UNIVERSITÄT PADERBORN
Die Universität der Informationsgesellschaft

ILH
INSTITUT FÜR
LEICHTBAU MIT
HYBRIDSYSTEMEN

Coating Materials
& Polymers

Organized Colloids

Self-Assembly of Spherical and Lamellar Colloids

Dissertation zur Erlangung des akademischen Grades
Doctor rerum naturalium

vorgelegt der Fakultät für Naturwissenschaften
der Universität Paderborn

von Arthur Oswald

Paderborn, 23. Mai 2022

Erstgutachter:	Prof. Dr. Wolfgang Bremser
Zweitgutachter:	Prof. Dr. Dr. h.c. Markus Antonietti

„You boil it in sawdust : you salt it in
glue :
You condense it with locusts and tape :
Still keeping one principal object in
view—
To preserve its symmetrical shape.“

Rev. Charles Lutwidge Dodgson
alias Lewis Carroll

From the poem

„The Hunting of the Snark“ (1876)

Acknowledgements - Danksagungen

Als Erstes möchte ich mich herzlich bei Herrn *Prof. Dr. Wolfgang Bremser* bedanken, der mir alle Freiheiten für das Anfertigen dieser Arbeit ermöglicht hat und mich darüber hinaus gefördert hat, unter anderem durch das Ermöglichen der Teilnahme an zahlreichen Konferenzen, zwei wundervollen Forschungsaufenthalten an der Fudan-Universität in Shanghai und die Chance verschiedene Projekte im Bereich der Technischen Chemie zu leiten.

衷心感谢武利民教授及其工作团队热情、友好的帮助，那些美味的节日大餐以及热烈有趣的学术讨论，令人难忘。**同**时感谢唐铭汇对此恰当的翻译。

Auch möchte ich mich herzlich bei Prof. *Dr. Hans-Joachim Warnecke* bedanken für sein immer offenes Ohr und die Vermittlung der Master- und der anschließenden Doktorarbeit im Arbeitskreis „Coatings, Materials & Polymers“.

Ein besonderer Dank gilt in diesem Zusammenhang dem gesamten *Arbeitskreis CMP* für das Arbeitsklima und im Speziellen:

Gilla und Maria, meine Labormuttis, die mir besonders in der Anfangsphase immer mit Rat und Tat in präparativen und persönlichen Belangen zur Seite standen.

Manuel und Nadine, meine Lieblings-Tech-Freaks, die mich in technischen Belangen über die gesamte Zeit kompetent unterstützt haben.

Dr. Daniel Briesenick, der meine vorangegange Masterarbeit angeleitet hat und dessen Geradlinigkeit eine Inspiration für meine Arbeiten war und immernoch ist.

Dr. Andreas Wolk alias Ulf, der mich (im positiven Sinne) regelmäßig auf die Palme gebracht hat bei den zahlreichen fachlichen Diskussionen mit vielen Barrel Kaffee und Hunderten von Zigaretten.

Dr. Horst Hintze-Brüning, der mit seinen scharfsinnigen Fragen und Anregungen bei jedem Aufeinandertreffen dabei geholfen hat meinen Horizont zu erweitern.

Den Bachelor- und Masterstudenten *Alexander Mai*, *Sarah Krüger*, *Johann Malsam* & *Aaron Neugebauer* und den studentischen Hilfskräften *Nicole Dickmann*, *Viktor Olenberg* und *Kevin Heetfeld* für die fruchtbare Zusammenarbeit und die außerordentliche Hilfsbereitschaft.

Dank gilt auch allen anderen Kollegen, die leider nicht auf diese Seite passen: *Dr. Anna Becker-Staines*, *Dr. Arne Rüdiger*, *Anne Büngeler*, *Deniz Dogan*, *Minghui Tang*, *Simon Ruthmann, Kai Zhao, Dr. Chen Zhao, David Wedegärtner, Daniel Appel, Tobias Buchholz, Stephan Berg, Fredrik Strothmann, Lea Senneka, Dominik Hense,…* und natürlich *Michaela Schuster*, *Martina Müller*, *Martin Samusch*, *Carlos Westermann, Dr. Oliver Strube* & *Dr. Oliver Seewald.*

Natürlich danke ich auch meinen zahlreichen Kommilitonen außerhalb des Arbeitskreises, im Speziellen *Heinrich Rempel*, *Dr. Stefan Waschke*, *Dr. Jens Timmermann* und *Dr. Baris Kaynak* für die schönen Stunden beim gemeinsamen Lernen und den Laporpraktika.

Der größte Dank gilt meiner Familie und meinen Freunden, die mich und meine übermäßige Begeisterung für die Thematik über die gesamte Zeit ertragen haben und (fast) immer gut darin waren mir das Gefühl zu geben, dass sie verstehen was ich vor mich hin fasele. ;-)

Declaration of Authorship / Eigenständigkeitserklärung

Hiermit erkläre ich, dass ich die vorliegende Arbeit mit dem Titel

Organized Colloids
Self-Assembly of Spherical and Lamellar Colloids

selbstständig und ohne unerlaubte fremde Hilfe angefertigt, keine anderen als die angegebenen Quellen und Hilfsmittel verwendet und die den verwendeten Quellen und Hilfsmitteln wörtlich oder inhaltlich entnommenen Stellen als solche kenntlich gemacht habe.

_____

Ort, Datum

_____

Unterschrift

Disclaimer: This is the updated digital version of the original that was printed earlier on the 17^{th} of January 2022. (Most of) the typos, incomplete sentences, and some format issues were corrected. Also, a few passages that may lead to confusion for the reader were clarified. A single dataset in Figure 138 was found to be incorrect and was also edited.

Abstract

Colloids with *Plate and Sphere symmetry* having different respective diameters are systematically prepared based on different synthesis compositions and partly different synthesis conditions in order to examine the self-assembly and ultimately the self-organization of the colloids in composite materials containing clays (plates), and organic polymers (spheres or coils) in water.

The ultimate goal of the thesis was to identify suitable preparation techniques, mixtures and geometrical proportions of the colloids with the ability to self-organize into polymer/clay composites with a brick-and-mortar morphology, so that the platelets are desired to be oriented parallel towards the coated surface. The central technique used in the thesis is the drying of aqueous colloidal dispersion droplets on a silicon wafer and the evaluation and characterization of the dried residue in close context with the properties of the colloids in the wet state. The examined mixtures of oppositely-charged plate and sphere colloids in the dispersions are regarded as already self-assembled by electrostatic forces. The term self-assembly implies equilibrium states, whereas self-organization implies non-equilibrium states, mainly occuring during drying and leading to organized colloid structures. The competing forces are essentially the electrostatic and the capillary force whereas also the occurrence of aging, mostly by ongoing and undesired chemical reactions take place.

Basic principles were examined with rigid spheres and rigid plates in water at room temperature, leading to the anticipated morphology which was obtained by two different pathways; by utilizing the electrostatic interaction @, namely the targeted use of ions, and also by utilizing the capillary interaction π and the targeted use of the diameter and thickness ratios of the involved colloids. Both approaches follow driving forces attributed to the compensation of the edge charge of the plate-shaped colloids.

Kurzfassung

Kolloide mit *Platten- und Kugelsymmetrie* mit jeweils verschiedenen Durchmessern wurden systematisch durch verschiedene Synthese-Zusammensetzungen und teilweise verschiedene Synthese-Bedingungen hergestellt um die Selbst-Assemblierung und die Selbst-Organisation der Kolloide in Kompositmaterialien bestehend aus Tonmineralien (Platten) und organischen Polymeren (Kugeln oder Knäuel) in Wasser zu untersuchen.

Das Ziel der Arbeit war es geeignete Präparationstechniken, Mischungen und geometrische Proportionen von Kolloiden zu identifizieren mit der Eigenschaft selbstorganisierte Komposite auszubilden, die möglichst parallel zur beschichteten Oberfläche ausgerichtete Platten enthalten, ergo eine Ziegel-Mörtel Morphologie aufweisen. Die zentrale Methode dieser Arbeit ist das Trocknen von Tropfen von wässrigen kolloidalen Dispersionen auf glatten Oberflächen (v.a. Silizium-Wafer) und die Evaluierung und Charakterisierung des getrockneten Rückstandes in engem Kontext mit den gemessenen Eigenschaften der Kolloide im nassen Zustand, also in Dispersion. Die untersuchten Mischungen von kolloidalen Platten und Kugeln mit entgegengesetzten Ladungen können im Nass-Zustand durch die Präsenz elektrostatischer Kräfte bereits als selbst-assembliert angesehen werden. Der Begriff Selbst-Assemblierung impliziert Gleichgewichtszustände, wohingegen die Selbst-Organisation Nicht-Gleichgewichtszustände impliziert, also hauptsächlich während des Trocknens eintritt und zu den antizipierten organisierten Kolloid-Strukturen führt. Die konkurrierenden Kräfte sind im Wesentlichen die Elektrostatik und die Kapillarkraft, wobei auch das Auftreten von Alterung, meist durch laufende und/oder unerwünschte chemische Reaktionen, stattfinden kann.

Die Grundprinzipien wurden mit rigiden Kugeln und rigiden Platten in Wasser bei Raumtemperatur untersucht und die gewünschte Ziegel-Mörtel-Struktur wurde darausfolgend mittels zweier Pfade erreicht; Nutzung der elektrostatischen Wechselwirkung @ durch Einsatz von Ionen und durch Nutzung der kapillaren Wechselwirkung π durch das gezielte Nutzen von Durchmesser- und Dickenverhältnissen der involvierten Kolloide. Beide Methoden zur Erreichung der gewünschten Struktur haben die Ladungskompensation an den Kanten der plattenförmigen Kolloide als Triebkraft inne.

Contents

I Introduction 1

1 Prologue 2

2 Aim of Work 3

3 Status Quo and Emphasis of the Thesis 4

II Theoretical Background 5

1 Colloids, Interfaces and Interphases 5

1.1 The Nano-Effect and Colloidal Dispersions 6

1.2 Charges at Interfaces 7

1.3 Interfaces and Interphases 10

2 Lamellar Colloids & Clays 12

2.1 Organization and Rheology of Clays 14

2.2 Layered Double Hydroxides 16

2.3 The Janus character of kaolinite 17

3 Colloidal Assembly 19

3.1 Electrostatic Assembly @ 20

3.2 Capillary Assembly π 21

3.3 Composite Materials and chemical interaction μ 24

4 Replicative Building Units 26

5 Analytic Methods 31

III Preparation & Synthesis of Colloids 33

1 Layered Double Hydroxides 34

1.1 Experimental Part 35

1.1.1 Synthesis of 400 nm sized Zn_2Al-BSA 36

1.1.2 Synthesis of 800 nm sized Zn_2Al-BSA 36

1.1.3 Synthesis of 3200 nm sized Zn_2Al-BSA 36

1.1.4 Synthesis of 1 µm sized Zn_2Al-NO_3 36

1.1.5 Kinetic Measurements 36

1.1.6 Examination of LDH stability 36

1.1.7 Reactive Intercalation with Trimethylethoxysilane 36

1.1.8 Ionic Exchange Reactions 37

1.2 Results and Discussion 38
1.2.1 LDH synthesis and kinetics 38
1.2.2 Control over LDH particle size 39
1.2.3 Examinations on the LDH stability 41
1.2.4 LDH Ionic Exchange 42
1.2.5 Liquid Exfoliation of LDH 45
2 Kaolinite 46
2.1 Sedimentation 46
2.2 Centrifugation 47
2.3 Ion Intercalation into kaolinite 48
3 Monodisperse and Spherical PS colloids 50
4 Polydisperse and coil-like PUR Colloids 52
4.1 Monomodal PUR Dispersions 53
4.2 Multimodal PUR Dispersions 55

IV Organized Colloids 56

1 Polystyrene @ Kaolinite Assemblies 57
1.1 Experimental Details 58
1.1.1 Manual Isoelectric Titration of pristine colloids 59
1.1.2 Auto-Titration of Organized Colloids 59
1.1.3 SEM observations of Basic Building Unit (3D @ 2D) 60
1.1.4 Preparation of Hollow Spheres on Kaolinite 60
1.1.5 Preparation Of Organized Kaolinite Colloids 61
1.1.6 Preparation of Composite Films 63
1.1.7 Contact Angle measurements on Composite Films 63
1.2 Results & Discussion 64
1.2.1 PS @ kaolinite deposition 64
1.2.2 SiO_2 coating of PS @ kaolinite assemblies 70
1.2.3 Surface Modification of PS_{95} @ K assemblies 73

2 Polystyrene @ Janus-Kaolinite Assemblies 76
2.1 Experimental Details 77
2.1.1 Silylation of Kaolinite 78
2.1.2 Janus deposition experiments 80

2.1.3 ζ-Potential measurements 80
2.1.4 Synthesis of PDMS @ Janus Kaolinite 80
2.1.5 Particle Adsorption on Carbon Fibres 80
2.1.6 Pull-Out tests 80
2.2 Results & Discussion 81
2.2.1 Analysis of Silane μ Kaolinite 82
2.2.2 Janus Deposition Experiments 85
2.2.3 Fiber Coatings consisting of PDMS μ Kaolinite 91

3 SiO_2 @ LDH – Stacked Assemblies 94
3.1 Experimental Details 95
3.1.1 Ultrafiltration 96
3.1.2 Separate Dispersion Method 96
3.1.3 Isoelectric Titration of pristine colloids 98
3.1.4 Isoelectric Titration of Organized Colloids 98
3.1.5 SiO_2 @ LDH deposition 99
3.1.6 Stacked SiO_2@LDH assemblies with ultrafiltration 100
3.1.7 Stacked Structures on LDH Monolayer 100
3.1.8 LDH edge-functionalization with Zr(IV) cations 101
3.1.9 SEM and FIB imaging of Stacked Structures 101
3.1.10 Mastersizer Measurements 101
3.2 Results & Discussion 102
3.2.1 Assemblies with exfoliated sheets 103
3.2.2 SiO_2 @ LDH assemblies 106
3.2.3 Stacked SiO_2 @ LDH assemblies 109

4 PUR / Clay Composites - Exfoliation & Intercalation 118
4.1 Experimental Details 119
4.1.1 LDH / polymer nanocomposites 119
4.1.2 LDH / PUR nanocomposites 120
4.1.3 Rheological Measurements 121
4.1.4 Kaolinite / Polymer Composites 122
4.2 Results & Discussion 123
4.2.1 PUR / Kaolinite Composites 124
4.2.2 Polymer / LDH Composites - Pretests 125
4.2.3 PUR / LDH Composites – Field Study 127

4.2.4 PUR / LDH Composites - Order and Disorder 130
4.2.5 PUR / LDH Composites - Structural Viscosity 141
4.2.6 PUR / LDH Composites - Dissipative Properties 147
4.2.7 PUR / LDH Composites - Scaling Law Analysis 148

5 Nacre-mimetics from protein/salt composites 152
5.1 Experimental Details 154
5.1.1 Preparation of Casein Dispersion 154
5.1.2 Preparation of Enzyme Dispersions 154
5.1.3 Biomineralization Experiments 155
5.1.4 Compositions of biomineralization experiments 156
5.2 Results & Discussion 157
5.2.1 Experiments in the absence of LDH colloids 162
5.2.2 Structural Features of Nacre and Formation Mechanism 167
5.2.3 Thoughts on applications of synthetic nacre 174

V Epilog 177
1 Summary 177
2 Conclusion 179
3 Outlook 179

VI References 180

VII Appendix 195

1 All Methods 195

2 Colloids 197
2.1 LDH synthesis 197
2.2 Kaolinite 201
2.3 Polystyrene Colloids 202
2.4 Polyurethane Colloids 204

3 PS @ kaolinite assemblies 206
3.1 Lateral Deposition Density Λ and Surface Affinity 206
3.2 Edge affinity of spherical colloids towards lamellar colloids 210

3.3 Janus deposition pattern of organized kaolinite 211
3.4 Autotitration curves 215
3.5 Dissipative CFRP 216

4 SiO_2 @ LDH assemblies 217
4.1 Ultrafiltration of lamellar colloids 217
4.2 Pommegranate Assemblies 218
4.3 Zirconium-based colloids 219
4.4 Aged morphologies of SiO_2@LDH assemblies 220

5 PUR/LDH composites 222
5.1 FIB cross-section of PUR/LDH clod 222
5.2 Polymer colloids above T_g on plate colloids 223
5.3 Influence of glycine on composite morphology 224
5.4 Aged PUR/LDH composites – rheological data 225

6 Casein / Chymosin / KCl composites 230
6.1 EDX results 230
6.2 Reference sample after 24 hours cleavage time 232
6.3 Reference sample with half the enzyme concentration 233

List Of Figures

Figure 1: True-to-scale illustration of lamellar and spherical colloids 1
Figure 2: Geometric representations of the used colloids and its interface shape 2
Figure 3: Examination procedure of the black box containing colloidal self-organization..... 2
Figure 4: Cross-sectional illustration of the desired coating morphology..... 3
Figure 5: Pathways to achieve a sequenced or functional Sphere @ Plate Assembly..... 3
Figure 6: Area / Volume ratio of a sphere vs diameter 6
Figure 7: The three classical electric double layer models 7
Figure 8: DLVO-based Interaction Force vs. distance for different ionic strengths. 8
Figure 9: Single-sphere deposition on a lamellar colloid by electrostatic forces 9
Figure 10: Distinction between the terms Colloid, Interface and Interphase..... 10
Figure 11: 3D polyhedron structures of lamellar colloids. 12
Figure 12: Growth of the interface of lamellar colloids 13
Figure 13: Area of the edges per volume of a single lamellar colloid vs. lateral diameter.... 14
Figure 14: Classical border cases of lamellar particle organization of LDH colloids 15
Figure 15: Most used rheometers types, in blue the examined substance..... 15
Figure 16: LDH formation in polyhedral depiction 16
Figure 17: Side-view on the ideal crystal structure of kaolinite 17
Figure 18: Scheme of 4D self-assembly 19
Figure 19: Ionic colloidal crystals 20
Figure 20: Colloidal crystals from nanoscale colloids showing hcp and ccp structures 21
Figure 21: Mechanism of Colloidal Crystal formation 22
Figure 22: Film-forming of the used PS and PUR dispersions..... 23
Figure 23: Composites with lamellar colloid structures 24
Figure 24: Nanoscale arrangement of lamellar colloids 25
Figure 25: Similar ordered structures 26
Figure 26: Cyclic vortices of proteins and water of *Patiria miniata* starfish 27
Figure 27: Enzymatically linked reactions and colloidal behavior of enzymes..... 28
Figure 28: Self-organization by the aid of gravity: temperature and pressure gradients 29
Figure 29: Information density for the case of statistically independent monomeric units .. 30
Figure 30: Scheme of LDH synthesis setup..... 34
Figure 31: LDH kinetics: electrical conductivity vs. time 39
Figure 32: Change in LDH morphology vs. addition time 39
Figure 33: pH vs *t* plot, SEM and DLS results of the different sized LDH-BSA colloids 40
Figure 34: Two morphologies obtained from the glycine-buffer synthesis route..... 40
Figure 35: XRD spectra after anionic exchange of LDH-NO_3 43
Figure 36: XRD spectra after anionic exchange of LDH-BSA..... 44
Figure 37: FIB cross section of (TMS μ LDH) colloids in a commercial PUR matrix..... 45
Figure 38: DLS measurements of raw kaolinite products..... 46
Figure 39: DLS measurements of Kaolin "SK-T 35"..... 47
Figure 40: DLS measurements of "SKT-13P" 48
Figure 41: XRD spectra of kaolinite and modified kaolinite 49
Figure 42: Size-Control of cationic PS colloids..... 50
Figure 43: DSC measurements on 95 nm PS colloids 51
Figure 44: DSC measurements and 1st derivates of monomodal 90 nm PUR colloids 52

Figure 45: SLS data of some drawn PS and PUR dispersions 52
Figure 46: Scheme of PUR particle synthesis 53
Figure 47: IR peak integrals of NCO-peaks of the PUR prepolymer 53
Figure 48: Size-control of the PUR colloids 54
Figure 49: Illustration of a sphere @ lamellar deposition 57
Figure 50: Illustration of the PS @ kaolinite assembly with increasing PS diameters 64
Figure 51: PS_{65} and PS_{95} colloids on K_{face} 65
Figure 52: PS^*_{105} @ K_{face} 65
Figure 53: PS^*_{135} @ K_{face} 66
Figure 54: Isoelectric Titration of Kaolinite and PS-dispersions 66
Figure 55: Apparent ζ-potential distributions of a PS_{95} @ K titration. 67
Figure 56: SEM images of PS_{145} / K and PS_{147} / K 68
Figure 57: SEM image*s* of PS_{145} π K_{edge} sample at lower magnifications 69
Figure 58: SEM images of PS^*_{135} @ K at different weight ratios 69
Figure 59: SiO_2 μ (PS_{95} @ K) assemblies based on different TEOS concentrations 70
Figure 60: SEM images of SiO_2-coated PS^*_{135} / K *after* PS combustion 71
Figure 61: SEM images of SiO_2-coated PS_{147} @ kaolinite *after* PS combustion 71
Figure 62: SEM images of SiO_2 μ PS_{95} @ K_{face} deposition patterns *after* PS combustion 72
Figure 63: SEM image of SiO_2-coated PS_{95} on kaolinite *before* PS combustion 72
Figure 64: Transformations of surface modified PS_{95} @ K_{face} assemblies 73
Figure 65: SEM images of the surface modified PS_{95}@K_{face} assemblies 74
Figure 66: TGA measurements and DTG of organized and functionalized kaolinite 75
Figure 67: Surface energies of polymer/organized kaolinite composite films 75
Figure 68: Representational Scheme of the Patchy Janus Kaolinite Coverage 76
Figure 69: Transformations of PS @ kaolinite Janus colloids 81
Figure 70: EDX and TGA results of amino-modified kaolinite in atom and weight percent 82
Figure 71: IRRAS measurement of modified (A10C2) and unmodified kaolinite 83
Figure 72: ^{27}Al-NMR spectrum of modified and unmodified kaolinite 83
Figure 73: ζ-Potential vs. centrifugation steps of kaolinite silylations. 84
Figure 74: Apparent ζ-potential of amino-modified kaolinite colloids. 84
Figure 75: PS_{65} @ kaolinite (left) and PS_{65} @ NH_2-kaolinite 85
Figure 76: Electrostatic Deposition of PDPE spheres on unodified and modified kaolinite . 85
Figure 77: Time evolution of Janus deposition patterns for PS@kaolinite 86
Figure 78: Deposition patterns of 600 nm modified kaolinite 88
Figure 79: Deposition patterns of 3400 nm modified kaolinite 89
Figure 80: Deposition patterns of 3400 nm modified kaolinite 90
Figure 81: Kaolinite silylation experiments with butoxyethanol as a solvent 91
Figure 82: SEM image of PDMS μ K 92
Figure 83: TGA traces of amino and PDMS modified kaolinite colloids 92
Figure 84: Carbon fiber coating comprising PDMS μ K 93
Figure 85: Interfacial Shear Strength estimation 93
Figure 86: Postulated stacking mechanisms 94
Figure 87: Photograph of the Ultrafiltration Unit 96
Figure 88: Illustration of Charge Switching Experiments 97
Figure 89: Transformations of organized [Sphere @ LDH] colloids 102

Figure 90: PS @ NaMMT titration 103
Figure 91: Chitin @ MMT titration 103
Figure 92: Diameter of SiO_2 @ LDH pommegranate structures 104
Figure 93: Film surface and cross-section of SiO_2@LDH assemblies in PVA matrix 105
Figure 94: Illustration of an electrostatic single sphere deposition 106
Figure 95: ζ-potential difference as a function of pH 107
Figure 96: A SEM image comparison of autotitration and separate dispersions method .. 108
Figure 97: SiO_2 @ LDH assemblies with different ratios 109
Figure 98: Isoelectric autotitration and postulated $(SiO_2@LDH)_n$ assembly mechanism ... 110
Figure 99: Isoelectric titration curves of freshly stacked structures 111
Figure 100: Assembly regime expressed as point of zero charge vs. SiO_2 mass content. ... 111
Figure 101: Overview of stacked assemblies with different weight ratios 112
Figure 102: FIB cross-section of stacked SiO_2 @ LDH assemblies in PVA 112
Figure 103: Pretreated Substrate for Stacking examinations 113
Figure 104: FIB-Cross Sections of Stacked SiO_2 @ LDH assemblies on a LDH monolayer 113
Figure 105: Apparently stacked and parallel oriented assemblies of LDH and SiO_2 114
Figure 106: Morphology of Zr-based colloids after stirring $Zr(SO_4)_2$ solution for 1 week.. 114
Figure 107: Monitoring of parameters during stacking coagulation 115
Figure 108: Time-resolved DLS measurement on stacked SiO_2@LDH assemblies 116
Figure 109: SiO_2@LDH assemblies treated with Zr-based dispersions in a PVA matrix ... 117
Figure 110: Primary, secondary, tertiary and quaternary structure. 118
Figure 111: Chosen program to examine thixotropic properties of LDH/PUR composites 122
Figure 112: SEM/FIB and DLS analysis of two polymer/clay nanocomposites 123
Figure 113: Different kind of stacked assemblies at similar magnifications 124
Figure 114: FIB-cross section of CTAB-kaolinite in a PUR matrix 125
Figure 115: Intercalation and Exfoliation of Layered Double Hydroxides 126
Figure 116: Cross-Section of exemplary PUR/LDH composite film 130
Figure 117: Cross-Sections of six samples with 4.5 vol.-% LDH in composite films 130
Figure 118: Size Distributions from FIB/SEM images 131
Figure 119: XRD patterns of 4 composite films 132
Figure 120: FIB/SEM images of the sample $PUR_{10}LDH_{400}$ 133
Figure 121: FIB/SEM images of the sample $PUR_{10}LDH_{800}$ 134
Figure 122: FIB/SEM images of the composite samples comprising LDH_{3200} 135
Figure 123: FIB/SEM images of the sample $PUR_{75}LDH_{400}$ 137
Figure 124: FIB/SEM images of the sample $PUR_{75}LDH_{800}$ 138
Figure 125: FIB/SEM images of the sample $PUR_{115}LDH_{400}$ 139
Figure 126: FIB/SEM images of the sample $PUR_{115}LDH_{800}$ 140
Figure 127: FIB/SEM images of the sample $PUR_{75}LDH_{800}$ 140
Figure 128: Shear program and output data 141
Figure 129: Flow curves of all 15 wt.-% PUR/LDH composites. 141
Figure 130: Structural viscosities H vs LDH volume concentration 142
Figure 131: Rheological data of the bare PUR dispersions 144
Figure 132: All 45 τ vs t plots of the last two ramps. 144
Figure 133: All 45 η vs t plots 145
Figure 134: All 45 τ vs γ plots 145

Figure 135: η vs γ plots 146
Figure 136: DMA measurement of all PUR/LDH composites 147
Figure 137: GPC data of the chosen PUR colloids. 148
Figure 138: D vs t plots. 149
Figure 139: Comparison of drying droplet and rheometer experiments 150
Figure 140: Anticipated coating and organization of LDH colloids with casein 152
Figure 141: Rrecently postulated mollusk shell formation mechanism 153
Figure 142: Scheme of examinations on the system Chy/LDH/Cas 157
Figure 143: Isolectric titration and SEM morphologies of Chy@LDH_{face} assemblies 158
Figure 144: SEM morphology from the (Chy@LDH) μ casein system 159
Figure 145: SEM images of casein μ LDH colloids 159
Figure 146: SEM images of the reference sample: KCl & chymosin 160
Figure 147: SEM images of composite crystals based on KBSA crystals 161
Figure 148: pH-dependent chymosin activity and ζ-potential 162
Figure 149: Ideal cleavage reaction of casein micelles 162
Figure 150: Time-dependent MALDI-ToF-MS results 163
Figure 151: Summary of AFM, MALDI and SEM results 164
Figure 152: SEM images of KCl/protein composites without MALDI matrix 165
Figure 153: SEM images of salt/protein composites with chymosin from Mucor Miehei 166
Figure 154: Terraced nacre vs towered nacre 167
Figure 155: Structures of natural *versus* mimicked nacre on different hierarchical levels 167
Figure 156: Time-dependent tablet-thicknesses: 0 *versus* 60 minutes cleavage time 168
Figure 157: Schematic representation of the postulated border cases of CMP gelation 169
Figure 158: Postulated mechanism of nacreous growth 171
Figure 159: SEM images showing *Platelets from Rods* 171
Figure 160: SEM images showing the structural feature *asperities & Mineral Bridges* 172
Figure 161: Simulation, AFM and DLS data on the *occlusion mechanism* 172
Figure 162: SEM images after 30 minutes cleavage time with bovine calf rennet 173
Figure 163: SEM images showing the structural feature of *not occluded protein micelles* 173
Figure 164: Synthetic nacre by biomineralization in a negative form 174
Figure 165: Digital microscope image of dried salt/protein composite on a silicon wafer 175
Figure 166: Symbiotic Ship Coating 176
Figure 167: Comprehensive overview of conducted transformations to organized colloids 177
Figure 168: Illustration of anticipated vs obtained cross-sectional coating morphology 179
Figure A-169: pH vs time curve of LDH synthesis in parallel reactor (2^{nd}) 197
Figure A-170: pH vs time data of LDH synthesis of 3^{rd} approach 198
Figure A-171: Evaluation of the synthesized LDH colloids 198
Figure A-172: pH-time data of the 2nd and 4th approach in comparison 199
Figure A-173: LabView Block Diagram of pH-stat regulation 199
Figure A-174: Net conductivities of LDH synthesis involved solutions 200
Figure A-175: Morphology of 5 µm LDH phase 200
Figure A-176: Book-Like Colloid of Kaolinite 201
Figure A-177: SEM image of a FIB-cut through a PUR/kaolinite composite 202
Figure A-178: All PVP containing PS-dispersions 203
Figure A-179: Glass transition temperature determination of PS via Proteus Software 203

Figure A-180: Glass transition temperature determination of PUR via Proteus Software 205
Figure A-181: Lateral Deposition Density 206
Figure A-182: Full deposition of PS spheres @ kaolinite 206
Figure A-183: TGA traces of kaolinite, PS @ kaolinite and hollow SiO_2 μ K 207
Figure A-184: PS (+) Colloidal Crystals at kaolinite crystal edges (+)..... 208
Figure A-185: 105 nm PS spheres on kaolinite after temperature treatment at 120 °C.... 208
Figure A-186: LDH/PUR composite dispersion after centrifugation..... 209
Figure A-187: Electrostatic Deposition of SiO_2 spheres (-) at kaolinite edges (+) 210
Figure A-188: PS65 @ LDH_{800}..... 210
Figure A-189: 1000-fold TEOS before calcination..... 211
Figure A-190: 19-fold TEOS before calcination 211
Figure A-191: 1000-fold excess on PS without PVP on kaolinite..... 212
Figure A-192: 4-fold TEOS after calcination 212
Figure A-193: Lamellar Particles SiO_2 from kaolinite edges 213
Figure A-194: PDPE @ kaolinite (reference) 214
Figure A-195: Zeta-Potential vs. PS content in 3D @ 2D assembly 215
Figure A-196: Isoelectric Titration of Sphere (+) @ kaolinite (-) deposition..... 215
Figure A-197: Isoelectric Titration of Sphere (-) @ LDH (+) deposition 216
Figure A-198: Results of three-point flexural test on PDMS-coated CF in CFRPs..... 216
Figure A-199: Conductivity vs. time during ultrafiltration..... 217
Figure A-200: Size determination of pomegranate structures of LDH-DS from LDH-NO_3 218
Figure A-201: Pomegranate structures with LDH-DS from LDH-BSA 218
Figure A-202: Morphology of colloids after stirring a $Zr(SO_4)_2$ solution for 1 week. 219
Figure A-203: Morphologies after 7 days of stirring 220
Figure A-204: Morphologies of the flotating fractions after 3 months of stirring 221
Figure A-205: FIB cut through a clod from pretests. 222
Figure A-206: LDH-ABSA in a commercial polyester resin containing co-solvent 222
Figure A-207: Comparison between PUR and PS above T_g 223
Figure A-208: FIB/SEM images of $PUR_{10}LDH_{800}$ composites..... 224
Figure A-209: 1 day aging 10 wt.-\% LDH in $PUR_{75}LDH_{1600}$..... 225
Figure A-210: 9 days aging of 10 wt.-% $PUR_{75}LDH_{800}$ and 5,10,15 wt.-% $PUR_{115}LDH_{3200}$226
Figure A-211: 18 days aging of 25 wt.-% $PUR_{10}LDH_{400}$ and 10, 15 % $PUR_{75}LDH_{400}$..... 227
Figure A-212: 36 days aging of all $PUR_{115}LDH_{400}$ 228
Figure A-213: 36 days aging of 5, 10, 15, 20 wt.-% $PUR_{115}LDH_{800}$ 229
Figure A-214: EDX results on Casein / Chymosin / LDH / KCl composites 230
Figure A-215: EDX results on Casein / Chymosin / LDH / KBSA composites..... 231
Figure A-216: Morphology of KCl/protein composites after cleavage time of 24 hours.... 232
Figure A-217: Identifying soft matter by electron beam 233
Figure A-218: Images and sketch of fibrous-ordered casein micelles 233

List of Tables

Table 1: Materials for LDH synthesis 35
Table 2: EDX results on the three LDH phases 41
Table 3: Examination of LDH stabilization after synthesis 41
Table 4: Most important properties of used zwitterions 42
Table 5: Compositions and resulting sizes of synthesized PUR colloids 54
Table 6: Materials for Sphere @ Lamellar Assembly 58
Table 7: Weighed portions of SiO_2 @ PS Core-Shell Colloids 61
Table 8: Weighed Portions of Films with Organized Kaolinite Colloids 63
Table 9: TGA mass losses of modified assemblies at 250 °C & 1000 °C 75
Table 10: Materials for Patchy Janus Kaolinite Coverage 77
Table 11: Weighed portions for silylations in 100 wt.-% ethanol 78
Table 12: Weighed portions for silylations in 80 wt.-% ethanol 79
Table 13: Silylation experiments in butoxyethanol as a solvent 79
Table 14: Molar silane excess per hydroxyl groups on kaolinite 82
Table 15: Results of IRRAS deconvolution, relative peak areas 83
Table 16: Materials for Stacking 95
Table 17: Separate dispersion method with equal mass concentrations 96
Table 18: Weighed Portions for separate dispersion method at equal volume 97
Table 19: Weighed portions of organized LDH/PVA composites 101
Table 20: Comparison of sizes and charges of the examined model systems 106
Table 21: Tabulated shear program 122
Table 22: Summary of the PUR / LDH field study results 128
Table 23: Flow index n from Ostwald-de-Waele fits 146
Table 24: Hierarchical levels 151
Table 25: Materials for Biomineralization experiments 154
Table 26: Overview of biomineralization experiments 156
Table 27: Solubilities/dispersibilities of reagents 169
Table A-28: Weighed portions of PS colloids 202
Table A-29: Weighed portions for PUR synthesis with polyester diol Priplast 1900 204
Table A-30: Weighed portions for PUR synthesis with polyester diol P-2010 204

I Introduction

In times of numerous possibilities to explore microscopic, mesoscopic and nanoscopic worlds, the high precision of analytic instruments is becoming a center part of manufacturing future materials. The tailoring of materials underlies an appropriate knowledge and a robust analysis of the structure-property relationship. The sum of all local interactions of the involved particles, in the following denoted as 'colloids' are responsible for the global properties of the resulting materials. The measurements of colloid sizes and morphologies are understood well these days, while the approaches to systematically analyze and understand the dynamic self-assembly of colloids are just in the beginning. The starting materials for the self-assembly examined in this work are simply chosen by geometry:
lamellar and spherical geometry – or simply said: plates and spheres (**Figure 1**).

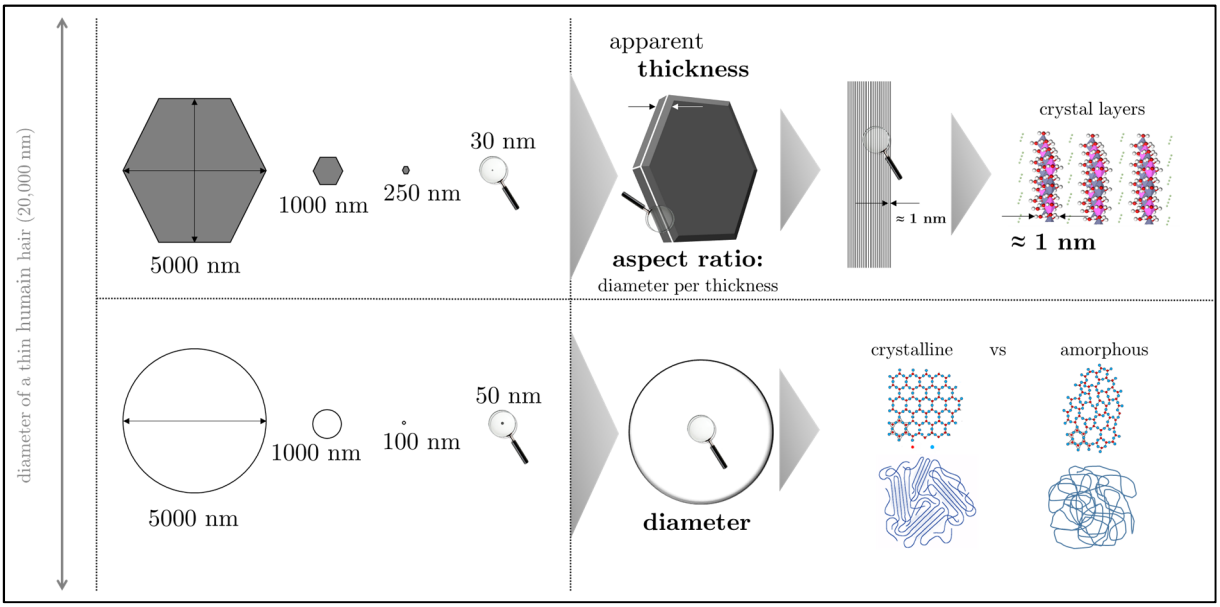


Figure 1: True-to-scale illustration of lamellar and spherical colloids

Besides the diameters and the shapes of the colloids, the electrical surface charges in water and the intrinsic properties of the respective colloids play a crucial role for designing applicable materials for a given purpose, such as a coating material. Especially the surface charges of the colloids play an important role, when it comes to directed, *static* self-assembly of lamellar and spherical colloids. A rigorous understanding of *dynamic* self-assembly processes, self-organization, of colloids will have an unprecedented impact on the future of materials science. The design of composite materials with well and homogeneously organized structures promise advanced property profiles and therefore pave the way for more efficient and multifunctional materials.
For example, readily assembled structures can have properties of metamaterials, which themselves have interesting applications with respect to the unique interactions with electromagnetic waves[1] and also allowing for a broader variety of constituents for the realization. In order to make use of the superior material properties of basic building units, essential self-assembly mechanisms of well-known model systems have to be studied. Herein, both kaolinite and layered double hydroxides are chosen as representatives of plate-shaped colloids, polystyrene and silica are chosen as representatives of spherical-shaped colloids and polyurethane as representative of coil-shaped colloids for the examination on organized colloids.

1 Prologue

The transformations of basic building units are from central interest for designing materials. **Chemical reactions** of small molecules can form colloids, such as polymerization reactions. The so obtained colloidal macromolecules in dispersions can undergo chemical transformations at the colloids' interface, so that in turn just a fraction of the initial monomer functionalities are accessible for further chemical reactions. The colloids can be transformed to desired basic building units with different sizes and functionalities, subsequently emerging into different properties, such as charge density.

The **physical interactions** of an ensemble of colloids are in general represented by attraction and repulsion, e.g. electric charges, surface tension, magnetic poles, gravity or entropy.

Mathematical representations of the small molecules, colloids and its interfaces are useful for characterizing the scaling and the geometrical shape of the basic building units. The formal mathematical transformations of basic geometric units by expansion and compactification are shown in **Figure 2**. In addition, the herein used basic building units are implemented.

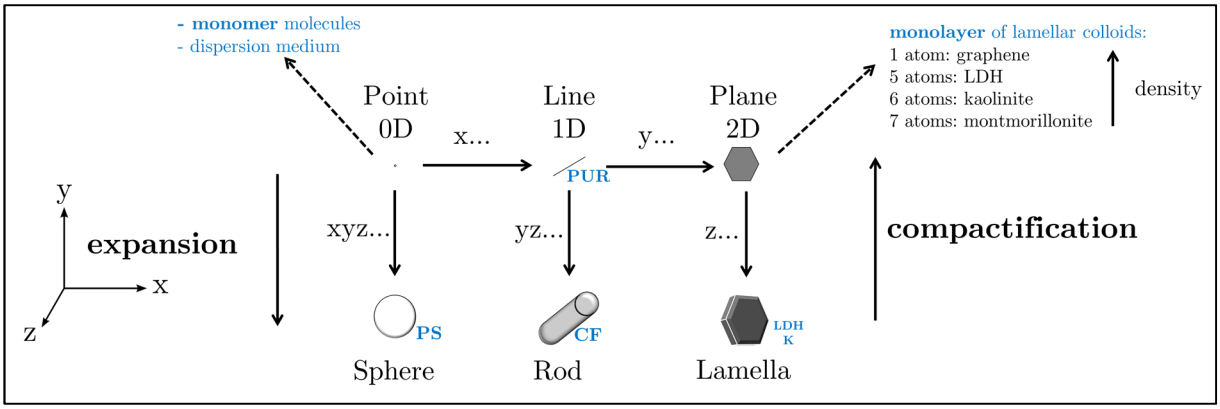


Figure 2: Geometric representations of the used colloids and its interface shape
The colloid types are depicted in blue font colour, with PUR: polyurethane, PS: polystyrene, CF: carbon fiber, LDH: layered double hydroxides and K: kaolinite

These considerations are useful to approximate examined systems to effective sizes. For example, a potassium ion K^+ (< 1 nm) can be considered as a 0D object compared to a 3D spherical polystyrene or silica colloid with a diameter of 100 nm. Obviously, the shown mathematical representations for a 1D line as a polymer chain or a 2D plane for a lamellar crystal layer is not perfectly rendering the reality. However, the consideration of the scaling and the geometry is helpful in order to describe colloids and interfaces so that the majority of this work is based on observations by scanning electron microscopy of dried colloidal dispersions – basically coating materials (**Figure 3**).

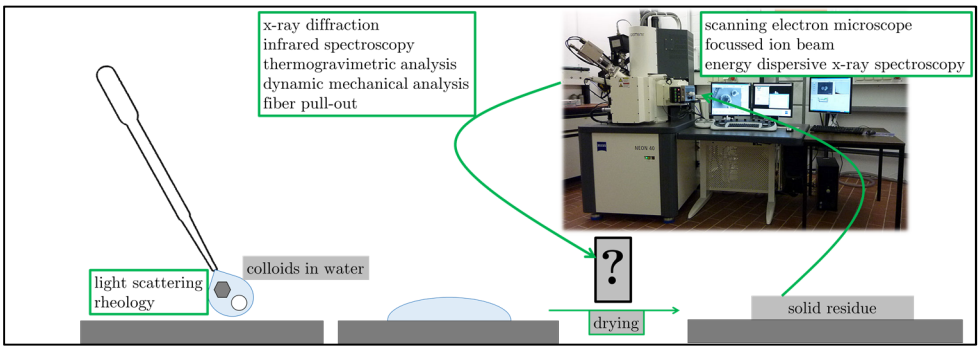


Figure 3: Examination procedure of the black box containing colloidal self-organization

2 Aim of Work

The main part of this work was to find a way to realize self-organized sphere & plate assemblies, preferably in a polymer/clay composite film with an alternating sequence of plates and spheres parallel to a flat surface, illustrated in **Figure 4**. The properties of such a coating material may have **i)** an improved mechanical and chemical barrier function, **ii)** functional rheology of the wet (and dry) coating material, **iii)** less need of material (lightweight & eco-friendly), **iv)** optical effects and may also allow **v)** implemented hollow spheres, which themselves allow further fine tuning of the coating materials' multifunctional properties.

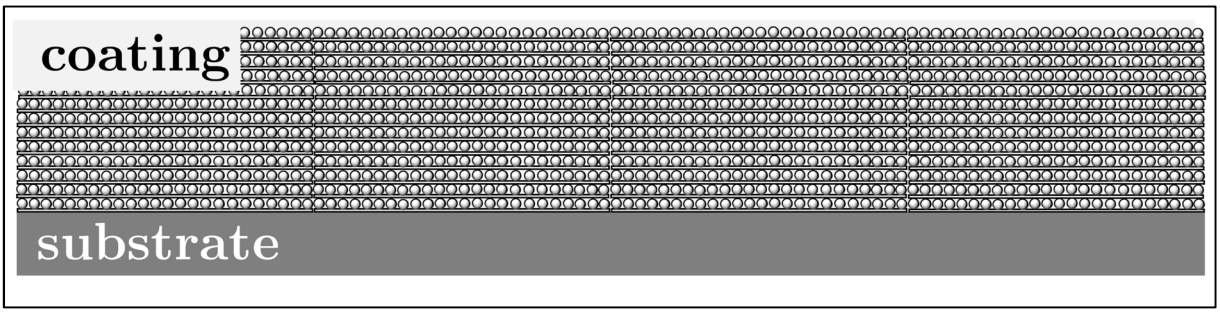


Figure 4: Cross-sectional illustration of the desired coating morphology

The examined pathways put into practice in order to reach the goal are shown in **Figure 5**. Obviously, Pathway ***A*** generates the highest interface between the individual colloids, a higher number of plate-sphere sequences and is therefore preferred with respect to a possible application as a coating material. A big interface between polymer and lamellar colloids is expected to overcome the mechanical properties of the pristine polymer by exfoliation or intercalation of the plates, as numerous publications already show.

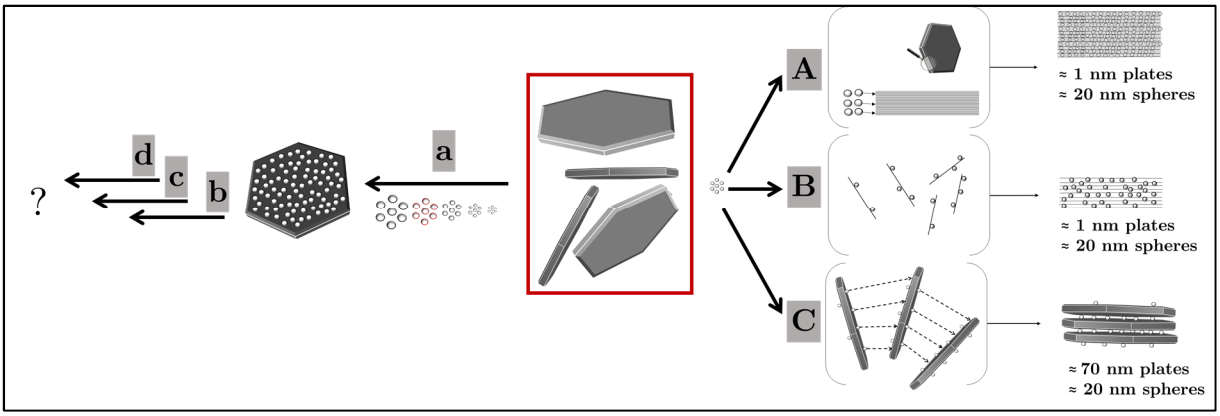


Figure 5: Pathways to achieve a sequenced or functional Sphere @ Plate Assembly

The organization to alternating sphere – plate assemblies is not limited to Pathway A, since it does not necessarily leads to the desired parallel orientation towards the substrate. In Pathway B and C, the selective hetero-coagulation of liquid exfoliated, 1-layer-thick (***B***) vs many-layer-thick lamellar colloids (***C***) with small spherical colloids lead to stacked assemblies and also do not necessarily leads to the desired parallel orientation. For a rather complete study, bigger spheres are examined first and the central question in the beginning of the thesis was how big a sphere is allowed to be in order to deposit on the face of a lamellar colloid (Pathway ***a***) and what further assembly or functionalization steps can be conducted from the obtained colloidal building units (***b, c, d***).

It should be noted, that the presented pathways are all favoured in aqueous systems, because of the high charge mobility of protons H^+ and hydroxide ions OH^- in water and allows for the exploitation of electrical fields in water. Further benefits of aqueous systems are lower toxic pollution by VOCs, lower cost and less waste. The main drawbacks of aqueous systems in coating materials are associated to the curing step and the final film-levelling. The use of water without addition of co-solvents usually leads to a inhibited curing of the coating material, usually leaving a rough surface. A covalent bonding between organic polymer and inorganic filler can further enhance the performance of nanocomposites,[2,3] which was not considered herein.

3 Status Quo and Emphasis of the Thesis

Composite materials from ceramic materials in organic polymer matrices enjoy broad research interest. An extensive review from the early 2000s shows a broad overview of polymer/layered silicate nanocomposites.[3] Clays, e.g. layered silicates in polymer matrices are reported there for a wide range of layered silicate loadings ranging from 0.1 to 100 wt.-%, whereas typical composites have clay loadings ranging from 1 to 10 wt.-%. The presence of polymer colloids tend to disturb the preferential parallel orientation of the clay platelets.
The preferred orientation of clay platelets in clay/polymer nanocomposites was examined in a systematic study for a variety of clays with different sizes and aspect ratios s with polyvinyl alcohol PVA.[4] It was found therein that high clay loadings tend to drive the clay colloids towards a more parallel alignment after drying of the respective composite dispersions, measured with x-rays of the solid phases with reported values for the order parameters S ranging from 0.80 to 0.95. For the lowest aspect ratio examined therein ($s = 25$), an order parameter of $S = 0.84$ with a 45 wt.-% clay loading in the composite was found. The composites moreover show higher stiffness for higher aspect ratios. The commonly known methods to produce parallel-to-substrate-ordered composite materials are:

i) centrifugation[5] (95 wt.-% montmorillonite MMT in polyimide PI), **ii)** sedimentation[4] (40-75 wt.-% clays with different aspect ratios (25–3,500) in polyvinyl alcohol PVA), **iii)** Layer-by-Layer spin coating (15-50 wt.-% silylated Al_2O_3 platelets in chitosan,[6] 14-97-wt.-% layered double hydroxides LDH in PVA[7]) or **iv)** vacuum-assisted magnetic alignment[8] (30-80 wt.-% modified TiO_2-coated Al_2O_3 in an aqueous polymer dispersion mixture, all commercial).

All of these approaches aim to limit the effective degrees of freedom of the platelets in order to derive the desired parallel orientation instead of a rather random orientation, which is usually the case. In all of these publications, mechanical tests are performed and compared to the mechanical characteristics of nacre as a biological coating material, with a 95 wt.-% $CaCO_3$ content in a biopolymer matrix with comparable anisotropic and ordered morphological features.
It remains to be ruled out, how polymer/clay nanocomposites with comparably low clay loadings < 25 wt.-% and also comparably low aspect ratios $s < 20$ can self-organize into the desired nematic ordered colloidal network structures within a coating material. This work aims to identify the underlying mechanisms and preparation techniques to do so.

II Theoretical Background

1 Colloids, Interfaces and Interphases

In general, the homogenous distribution of a substance in a medium such as water is called a colloidal dispersion, if at least one dimension of the colloid is below 1 µm and bigger than 1 nm. The term "colloid" was firstly introduced in 1861 by Graham[9] after dialyzing gelatin, dextrin and many more colloids with a porous membrane. The examined types of colloidal systems are two-phasic dispersions with either i) a soluble phase, such as polyelectrolyte molecules in water; ii) an insoluble phase, such as some mineral or some oil in water and iii) both-in-one; associative colloids such as surfactants/amphiphiles. The combination of these exemplary colloidal systems can be found in biological systems such as proteins, e.g. casein micelles in milk, which have a predominantly hydrophobic part which is covalently bonded to electrostatically charged, hydrophilic chains oriented towards the water, together forming a so-called electrosteric stabilized micelle.
The tailoring of the size and the colloidal shapes are of central interest within this work. The emergence of shape and size of the effective interfacial area A between colloid and the surrounding medium depends on both the chemical nature of the colloid and the surrounding medium. The functional groups of the colloids at the interface A assemble in dependence of the polarity, best described by the surface energy γ, the thereby excluded volume V and electrostatic forces, which can cause stabilization of the colloids against settling, especially in water. A big variety of functional groups at colloidal interfaces can be used to tailor materials for a given purpose. The engineering at the interfacial region is not just a question of the chemical composition. The morphology of actual interfaces is closely linked to the processing history of the materials, which also determine the size and shape of the resulting colloids.
The region near the interface can be called an interphase volume which has different properties compared to the respective bulk phase volume. The medium can be any solvent or a polymeric phase. The interphase is therefore a voluminous phase near the colloidal surface, where the degrees of freedom become less compared to the bulk phase.

1.1 The Nano-Effect and Colloidal Dispersions

The Nano-Effect can be described by a spherical Archimedean solid. The share of interface A of the A/V ratio grows exponentially with decreasing radius r and corresponding volume V. The A/V ratio of a spherical colloid versus the diameter d is shown in **Figure 6**. The higher the ratio for the same volume, the higher is the number N of atoms at interfaces, which are accessible for interaction, e.g. by chemical reactions or physical interaction. The distribution of interfaces within a material is modifying the properties, e.g. found in well-dispersed nanocomposite materials or nano-/mesoporous materials.

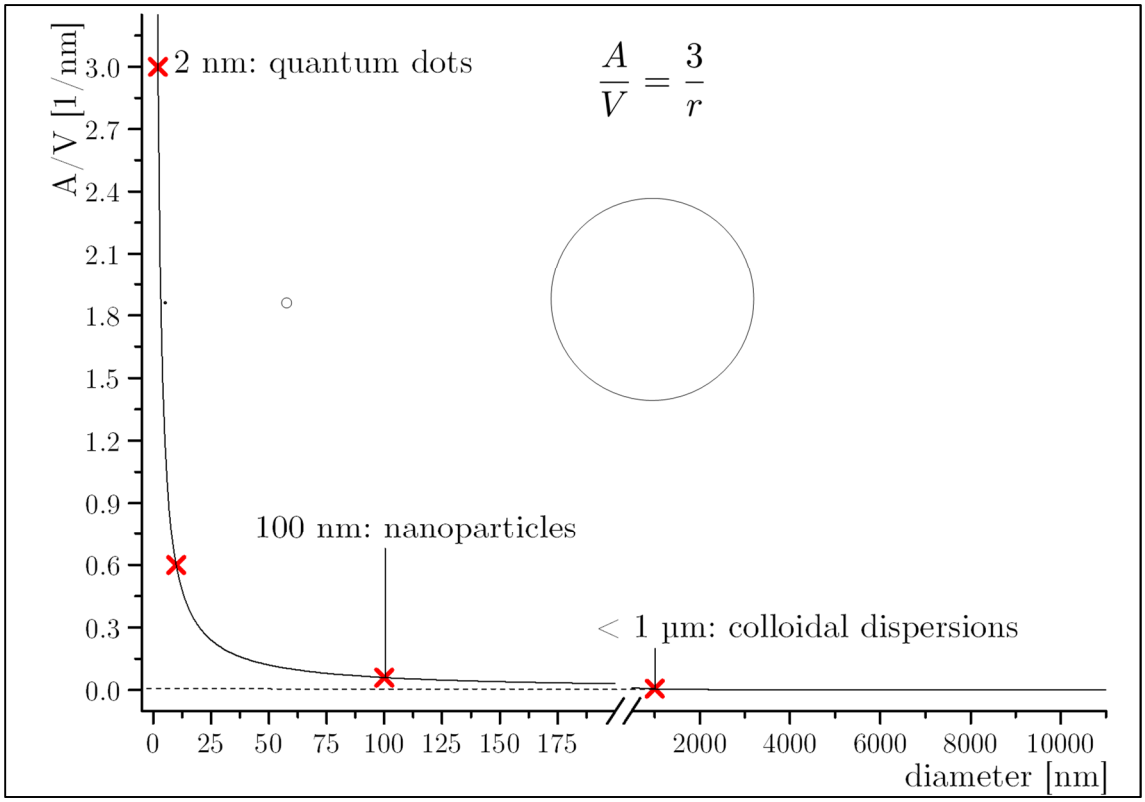


Figure 6: Area / Volume ratio of a sphere vs diameter
The visualization of 10, 50 and 1000 nm spherical colloids are true to scale.
Examples:

- Formally, a single sodium ion with a diameter of 0.2 nm has an A/V ratio of 30 m^2/m^3. A proton has an A/V ratio of $> 10^6$.
- A quantum dot has about 10^4 atoms

The electrostatic stabilization of nanoscaled colloids in aqueous dispersions ($d \leq 100$ nm) is possible by the help of functional groups which are able to form charges in water, typically ammonium (NH_3^+) or carboxylate groups (COO^-), which can lead to a strong electrostatic repulsion and therefore stabilization or more interesting in the context of this work: attraction when mixed together. The composition of a polymer colloid synthesis determines the number of the charged functional groups at the interface and subsequently the resulting size. The resulting size distribution depends on the molecules and the number of the charged groups used, which then can self-assemble at the colloid/water interface. The pH of the water phase is therefore a determining parameter in aq. nanoparticle synthesis, since it alter the present charges and therefore the resulting electrostatic fields.

1.2 Charges at Interfaces

The homogenous distribution of colloids in a dispersion medium remains stable, in case the repulsive forces between the colloids are sufficiently high compared to the competing attractive forces, which cause coagulation/association/aggregation/agglomeration, therefore higher weight and subsequently settling/sedimentation. The repulsion originates from electrostatic forces, whereas attractive van-der-Waals forces oppose the repulsion, described in the DLVO-theory by Derjaguin & Landau (1941)[10] and Verwey & Overbeek (1948)[11], respectively. The repulsive electrostatic force can be triggered by protonation or deprotonation of functional groups on the surface of the colloids. However, especially water contains charges originating from autoprotolysis and/or present ions. The pH value in the dispersion can be changed to switch the sign and/or the strength of the surface charges, depending on the nature and amount of accessible charged functional group present at the interface. In the simplest conceivable case, the counter-ions cover the charged colloidal surface, what leads to a compensation of the surface potential Ψ_0.

The described case is the Helmholtz model (1853)[12], which is shown in **Figure 7**. The surface potential has a linear dependence and drops to zero at the outer boundary δ, acting like parallel plate capacitors. In the equation, δ is the thickness of the adsorbed ion layer, σ is the surface charge density and ε is the dielectric constant of the dispersion medium. An extended model was proposed by Gouy (1910)[13] and Chapman (1913)[14], taking into account thermal fluctuations of the ions. The model describes an exponentially decreasing surface potential Ψ, where x is the distance from the surface and κ the reciprocal Debye length – the distance where the surface potential Ψ_0 drops to Ψ_0/e (e = Euler's number, not elementary charge!).

The Stern model (1924)[15] combines the two border cases with a linear charge decay, followed by an exponential decay. The linear dependence is positioned in the fixed layer regime and an exponential dependence beyond the fixed layer distance δ.

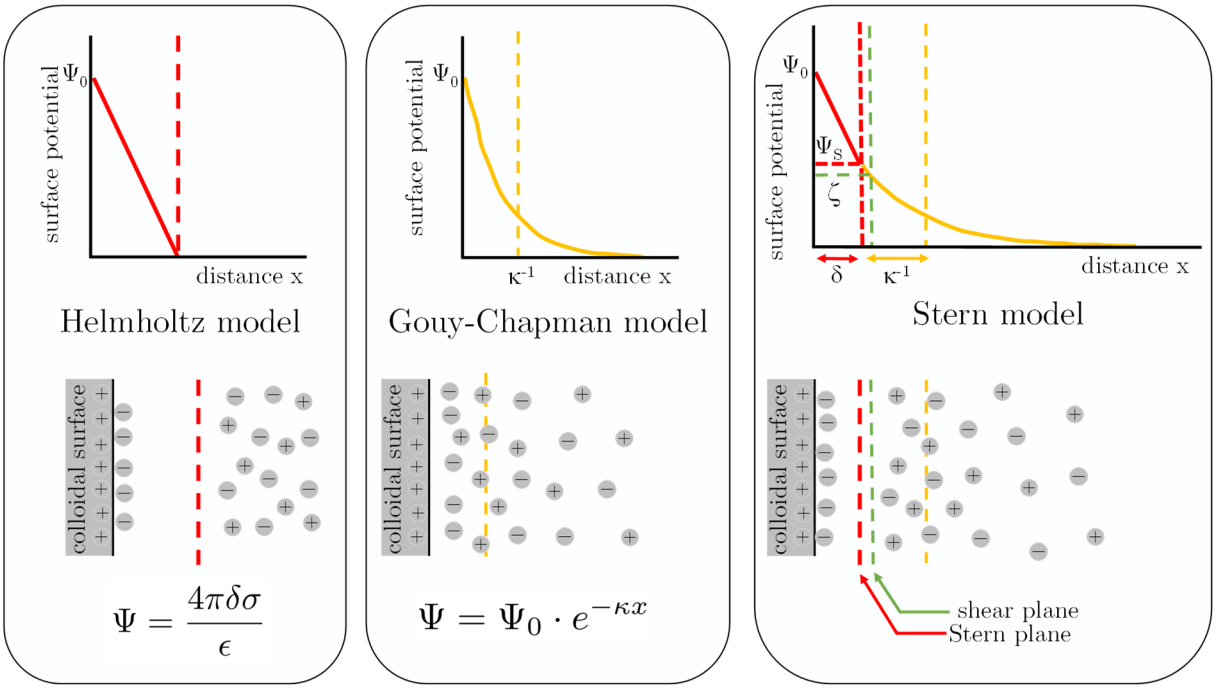


Figure 7: The three classical electric double layer models

The width of the double layer can be changed by varying the concentration of charge carriers such as salts, as mentioned before. In general, the repulsive forces become smaller, if the ion

concentration is increased. The values of the layer thicknesses δ and κ^{-1} decrease, and the repulsion decrease also (see **Figure 8**), so attraction becomes more likely. The diagram is based on the equations of the DLVO theory and shows the interaction between spherical colloids with fixed parameters (radius $r = 100$ nm, surface potential $\Psi_0 = 30$ mV, Hamacker constant $A_H = 7 \cdot 10^{-21}$ J). The most suitable measurement of the surface charge (density) is the ζ-potential. For example, the ζ-potential of low ionic strength dispersions is also found to be higher. The ζ-potential of a dispersion is measured by appliying an electrical field which causes a shear plane around the electrophoretic moving colloid. A colloid exposed to an electrical field in a folded capillary cell move in the direction of the counter-charged electrode. The electrophoretic mobility and the drift velocity of the colloids are dependent on the surface potential of the colloid and the ionic strength of the bulk solution (Smoluchwoski, 1903).[16]

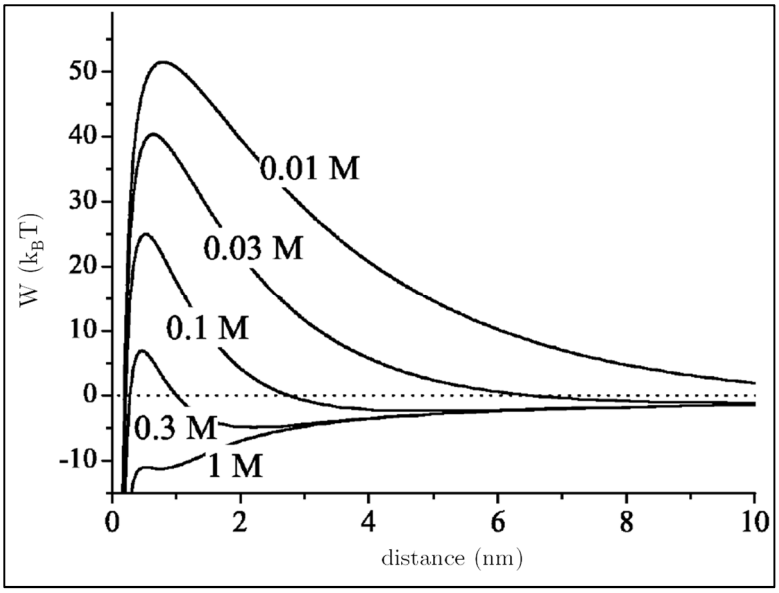


Figure 8: DLVO-based Interaction Force vs. distance for different ionic strengths. diagram taken from Butt et al.[17]

The ζ-Potential can have a positive or a negative sign, which represent the sign of the colloidal surface charge and the direction of the movement. The dynamic viscosity η, the permittivity of the medium ε, the ζ-potential of the colloid, the applied voltage, and the Henry-function $f(\kappa r)$ determine the (ideally) constant velocity v of the colloid in the electric field. The Henry-function represent an approximation, which includes the ratio of the ionic layer thickness (κ^{-1}) and the radius r of the colloid. There are approximations named after Hückel and Smoluchowkski for different ranges of radii. Measuring the velocity v can be made with a camera and the so called ζ-Potential can be calculated with (1).

$$v = \frac{2\epsilon \cdot \zeta \cdot f(\kappa R)}{3 \cdot \eta} \tag{1}$$

The "M3 PALS" technique* allows a fully automatized approach to measure the ζ-Potential of colloids by measuring movement frequencies with Laser Doppler Electrophoresis to calculate the velocity of the colloids.

The resulting ζ-Potential is strongly dependent on the charge carrier distribution surrounding the colloid. Moreover, since colloids in colloidal dispersions can be agglomerates of primary colloids (cf. Ostwald's step rule), the obtained ζ-Potential is better described as an apparent

* Mixed Mode Measurement - Phase Analysis; Malvern Instruments

ζ-Potential. The change of the apparent ζ-Potential of a colloid is made by addition of acids/bases, charge carriers or other charged colloids, practically by change of pH, addition of salt solutions or colloidal dispersions. The pH of the surrounding solution can form charges or neutralize charges on the surface.
In the thesis, the heterocoagulation of spherical and lamellar colloids with opposite charges are examined (**Figure 9**). With no ions present, the deposition of a single sphere onto a counter-charged platelet changes the apparent electrostatic field of the sphere from isotropic to anisotropic. The coagulation of such platelets, clays, to different structures and the resulting structure-property relationship are presented in Section II-2.1.

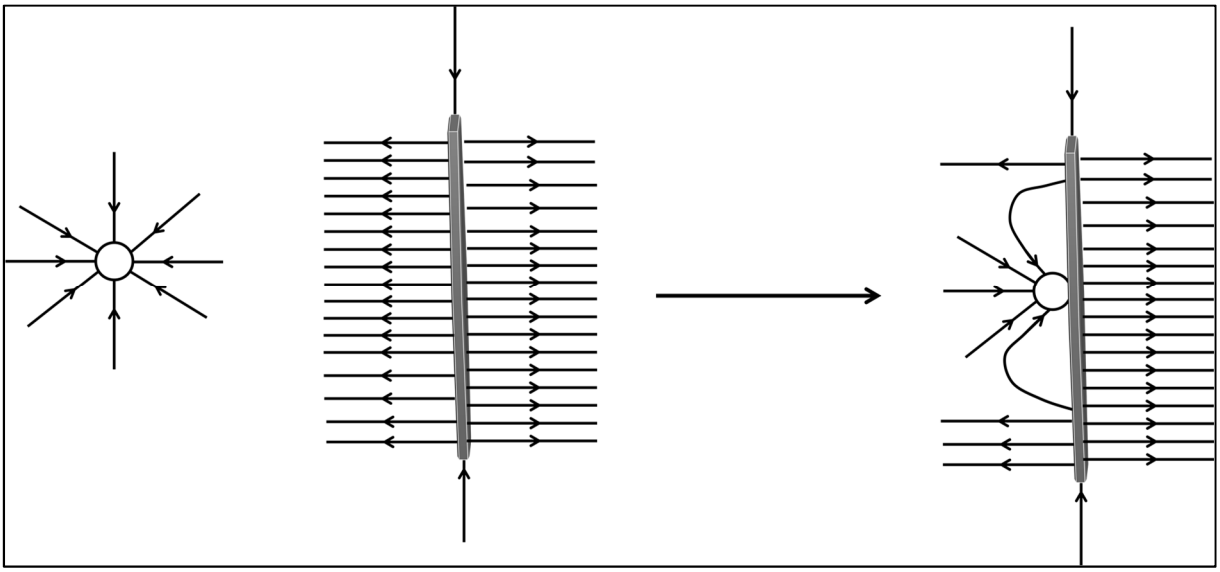


Figure 9: Single-sphere deposition on a lamellar colloid by electrostatic forces

May a colloid with a point mass m accelerate due to the electrostatic force F with a constant permittivity of the medium. The effective surface charges q of two colloids in water with oppositely charged interfaces should be adequate to Newton's and Coulomb's law (with a constant permittivity ε):

$$F = ma \propto \frac{q^{+}q^{-}}{r^{2}} \tag{2}$$

The field lines between the colloids (formal charges q^{+} and q^{-} of mass point m) are assumed to perform a directed assembly of the e.g. isotropic charged silica colloids (q^{-}) and the anisotropic lamellar LDH colloids (q^{+}). When additional ions are added, e.g. in order to perform a pH adjustment, the electric field lines are less directed, since the permittivity ε changes.

1.3 Interfaces and Interphases

In the previous section, the charge of a colloid was described with a charged *interface A* which in turn changes the properties in the surrounding *interphase* volume, *V**. This volume is more pronounced, if the particle volume *V* becomes smaller than the charge compensating shell with the volume *V** of this interphase (cf. subsection about the nano-effect). Those interphases are found in polymer nanocomposite materials. In the Multi-Core model of Tanaka, three different interphases with different properties are suggested (**Figure 10**). When a functional group of a polymer chain is covalently bonded to a nano-scaled particle, the polymer chains organize in a different way compared to the bulk of the polymer, in turn changing measurable material properties. The interphase can cause a shift of the glass transition temperature T_g, which is a measure of the polymer chain mobility at a given temperature (e.g.: r.t.). The shift of T_g can be measured with DSC (Differential Scanning Calorimetry)[18]. The origin of the Tanaka model is from the field of nano-dielectrics, since polymers are used as insulating material for many applications. Within the theory, it is suggested, that ions can be trapped in the second and third layer, because of a locally lowered density and the superimposed surface potential Ψ near the interface. However, the charge-trapping effect becomes more pronounced for higher interphase volumes *V**, especially for nanoparticles. As a consequence, a high interphase volume *V** arises from a high specific interface *A/V*. So the dielectric breakdown strength of dispersed nano-scaled fillers is much higher than for micron-scaled fillers.[19]

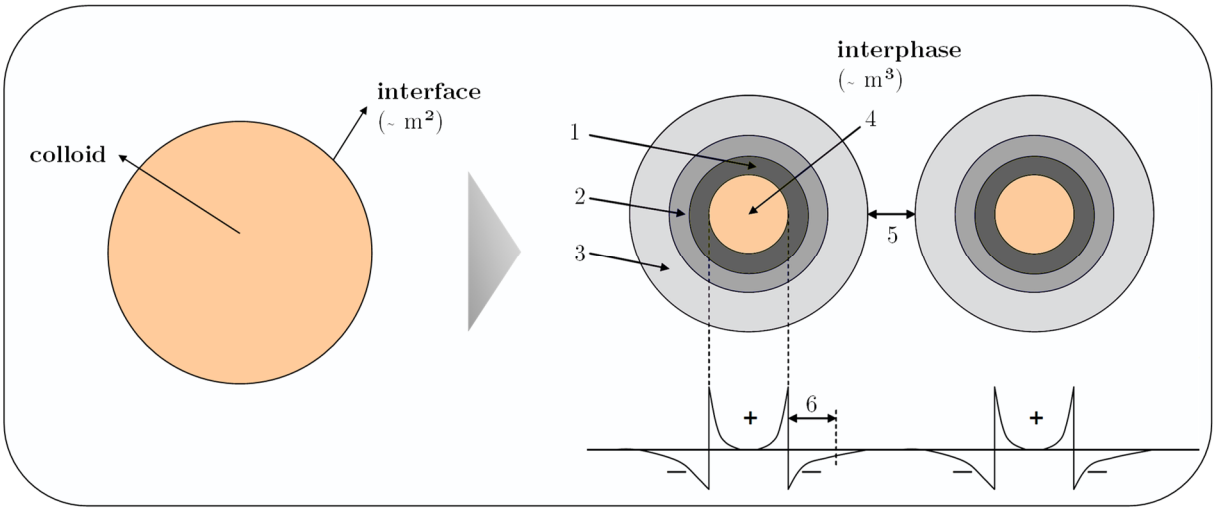


Figure 10: Distinction between the terms Colloid, Interface and Interphase
recolored from Multi-Core Model according to T. Tanaka[20]

1	several nanometers:	tight binding of polymer (ionic/covalent)
2	≈ 10 nm:	loose interaction between polymer chains attached at the interface
3	several ten nanometers	deviant chain conformation & mobility vs. bulk caused by interphase 1 & 2
4	20 to 50 nm:	diameter of nanoparticle
5	40 to 100 nm:	distance between two interphases
6	up to 100 nm:	superimposed Debye shielding

The term "interphase" is used in many disciplines with partially different interpretations in different scientific fields. As a related example, the adhesion of polymers on a metal surface ideally leads to complete wetting and thereby comprise mechanical interlocking due to an interposing mechanism between micron-scaled cavities of the metal surface and entangled polymer chains. The interphase volume *V** between polymer and metal in this case has a thickness in the range of the surface porosity of the metal surface. The interphase of the metal

surface is optimally sealed when the interface is entirely wetted. In the following, some general considerations about the degrees of freedom D_f of a polymer chain are described on a theoretical basis.

The diffusion of a linear polymer chain can be described as "reptation" (de Gennes (1971)[21]). The word is derived from the word "reptile" and wants to describe the polymer entanglement, which can be compared to snakes slithering through one another. In the model, a number of N entangled mass points (0D) move by diffusion (2-dimensional, $[m^2s^{-1}]$) along a 1-dimensional line, resulting in a 3-dimensional tube, in which the enangled polymer units are trapped. The simple model predicts that the relaxation time T_r, so the time needed for N units to pass its own volume rises with the cube of the molar mass M of a linear polymer chain and is related to the dynamic viscosity η:

$$T_r \sim \eta_0 \sim M^{3.0} \tag{3}$$

However, a irrational number is obtained in experiments on linear polymers is directly proportional to the zero shear-viscosity: $\eta_0 \propto M^{3.4}$. The relaxation time T_r is then described as the required time t in which the polymer chain recover its original state after a (small) constant force F is applied by which the chains "reptate", describing a rather steady-state. In the related blob-models, interlocked segments in a long chain are added: the overall shape however retain to be in the tube-like trajectory.

The reptation model does not take into account any chemical composition of the polymers, moreover polarity, conformation or presence of solvent is not included. The drift velocity v of the polymer chain is dependent on the effective degrees of freedom D_f^* of the polymer. The effective degrees of freedom D_f^* at room temperature are smaller or equal to the actual degrees of freedom D_f of a polymer chain:

$$D_f^* \leq D_f \tag{4}$$

In real systems, attractive vs repulsive forces (non-polar, polar or ionic) of the molecules to each other can be viewed as frictional forces vs. slipping forces, respectively. In this context, near the melting point, at the glass transition temperature T_g of a polymer, the crystal phases could be assumed to start "reptating", therefore slipping through each other and overcome friction.

The examined systems in this thesis are mainly polyurethane-based (PUR) und polystyrene-based (PS) dispersions. The glass transition temperature T_g of the used PS is much higher than in the PUR systems, so that the PS spheres are hard at room temperature, whereas PUR is a sticky, viscous liquid. SEM imaging show, that the monodisperse PS colloids form colloidal crystals of hard spheres, whereas PUR colloids form films at room temperature and therefore have, technically said, a lower MFFT than the PS systems examined. In coatings technology, the Minimum Film Forming Temperature (MFFT) of a polymer plays a crucial role in designing coating materials.

2 Lamellar Colloids & Clays

The most suitable and notable lamellar colloids are well-known clays, especially layered silicates or phyllosilicates. Clays are low-cost and they are used in many commercial products. There are many structural groups covering at least over 100 types with different geometry and composition of phyllosilicates, without taking into account polytypism or interstratification. Clays are abundant on earth, whereby their geometry is believed to store information (by replication of stacking-faults, dislocations and substitutions).[22] The interlamellar void could be interpreted as protected reaction machineries with a huge charged interface which can catalyze the polymerization of complex biopolymers such as RNA[23] or polypeptides[24]. Clays, more generally the interface and geometry of clays are therefore discussed to play a central part in the origin of life, described by the 'crystals as genes' hypothesis of A.G. Cairns-Smith.[25]
The lamellar geometry is useful to design coating materials with enhanced barrier properties towards environmental stress. In general, one of the most interesting geometrical properties of clay colloids is the aspect ratio, which is the quotient of the equivalent diameter d and the thickness d^* of the lamellar colloid. As pointed on in the introduction, a single crystal layer can be interpreted as a geometric 2D plane, because the thickness is in the sub-nanometer range (≤ 1 nm). The 2D planes stack on each other with alternating (partial) charges (**Figure 11**). The TO structure is polar along the z-axis and therefore stack (T: tetrahedral; O octahedral). In other clays, the polarity for the crystal layer stacking is reached by charges compensating the layer charge (O, TOT). The layer charge is a result of the superposition of isomorphic substitutions (cf. Goldschmidt tolerance factor (1926)[26]).

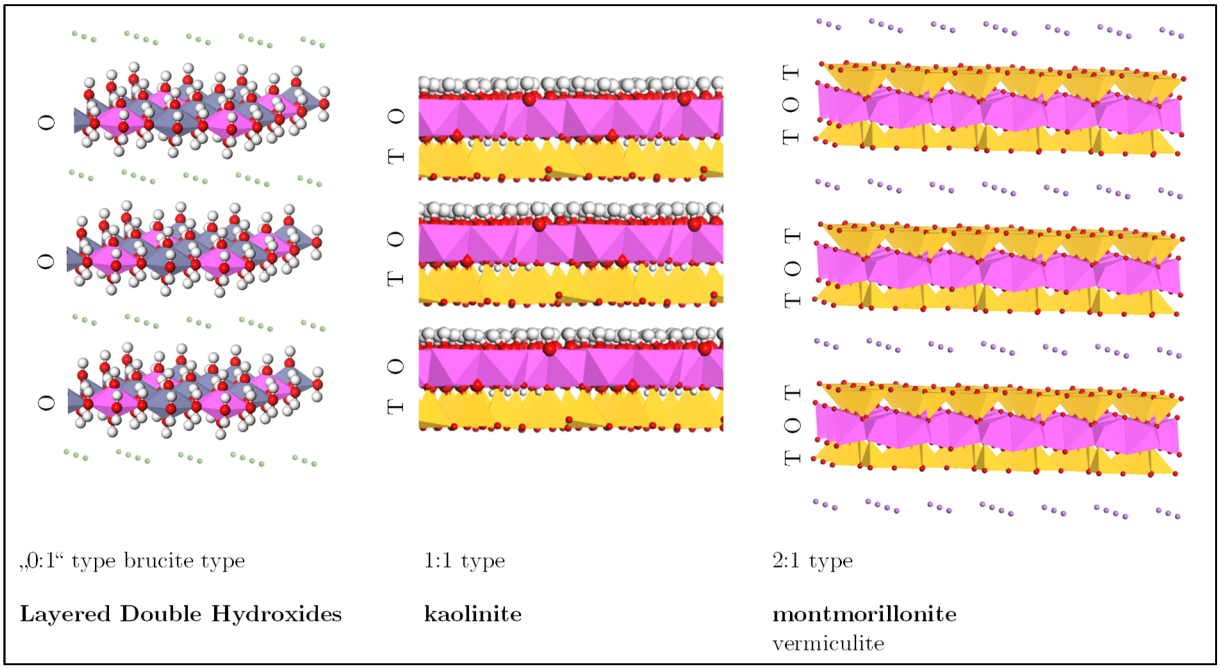


Figure 11: 3D polyhedron structures of lamellar colloids.
SiO_4 tetrahedrons: yellow; $M(OH)_6$ octahedrons: M=Al (pink), M=Zn (grey); green interlayer anion: chloride; violet interlayer cation: sodium

The layered structure allows to build a barrier towards environmental stress such as corrosion,[27] mechanical impact such as stone-chip resistance[28,29] or dielectric breakdown strength[18].

There are a lot of possibilities to obtain lamellar colloids on a synthetic way. For example, nanometer thin, amorphous lamellar structures with Janus character[†] can be formed by template sol-gel chemistry.[30] Another representative, the so-called MAX alloy phases are layered hexagonal carbides or nitrides (X) with a main group element (A) and an early transition metal (M).[31] Another very interesting representative of synthetic lamellar colloids are Layered Double Hydroxides (LDH), which will be presented in section II-2.2.
The lamellar structure of clays has perfect "Cleavage" along the (001) crystal plane, which means by a mineralogist's definition a very good cleavage, leaving a shiny cleavage surface. Cleavage is macroscopically observable by e.g. peeling off centimeter-scaled muscovite in sheets or removing thin flakes from thermally treated vermiculite. Herein, the term exfoliation is used. In the case of montmorillonite, the lamellar structure is tangible by the rheological behaviour, which is utilized in many commercial cosmetic products. An elaborate melt synthesis of a near relative (Na-fluorohectorite) is known for years and easily exfoliate (cleave) to very high aspect ratios.[32]

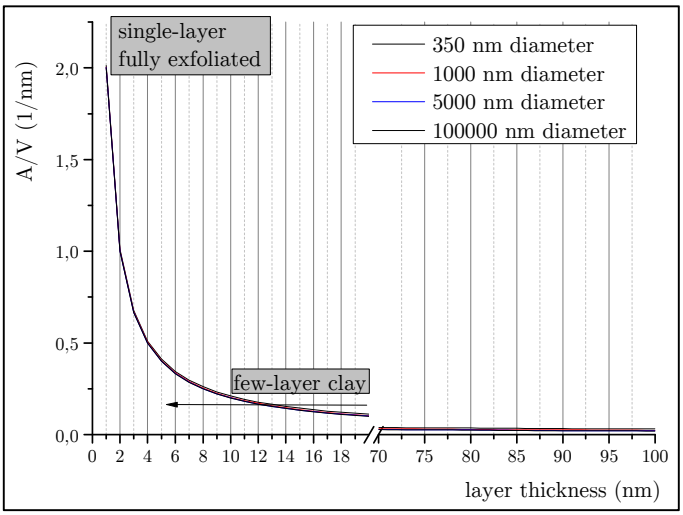


Figure 12: Growth of the interface of lamellar colloids

A fully exfoliated clay particle has the highest interface per volume. The different diameters have the same interface to volume growth rate, since the edges represent a neglectable contribution to the total interface of a lamella. Furthermore, no edge area is generated by exfoliation, since the interface of the lamellar colloids is per definition at the particle/water interface.

Typical representatives of lamellar colloids are: layered silicates, layered double hydroxides, chitin, chitosan, graphite, α-zirconium phosphate, hydrotalcite, brucite, talcum, MAX phases and many more. The following subsections will focus on the three types of lamellar colloids used in this work. In Figure 11 the layered colloids studied herein are shown: layered double hydroxides, kaolinite and montmorillonite.
It becomes apparent from **Figure 12** that the interface per volume A/V of a clay platelet with cylindrical shape rises exponentially by exfoliation (reducing the number of sheets stacked together), almost independent on the lateral size of the lamellar colloid. In contrast, the interface generated by the edges A_{edge} rises exponentially with smaller diameter (**Figure 13**).

[†] Janus Colloids are named after the two-faced god Janus. A particle with asymmetric and anti-directed orientation of the surfaces with different surface chemistry are called Janus colloids.

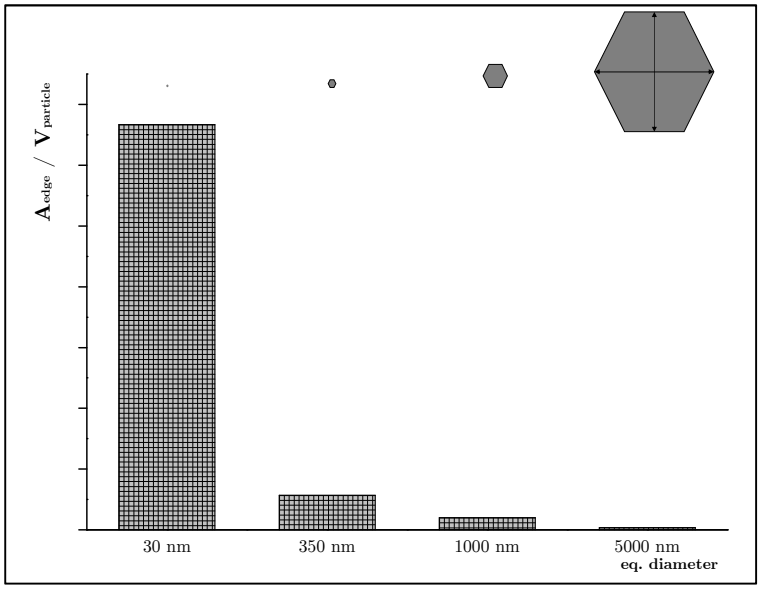


Figure 13: Area of the edges per volume of a single lamellar colloid vs. lateral diameter
For the calculation, a cylindrical geometry is assumed. The chosen equivalent diameters refer to relevant diameters examined in the thesis.

The predominant edges of small lamellar colloids change the charge distribution of the surrounding ions and the particle-particle interaction, leading to rheological effects.

2.1 Organization and Rheology of Clays

The organization of clays is mainly dependent on the surface charges, the edge charges and optionally the intercalated charge carrying ions. The classical border cases of clay organization are the house-of-cards and the band-type organization[33] (**Figure 14**).
By changing the pH or ionic strength of the clay dispersion, the charges, the organization of the clay colloids and subsequently the flow characteristics such as the viscosity η changes. The flow characteristics are obtainable by rheological measurements in dependence of a lot of parameters (e.g. particle concentration, pH, ionic strength of the electrolyte, charge density of the ionic species of the electrolyte, type, charge and size of the clay, presence of oppositely, same charged or non-charged colloids, applied shear forces,...[34]). Air inclusions in the dispersion significantly changes the results of the measurements and have to be avoided for reproducible results. **Figure 15** shows the most-used types of rheometers. The top component of the rheometers is rotating with the shear rate $\dot{\gamma}$ and the shear strength τ, the bottom part is static. Roughly speaking, the viscosity η of the clay suspension results from the applied shear force τ and the shear rate $\dot{\gamma}$ of the upper dynamic part $(\tau = \eta\,\dot{\gamma})$. These parameters are obtainable with a force transducer.
A well-known clay is the commercial product "Laponite", a synthetic hectorite. These lamellar colloids are very small (eq. ø = 30 nm) and have much more exposed edge charges compared to naturally occurring montmorillonite (eq. ø = 350 nm). The small size of the product "Laponite RD" ensure that the colloids form a viscous gel, which is a consequence of the house-of-cards organization. By applying shear forces to the suspension (e.g. shaking), the band-type organization becomes more dominant, since the viscosity of the dispersion becomes very low compared to the initial gel state. After a period of rest, the viscous gel regenerates. This rheological property is called "thixotropy" and is usually quantified by the hysteresis area in the flow curve (τ vs $\dot{\gamma}$). The organization in "Laponite RDS" is achieved by addition of tetravalent pyrophosphate anions to compensate the positive charges at the edges. In this case,

the gel-forming house-of-cards organization cannot occur, because the sign of the charge is the same at the edge and at the face of the lamellar colloid. However, thixotropy is not the only rheological effect occurring in clay suspensions.

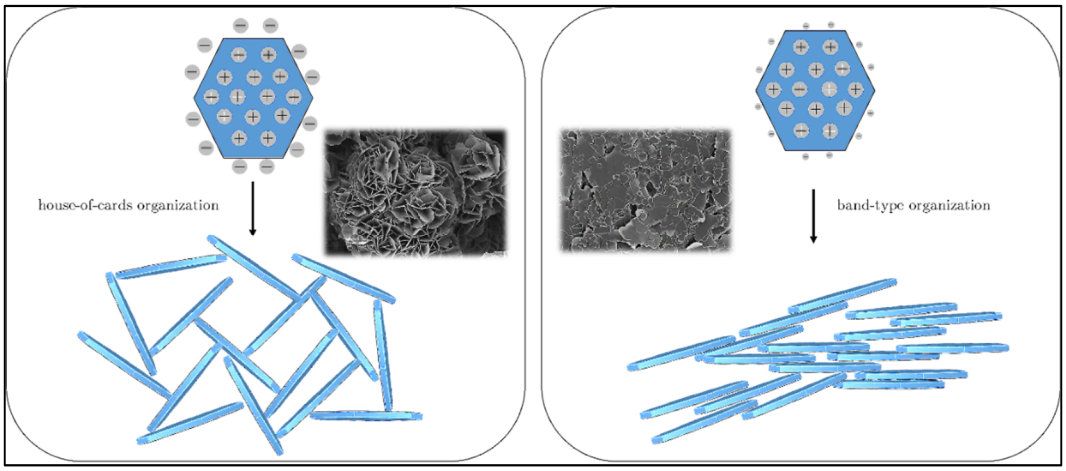


Figure 14: Classical border cases of lamellar particle organization of LDH colloids
top: When the edges of the clay are highly charged, the house of cards organization is favored; when the edge charges are small compared to the basal surface charge, the band-type organization is favored.

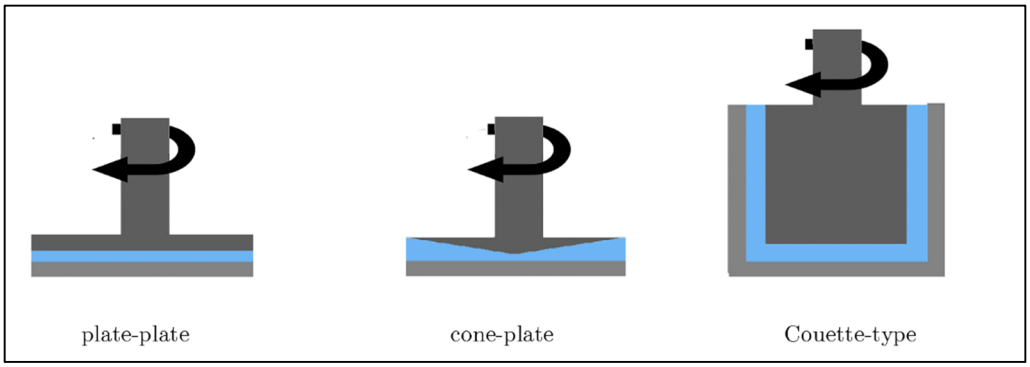


Figure 15: Most used rheometers types, in blue the examined substance.

Other known flow characteristics of clay suspensions are "anti-thixotropy" (rheopexy) and Bingham fluidic at high clay concentrations and apparently Newtonian at low clay concentrations or high ion concentrations.[35] For example, examinations on the flow behavior of oppositely charged, heterocoagulated clays in oil/water emulsions show rheopexy at distinct compositions.[36] The morphological changes in the suspension leading to anti-thixotropy are not fully understood. Clay dispersions often behave like Bingham fluids. The resting dispersion behaves like a rigid body. Even at distinct shear stress values τ below the yield stress value τ_B, the dispersion has a high viscosity. The yield stress value τ_B is a measure for the inner adhesive forces of the clay network structure. When the stress value is higher than τ_B, the fluid begins to flow. The effect is useful for classical wall coatings: when a paint roller is dipped into a paint bin, the shear force is insufficient to destroy the inner structural network and the paint do not drip. During the application of the paint, the structural network is broken apart by shearing, the paint distributes over the wall and subsequently thickens after rebuilding the network. The rheological behavior of clays have a broad application in personal care products such as creams, gels or paste, in paper production, in oil recovery as electrorheological fluids, in printing inks, in plant rooting gels and may others.[37] In a recent publication, LDH-coated SiO_2 assemblies

were examined as electrorheological fluid.[38] However, in this work, the thixotropic properties of LDH/PUR with varying compositions and colloid sizes are studied.

2.2 Layered Double Hydroxides

The chemical formula of layered double hydroxides is similar to the naturally occurring hydrotalcite-type $Mg_6Al_2(OH)_{16}[CO_3] \cdot 4\ H_2O$. The corresponding Mg^{2+}-based hydroxide is charge neutral, whereas the Al^{3+} sites give a positive layer charge by isomorphic substitution. These cationic clays can be synthesized by precipitation at ambient conditions and broad ranges of pH values, depending on the ions involved in the precipitation. The more precisely the pH is controlled, the bigger the colloids can potentially grow. The lamellar structure is formed by olation. Olation is the (poly)condensation of metal complexes, which can lead to lamellar polymeric structures, e.g. layered double hydroxides (**Figure 16**). The olation reaction is e.g. used as a protein crosslinking reaction in the tanning process of leather.

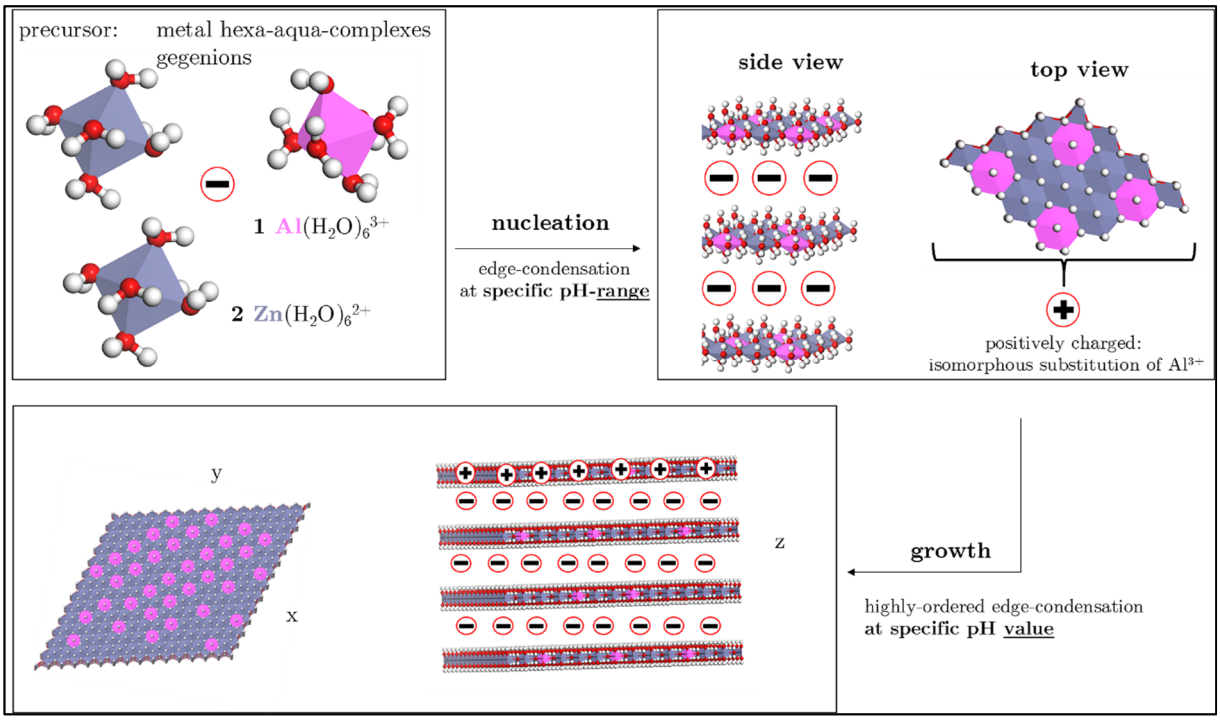


Figure 16: LDH formation in polyhedral depiction
The first affirmative LDH coprecipitation reaction at constant pH was performed 40 years ago[39]

The rheological properties of LDH colloids are not intensively studied, compared to the prominent clay montmorillonite. In comparison to montmorillonite, LDH colloids have a high surface charge density. The intercalated ions can serve as a release agent, e.g. for controlled catalyst or drug release or for the inhibition of corrosion with e.g. benzotriazolates[40,41]. By adding Li-salts into coating compositions for aluminum alloys, the Al^{3+} and Li^{+}-ions form a protective layer of Layered Double hydroxides at defect sites.[42]
In this work, the mainly examined LDH phases consist of a $[Zn_2Al(OH)_6BSA]$ phase, whereas BSA indicate the intercalated benzenesulfonate ion.

2.3 The Janus character of kaolinite

Kaolinite is an abundant clay mineral, which can be mined in almost every country on planet earth. By modifying kaolinite, two-dimensional 'Janus colloids' can be obtained on technical scale for a huge field of applications.
In general, Janus colloids have an amphiphilic character and can be useful for compatibilization of polymers.[43] Moreover, Janus colloids can be fine-tuned to obtain interesting magnetic properties for medical uses[44], chemotactical behavior towards catalytic species[45], or combined properties like electrorheological[46] properties. Organisms called "disco clams" make use of the switchable optical properties of Janus colloids,[47] which are known also from the e-paper technology.[48]

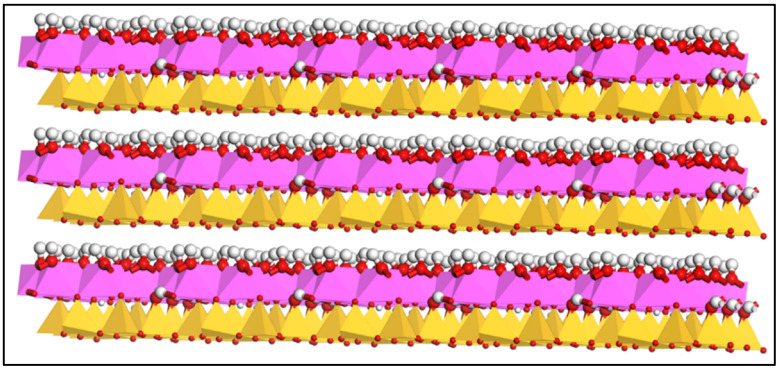


Figure 17: Side-view on the ideal crystal structure of kaolinite
Mixed polyhedral/ball-and-stick representation. SiO_4 tetrahedrons: yellow; $Al(OH)_6$ octahedrons: pink; OH groups red/white

Up to now, the synthesis of Janus colloids is complex and in most cases very expensive. Typical procedures are microfluidic synthesis[49,50], the "Gyricon Method" used for electronic paper displays[51], phase separation of tailored block copolymers[52], procedures from particle monolayer adsorbed on a sacrificial layer on a planar surface including plasma-treatment[53], lithographic techniques[54] and templated sol-gel techniques.[55]
Kaolinite has no interlayer charge and is weakly swellable in water. Therefore, the separation of the layers is intrinsically impeded. Kaolinite is a cheap raw material, which is also structurally a raw Janus particle. The crystallographic structure (**Figure 17**) of kaolinite shows a distinct asymmetric, so-called 'Janus particle' character with respect to the distribution of hydroxyl groups. By modification with an functional group (-NH_2, -SH, alkyl,...) by sol-gel chemistry there is a huge potential to use this material for organizing the obtained Janus kaolinite with other colloids and/or molecules. At this point, it should be noted, that natural grown colloids have a lot of polytypes[56] and substituted ions (compare 'rock cycle'), so that a geometrically ideal Janus particle from natural grown kaolinite is unlikely to achieve. According to a force-field molecular dynamics study, the basal contact angle of water on the ideal $Al(OH)_6$ octahedral layer is 0° and on the ideal tetrahedral layer 105°.[57] However, contact angle measurements on kaolinite show a contact angle around 17°.[58] Kaolinite is regarded as a pigment or filler in coatings industry and most of the time it is used as a rheological additive. Because of its cheap price, kaolinite is used in coatings everywhere in the world without taking into account the inherent Janus character.
The preparation of kaolinite Janus colloids is already reported. In the first publication to this topic, kaolinite is purified by removal of calcium and magnesium ions with EDTA, a removal of ferrous species by the DCB-method ("dithionite-citrate–bicarbonate") followed by a final

ozonisation. The selective adsorption of molecules on the different basal surfaces was examined by a ToF-SIMS analysis with Ru-complexes (tetrahedral side) and phosphorous-catechol complexes (octahedral side) with P and Ru as marker atoms.[59]
In another publication, kaolinite/polymer hybrid Janus colloids were prepared by an initial modification with 3-aminopropyltriethoxysilane. The assumed covalent bond was achieved by a 60°C/vacuum curing step. The Janus morphology appears, even though patchy, when colloids were deposited on the modified kaolinite, which then has positively charged sites from the silane ($-NH_3^+$) and negatively charged areas of the pristine basal surfaces of kaolinite. Moreover, the kaolinite Janus colloids enhance the stabilization of water−oil emulsions, similar to Pickering dispersion colloids with a hydrophilic and a hydrophobic polymer on the different sides of the kaolinite platelets.[60]
The proof of the Janus character is tricky. Assuming a thickness of 100 nm at any eq. diameter of one kaolinite particle, all functional groups located at the outer surface account to 1 mol.-%. Further assuming, that about one half of the total surface is reactive and the (reactive) edges do not contribute to the Janus character, the total reactive surface is therefore around 0.55 mol.-%.
In a recent publication, solid-state ^{19}F-NMR and assisting measurements were combined to obtain the minimal reactive surface of clays with a monofunctional trifluorinated silane (TFS). The obtained values of the silane were between 0.49 mol.-% and 0.26 mol.-% for the TFS molecules.[61] The experimental data from the literature cover the simple assumption described above, ending up in a theoretical surface yield of 89 % of the assumed accessible OH groups of kaolinite. Interlayer grafting of APTES molecules between the interlamellar void was also reported and shown by interlayer distance measurements with x-ray diffraction XRD.[62]

This thesis focuses on the Janus character of kaolinite and the assumed Janus deposition pattern of spherical colloids on APTES-modified, preferably Janus kaolinite surfaces.

3 Colloidal Assembly

The possibilities of assembling colloids are seemingly high with respect to the variety of atomic and colloidal structures, which are accessible via chemical synthesis of small molecules which in turn give colloidal basic building units (bottom-up approach). Also, colloids can be mined and processed afterwards to commercial products, for example by milling to different grades or qualities of powders (top-down approach). The following parameters and terms for the assembly of colloids in this thesis are:

•	charges q	electrostatic assembly @
•	surface tension γ	capillary assembly π
•	atmospheric pressure p	capillary assembly π
•	reactivity / chemical potential μ	chemical assembly μ
❖	type of colloid	chemical nature i
❖	quantities and concentrations	of ion/molecule/colloid species i
❖	degrees of freedom D_f	of ion/molecule/colloid species i
❖	shape & size distribution	lamellae, spheres, coils of different sizes i
○	temperature T	thermal energy: preferably room temperature
○	crystallinity T_g	inner frictional energy: hard *vs* soft matter at r.t.
○	solvents & solubilities θ	mixing energy / entropy

The letter **@** is used for the electrost**at**ic assembly of colloids. The letter $\boldsymbol{\pi}$ is used for ca**pi**llary assembly of colloids. The letter $\boldsymbol{\mu}$ is used for any significant che**mi**cal transformation during, prior or after colloidal assembly. The letter $\boldsymbol{i}$ stands for **i**nformation. For basic research experiments net effects have to be studied. Therefore, the premise for the colloidal assemblies studied here is a well-defined, preferably unimodal size distribution of the used colloids. Moreover, time-dependent effects (4D dynamic self-assembly, also: self-organization) are studied here (cf. **Figure 18**).

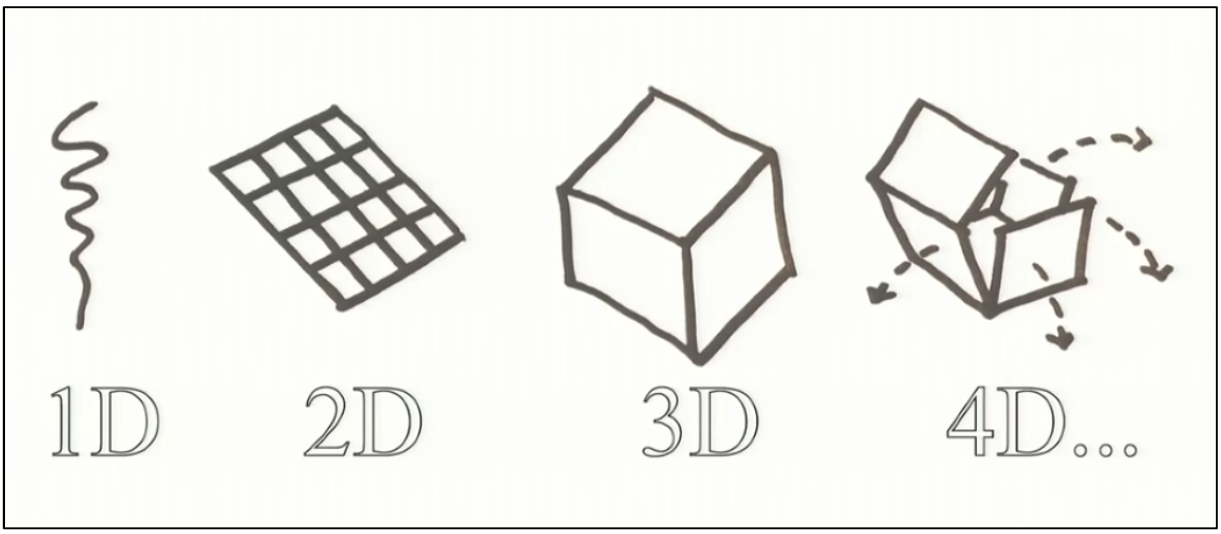


Figure 18: Scheme of 4D self-assembly
taken from S. Tibbits' TED talk (2013) on "4D printing"[63]

3.1 Electrostatic Assembly @

The electrost**at**ic asssembly @ is based on attractive opposite Coulombian charges. In this subsection, the general electrostatic assembly types examined in the literature are shown. The simplest case for an electrostatic assembly may be the generation of a salt crystal with ions smaller than 1 nm, considered as 0D mass points. The preparation of rather big colloids in water is based on the electrostatic repulsion by the help of these 0D ions. However, the close-packing of monodisperse colloids , for example with a diameter of 1000 nm behave in the same way and are therefore called colloidal crystals. In **Figure 19**, such a (**0D** @ **0D**)$_n$ assembly with dyed silica colloids is shown.

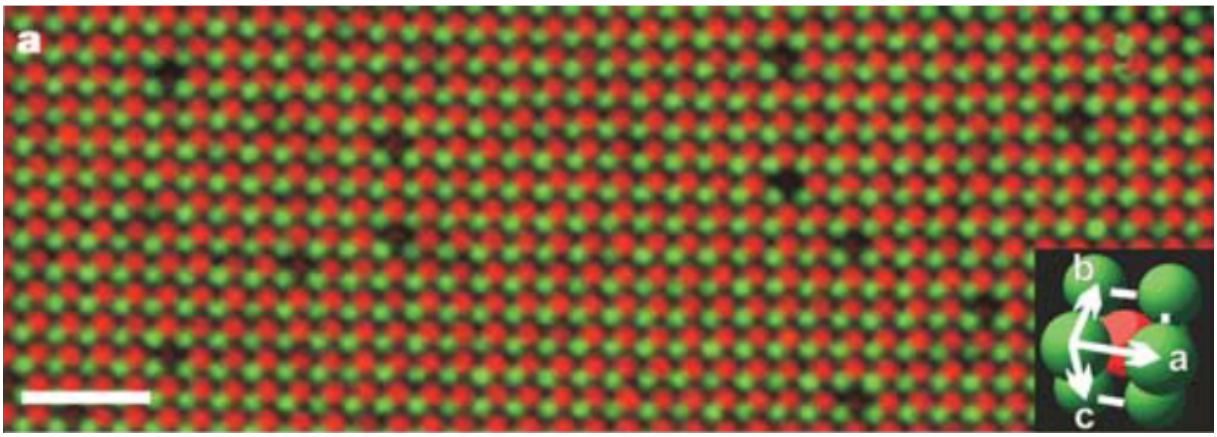


Figure 19: Ionic colloidal crystals

Images were published in a letter by van Blaaderen et al.[64] Confocal laser scanning microscopy with dyed colloids: green spheres: positively charged colloids; red: negatively charged colloids with a diameter of ≈ 1 μm

The Layer-by-Layer technique with dissolved and oppositely charged polymer chains (1D) engage the materials scientists interest since the early 90's, when Decher et al. published his results of at least 35 consecutively alternating layers (**1D** @ **1D**)$_{35}$ of oppositely charged polyelectrolytes.[65] The principle is quite simple: A substrate (e.g. glass) is electrically charged by an acidic (+) or basic (-) pretreatment and dip-coated in a diluted solution of oppositely charged and dissolved macromolecules. Subsequently, the weakly attached excess of macromolecules is rinsed off the substrate with water and the substrate is immersed again in a diluted solution of an again oppositely charged and dissolved macromolecule solution, followed again by a rinsing step. The procedure is repeated until the desired film thickness is reached. The LbL-technique is also applicable on colloidal surfaces of spheres or tubes.
The selective coagulation of clay minerals (**2D** @ **2D**)$_n$ is achieved by changing the surrounding charge distribution of the surface and the edges.[66] The border cases of this assembly are described above (subsection 2.1).
The deposition of comparably small spherical colloids (0D spheres) on big spherical colloids (3D spheres) can lead to raspberry like colloids[67] with a 0D @ 3D configuration. In general, the electrostatic assembly can be easily used for the organization of many other colloid shapes. The herein examined assemblies are best described as 0D @ 2D or 3D @ 2D, meaning colloidal spheres on the suface of colloidal plates.

3.2 Capillary Assembly π

The ca**pi**llary assembly **π** occurs during drying of colloidal dispersions. In colloidal dispersions, the distribution of electrostatically stabilized spheres is entropy-driven and strive for *maximum space-filling* of the liquid phase. The colloids distribute with an average maximum distance like an ideal gas, because of strong electrostatic repulsion between the colloids. An ideal gas is defined by the amount of atoms which have no volume (0D), compared to a colloid with a reasonable mass m and volume V (3D). Moreover, the ideal gas theory does not take into account charges, which is covered by the assumption that the collision between idealized gas points is perfectly elastic. For stable dispersions of hard spherical colloids in water at room temperature, made of SiO_2 (T_g: 500 °C) or polystyrene (T_g: 105 °C), the assumption of elastic collisions and zero-dimensionality (0D) is realistic at room temperature. The more narrow the size distribution, the more closely the dispersion behave like an ideal gas. However, when a droplet of aqueous colloidal dispersion is dried on a surface, the *maximum space-filling* effect in the dried state ends up in a colloidal crystal phase from visual 3D spheres, shown in **Figure 20**.

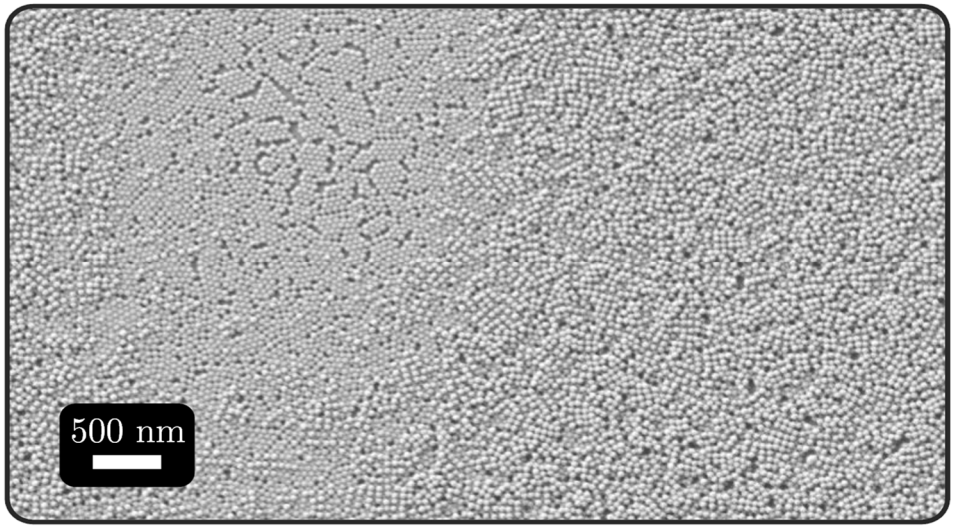


Figure 20: Colloidal crystals from nanoscale colloids showing hcp and ccp structures
The SEM image is taken from the dissertation of K. Briesenick (2017)[68]. The polymer colloids (50 nm) are synthesized with the DPE-technology described therein. The close-packed colloidal crystal structures observed here are the same described known from atomic scale to macroscopic scale (Kepler conjecture, 1611,[69] proofed formally in the 2000s[70]). Hexagonally-packed structures of same-sized spheres (hcp) have maximum space-filling with a value of 74 vol.-%, whereas the second-best are cubic structures (ccp) with a space filling of 52 vol.-%.

The sphere organization can then be interpreted as a dynamic $(3D\ \pi\ 3D)_n$ collapse on a 2D surface. At the beginning of the evaporation, the dispersion behave like an ideal gas and fill the space homogenously. In terms of thermodynamics, the drying of a colloidal dispersion droplet is in a highly non-equilibrium state. Just before the end of the evaporation, when the ratio of water level and colloidal diameter becomes ≤ 1, the system underlie the external restriction of the finite wetted surface and the forces on the colloids $|F_c|$, especially the immersion force, dramatically change (see **Figure 21**, lateral capillary force). When the water level reaches the diameter d of the colloids, a 3-phase point emerges (colloid/water/air), the planar water surface is significantly perturbed (dA) by the generation of menisci with wetting angles originating from the local wettability (surface tension γ) of the colloid at the respective height h of the water film. The capillary potential ΔW consists of two terms: one

thereof is the surface energy $W(\gamma_c)$ and one is a gravitational Archimedean term $W(\Gamma_c)$ which strongly decreases with smaller distance L between two colloids.[71] The change in geometrical shape of the air/water interface ΔA_* and the change of the (rather neglible) excluded volume dV_* of spherical colloids is further described in a model of Kralchevsky & Denkov (1993)[72]. The shortened version of the equation described therein for two spheres immersed into water along the z-axis reads

$$\Delta W_\pi = W(\gamma_c) + W(\Gamma_c) = -\sum_* \left\{ \pi\gamma \left[\Delta A_*\right] - \Delta\rho g \left(\Delta \int_* |z| \cdot dV_* \right) \right\}. \qquad (5)$$

The distance between the colloids L, the height h, the radius r of the colloid and the respective wetting angles are incorporated into their model and experiments. The attractive capillary forces overcome the repulsive electrostatic forces during the described final evaporation and after passing a non-equilibrium state, the colloids remain dried and immobile on the surface. During the drying process of a drying droplet, ordered regions (colloidal crystals) form and the water and colloids are pulled from the center towards the ordered regions.

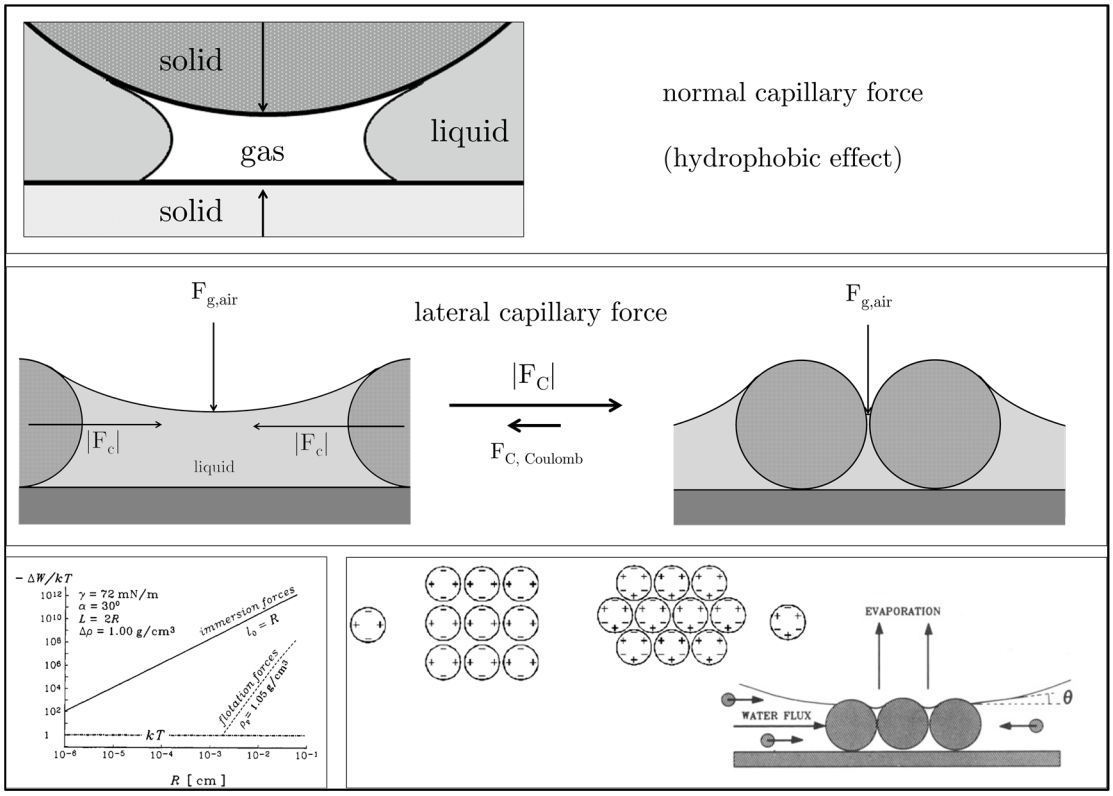


Figure 21: Mechanism of Colloidal Crystal formation

top: normal capillary force between two solid phases

middle: Nucleation due to the forces on the colloids F_C. In this special case, the force is called immersion force. The immersion force lead to nucleation and ordered growth by attachment.

bottom left: calculated immersion force[73] and flotation force[72] (as work ΔW) vs. radius R of the colloid. Even for 200 nm spheres, the attractive force is 100 times higher than kT. The picture is taken from reference.[74]

bottom right: The local deviations of the meniscus visualized here, are called capillary charges.[71] For spheres, quadrupole & hexapole symmetry of the fluctuating amplitudes are thinkable. The mathematical expression leads to a Coulomb-like expression and is therefore called capillary charges.

Again, the system "drying aqueous dispersion droplet" is in a highly non-equilibrium state. Air molecules have a reasonable weight at atmospheric pressure (approx. 1 kg/cm² air column) and hit the surface (e.g. 1 cm²) of a single water droplet (approx. 30 mg) with the thermal energy kT. The collisions lead to evaporation of water and there is less space for the colloids to distribute by repulsion with progressing time. At the 3-phase line around the water

droplet, the evaporation is fastest and lead to the prominent coffee-ring effect. Water molecules at the 3-phase point have less degrees of freedom D^*_f compared to the molecules in the bulk, so that a water flux is induced towards the radial 3-phase line, where the colloidal crystals start to form. Moreover, the sum of degrees of freedom ΣD for the system become smaller, since water molecules are removed by evaporation.
The surface energy of water leads to a minimization of the air/water interface by collective movement (convection) of water molecules to the colloids, inhibiting the evaporation and decreasing the contact line. So the collective movement of water leave the colloids in a maximum-space-filling phase, as it was in dispersion.
Apart from the rather simple colloidal crystal formation, the acting capillary forces during drying of colloidal dispersions can also form i) deformation of the colloids by the air/water interface and act on more interfaces leading to ii) wet sintering (polymer/water), iii) dry sintering (polymer/air) or iv) skinning by coalescence during drying, all described within the prominent Routh-Russel model.[75,76] A recent review by A. Routh about drying of thin colloidal films from 2013 states that the particle size distribution of the involved colloids are not that well known in most studies on the model so that numerous complications arise and the ability to predict the drying process by the help of evaporation rates is hindered.[77] Within the context of the thesis, the dependence of the glass transition temperature T_g on the film formation of colloids is from central interest. The detection of water in drying polymer dispersions by GARField NMR[78] with glass transition temperatures T_g ranging from -22 to 19 °C end up in coalescence and skin formation for the low T_g polymer (-22 °C), having low surface roughness versus high surface roughness by particle deformation and crack formation for the higher T_g polymer (19 °C). Herein, PS with a T_g of 105 °C and PUR with a T_g of -45 °C are examined, representing border cases: no capillary deformation and pronounced cracking for the PS films at r.t. and in contrast to PS, coalescence at room temperature for PUR (cf. **Figure 22**). Later on, the coalesence of PUR is enhanced by the addition of co-solvent and crosslinker.

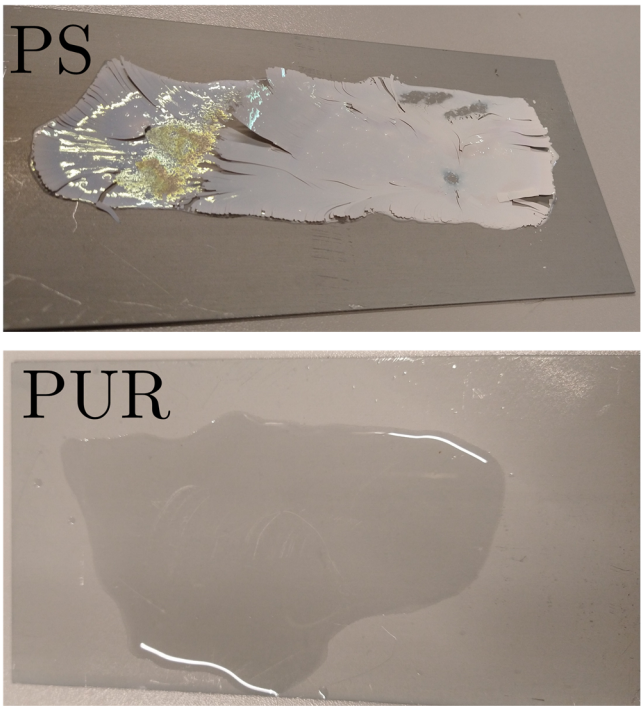


Figure 22: Film-forming of the used PS and PUR dispersions

A more mechanistic view of drying suspension is provided in a recent paper from 2016 by distinguishing four stresses: hydrodynamic, elasto-capillary, shrinkage and capillary stress; and

the examination of phenomena like wrinkling, cracking and air invasion via transmission optical microscopy. It is demonstrated therein, that different crosslinker concentrations in the dried films can also lead to altered capillary deformation and coalescence of the colloids.[79]
The examined PUR systems herein form tacky films without crosslinker so that the use of crosslinker is inevatible for the mechanical characterization of PUR/LDH composite films.

3.3 Composite Materials and chemical interaction μ

Chemical assembly μ. The preparation of composite materials with a high interface are expected to enhance the mechanical properties of the pristine organic polymer materials such as the modulus, crack resistance, stone-chip resistance or scratch resistance. The further expansion of the interface can be made by grafting reactions between polymer and filler, which forms a covalent bond at the composite interfaces (e.g. with an organosilane), so that the actual wetted surface is higher. Covalent bonds therefore lead to an increase of stiffness (D. Briesenick et al. (2015)[2]). Complex hierarchically organized colloids in biological composite materials such as nacre emerge in composite materials with roughly 1000-fold stiffer (protein) and 1000-fold tougher materials (calcite), compared to the pristine building units (**Figure 23**, black box).

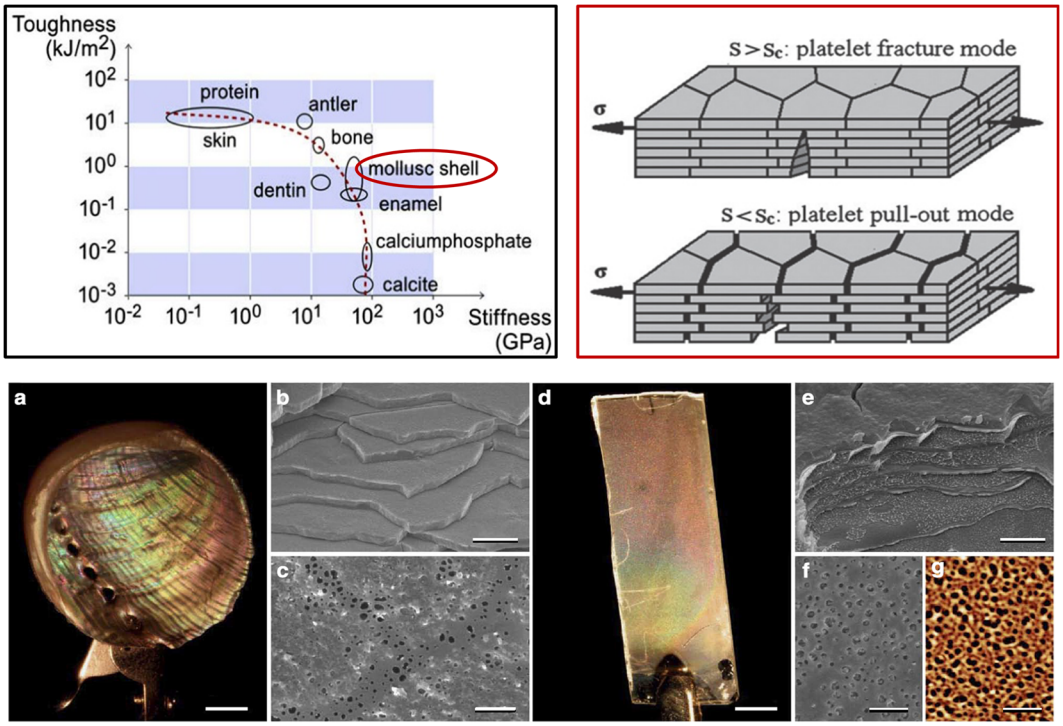


Figure 23: Composites with lamellar colloid structures
black box: "banana curve". Diagram taken from Espinosa et al (2009)[80]
red box: border Cases of failure mechanisms of lamellar colloid based composites
bottom: Mimicking nacre of a mollusk shell by the LbL-method. *left*: natural nacre; *right*: artificial nacre on metallic surface. Photographs taken from Finnemore et al. (2012)[81].

The banana shaped curve indicate the striving of biological material systems for the most efficient materials made of the available basic building units. It is well-known that the organization of the basic building units allow for the enormous enhancement of the pristine material properties and the pertinent self-organization within living organisms maintain and repair such material structures. Man-made composite systems can reach the mechanical

characteristics, whereas the focus lies on the adequate choice and development of materials with inherent characteristics rather than the hierarchical organization of available materials.
For example, the influence of the aspect ratio s of different layered silicates was examined in a non-ionic PVA matrix by Das et al. (2015) for aspect ratios ranging from s = 25 to s = 3500.[4] It was found, that composites with lower aspect ratios have higher toughness, whereas higher aspect ratios have a higher stiffness. The two border cases for the failure mechanisms in such systems are shown in the red box of **Figure 23**.
In case the tensile strength of the lamellar platelet σ_p is higher than the shear strength of the polymer matrix τ_y, the fracture of the lamellar platelet is more likely. A platelet pull-out mode is therefore favored, when the shear strength of the polymer matrix dominates over the tensile strength of the platelets. The border cases can be easily described by the critical aspect ratio s_c, which was also experimentally demonstrated by (Bonderer et al (2008)[82]):

$$s_c = \frac{\sigma_p}{\tau_y} \tag{6}$$

The parallel alignment of lamellar colloids is assumed to strengthen the composites, so that several Layer-by-Layer techniques or gravitational forces (sedimentation) are mostly used as the driving force. For example, Layer-by-Layer examinations on parallel aligned LDH/PVA composites with nacre-like aspect ratios were examined in the literature.[7]
A Layer-by-Layer mineralization approach of nacre-like structures is shown in Figure 23 (bottom). It should be noted that, the hierarchical structure of naturally occurring nacre is far more complex than just parallel aligned platelets with an efficient aspect ratio. The interface is maximized by closely packing of nanometer-sized aragonite colloids, enwrapped into proteins between a chitin matrix.[83] The LbL-method lead to materials with just about 50 % of the modulus of naturally occurring nacre.

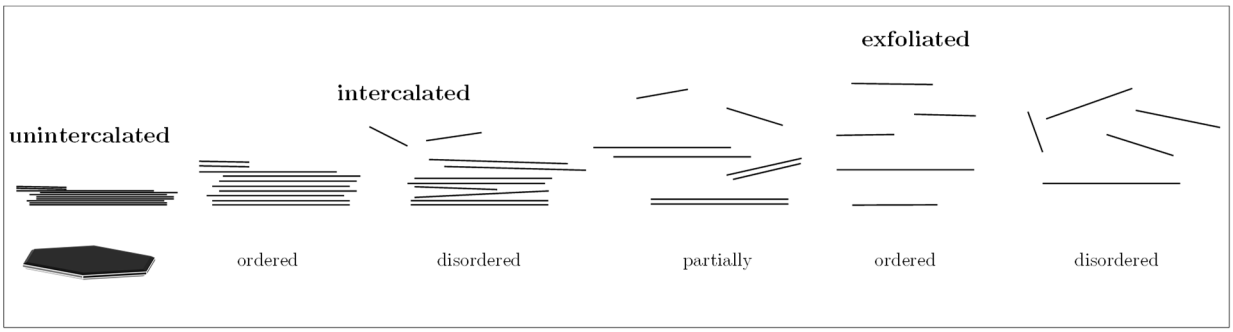


Figure 24: Nanoscale arrangement of lamellar colloids
The picture was taken from Vaia (2000)[84]

As stated before, the goal of the thesis is the parallel alignment of clay colloids by the self-assembly of spherical and lamellar colloids, whereas an exfoliation or intercalation of the lamellar colloids by the polymer colloids is desired in order to enlarge the effective interface between the components (**Figure 24**).

4 Replicative Building Units

This section is attributed to Section IV-5 (p. 152f) which deals with biomineralization experiments on proteins. Life on earth is known as a highly organized non-equilibrium system, which resist against the rise in entropy by forming steady states in the form of cycles in the form of circular cells. A prominent example for the replication of building units is the reoccurrence of clay minerals having reoccurring compositions within the so-called rock-cycle of the earth. The rock cycle is possible, because planet earth is in a thermodynamic non-equilibrium state. Reoccurring cyclic patterns throughout the space dimensions are evident (cf. **Figure 25**). A single cycle is called a limit cycle in the field of mathematics, initiated by Henri Poincaré in 1882,[85] put onto the list of David Hilbert's problems in 1900[86] (16. problem, not fully solved yet), whereas the application of those mathematical constructions to biological systems and the evolutionary behaviour thereof by the use of interacting cycles are called hypercycles, initiated by Manfred Eigen in 1978[87,88].

Our surroundings and ourselves are full of steady-state cycles moving around an equilibrium state. Celestial bodies follow cycle patterns: **Galaxies** have a spiral shape, one year accounts to one Earth cycle around the Sun, and one month is one Moon cycle around the Earth, whereas our solar system is part of **Milky Way**, which itself has a spiral pattern. The **streams of the oceans** of the earth show turbulent superstructures with cyclic shapes, so the gaseous troposphere and the crust on the liquid core (rock-cycle). The collision of such spiral structures emerge into so-called **spiral defect chaos** patterns, e.g. observable on the surface of **brain coral colonies**. Stable limit cycles spontaneously form out of chaotic into ordered patterns and attract the environment to copy the cyclic behavior. Such cycles are called attractors and can be compared with nucleation centers, which ultimately lead to an equilibrium state. Autocatalytic, therefore self-replicating species in reactions also have a cyclic/spiral/target shape and can be modelled if the kinetics are applied to diffusion laws.

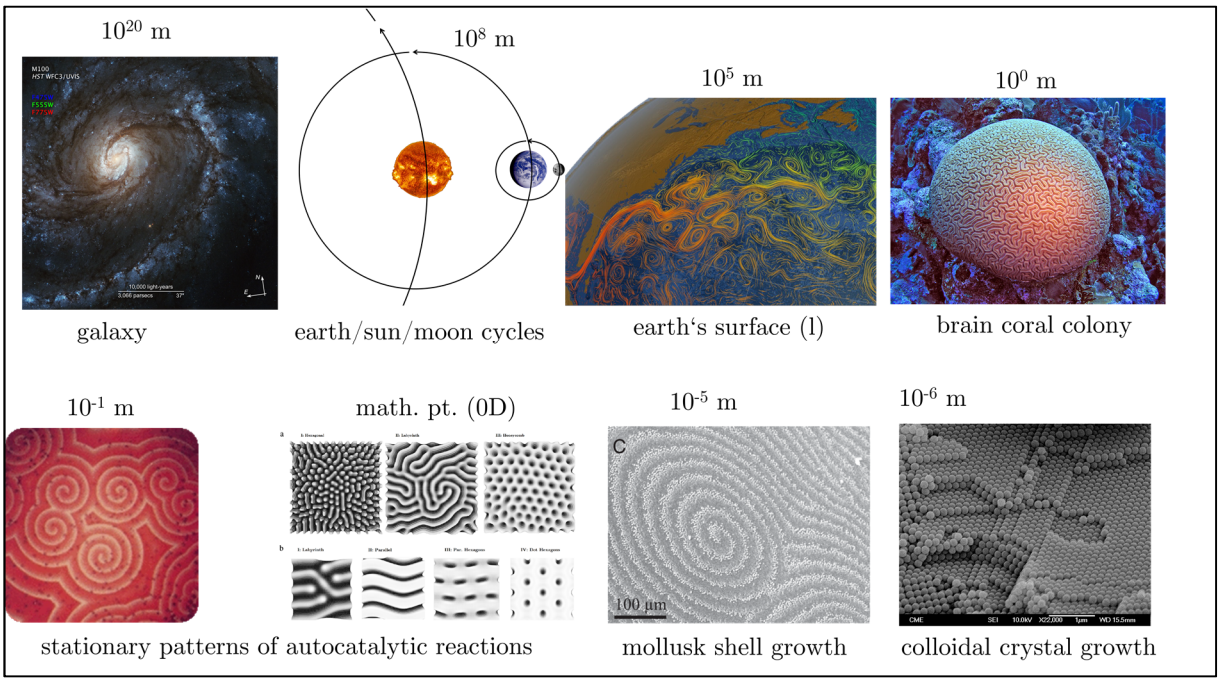


Figure 25: Similar ordered structures
at many scales with cycles, spirals, defects, chaos & order
UV-Vis image of M100 spiral galaxy[89] UV-Vis image of the sun[90] image (vis) of earth[91] image (vis) of moon[92] sea surface currents calculated from surface temperature[93] brain coral colony, 3x5m[94], BZ-reaction[95] numerical simulation of a coupled Brusselator kinetic-diffusion model[96] spiral pattern of growing nacre on a mollusk shell[97], colloidal crystal from monodisperse PS latex (200 nm)[98].

Autocatalytic cycles of inorganic, therefore rather "dead" species are known from the **BZ-reaction**, named after Belousov (1951)[99] and Zhabotinsky (1964)[100]. Further mathematical models followed by Prigogine et al. (1968)[101] (**Brusselator**: reaction & diffusion model) or already described by Turing (1952)[102] in a more general way earlier. Such wave patterns were recently observed and modelled by Tan et al. (2020) during the very early stages of life on the egg cells' surface of *Patiria miniata* starfishes[103], cf. **Figure 26**. In this context, one usually speaks of a 2D excitable medium.

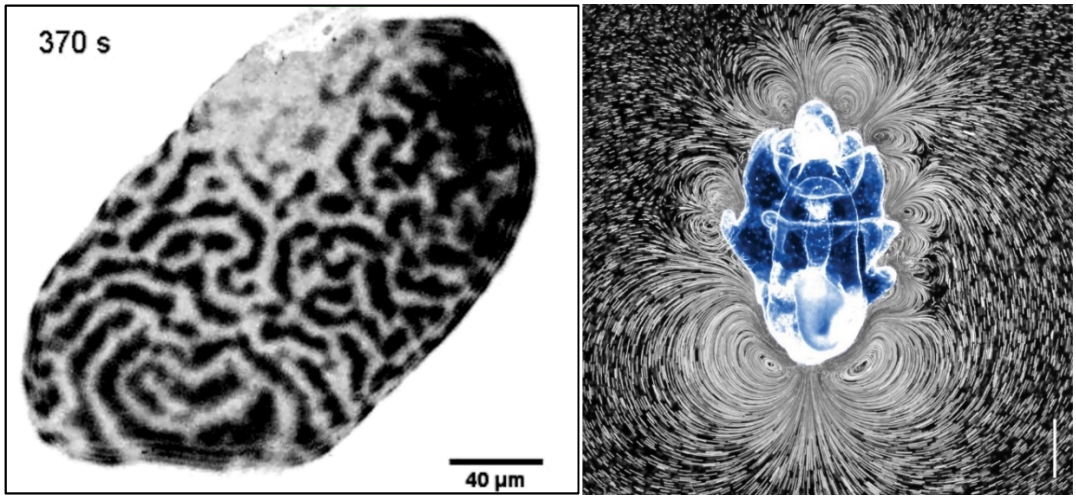
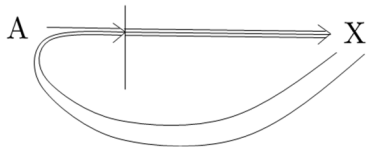


Figure 26: Cyclic vortices of proteins and water of *Patiria miniata* starfish
left: snapshot of signalling protein waves on the membrane of a starfish egg cell. Image taken from Tan et al. (2020)[103] with inverted B/W.
right: Starfish larva, about eight weeks old. Nine counter-rotating vortices are visible by 6 µm algae tracer particles in a dark-field movie. The swimming direction is upwards and the scale bar accounts to 350 µm. Image taken from Gilpin et al. (2017)[104].

The colloidal structures of **grown colloidal crystals** (and **early nacre growth**) shown in Figure 25 can be interpreted as 2D-screened gravitationally-collapsed structures[105] into an ordered and space-filling shape by the afore-introduced capillary assembly π, where the action of gravitation Γ and the surface energy γ act on the colloidal PS spheres (cf. II-3.2, p.21f). A colloidal crystal from PS spheres forms by the evaporation of water from an aq. colloidal dispersion droplet, whereas the colloidal crystals of mollusk shells, such as nacre, form under water, both representing non-equilibrium systems. The formation of nacre is much slower and controlled by a living organism, which has a high dynamical depth with many linked cycles at different scales and different functionalities allowing to sense the environment, whereas the drying droplet is maybe the simplest accessible case of a non-equilibrium state.
An oriented attachment of basic PS building units to colloidal crystals of PS can be described as an autocatalytic cycle, so that the mere existence of the species $2X$ (colloidal crystal PS colloids) and some active species A (single PS colloid) leads to more X after time and therefore growth of the colloidal crystal ($3X$). As long as active species A are present, the colloidal crystal grows and literally acts as an attractor. The simplest case and the nonlinear concentration dependence of such process can be written as:



$$A + 2X \rightarrow 3X \tag{7}$$

$$\frac{dX}{dt} = kAX^2 \tag{8}$$

In the earlier-mentioned Brusselator model, the catalysis is more complex and behave reciprocal, meaning that catalysis and inhibition interact by feedback-loops, so that these states are far away from equilbrium, ergo non-equilibrium states. The feedback-loops play a crucial role in molecular biology: for example the nucleic acids contain information to produce proteins, proteins produce nucleic acids and so on (cf. **Figure 27**). The coupling of such self-replicative networks of limit cycles - Hypercycles -were theoretically described by Eigen (1978)[87]. The model conclude the following properties of hypercycles:
The coexistence of cyclic species are stable and controlled via cyclic linkage and coherent growth is allowed. The coupling of the cycles can be attractive or repulsive, dependent on the stability of the cycle. A stable limit cycle is attractive. The cycles compete with any other outer replicative unit, e.g. an other limit cycle, hypercycle or a 'parasitic coupled' cycle. The enlargement or reduction of the size is done by selective advantage, whereas maintaining the stability of information and promoting the evolution of the information (in phenotype and genotype). The linkage of cycles is not easily done and needs high order linkage. The internal linkage evolve to optimal function.

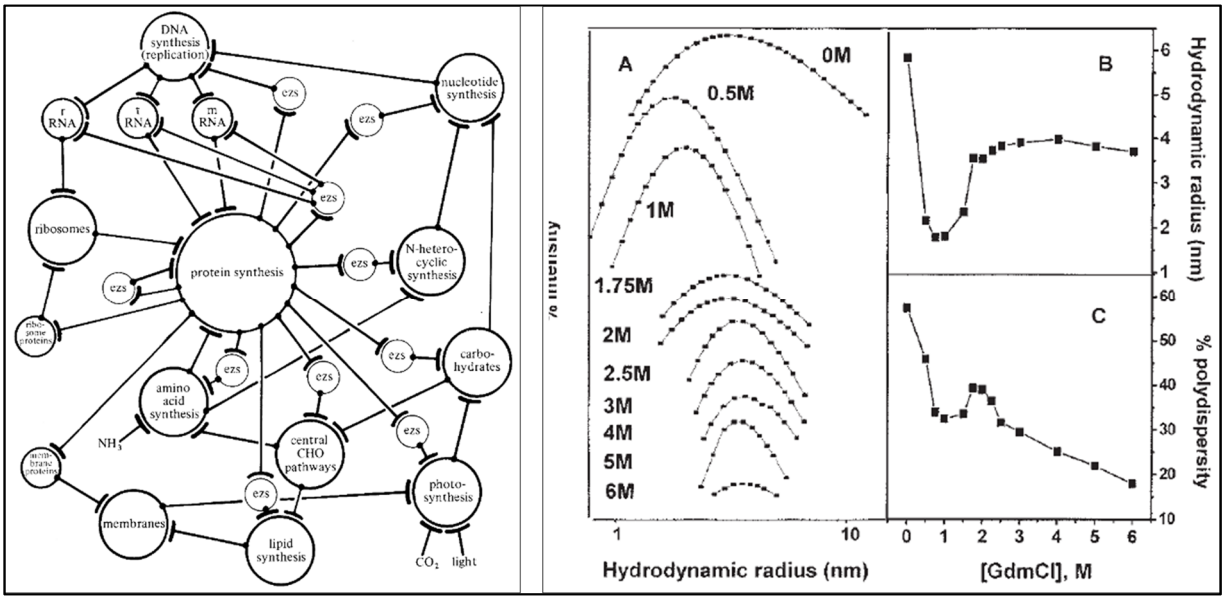


Figure 27: Enzymatically linked reactions and colloidal behavior of enzymes
left: Some interdependences of central biochemistry by Cairns-Smith (1982)[25]. ezs: enzymes
right: Lipase size in dependence of ionic strength. The broadness of the size distribution of this enzyme change with the surrounding charge distribution.[106]

Cells are based on complex composite materials, which resist outer pressure and organize to room-efficient structures with the help of lipid-layers, which form a stable, closely packed, charged and permeable coating towards the environment. The thrive for energy-efficient design of interfaces and interphases by organisms is omnipresent and acts beyond the scale of cells, emerging into the allometry of living organisms. Resistance against pressure is optimized in multicellular organisms, because the interface towards air or water becomes smaller and specialized cells create the boundary towards the environment (e.g. skin cells, mollusk shells). Viruses, which are not considered as 'living' do the same, such as a bacteriophage protects its DNA within an icosahedral structure.
Moreover, it is interesting to have a look on the allometric-scaling of living systems, since it is closely related to the introduced Nano-Effect (II-1.1, page 6), where the surface area A per volume V of non-living spheres and plates are considered. Moreover, non-living systems also form symmetric structures against temperature and pressure, shown in **Figure 28**:

Thermally-driven cyclic trajectories of molecules (such as water molecules) in a flat dish was experimentally described by Bénard (1900)[107] and mathematically described by Rayleigh (1916)[108], and also found herein by accident during experiments with vermiculite dispersions (not further described). The occurrence of capillary hexapoles was already described above in the section about capillary assembly π. Both have in common, that these "cells" form structures with six neighbours for maximum space filling.

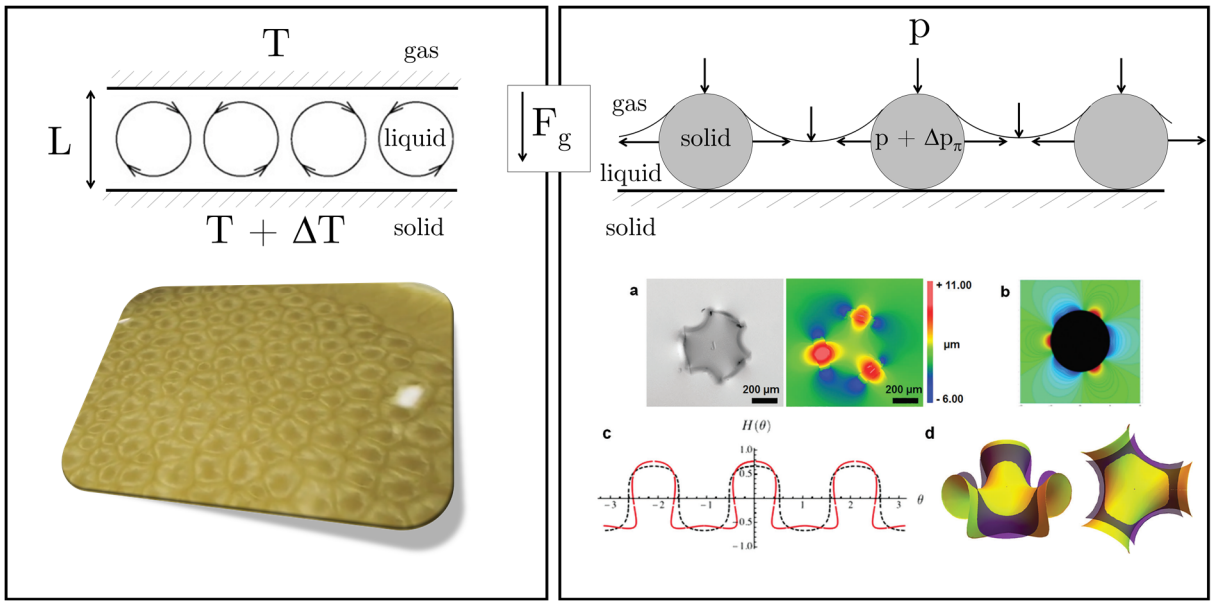


Figure 28: Self-organization by the aid of gravity: temperature and pressure gradients
left: Rayleigh-Bénard convection cells from a clay suspension in a water/ethanol/mixture, top scheme is adapted from the literature[109]
right: capillary hexapoles of floating particles, Bae et al. (2017)[110], top figure shows how atmospheric pressure p and capillary pressure Δp_π acting on colloids

Living organisms are highly organized dynamic systems, which permanently perform self-repair of teeth, skin and many more important biomaterials. The controlled assembly of colloids is realized in nature in order to tailor the necessary functionalities. Superorganisms like coral or ant colonies are synergistically acting organisms of a single species, which form organized structures with emerging new properties by behaving like one organism (cf. also swarm behaviour of fishes). A multicellular organism like a mammal is assumed to have a higher selective linkage between the cells, forming (hyper)cycles. Thereby, the occurrence of multicellular organisms most likely evolved by trial and error cycles, thereby gaining information exchange densities and cyclic linkages with high selectivity. Deacon et al (2014) claim in a paper on information theory[111] that *information density* can be interpreted as the compactness with respect to the amount of detail some information accounts for, whereas the number of *dynamic levels* of the organization pattern account to the *dynamical depth*. The nested dynamical levels behave in a way in order to reduce local entropy. Thus, a drying droplet has lower dynamical depth than the oscillating BZ-reaction and living systems have a high dynamical depth, e.g. local dynamical levels of the human organism:
10^{-9} m: DNA diameter; 10^{-8} m: ribosomes & DNA; 10^{-7} m: microtubule organizing center; 10^{-6} m: cells & chromosomes; 10^{-5} m: blood cells; 10^{-4} m: human egg, skin cells; 10^{-3} m: skin thickness; 10^{-2} m: inner organs; 10^{-1} m: extremities; 1 m: human organism.
It should be noted in this context that also any protein molecule has a much higher information density than a monodisperse polystyrene colloid or a polydisperse polyurethane colloid, both

being used throughout the thesis (cf. information densities bit/N in **Figure 29**, based on the works of C.E. Shannon on information entropy[112]). An extra section describes drying droplets containing proteins (Section IV-5, page 152f). The enzyme chymosin selectively cleave κ-casein chains at a distinct location of the amino acid sequence, so that the hydrophilic part caseinomacropeptide CMP of the casein colloid is separated from the more hydrophobic proteins α_{S1}, α_{S2}, β, and the residual para-κ-casein.

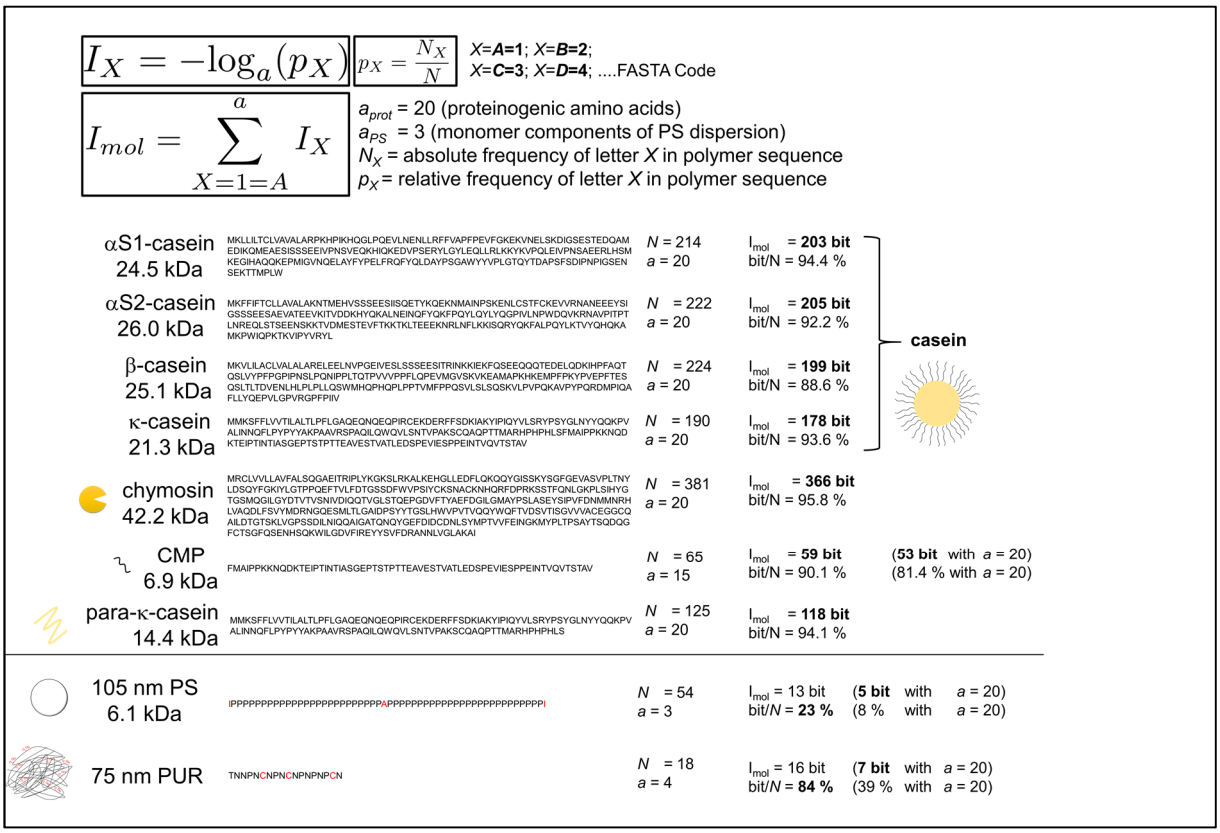


Figure 29: Information density for the case of statistically independent monomeric units
The used equation is based on information theory (Shannon entropy). For the synthetic products PS and PUR, the theoretical number average of the molar mass was calculated from the weighed portions and correlated with GPC measurements on PUR (Figure 137, page 148). GPC measurement on PS dispersion failed in standard solvents.

With respect to the (coating) materials' properties one have to note that the glass transition temperature T_g of casein is a function of the moisture content and the measuring method and cannot be defined easily, whereas measured values of 20 to 140 °C are reported.[113]

5 Analytic Methods

The central analytic tools used in the thesis are presented in the following. For a deeper understanding and for further possibilities on usage of the techniques, literature references are provided in the following text, if not already described above.

The size distribution of spherical and lamellar colloids and their organization in dried state can be measured manually from **Scanning Electron Microscopy (SEM)**[114] photographs (Zeiss NEON 40)[115]. Two different detectors (SE2, Inlens) analyze electrons from the sample surface and can give complemental information, e.g. about the 3D morphology (SE2) and material contrast (Inlens). In almost all cases and if not stated otherwise, the sample substrate is a flat silicon wafer, cut to quadratic or triangle-shaped pieces prior use (approx. 1 x 1 cm). The silicon wafers are stored in iso-propanol, dried prior use and glued with silver flakes containing glue on a sample holder. A droplet of the mostly aqueous dispersion is placed on the silicon wafer with a disposable pipette and dried at ambient conditions. Thereafter, a 3 nm thin Au/Pd plasma sputtered coating under reduced pressure is applied on the sample to provide electron conductivity.

The organization in composite films is examined by preparing cross-section with a **Focussed Ion Beam (FIB)**[116] of the aforementioned Zeiss NEON 40 SEM unit. The graphic analysis of the SEM cross-section images was made with ImageJ and calculated to analyze particle-particle distance distributions (e.g. compare Figure 24 on page 25). Moreover, the qualitative analysis of the colloidal morphologies in the cross-sections of the composite materials was conducted to obtain information of the assembly mechanisms.

Dynamic Light Scattering (DLS)[117] measurements, also known as photon correlation spectroscopy (PCS), were performed in order to obtain colloid size distributions. The measurements were conducted with a Malvern Zetasizer Nano ZS with disposable cuvettes (if not stated otherwise). The measurement of bigger colloids were performed with a Malvern Mastersizer 2000 in a MS-1 sample unit and a 300RF lens, which allows detection of colloid sizes from 0.05 to 880 µm. Alternatively, a "MS-7" magnetic stirred cell (beam length 10 mm, 300F lens) was used to perform time-dependent measurements on the size of organized colloids.

A feasible method to measure the surface charges of colloids is a **ζ-Potential** Measurement[118]. Measurements were performed with a Malvern "Zetasizer Nano ZS" in disposable, U-shape folded capillary cells. Optionally, the autotitration unit "MPT-2" with Vacuum Degasser is installed to add colloids, salts, acids or bases automatically.

The *d*-spacing of lamellar colloids was measured by **X-Ray Diffraction (XRD)**[119] with a Bruker D5005 (Cu-Kα = 0.154 nm).

The shape of some synthesized polymer colloids (PUR & PS-based) was determined via **Multi-Angle Static Light Scattering (SLS)**[120,121]. The measurement was conducted on an ALV "5000E CGS". The measured angles were 30 to 150 ° with 5 ° steps and 3 measurements á 10 s for each angle. The calculation of the gyration radius (R_g) and hydrodynamic radius (R_h) was performed by associated members of AK Huber at Paderborn University.

Moreover, the extent of particle-particle interaction of two-component systems (spherical & lamellar) was measured with a **Couette Rheometer** "Anton Paar Rheolab QC" (compare II-2.1, page 14). The thixotropic properties of wet composite material was examined systematically in dependence of the size of the colloids.

The solid content of diluted dispersions or indications for the yield of grafting reactions were examined with **Thermogravimetric Analysis (TGA)** "Mettler-Toledo TGA/SDTA 851e",

mostly with a heating rate of 5 °C/min with synthetic air as carrier gas. A Thermogravimetric analysis monitors the change in mass by applying a temperature program on the sample.
The chemical environment of modified kaolinite colloids was examined via **Nuclear Magnetic Resonance (NMR) spectroscopy**[122,123,124,125]. Herein, ^{27}Al-NMR measurements are conducted to examine the bonding state of aluminum species in kaolinite and their change after silylation with APTES.
Elemental analysis is performed parallel to SEM examinations with an additional **energy dispersive x-ray spectroscopy (EDX)**[126] detector, with the commercial name "Thermo Fisher Scientific Ultra Dry" . The combined SEM/EDX technique allow for a spatial resolution of elemental analysis**.**
The isocyanate conversion of the polyurethane synthesis was monitored by Attenuated Total Reflection Fourier-Transformed **Infrared Spectroscopy**[127] **(ATR-FTIR) "**Bruker Alpha-P" (λ = 633 nm). Modified kaolinite particles were analyzed also by Infrared Spectroscopy (**IRRAS**: Infrared Reflection Absorption Spectroscopy) on a Bruker "VERTEX 70". Characteristic frequencies are taken from the literature.[128]
The surface energies of organized colloid films were measured by a **Contact Angle Measurement** with a KRÜSS "Drop Shape Analyzer 25E". The surface energies of the surfaces was determined by the "OWRK-method" (Owens-Wendt[129]-Rabel[130]-Kaelble[131]).
Phase transitions of freeze-dried polymer dispersions were examined with **Differential Scanning Calorimetry (DSC)**[132]. The samples were freeze-dried and pre-examined by TGA in order to rule out the presence of solvent in the examined temperature range of the DSC measurement.
Further tools, methods and details concerning the functional principles are described in the respective experimental details and are fully listed in the Appendix (page 195).

III Preparation & Synthesis of Colloids

Before starting to introduce any assembly-related experiments, the conducted colloid preparation & synthesis are presented and the evaluation of the colloids with respect to

- surface charge (meas. ζ-potential)
- primary colloid size (meas. DLS and SEM)
- composition and structure (meas. EDX/TGA/IR/XRD/NMR)

are presented in the following.

Again, the most important colloids in this work are layered double hydroxides LDH, kaolinite K, polystyrene PS, silica SiO_2 and polyurethane PUR colloids. In the next step, the prepared colloids are mixed with different plate/sphere mass ratios by simultaneously varying the size and thickness of either the lamellar or spherical colloids, depending on the case of assembly, all described in **Section IV** (page 56ff).

This work provides a look over a broad range of examined colloids: with spheres ranging from approx. 10 to 500 nm in diameter with preferably monodisperse size distributions, and plates ranging from 300 nm to 5,000 nm in lateral size (also long cylinders with a 6,000 nm diameter, meaning carbon fibers). In addition to the synthesized colloids of this chapter, some commercially available colloids were examined.

1 Layered Double Hydroxides

In the following, the applied procedures of the synthesis and modication of LDH phases are presented. The preliminary testing of the synthesis include four different set-ups. In a first approach, a syringe driver conducted the constant flow of the metal salt solution and the pH-regulating flow was tried to do by hand. In a second approach, an automated parallel reactor system by Hitec Zang GmbH is used to keep the pH constant. The reactor system is working with solenoid valves and gravimetric dosing module ("GraviDos"). In a third approach, a syringe driver is used as the constant flow instrument and a programmed pH electrode/peristaltic pump system is used.

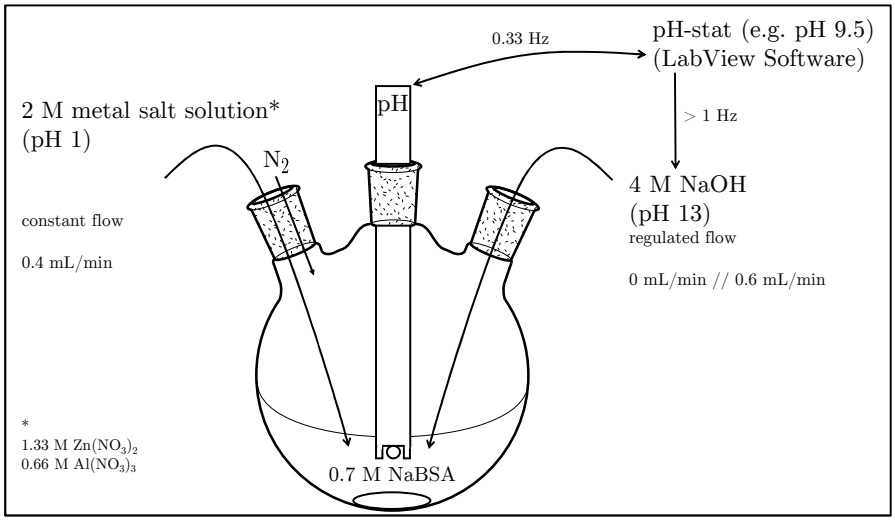


Figure 30: Scheme of LDH synthesis setup
The flask is air-tight, the tubings have an inner diameter of 0.8 mm

In the last and fourth approach, a peristaltic pump is used as the constant flow and a programmed pH electrode/peristaltic pump system is used as a pH-regulating flow. The pretested approaches 1-3 are shown in the Appendix in more detail (page 197f). In **Figure 30**, the final experimental setup is illustrated. The standard composition of the synthesized LDH phases are $Zn_2Al(OH)_6[BSA]$ and $Zn_2Al(OH)_6[NO_3]$, respectively.

1.1 Experimental Part

Materials

Table 1: Materials for LDH synthesis

Name	Purity/ NVC	Supplier
pure water		
acetonitrile	≥ 98%	Sigma Aldrich
ethanol	≥ 98%	Sigma-Aldrich
zinc nitrate hexahydrate	≥ 98%	Alfa Aesar
aluminum nitrate nonahydrate	≥ 98%	Carl Roth
sodium hydroxide	≥ 98%	Sigma-Aldrich
sodium benzenesulfinate	≥ 98%	Acros Organics
taurine	≥ 99%	ACS
glycine	≥ 98.5%	Merck
betaine	≥ 98%	Sigma-Aldrich
lecithine ("Phospholipon® 90G")	≥ 94%	Phospholipid GmbH
sodium dodecylsulphate		Sigma-Aldrich
sodium carbonate		STOCKMANN
sodium lactate solution	60 wt.-% in H_2O	Sigma-Aldrich

Methods

Dynamic Light Scattering (DLS)
Malvern Zetasizer Nano ZS, Malvern Mastersizer 2000
Zeta Potential Measurement
Malvern Zetasizer Nano ZS
Scanning Electron Microscopy (SEM)
Zeiss NEON 40
Elementary Analysis
EDX of Zeiss NEON 40
X-Ray Diffraction (XRD)
Bruker D5005 (Cu-K_α = 0.154 nm).
Parallel Reactor System
Hitec Zang LabKit #2026
pH Electrode
Mettler Toledo SevenMulti pH-Meter
Syringe Driver
B. Braun PERFUSOR IV
Peristaltic Pump
Heidolph PD5201 (constant flow); Heidolph Hei-FLOW Precision 01 (regulated flow)
Regulating Software
LabView 2014 (block diagram in Appendix, p.199)

1.1.1 Synthesis of 400 nm sized Zn_2Al-BSA

Zn_2Al-BSA is prepared by using the co-precipitation method. Therefore, 130 mL of a 2 M metal salt solution containing $Zn(NO_3)_2 \cdot 6\ H_2O$ and $Al(NO_3)_3 \cdot 9\ H_2O$ in a 2:1 molar ratio was added into 250 mL of a 0.7 M Sodium Benzenesulfonic acid (NaBSA) solution under nitrogen atmosphere. The flow of the metal salt solution is held constant at 0.6 mL per minute. Simultaneously, a 4 M NaOH solution is added in a regulated flow to keep the pH constant at 9.0.

1.1.2 Synthesis of 800 nm sized Zn_2Al-BSA

Zn_2Al-BSA is prepared by using the co-precipitation method. Therefore, 130 mL of a 2 M metal salt solution containing $Zn(NO_3)_2 \cdot 6\ H_2O$ and $Al(NO_3)_3 \cdot 9\ H_2O$ in a 2:1 molar ratio was added into 250 mL of a 0.7 M sodium benzenesulfonic acid (NaBSA) solution under nitrogen atmosphere. The flow of metal salt solution is held constant at 0.6 mL/min. Simultaneously, a 4 M NaOH solution was added in a regulated flow to keep the pH constant at 9.5. After the synthesis, the precipitate is washed seven times by centrifugation and transferred into an airtight and nitrogen flushed sample container.

1.1.3 Synthesis of 3200 nm sized Zn_2Al-BSA

To obtain bigger LDH colloids, the synthesis was conducted using a glycine-NaOH buffer at 9.5 according to Ruzin (1999)[133]. Therefore, 0.94g of glycine and 0.23g of NaOH were added and dissolved in the 0.7 M NaBSA solution at the beginning of the synthesis.

1.1.4 Synthesis of 1 µm sized Zn_2Al-NO_3

Zn_2Al-NO_3 is prepared by using the co-precipitation method. Therefore, 130 mL of a 2 M metal salt solution containing $Zn(NO_3)_2 \cdot 6\ H_2O$ and $Al(NO_3)_3 \cdot 9\ H_2O$ in a 2:1 molar ratio was added into 250 mL pure warer under nitrogen atmosphere. The flow of metal salt solution is held constant at 0.6 mL/min. Simultaneously, a 4 M NaOH solution was added in a regulated flow to keep the pH constant at 9.5. After the synthesis, the precipitate is washed seven times by centrifugation and transferred into an airtight and nitrogen flushed sample container.

1.1.5 Kinetic Measurements

During the synthesis, small parts (2 mL) of the suspension are removed, centrifuged (one time, 5 minutes, 13,000 rpm) and the electrical conductivity of the supernatant is measured using Malvern Zetasizer Nano-ZS. The net conductivities of relevant concentrations of aq. NaBSA, aq. $Zn(NO_3)_2$, aq. $Al(NO_3)_3$ and aq. NaOH solutions were also measured (Appendix, page 200).

1.1.6 Examination of LDH stability

The post-treatment of the synthesis described in 1.1.2 is a seven-step centrifugation. To examine the LDH stability, two small portions (approx. 0.2 g) of each step were isolated as a slurry and as a dispersion in pure water, respectively. The individual pH values of the dispersions were measured immediately and one more time after 48 hours. Moreover, the particle size of each slurry and each dispersion was measured using DLS (28 samples). The mass content for the measurements of the slurries and dispersions are diluted to approx. 0.1 wt.-%.

1.1.7 Reactive Intercalation with Trimethylethoxysilane

In a polymeric vessel, 0.64 g of a 1 µm LDH-BSA slurry (15.8 wt.-%) is dispersed in 65 g EtOH by magnetic stirring. Subsequently, 260 µL trimethylethoxysilane (TMS) were added stepwise to prevent dimerization (0 min: 10 µL, 1 h: 50 µL, 1.5 h: 50 µL, 22 h: 50 µL, 24 h: 50 µL, 26 h: 50 µL). The total addition of TMS structural OH-groups of the LDH phase. The mixture is refluxed at 70 °C in a round-bottom flask with reflux condenser for 24 hours. After cooling

to r.t., the mixture is placed into a snap-cap vessel and allowing sedimentation to the colloids until a clear and blue dispersion appears above the sediment (days).
The supernatant dispersion (approx. 0.05 wt.-%) is then mixed with a commercial polyurethane dispersion (Bayhydrol® UH 2621; 40 wt.-%) to obtain a LDH content of approx. 1 wt.-% in the resulting dry film. The dispersion is applied with a 50 µm doctor blade and dried at 80 °C for 45 min. Subsequently, the resulting film is sputtered with Au/Pd and examined via SEM and FIB technique.

1.1.8 Ionic Exchange Reactions

Ionic Exchange reactions were carried out at different conditions and requirements throughout the thesis. LDH phases have anions trapped in the intergalleries. The two compositions $Zn_2Al(OH)_6[BSA]$ (M = 417.01 g/mol) and $Zn_2Al(OH)_6[NO_3]$ (M = 321.80 g/mol) were investigated.
In most cases, a 10-fold molar excess of the respective exchange ion is added to a LDH dispersion in water or water/solvent mixtures (0.5 to 10 wt.-% LDH) and mixed for 48 hours. The pristine LDH dispersion should have a low conductivity (lower than 0.1 mS/cm) and a low mass content (1 wt.-%) for the exchange to succeed. Subsequently, the colloids are centrifuged until the electric conductivity has values near pure water (at least 0.1 mS/cm, mostly 6-7 centrifugation steps). Zwitterions do not have an electric conductivity; the samples were centrifuged accordingly.
The preparation of LDH-taurine in water was difficult, since the solubility auf taurine is low. Therefore, 1.4 g LDH-NO_3 slurry (NVC approx. 40 wt.-%) were dispersed in 22 g acetonitrile by magnetical stirring. 20 g of saturated aq. 0.5 M taurine solution were mixed (10-fold excess) and stirred for 48 hours. Accordingly, 2 g LDH-BSA were mixed with 34.5 g acetonitrile and 22.5 g of 0.5 M taurine solution is added (5-fold) and stirred for 48 hours.
The preparation of LDH-betaine was conducted by mixing 30 g ethanol, 1.4 g LDH-NO_3 slurry (NVC approx. 40 wt.-%)and 2.3 g of aq. 4.2 M betaine solution (10-fold excess, pH 9 with 0.5 M NaOH). The mixture is stirred for 48 hours. Accordingly, 2 g LDH-BSA were dispersed in 37 g EtOH, then 5.2 g aq. 4.2 M betaine solution (pH 9) was added and stirred for 48 hours.
The LDH-dodecylsulphate phase was prepared from LDH-BSA and LDH-NO_3 in the same way. A SDS solution is prepared from 3.6 g SDS in 13.8 g water and is added to a dispersion of 2 g LDH-slurry in 20 g water and stirred for 48 hours.
The LDH-glycine was used in rheological experiments and are described in more detail below. 5.9 g LDH slurry is dispersed in 55 g of water. Then, 4.35 g glycine dissolved in 100 g water is added and stirred for 48 hours.
As a reference, LDH-carbonate phases were prepared. 1 g LDH-BSA, 1.3 g Na_2CO_3 and 20 g H_2O were mixed and stirred for 48 hours. Accordingly, 1 g LDH-NO_3, 1.7 g Na_2CO_3 and 28 g H_2O were mixed and stirred for 48 hours.

1.2 Results and Discussion

In the following subsection, the synthesis, kinetics, stability and ionic exchange reactions of LDH phases are discussed. The colloids are synthesized by the co-precipitation method. A 2 eq. intercalator (NaBSA) solution was prepared, the mixed metal nitrate solution (Zn:Al 2:1 mol:mol) is added with a constant flow, whereas the NaOH solution is added as soon as the transmitted pH value from the pH meter drops below pH 9.5. It is well known in literature, that reproducible particle size distributions can be synthesized by keeping the pH at a specific value.[134] The smaller the deviation from the preset pH value is, the bigger the colloids are allowed to grow. The deviation from the pH is strongly connected to the flow rate of the solutions and the signal transmitting time. The chosen systems keep the metal salt nature and ratio constant ($Zn_2Al(OH)_6$). Zinc and aluminum are chosen because of the cheap price and suitability as a multifunctional filler for coatings.[27] The flow rates throughout all experiments is kept at the lowest possible level. The synthesis pH was set to 9.0 to obtain smaller LDH colloids. In all experiments, a 2-fold excess of the intercalated ion is provided.

1.2.1 LDH synthesis and kinetics

The formal precipitation reaction of the LDH synthesis is best described by the following reaction equation:

$$2\ Zn(NO_3)_2 + Al(NO_3)_3 + 6\ NaOH + 2\ NaBSA \rightarrow Zn_2Al(OH)_6[BSA]\downarrow + 7\ NaNO_3 + 1\ NaBSA$$

The reaction is monitored using electrical conductivity measurements (cf. **Figure 31**). The spectator salts sodium nitrate and sodium benzenesulfinate are highly soluble and remain in the bulk solution during the precipitation. After centrifugation, the supernatant is measured. The resulting conductivity should represent the concentration of the mentioned soluble salts. In order to interpret the conductivity values, the conductivity measurements are conducted on solutions of NaOH, $Zn(NO_3)_2$, $Al(NO_3)_3$ and NaBSA in dependency of the relevant concentrations. These measurements are shown in the Appendix on page 200. The dependency of $NaNO_3$ conductivities against the concentration are taken from the literature.[135] The conductivity of the used pure water is 0.025 mS/cm (c=0). The electrical conductivities at known concentrations are extracted from polynomial fits. The measured and theoretical electrical conductivity vs. time of the synthesis is shown in Figure 31.
Theoretical calculations on the synthesis need an accurate concentration profile of the reaction. The concentrations of the individual ions i are calculated with equation (9).

$$c_i(t) = c_i(0) + \frac{c_i \cdot \dot{V} \cdot t}{V(t)} \tag{9}$$

The flowrate $\dot{V}$ is fixed at 0.55 mL/min (measured 10 times by volumetric measurement). In the equation, *c(t)* and *V(t)* are the concentration and the volume of the reactants in the reactor at time t. The value $c_i(0)$ represents the concentration of the ions i in the reactor at t=0 min and c_i represents the concentration of the ion i in the feed solutions.

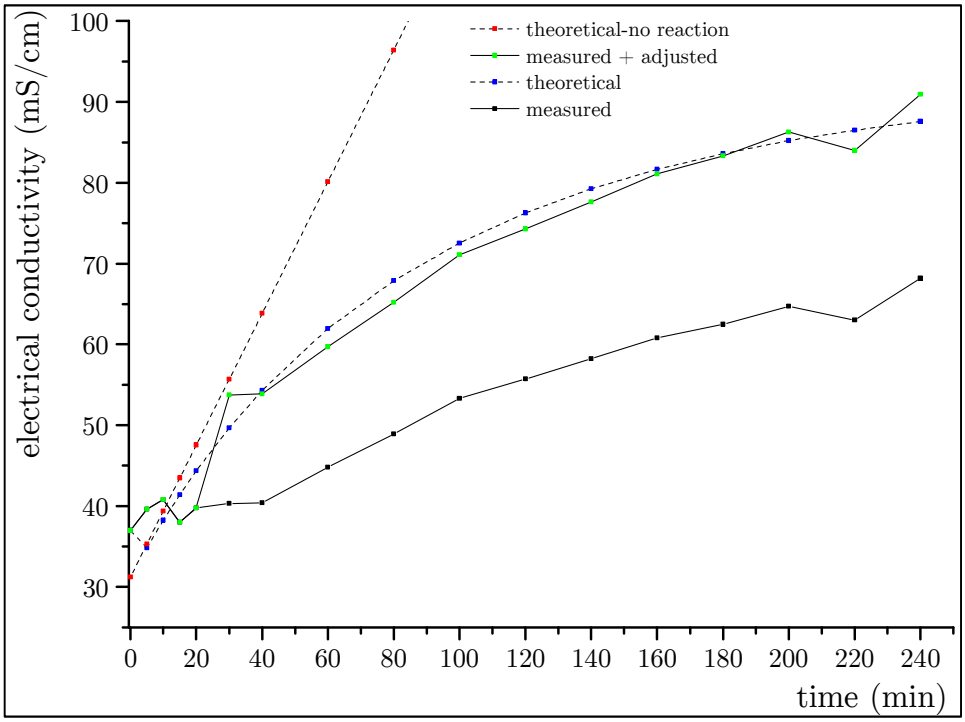


Figure 31: LDH kinetics: electrical conductivity vs. time
The adjustment of the measured values (▪) is done for measurements with $t > 20$ min, more specifically at mass fractions higher than 1 wt.-% during synthesis. Approximately one third of the ions stay in the solid phase after the first centrifugation (see **Table 3**, Z0 → Z1). Therefore one third of the measured value is added on the initial measured value.

In early stages of the synthesis, the solid content is smaller than in later stages of the synthesis. Therefore, the measured conductivity values in later stages of the synthesis lead to comparably smaller values due to adsorbed ions in the solid phase. The side product ZnO also lead to inaccuracy of the measured kinetics. In the first 40 minutes, the nucleation of LDH colloids is believed to dominate over growth, followed by 200 minutes of growth dominating over nucleation. Moreover, SEM images show that the thickness build-up happens at $t < 30$ min, followed by lateral growth at almost same thicknesses (**Figure 32**).

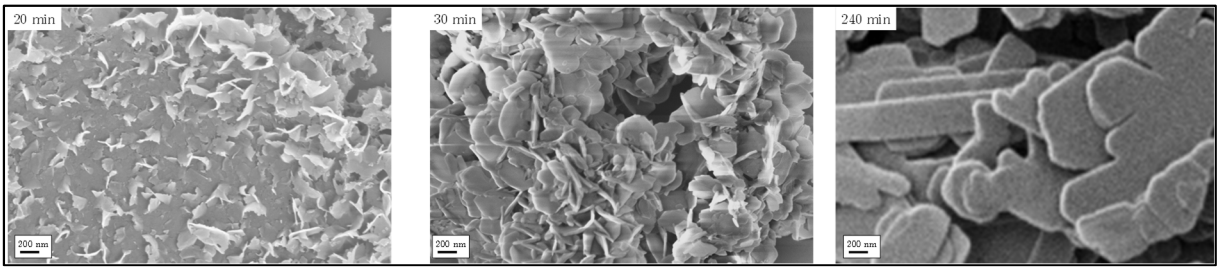


Figure 32: Change in LDH morphology vs. addition time

In summary, it can be stated, that the LDH coprecipitation reaction was successfully done with a yield near 100 % with considerable losses during the centrifugation post-treatment.

1.2.2 Control over LDH particle size

As it is known from literature and the described preliminary tests, LDH phases nucleate at specific pH ranges depending on the ion species and grow at held-constant pH values. Here, the chosen value is 9.5 in order to prevent surpassing the lower border of pH 8.5, attributed to LDH dissolution and the upper border of pH 10.0, attributed to precipitation of ZnO.[136] Without the use of a buffer system, the deviation of the pH in the beginning of the synthesis

is very high (ΔpH = $\pm$1). By using a glycine buffer, the deviation of the pH throughout the synthesis is way smaller (ΔpH = $\pm$ 0,075) and leads to much bigger colloids with about 5 µm in lateral size, whereas the other samples have lower diameters (cf. **Figure 33**).
The buffering capability of glycine containing solutions is comparably high at low ionic strength because of the amphoteric character of glycine. The carboxyl group of the glycine ion is most likely deprotonated and negatively charged at pH 9.5 (IEP: pH 6)[137] and therefore should be able to intercalate into the LDH interlamellar voids. The concentration of glycine during the synthesis is low, compared to NaBSA (50 mM Gly vs 700 mM BSA). The proton acidity and therefore the effective charge of benzenesulfonic acid is also higher ($pK_{a,BSA}$: -2,8)[138] compared to the carboxylic acid group of glycine ($pK_{a1,Gly}$: 2,3)[137].

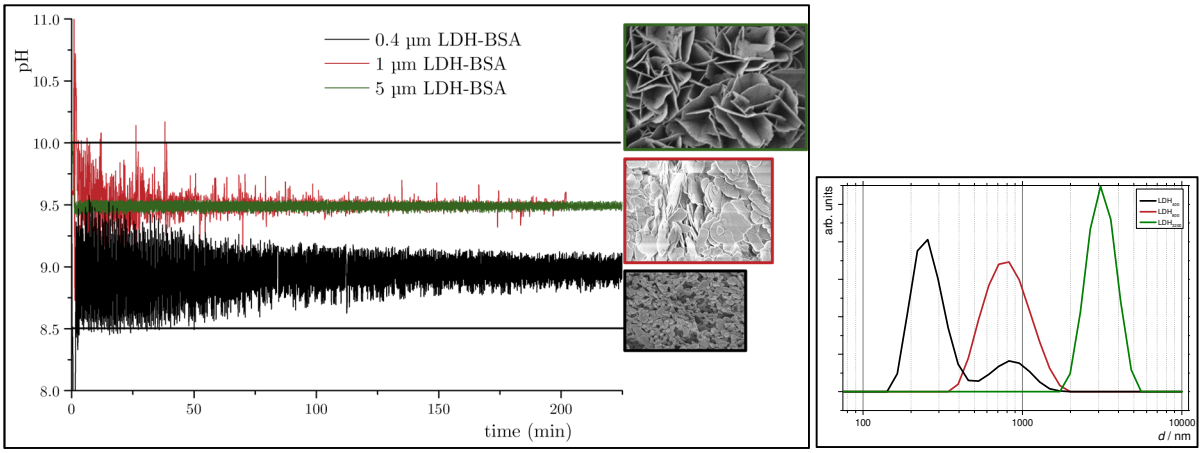


Figure 33: pH vs t plot, SEM and DLS results of the different sized LDH-BSA colloids
The colored frames of the SEM image relate to the colored pH/time curves. The SEM images all have the same magnification.

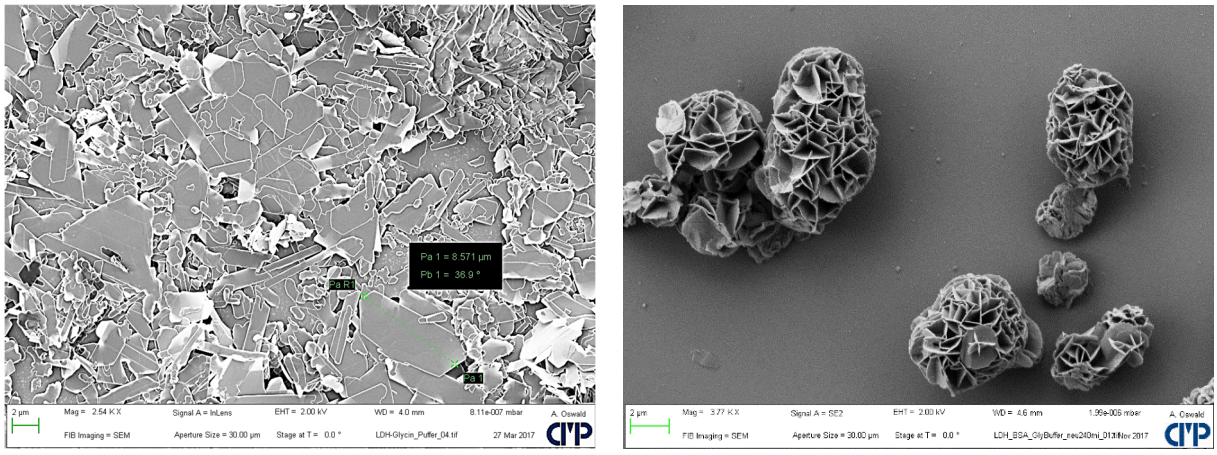


Figure 34: Two morphologies obtained from the glycine-buffer synthesis route

To the best of my knowledge, the presented glycine-based buffer synthesis route is not reported in the literature yet. However, two different morphologies were obtained by using seemingly same reaction conditions, shown in **Figure 34**. In this work, the intertwined structures (right image) was obtained in 9 out of 10 syntheses, whereas no reason was identified, why the left structure emerged, where no intertwined structures were found throughout the sample. From the resulting Zn/Al ratios (cf. **Table 2**), it is evident, that the bigger sizes tend to have a higher surface charge.

Table 2: EDX results on the three LDH phases

Element	**LDH_{400}**		**LDH_{800}**		**LDH_{3200}**	
K line	**atom.-%**	**Δ atom.-%**	**atom.-%**	**Δ atom.-%**	**atom.-%**	**Δ atom.-%**
Zn	14.4	0.3	12.8	0.2	11.5	0.2
Al	7.1	0.1	7.4	0.1	7.0	0.1
S	5.1	0.1	5.3	0.1	5.2	0.1
O	49.0	0.4	48.6	0.4	49.2	0.4
C	17.2	0.4	17.4	0.4	18.8	0.4
Na	7.1	1.7	8.5	1.7	8.2	1.5

1.2.3 Examinations on the LDH stability

During the LDH synthesis there are a lot of extant ions, which do not precipitate. A centrifugation process removes these ions. The presence of the ions can alter the size and morphology of the LDH colloids, especially, when the pH drops below 8.5. In order to evaluate the stability, the size of the colloids in the precipitate is measured via DLS immediately after each centrifugation step and another time 48 hours later. Additionally, the pH of a 2 wt.-% dispersion from the precipitate in pure water was measured. The results are shown in **Table 3**. After the 7^{th} centrifugation step, the conductivity drops below 1 mS/cm and the colloids keep their size.

Table 3: Examination of LDH stabilization after synthesis

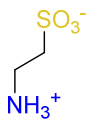
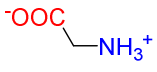
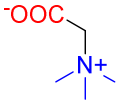
# step	Conductivity [mS/cm]	pH 0 h	pH after 48h	ΔpH	Δ size (DLS) [nm]
C1	78.4	-	-	-	reference
C2	26.1	8.7	10.1	+ 1.4	bigger
C3	12.8	8.2	9.2	+ 1.0	smaller
C4	4.2	7.6	8.6	+ 1.0	smaller
C5	1.5	6.9	7.9	+ 1.0	smaller
C6	1.1	6.8	7.6	+ 0.8	smaller
C7	0.9	7.2	7.9	+ 0.7	same size

The centrifugation process is therefore conducted as fast as possible after synthesis and was ended, whenever the conductivity drops at least below 1 mS/cm. It is well-known, that DLS size measurements of lamellar colloids are not ideal. Nevertheless, SEM images and the DLS measurements correspond well. Moreover, the colloids are kept away from carbonate contamination by sealing the nitrogen flushed sample containers with plastic paraffin film. It is evident, that in all experiments the pH value rises after 48 hours, even if the size of the colloids stay the same. The dissolution of LDH colloids below pH 8.5 is believed to release hydroxide ions, therefore an increase of the pH is the result. Interestingly, the particle size after the 7^{th} centrifugation step also rises, even if the particle size do not change significantly. The reason for the increase in size could be the dissolution of ZnO colloids,[139] which are also present in a reasonable amount (XRD spectrum, Appendix, page 198).

1.2.4 LDH Ionic Exchange

For Ionic Exchange experiments, the LDH colloids are centrifuged to electrical conductivity values of about 0.1 mS/cm, to further remove competing ions within the process.
It was assumed that a charge-driven intercalation of small polymer colloids in aq. dispersion into the here described LDH^{+}-BSA^{-} phase should be possible with a cationic polymer dispersion. Most polymer colloids have an anionic surface charge. To maximize the compatibility to the synthesized LDH-phases the ionic exchange with zwitterionic species was examined, with different characteristics (cf. **Table 4**). A set of ionic exchange experiments with pH adjustment showed, that the particle size decreases, even at basic conditions. Not shown in the table, a commercial lecithine ("Phospholipon 90G", kindly provided by Lipoid) was used as a zwitterionic species with a long organic chain.
The XRD measurements and some relevant distances are illustrated on the next pages for the examined LDH phases (**Figure 35**: LDH-NO_3 and **Figure 36**: LDH-BSA). It is clear from both LDH phases, that only the intercalation of dodecylsulphate was almost complete. The other phases not even change in distance. SEM observations and DLS measurements show a decrease of the LDH primary particle size, when zwitterions are added, already indicated by the intensities of the XRD diffraction peaks.

Table 4: Most important properties of used zwitterions

	 **taurine**	 **glycine**	 **betaine**
p$K_{A,1}$	1.50	2.34 (2.21)	-
p$K_{A,2}$	8.74 (9.08)	9.60 (9.15)	-
IEP	5.29	5.97	-
mol. solubility (H_2O)	0.5	3.3	5.2
eq. length [nm]	0.49	0.47	0.59

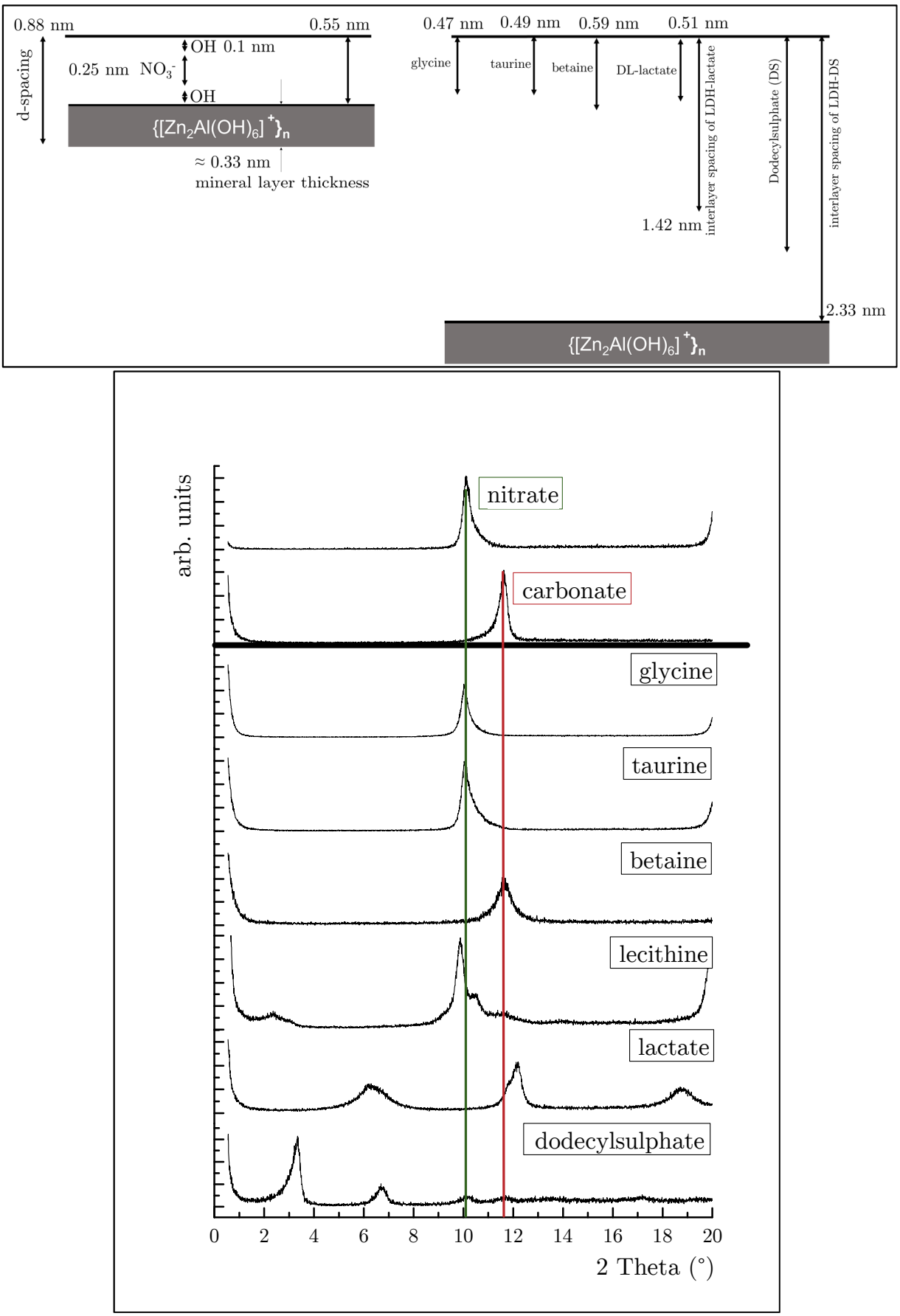
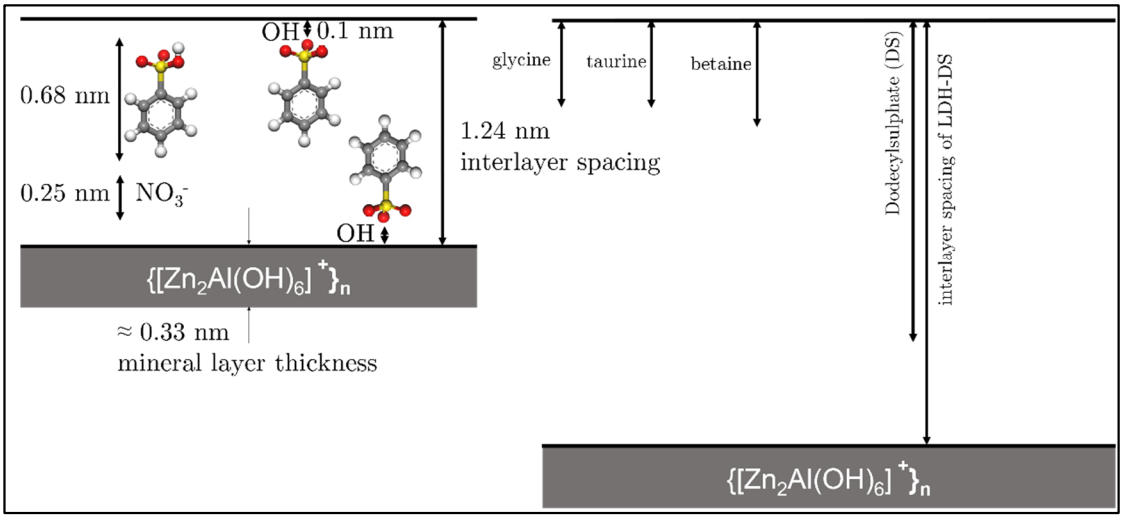


Figure 35: XRD spectra after anionic exchange of LDH-NO_3



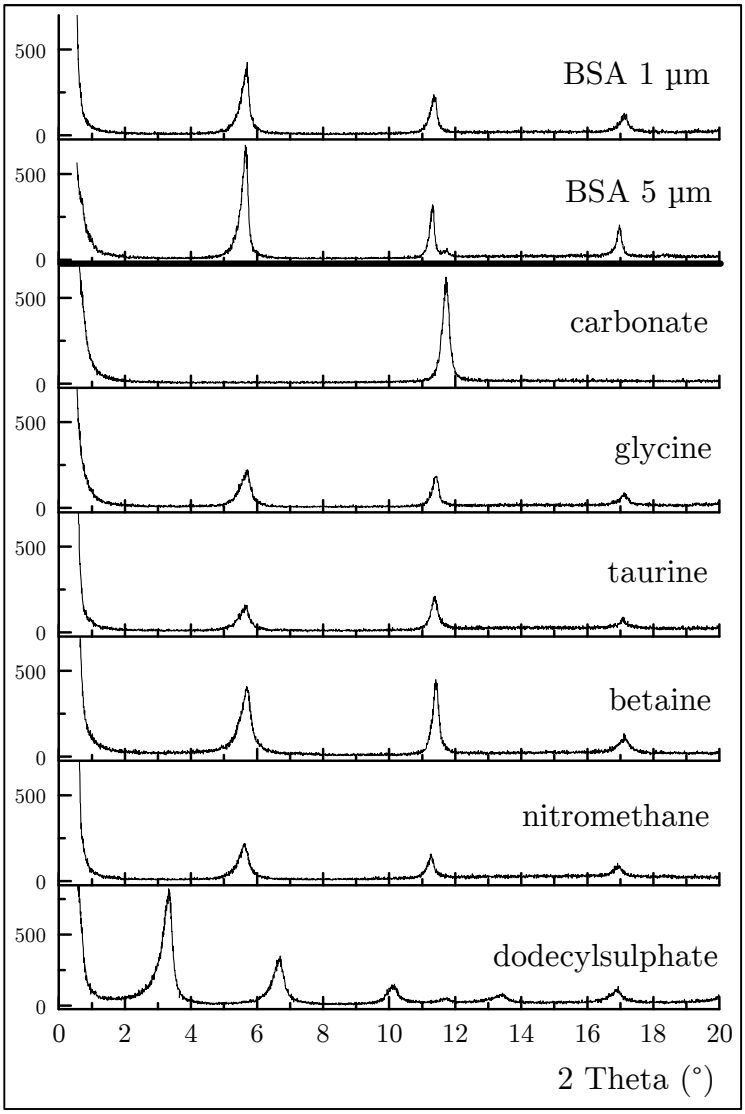


Figure 36: XRD spectra after anionic exchange of LDH-BSA

1.2.5 Liquid Exfoliation of LDH

The separation to single sheets by exfoliation as it is the case for the prominent montmorillonite was not observed for LDH, as it is expected for high surface charge densities, present in LDH. The liquid exfoliation of LDH colloids in water by lactate ions is reported for lactate ions introduced directly in the synthesis.[140] Moreover the liquid exfoliation of LDH in formamide[141] and amino acid/solvent combinations are reported[142]. The liquid exfoliation by a mixture of solvents (DMF/EtOH) is also reported elsewhere.[143]
Here, the LDH-dodecylsulphate phase after ionic exchange was dispersed in butanol in a 0.12 wt.-% dispersion, according to the reported method of Adachi-Pagano et al. (2000)[144]. The mixtures were homogenized by ultrasonic treatment in a snap-cap vial for three days. Both dodecylsulphate phases (pristine phase: LDH-BSA & and LDH-NO3) were used in a later section IV-3.1.5 (page 99) for experiments on organized colloids.
Another approach conducted here was the hydrophobization of the LDH intergalleries with a reactive trimethylsilane. In **Figure 37**, an example for the TMS-treated LDH colloids in a waterbased PUR matrix is shown. The basal spacing of the LDH colloids is expanded, whereas the lateral size shrinked drastically. As a reference, the same LDH phase was dispersed in the same matrix, without any indication of intercalation by the polymer colloids. Most of the prepared LDH colloids are not intercalated or swollen by the silane and remained at the bottom of the glass vessel after reaction.

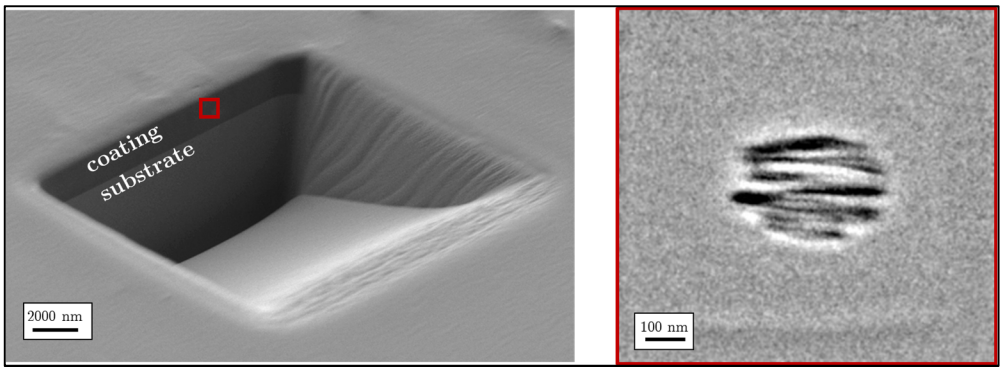


Figure 37: FIB cross section of (TMS μ LDH) colloids in a commercial PUR matrix

2 Kaolinite

In general, it is possible to synthesize kaolinite colloids in a hydrothermal process.[145] Within this work, no kaolinite synthesis is performed. Raw kaolinite is kindly provided by BASSERMANN Minerals[‡] with a multimodal size distribution and iron-containing, magnetic impurities. The raw product can be transformed into a rather monomodal size distribution from different size fractions by sedimentation and/or centrifugation. The first product, "SKT-35" contains big size fractions with book-like stacked kaolinite colloids (SEM image in Appendix, page 201). These huge colloids shall be removed for the following experiments. The goal is to achieve lamellar colloids with the highest possible aspect ratio in order to obtain Janus colloids (Section IV-2, p. 76f).

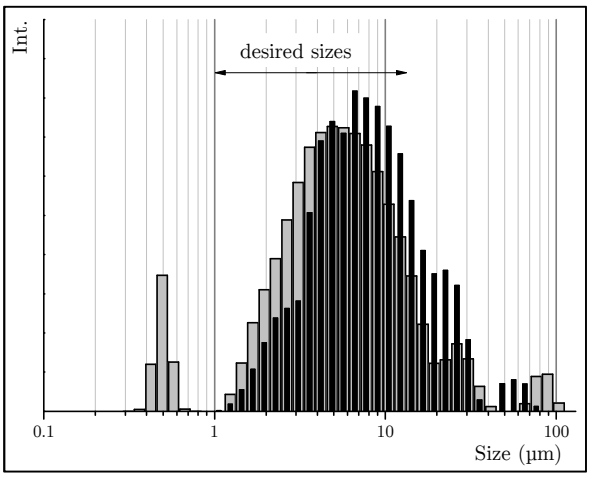


Figure 38: DLS measurements of raw kaolinite products SKT-35 (black), SKT-13P (grey)

The second kaolinite product used herein, "SKT-13P", has many kaolinite colloids with small size fractions below 1 µm. Both kaolinite products have the same origin, whereas they supposed to have different size distriutions due to different processing by the supplier. The supplier "delaminated", flotated and finally spray-dried the "SKT-35" raw product. In the following, the sedimentation and centrifugation processes to obtain monomodal size distributions at same measurement conditions are described.

2.1 Sedimentation

In a typical sedimentation procedure, 1.0 - 2.5 L of 1.0 - 1.5 wt.-% aqueous kaolinite dispersion are placed in a 1 - 3 L beaker and stirred overnight. Subsequently, the beaker is placed in an ultrasonic bath for 30 minutes and magnetically stirred up. The stirring is stopped when the dispersion appears homogeneous and no sediment is visible at the bottom. When the dispersion is at rest, the level of the dispersion in the beaker h is measured with a ruler and the required sedimentation time t for the desired equivalent diameter ($2r$) is calculated from equation (11). The settling velocity v_p of spherical colloids with radius r can be calculated according to Stokes' law:[146]

$$v_p = \frac{2}{9} \cdot \frac{r^2 \cdot g(\rho_p - \rho_f)}{\eta} \tag{10}$$

[‡] USA kaolinite from Thiele Kaolin Company®. Two products used: SK-T 13 (P) & SK-T 35

$$t = \frac{2}{9} \cdot \frac{r^2 \cdot g(\rho_p - \rho_f)}{\eta \cdot h} \tag{11}$$

where g is the gravitational acceleration, ρ_p and ρ_f the densities of the colloids and the fluid, respectively (kaolinite: 2580 kg/m^3; water: 1000 kg/m^3) and η the kinematic viscosity of water ($\eta = 0.001$ Ns/m^2).
The diameters ($2r$) chosen for the sedimentation experiments of the product "SKT-35" are 1 µm and 6 µm. The DLS measurement (**Figure 39**) shows a mean particle size of 3.43 µm, which is in good agreement with the formal theoretical value of 3.5 µm (mean of 1 and 6 µm).

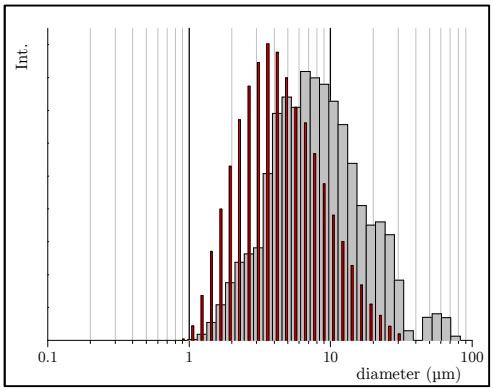


Figure 39: DLS measurements of Kaolin "SK-T 35"
before (grey) and after (red) the sedimentation process. The SEM structure shows the book-like

In the whole process, eight sedimentations are conducted. The first five sedimentation processes took approx. 110 minutes and the sediment is discarded. The subsequent three sedimentation processes took approx. 65 hours and the supernatant is discarded.

2.2 Centrifugation

The centrifugation process is used in a similar way to the sedimentation in order to accelerate the process. Stokes' law is modified with a factor x, which is a multiple of the gravitational acceleration g and can be set at the centrifuge. ($r = 0.4$ µm, $x = 1300$, $t = 14$ min, $h = 14.8$ cm)

$$t = \frac{2}{9} \cdot \frac{r^2 \cdot x \cdot g(\rho_p - \rho_f)}{\eta \cdot h} \tag{12}$$

Since the centrifuge has a tilted geometry, the containers are filled to a fixed height, and the sedimentation height was. measured with a scale by tilting the container in the same angle. This process was used for the product SKT-13P (29 % yield).

After 10 centrifugation steps, no colloids below 1 µm can be detected via Mastersizer DLS measurement, whereas a considerable amount of small particles is still present, as detected by SEM imaging.

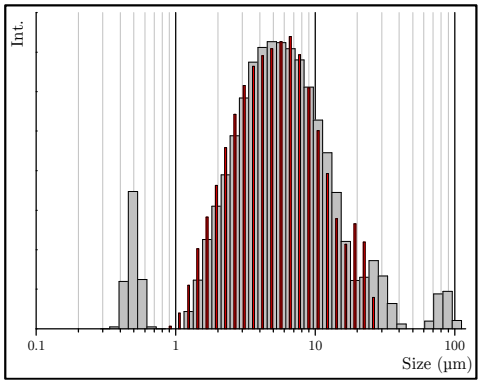
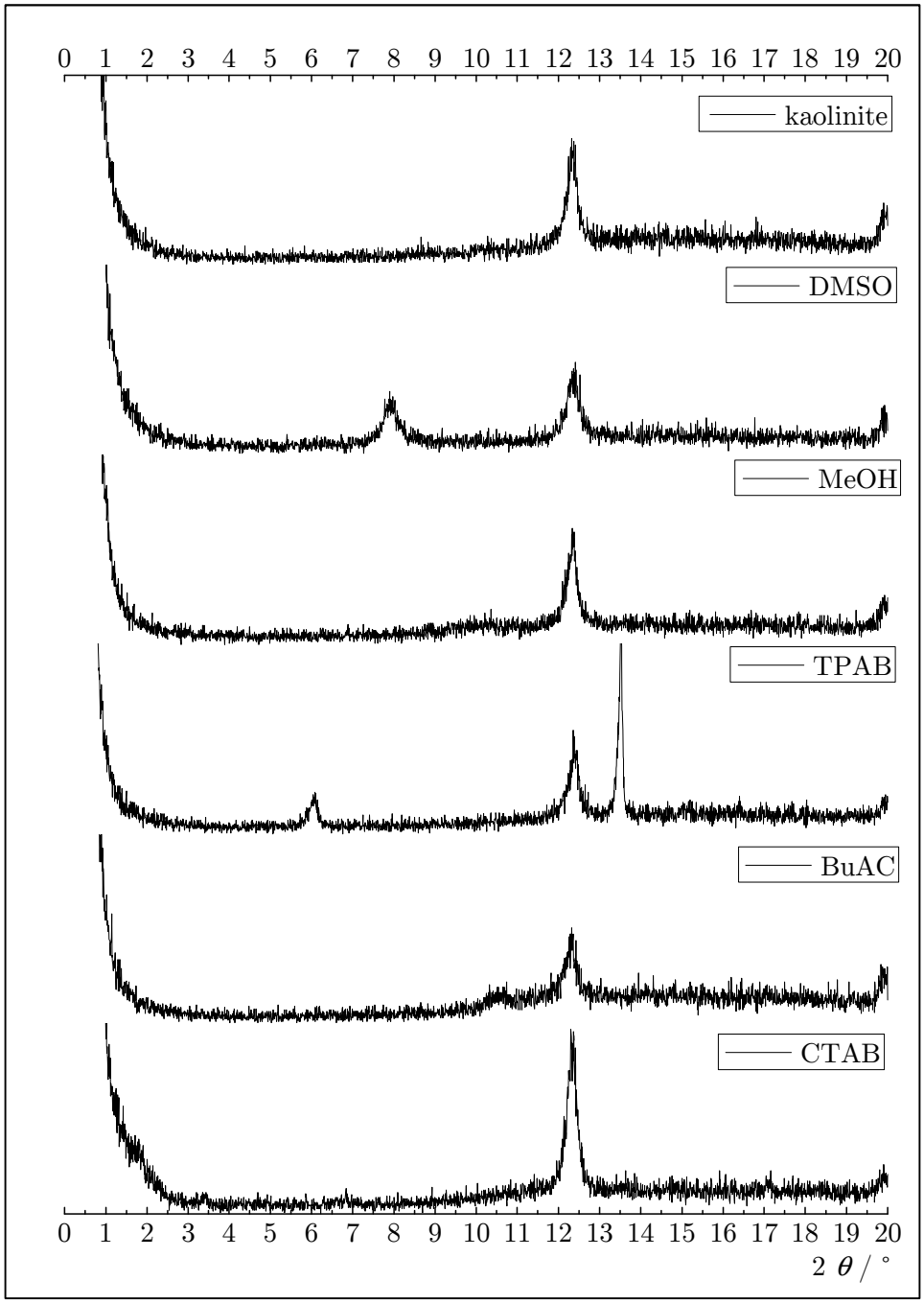


Figure 40: DLS measurements of "SKT-13P"
before (grey) and after (red) centrifugation and sedimentation process

2.3 Ion Intercalation into kaolinite

In kaolinite there are no ions to exchange, so that it is more an intercaltion by introducement of ions into kaolinite intergalleries. The product "SKT-63" is chosen over the aforementioned types because of the smaller lateral size. Since kaolinite has a very small ionic exchange capacity and a comparably weak swelling in water,[147] the kaolinite colloids are intercalated first with DMSO and then with methanol according to the method of Matusik et al.:[148]
2 g kaolinite, 27 mL DMSO (29.7 g), 3 g H_2O, are placed in a flask with a magnetic stirrer and a reflux condenser. The mixture is heated to 70 °C and is stirred for 2 hours. After the dispersion cooled down to room temperature, the DMSO-intercalated kaolinite is centrifuged one time and dried at 60 °C.
Subsequently, 2 g of DMSO-intercalated kaolinite is mixed with 40 mL methanol, stirred for 24 hours at room temperature and was centrifuged 6 times in methanol. The methoxy-kaolinite slurry is sealed with plastic paraffin film until further use.
The two ammonium salts used in this work are cetyltrimethylammonium bromide (CTAB) and tetrapropylammonium bromide (TPAB). 1 M solutions of CTAB and TPAB in methanol and a 50/50 mix of CTAB/TPAB were prepared and mixed with 1 g of methoxy-kaolinite. The dispersions were stirred for 48 hours at r.t. and centrifuged 4 times in methanol to obtain ammonium intercalated kaolinite (K-CTA, K-TPA). All steps were monitored using XRD measurements.
From the XRD measurements (**Figure 41**), it is evident that a partial intercalation of DMSO, tetrapropylammonium, and butylammonium is realized. The butylammonium reflex is rather small. In the case of partially intercalated tetrapropylamine, the interlayer spacing of kaolinite is 10-fold increased, compared to the initial kaolinite interlayer spacing.
The intercalated kaolinite phases underwent mixing with polyurethane colloids, described in section IV-4.1.4 (page 122).



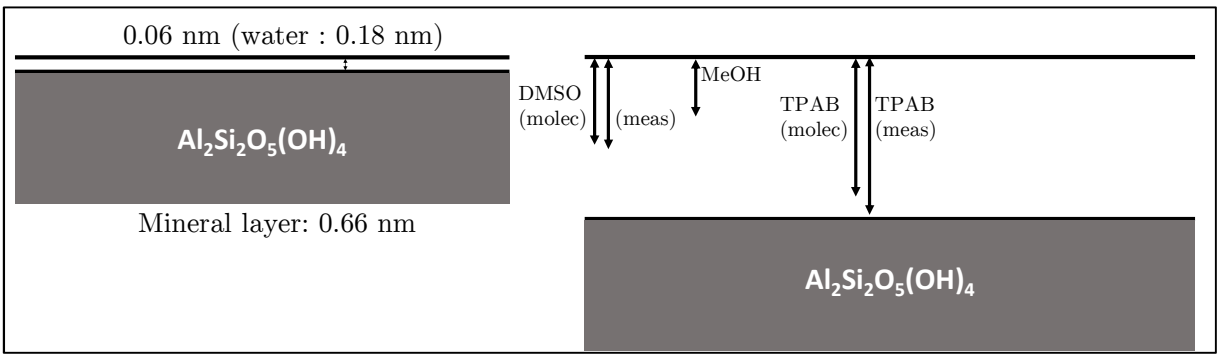


Figure 41: XRD spectra of kaolinite and modified kaolinite

3 Monodisperse and Spherical PS colloids

Since polystyrene is an easy-to-handle, cheap and well-documented polymeric material, it is used for model experiments on organized colloids (Section IV-1 & IV-2). The comparably high glass transition temperature T_g (cf. **Figure 43**) of polystyrene towards the polyurethane used herein (cf. Figure 44) is crucial for further experiments to prevent the solid spheres from film formation at room temperature. The size control can be expressed by logarithmic functions.[149] The polydispersity index ranges from 0.002 to 0.063 for the further examined PS dispersions. All prepared PS dispersions are monodisperse, with a few exceptions. In **Figure 42**, the influence of the METAC/styrene ratio on the sphere diameter is shown. Moreover, at METAC/styrene ratios > 0.12, the colloids result in bigger sizes around 90 nm (see Appendix for full data set, page 203).

The polymerization was conducted in a 250 mL three-neck round-bottom flask equipped with a magnetic stirrer, nitrogen inlet, a septum and a reflux condenser. The septum is transfixed with the programmable temperature sensor (from magnetic stirrer) and immersed into the dispersion. 100 g water, 7.7 g of styrene, 0.6 g PVP K-30 and various amounts of 80% aq. METAC[§] solution (cf. Appendix, Table A-28, page 202) were placed in the flask and the emulsion was stirred vigorously under decent nitrogen flow for 30 minutes. The emulsion is heated to 70° C and 3 mL of aq. AIBA (0.4 g) solution was added when the temperature is reached. The reaction is carried out for 24 hours and was cooled down. The resulting colloid dispersions need no further filtration or other purification processes and are used as diluted dispersions.

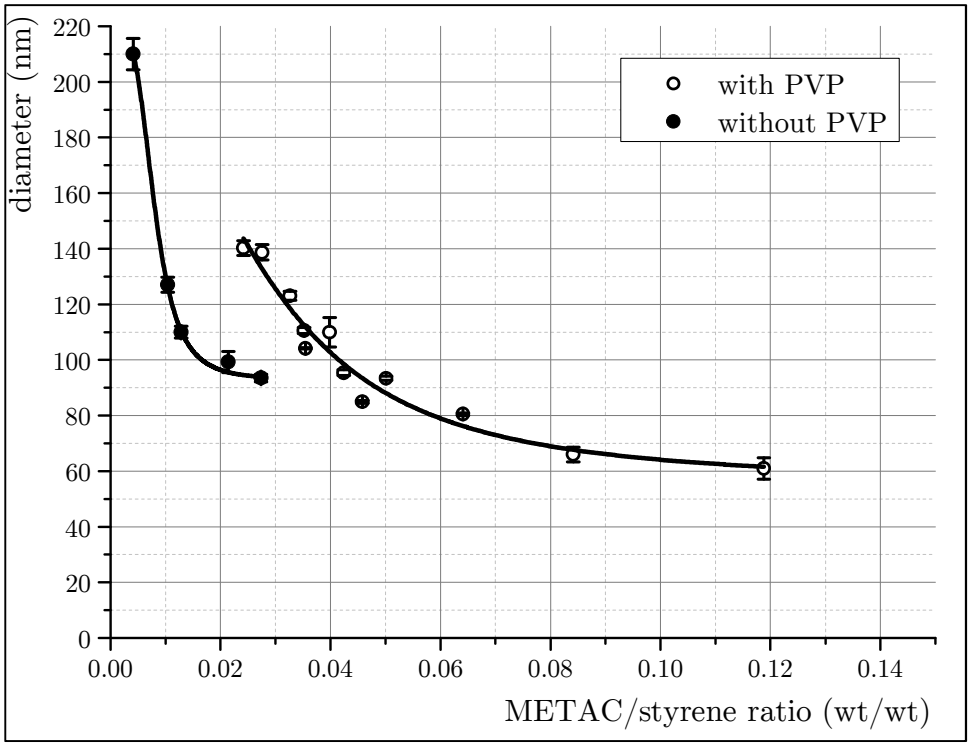


Figure 42: Size-Control of cationic PS colloids with PVP and without PVP
The Sigmoidal – Logistic Fits converged with $R^2 = 0.941$ (○) and $R^2 = 0.996$ (●)

[§] [2- (Methacryloyloxy)ethyl]trimethylammonium chloride

It is assumed, that the synthesis formed a copolymer with a positive charge-enriched surface. Zeta potential measurements in the chapters about organized colloids show a positive zeta potential, which was the initial goal of the synthesis in order to examine PS/K composites.

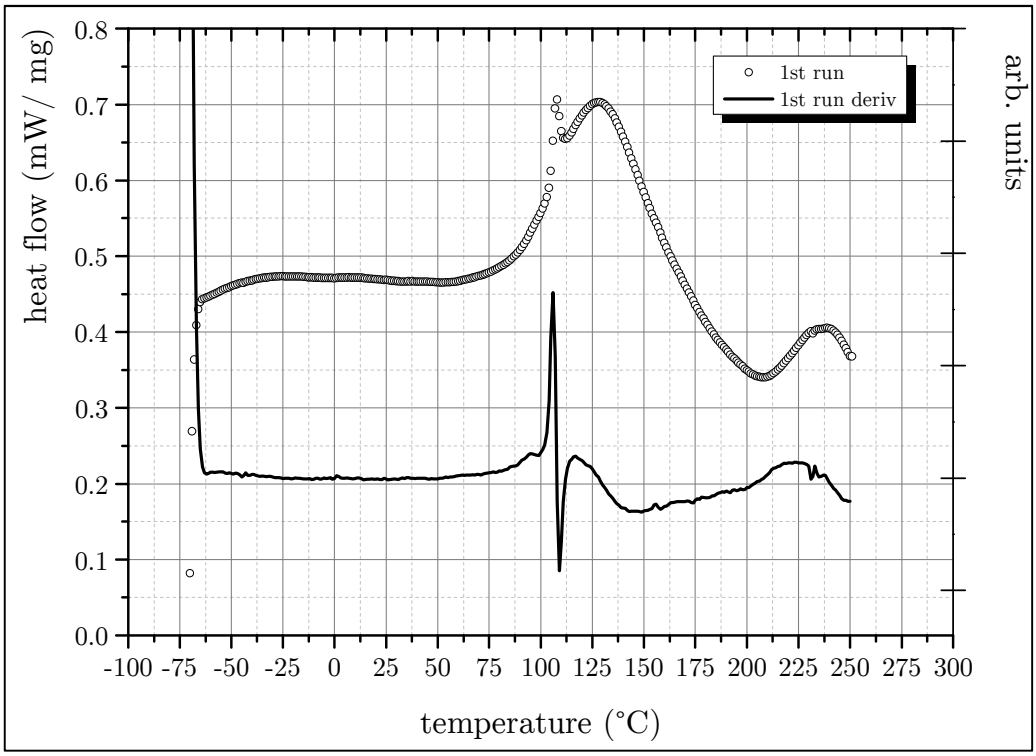


Figure 43: DSC measurements on 95 nm PS colloids

The glass transition temperature was also determined graphically with the software provided for the DSC apparatus (see Appendix, page 203). The onset of T_g is at 103 °C and ends at 108 °C. The T_g is 106 °C. The broadness ΔT_g is therefore 5 °C.

A gel permeation chromatography (GPC) measurement was not conducted for PS, because the freeze-dried powder was not soluble in THF, surprisingly. The ionic shell may prevent the solution of the PS colloids.

4 Polydisperse and coil-like PUR Colloids

The glass transition temperature T_g of the here prepared polyurethane colloids is lower than the PS colloids, described above and shown as DSC measurement in **Figure 44**. Static Light Scattering experiments show, that the PS colloids behave like hard spheres and the PUR colloids behave like coils, shown in **Figure 45**.

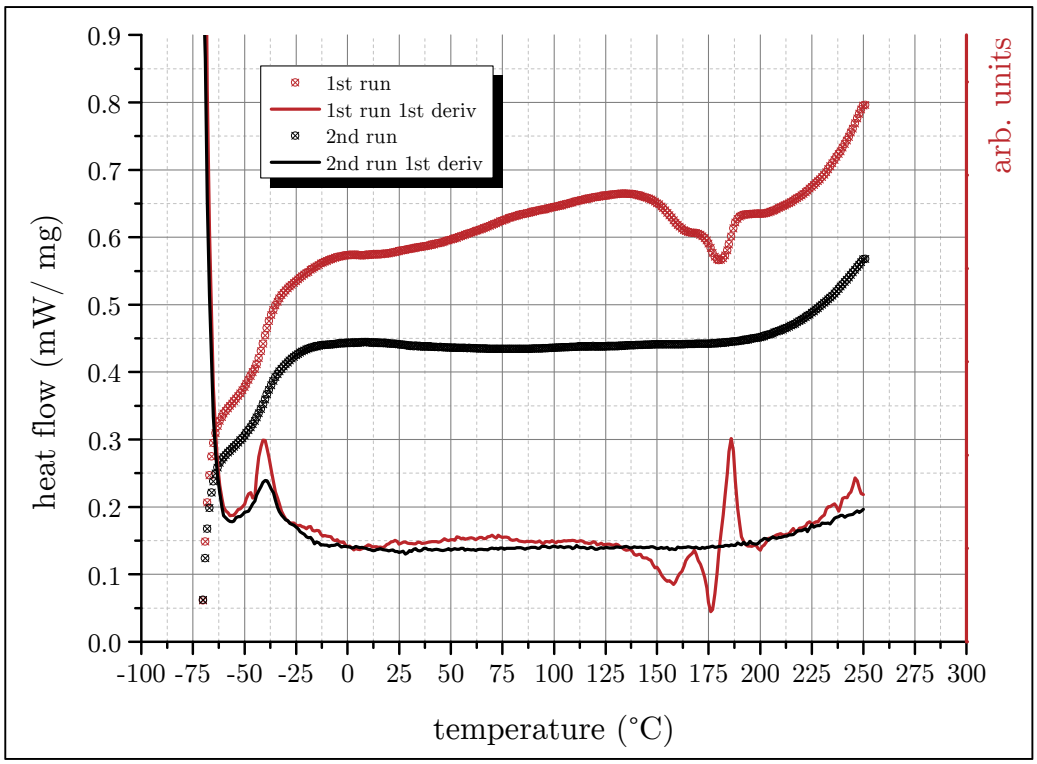


Figure 44: DSC measurements and 1st derivates of monomodal 90 nm PUR colloids
The glass transition temperature T_g was also determined graphically with the software provided for the DSC apparatus (see Appendix, page 205). The onset of T_g is at -46 °C and ends at -32 °C. The T_g is -40 °C. The broadness ΔT_g is therefore 14 °C.

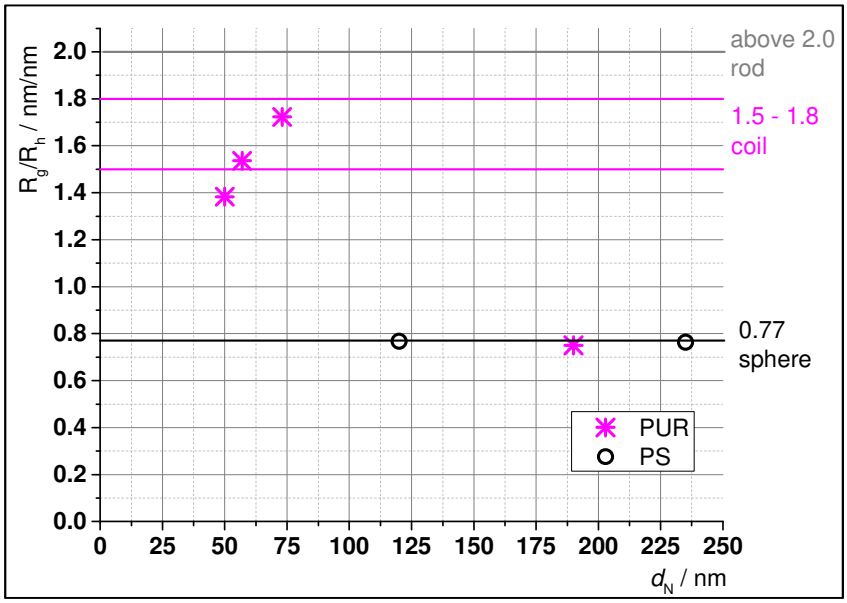


Figure 45: SLS data of some drawn PS and PUR dispersions

For the PUR syntheses, the used commercial polyester diol has a flexible cyclohexane-based C_{36}-spacer and an unknown spacer, indicated by blank boxes in **Figure 46**. The other used diol has a carboxylic acid group. The molar ratio of the diol monomers determinate the diameter of the synthesized colloid, as it is the case for PS colloids. As the diisocyanate, an aromatic meta-substituted type was chosen. The procedure is based on the acetone process.[150]

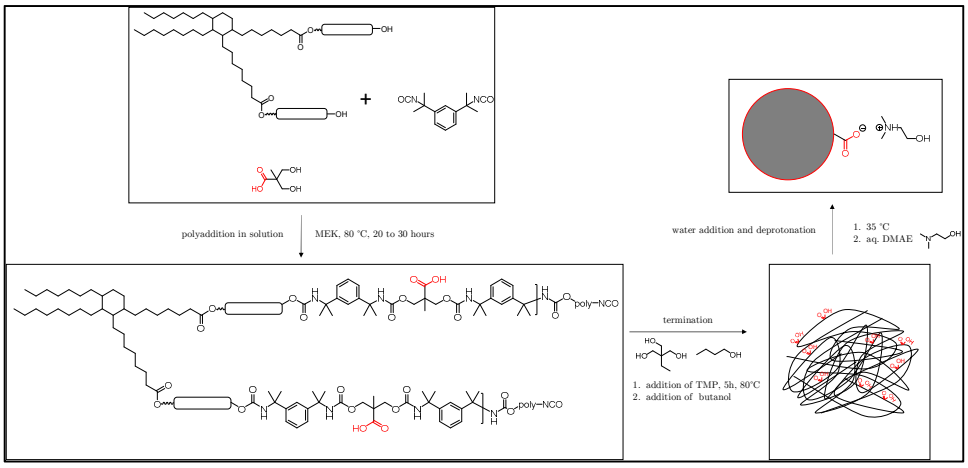


Figure 46: Scheme of PUR particle synthesis

The conversion of NCO was measured via integration of the NCO-signal in an ATR-FTIR spectrum (cf. **Figure 47**). The reaction time for the presented polymerizations is different, depending on the ratio of added monomers and their viscosity.

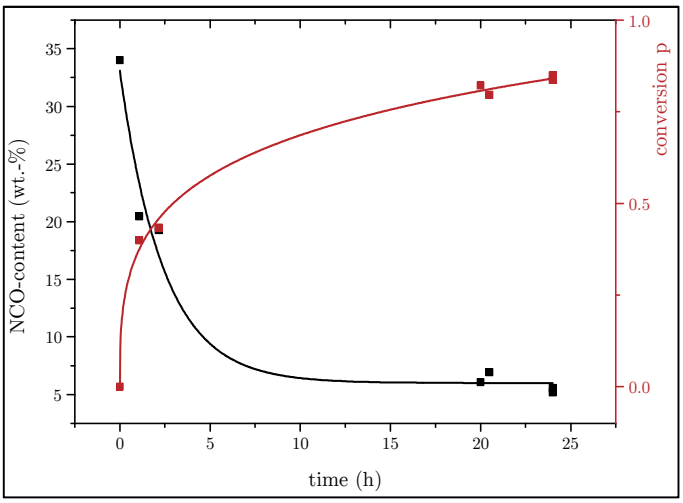


Figure 47: IR peak integrals of NCO-peaks of the PUR prepolymer

4.1 Monomodal PUR Dispersions

The polymerization was conducted in a 500 mL three-neck round-bottom flask equipped with a foldable centrifugal blade stirrer, a reflux condenser and a turnover septum. The procedure is based on the aceton process.[150]
104.4 g commercial polyester diol (49 mmol, 2000 g/mol; Priplast P1900; CRODA GmbH), various amounts of Dimethylolpropionic acid (DMPA), e.g. 6.7 g (49 mmol) and 50 g 2-Butanon (MEK) were placed in the flask and the mixture was homogenized for about 20 minutes. Subsequently, 28 g (114 mmol) of Tetramethylxylylendiisocyanate (TMXDI) was added and the temperature was increased to 85 °C. The amount of unreacted isocyanate was

monitored using ATR-IR measurements, until 1% of the initial isocyanate groups are left. Then, 2.7 g TMP (20 mmol, Trimethylolpropane) was added and the mixture was stirred another 5 hours. The reaction was terminated with 4 g butanol and cooled down to 35 °C. 405 g water and 5.33 g Dimethylethanolamine (DMAE) (59 mmol, molar amine-carboxy ratio $\alpha = 1.20$) was added under stirring with a flowrate of 0.5 mL/min with a peristaltic pump. In the end, the remaining MEK was removed with a rotary evaporator. The colloidal diameter was controlled by the content of carboxylic acid content of DMPA monomers. The more DMPA is present, the smaller the resulting colloids (cf. **Table 5**, weighed portions in Appendix, page 204).

Table 5: Compositions and resulting sizes of synthesized PUR colloids

DMPA/polyesterdiol ratio [mol/mol]	**colloid diameter** [nm]
0.50	190
0.63	114
0.74	30
0.74	82
0.74	97
0.77	28
0.79	75
0.80	76
0.80	49
0.83	45
0.90	47
1.00	13
1.03	34
1.25	9
2.00	3
2.00	10
2.00	9
3.03	11
5.00	17
10.00	22

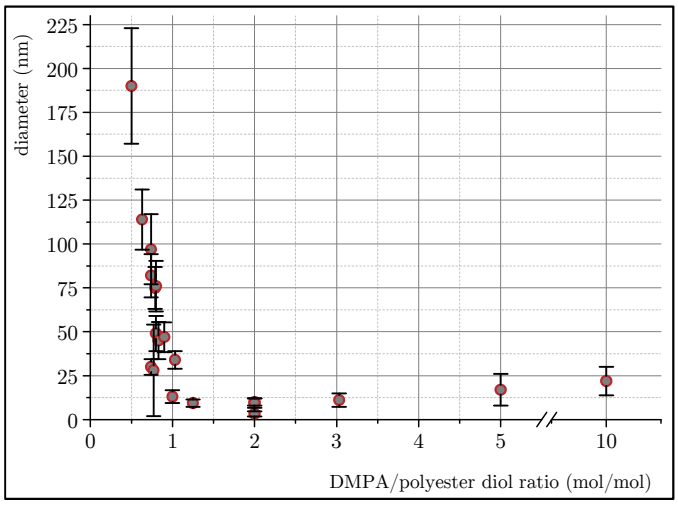


Figure 48: Size-control of the PUR colloids

Gel permeation chromatography (GPC) of freeze-dried PUR colloids was conducted with THF as eluent, a Merck LC-6200 pump, three columns; PSS-SDV guard 5 µm, PSS-SDV10^5 Å, 5 µm, PSS-SDV 10^3Å, 5µm; and two detectors, a Knauer RI 2300 detector and a Merck UV/VIS L-4200 detector. The standard is a narrow-distributed linear PS in THF. Results are shown and discussed on page 148.

4.2 Multimodal PUR Dispersions

The polymerization was conducted in a 500 mL three-neck round-bottom flask equipped with a foldable centrifugal blade stirrer, a reflux condenser and a turnover septum. The septum is transfixed with the programmable temperature sensor (from magnetic stirrer) and immersed into the solution. 104.41 g polyester diol (50 mmol; Priplast P1900; CRODA GmbH), 6.68 g of dimethylolpropionic acid (50 mmol; DMPA) and 45.50 g 2-butanone (MEK) were placed in the flask and homogenized for 20 minutes. Subsequently, 27.97 g (114.5 mmol) tetramethylxylylendiisocyanate (TMXDI) was added and the temperature in the reactor is increased to 70 °C. The amount of unreacted isocyanate was monitored using ATR-IR measurements, until 1 wt.-% of the initial isocyanate groups are left (24 hours, see **Figure 47**). Then, 2.69 g (20 mmol) TMP (trimethylolpropane) were added and the mixture was stirred another 5 hours. The reaction was terminated with 1 g butanol and cooled down to 35 °C. The non-volatile content of the mixture is measured (75 wt.-%). Defined portions of e.g. 10 g were added into a flask with a centrifugal stirrer and the temperature is adjusted to 35 °C. Different amounts of dimethylethanolamine (DMAE) were added with protolysis degree α of 0.8, 0.9 and 1.0 and 22 g water with a peristaltic pump. In the end, the remaining MEK was removed with a rotary evaporator.

molar amine-carboxy ratio α	N-Avg. [nm]	PdI
0.4	99	0.33
0.6	112	0.45
0.8	50	0.80
0.9	190	0.25
1.0	69	0.39
1.2	45	0.28

IV Organized Colloids

In the following chapter, the focus is on the actual topic of the thesis: the self-assembly of lamellar and spherical colloids in aqueous dispersions with the goal to obtain well-organized colloid structures. The examinations on model systems in this work is connected to some uncertainties with respect to the ratios of the weighed portions of lamellar and spherical colloids, what may usually known as stoichiometry in the classical sense. With the electrostatic interaction @ as a driving force, the dispersions are diluted to small concentrations ($\geq$ 0.5 wt.-%) to allow the colloids to agglomerate in a homogenous way.[68] Furthermore, the surface charge of the colloids can be triggered by the pH value in the colloidal dispersions and is measured as the electrophoretic mobility, expressed as the ζ-Potential. Especially, when the primary colloid sizes are varied, the composition for a full and homogenous coverage, if possible at all, changes (S. Neuhaus (2015)[151]). It is expected and was already found, that the smaller the lateral size of the lamellar colloids, the smaller the spherical colloids have to be for a homogenous coverage. Moreover, with decreasing size of the spherical colloids, the less weight is necessary to cover the full surface area of the lamellar colloid due to the increasing interface of the colloids. From the electrostatic assembly @ experiments on drying droplets, the capillary assembly π emerges as an effect for bigger becoming spherical colloids. The major part of the preparative work was to find appropriate techniques to obtain well-organized structures by controlled agglomeration for many different combinations of materials, therefore their properties and scale.

The homogenously distributed deposition of spherical PS colloids on the lateral area of lamellar kaolinite colloids and the further modification by chemical interaction μ is described in **Section IV-1**, page 57f. The functionalization of kaolinite with an oppositely charged silane can change the deposition pattern and allow for a partial occupation (**Section IV-2**, page 76f). At compositions below the full electrostatic deposition, the colloids can undergo an agglomeration to stacked assemblies by defects, described in **Section IV-3**, page 94f. The exfoliation and intercalation of polymers with different sizes into interlamellar voids is presented in **Section IV-4**, page 118f.

In the final **Section IV-5**, page 152f, enzymes are introduced as candidates for model systems which are able to perform all types of assembly, namely the electrostatic assembly @, capillary assembly π and the chemical interaction μ, all in a single drying droplet and subsequently form lamellar structures similar to nacre.

1 Polystyrene @ Kaolinite Assemblies

The electrostatic deposition @ of spherical on lamellar colloids PS @K takes place very fast. Former studies[68] and the literature (section II-1.2) show homogenous deposition patterns by strong electrostatic attraction in case of opposite charges and low ionic strength (cf. **Figure 49**).
The deposition density **Λ** describe the number of spheres N_{sph} per surface area of a lamellar particle A_{lam}:

$$\Lambda = \frac{N_{sph}}{A_{lam}} \tag{13}$$

The equation does not take into account the volume V_{sph} of the spheres, so that the spherical colloids can be seen as a mass point, since the surrounding ions, which can be interpreted as such 0D objects determine the colloidal assembly. Therefore, the system can be seen as a deposition of finite 0-dimensional colloids N on a finite area A of lamellar colloids. The approximation is useful to predict the composition of a homogenous sphere deposition over the full face area of the lamellar colloids. After a short SEM observation and some simple geometric considerations, the full area occupation can be calculated, tested and if necessary fine-tuned in a third try. This approach is assisted by ζ-potential measurements of the pristine and assembled colloids within this section.

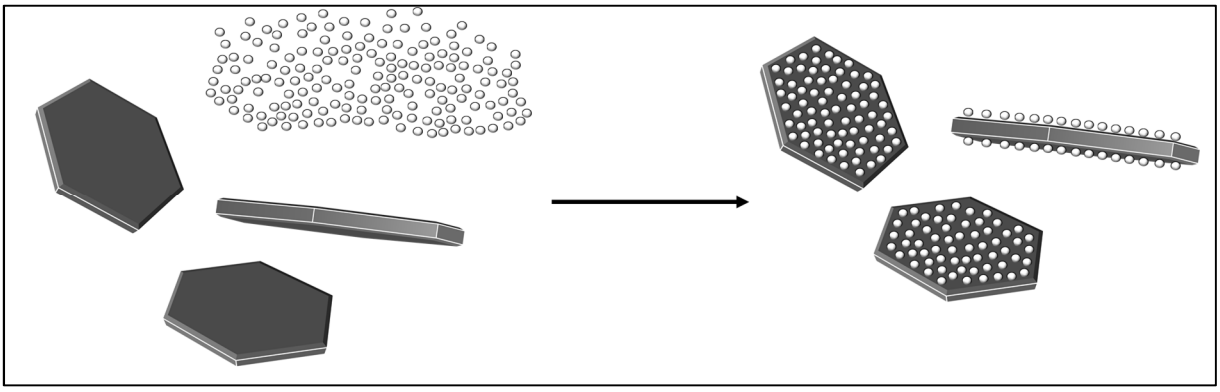


Figure 49: Illustration of a sphere @ lamellar deposition

The here shown basic building unit PS @ K undergo a systematic modification to more complex building units. In this section, the possibility to tailor the surface energy of the organized colloids is examined.

1.1 Experimental Details

The experimental details on the electrostatic deposition of spherical colloids on lamellar colloids are presented in the following subsections. All of the used dispersions were homogenized before measuring the ζ-Potential, whereas the NVC of the respective dispersion is measured to ensure the actual weight ratios of the colloids.

Materials

In Table 6, the different lamellar and spherical colloids for Coverage experiments are presented. The lamellar phases examined here are Layered Double Hydroxides and Kaolinite. The spherical phases are different polymer dispersions and silica sols with varying sizes.

Table 6: Materials for Sphere @ Lamellar Assembly

Name	Size/Purity	Supplier
kaolinite "SKT-35"	2,5 µm** / 4,8 µm††	BASSERMANN Minerals
kaolinite "SKT-13P"	0,6 µm** / 4,5 µm††	BASSERMANN Minerals
polystyrene Latex	60 - 500 nm‡‡	see section III-3
Perglutin K532	30 nm‡‡	Kurita Europe GmbH
DPE-based latex dispersion	50 nm‡‡	K. Briesenick (2017)[68]
Snowtex®-O (SiO_2)	10-20 nm‡‡	NISSAN Chemicals
chitin	400 nm, ≥75% deacytelated	Sigma-Aldrich
Na-montmorillonite	300-400 nm	BYK
kaolinite "SKT-13P"	4.3 µm	(see section III-2.2)
Methyltriethoxysilane	98 %	abcr
Tetraethylorthosilicate	98 %	abcr
Monohydride terminated PDMS	850 g /mol, 5-9 cSt	abcr
Pt-divinyltetramethyldilisoxane	3.0-3.5 wt.-% Pt	abcr
SILRES® BS 45	54% NVC	Wacker Chemie
PS latex 105 nm	7.8% NVC	#6, page 202
pure ethanol	99.5 %	commercial
pure water		

Methods

Dynamic Light Scattering (DLS)
Malvern Zetasizer Nano ZS
Malvern Mastersizer 2000
Zeta Potential Measurement
Malvern Zetasizer Nano ZS
optionally equipped with Autotitration Unit MPT-2 and Vacuum Degasser
Scanning Electron Microscopy (SEM)
Zeiss NEON 40
Thermogravimetric Analysis (TGA)
Mettler-Toledo TGA/SDTA 851e, 5 °C/min, synthetic air

** Measured mean diameter by BASSERMANN Minerals with Sedigraph (D50)
†† measured mean diameter with Mastersizer 2000
‡‡ Measured with Zetasizer Nano ZS

Centrifuge
BECKMAN COULTER Avanti® J-E with a JA-10 Rotor
Peristaltic Pump
Heidolph PD5201 (tubing diameter 0.8 mm)
pH monitoring
Mettler Toledo SevenMulti
optionally connected per USB to a PC (live pH vs. time monitoring for manual isoelectric titrations)
Drop Shape Analyzer
KRÜSS Drop Shape Analyzer 25E

1.1.1 Manual Isoelectric Titration of pristine colloids

The Apparent ζ-potential and the size of the colloids in dependence of the pH value and electrical conductivity is measured with a Malvern Zetasizer Nano ZS, optionally equipped with the Autotitration Unit "MPT-2". The sample dispersion is diluted to ≤ 0.17 wt.-% and placed into a special disposable screw-capped polymer vessel, which can be connected to a magnetic stirrer and a pH meter of the MPT-2 unit.
The acidic/basic solutions are placed in the autotitration unit and then can be used to pump the respective solution into the main sample container per Malvern software. The pH increment is $\Delta pH \approx 0.5$ in all experiments.
In order to obtain comparable ionic strengths, two measurements are conducted. The first titration is conducted into the acidic medium until pH 2 is reached (0.5 M HCl). The second titration is conducted into the basic medium until pH 12 is reached (0.5 M NaOH).
Alternatively, the dispersion is stirred by a magnetic stirrer in an external vessel and the acidic/basic solution is added manually with a peristaltic pump (flow rate 0.4 $\frac{mL}{min}$). The pH is controlled by monitoring the pH (pH vs. time) per computer software (LabView) throughout the titration. After reaching an approx. constant pH, a small volume is removed, measured and readded to the dispersion. Here, also two samples of dispersion (acid/base) were measured.

1.1.2 Auto-Titration of Organized Colloids

The agglomeration of colloids is observable via size and ζ-potential measurements described above. Therefore, a known quantity of lamellar colloids is weighed (mostly 10 g, 0.17 wt.-%) into the sample holder (stock dispersion) and a diluted dispersion (0.02 - 0.20 wt.-%) of spherical particle dispersion is added (additive dispersion) with the programmable autotitration unit. The autotitration unit adds dispersion stepwise until the desired volume is reached (max. 20 mL).The number of programmed steps in all experiments is 10, with 3 ζ-Potential (mostly 12 runs) and 1 size measurement (30 runs) at each step. The sample is recirculated after each single measurement (40 times in total), as well as before the first and after the last measurement. For this configuration, each step takes approx. 13.5 min. Prior start and in the end of the autotitrations, all tubings were rinsed multiple times with water. Just before the autotitration, the tubings are inspected to eliminate air bubbles to prevent the measurement of dead volume. The Autotitration Unit is therefore equipped with a Vacuum Degasser Unit. Performing the Autotitration method, small air bubbles in the tubes can occur in an irregular fashion, which leads to false calculations of the computer software, because the dead volume is not measurable with the equipment. Therefore, the degasser is installed between the additive container and the stock dispersion container. The setup of the autotitration unit is a circulation of an assembled stock dispersion and is optimized and developed for pH-dependent

measurements.[§§] Therefore, it is unknown, which particle ratio is indeed present during the measurement in the cuvette, especially near the Point Of Zero Charge (POZC). In this region, the gravitational force of the agglomerates become bigger and the agglomerates are able to settle. Therefore, the samples are magnetically stirred to prevent those effects.

The relevant dispersions are prepared as follows:
The NVC of the *cationic dispersion* ("Perglutin") is measured (1 g dispersion, 110 °C, 30 min) and diluted as to 0.02, 0.08 and 0.12 wt.-% with pure water. The dispersion is used as additive.
The NVC of *cationic PS dispersions* (see III-3) is measured (1 g dispersion, 110 °C, 30 min) and diluted to 0.02, 0.08 and 0.12 wt.-% with pure water. The dispersion is used as additive.
The *kaolinite* colloids are used with the resulting NVC after sedimentation (approx. 3 wt.-%). The dispersion is diluted to 0.17 to 0.20 wt.-% with a total mass of 10 to 10.7 g. The dispersion is used as the stock dispersion. In almost all experiments, SKT-13 P was used. In a typical experiment 0.36 g (analytical balance) of a 4.8 wt.-% kaolinite dispersion is mixed with 10 g of water in the sample holder.

1.1.3 SEM observations of Basic Building Unit (3D @ 2D)

In a typical experiment, a single droplet of an approx. 2 wt.-% (NVC_{lam}) aq. kaolinite dispersion is weighed into a small vessel and the weight is determined by an analytical balance. The e.g. polystyrene dispersion is mostly adjusted to approx. 0.02 wt.-% (NVC_{sph}) with pure water. The resulting weight of required polystyrene dispersion (m_{sph}) for a desired factor x is calculated with equation (14) and subsequently added to the kaolinite dispersion as precise as possible.

$$m_{sph} = \frac{m_{lam} \cdot \mathrm{NVC}_{lam}}{x \cdot \mathrm{NVC}_{sph}} \tag{14}$$

For example, 0.03 g of kaolinite dispersion is mixed with 0.3 g of PS dispersion to obtain a 1 to 10 ratio (PS @ Kaolinite, wt/wt).
The actual weighed portion of m_{lam} (4 fractional digits) is noted and the desired mass m_{sph} is calculated with Excel-Software before addition to keep deviations small. The organized dispersions are agitated 5 times with a disposable pipette and a single drop is dried on a silicon wafer at room temperature. The dried sample is sputtered with Au/Pd (ρ = 16.7 g/cm³) to an eq. thickness of 3 nm (QCM) and imaged via SEM.

1.1.4 Preparation of Hollow Spheres on Kaolinite

In a typical experiment, 0.35 g of monomodal kaolinite dispersion ("SKT-35", page 47, NVC 2.21 wt.-%) is mixed with 3.55 g cationic polystyrene dispersion (#6 on page 202, NVC 0.02 wt.-%) in a screw-capped polymer vessel and finally 17 g of EtOH is added to obtain 80 wt.-% EtOH in H_2O. After 5 minutes ultrasonication, 0.08 g of 25% NH_4OH solution is added and stirred magnetically for another 2 minutes. The mixture is placed into a water bath (50 °C) under stirring. After 10 minutes at 50 °C, different TEOS weight equivalents based on the PS content are added (**Table 7**).

[§§] https://www.malvernpanalytical.com/de/assets/MRK552_tcm57-17209.pdf timestamp: 05.04.2018

Table 7: Weighed portions of SiO_2 @ PS Core-Shell Colloids

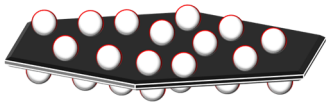
#	105 nm PS + SKT-35 kaolinite					PS w/o PVP
	1	**2**	**3**	**4**	**5**	**6**
kaolinite disp (g)	0.36	0.3625	0.3584	1.5169	0.5000	0.2571
PS disp (g)	3.5500	3.6196	3.9849	5.1889	5.4440	5.0000
EtOH (g)	17.00	17.40	18.45	27.60	23.69	21.21
TEOS (g)	0.0136	0.0268	0.0040	0.1700	1.9600	1.0100
ammonia (g)	0.0840	0.0825	0.0818	0.0800	0.1000	0.1000
TEOS/PS (wt/wt)	19	37	5	164	1000	1010
K/PS (wt/wt)	11	4	3	11	10	10
conditions	2h, 50 °C	2h, 50 °C	2h, 50 °C	2h, 50°C	2h, 50°C	2h, 50°C

The overall particle concentration accounts to 0.35 - 0.40 wt.-% in all experiments. After 2 hours of stirring at 50 °C, the dispersions are cooled down to r.t. and are washed in pure ethanol four times by centrifugation. Small parts of the slurry are diluted in EtOH and poured into a crucible. After EtOH evaporated at r.t., the crucible is placed in a programmable oven, which heats from r.t. to 550°C in steps of 1 °C/min. The temperature is held for another 2 hours at 550 °C and the program ends. The residue is collected for TGA measurement and for morphological SEM observations.

1.1.5 Preparation Of Organized Kaolinite Colloids

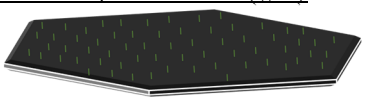
In all experiments of this part, the product kaolinite "SKT-13P" was used. In this product, the appearance of book-like kaolinite structures is at the lowest level. The supplier "delaminated", flotated and finally spray-dried the SKT-35 raw product, so that SKT-13P was used. All centrifugations were performed for 10 minutes at 8000 rpm.

PS @ kaolinite (#1)



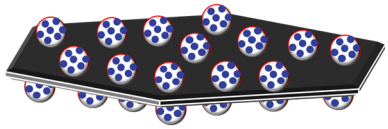
4 g of kaolinite is suspended in 800 g pure water to obtain a 0.5 wt.-% dispersion. Subsequently, 5.13 g of a 105 nm PS dispersion (7.8 wt.-%) is added to obtain a 1 to 10 weight ratio of PS @ kaolinite. The pickering dispersion is stirred for 1 hour and settled overnight. A peristaltic pump removes the supernatant carefully. The obtained organized colloids "PS @ kaolinite" are dried at 70 °C overnight.

MTMS μ kaolinite (#2)



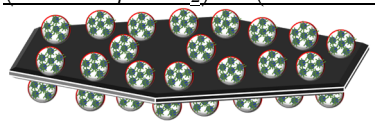
1 g of kaolinite is suspended in 200 g pure ethanol and 1 g pure water with pH 4.5 until a homogenous 0.5 wt.-% dispersion is formed. 0.25 g MTES is added and stirred 2 hours at room temperature. After one centrifugation step, the slurry is dried at 120 °C for 2 hours.

μ SiO_2 @ (PS @ kaolinite) (#3)



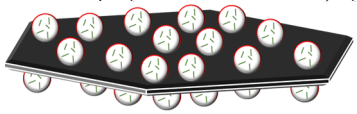
2 g of PS @ kaolinite (#1) are suspended in 400 g pure ethanol and 0.2 g aq. 25% NH_4OH until a homogenous 0.5 wt.-% dispersion is formed. The dispersion is heated to 50 °C and 0.2 g TEOS was added. The mixture was vigorously stirred at 50°C for 2 hours and centrifuged 5 times. The slurry was dried at 70°C overnight.

(MTMS μ SiO_2) @ (PS @ kaolinite) (#4)



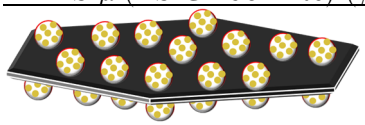
1g of SiO_2 @ PS @ kaolinite (#3) is suspended in 200 g pure ethanol until a homogenous 0.5 wt.-% dispersion is formed. 0.25 g MTES is added and stirred 2 hours at room temperature. After one centrifugation step, the slurry is cured at 120 °C for 2 hours.

MTMS μ (PS @ kaolinite) (#5)

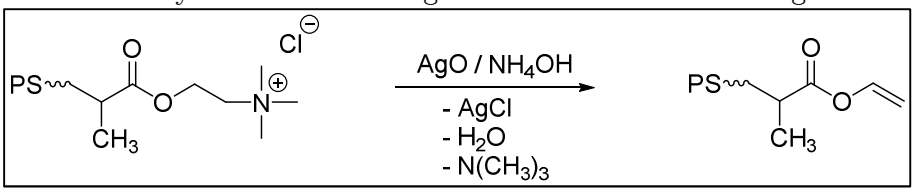


1 g of PS @ kaolinite (#1) is suspended in 200 g pure ethanol and 1 g pure water with pH 4.5 until a homogenous 0.5 wt.-% dispersion is formed. 0.25 g MTES is added and stirred 2 hours at room temperature. After one centrifugation step, the slurry is cured at 120 °C for 2 hours.

PDMS μ (PS @ kaolinite) (#6)



0.49 g of PS @ kaolinite (#1) is dispersed in 100 mL of 0.5 M NH_4OH and 5.4 mg AgO is added and stirred for 20 minutes. The dispersion was centrifuged () and the slurry was redispersed another time in 100 mL of 0.5 M NH_4OH, another 5.4 mg AgO is added and stirred for 20 minutes. The slurry then was centrifuged 3 times and dried overnight at 80 °C.



The resulting product (0.2846 g) is dispersed in 6.1 g toluene. 0.91 g of hydride functionalized PDMS (Polydimethylsiloxane, monohydride terminated, 5-9 cSt, ca. 850 g/mol) and 0.05 g of catalyst (Pt in vinyl terminated PDMS: 3-3.5 wt.-%) is added to the dispersion. The dispersion is stirred for a total of 24 hours, washed 3 times in toluene, 2 times in EtOH and dried at 40 °C.

1.1.6 Preparation of Composite Films

The obtained organized kaolinite colloids are mixed into a commercial silicone resin ("SILRES BS 45"; NVC 54 wt.-%) in order to obtain a film with 34.5 wt.-% content of kaolinite based on the resulting film. The chosen weight content of kaolinite was chosen after preliminary experiments with the commercial resin and the kaolinite product, mixed with a dissolver.

Table 8: Weighed Portions of Films with Organized Kaolinite Colloids

#		kaolinite (g)	resin (g)	water (g)	EtOH (g)	org. colloids in film (wt.-%)
#0	K (13P, reference)	5.40	20.00	0	0	33.3%
#1	PS @ K	0.67	2.36	1.38	0	34.4%
#2	MTMS μ K	0.67	2.34	1.41	0	34.7%
#3	μ SiO_2 @ (PS@K)	0.67	2.34	1.37	0.42	34.6%
#4	(MTMS μ SiO_2) @ (PS@K)	0.68	2.43	1.38	0.40	34.1%
#5	MTMS μ (PS@K)	0.67	2.38	1.40	0.41	34.2%
#6	PDMS μ (PS@K)	0.23	1.02	0	0.56	29.7%

1 g of the respective organized kaolinite colloids were mixed with 3.4 g of aqueous silicone resin (54% wt NVC; SILRES® BS 45) in order to obtain a dry composite content of 35 wt.-% kaolinite. In some composites, the addition of solvent was required.The composite is applied on hdg-steel with a 100 µm razor blade. The films are cured for 20 min at 80 °C. The surface energy of the films were measured with a Drop Shape Analyzer (contact angle measurement).

1.1.7 Contact Angle measurements on Composite Films

Contact Angle measurements were made on a KRÜSS "Drop Shape Analyzer 25E". On two different spots of the sample surface, the contact angle of water and diiodomethane droplets were measured live via camera and the included software. First, a droplet of water is placed on the surface and after 10 s, then the drop shape analyzer performs 20 measurements in 20 seconds. Subsequently, diodomethane is placed on the surface (different spot) and the same measurement procedure is conducted (10 s wait, 20 measurements in 20 seconds).

1.2 Results & Discussion

In order to examine the surface deposition affinity of PS on platy kaolinite colloids with thicknesses of 70 to 140 nm, the lateral size and therefore the aspect ratio of the platy kaolinite colloids is crucial and the aforementioned stacked structures with kaolinite colloid thicknesses higher than 1000 nm are not desired. Therefore, the colloids were separated by sedimentation in water according to Stokes' settling velocity assuming spherical particle geometry. The sedimentation process reduced the number of stacked structures, but did not lead to complete elimination of the undesired kaolinite colloids.

The crystal structure of ideal kaolinite has a so-called Janus character, because of the different functional groups on the two basal surfaces, namely Al-OH octahedrons on one side (reactive) and fully condensed SiO_4 tetrahedrons on the other (defects are reactive). Therefore, the local reactivity (i.e. μ, chemical interaction), the local wettability (i.e. π, capillary interaction) and the local surface charges (i.e. @, electrostatic interaction) are different for both kaolinite basal surfaces as well as for the lateral edges.

The heterocoagulation of polystyrene and kaolinite colloids was examined empirically, mainly via SEM imaging of dried PS/K dispersion residues. The biggest diameter of PS spheres with deposition affinity towards the face of the kaolinite colloids K_{face} was identified, whereafter the PS spheres were coated and thereby fixated with SiO_2 by the use of TEOS ($Si(OEt)_4$). After consecutive combustion of PS from the assembled SiO_2/PS/K colloids, hollow SiO_2 spheres are desired to remain on K_{face}. The ideal PS diameter for that purpose was found to be 95 nm, in the following denoted as PS_{95}.

The deposition of spherical colloids was systematically studied by ζ-potential (charges) and DLS measurements (sizes) in the wet state and SEM measurements in the dried state (morphology of PS/K assemblies). The maximum diameter of the prepared PS colloids with affinity towards the faces of kaolinite K_{face} after drying was identified and the homogenously covered PS @ K_{face} assembly then was used as a basic building unit for preparing modified assemblies with alkoxysilanes, resulting in different surface energies of the assemblies, measurerd by contact angle measurement of PS/K colloids in a PDMS matrix.

1.2.1 PS @ kaolinite deposition

The surface deposition affinity of cationic polystyrene spheres on the kaolinite platelets faces K_{face} with a lateral diameter of 3.4 µm was examined with different sizes of monodisperse polystyrene colloids, illustrated in **Figure 50**.

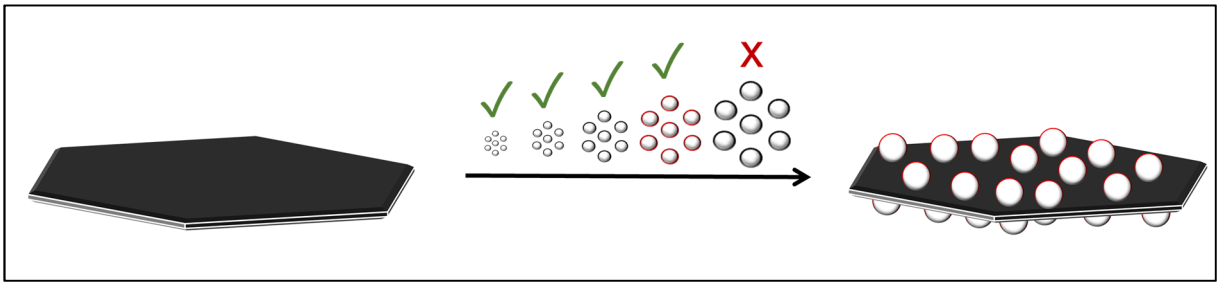


Figure 50: Illustration of the PS @ kaolinite assembly with increasing PS diameters

In order to obtain PS @ K_{face} assemblies with the highest possible PS diameter, some of the PS dispersions were synthesized without the use of the non-ionic emulsifier PVP and are indicated in the following by the denotation PS^*_d and a blue colour, whereas the indices d

represent the respective diameter of the PS spheres, for example PS^*_{105} for PS *without* PVP and PS_{95} for PS *with* PVP used in the synthesis. According to the expectation , the surface charge density of the resulting PS colloids is higher without the non-ionic surfactant PVP, since $\zeta_{PVP} \approx 0$ mV (meas. with a conductivity of 0.04 mS/cm in pure water), explained by shielding of charged groups by PVP.

The surface charge density (and the size) of the PS spheres has a dominating influence on the deposition affinity of the spherical PS colloids towards K_{face}, visible for assemblies examined via SEM imaging of dried PS/K dispersion droplets (cf. **Figure 51**, **Figure 52**, **Figure 53**, **Figure 56**, **Figure 57** and **Figure 58**). The PS dispersions with the highest diameters and reasonable deposition affinity (indicated by green colour) towards K_{face} are PS_{95} and PS^*_{135}. Higher PS diameters lead to the formation of colloidal crystals and a deposition affinity towards K_{edge} during drying by the capillary interaction π (PS π K_{edge}, cf. red-framed Figure 56, Figure **57** and Figure 58) described in the theoretical part (II-3.2, page 21).

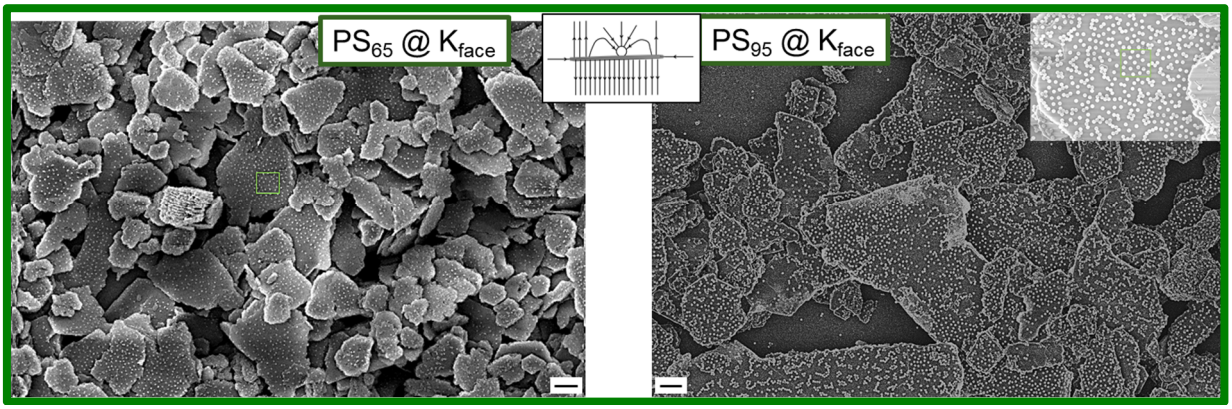


Figure 51: PS_{65} and PS_{95} colloids on K_{face}

The scale bars account to 1 µm. The shown PS/K composites have an affinity towards K_{face} by electrostatic interaction @. The inlet show the local interaction field lines as a minimal example. The deposition density Λ was determined from the light green frames: PS_{65} with N = 23 spheres on A=0.808 μm^2 and PS_{95} with N = 17 spheres on A=0.59 μm^2, both resulting in Λ = 30 PS spheres/μm^2.

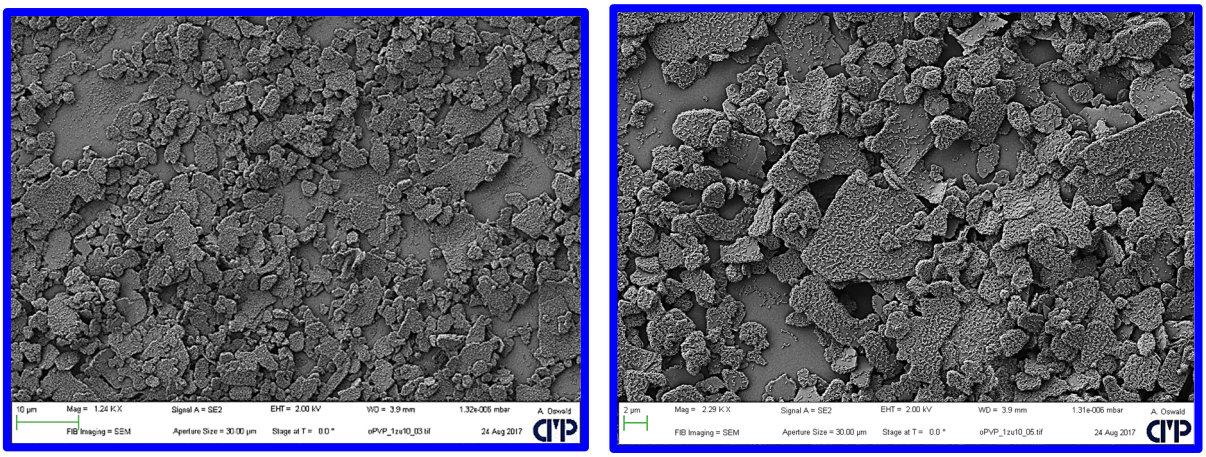


Figure 52: PS^*_{105} @ K_{face}

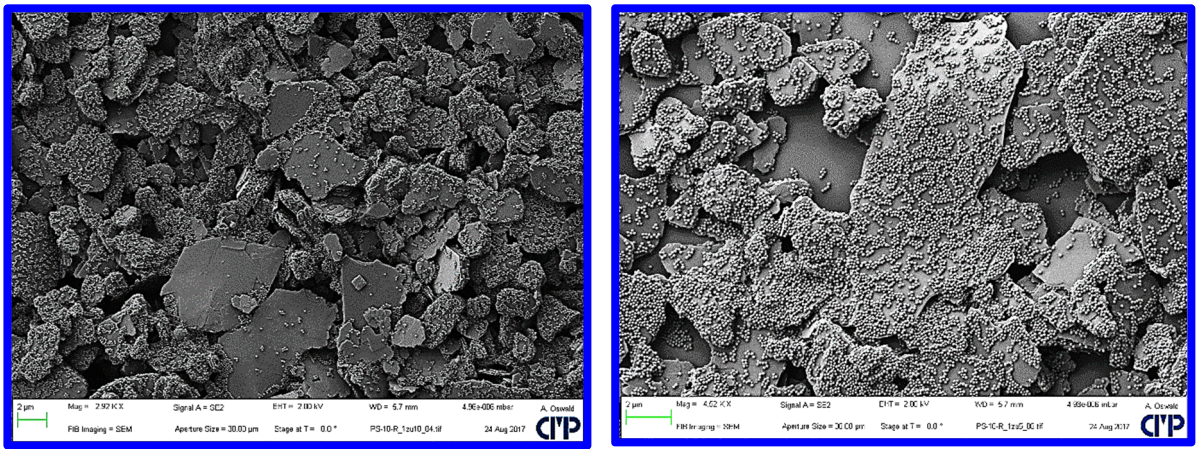


Figure 53: PS^*_{135} @ K_{face}

All of the synthesized PS colloids have a cationic charge and therefore positive ζ-potentials throughout the examined pH range from 2 to 12. The optimal pH for the PS/K assemblies in water was expected to be accessible by ζ-Potential vs pH measurements on the pristine colloids, shown in **Figure 54**. As it can be seen in the set of isoelectric titration curves in Figure 54 (*left*), the surface charge density of the PS colloids (meas. ζ-potential) becomes weaker with increasing size, since the weighed in quantity of charges determine the size of the resulting PS colloids.

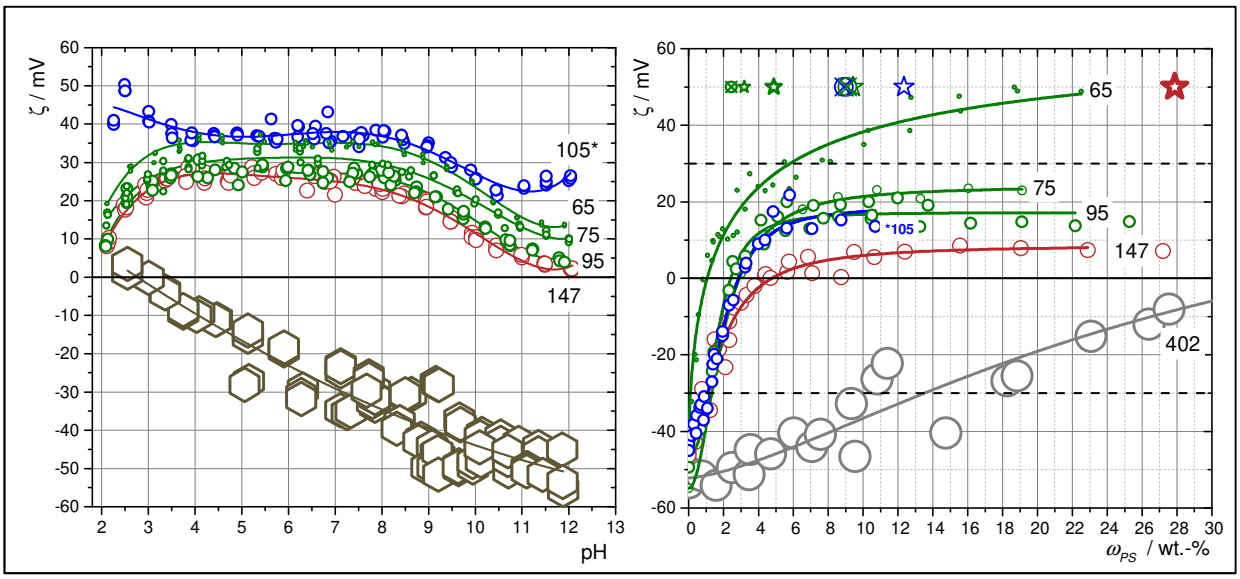


Figure 54: Isoelectric Titration of Kaolinite and PS-dispersions

left: isoelectric titration of pristine PS and kaolinite colloids. The ζ-potential deviations are very high with up to Δζ=30 mV and are not included for better visualization. Brown hexagons are attributed to kaolinite colloids. Green circle data points are indicated by increasing symbol size: 65 nm, 75 nm, 95 nm, the blue circles are PS without PVP: *105 nm, all having deosition affinity towards the K_{face} and red circles: 147 nm; with corresponding lines from 5th polynomial fitting.

right: titration of PS as additive and kaolinite as stock dispersion. The symbol attributions are equal to the *left* figure. A reference sample with 402 nm PS spheres is added (grey). The circled crosses are based on empirical findings from SEM imaging and the star symbols are predicted PS/K ratios from a geometrical model, based on the empirical findings from SEM imaging. The lines are based on logarithmic fitting. More isoelectric titrations are shown in the Appendix (page 215f).

The ratios of PS @ K for the full coverage of K_{face} by PS were estimated empirically via SEM imaging of dried PS/K dispersion droplets: e.g., for the PS_{65} samples, a 1 to 40 PS @ K ratio (wt/wt) result, whereas for the PS_{95} and PS^*_{105} samples a weight ratio of 1 to 10 PS @ K was

found, depicted as *circled cross symbols* in Figure 54. A constant deposition density Λ of approx. 30 PS spheres per μm^2 on K_{face} for PS_{65} and PS_{95} was estimated from the SEM images shown herein (Figure 51, light green frames). From the empirically estimated deposition density Λ, a simple geometrical model of hexagon-shaped kaolinite platelets and PS spheres was deployed, depicted as *star symbols* in Figure 54 (model data: ρ_K=2.58 g cm^{-3}, ρ_{PS} =1.04 g cm^{-3}, d_K=3.43 μm, h_K=0.10 μm and d_{PS} = 65 and 95 nm). The other samples did not show a constant deposition density Λ and the geometric model volume ratio (and therefore mass ratio) for $PS^*_{105}$was calculated with the assumption that Λ=30 PS spheres per μm^{-2} on K_{face} holds.

From the isolectric titration curves 'ζ vs pH' of the pristine colloids, one would expect that for the additive titration 'ζ vs ω_{PS}' that the PS @ K assemblies for the PS^*_{105} sample have the steepest increase, if one neglect the effect of the size. The geometrical model helps to approximate the net effect of the size.

The PS @ K assemblies tend to be less homogeneous after drying if more ions are present, such as increased chloride concentrations at high PS concentrations or ambient carbonate uptake. In this context, pH adjustment also adds ions to the dispersions - so inhomogeneous distributed spheres on the kaolinite surfaces can be the result. For PS_{65} spheres, a pronounced homogeneous distribution of the PS spheres was achieved all over the dried sample, not observed in any sample with higher diameter. This finding correlates well with the lower limit of layer thicknesses of the used kaolinite platelets (cf. Appendix, page 202). The well-kept distance of PS_{65} spheres after drying seemingly resemble the shielding effect of the electrical field lines from the initial wet state. Similar assemblies were already observed and examined for negative charged polymer spheres @ LDH.[68]

The *apparent* ζ-Potential is interpreted as the average surface charge of the agglomerated structure. A single deposition step of a sphere on a lamellar colloid changes the initial surface charge of the lamellar colloid, so that the initial electrophoretic mobility of the lamellar particle is weakened. The shift and broadening of Apparent ζ-Potential distributions of an autotitration experiment is shown in **Figure 55**.

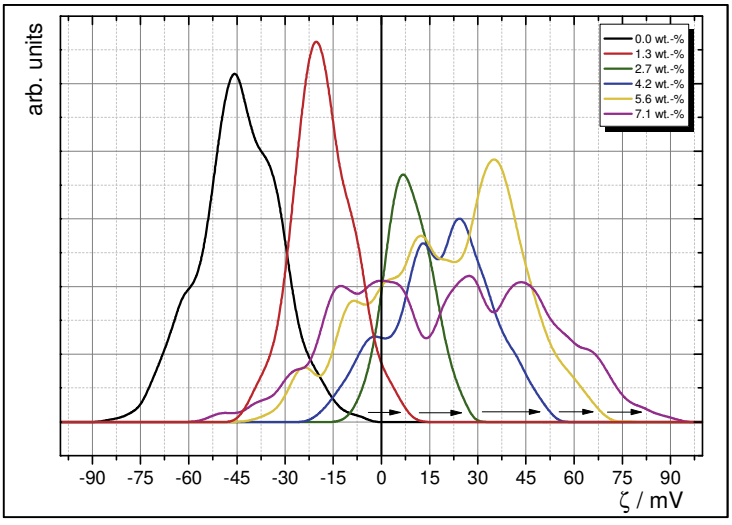


Figure 55: Apparent ζ-potential distributions of a PS_{95} @ K titration.
The conductivities were all 0.1 mS cm^{-1} throughout the addition. The results originate from an autotitration of 95 nm PS colloids (0.08 wt.-%) added to a kaolinite dispersion (0.17 wt.-%). The peak of the red colored distribution curve are 2.9 · 10^8 Counts. The intensity of the ζ-Potential distribution decreases with the added amount of spherical colloids in the dispersion, simultaneously the mean of the distribution increases (cf. arrows).

Low ionic strengths lead to increase of the ζ-potentials at constant pH. It was found, that the removal of ions is more crucial than controlling the pH in order to obtain homogenously organized PS/K assemblies after drying. The control over the ionic strength was realized by dilution of the dispersions. This fits well into the requirement of diluted dispersions for the ζ-potential measurements. The ζ-potential measurements were all conducted at the lowest possible ion (and colloid) concentrations, measured as low conductivities down to 4 µS cm^{-1}.
However, the biggest found PS diameter with a reasonable affinity to K_{face} after drying was found to be PS^*_{135}, whereas higher diameters show affinity towards K_{edge}, seemingly irrespective of the surface charge density, but strongly attributed to the kaolinite edge height distribution, shown in the SI.
Again, the ζ-potentials of PS_{95} and PS^*_{105} have a considerable difference in surface charge density ($\Delta\zeta = +10$ mV) but the addition lead to almost the same response, as already mentioned. The surface charge density (meas. ζ-potential) is directly linked to the composition of the PS colloids from synthesis. Therefore, the composition has some influence on the resulting surface energy γ of the PS colloids, attributed to resulting capillary interactions π.
The formation of PS colloidal crystals by the capillary interaction π is known to start during the drying process, more precisely, when the diameter is equal to the level of the evaporating water film (cf. theoretical part). Therefore, bigger PS colloids have more time to organize to colloidal crystals, if the drying conditions are the same. The electrostatic interaction @ is overcome by evaporation of water as medium of the electrostatic forces. The arising capillary forces during the drying of a dispersion droplet can be described in short as π $2D_{inf}$. The symbol π is the capillary interaction, whereas the expression $2D_{inf}$ means, that the droplet is dried on an (quasi-)infinite flat 2D surface (Si-wafer). The interaction of negatively charged spheres (PDPE and SiO_2)with the edges of kaolinite colloids is shown in the Appendix (page 214).
Size measurements on the assemblies were also performed during the autotitration process by DLS. The DLS results are from marginal interest and do not have any significance, because the detectectable size ranges by the used equipment are too narrow and are believed to surpass 10 µm for the assemblies.
The main reason why PS colloids at a particular size do not deposit on the kaolinite surface are competing capillary interactions, which induce the formation of colloidal crystals (PS π PS)$_n$ during the drying process (compare theoretical part, II-3.2, page 21ff) and also assemblies of the type PS π K_{edge} (cf. **Figure 56** and **Figure 57**).

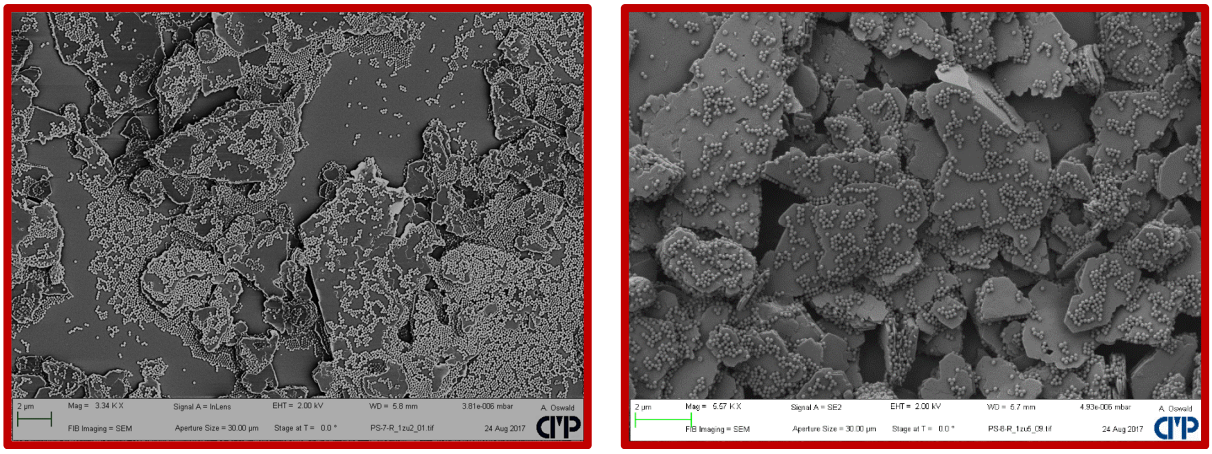


Figure 56: SEM images of PS_{145} / K and PS_{147} / K
left: PS_{145} / K showing moderate edge and moderate face affinity (1 to 2, wt/wt).
right: PS_{147} / K showing *clear* edge affinity (1 to *5*, wt/wt).

Also, the capillary interaction π is able to pull the PS colloids towards the ordered regions at the perimeter of the drying droplet at high PS concentrations. Higher concentrations and sizes of PS are therefore able to prevent surface affinity, shown in **Figure 58**. At intermediate ratios and near the perimeter of the droplet, colloidal PS crystals can also form on K_{face} after drying(cf. Appendix, page 206), whereas this effect was not found to be easily reproducible and had minor attention throughout the thesis, therefore may need deeper investigation with respect to fluid mechanic topics such as the prominent marangoni flow ($\propto \Delta T$, $\Delta\gamma$).

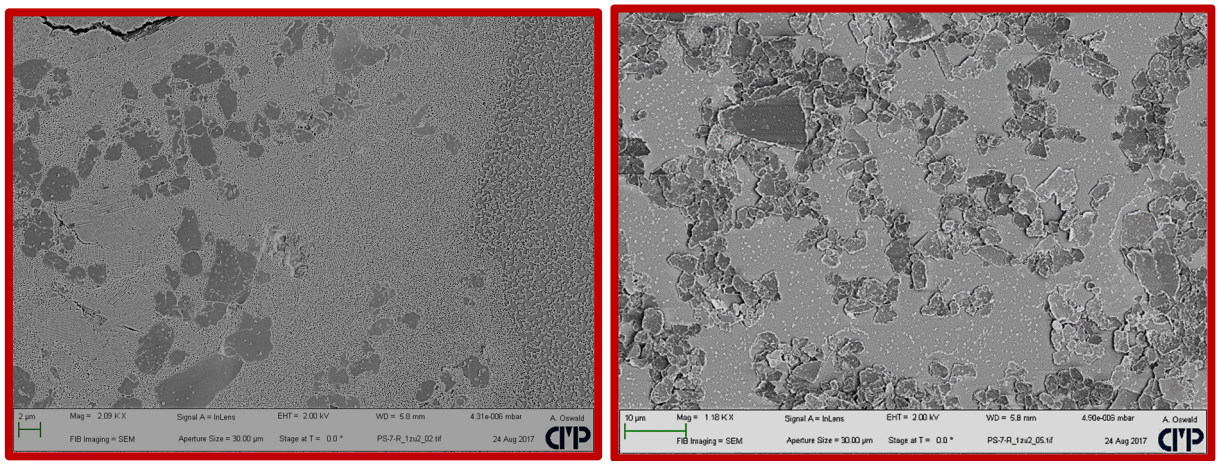


Figure 57: SEM image*s* of PS_{145} π K_{edge} sample at lower magnifications
including the disordered regions with no surface affinity (*left image*). The left-hand side of the left figure is directed to the droplets perimeter, the right-hand side is directed to the middle of the sample (*right image*).

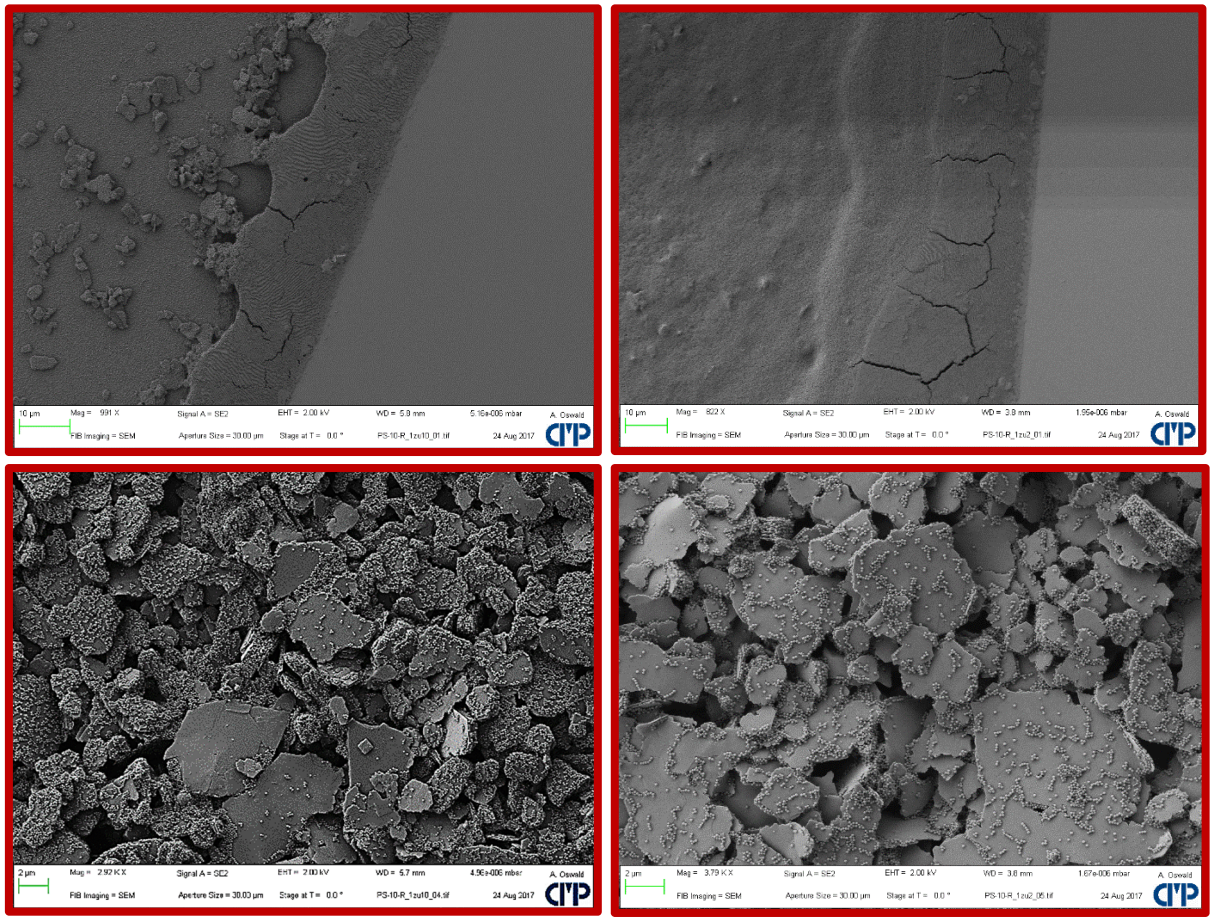


Figure 58: SEM images of PS^*_{135} @ K at different weight ratios
1 to 10 (left) and 1 to 2 (right). Also for the PS π PS assemblies, a border between ordered and less-ordered patterns established after drying.

Some side experiments were conducted with small concentrations of different salts (NH_4F, NaF, NH_4Cl, tetrapropyl-ammoniumbromide), which did not lead to an enhanced electrostatic deposition of higher PS diameters within PS@K_{face} assemblies (not shown herein).

1.2.2 SiO_2 coating of PS @ kaolinite assemblies

The wet-state morphology of the PS@K_{face} assemblies is hardly accessible. Therefore, the deposited PS spheres were fixated to the kaolinite surface by covalent bonds by the use of TEOS. In a related publication about SiO_2 hollow spheres, PS was used as template and PVP was also added during the PS synthesis to obtain the desired SiO_2 hollow spheres from the reaction of PS with TEOS and subsequent combustion of PS. The described procedure lead to monodisperse hollow silica spheres and is adapted here. Bare monodisperse silica hollow spheres (not shown here, Wu et al. (2006)[152]) were reproduced with a diameter of 325 nm during a visit in Shanghai at the Fudan University. The reaction conditions were the same in all experiments, despite the TEOS concentration (**Figure 59**). Raspberry-like SiO_2 @ PS and core-shell SiO_2 @ PS colloids are obtained on the kaolinite surfaces K_{face}. After combustion of PS, three border cases of morphologies were obtained: crumbled, raisin-like and hollow.

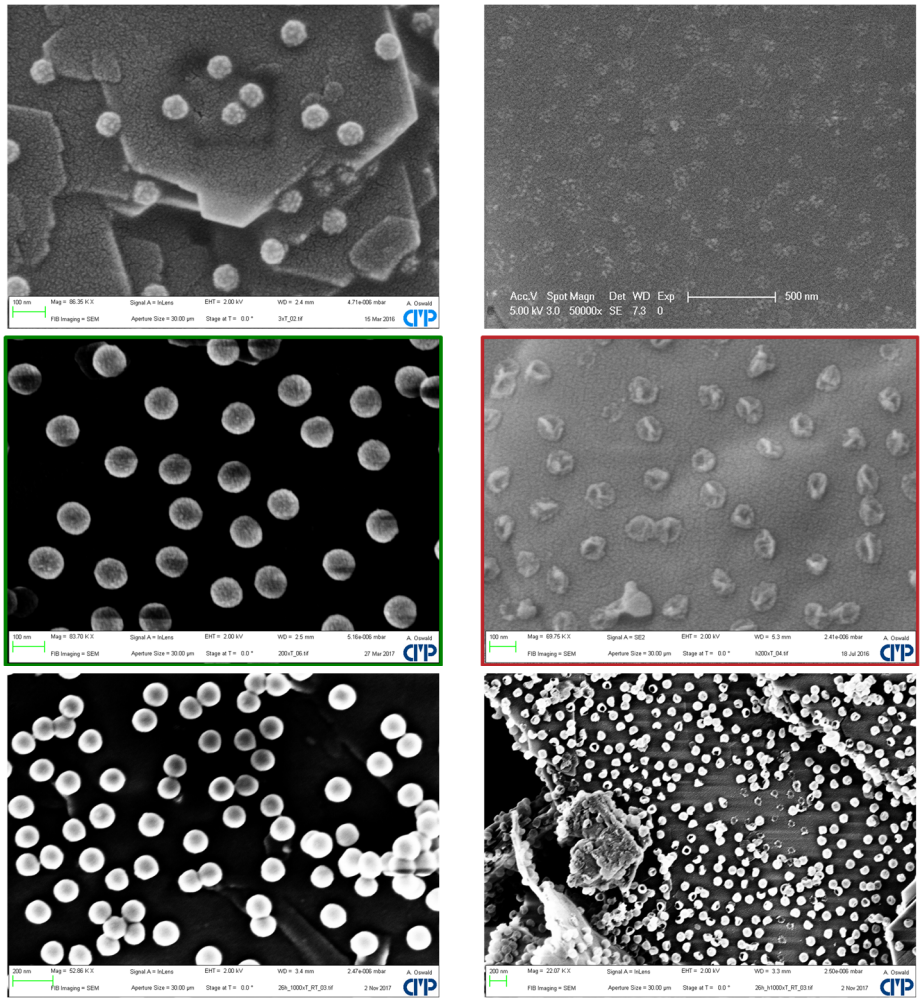


Figure 59: SiO_2 μ (PS_{95} @ K) assemblies based on different TEOS concentrations
The left side shows the assemblies before heat treatment, the right side shows the same assemblies after heat treatment. The TEOS concentrations from top to bottom are 3-, 200- and 1000-fold TEOS weight based on the PS mass content.

The reaction of TEOS with the aforementioned PS_{135}* @ K_{face} assemblies (Figure 53, w/o PVP in PS synthesis) result in aggregates of SiO_2 and PS spheres, resulting in poor sphere deposition on the surface of kaolinite K_{face} (cf. **Figure 60**). In contrast, the aforementioned PS_{147} **π** K_{edge} assemblies of the previous subsection (cf. Figure 56) has an affinity towards K_{face}, therefore resulting in the desired SiO_2 μ (PS_{147} @ K_{face}). The usage of PVP for the successful preparation of SiO_2-coated particles is often reported in the literature[153,154] and the present work confirms that PVP enhance the formation of homogenous SiO_2 shells surrounding PS.

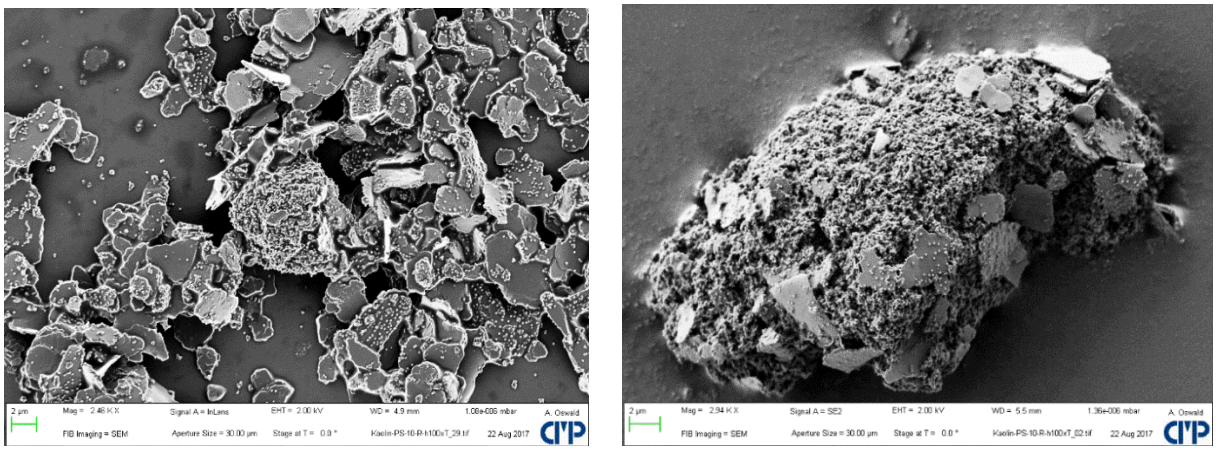


Figure 60: SEM images of SiO_2-coated PS^*_{135} / K *after* PS combustion with a 100-fold TEOS/PS excess (wt/wt)

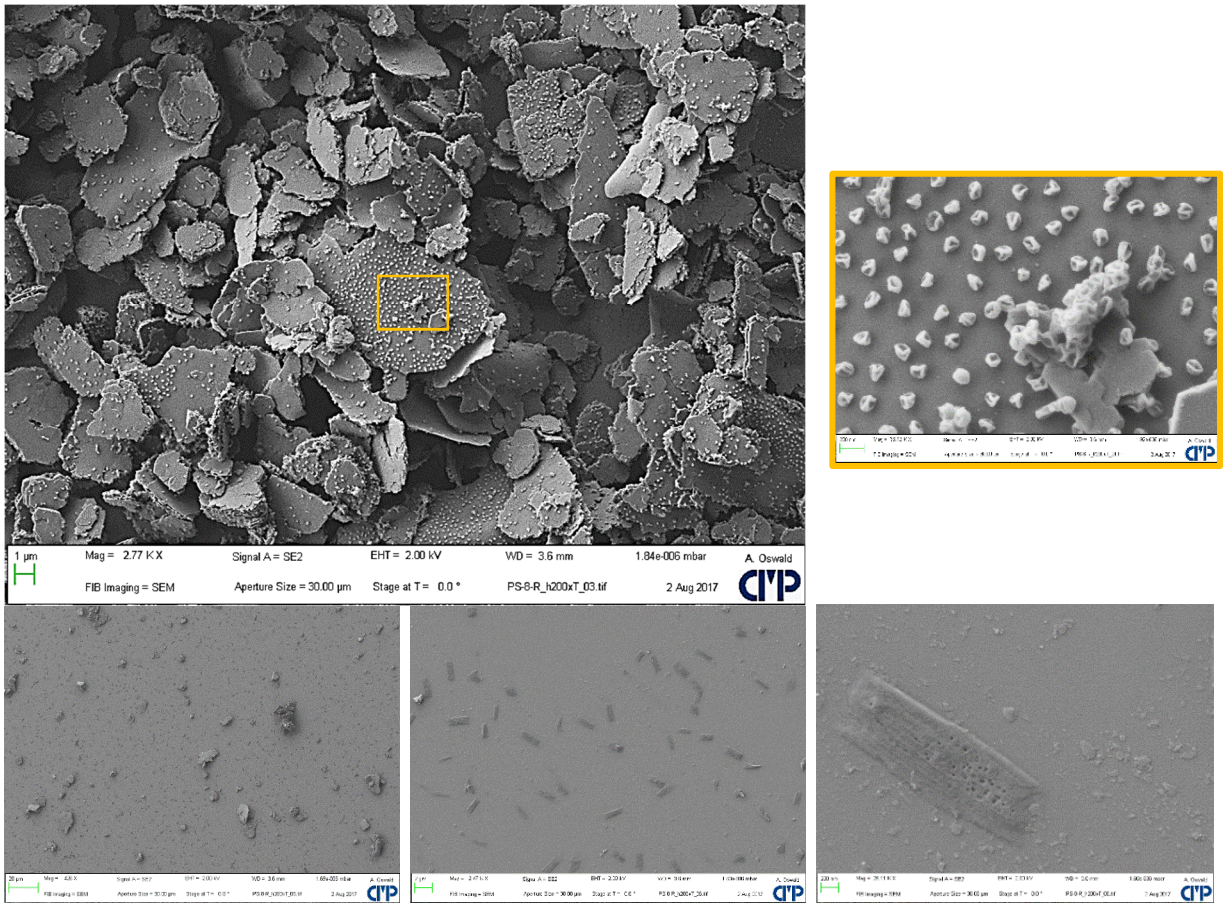


Figure 61: SEM images of SiO_2-coated PS_{147} @ kaolinite *after* PS combustion prepared with a 200-fold TEOS/PS weight ratio. Bottom SEM images shows large SiO_2 sheets with K_{edge} imprints

After reaction with TEOS, the resulting SiO_2 μ (PS @ K_{face}) assemblies tend to show a Janus deposition pattern, visible in Figure 61 and **Figure 62**. As already pointed out, the Janus character of the ideal crystal structure of kaolinite is believed to induce the obtained deposition behavior. During the heat treatment from r.t. to 550 °C, kaolinite is transformed to metakaolinite by dehydroxylation above 450 °C (TGA, Appendix, page 207). It is assumed that SiO_2 is covalently bonded to the hydroxyl functions of the octahedral kaolinite surface due to the calcination process. From the SEM morphologies it seems that SiO_2 is bound to the octahedral layer, to defects of the tetrahedral layer and at the edges of kaolinite.

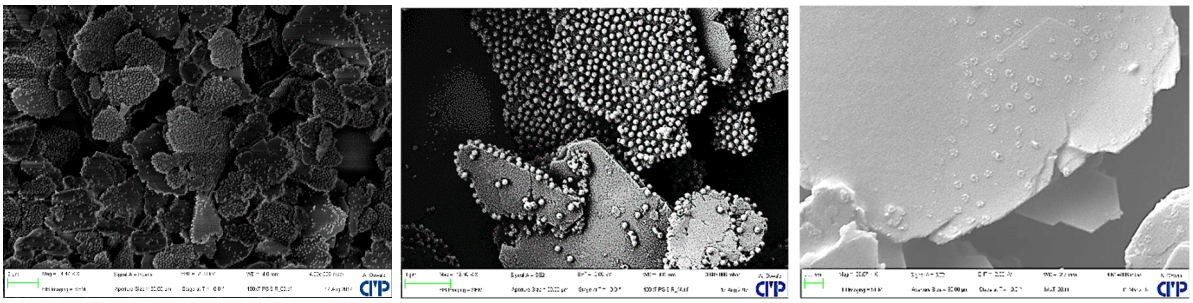


Figure 62: SEM images of SiO_2 μ PS_{95} @ K_{face} deposition patterns *after* PS combustion

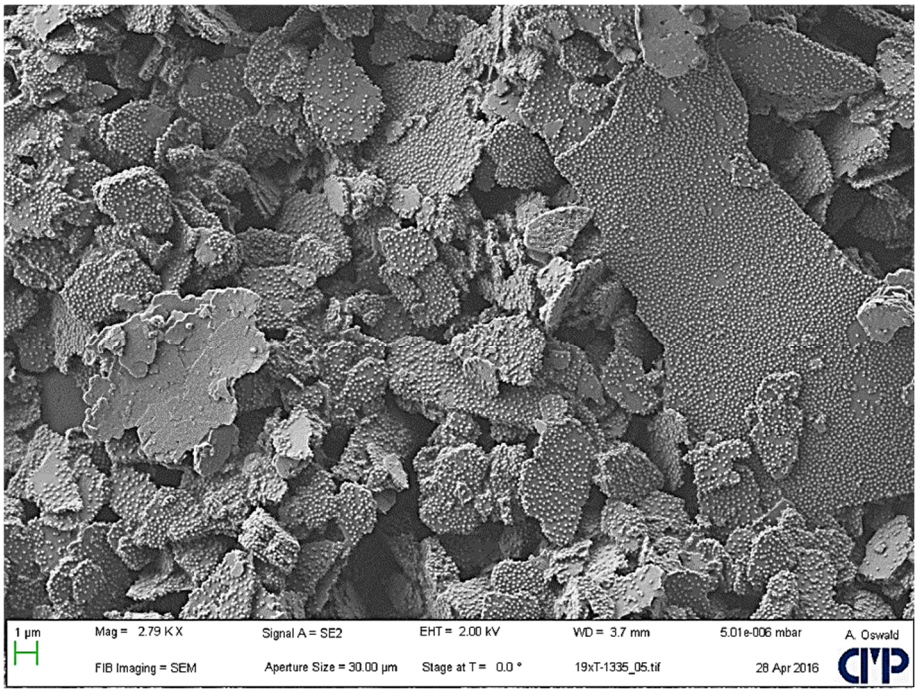


Figure 63: SEM image of SiO_2-coated PS_{95} on kaolinite *before* PS combustion treated with a 19-fold TEOS/PS weight ratio

The wall thicknesses of the hollow spheres are approx. 8 nm thick, which corresponds to a ratio of shell thickness to PS_{95} diameter ratio of 7.8 %, whereas the aforementioned 430 nm hollow spheres have a ratio of 5.6 %.

1.2.3 Surface Modification of PS_{95} @ K assemblies

A comprehensive overview of the transformations within this subsection is shown in **Figure 64**, the corresponding SEM images of the morphologies in **Figure 65** and the thermogravimetrical analysis in **Figure 66** and **Table 9**. The surface modification was done by silylation with TEOS ($Si(OEt)_4$) and/or MTES ($Me\text{-}Si\text{-}(OEt)_3$). The methylene group of the organosilane MTES was applied on three different colloidal assemblies by chemical assembly μ (hydrolysis, condensation). Moreover, a treatment with the more hydrophobic PDMS was applied. The modified organized colloids were incorporated into a commercial PDMS-based matrix with a constant mass concentration of the assemblies in the matrix and the surface energy of the composite films was measured (**Figure 67**).
The obtained hollow spheres on kaolinite (light blue box) do show a Janus deposition pattern, in case of using the kaolinite product SKT-35 after sedimentation procedure. The other kaolinite product (SKT-13P) was used for all other assemblies shown here and the kaolinite-based assemblies with Janus characteristics are further examined in the next section by using aminofunctional silanes before the assembly.

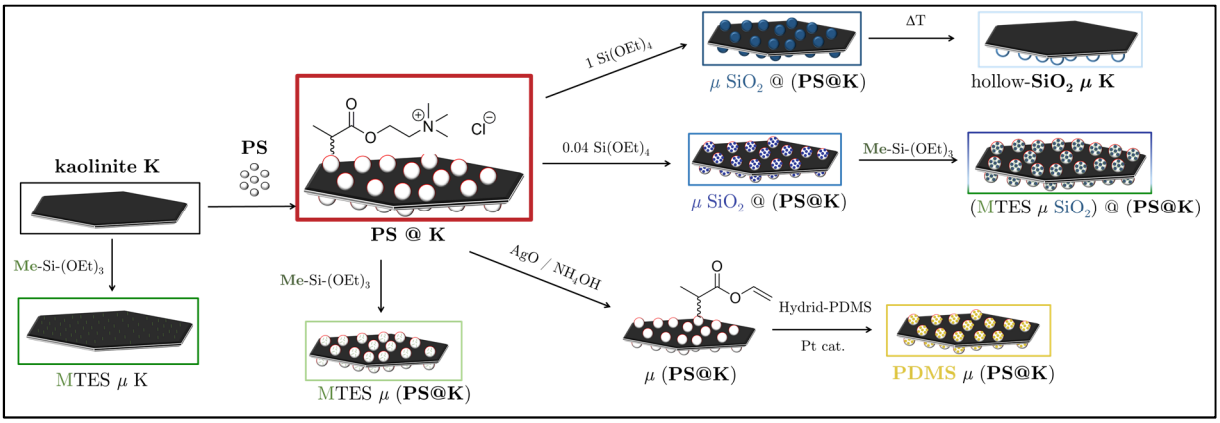


Figure 64: Transformations of surface modified PS_{95} @ K_{face} assemblies
The transformed colloids are described by μ = chemical reaction and @ = electrostatic assembly.

The modification of the PS_{95} @ K assemblies with MTES lead to a partial coalescence of the PS spheres. The assemblies which underwent a Hofmann elimination reaction μ (PS@K) were intact and the subsequently PDMS-modified assemblies PDMS μ (PS@K) show a loss of the spherical polystyrene morphology. The morphologies of the assemblies treated with TEOS are shown in the previous subsection with intact spherical morphology, showing either raspberry, core-shell or hollow morphologies. The modification of kaolinite K with MTES (MTES μ K) as a reference show no change of the morphology of the initial kaolinite K colloids, whereas the thermogravimetrical analysis and the surface energy changed, described in the following.
The modification of kaolinite K with MTES (MTES μ K) lead to a minor mass loss compared to pristine kaolinite (cf. Table **9**). The mass loss of kaolinite K originates from the surface water content, which is assumed to be readily evaporated below 250 °C (1.15 wt.-%) and the dehydroxylation of the structural hydroxyl groups (13.75 wt.-%). The lower surface water loss of the MTES-modified samples can be explained with the decreased water content by the hydrophobic surface, also measured via contact angle measurement. The highest mass loss is obtained for the *basic building unit*: unmodified kaolinite with cationic PS spheres (PS @ K), whereas any silylation by TEOS and MTES lead to minor mass losses, since the overall combustible part is decreased by the introduced silicon oxide.

However, the emphasis in this subsection is on the altered surface energies of the modified PS_{95} @ K assemblies: the permanently charged quaternary ammonium groups of the PS colloids increase the hydrophilicity of the pristine kaolinite. The dispersive part of the surface energy increases almost linearly in the order (cf. Figure 67, *left*).

PS@K<$SiO_2\mu$(PS@K)<(MTESμSiO_2)@(PS@K)<MTESμ(PS@K)<K<MTESμK<PDMSμPS@K.

When the MTES is reacted on the PS @ K assemblies, the polar part of the surface energy decreases by 66 %, whereas when TEOS is applied the films are 20 % less polar, and the combination of TEOS and MTES result in a decrease of the polar content of the surface energy of just 40 %. The surface of the PDMS containing assemblies has the highest dispersive part of the surface energy with 100 %. By the help of this framework, one can tailor the compatibility of nanofillers for commercial coatings. In the upcoming section, the emphasis is on the Janus character and the assembly after silylation.

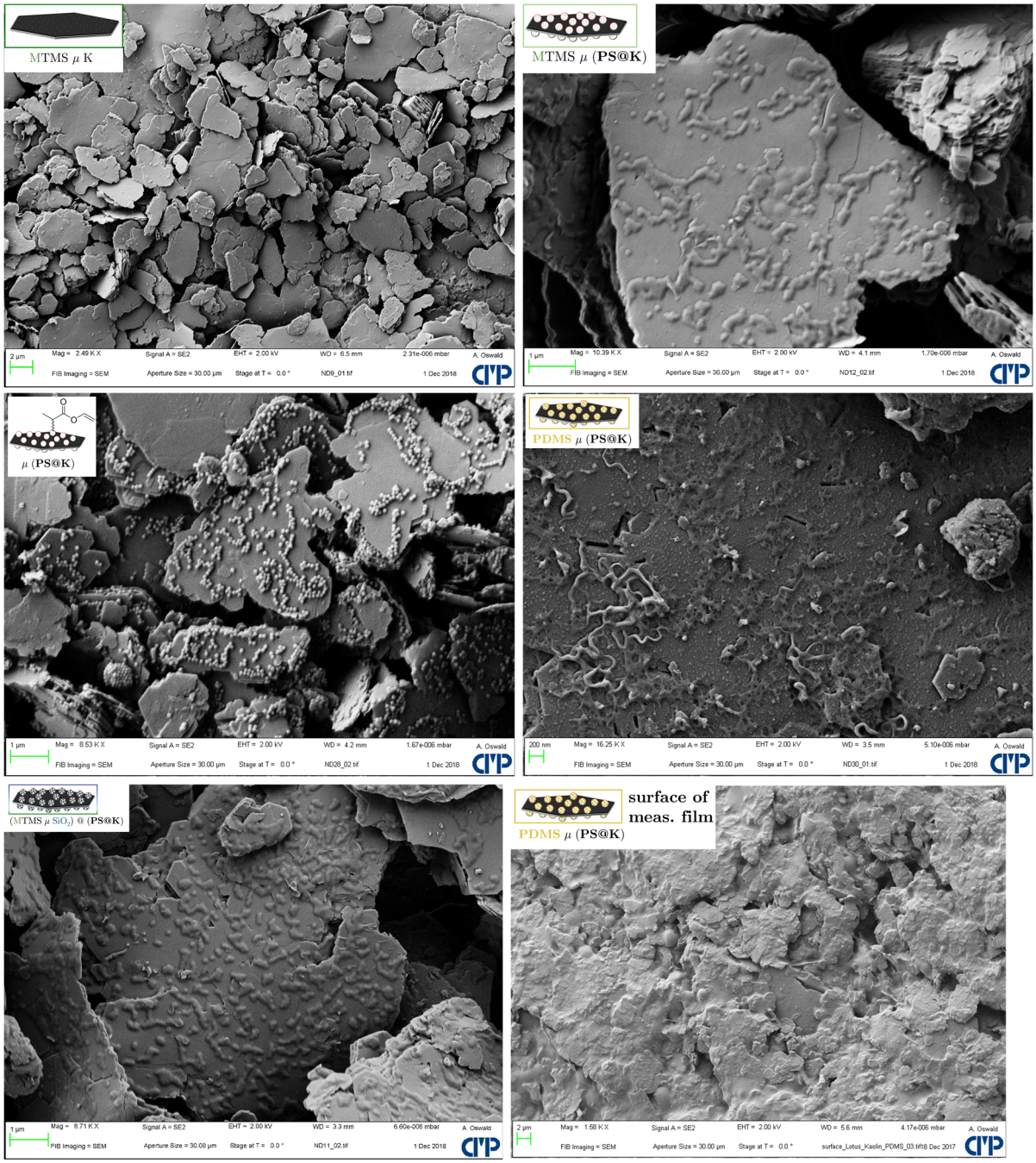


Figure 65: SEM images of the surface modified $PS_{95}@K_{face}$ assemblies

Table 9: TGA mass losses of modified assemblies at 250 °C & 1000 °C

	mass loss at...		combusted part
	1000 °C	250 °C	Δm (1000 – 250) °C
K	14.90%	1.15%	13.75%
K+MTES	14.40%	0.68%	13.72%
K+PS+TEOS+MTES	19.45%	0.62%	18.83%
K+PS+TEOS	20.33%	1.26%	19.07%
K+PS+MTES	20.23%	1.01%	19.22%
K+PS	20.37%	1.10%	19.27%

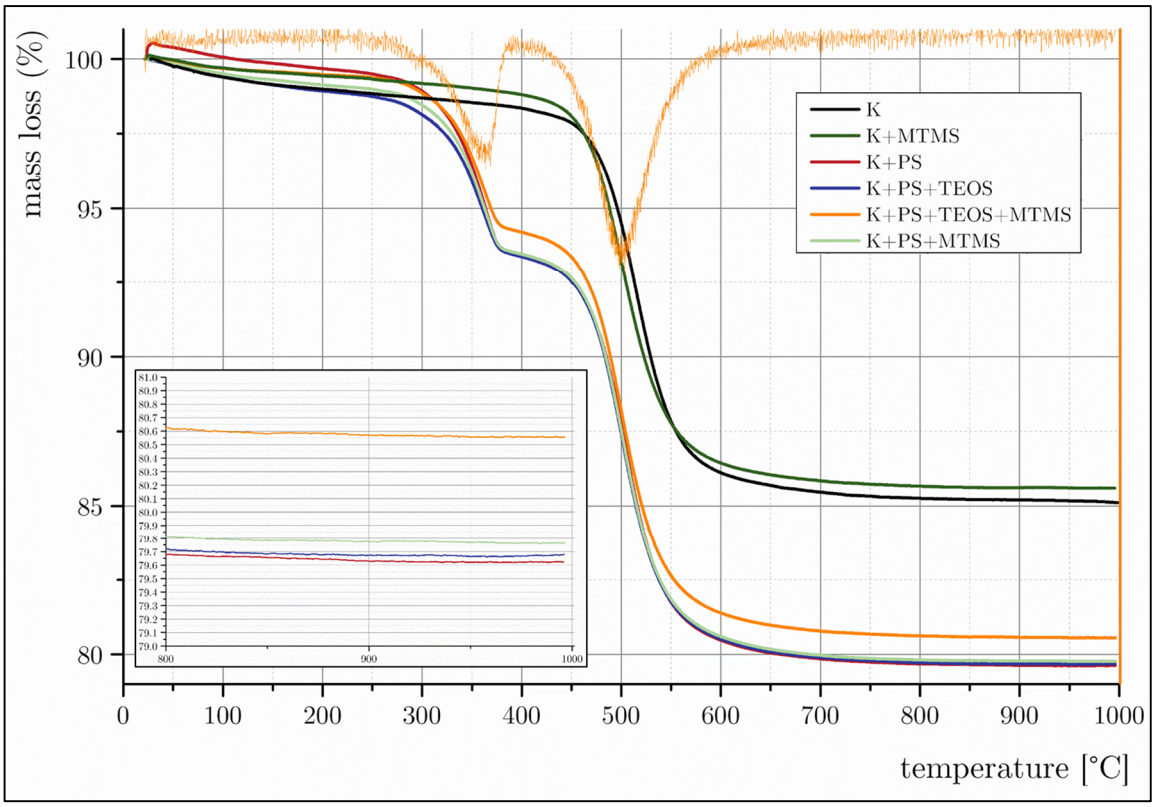


Figure 66: TGA measurements and DTG of organized and functionalized kaolinite

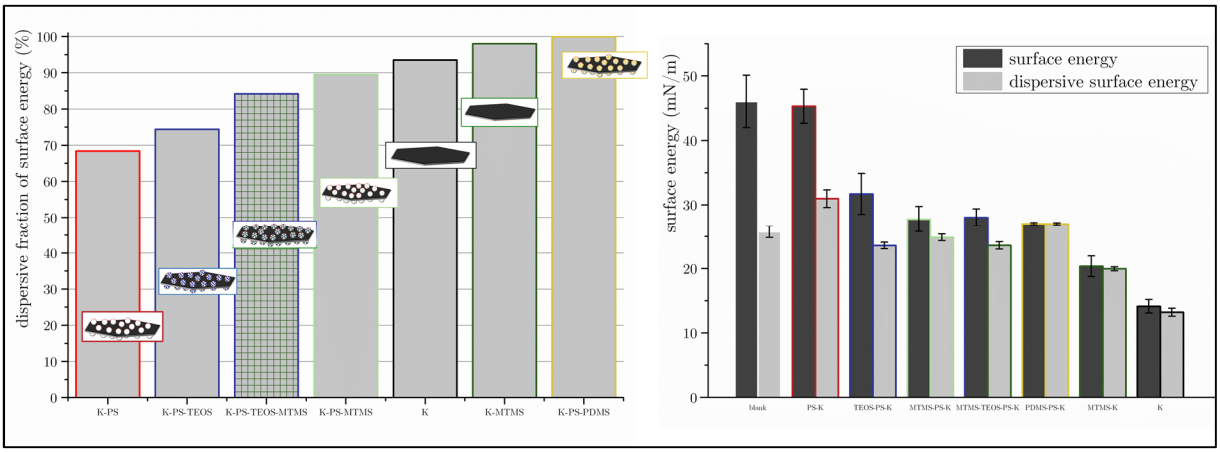


Figure 67: Surface energies of polymer/organized kaolinite composite films

2 Polystyrene @ Janus-Kaolinite Assemblies

The Janus character of kaolinite is an interesting and outstanding property, which is poorly documented and almost unregarded. In the previous subsection, Janus deposition patterns emerged from fixating PS spheres on kaolinite surfaces in order to rule out the colloidal state of the PS @ K_{face} assemblies. The possibilities to make use of Janus colloids is tremendous and are described in the theoretical part (section II-2.3, page 17). Usual manufacturing of Janus colloids is usually elaborate, therefore it seemed worth doing more work on cheap and abundant kaolinite.

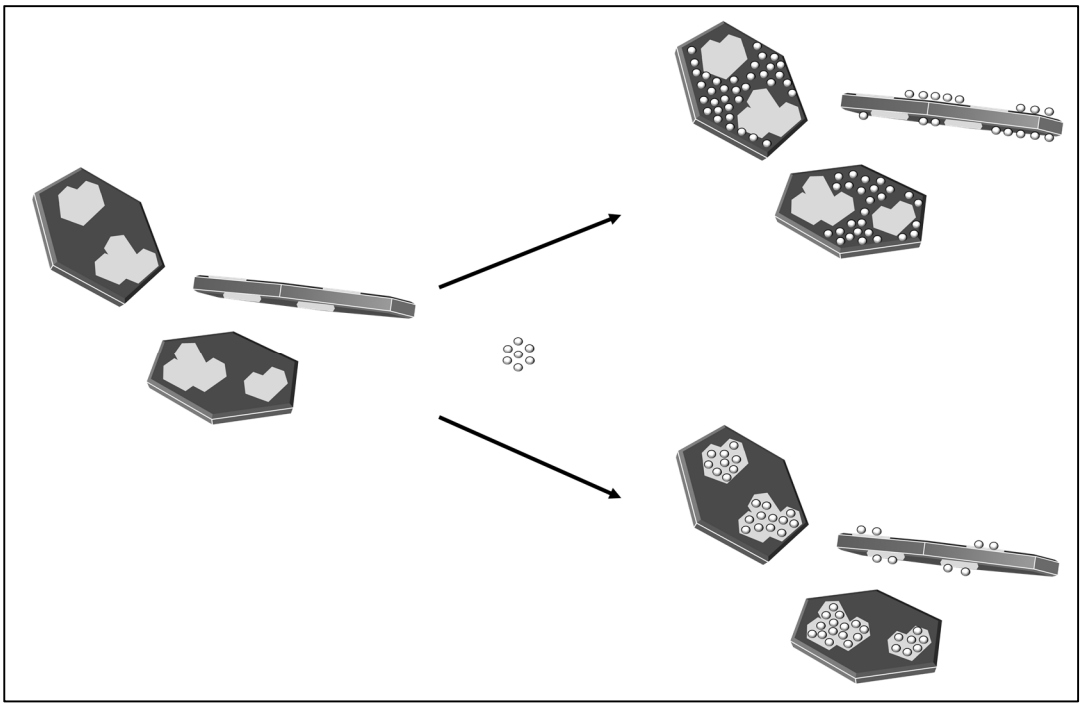


Figure 68: Representational Scheme of the Patchy Janus Kaolinite Coverage

Within this subsection, several silylation reactions of kaolinite colloids are conducted (cf. **Figure 68**). The obtained positive charge ($-NH_3^+$) can hinder alike charged spherical colloids to deposit on the surface by electrostatic shielding, whereas the same spheres are deposited on the unmodified spots on the kaolinite surface. Consistently, for negatively charged spheres, the deposition on the modified spots is expected. The obtained functionalities can also be used for a further grafting reaction to obtain a deposition pattern based on covalent bonding. All of these possibilities are presented in the upcoming subsections.

2.1 Experimental Details

Materials

Table 10: Materials for Patchy Janus Kaolinite Coverage

Name	Size/Purity	Supplier
Kaolin SKT-13P	pristine, multimodal	BASSERMANN minerals
Kaolin SKT-35	3.43 µm, monomodal	BASSERMANN minerals
PS nanoscale dispersion	61 nm	see section III-3, page 50
Perglutin	30 nm	BK Giulini
Epoxy-PDMS "Tegomer E-Si 2330"	5-15 nm	EVONIK
3-Aminopropyltriethoxysilane	97%	abcr
3-Aminopropylmethyldiethoxysilane	97%	abcr
3-Aminopropyldimethylethoxysilane	95%	abcr
pure ethanol	≥99.5%	Merck
2-butoxyethanol		

Methods

Dynamic Light Scattering (DLS)
Malvern Zetasizer Nano ZS
Zeta Potential Measurement
Malvern Zetasizer Nano ZS
Scanning Electron Microscopy (SEM)
Zeiss NEON 40
Elementary Analysis
EDX (Zeiss NEON 40)
Thermogravimetric Analysis (TGA)
Mettler-Toledo TGA/SDTA 851e, optionally Pfeiffer Vacuum OmniStar, mostly 5 °C/min
Infrared Spectroscopy (ATR-FTIR)
IRRAS Bruker VERTEX 70
Centrifuge
BECKMAN COULTER Avanti® J-E with a JA-10 Rotor
Ultrasonic Bath
BANDELIN "SONOCOOL 255 "
Pull-Out measurement
"MTS Criterion C45.105" with an "HBM/S2M/10" load cell

2.1.1 Silylation of Kaolinite

Silylations of kaolinite colloids are conducted with the extracted size fractions around 4 µm obtained from the sedimentation and/or centrifugation processes described in section III-2 (page 46). The small fractions (mean eq. diameter 0.6 µm) are not examined, primarily to limit the number of samples. Another reason is that the smaller kaolinite particle fractions are always present in the extracted size fractions and are therefore in indirect examination. The weight fraction of kaolinite is kept constant at values around 0.3 to 0.4 wt.-% throughout all silylation experiments, which should allow for a proper particle-to-particle distance for the silylation taking place on the surface hydroxyl groups. The reaction time and the temperature dependence of self-condensation products of APTES are taken from Brochier Salon et al.[155] Therefore, the chosen reaction time is 12 hours at r.t., where 80% of T^3 and 20 % of T^2 species are present. The addition of water is another option and therefore reduces the reaction time in general, so that 5 hours in presence of water are chosen. Silylation reactions are usually performed in a sealable polymeric vessel to prevent silylation of glass utilities. On the other hand, it was found in the literature, that the size of the self-condensed colloids do not vary with the used vessel material.[156] Both conditions are tested on classical Stoeber reactions and it is found, that there is in fact no difference between polymer and glass vessels. All silylations performed at higher temperatures than r.t. are performed in glass flasks with reflux condenser to prevent building up pressure. In some experiments, the silylation was conducted at 50 °C and an undetermined inner pressure in a screw-capped polymer vessel. The samples are denoted as A1C1 with A1 indicating the aminosilane concentration (1%) and C1 the number of centrifugation (1^{st} step). The samples are dried and redispersed in water for further use.

a) Aminosilane in 100% Ethanol

In a typical experiment, a 0.4 wt.-% kaolinite dispersion in pure ethanol is prepared, and 1, 3, 5, 7 and 10 wt.-% APTES based on the overall dispersion was added. For example, 0.1 g kaolinite is dispersed in 25 g ethanol and 0.25 g APTES is added. After 12 hours, the samples are centrifuged 4 times (4500 rpm, 5 minutes).

After each centrifugation, 10 mL EtOH are used for the redispersion, subsequently 5 mL are taken and dried in an convection oven in a stainless steel dish until the solid phase appears lucid (45 °C; 20 to 30 minutes). The semi-dry powder is then treated at 120 °C for 48 hours. Thereafter, an aqueous dispersion with a NVC of 2 wt.-% is prepared for examination via SEM (IV-2.1.2).

Moreover, one attempt was on the raw product "SKT-13P" (no size fraction isolated). This multimodal type is used for the experiments described in IV-2.1.4 to IV-2.1.6.

Table 11: Weighed portions for silylations in 100 wt.-% ethanol

	1 wt.-% APTES	3 wt.-% APTES	5 wt.-% APTES	7 wt.-% APTES	10 wt.-% APTES
Kaolin dry	0.10	0.10	0.10	0.10	0.10
EtOH	25	25	25	25	25
APTES	0.2703	0.7870	1.2600	1.8550	2.5239
mmol APTES/g kaolinite	12	36	57	84	114

b) Aminosilane in 80% Ethanol

In a typical experiment, an aq. kaolinite dispersion, ethanol and various concentrations of APTES (1, 3, 5, 7, 10 wt.-% on overall dispersion) are stirred for 5 hours at room temperature. For example, 0.1 g kaolinite is dispersed in 5 g water and 23.6 g ethanol (80/20 wt), thereafter 0.3 g of APTES is added. Both of the monomodal kaolinite types were used. The samples are centrifuged 4 times.

After each centrifugation, a small portion (approx. 15 wt.-%) of the resulting solid phase is taken and dried at 70 °C (1 hour) for further examinations.

Alternatively, after each centrifugation, 10 mL EtOH are used for the redispersion, subsequently 5 mL are taken and dried in an convection oven in a stainless steel dish until the solid phase appears lucid (45 °C; 20 to 30 minutes). The powder is then treated at 120 °C for 48 hours.

Table 12: Weighed portions for silylations in 80 wt.-% ethanol

	1 wt.-% APTES	3 wt.-% APTES	5 wt.-% APTES	7 wt.-% APTES	10 wt.-% APTES
kaolinite disp 5.36 wt.-%	2	2	2	2	2
H_2O	4	4	4	4	4
EtOH	23.6	23.6	23.6	23.6	23.6
APTES	0.33	0.89	1.48	2.08	2.97
mmol APTES/g K	14	38	62	88	125

c) Aminosilane in Butoxyethanol

Another experiment is carried out in butoxyethanol as reactive solvent (bp.: 171 °C). All reactions were carried out in 50 mL volume (55.6 g). The reaction was carried out in a 100 mL three-neck round-bottom flask equipped with a reflux condenser and magnetic stirrer. Therefore, a 0.4 wt.-% Kaolinite dispersion in Butoxyethanol is prepared and heated to 93.5 °C (oil bath 110 °C). Then, APTES is added to obtain a 0.1, 0.9 and 8.1 wt.-% APTES concentration based on the overall dispersion (see **Table 13**). The dispersion is stirred for another 2 hours, centrifuged six times (6000 rpm, 7 minutes) and dried at 80°C overnight.

In one experiment a trimethylammonium silane (0.1 wt.-%) is used (#4).

Table 13: Silylation experiments in butoxyethanol as a solvent

	#1	**#2**	**#3**	**#4**
kaolinite	0.2062	0.20	0.20	0.20
butoxyethanol	43.943	44.02	44.76	43.95
H_2O	2.00	1.99	2.01	2.02
APTES	4.09	0.41	0.05	0.05
APTES conc (wt.-%)	8.14%	0.89%	0.10%	0.12%

d) Analogous Aminosilanes in 95 % Ethanol

The silylation grafting reactions were performed in a three-neckedround-bottom flask equipped with a reflux condenser, magnetic stirrer and a Heat-On (Heidolph). A 0.6 wt.-% kaolinite (1.2 g) dispersion in 198 g of a ethanol/water mixture (95/5, wt/wt) was prepared by magnetical stirring for 15 minutes. Then, approx. 11 mmol silane per g of kaolinite was added with

adjustable micro pipettes, corresponding to 2.16 g APMS, 2.51 g APDS and 2.87 g APTS, respectively. All mixtures were stirred for 24 h at r.t., followed by 24 h at 120 °C Heat-On temperature (approx. 80 °C inner temperature) and finished by 24 h stirring, resulting in slow cooling to r.t. in the Heat-On. After reaction, the dispersions were centrifuged five times in pure ethanol (7000 rpm, 10 min). In a final step, the modified kaolinite slurries were i) freeze-dried, denoted as FD or ii) treated in an oven at 120 °C, denoted as OV.

2.1.2 Janus deposition experiments

The examination of the Janus character after silylation was carried out by mixing the modified kaolinite colloids in a 1 to 40 ratio (PS @ kaolinite) in the same way already described in Section IV-1.1.3. In short, a 2 wt.-% dispersion of kaolinite is mixed with a 0.02 wt.-% PS dispersion (65 nm) to obtain the desired ratio and dropped on a silicon wafer. The morphology of the samples was examined via SEM.

These simple experiments has been conducted many times with many weight ratios, sphere sizes and charges (ζ-Potential).

2.1.3 ζ-Potential measurements

All ζ-Potential measurements were conducted on a Malvern Zetasizer Nano ZS, already described in previous sections.

2.1.4 Synthesis of PDMS μ Janus Kaolinite

The amino functionality can be used for further grafting reactions. A very quick and reliable reaction is a reaction with an epoxide group. The grafting of Epoxy-PDMS (epoxide functionalized polydimethylsiloxane) is described here.

For example, the samples A10C2 and A7C2 (obtained from untreated multimodal kaolinite "13 P", 100% ethanol) were dispersed (approx. 0.4 wt.-%) in 30 g ethanol, and 12 g of commercial epoxy modified PDMS (Evonik) is added and stirred for 48 hours. After reaction, the samples were centrifuged six times in ethanol (7000 rpm, 10 min). As a reference, the epoxide-modified PDMS was stirred for 48 hours in unmodified kaolinite of the same origin.

2.1.5 Particle Adsorption on Carbon Fibres

The obtained PDMS @ Janus kaolinite colloids from A10C2 and A7C2 are dispersed in 20 g water (0.4 wt.-%) by ultrasonication in a snap-cap glass container. Some untreated, endless carbon fibers were added and magnetically stirred for 1 hour. Alternatively, EtOH was used as a solvent. The fibres are withdrawn and dried in an oven at 80 °C.

2.1.6 Pull-Out tests

The procedure details, theoretical background and more about carbon fiber pull-out experiments are described in the PhD thesis of Anna Becker-Staines[157] and also for the upcmoing PhD thesis of Minghui Tang. In the following, the crucial procedure is described.

A frame of millimeter paper was cut to 20 mm x 30 mm with square holes of 10 mm x 10 mm. Subsequently epoxy resin (BECKOPOX, EP140) and hardener (BECKOPOX, EH637) were mixed in a ratio of 100:54 (wt/wt) at r.t. for forming the droplet-bonded single fiber specimens. A single carbon fiber was fixed by a droplet of epoxy resin / hardener mix above the central hole. With help of the auxiliary line of millimeter paper the fiber was aligned straightly. The other fiber end was cut by a scalpel at the edge of the paper, and then fastened by a second droplet of epoxy resin/hardener mixture with an embedded length between 70-300 µm. After one week of drying at r.t., the specimens were measured by the material test system "MTS Criterion C45.105" with an "HBM/S2M/10" load cell. Both ends of the paper frame were clamped erectly by clamping jaws. The left and right sides were cut off and the fiber and the test was done with a speed of 0.03 mm/min until the fiber was pulled out from the epoxy resin droplet.

2.2 Results & Discussion

A silylation reaction on the octahedral layer of kaolinite was conducted by using many different conditions and three different aminosilanes. Mostly, the organofunctional silane 3-aminopropyltriethoxysilane (APTES) was chosen, because the amino group of the silane is capable to introduce a positive charge by protonation on the negatively charged kaolinite colloids and moreover is accessible for reaction with epoxide functions. The obtained charge-modified kaolinite colloids are tested on the Janus character with cationic charged PS colloids or anionic charged DPE-based colloids (PDPE) as a marker. The mixture should lead to a Janus deposition pattern with sufficiently small colloids (here: PS: 58 nm, PDPE: 50 nm). An overview of the Janus kaolinite assemblies is shown in **Figure 69**.

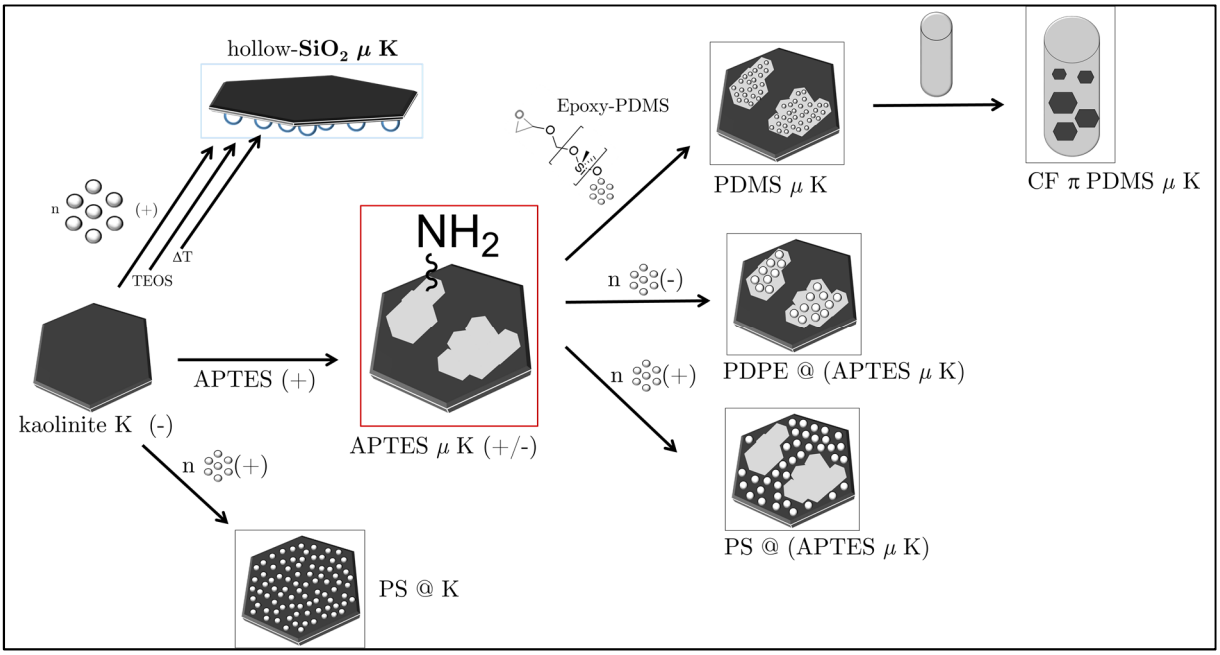
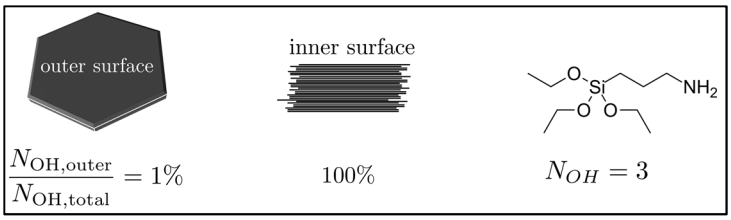


Figure 69: Transformations of PS @ kaolinite Janus colloids

2.2.1 Analysis of Silane μ Kaolinite

In this subsection, the bond between APTES and kaolinite is analyzed via EDX, TGA, IR- and NMR spectroscopy. As listed in **Table 14**, all experiments were conducted with a high molar excess of silane. From a geometrical perspective, one single, ideal kaolinite colloid with any diameter has an accessible surface for grafting of 1 mol.-%, with 100 kaolinite layers. The conditions are chosen in that way because the aminosilane condensation proceeds very fast as known from the literature.[155]
It is known and also found herein, that the silane does not intercalate in the used solvents, therefore the silane does not react with the OH groups in the intergalleries of kaolinite. The intercalation of ammonium salts into kaolinite by the help of DMSO and methanol is described in III-2.3 (page 48) and the subsequent dispersing in a PUR matrix in IV-4.2.1 (page 124).
After silylation, the samples were washed once after reaction (C0) and subsequently centrifuged up to 4 times (C1 to C4). In the following, the analysis of the C2 fractions are analyzed.

Table 14: Molar silane excess per hydroxyl groups on kaolinite
The shown molar excess is a calculation which relies on the approximation that the kaolinite colloids have 100 crystal layers and 1 of these layers is accessible for reaction. Neglecting the trifunctional character of the silane, the molar excess accounts to a molar excess the smallest shown molar excess is 0.7.



APTES concentration (wt.-% in solution)	1 %	3 %	5 %	7 %	10 %
inner molar excess (mol.-%/mol.-%)	2	6	10	13	19
outer molar excess (mol.-%/mol.-%)	213	574	955	1340	1916

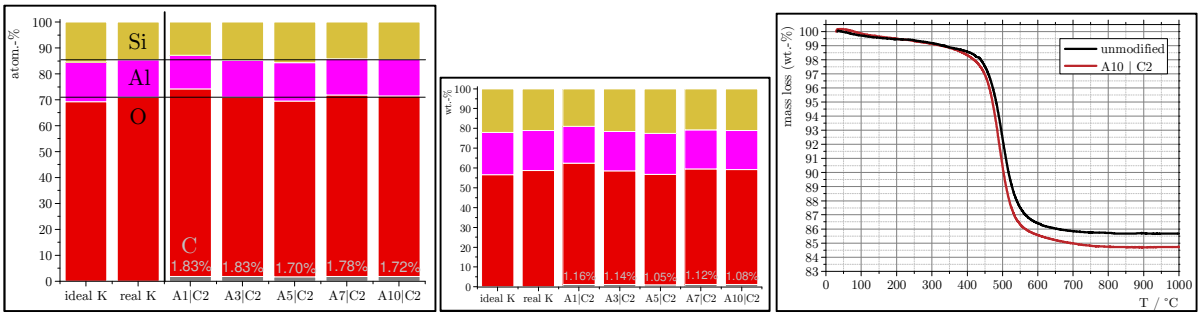


Figure 70: EDX and TGA results of amino-modified kaolinite in atom and weight percent

In **Figure 70**, the kaolinite products after two centrifugation steps "C2" at different aminosilane concentrations (A1 to 10 wt.-%) are shown. The carbon content in wt.-% correlate well with the TGA data. From the EDX data in atom.-%, one can calculate that 3.8 to 4.7 silane molecules per aluminum center are present, accounting to equivalent thicknesses between 21 and 26 nm within the simplified model. The deviation from the actual detected thicknesses can be explained by defects in the the tetrahedral layer and exposed broken edges from stacking defects. Unfortunately, the detection of nitrogen N was not possible using the EDX technique. The IRRAS spectrum of the sample A10C2 is shown in **Figure 71**. After the modification, the IR peaks decently shift and one new peak arise at 1074 cm^{-1}, attributed to a Si-O-Si stretch

vibration from self-condensed silanes. The attribution of the peaks of the unmodified kaolinite was made by the help of the literature.[158,159,160] The altering of the IR spectra after silylation indicate, that a covalent bond was established. The deconvolution of the IR peaks and the obtained peak areas (cf. **Table 15**) gives similar quantitative results compared to the obtained range of the EDX and TGA results.

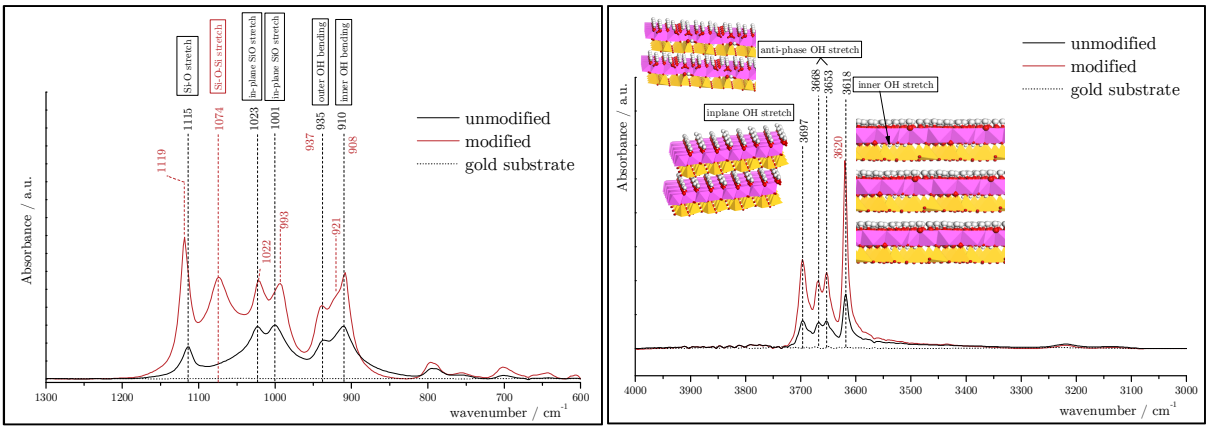


Figure 71: IRRAS measurement of modified (A10C2) and unmodified kaolinite

Table 15: Results of IRRAS deconvolution, relative peak areas

	reference	A10C2	gain/loss
inplane	24%	29%	+4.7%
anti-phase	21%	19%	-2.7%
anti-phase	18%	18%	-0.1%
inner	36%	34%	-2.0%

A rather qualitative analysis was done by ^{27}Al-NMR, shown in **Figure 72**. The three signals are originating from Al_4-, Al_5- and Al_6-centers of the kaolinite structure (from left to right).[161] After the silylation, the signals are slightly shifted and also slightly change their shape. Herein, the Al_5 signals are assumed to be structural defects, such as Si(Al)-substitutions in the tetrahedral layer. The Al_6-centers are attributed to the faces of the octahedral layer of kaolinite K_{face}, whereas the Al_4 signals are attributed to the (broken) edges of kaolinite K_{edge}.

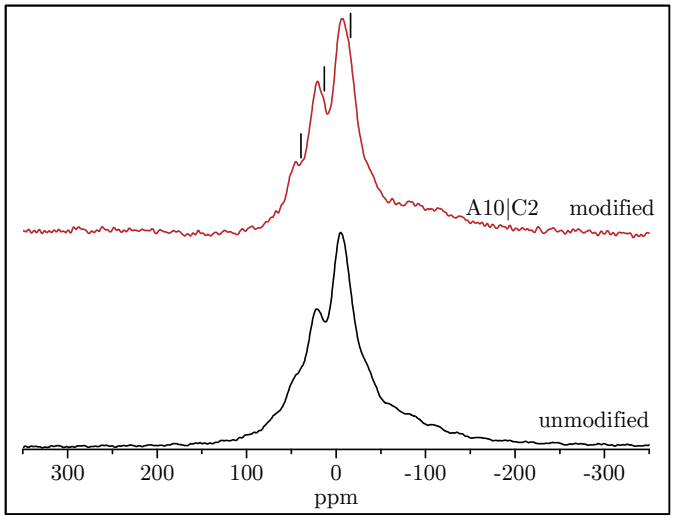


Figure 72: ^{27}Al-NMR spectrum of modified and unmodified kaolinite

The change of the apparent surface charge density was estimated by ζ-Potential measurements (cf. **Figure 73** and **Figure 74**). The water content in the silylation experiments tend to result in higher, more positive ζ-Potentials. The higher ζ-Potential indicate, that more NH_3^+ moeities are present and accessible on the kaolinite surfaces. Higher kaolinite diameters and higher water contents during the silylation process lead to more positive surface charges, whereas also the number of centrifugation steps alter the result.

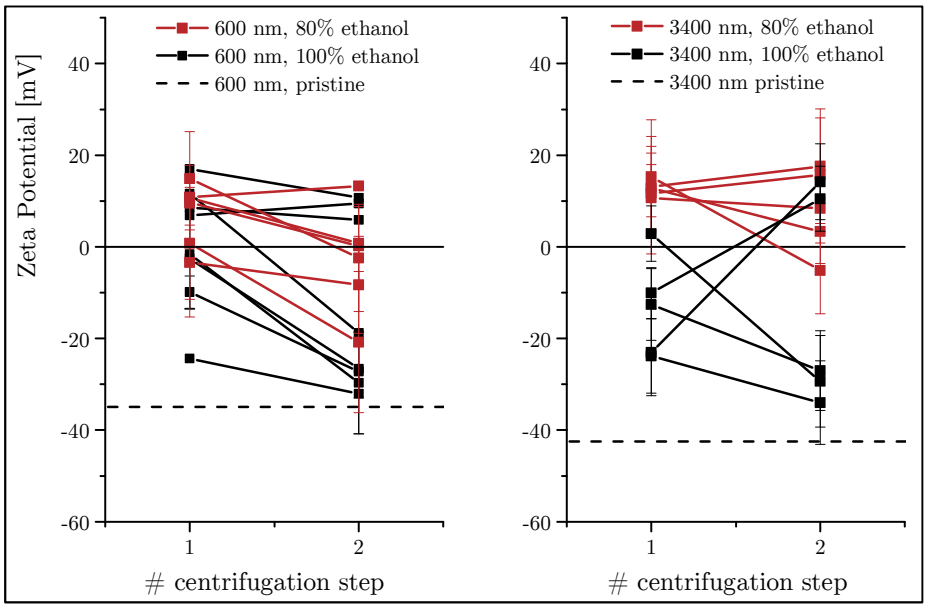


Figure 73: ζ-Potential vs. centrifugation steps of kaolinite silylations.
The measurement was conducted on 120 °C treated kaolinite colloids (13 P, multimodal). The black dashed line is attributed to the ζ-Potential of unmodified kaolinite.

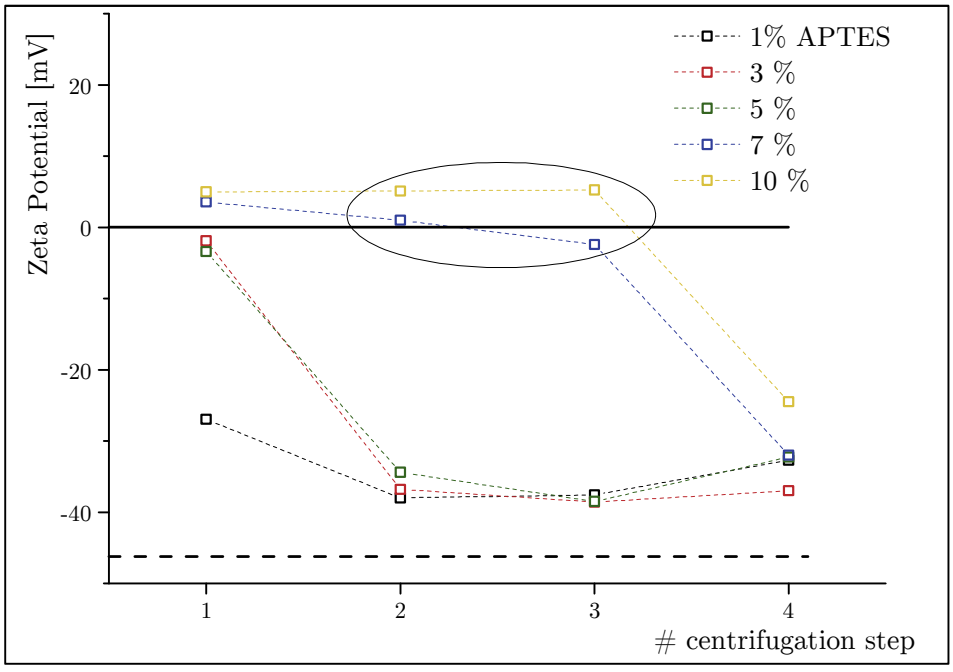


Figure 74: Apparent ζ-potential of amino-modified kaolinite colloids.
The measurement was conducted on 120 °C treated kaolinite colloids (13 P, multimodal). The black dashed line indicate the ζ-Potential of the unmodified kaolinite.

In the following, the surface charge was further examined by spherical colloids with positive and negatively charges on the modified surface of kaolinite K_{face}.

2.2.2 Janus Deposition Experiments

In order to examine the Janus character of kaolinite, the deposition pattern of pristine kaolinite colloids were compared with the deposition pattern of aminosilane-modified kaolinite. The used PS marker particles have positive charges and diameters in the range of 30 to 65 nm. The weight ratio, which lead to a full and homogenous deposition of the kaolinite surface K_{face} was determined as 1 to 40 for PS_{65} (cf. previous subsection). By mixing modified kaolinite with the same weight ratio, patchy Janus deposition patterns were obtained, exemplary shown in **Figure 75**. The grafted sites are positively charged and therefore shield the electrostatic deposition of alike charged colloids.

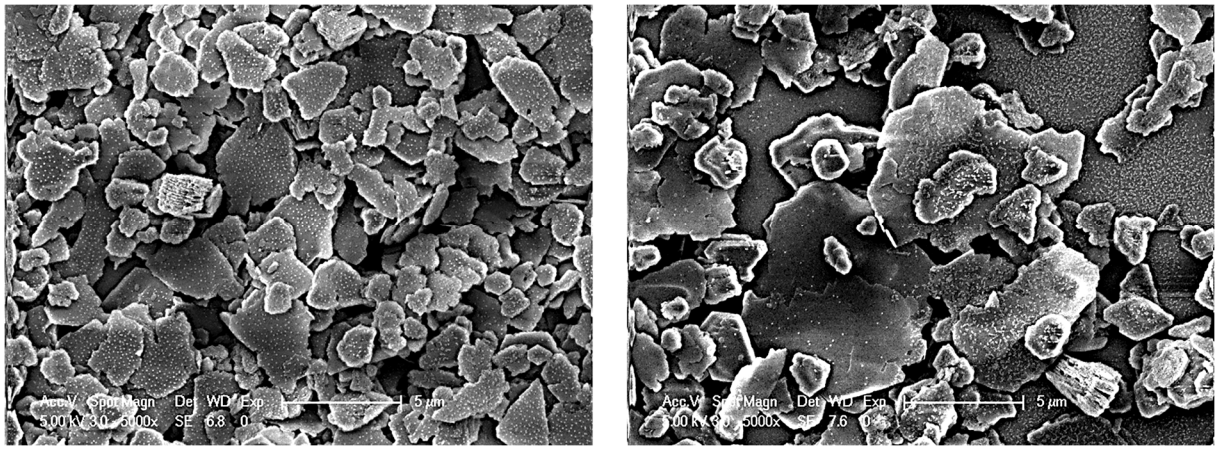


Figure 75: PS_{65} @ kaolinite (left) and PS_{65} @ NH_2-kaolinite with a 1 to 40 weight ratio. Modification of kaolinite was done with a 3 % APTES (A3) in a 80/20 EtOH/H_2O wt/wt after 3 centrifugation steps (C3) and drying at 70°C.

For negatively charged DPE-based colloids with a diameter of 50 nm, the weight ratio for full and homogenous deposition on K_{face} can not be estimated, because the alike charges. More examples on alike charged lamellar and spherical particles are shown in the Appendix on page 210 (SiO_2 @ K and PS @ LDH), showing the same behaviour. However, on modified kaolinite, patchy Janus deposition patterns emerge (**Figure 76**). However, the favored marker particles are the cationic PS colloids.

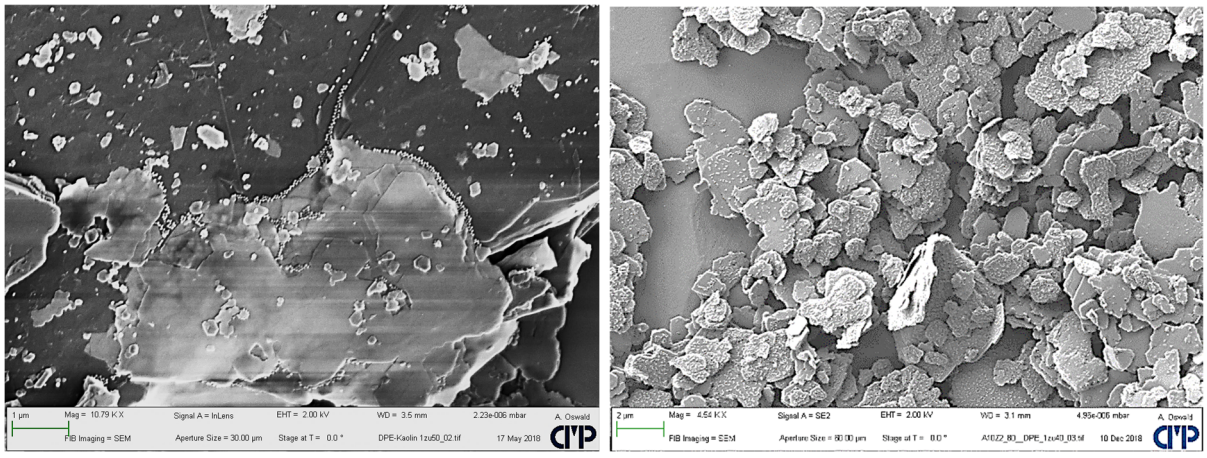


Figure 76: Electrostatic Deposition of PDPE spheres on unodified and modified kaolinite
left: PDPE particles (-) and kaolinite (-) lead to edge deposition
right: Janus deposition pattern of PDPE @ kaolinite (A10C2, 80% ethanol, 120°C curing, 1 to 40 ratio wt/wt)

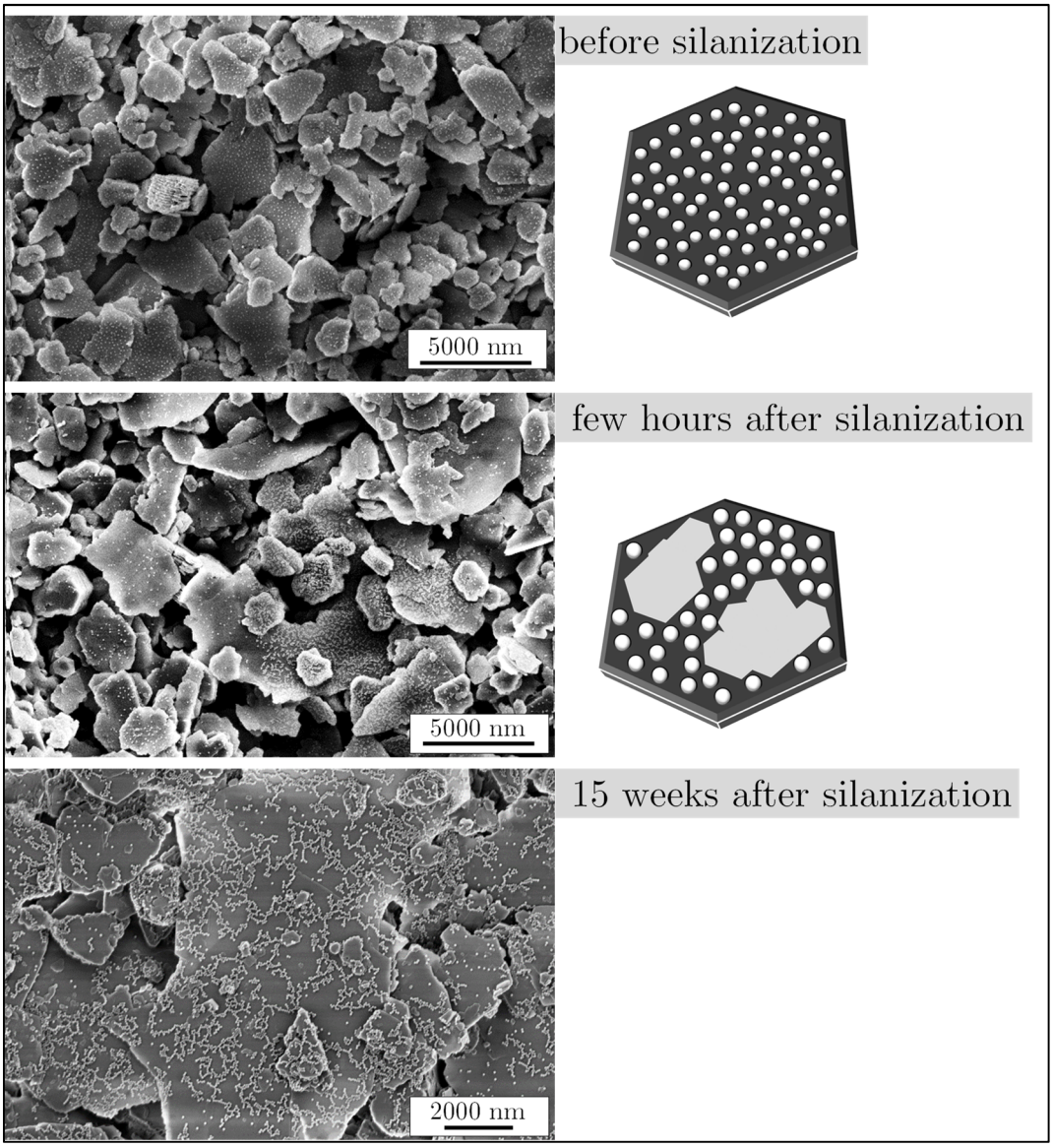


Figure 77: Time evolution of Janus deposition patterns for PS@kaolinite

top: deposition pattern of PS_{65} @ unmodified kaolinite with a 1 to 40 ratio.

middle: PS_{65} @ modified kaolinite with a 1 to 80 ratio. The modified K was modified with a 5 wt.-% APTES in 80/20 EtOH/H_2O wt/wt, 3 centrifugation steps, curing at 70°C, PS: 65 nm, kaolinite "SKT-35" after sedimentation. The Janus deposition pattern emerged also with a 3 and 7 wt.-% APTES in the silylation reaction

bottom: The same sample after 15 weeks storage in water and subsequent addition of PS_{65}.

However, the modified kaolinite colloids show clear Janus deposition patterns if the silane was physically adsorbed (dried at 70 °C). After the storage in water for 15 weeks, the deposition pattern of these samples changed to a non-Janus deposition pattern. In the first studies, five different samples (varying APTES concentration, therefore also varying pH) with kaolinite colloids (SKT-35, 3.4 µm) were used. In addition to the five different silane concentrations during the actual reaction time, four additional concentrations of each sample are generated by the centrifugation steps. The method generates therefore 20 samples in total. As an example, the denotation A3C4 means an aminosilane concentration of 3 % and the concentration resulting from the 4^{th} centrifugation step. Each of these samples are dried at 70 °C and redispersed in water. What is clear from the experiments, is that the aq. modified kaolinite dispersion changes the coverage behavior after 15 weeks of storage. The reason for the change

of the behavior is believed to be the insufficient bonding strength of the silane in the physisorbed state and a subsequent migration of the oligomeric APTES over time. The desorption of silanes in the presence of water is known from the literature on experiments examining for example glass fibre surfaces.[162]
In order to create a covalent bonding between the octahedral layer of kaolinite and APTES, a curing step was performed at 120 °C immediately after the synthesis and the respective centrifugation steps. The deposition patterns show more or less colloids on the kaolinite surfaces, but the sharp distinction like in the physisorbed samples is not obtained in any of the samples cured at 120 °C. Therefore, further experiments were made with smaller, commercial cationic colloids with a rather high dispersity (Perglutin, 20-30 nm), acidic and basic pH and also small kaolinite colloids (600 nm) are compared to big kaolinite colloids (3400 nm), shown in **Figure 78**, **Figure 79** and **Figure 80** on the following pages.
The kaolinite colloids having small diameters (600 nm) show a patchy deposition behaviour at pH 9 for almost any case examined. The only sample which shows full deposition is A7C2. For kaolinite colloids having big diameters (3400 nm) show full deposition in any case at pH 9, whereas at pH 4.5 both kaolinite colloid fractions show poor deposition without reasonable patchiness for the samples with one centrifugation step C1 and absent Janus deposition patterns. After 2 centrifugations C2, all samples show full deposition patterns. From these experiments it can be concluded that the size ratio of the marker colloids and the modified kaolinite colloids play a crucial role if one wants to detect the Janus deposition behaviour, whereas also the number of centrifugation steps, the curing method and also the amount of present water during synthesis alter the resulting deposition behaviour.

Based on the present findings, one can say that clear Janus deposition patterns are obtained more likely for

1. physisorbed samples (curing at 70° C)
2. fewer centrifugation steps (C1, C2)
3. high APTES concentrations (3, 5, 7, 10 wt.-%)
4. high water content

and less likely for

1. chemisorbed samples (curing at 120 °C)
2. many centrifugation steps (C3, C4)
3. low APTES concentrations (1 wt.-%)
4. low water content

More effects on the deposition patterns that could be examined are other solvents than ethanol, the reaction time, the reaction temperature and also the nature of silane, such as dialkoxy-aminosilanes or monoalkoxy-aminosilanes. Reaction time-dependent examinations were already examined for mono- and trialkoxysilanes on laponite[163] and were used herein as an orientation for the final subsection, where amino-modified kaolinite is reacted with epoxide-functional PDMS and the PDMS μ kaolinite colloids were used as a coating for carbon fibers in order to enhance energy dissipation of carbon fiber reinforced plastics CFRP.

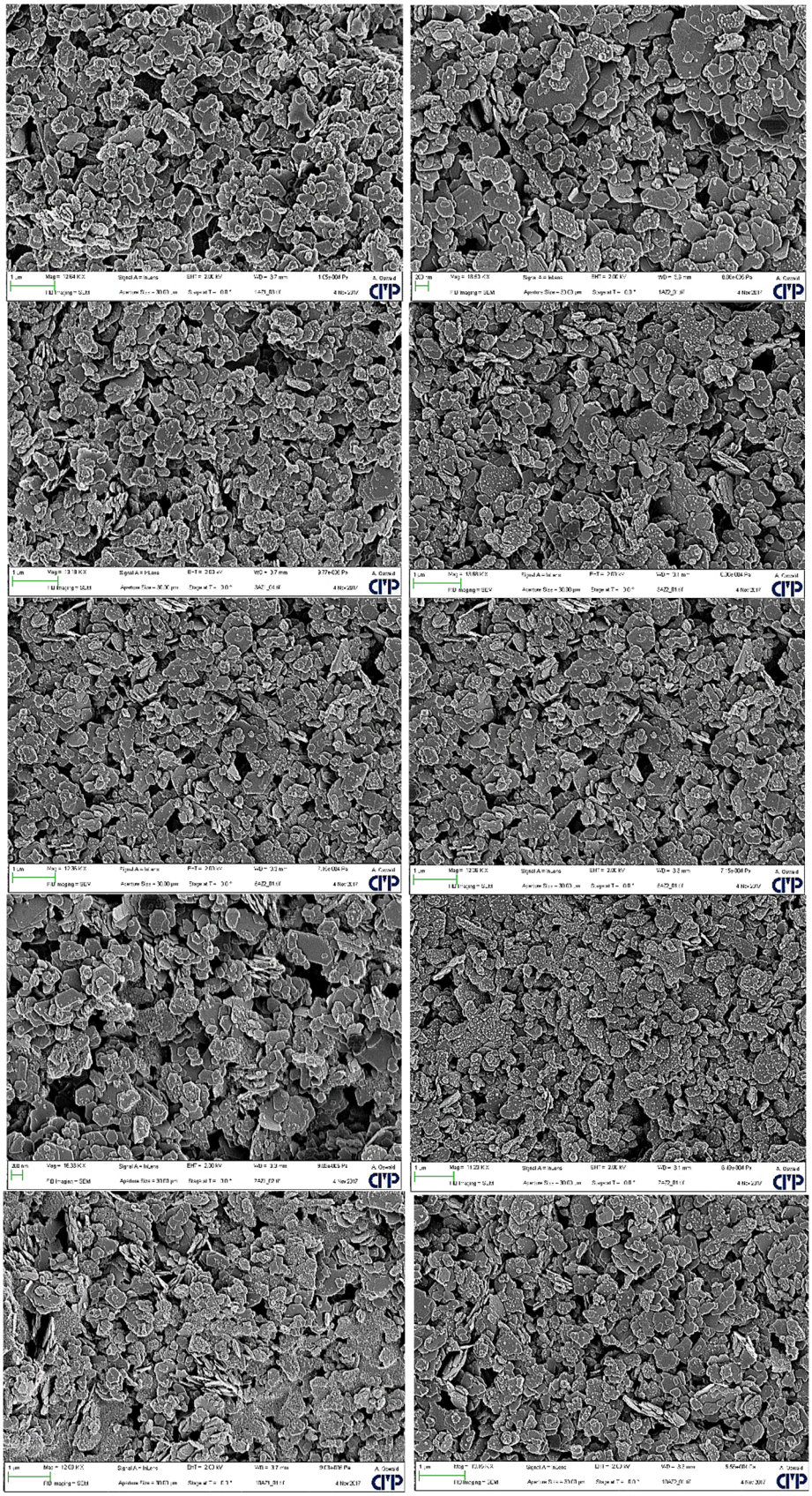


Figure 78: Deposition patterns of 600 nm modified kaolinite

All dried samples had pH 9, a 1 to 30 PS @ K ratio, 100% ethanol during modification and were cured at 120 °C. The left hand side shows the samples after 1 centrifugation step C1, the right hand side shows samples after 2 centrifugation steps C2. The APTES concentration were from top to bottom 1, 3, 5, 7 and 10 wt.-% APTES during modification.

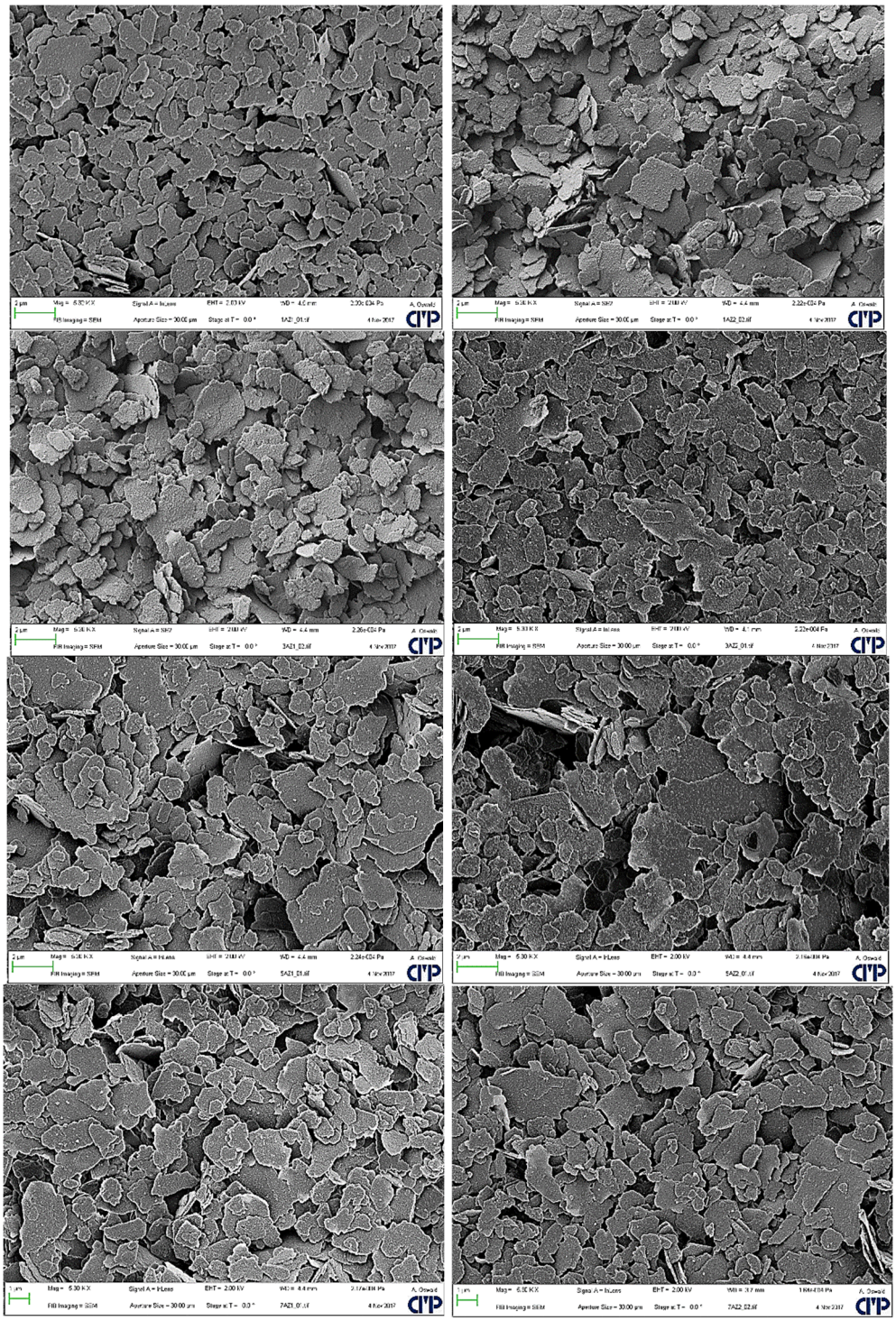


Figure 79: Deposition patterns of 3400 nm modified kaolinite

All dried samples had pH 9, a 1 to 30 PS @ K ratio, 100% ethanol during modification and were cured at 120 °C. The left hand side shows the samples after 1 centrifugation step C1, the right hand side shows samples after 2 centrifugation steps C2. The APTES concentration were from top to bottom 1, 3, 5 and 7 wt.-% APTES during modification.

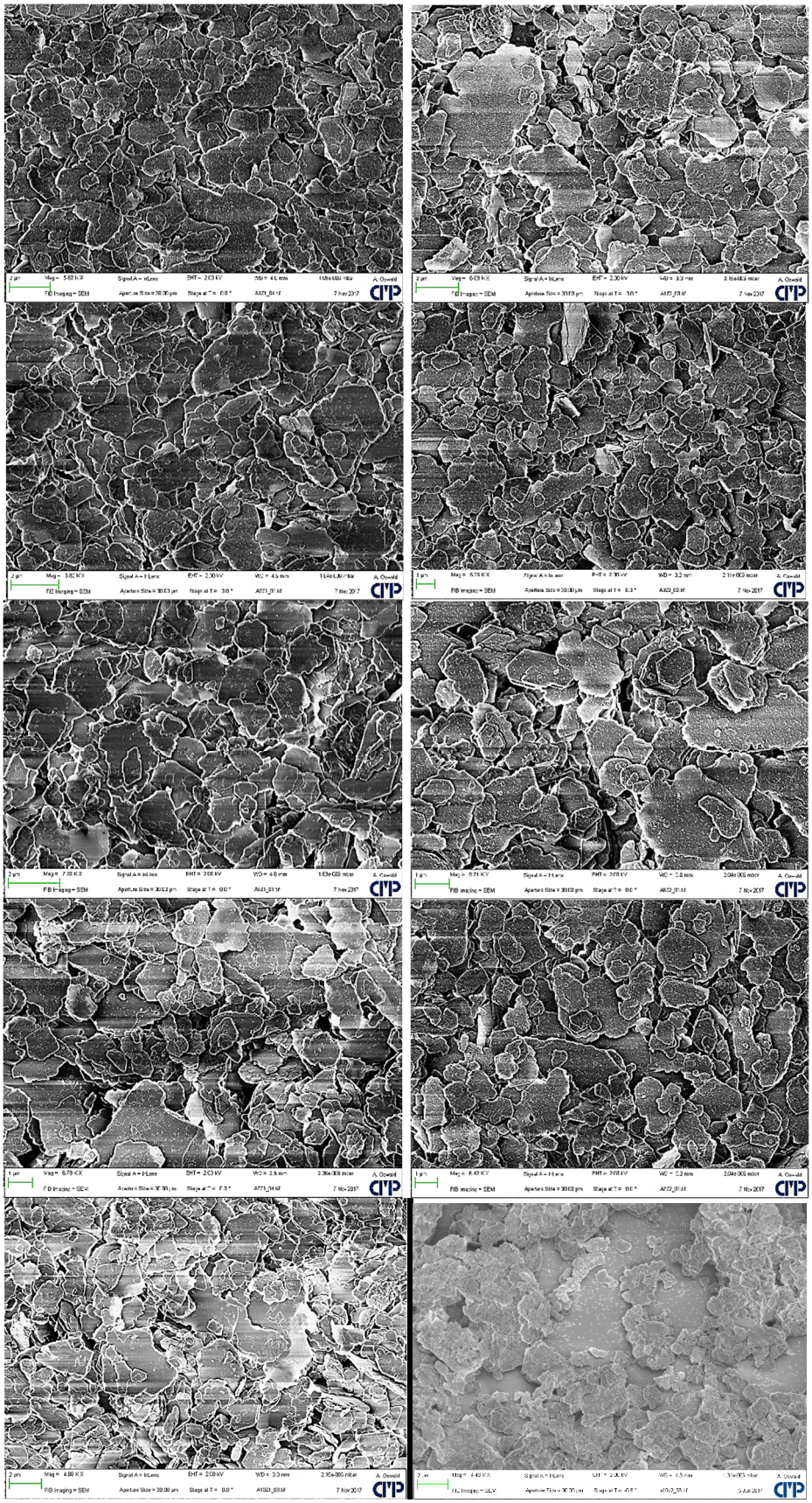


Figure 80: Deposition patterns of 3400 nm modified kaolinite

All dried samples had pH 4.5, a 1 to 30 PS @ K ratio, 100% ethanol during modification and were cured at 120 °C. The left hand side shows the samples after 1 centrifugation step C1, the right hand side shows samples after 2 centrifugation steps C2. The APTES concentration were from top to bottom 1, 3, 5, 7 and 10 wt.-% APTES during modification.

Within the thesis, 2-butoxyethanol was used as an alternative to ethanol, in order to enhance the covalent bonding in the wet state. Butoxyethanol is a suitable solvent for the purpose, since it is miscible with water and has a boiling point higher than water (171 °C). However, grafting reactions with 2-butoxyethanol lead to spherical colloids with diameters of up to 200 nm and the dispersion turned orange. Without kaolinite present in the synthesis as a reference, the colloidal dispersion also appeared orange. The ζ-Potentials of the colloids after synthesis in 2-butoxyethanol and after 6 centrifugation steps show a clear upward trend.

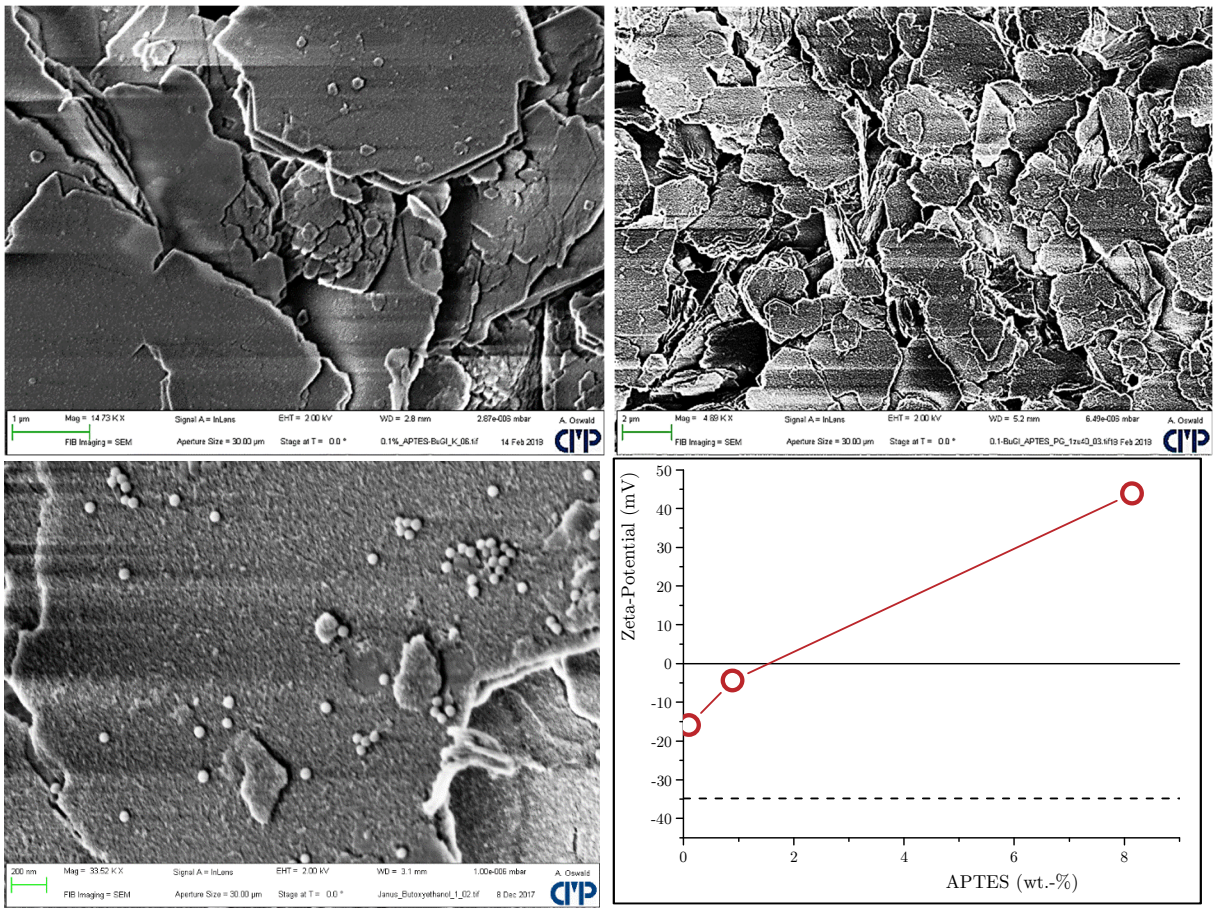


Figure 81: Kaolinite silylation experiments with butoxyethanol as a solvent
upper left: amino-modified kaolinite with an APTES concentration of 0.1 wt.-%
upper right: same sample with 30 nm PS colloids, showing full deposition
lower left: amino-modified kaolinite with APTES concentration of 1 wt.-% and PS_{65} colloids
lower right: ζ-potentials of amino-kaolinite as a function of APTES concentration

As a conclusion of the silylation experiments, it can be said, that the synthesis of long-term stable Janus kaolinite colloids was not successful, whereas the Janus character of kaolinite became visible.

2.2.3 Fiber Coatings consisting of PDMS μ Kaolinite

From the previous subsections one can say that the silylation of kaolinite to stable and reliable Janus amino-kaolinite is not fully understood and remains a challenge. However, the ζ-potential measurements at least indicate, that the surface charge of the kaolinite colloids switched to more positive values by immobilized protonated amine functions. For the carbon fiber coatings, the kaolinite modification was done with homologous silanes (described on p. 79). The reaction between the surface amino-groups and epoxide-PDMS colloids in

ethanol was conducted to obtain covalently bonded PDMS colloids on the kaolinite surface (**Figure 82**). The deposition pattern of PDMS colloids on the kaolinite surface was not visible at low magnifications, because the material contrast in the SEM between PDMS and kaolinite is insufficient due to high silicon contents in both materials.

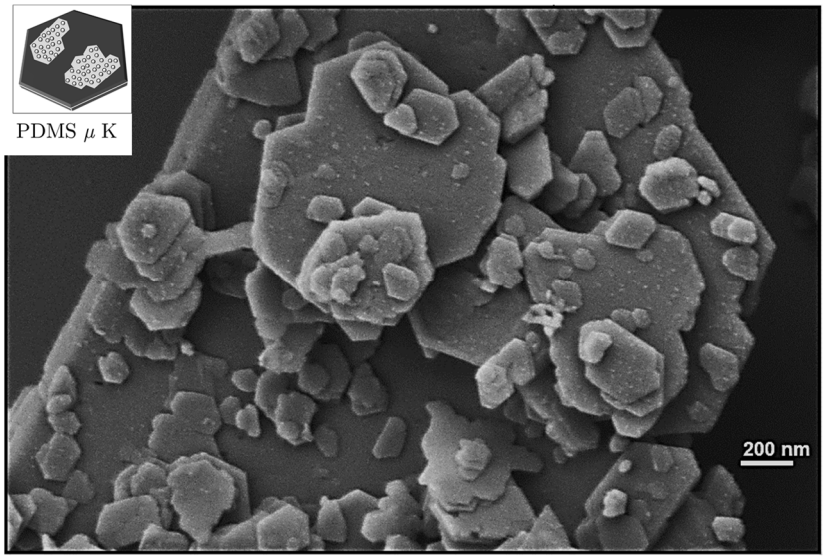


Figure 82: SEM image of PDMS μ K

As a reference, the unmodified kaolinite underwent the same reaction conditions and result into identical TGA traces. This results confirm, that the PDMS colloids graft onto the modified kaolinite surface by epoxide-amine reaction. The thermogravimetric analysis of the grafted samples is shown in **Figure 83**.

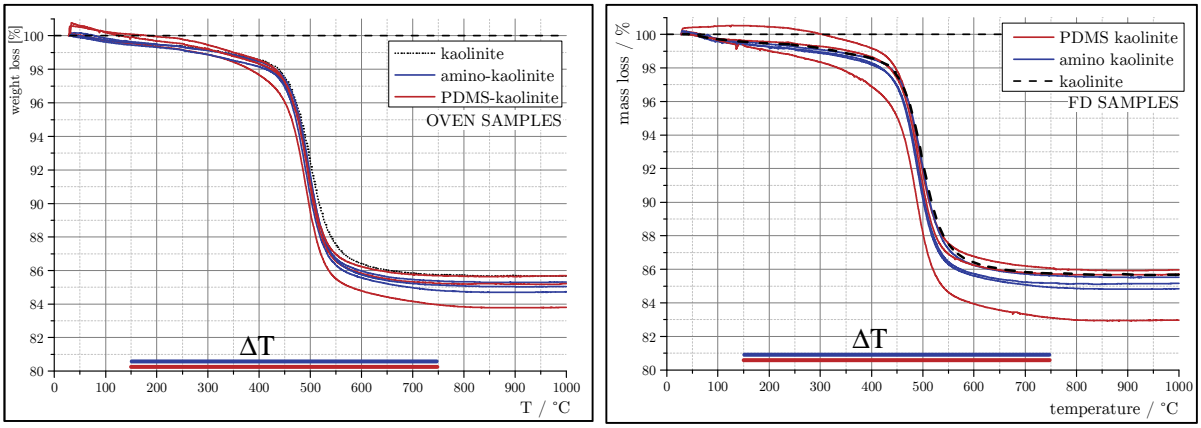


Figure 83: TGA traces of amino and PDMS modified kaolinite colloids

The resulting colloids can be dispersed in water by ultrasonication and flocculate after rest due to agglomeration of the immobilized PDMS. The subsequent coating of the carbon fibers was done in water in order to make use of the differences of the surface energies with water having high surface energies and the carbon fibers and PDMS having similar surface energy values ($\gamma_{H2O} \gg \gamma_{PDMS} \approx \gamma_{CF}$). For PDMS μ kaolinite colloids with high amounts of PDMS, the dispersing procedure was aggravated and EtOH was used as a solvent for the fiber coating. In

fact, the use of EtOH as a medium for the fiber coating turned out to be a good alternative in all cases. Examples of the coated fibers are shown in **Figure 84**.

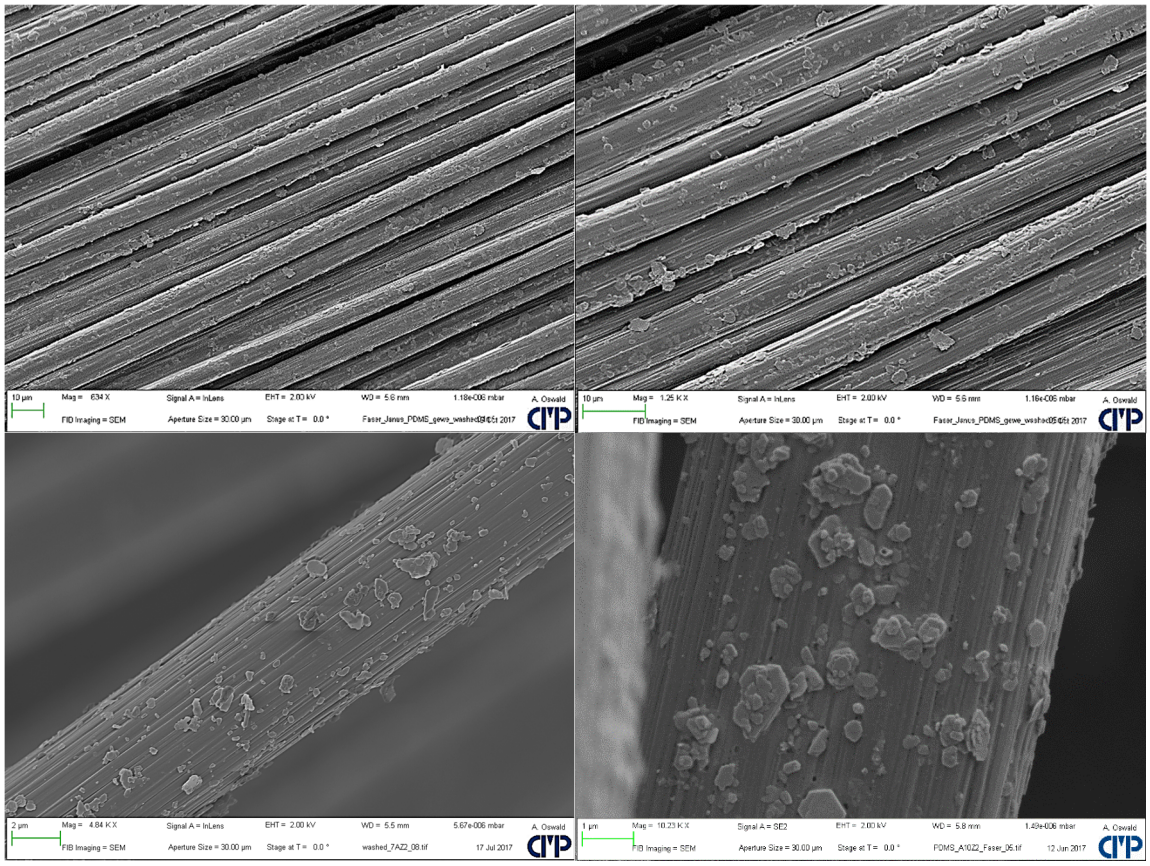


Figure 84: Carbon fiber coating comprising PDMS μ K

In **Figure 85**, an illustration from Anna Becker-Staines' work[157,164] on estimating the interfacial shear strength IFSS is shown. The motivation behind the weakening of the IFSS of CFRP materials by a PDMS coating is the reduction of undesired stress amplitudes and splintering of carbon fibers after impact by the help of energy dissipation at the interface carbon fiber/ polymer interface. Due the implementation of PDMS and kaolinite, the epoxy-amine polymer network density is lowered, the tribological characteristics at the interface are changed (especially by PDMS) and lead to higher deformation and lower moduli (cf. Appendix, page 216). Follow-up work on IFSS and CFRP are about to be made by Minghui Tang.[165]

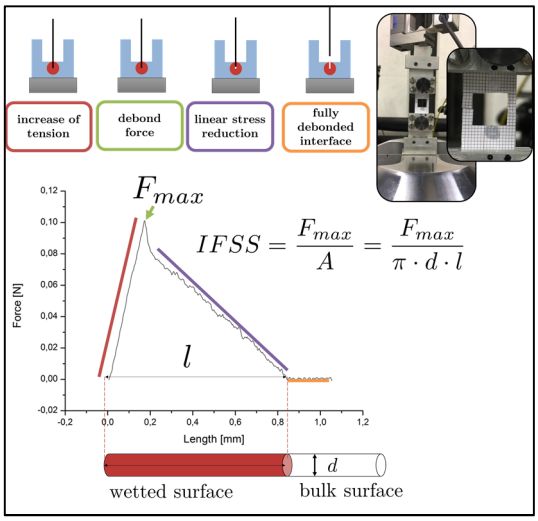


Figure 85: Interfacial Shear Strength estimation

3 SiO_2 @ LDH – Stacked Assemblies

The coagulation of lamellar colloids, especially natural occuring clays, are well-documented (cf. section II-2.1, page 14). The coagulation is best described by two classical border cases: the house-of-cards structure (edge-to-face coagulation) or a band-type structure (face-to-face coagulation). In the literature, coagulation and hetero-coagulation mechanisms for a lot of clays are also reported.[166,167,36]

In this section, the focus lies on the heterocoagulation of spherical colloids with lamellar colloids with the goal of electrostatic-driven and defect-directed stacking of the intact and also of exfoliated LDH colloids (**Figure 86**). The mainly examined system here is 1 µm LDH-BSA and 10-20 nm SiO_2 ("Snowtex-O"). As in the previous sections, the most important parameter for the assemblies is a low ionic strength in the dispersions, because the electrostatic forces are higher at low ionic strength. The control over pH is connected to a lot of effort and other issues discussed below. The organized colloids are examined by ζ-Potential measurements, the electric conductivity, size, pH and a morphological examination by SEM and FIB technique.

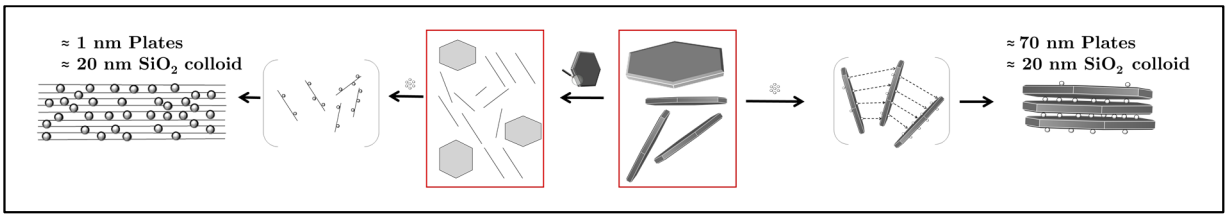


Figure 86: Postulated stacking mechanisms

Furthermore, the deposition behaviour of hard spheres with different diameters and charges on 2D-shaped, positively charged LDH colloids with different thicknesses is examined further in this chapter.

In the very beginning of this chapter, the apparent ζ-Potential of thin lamellar colloids with opposite charges are described. In this chapter, all colloids used are hard. A hard colloid is characterized by the glass transition temperature in comparison to the room temperature (compare II-3.2) and are not able to intercalate into the LDH intergalleries.

3.1 Experimental Details

The experimental details on the organization to sequenced layers of LDH colloids and SiO_2 colloids are presented here in detail. The small 0.4 µm colloids are discarded from the experiments because of the low aspect ratio, whereas

Materials

All used materials are listed in **Table 16**.

Table 16: Materials for Stacking

Name	**Size/Purity**	**Supplier**
LDH-BSA 800 nm	800 nm	see section III-1.1.2
LDH-NO_3-DS	1 µm	see section III-1.1.8
Snowtex® ST-O (commercial SiO2)	20 nm	NISSAN Chemical
PVA	22,000 g/mol	Kuraray Europe GmbH
PVA-VTES Copolymer "POVAL 95-98R"		Kuraray Europe GmbH
Magnesium nitrate hexahydrate		Carl Roth
Aluminum nitrate nonahydrate		Carl Roth
Urea		
DPE latex	50 nm	K. Briesenick[68]

Methods

Dynamic Light Scattering (DLS)
Malvern Zetasizer Nano ZS
Malvern Mastersizer 2000,
MS-1 sample unit and a 300RF lens, which allows detection of colloid sizes from 0.05 to 900 µm.
MS-7 Magnetically Stirred Cell (beam length 10 mm, 300F lens)
Zeta Potential Measurement
Malvern Zetasizer Nano ZS with Autotitration Unit MPT-2
Scanning Electron Microscopy (SEM)
Zeiss NEON 40
Focussed Ion Beam (FIB)
Zeiss NEON 40
Ultrasonication
BANDELIN "SONOCOOL 255"
Ultrafiltration
Feinmechanik-Werkstatt Paderborn University
pH Electrode
METTLER TOLEDO SevenMulti pH-Meter
Autoclave steel bomb
Teflon-lined autoclave steel bomb

3.1.1 Ultrafiltration

The fine adjustment of the electrical conductivity in the bulk solution is possible with an ultrafiltration unit. The system shown in **Figure 87** was manufactured at the "Feinmechanik-Werkstatt Paderborn" at Paderborn University. This system can be used with customary filter membranes with a pore diameter down to 15 nm and pressures up to 3 bar. By monitoring the electrical conductivity of the permeate (Zetasizer), the conductivity of the retentate can be controlled in that way. In this work, the electrical conductivity is brought to a minimum in order to have a minimum of charge carriers around the colloids. In general, the system can be also useful with organic solvents by changing some parts. The centrifugation of the particles is favoured in all experiments within the thesis, whereas the ultrafiltration unit was used when mentioned.

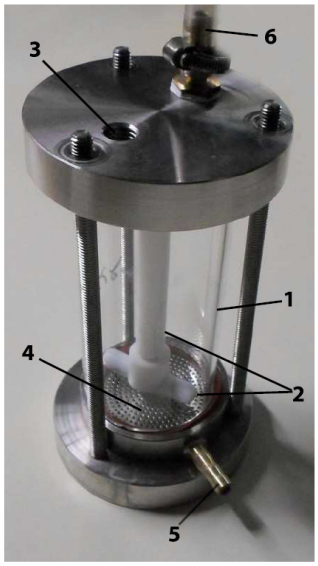


Figure 87: Photograph of the Ultrafiltration Unit

1. cylindrical pressure chamber
2. magnetical stirrer with rod
3. Dispersion-Inlet with screw thread
4. perforated plate, filter, O-ring
5. filtrate outlet
6. gas inlet

The three threaded rods are fixed with three compatible nuts

3.1.2 Separate Dispersion Method

Both, lamellar and spherical particle dispersions are adjusted to the same concentration (e.g. 0.2 wt.-%, **Table 17**). The addition of the dispersions to one another is done with a disposable pipette and measuring the weight of the dispersions at different ratios. The addition is conducted fast and drop-by-drop (0.03 g), quickly followed by a ζ-Potential measurement. After 2 and 24 hours, all (unstirred) samples undergo another ζ-Potential measurement.

Table 17: Separate dispersion method with equal mass concentrations

#	LDH disp [g]	SiO_2 disp [g]	SiO_2 in assembly [wt.-%]	NVC of dispersion [wt.-%]
#1	0.5951	0.3194	35%	0.20
#2	3.0081	1.2289	29%	0.20
#3	3.0132	0.9157	23%	0.20
#4	6.0346	0.3207	5%	0.20
#5	7.5184	0.2961	4%	0.20
#6	9.0333	0.3002	3%	0.20
#7	10.5255	0.3277	3%	0.20
#8	12.0039	0.3060	2%	0.20

#9	15.0319	0.3131	2%	0.20
#10	18.0133	0.3096	2%	0.20
#11	21.0310	0.3001	1%	0.20
#12	24.0516	0.2997	1%	0.20

Alternatively, in order to keep the overall dispersion volume constant during the assembly, a 0.2 wt.-% SiO_2 and a 2.96 wt.-% LDH dispersion is prepared. The LDH dispersion is weighed in first, followed by water addition (cf. **Table 18**). In the end, the SiO_2 dispersion is added and the ζ-Potential is subsequently measured. The samples were measured after a short and intense shaking in a screw-capped polymer vessel and withdraw/readdition cycles with a disposable polymer pipette to ensure a reasonable mixed state.

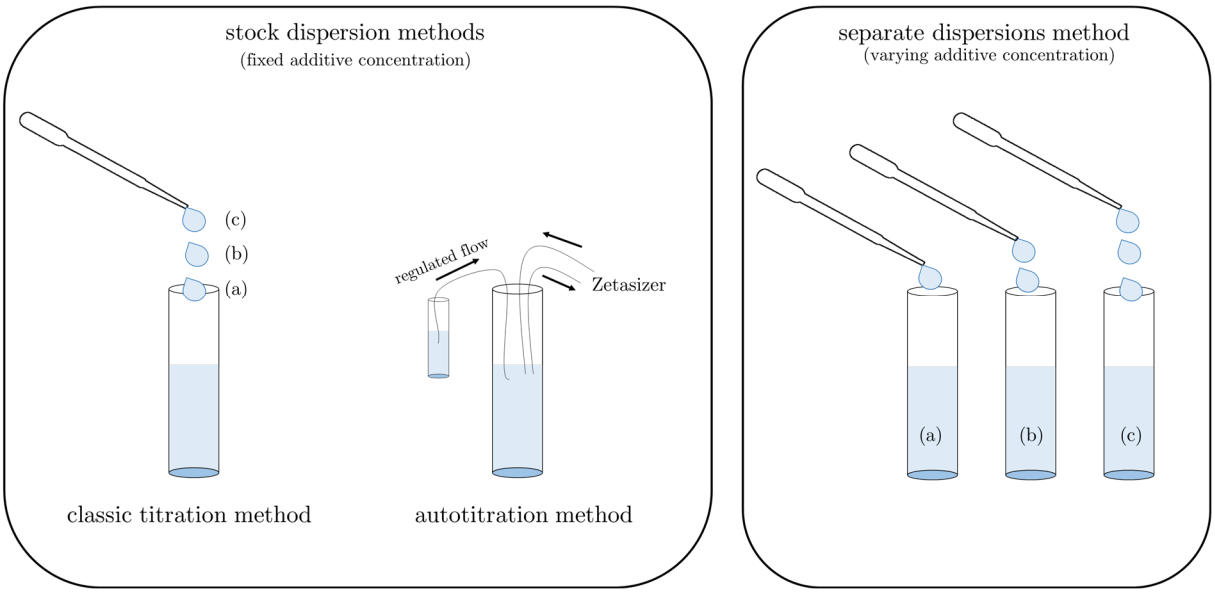


Figure 88: Illustration of Charge Switching Experiments
(a), (b) & (c) illustrate the different samples arising by the addition history of either lamellar or spherical colloids to a stock dispersion

Table 18: Weighed Portions for separate dispersion method at equal volume

#	SiO_2 in assembly [wt.-%]	LDH disp [g]	water [g]	SiO_2 disp [g]	NVC of dispersion [wt.-%]
1	0.3%	0.6729	9.2965	0.0306	0.20
2	0.6%	0.6709	9.2679	0.0612	0.20
3	1.3%	0.6665	9.2061	0.1274	0.20
4	1.5%	0.6648	9.1823	0.1529	0.20
5	2.0%	0.6614	9.1347	0.2039	0.20
6	2.5%	0.6581	9.0871	0.2548	0.20
7	5.0%	0.6412	8.8491	0.5097	0.20
8	10.0%	0.6074	8.3732	1.0194	0.20
9	15.0%	0.5737	7.8973	1.5290	0.20
10	20.0%	0.5400	7.4213	2.0387	0.20

Within preliminary tests, the separate dispersion method was used to examine the influence of the choice of additive or stock solutions on the outcome of the Apparent Zeta-Potential measurement. Therefore, two sets of samples with equal mass concentrations were prepared (0.5 wt.-% montmorillonite and 0.5 wt.-% Perglutin, for weighed portions compare **Table 17**). Here, the ζ-Potential was measured for a sphere-to-lamellar and a lamellar-to-sphere addition sequence, respectively. Moreover, the addition sequences of positive to negative lamellar phases are examined. The primary colloids have comparable sizes (montmorillonite and dispersed chitin).
The separate dispersion method was mostly used for SEM observations. The relevant dispersions, if not described above are prepared as follows:
0.5 g chitin is stirred in 100 g of 4 wt.-% acetic acid overnight. The sample is allowed to sediment overnight, and the supernatant is carefully discarded. The resulting NVC of the supernatant is 0.17 wt.-% (1 g dispersion, 110 °C, 30 min).
1 g *Na-montmorillonite* was dissolved in 100 g of pure water. Prior use, the resulting dispersion is purified by ultrafiltration (pore diameter : 0.05 µm) until the electrical conductivity reaches 0.01 mS/cm. The dispersion is diluted to approx. 0.1 wt.-%.
The SiO_2 particle dispersion (Snowtex-O) are filtered through a syringe filter and the NVC is measured (1 g dispersion, 110 °C, 30 min). The dispersion is diluted to 0.20 wt.-% with pure water and ultrasonicated prior use.
The *LDH* colloids are optionally ultrafiltrated (0.05 µm), followed by a 30 minute ultrasonic treatment in a glass vial (20 mL).

3.1.3 Isoelectric Titration of pristine colloids

The Apparent ζ-potential and the size of the colloids in dependence of the pH value and electrical conductivity is measured with a Malvern Zetasizer Nano ZS, optionally equipped with the Autotitration Unit "MPT-2". The sample dispersion is diluted to ≤ 0.17 wt.-% and placed into a special disposable screw-capped polymer vessel, which can be connected to a magnetic stirrer and a pH meter of the MPT-2 unit.
The acidic/basic solutions are placed in the autotitration unit and then can be used to pump the respective solution into the main sample container per Malvern software. The pH increment is ΔpH ≈ 0.5 in all experiments.
In order to obtain comparable ionic strengths, two measurements are conducted. The first titration is conducted into the acidic medium until pH 2 is reached (0.5 M HCl). The second titration is conducted into the basic medium until pH 12 is reached (0.5 M NaOH). The experiments were already conducted on the here examined pristine colloids 1 µm LDH-BSA and silica "ST-O" in previous works (K. Briesenick (2017), S. Neuhaus (2015)). A comprehensive graph is shown in the results.

3.1.4 Isoelectric Titration of Organized Colloids

The agglomeration of colloids is observable via size and ζ-potential measurements described above. Therefore, a known quantity of lamellar colloids is weighed (mostly 10 g, 0.17 wt.-%) into the sample holder (stock dispersion) and a diluted dispersion (0.02 - 0.20 wt.-%) of spherical particle dispersion is added (additive dispersion) with the programmable autotitration unit. The autotitration unit adds dispersion stepwise until the desired volume is reached (max. 20 mL).The number of programmed steps in all experiments is 10, with 3 ζ-Potential (mostly 12 to 100 runs, dependent on software algorithm & settings) and 1 size measurement (30 runs) at each step. The sample is recirculated after each single measurement (40 times in total), as

well as before the first and after the last measurement. For this configuration, each step takes approx. 13.5 min. Prior start and in the end of the autotitrations, all tubings were rinsed multiple times with water. Just before the autotitration, the tubings are inspected to eliminate air bubbles to prevent the measurement of dead volume. The Autotitration Unit is therefore equipped with a Vacuum Degasser Unit.
The relevant dispersions are prepared as follows:
The *LDH* colloids are used with the resulting NVC after synthesis (approx. 40 wt.-%). First, an approx. 5 wt.-% dispersion is prepared with pure water by magnetic stirring and ultrasonication. The dispersion is diluted to 0.17 - 0.20 wt.-% with a total mass of 10 to 10.7 g. The dispersion is used as the stock dispersion. In a typical experiment, 0.36 of a 6.6 wt.-% LDH dispersion and 10 g of water are mixed in the sample holder.
The commercial *SiO₂* colloids "ST-O" (diameter 20 nm) and "ST-ZL" (diameter 120 nm) were used. ST-O was filtered through a 0.20 µm syringe filter prior use and the NVC was measured in both cases (1 g dispersion, 110 °C, 30 min). The dispersion is used as additive after dilution to e.g. 0.02 wt.-%.
The DPE-based dispersion (50 nm) is taken from former studies (see Table above). The colloids were dialyzed and are stable since 2012. The dispersion is used as additive dispersion after dilution to e.g. 0.02 wt.-%.

3.1.5 SiO_2 @ LDH deposition

In a typical experiment, a single droplet of an approx. 2 wt.-% (NVC_{lam}) aq. LDH dispersion is weighed into a small vessel and the weight is determined by an analytical balance. The e.g. SiO_2 dispersion is mostly adjusted to approx. 0.02 wt.-% (NVC_{sph}) with pure water. The resulting weight of required SiO_2 dispersion (m_{sph}) for a desired ratio x is calculated with equation (14) and subsequently added to the kaolinite dispersion as precise as possible.

$$m_{sph} = \frac{m_{lam} \cdot \mathrm{NVC}_{lam}}{x \cdot \mathrm{NVC}_{sph}} \tag{15}$$

For example, 0.03 g of LDH dispersion is mixed with 0.3 g of SiO_2 to obtain a 1 to 10 ratio (SiO_2 @ LDH, wt/wt).
The actual weighed portion of m_{lam} (4 fractional digits) is noted and the desired mass m_{sph} is calculated with Excel-Software before addition to keep deviations small. The organized dispersions are agitated 5 times with a disposable pipette and a single drop is dried on a silicon wafer at room temperature. The dried sample is sputtered with Au/Pd (ρ = 16.7 g/cm³) to an eq. thickness of 3 nm (QCM) and imaged via SEM.
The commercial *SiO₂* colloids "ST-O" (diameter 20 nm) used. ST-O were filtered through a 0.20 µm syringe filter prior use and the NVC was measured in both cases (1 g dispersion, 110 °C, 30 min). The dispersion is used as additive after dilution to e.g. 0.02 wt.-%.
The DPE-based dispersion (diameter 50 nm) is taken from former studies (see Table above). The colloids were dialyzed and are stable since 2012. The dispersion is used as additive dispersion after dilution to e.g. 0.02 wt.-%.

Pommegranate-like coagulation (*hollow*)

In the very beginning of the work, it was tried to achieve alternate stacking of with the thinnest lamellar building block possible. The exfoliation into thin LDH sheets in water is documented in the literature, but the aspect ratio of these lamellar colloids Therefore, the method of Adachi-Pagano et al.[144] was applied to obtain exfoliated LDH sheets in butanol (0.12 wt.-% LDH).

Therefore, the chosen LDH phase is LDH-dodecyl sulfate from LDH-NO_3, as described in the paper. An aqueous 0.12 wt.-% ST-O dispersion is added in different weight ratios:
LDH/SiO_2 (wt/wt): 0/100, 25/75, 50/50, 75/25, 80/20, 90/10 and 100/0.
The mixed dispersion is dried on a wafer.

3.1.6 Stacked SiO_2@LDH assemblies with ultrafiltration

3 g of a LDH-BSA slurry (NVC: 17 wt.-%, DLS: 1 µm) and 100 mL pure water were stirred magnetically for 20 minutes in a 100 mL beaker. The ultrafiltration unit is placed on a magnetical stirrer to ensure mixing during the filtration. The dispersion is filled into the ultrafiltration unit and the inlet was closed with a screw, optionally reinforced with Teflon tape. Nitrogen was used to build up a pressure of approx. 2 bar. The filter is a nylon membrane filter (Whatman) with a pore size of 200 nm. The LDH colloids were filtrated until the conductivity is at about 0.05 mS/cm (Zetasizer). The dispersion volume is refilled with pure water and waited until the volume is at approx. half the volume. Then, different portions of 0.55 wt.-% SiO_2 dispersion (20 nm, ST-O) was added to obtain desired weight ratios of 1 to 30, 1 to 400, 1 to 800 and 1 to 1200. Usually 3.35 g SiO_2 (1 to 28) dispersion was mixed with 10 g of water and added into the ultrafiltration unit, subsequently the container was refilled to the top with pure water again, and the pressure is applied. When the dispersion in the ultrafiltration unit is at about 10 % of the initial level, pure water is added and the pressure is applied again. This process is repeated another time, whereas this time, the ultrafiltration is applied until most of the water is removed. During the ultrafiltration, the permeate was studied on SiO_2 colloids passing the filter via DLS.
2 g of the obtained slurry (NVC: 11 wt.-%) were mixed in 5 g of a 13 wt.-% PVA solution (M_w: 22,000 g/mol) with a dissolver (VMA DISPERMAT®; smallest disk diameter available Ø = 30 mm). In a small PTFE vessel, the PVA solution is placed and placed into a) with the. The composite is mixed at 1000 rpm for 10 minutes. A single droplet of the composite dispersion is placed on a substrate, dried at r.t. for 30 minutes and dried at 50 °C overnight. The weighed SiO_2@LDH colloids correspond to 25 wt.-% in the resulting film.

3.1.7 Stacked Structures on LDH Monolayer

In order to enhance the parallel orientation of the stacked structures towards the substrate, a LDH Monolayer was prepared based on the method of Duan et al.[168,169]. Before the synthesis, the silicon wafers were thoroughly cleaned by ultrasonication in ethanol and in water for 15 minutes in both cases. The wafers were then dried at 200 °C for 2 hours before use. Subsequently, the wafers were glued by double faced adhesive tape on a SEM specimen stub and clamped into a screw machine. A single drop of a 4 wt.-% solution of a PVA/VTES copolymer was placed on the wafer and spin-coated at approx. 5000 rpm for 5 minutes. The coated wafer is annealed at 200 °C for 30 minutes and after cooling, the wafer was placed at the bottom of a 100 mL teflon-lined stainless steel bomb. A solution of 1,71 g $Mg(NO_3)_2 \cdot 6\ H_2O$ (6.7 mmol), 1.25 g $Al(NO_3)_3 \cdot 9\ H_2O$ (3.3 mmol) and 5.60 g urea (93 mmol) in 100 mL pure water was prepared and stirred for 10 minutes. A small part of the solution was added to the Teflon-lined steel bomb until the meniscus of the solution is just above the silicon wafer. The steel bomb was tightly closed and carefully placed in an oven at 90 °C for 9 hours, cooled at room temperature and carefully opened. The wafers were washed thoroughly with pure water and dried under ambient conditions. Finally, the composites described in subsection 3.1.6 were placed on the $\{[Mg_2Al(OH)_6]NO_3\}$ LDH monolayer and examined via SEM and FIB technique.

3.1.8 LDH edge-functionalization with Zr(IV) cations

Another way to enhance the parallel orientation of stacked LDH structures is an addition of zirconium cations. The stacked structures are prepared without ultrafiltration and a 1 to 800 (wt/wt) ratio (according to) and mixed with a $Zr(SO_4)_2 \cdot 4\ H_2O$ solution to obtain an overall concentration of 10 mM in the resulting composite. In all experiments, the $Zr(SO_4)_2$ concentration is adjusted in such a way that the required added volume is 1 mL.

The appearance of rods and spheres with a thickness of 2.7 µm were observed after stirring for 7 days (Appendix, page 219), so that another experiment was conducted by filtering the solution through a 200 nm syringe filter, as follows:

A 500 g LDH dispersion (0.40 wt.-%), 30 g of a 20 nm SiO_2 dispersion (0.01 wt.-%) and 100 mL of a 0.01 M $Zr(SO_4)_2$ solution (equal to 0.35 wt.-%) in deionized water were prepared. The Zr-containing solution was stirred for 1 week, whereas a transparent solution forms after 1 hour, and a birefringent dispersion is formed after about 48 hours. After 5 days of magnetic stirring, the dispersion is filtered through a 200 nm syringe filter to obtain a transparent liquid. The conductivity was measured before and after the filtering (no change). The LDH dispersion is magnetically stirred in a 1 L screw-capped bottle. A mixture of the 25.33 g SiO_2 dispersion and 25 g water is added to the LDH dispersion with a peristaltic pump (0.4 mL/min, 125 min). Subsequently, A mixture of 15.93 g of the filtered 0.01 M $Zr(SO_4)_2$ solution and 8 g deionized water was added with a peristaltic pump (0.4 mL/min, 40 min). After another 30 minutes of magnetic stirring, 450 g of the dispersion is centrifuged at 10.000 rpm for 10 minutes. The remaining dispersion and the slurry obtained after centrifugation were mixed in a PVA matrix.

Table 19: Weighed portions of organized LDH/PVA composites

	organized LDH [g]		PVA [g]				
	slurry	dispersion	gel	dispersion	H_2O	NVC	filler content
#1	0.25	-	-	2.53		14.4%	25%
#2	0.24	-	-	1.60	2.14	7.2%	34%
#3	-	10.27	-	1.00		1.4%	25%
#4	0.38	-	2.00	-	4.50	8.5%	26%
#5	0.29	-	1.10	-	3.00	8.1%	33%
#6	-	13.50	2.83	-		4.1%	8%
#7	-	20.88	1.22	-		1.6%	23%

The portions shown in **Table 19** were weighed in and magnetically stirred in a 20 mL snap-cap vial for 1 day (PVA dispersion) and 5 days (PVA gel), respectively. One droplet of the composite dispersion is placed on a silicon wafer, dried 1 hour at r.t., and at 50 °C overnight.

3.1.9 SEM and FIB imaging of Stacked Structures

A single droplet of the coagulated particle mixture samples was dried on a silicon wafer for SEM examination. The samples are sputtered with Au/Pd ($\rho = 16.7\ g/cm^3$) to an eq. thickness of 3 nm (measured simultaneously by QCM).

3.1.10 Mastersizer Measurements

A LDH dispersion with a NVC of 0.4 wt.-% is placed into the sample unit and the dispersion was measured. The obscuration was adjusted by dilution until a meas. NVC of 0.016 vol.-% LDH is present. Then, a single SiO_2 (20 nm) dispersion droplet (0.03 g) was added in order to obtain an approx. weight ratio of 1 to 800 (SiO_2 @ LDH). A program conducted a measurement every 30 minutes for 24 hours.

3.2 Results & Discussion

In a previous work on organized colloids, the liquid delamination of LDH colloids in DMF and assemblies thereof were examined in model composites (K. Briesenick (2017)[68]).
In this subsection, the focus is on stacked assemblies of spherical and lamellar colloids, shown in **Figure 89**. Some preliminary experiments focus on Na-montmorillonite (NaMMT) assemblies with lamellar chitin and spherical PS. Liquid exfoliated LDH colloids in butanol and a subsequent organization with SiO_2 colloids in water lead to hollow structure with SiO_2 @ LDH assemblies as a shell. The non-exfoliated LDH colloids form stacks $(SiO_2 @ LDH)_n$ by electrostatic self-assembly with low amounts of SiO_2, which can be further organized by addition of zirconium ions (Zr^{4+}). The zirconium ions are assumed to adhere to the edges of the LDH particles, comparable to pyrophosphate ions ($P_2O_7^{4-}$), which adhere to the edges of synthetic laponite and induce a more parallel alignment of the lamellar clay and significantly alter the rheological characteristics.[37] Moreover, the parallel alignment was enforced by first forming parallel-aligned LDH on the substrate and subsequently apply different $(SiO_2@LDH)_n$ assemblies in a PVA matrix on the pretreated substrate. The non-exfoliated LDH particles can also be mixed with spherical colloids to obtain a homogenous deposition on the surface of the LDH colloids LDH_{face}, similar to the previous subsections.

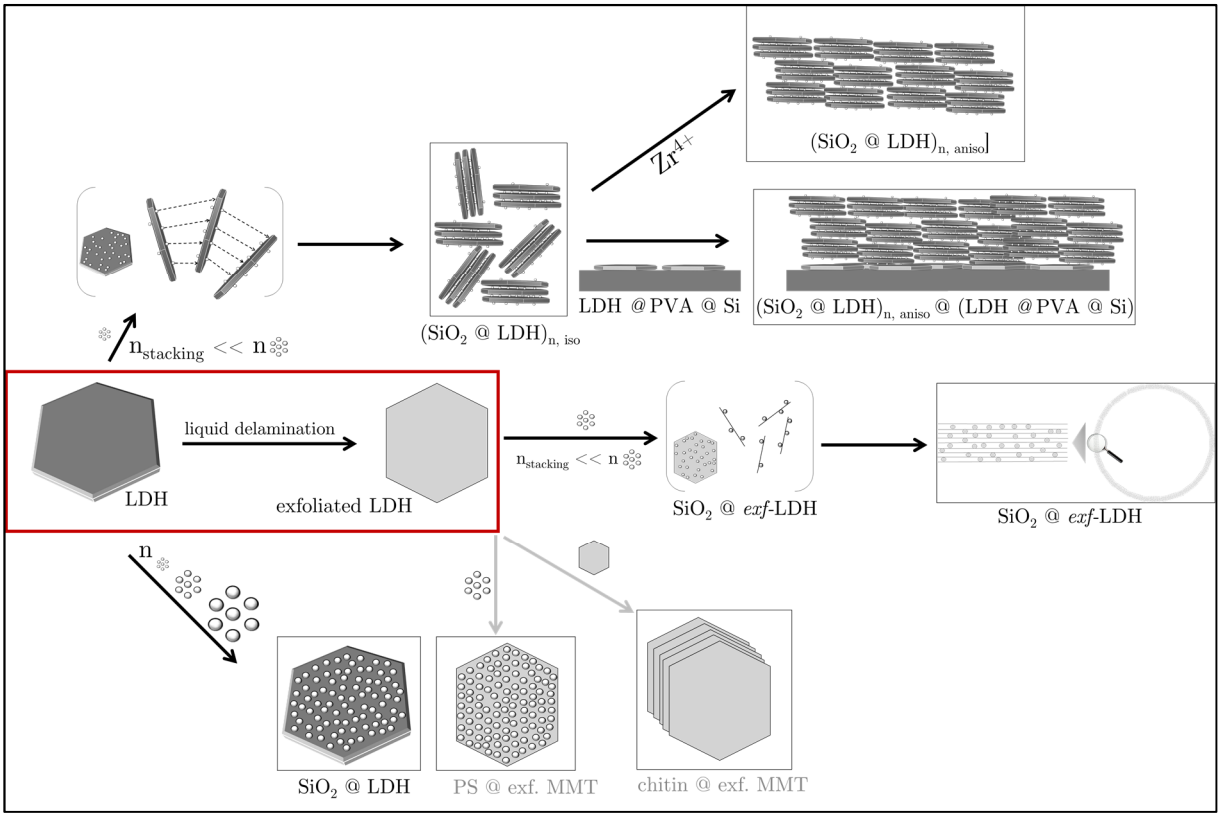


Figure 89: Transformations of organized [Sphere @ LDH] colloids
All assemblies start with LDH tactoids with 2D geometry.
iso: isotropic; aniso: anisotropic; exf.: exfoliated; PVA: polyvinyl alcohol; MMT: montmorillonite

3.2.1 Assemblies with exfoliated sheets

The influence of the addition sequence on the apparent surface charge of organized colloids in the wet state was examined on chitin @ MMT and PS @ MMT assemblies, respectively. The deposition of cationic polymer spheres PS @ MMT ("Perglutin", PS-acrylate copolymer) and the deposition of cationic lamellae chitin @ MMT on anionic lamellar and ultrafiltrated montmorillonite colloids is examined with the separate dispersion method in order to estimate the point of zero charge POZC (cf. experimental part 3.1.8).

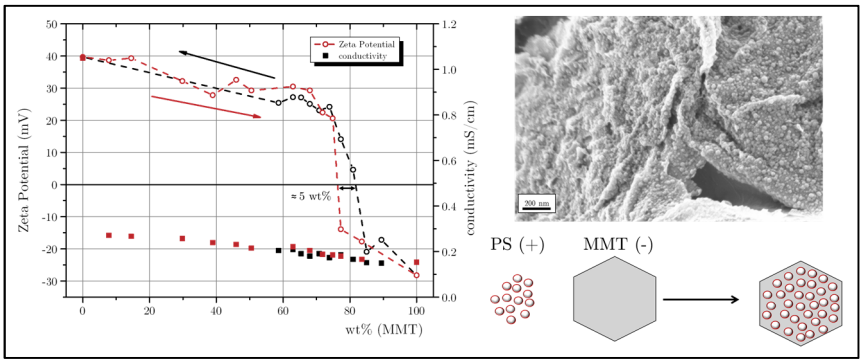


Figure 90: PS @ NaMMT titration
The black depicted data points are attributed to the addition of NaMMT, whereas the red data points are attributed to the addition of PS dispersion. The measured POZCs have different values with a gap of about 5 wt.-%.

In **Figure 90**, the isoelectric titration of cationic spheres on MMT and a reversed titration of MMT to cationic dispersion is shown. The big gap of the POZC values (5 wt.-%) could be related to the ability of the flexible montmorillonite colloids to enwrap the small PS colloids and shield the charges therefrom. It is assumed that the assembly behavior should take place in other Sphere @ Lamellar colloid assemblies with comparable sizes. The isoelectric titration of a Lamellar @ Lamellar colloid assembly has a much smaller gap of the POZC values (cf. **Figure 91**) and is conducted at higher conductivities. The gap between the POZC values is at approx. 0.7 wt.-%. The apparent diameter in aqueous medium is almost the same for both lamellar colloids. In these measurements, the pH of the mixed dispersion was not measured. It is known from the preparation, that the chitin dispersion (pH 2.6) and the perglutin dispersion (pH 3.7) are acidic.

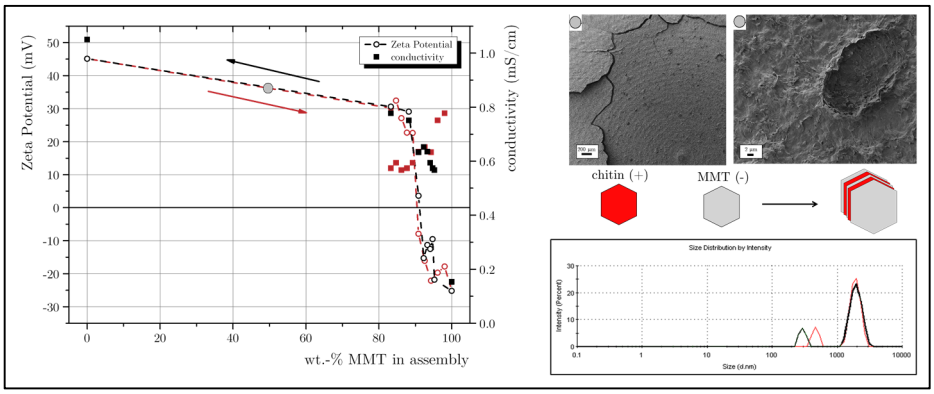


Figure 91: Chitin @ MMT titration
The black depicted data points are attributed to the addition of NaMMT, whereas the red data points are attributed to the addition of PS dispersion. The measured POZCs have different values with a gap of about 5 wt.-%.

A different morphology was found for amino-functionalized silica and epoxy-modified montmorillonite SiO_2 μ MMT in a previous work (A. Oswald (2014)[170]). There, the self-assembled colloids form by chemical interaction μ in NMP as a solvent and subsequently was dispersed in a poly amide imide (PAI), where massive agglomerates are found, comparable to pommegranate structures. The assembly is preserved in the film cross-section (FIB) of the composite material.

Herein, mainly different LDH phases were tested on the ability to form stacked structures from exfoliated LDH. Among them the metals zinc, magnesium and aluminum in different metal ion ratios and different intercalating species ($HBSA^-$, NO_3^-, $ABSA^{-/+}$, BSA^-) were tested. The aspect ratios, lateral sizes and subsequently the stiffness of these lamellar colloids vary strongly, so the results.[68,151]

Theoretically, the highest interface is reached, if the particle dimensions become small. For this reason, liquid exfoliated LDH sheets (1000 nm) in butanol were mixed with aq. SiO_2 dispersion (20 nm) with different ratios and equal NVCs in the initial dispersions. The dodecylsulfate-intercalated LDH colloids were prepared from LDH-BSA and LDH-NO_3 as initial phases and mixed with the SiO_2 colloids in different ratios. A similar 'pommegranate' structure is obtained (**Figure 92**), which turned out to be hollow after dispersing in a PVA matrix (**Figure 93**). At 90/10 (wt/wt) compositions of LDH/SiO_2 the shown microspheres appear.

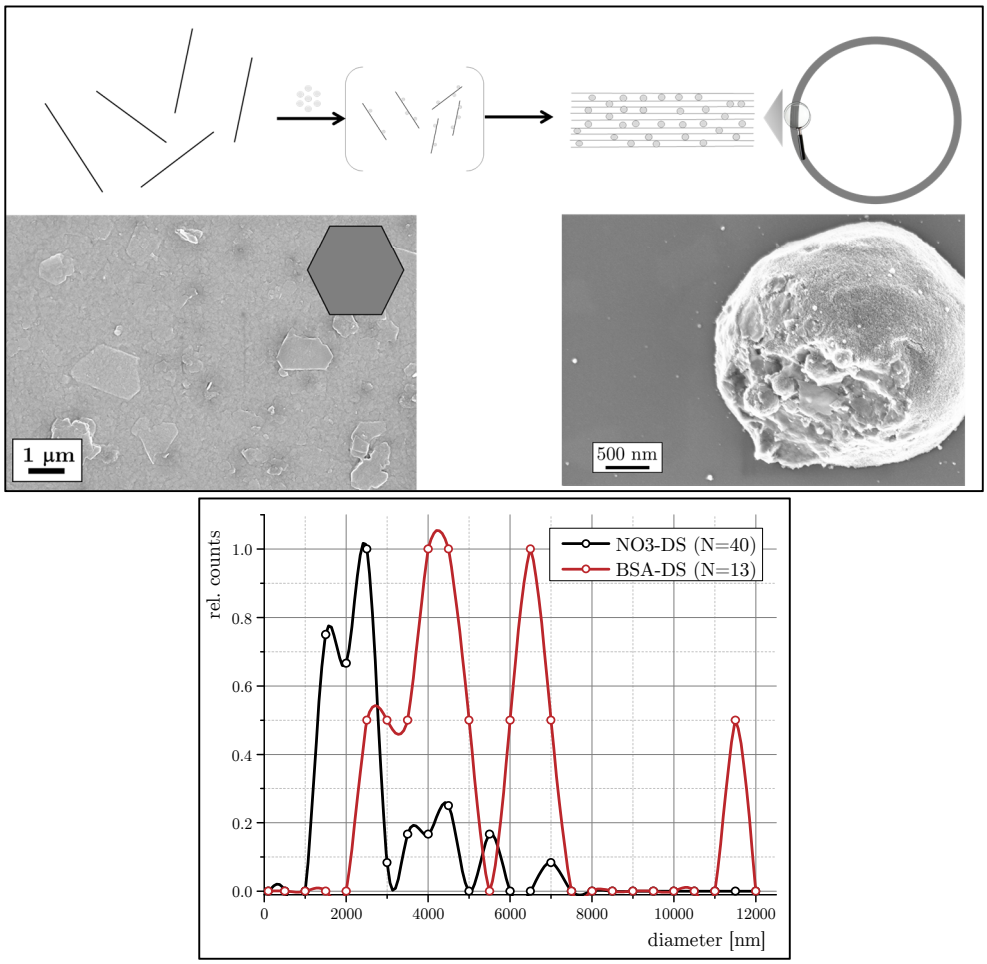


Figure 92: Diameter of SiO_2 @ LDH pommegranate structures with different LDH species. The upper illustrations and images show the obtained organization. The size distributions of the pomegranate structures are obtained by optical measurement on SEM images (see Appendix page 218).

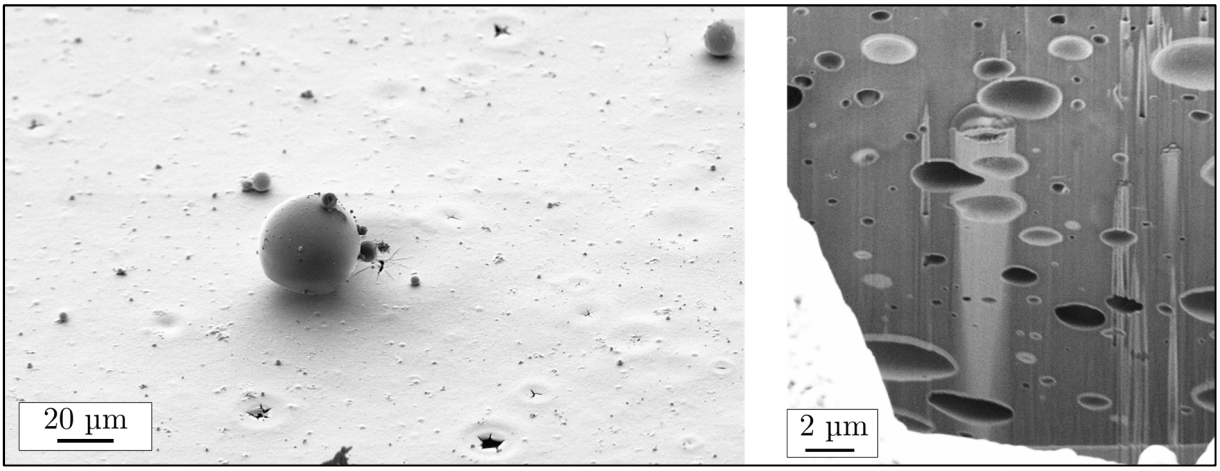


Figure 93: Film surface and cross-section of SiO_2@LDH assemblies in PVA matrix
left: Film surface. Hollow structures in the film and stabilized hollow structures on the film.
right: Film cross-section. The film thickness is about 20 µm.

The hollow morphology of the SiO_2 @ *exf*-LDH assemblies are preserved and are visible within the FIB film cross-section. The solubility of butanol in water is low, so that a phase-separation mechanism of the solvents is assumed. The colloidal and the dried state seem to be similar, since the cross-section of these assemblies in a PVA matrix show a preservation of the spherical (hollow) structures. All in all, these assemblies did not lead to the desired stacking parallel to the surface and was therefore not further examined. The liquid exfoliation in water of all tested LDH colloids was not successful.

3.2.2 SiO_2 @ LDH assemblies

In order to introduce this subsection, some general similarities and differences to the PS @ K assemblies and conclusions from the previous subsections are described in the following.
A single colloid can be described as a mass point m and is therefore accelerated by the force F. The effective surface charges q of two dispersed colloids in water with oppositely charged interfaces satisfy Newton's and Coulomb's law:

$$F = ma \propto \frac{q^+ q^-}{r^2} \tag{16}$$

The field lines between the colloids from the formal charges q^+ and q^- are assumed to perform a directed assembly of the isotropic charged SiO_2 colloids (q^-) and the anisotropic lamellar LDH colloids (q^+), cf. **Figure 94**.

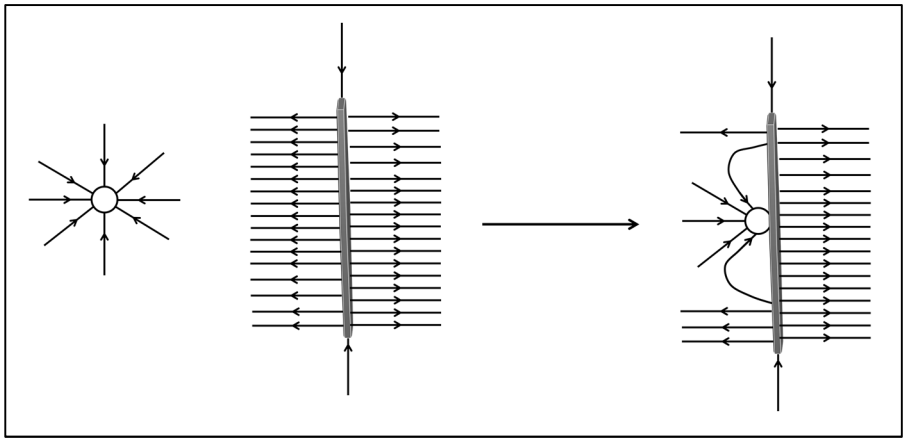


Figure 94: Illustration of an electrostatic single sphere deposition

When additional ions are present, e.g. in order to perform a pH adjustment or present ionic residues of the synthesis, the electric field lines are weakened and less directed, so the assemblies. An increase of the ionic strength is assumed to perturb the field lines, and less directed colloidal assemblies are observed[68]. Moreover, the storage of montmorillonite MMT, layered double hydroxides LDH or kaolinite colloids K in dispersion with low ionic strength partially dissolute the colloids and an additional carbonate uptake takes place, measurable as electric conductivity. Therefore, the colloids are stored as slurries or powders to inhibit the formation of ions by dissolution and carbonate uptake.
Moreover, the ratio of the diameters of the lamellar and spherical colloids is from central interest for the herein described and desired stacking assembly of lamellar and spherical colloids. Also the charge differences of the colloids, measured as ζ-potential are compared in **Table 20**. Not shown, but also important is the density of LDH colloids which is lower than for K colloids, leading to higher mobility.

Table 20: Comparison of sizes and charges of the examined model systems

Assemblies	**eq. plate diameter** [nm]	**sphere diameter** [nm]	**diameter ratio** [nm/nm]	**max Δζ** [mV]
PS @ kaolinite	4300	65-105	40-60	70
SiO_2 @ LDH	1000	10-15	70-100	110

The isoelectric titration of the pristine colloids SiO_2 and LDH were already measured in previous works[151] and the results are recapitulated in **Figure 95**.

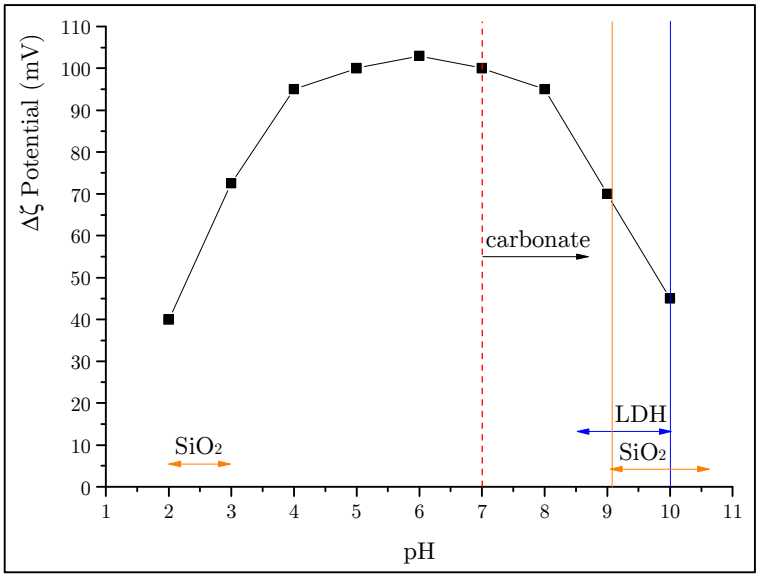


Figure 95: ζ-potential difference as a function of pH

The ζ-potential difference Δζ reveal the difference of surface charges of the pristine colloids in dependence of the pH. LDH colloids are most stable between pH 8.5 and pH 10. The used SiO_2 colloids are unstable above pH 9 and below pH 3. The ζ-potential difference at the stability optimum pH 9 is about 70 mV, compared to pH 7 with about 100 mV. Carbonate uptake in the basic region is favored, so that no pH adjustment was conducted throughout the experiments.

The assembly of hard and spherical SiO_2 colloids (20 nm) on stiff lamellar LDH colloids (1 µm) was examined with the separate dispersions method and the autotitration method in comparison (**Figure 96**).

As a result, the isoelectric titration measurement results mainly depend on:

- the ion concentration
- the addition sequence (time of assembly, time of the addition)
- the concentrations of colloids in additive and stock dispersions
- the choice of the stock and the additive dispersion (lamellar - spherical; charge)
- mixing characteristics (rest, magnetic stirring, shaking,....)

The apparent ζ-Potential was measured in dependence of the respective weight ratio of the colloids. The underlying logistical fits (not shown in the figure) of the separate dispersions method converge well (e.g.: ultrafiltrated-LDH : $R^2 = 0.990$). Autotitration experiments on bigger spheres (50 nm PDPE and 120 nm SiO_2) are shown in the Appendix (page 216).
The Point Of Zero Charge (POZC) for the ultrafiltrated LDH is at approx. 3 wt.-% (equal to 1 to 32, SiO_2 @ LDH, wt/wt) and confirm the SEM findings. The SEM images in **Figure 96** show the deposition pattern above and below this ratio. At a ratio of 1 to 35, some of the lamellar LDH colloids are not covered by spherical colloids. At a ratio of 1 to 28, the surface is visibly covered and the distance between the spherical colloids is homogenous. The ζ-potential at this particular ratio (1 to 28) is at approx. 1 mV according to the logistic fit. At the POZC, the charge of the lamellar colloids is fully compensated with a heterogenous surface charge distribution and a homogenous deposition of spherical colloids.

For low SiO_2 contents, more blank LDH surfaces are present. At blank LDH surface spots, the local charge is positive, whereas sphere-covered LDH surface spots are negatively charged. The addition of more spherical colloids leads to shorter distances between the SiO_2 spheres on the LDH_{face} and a more negative ζ-Potential.

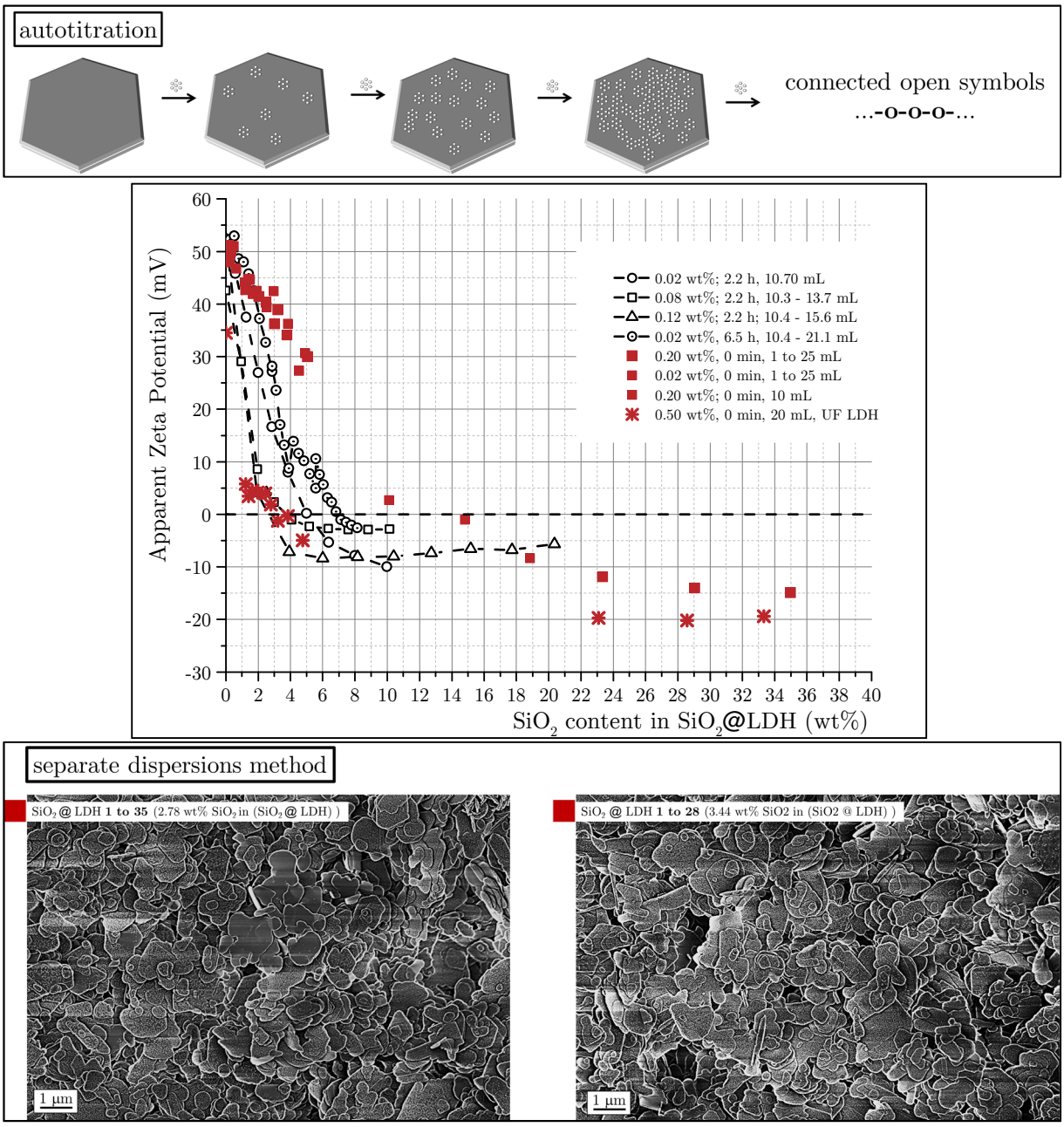


Figure 96: A SEM image comparison of autotitration and separate dispersions method

Connected open symbols refer to the *autotitration method*, scattered red symbols refer to the separate dispersions method.

In all shown data points, 1 µm LDH-BSA is the stock dispersion and 20 nm SiO_2 (ST-O) as additive was used. The SiO_2 additive concentrations are shown in the legend. The SEM images at the bottom show SiO_2@LDH assemblies (▪) (w/o ultrafiltration, w/o ultrasonic treatment) around the POZC (approx. 3 wt.-%) of the ultrafiltrated LDH-BSA phase (✳).

The addition of spherical SiO_2 colloids to LDH dispersions was favored over the corresponding reversed addition, because of the easier handling of small batches, since the concentration of the SiO_2 colloid dispersion is much smaller compared to the LDH concentration. Therefore, the reversed addition was beyond the scope and not examined.

The diffusion and electrostatic agglomeration dynamics of organized colloids can be compared to the "musical chairs" game. The stock dispersion method (e.g. autotitration) gives an unequal chance for later added spherical colloids to interact with free LDH colloid surfaces. Ideally, the separate dispersions method gives any spherical particle the same time to occupy free surfaces. Therefore, the stock dispersion method is strongly depended on the addition sequence, visible in **Figure 96**. The correlation of the POZC and full deposition of the LDH colloids is a useful tool to qualitatively and quantitatively evaluate the effective interface between the colloids.
Either way, from a technical point of view the fast addition of a fixed amount of dispersion has a big advantage because of the reproducibility, precision and the easy procedure. In general, the ζ-Potential measurements are an elaborate method to find the right ratio of lamellar and spherical colloids and confirm findings of SEM observations. More simple and convenient is the qualitative observation of dried dispersions on a surface with different ratios through a Scanning Electron Microscope (cf. **Figure 97**).

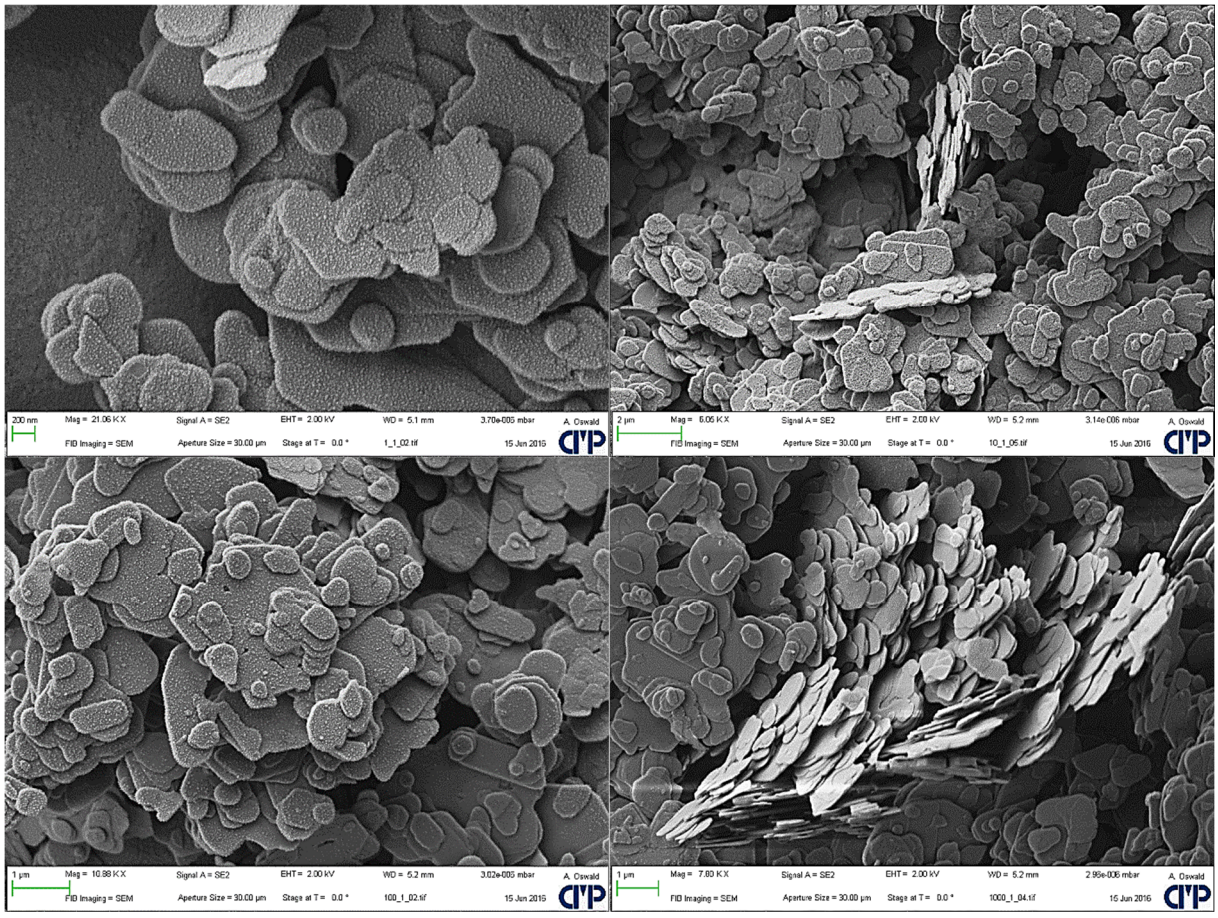


Figure 97: SiO_2 @ LDH assemblies with different ratios
from *upper left* to *lower right*: 1 to ...1, 10, 100, 1000)

The results for SiO_2 @ LDH assemblies with weight ratios ranging over 4 powers of ten lead to the working hypothesis that the interesting ratios in order to examine the stacking behaviour are between 1 to 100 and 1 to 1000.

3.2.3 Stacked SiO_2 @ LDH assemblies

It was found, that the $Zn_2Al(OH)_6[BSA]$ phase shows the most suitable properties to examine the stacking of lamellar and spherical colloids, because of rigid morphology. The strong coordination of the BSA ions is assumed to be the reason for the rigidity and the poor

exfoliation tendency of these LDH-BSA phases. Moreover, these colloids were much easier to dialyze by ultrafiltration to dispersions with low ionic strength (pore size: 0.05 µm). For example, the ultrafiltration of the nitrate analogue phase $Zn_2Al(OH)_6[NO_3]$ took about 10 times longer, because these thinner and more flexible colloids tend to block the filter membrane (cf. Appendix, page 217). The weak coordination of nitrate ions form semi-rigid lamellar colloids and have a higher exfoliation tendency, indicated by the results above on the hollow SiO_2 @ *exf*-LDH assemblies.

The measured apparent ζ-Potential with SiO_2 present in the mixture has always smaller values towards the pristine LDH-BSA phase, whereas after time, the positive charge re-establish to some extent. The stacking mechanism lead to a shielding of the small SiO_2 spheres, so that the ζ-Potential "hops" to more positive values. The autotitration of the model system show regular "hops", which vanish for higher sphere concentration, shown in **Figure 98**. This effect is attributed to a stacking mechanism. Intriguingly, the same behaviour was found for the PS@K model system from the previous subsections, whereas the emerging ζ-potential deviations are much higher in all cases. Morphologies of stacked PS@K assemblies were not observed in any dried PS@K sample within the thesis, whereas a stacking mechanism in the wet state can not be fully excluded.

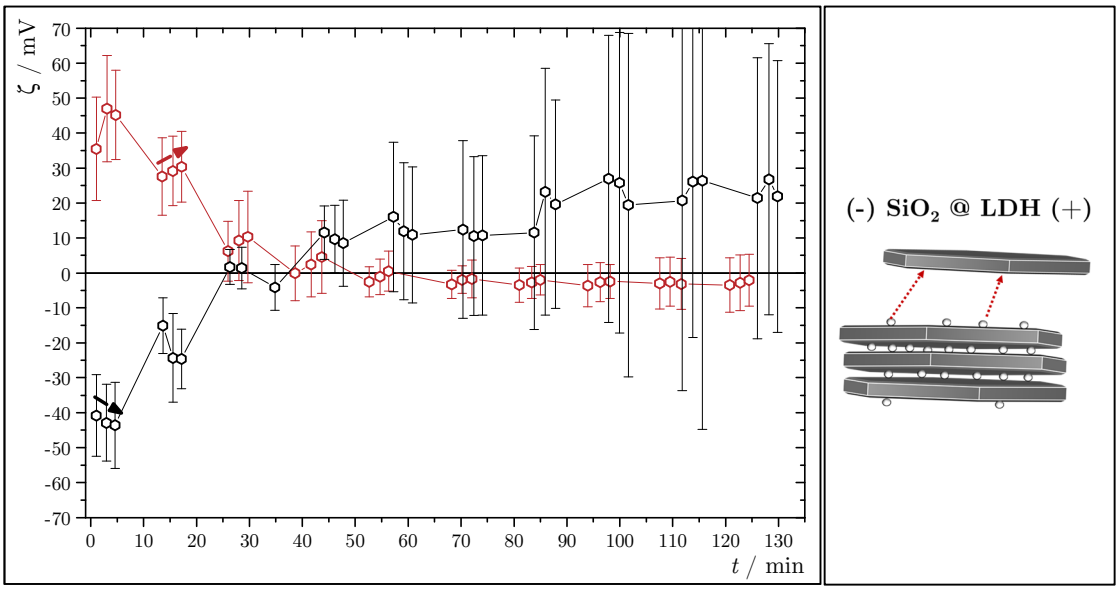


Figure 98: Isoelectric autotitration and postulated $(SiO_2@LDH)_n$ assembly mechanism

black data sets:	0-9 vol.-% **PS@K**,	additive 0.015 wt.-%, 65 nm PS.
red data sets:	0-16.6 vol.-% **SiO_2@LDH**,	additive 0.080 wt.-%, 20 nm SiO_2.

The addition of SiO_2 colloids (20 nm) to the LDH colloids (1 µm) lead to agglomeration due to strong electrostatic attraction, like described before. As it already can be seen in Figure 95, the highest attraction is expected between pH 5 and pH 9, measurable as the ζ-potential difference ($\Delta\zeta = 100$ mV). For the SiO_2@LDH assemblies, the point of zero charge of the assemblies was measured for different ratios ranging from 1 to 100 to 1 to 1000, shown in **Figure 99** and summarized in **Figure 100**.

The "hops" of the ζ-potential attributed to a stacking mechanism also appear in the determination of the POZC for the ratios 1 to 200, 300, 400, 500 and 800, whereas ratios of 1 to 100, 600, 700 and 1000 do not show this behaviour. Moreover, pristine LDH does not show the behaviour. The results of the estimated POZC values, expressed as pH, and the respective mass concentrations of the SiO_2@LDH assemblies have a significant correlation, shown and described in Figure 100.

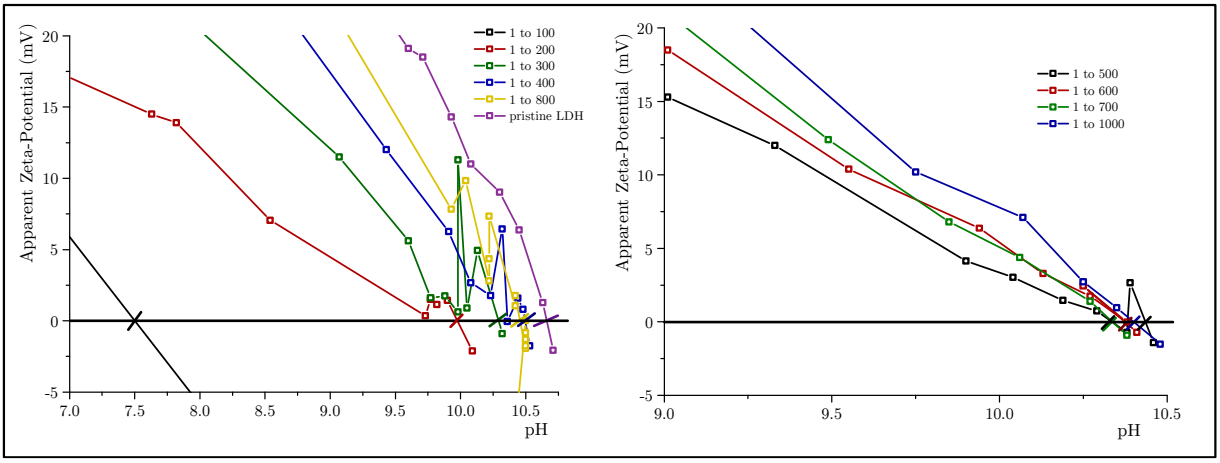


Figure 99: Isoelectric titration curves of freshly stacked structures

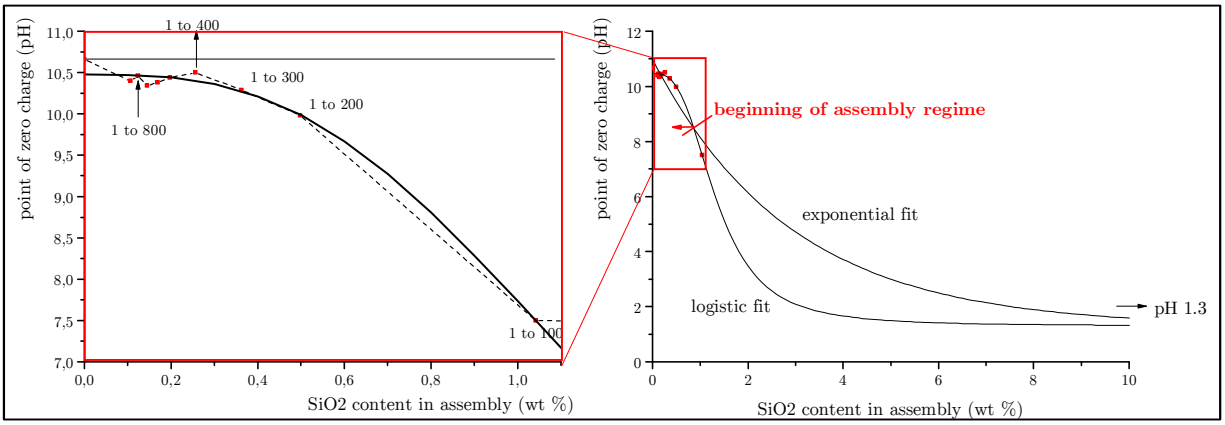


Figure 100: Assembly regime expressed as point of zero charge vs. SiO_2 mass content.
right: The exponential fit of all measured POZC values and the POZC of pristine colloids describes the theoretical case of no agglomeration and no assembly of the colloids (with $10^{\hat{}10}$ wt.-% substituted for zero). The exponential fit of the data se do not converge, because of a mutual dependency of the parameters (χ^2=0.159; R^2=0.980) due to the aforementioned agglomeration. In turn, the logistic fit converges with χ^2=0.010 and R^2=0.999. The intersection point of both fits is interpreted as the "assembly regime" of the examined model system.

The postulated assembly regime at low SiO_2 mass contents was further examined for dried samples and the resulting morphology.

The full coverage at a SiO_2 @ LDH ratio of 1 to 28 has also fractions of stacked assemblies, whereas for example ratios of 1 to 400 and 1 to 800 appear to undergo assembled stacking more likely, based on detailed observations of dried assemblies via SEM imaging (**Figure 101**). The mechanism behind the stacking is assumed to be a partial coverage of LDH colloids, followed by an electrostatic attraction of oppositely charged spots ("defects") and is shown in Figure 86, at the beginning of the subsection. The trapped SiO_2 colloids between the LDH colloids are not clearly visible in the presented SEM images, because of a low probability to see the SiO_2 at low concentrations and issues based on the resolution. A single stacked assembly is shown for an excess of SiO_2 in **Figure 102**, where the SiO_2 particles are visible in a FIB cross-section of a SiO_2/LDH/PVA composite with a magnification of approx. 28,000 X. The distances between the LDH colloids in the SEM images are equal to the primary particle size (20 nm) of the SiO_2 colloids. The distances were measured with "ImageJ" software. These measurement of the distances in the images indicate, that the colloids are stacked by the assumed mechanism.

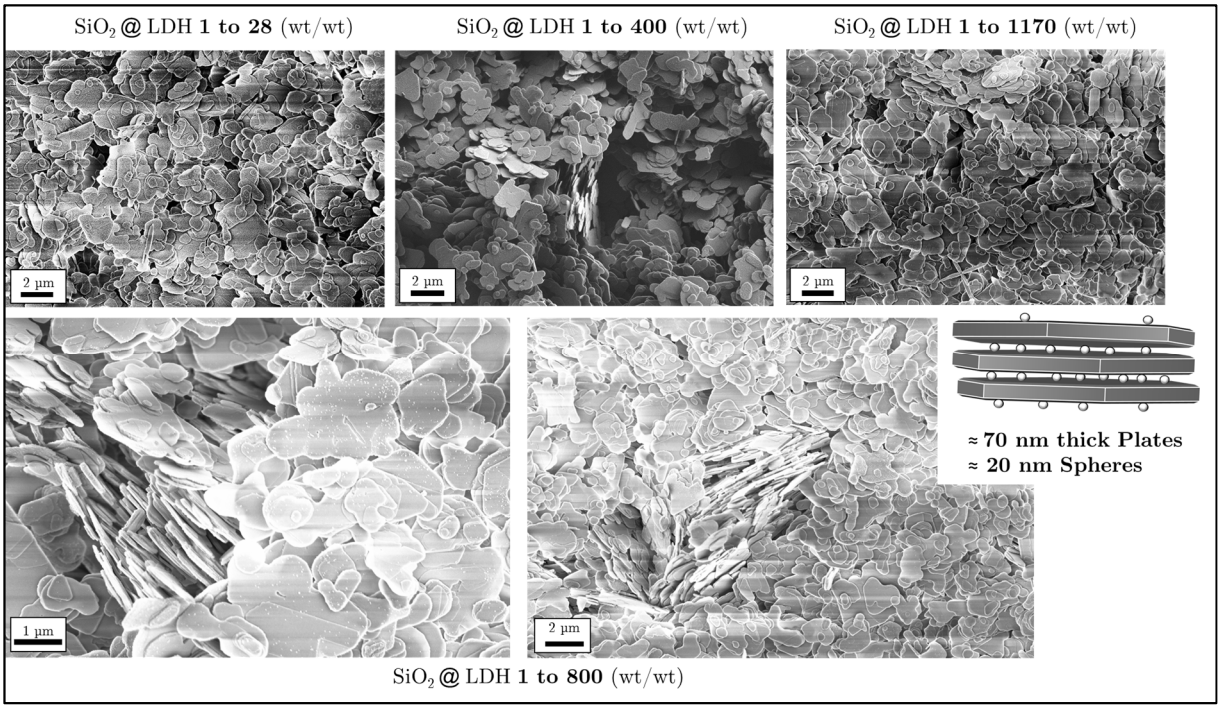


Figure 101: Overview of stacked assemblies with different weight ratios

All of these images are made with ultrafiltrated LDH-BSA colloids. The distances between the sheets were measured with ImageJ image-processing program and are comparable with the SiO_2 colloid diameter.

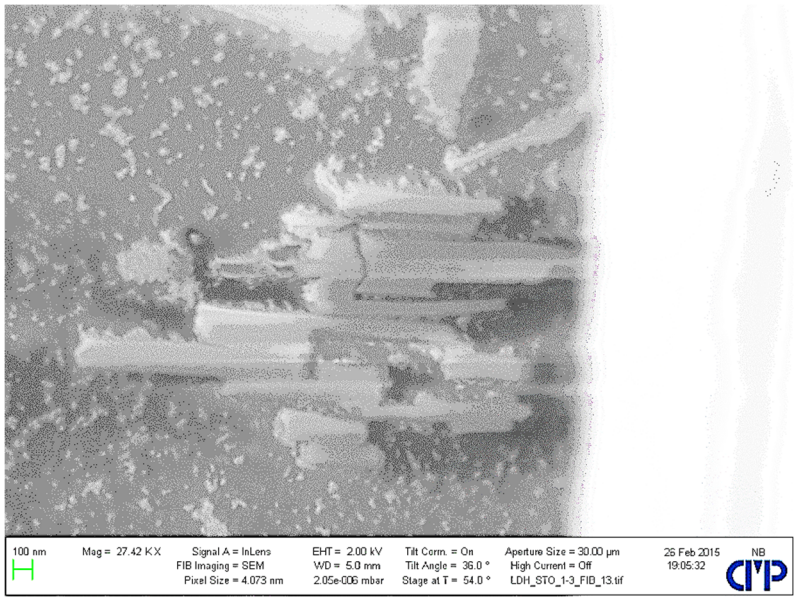


Figure 102: FIB cross-section of stacked SiO_2 @ LDH assemblies in PVA

SiO_2 @ LDH (1 to 1, wt/wt) and (SiO2@LDH) to PVA of 1 to 3 (wt/wt)

The hetero-coagulation to stacked structures with bigger spherical colloids (PDPE, 50 nm) with the same charge did not lead to visible morphologies of stacked structures. It is assumed, that the presented mechanism is valid for a particular size and charge ratios of the lamellar and spherical colloids (listed in Table 20, where PS @ K and SiO_2 @ LDH are compared).

However, in the first experiments on the parallel orientation of the stacked SiO_2 @ LDH assemblies in PVA, a face-edge attraction of the stacked assemblies took place. In order to obtain a parallel alignment towards the substrate, other strategies were applied. The chosen polymer matrix PVA has a negligible charge in water and is therefore not capable of exfoliation or even intercalate the LDH colloids, therefore just act as a model polymer matrix.

The desired parallel alignment of the stacked assemblies in a composite was tried to accomplish by a pre-treatment of the silicon substrate with a LDH monolayer, first described by Duan et al.[169]. The reproduced LDH monolayers are shown in **Figure 103**, right. The PVA thin films show a multicolored interference pattern indicating that the film thickness is below 100 nm. The film thickness differs from the middle region to the edge region of the silicon wafer. The *in-situ* hydrothermal synthesized LDH monolayers have a parallel alignment, as desired.

The stacked colloidal assemblies $(SiO_2@LDH)_n$ were dispersed in PVA with 25 wt.-% in the resulting film and a total NVC of the SiO_2/LDH/PVA composite of about 30 wt.-% and were finally applied on the pre-treated substrates. The corresponding FIB cross-sections are shown in **Figure 104**. The mentioned face-edge interactions of the stacked assemblies are still present in every sample, especially at high distances from the substrate. Again, the probability to see the SiO_2 colloids becomes very low due to the fact, that cross-sections reveal just a thin part of the composite. However, at a SiO_2@LDH weight ratio of 1 to 28, the SiO_2 colloids are visible on the surface of the LDH colloids (inlet).

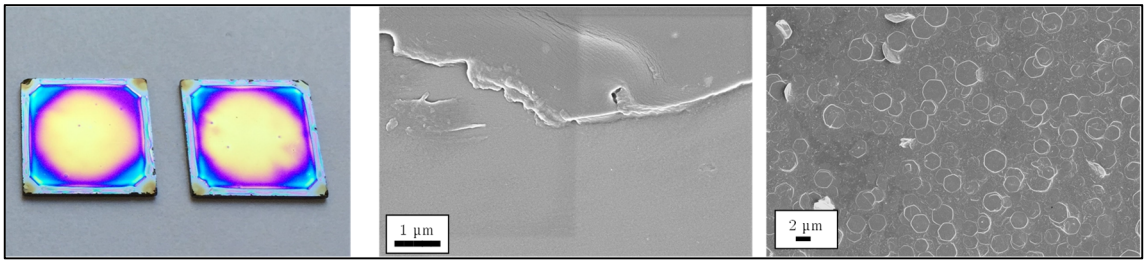


Figure 103: Pretreated Substrate for Stacking examinations
left: thin PVA films on 1x1 cm silicon wafer made by spin-coating;
middle: SEM image of a scratch on thin PVA film;
right: SEM image of LDH monolayer on thin PVA film

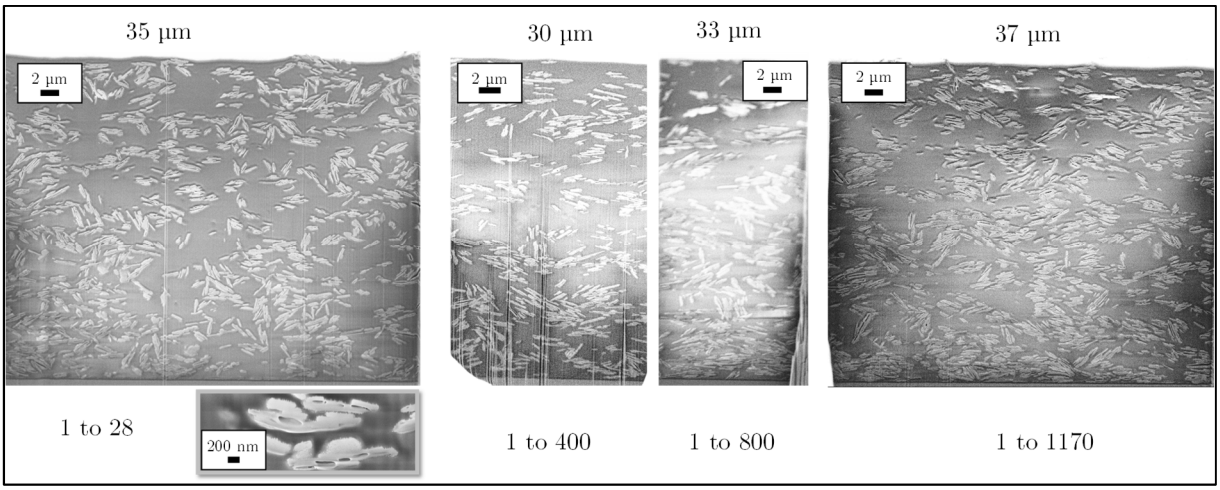


Figure 104: FIB-Cross Sections of Stacked SiO_2 @ LDH assemblies on a LDH monolayer

The parallel alignment near the substrate is especially visible at the ratios 1 to 800 and 1 to 1170. The other two samples however did not show this behavior, even though stacking was observed in the 1 to 400 sample before dispersing in PVA solution. Alternatively to the rather inconvenient method presented here, a silylation of the substrate with a positive charge could be conducted. However, the parallel orientation did not take place as desired all over the composite so that other approaches were examined. For further experiments a ratio of 1 to 800

is used, because the pH is most optimal with respect to the LDH stability, low SiO_2 concentrations and therefore impeded aging.
In a subsequent experiment, the ratio of the stacked assemblies were mixed with zirconium (IV) sulfate $Zr(SO_4)_2$. Apparently, the resulting cross-sections show a parallel alignment of the stacks up to about 30 alternating stacked layers (**Figure 105**). The assumed mechanism behind this parallel assembly is the compensation of the negative edge charge by Zr^{4+} ions, analogue to the edge-charge compensation of Laponite colloids by also tetravalent pyrophosphate anions $P_2O_7^{4-}$.[171]
Unfortunately, it turned out, that the obtained stacked structures are most likely Zr-based colloids. After dissolution of $Zr(SO_4)_2$ in water, a transparent solution is obtained, whereas after a longer period of time of stirring, the solution changes to a birefringent dispersion of Zr-based colloids with the desired morphology (cf. **Figure 106**).

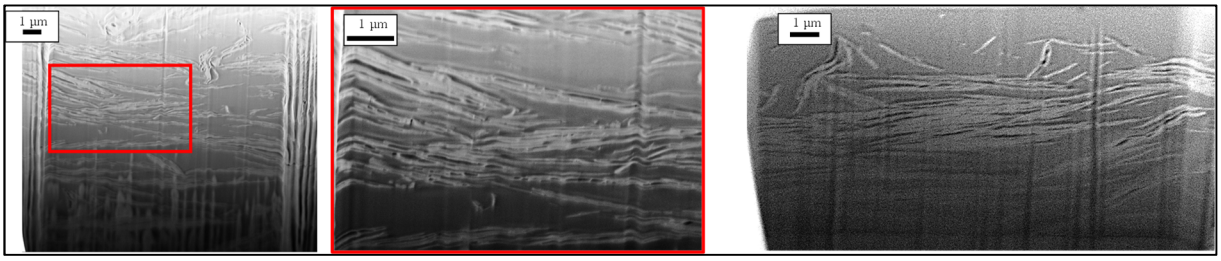


Figure 105: Apparently stacked and parallel oriented assemblies of LDH and SiO_2
Film thicknesses are 25 µm (*left*) and 8 µm (*right*)

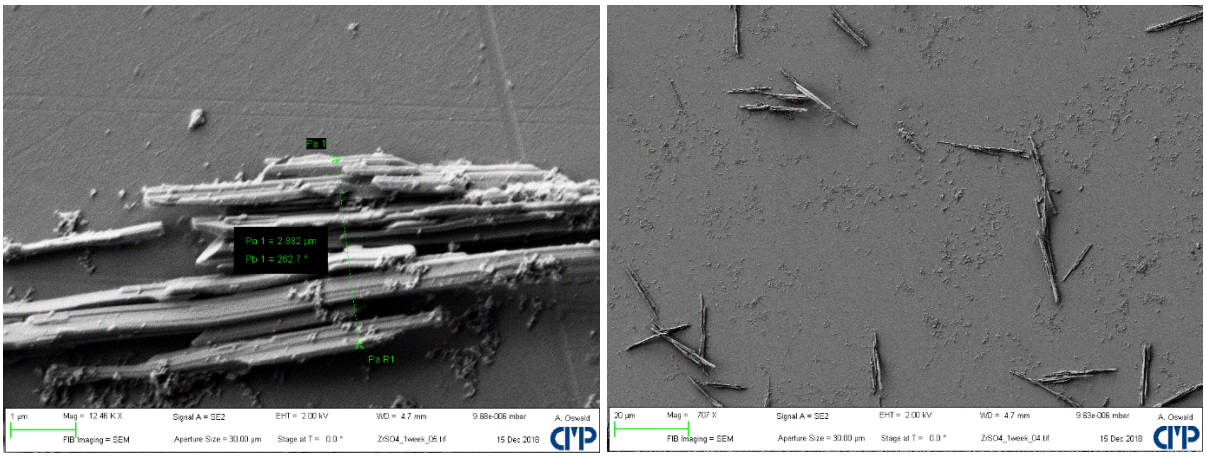


Figure 106: Morphology of Zr-based colloids after stirring $Zr(SO_4)_2$ solution for 1 week.

In order to eliminate the Zr-based colloids, the birefringent parts were eliminated after 1 week of stirring with a syringe filter, leaving a blue, transparent dispersion. Further formation of birefringent colloids was not observed and the elctrical conductivity was not changed after filtering. The Zr-containing dispersion was then added after a defined period of time, leading to parallel oriented and stacked $(SiO_2@LDH)_n$ assemblies, shown in the end of this subsection. The assemblies themselves undergo time-dependent effects, such as reactions, dissolution and carbonate uptake. In the following, the time-dependent studies on the stacked assemblies are presented.
Like in many other clay/oxide systems, the system LDH/SiO_2 leads to undefined chemical reactions after some time.[34] In the here presented experiments, the size of the organized colloids, the macroscopic morphology (flotating skin) and microscopic morphology (see Appendix for SEM images, page 220ff) alters by complex geopolymerization reactions, which were not

examined further. The altering of the organized colloids was characterized by the time-dependent conductivity, ζ-Potential, pH, and dynamic light scattering vs time (**Figure 107**).

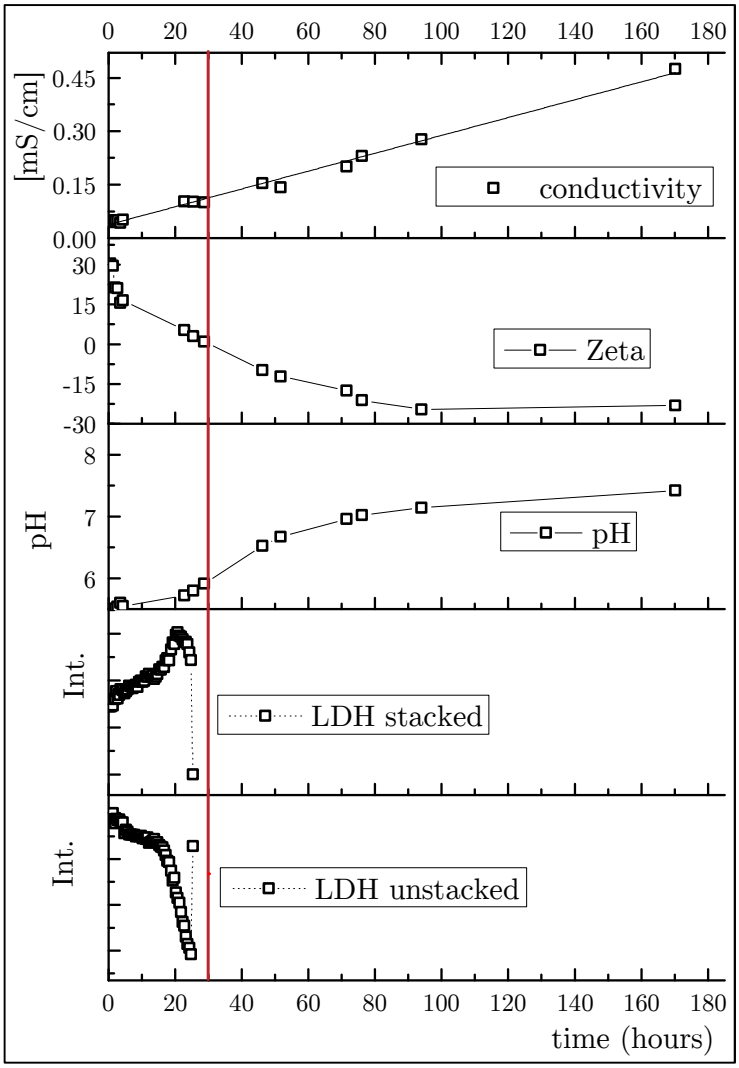


Figure 107: Monitoring of parameters during stacking coagulation

The red line indicate the time, when the POZC is reached (ζ = 0 mV). The top three measurements were measured from a single batch without N_2-atmosphere, whereas the bottom two measurements were measured in a stirred cell of a Mastersizer (cf. **Figure 108**). The stirring of the Mastersizer cell was not possible to prepare with nitrogen atmosphere and the stirring part of the instrument lead to a temperature increase. It is assumed, that the dramatic change of the measured intensities is attributed to the described red line based on measurements at r.t., whereas the change happens earlier due to increased temperature and missing N_2-atmosphere.

The populations of "LDH stacked" and "LDH unstacked" are obtained from the integration of the peaks from the DLS measurements in the range below 1 µm and above 2 µm, respectively, shown in **Figure 108**.

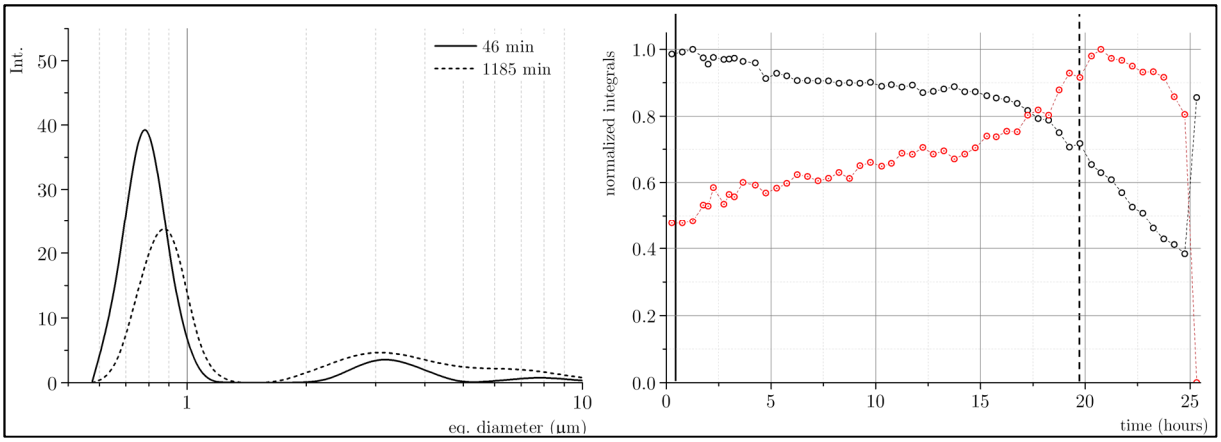


Figure 108: Time-resolved DLS measurement on stacked SiO_2@LDH assemblies with a ratio of 1 to 800. Thermal energy input of the stirring unit was not recorded but noticed after the measurement

To sum up the results on the time-dependent effects, the following text tries to conclude the findings. A dissolution to smaller units (monomeric or oligomeric) becomes more likely with time, indicated by the rise of conductivity and pH. These smaller units can be metal-aqua complexes, -hydroxyl complexes, -oxides and mixes thereof (LDH) or silicic acid units $Si(OH)_4$ by dissolution of SiO_2. However, the direct contact between the phases also leads to reactions after time and amorphous phases form and flotate (cf. SEM images in the Appendix, page 221). The reaction of SiO_2 and the LDH colloids is comparable to complex "geopolymerization" processes, with amorphous microstructure which are documented, but still poor unterstood.[172] The appearance of amorphous and crystalline phases with other morphologies became evident but was not further analyzed. The emerged phases can be probably gibbsite ($Al(OH)_3$) or zinc hydroxide ($Zn(OH)_2$), SEM images thereof are shown in the Appendix, as already mentioned. The examinations on the altering is a very complex topic, which was beyond the scope of the thesis and was therefore not further examined.

The pure water used throughout the experiments has a measured pH of around 5, because of a very low electrical conductivity and a very low buffering capability. Usual pH meters show erroneous measurements at very low ionic conductivity and buffering capability. The water is therefore assumed to be not acidic and assumed to be pH 7, based on the findings that LDH colloids do not shrink in size after storage in the used pure water, whereas LDH colloids stored in acidic medium around pH 5 do shrink. The N_2-atmosphere was applied in order to prevent the influence of CO_2 uptake on the measurement.

The mechanism is found to not take place to the presented extent at colloid concentrations significantly higher than 1 wt.-% and electrical conductivities above 0.2 mS/cm in water. Moreover, reference samples without stirring overnight did not lead to well-stacked structures. In summary, the overall colloid concentration has to be around 0.5 wt.-%, the electrical conductivity below 0.1 mS/cm and the assembly process should have about 12 hours to equilibrate. The pH of the dispersions are not adjusted to prevent the presence of ions in the dispersions and allow the assumed stacking mechanism to operate.

From these pre-examinations, a final preparation strategy was applied in order to obtain assemblies with parallel oriented stacks towards the substrate. The SiO_2@LDH assemblies were allowed to form in water for several hours, the filtered Zr-based dispersions were added and finally mixed with PVA with different amounts of assemblies and water. The resulting FIB/SEM cross-sections are shown in **Figure 109**. The obtained images clearly show enhanced parallel orientation of the assemblies towards the substrate.

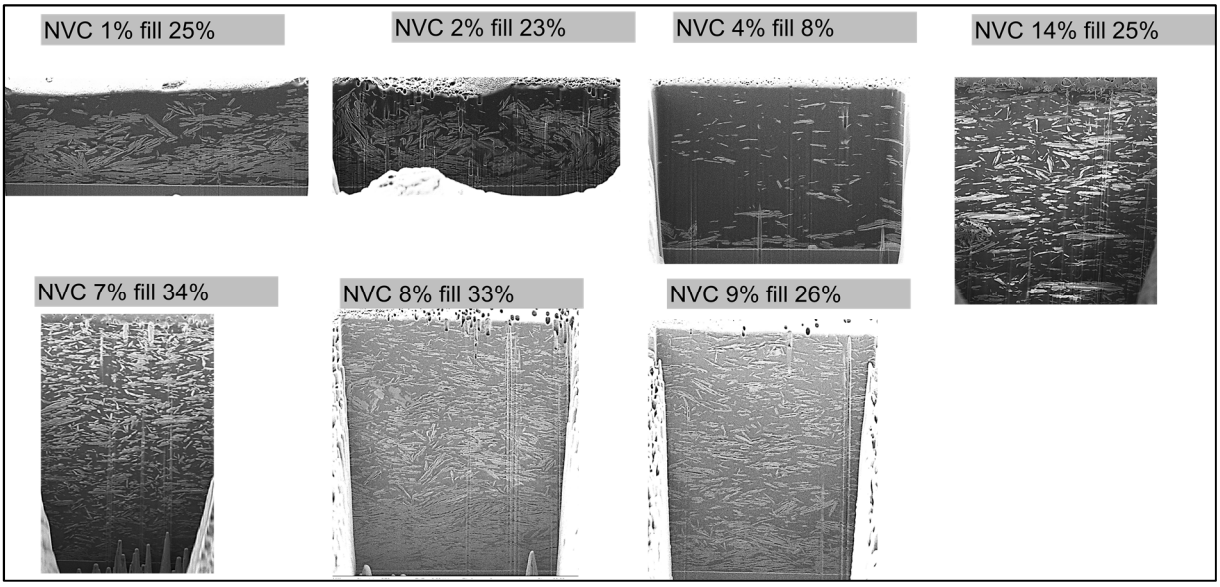


Figure 109: SiO_2@LDH assemblies treated with Zr-based dispersions in a PVA matrix

The ideal amount of zirconium was not further examined, because these preliminary tests act as an orientation for designing materials in other polymer matrices within a project. The composition of the organized colloids here are approximately 97 wt.-% LDH, 2.9 wt.-% Zr-salt, 0.1 wt.-% SiO_2. Dissolved Polyvinyl alcohol (PVA) is an appropriate matrix system to study the structure-property relationship of aqueous clay organization, because it has - similar to water - a high density of hydrogen bonds, without having a charged interface.

For example, the influence of the aspect ratio on the mechanical properties of different clay/PVA composites is already intensively investigated by Walther et. al. for much less PVA in the composites, so that the platelets are forced to align parallel by sterical constraints.[4]

4 PUR / Clay Composites - Exfoliation & Intercalation

For layered crystal structures with ions in the interlayer space, the charge of the layered crystal and the interlayer ion have opposite charge. For example, Layered Double Hydroxides (LDH) have a positive layer charge and a negative ion in the interlayer, whereas for example montmorillonite (MMT) has a negative layer charge and a positive ion in the interlayer. In order to enforce an intercalation of polymer colloids, the interlayer ions and an intercalating polymer colloid have to carry same charges. For the systems under examinations here, the addition of negatively charged PUR colloids to glycine-modified LDH was applied.
The electrostatic-driven penetration of PUR colloids into the LDH platelet staples lead to alterations of the primary structure 1°, on the secondary 2°, tertiary 3° and on the material properties as the quaternary structure 4°, indicated in **Figure 110**.

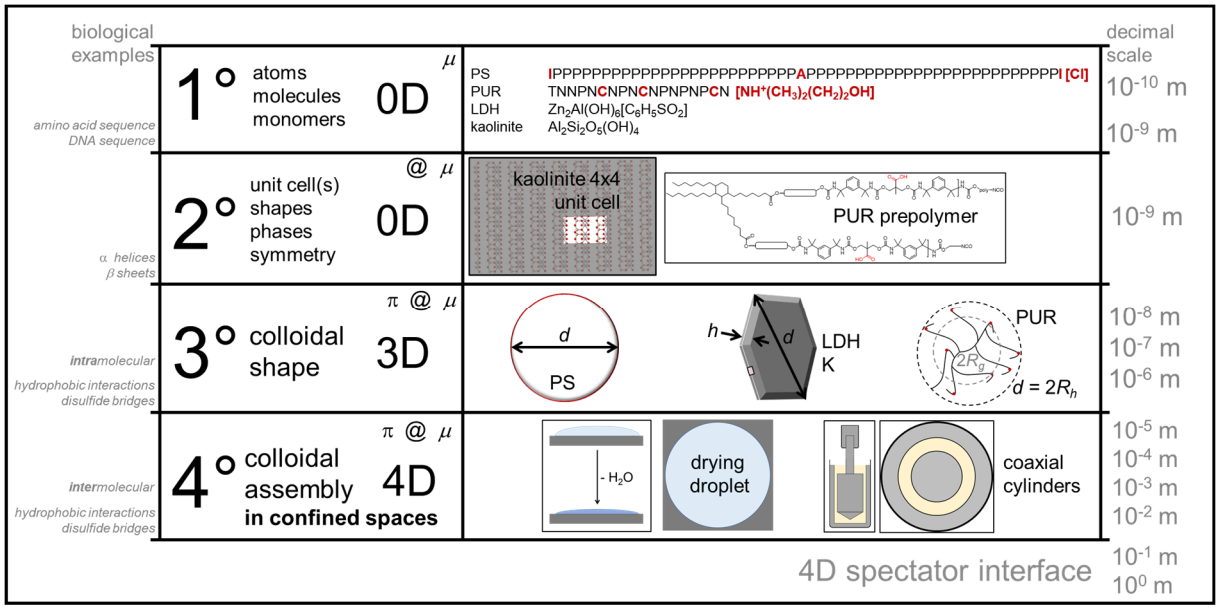


Figure 110: Primary, secondary, tertiary and quaternary structure.
The letters π, @ and μ represent the capillary, electrostatic and chemical interaction, respectively. The monomer sequences of PS and PUR are just exemplary in order to illustrate the similarity to amino acid sequences. Red coloured letters (PS and PUR), dots (PUR) and curvature (PS) indicate charge carrying groups. The red coloured frame in case of kaolinite indicate the siting position of the unit cell.

The penetration of PUR colloids into the platelet staples by mixing lead to alterations of the overall primary structure 1° by ion exchange, therefore also on the secondary 2°, tertiary 3° and finally on the quaternary structure 4°, which is based on the interaction of the 3° structures, leading to colloidal network structures such as intercalation, exfoliation or nematic order in PUR/LDH composites, described below.
In the literature on polymer/clay composites, the morphology of layered crystals are divided in the three states aggregated, intercalated and exfoliated. In this context, the 1° LDH structure is only stable for *aggregated* LDH, where the atoms building the LDH crystal phase (2°) and also the resulting colloidal shape (3°) remains intact after mixing with PUR. *Exfoliation* of LDH lead to a quantitative decrease of the initial 1° and 2° LDH structures and an increase of the aspect ratio (change in 3° structure), whereas *intercalated* LDH have changed 1° and 2° LDH structures.

4.1 Experimental Details

All lamellar colloids used in this thesis were tested on the intercalation and exfoliation behavior in combination with the experimental parameters.

Materials

Name	Size/Purity	Supplier/Synthesis
LDH 400 nm	400 nm	see section III-1.1.1
LDH 800 nm	800 nm	see section III-1.1.2
LDH 3200 nm	3200 nm	see section III-1.1.3
polyurethane Latex	10 - 180 nm	see section III-4
polystyrene Latex	50 - 200 nm	see section III-3
kaolinite SKT-63	650 nm	BASSERMANN minerals
dimethylsulfoxide		
methanol		
tetrapropylammoniumbromide		
2-butoxyethanol		
RESIMENE® HM 2608	90% in isobutanol	INEOS Melamines

Methods

Dynamic Light Scattering (DLS)

Malvern Zetasizer Nano ZS

Malvern Mastersizer 2000

Zeta Potential Measurement

Malvern Zetasizer Nano ZS

Scanning Electron Microscopy (SEM)

Zeiss NEON 40

Focussed Ion Beam (FIB)

Zeiss NEON 40

X-Ray Diffraction (XRD)

Bruker AXS D8 ADVANCE for Structure Solution (Cu-Kα = 0.154 nm)

ULTRA-TURRAX®

IKA® T10

Ultrasonic

BANDELIN "SONOCOOL 255 "

Rheology measurements

Anton Paar Couette Rheometer "Rheolab QC"

4.1.1 Polymer/LDH nanocomposites

The LDH phase $Zn_2Al(OH)_6[NO_3]$ was derived from F. LEROUX (Institut de Chimie de Clermont-Ferrand). All composite dispersions described here were applied with a doctor blade. 2 g of 30 wt.-% LDH slurry is mixed with 20 g water under magnetic stirring, until the dispersion is homogenous. Subsequently, 2.3 mmol per g LDH of sodium DL-lactate, sodium acetate, sodium dodecylsulphate, lecithine, glycine, *p*-aminobenzenesulfonic acid (ABSA), Pluronic P-123 (5800 g/mol; block copolymer PEG-PPG-PEG), Tergitol NP-9 (polyethylene

glycol nonyl phenyl ether), Polysorbate 60 (1312 g/mol; 16 PEG units in 4 branches, bonded to octadecyl) and Tween 20 (1228 g/mol; 20 PEG units in 4 branches, bonded to dodecyl) were added in a small volume of water (5 to 10 g water). After mixing, the LDH suspensions were shaken for 48 h "Certomat U" and centrifuged six times.
The solid content of the resulting LDH slurries is determined (0.1 g, 30 min 110 °C). 0.1 g of the respective LDH slurry (e.g. 30 wt.-%) is mixed with the polymer matrix (10 wt.-% LDH content in resulting film).
Different polymer matrix systems were chosen, depending on the system. For the commercial non-ionic surfactants P-123, NP-9, P-60 and T 20, PVA (11 wt.-%, e.g. 2.46 g) and HMMM[***] (99 wt.-%, e.g. 0.27 g) were chosen. In case of PVA, the composite is dried at ambient conditions, followed by drying at 80° C for 1 hour. The LDH/HMMM films were dried for 16 hours at 80° C, followed by 30 minutes at 180 °C.
The anions lactate, acetate, dodecylsulphate and the zwitterions lecithine, glycine, ABSA were mixed into undisclosed polyurethane dispersions (BASF Coatings), respectively.
Moreover a undisclosed polyester dispersion (BASF Coatings) was used. The LDH phase $Zn_2Al(OH)_6$[ABSA] was also derived from F. LEROUX (Institut de Chimie de Clermont-Ferrand).

4.1.2 PUR/LDH nanocomposites

The preparation of the bare LDH and PUR colloids is shown above (Chapter III, page 33ff.). The obtained phases contain the zwitterions lecithine, *p*-aminobenzenesulfonic acid, taurine, glycine and betaine. All of these LDH phases were dispersed in aqueous PUR matrices (section III-4, page 52) containing small (10-180 nm) and negatively charged colloids.
In a typical experiment, 1 g of approx. 40 wt.-% slurry of the respective LDH phase is mixed with an approx. 30 wt.-% aq. PUR dispersion (5.33 g), magnetically stirred for 5 days in a snap-cap vial to obtain a composition 20 wt.-% LDH and 80 wt.-% PUR in the solid content. The resulting non-volatile content (NVC) of the dispersion is approx. 32 wt.-%. Other compositions with 1 to 25 wt.-% LDH in the solid content are prepared accordingly.
Thereafter, a droplet of the composite dispersion is placed on a silicon wafer and pre-dried at ambient conditions for 1 to 5 hours. In the following, the droplet is dried at 40 °C for 12 hours, at 80 °C for 12 hours, at 95 °C for 6 hours, at 100 °C for 12 hours, at 120-130 °C for 6 hours. Mainly, the prevention of trapped solvent/air inclusions is tried to prevent throughout the drying process.
Optionally, HMMM is added to the composite dispersion as a cross-linking agent (typical: 40 wt.-% in resulting film, 1.35 g) or butoxyethanol as a co-solvent (typical: 20 wt.-% in resulting film). Mostly, both were added. In these cases, the films were dried for 16 hours at 80° C, followed by 30 minutes at 180 °C. In some cases, the composite dispersion is applied with a doctor blade and pre-dried for 1 to 5 hours, followed by the same drying procedure.
In some experiments, yttrium stabilized Zr-beads (diameter 0.7 to 1.2 mm) were added to the snap-cap vial in order to enhance the mixing process. This method appeared to disperse the composites very quickly (6 hours instead of 5 days). Moreover, other mixing instruments were used such as dissolver or ULTRA-TURRAX, before application on a substrate. The use of these high-shear tools mostly lead to foaming and requires undesired dilution (dissolver) of the LDH slurries to obtain reasonable mixing times. The dilution leads to smaller shear forces.

[***] Hexamethoxymethylmelamine

4.1.3 Rheological Measurements

LDH Slurry

The three different LDH products of section III-1.2.2 (p. 39) with diameters of 0.4, 1 and 5 µm were taken as three equivalent representatives of LDH-phases. The 5 µm LDH colloids are prepared with small amounts of glycine as a buffer. In order to make the samples more comparable, the LDH phases underwent an ionic exchange treatment with a 3-fold excess glycine (5 wt.-% LDH in water), shaken for 48 hours (Certomat U), centrifuged and washed in water 7 times. The resulting LDH slurries have a non-volatile content NVC of up to 50 wt.-%. For the rheological measurement, one single batch (760 mL) of a LDH synthesis was used for a better comparability.

Polyurethane Dispersions

For the rheological measurements, three monomodal polyurethane dispersions were prepared with different sizes according to III-4.1. The polyurethane colloids have diameters of 15, 75 and 135 nm originating from the carboxyl group content of the polymer chain. The polyurethane dispersions have a non-volatile content NVC of 33 ± 2 wt.-%. .-%. For the rheological measurement, one single batch of a PUR synthesis (1.1 L) was used for a better comparability.

PUR/LDH Composite Dispersion

The three different LDH colloids (0.4, 1 and 5 μm in eq. diameter) are dispersed in the PUR dispersions with diameters 15, 75 and 135 nm by shaking, magnetic stirring and a final ULTRA-TURRAX treatment with different weight ratios. Compositions with 0, 2, 5, 8, 10 and 13 vol.-% LDH (5, 10, 15, 20 and 25 wt.-%) in the composite dispersion based on the non-volatile content were prepared. For all measurements, the overall non-volatile content in water is kept constant at 32.1 wt.-%. After settling for 2 days, gas bubbles are removed by ultrasonication and further gentle stirring until visible gas bubbles are removed. The density of the LDH colloids is assumed to be 2 g/cm^3 and the density of PUR as 1 g/cm^3.

Thixotropy Measurement

20 mL of the respective PUR/LDH composite material was put carefully into a Couette Rheometer (listed above) and the measurement program (**Figure 111**) is started. The measured shear stress τ vs. the applied shear rate γ are plotted and analyzed.

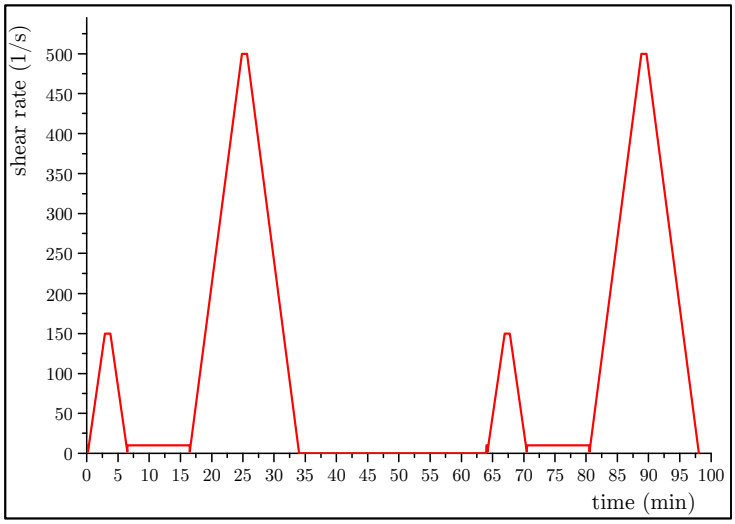


Figure 111: Chosen program to examine thixotropic properties of LDH/PUR composites

Table 21: Tabulated shear program

# N pts.	Δt s	$\dot{\gamma}$ s^{-1}
10	1	10
33	5	2...150
10	5	150
33	5	150...2
10	1	10
100	5	2...500
10	5	500
100	5	500...2
0	600	0
10	1	10
33	5	2...150
10	5	150
33	5	150...2
10	1	10
100	5	2...500
10	5	500
100	5	500...2

4.1.4 Polymer/Kaolinite Composites

In a previous chapter, the ionic exchange of LDH colloids is shown (III-2.3, page 48). The obtained kaolinite phases contain the cations tetrapropylammonium, cetyltrimethylammonium and both in a 50/50 (mol/mol) mixture in methanol. All of these kaolinite phases were dispersed in an aq. PUR matrix (< 20 nm, section III-4, page 52) and negative charged colloids as an intercalating agent. Some experiments were conducted with the PUR prepolymer in the absence of water or addition of butoxyethanol. The composites were casted with a razor blade on an hdg-steel substrate and the cross-section was analyzed by FIB.

4.2 Results & Discussion

In the following subsection, all attempts on the separation of layered crystal planes of Layered Double Hydroxides and Kaolinite in polymer matrices are presented. In **Figure 112**, a comparison of two known systems are shown from recent studies on montmorillonite (D. Briesenick (2016)[18]) and Layered Double Hydroxides (H. Hintze-Brüning (2011)[173]).

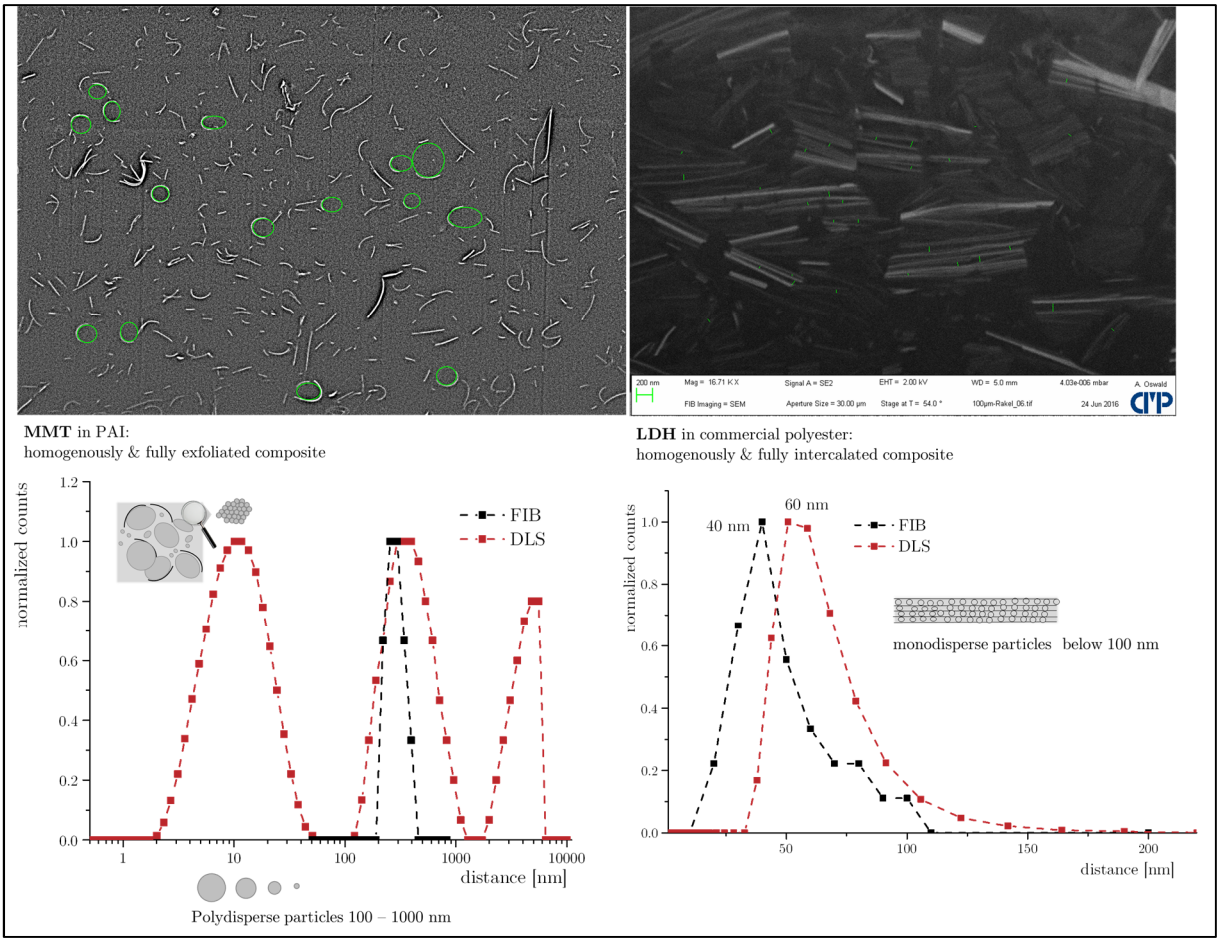


Figure 112: SEM/FIB and DLS analysis of two polymer/clay nanocomposites

The green drawings in the SEM/FIB cross-section photographs account to the distance distribution "FIB" in comparison to the diameter measured via DLS of PAI colloids in NMP as a solvent. The left picture has 0.8 wt.-% MMT based on poly amide imide. The right picture has a LDH content of 10 vol.-% based on polyester. It is evident from the pictures, that the hydrodynamic radius is slightly bigger than the measured distances between the lamellar units after drying.

In both cases, the layered colloids share high interfaces with the polymer colloids, whereas the resulting organization differ from each other, indicated by the inlet sketches. The highly exfoliated composites (left) are prepared in absence of water (NMP as solvent for PAI as polymer) and with organophilic montmorillonite. The LDH phases presented on the right are a mixture of LDH with intercalated zwitterions i) ABSA: introduced within LDH synthesis, and ii) an ion exchanged LDH-NO_3 with an organophilic zwitterion (lecithine) in a mixed polyester/polyurethane system. The hydrophilic polyester dispersion intercalated into the LDH-ABSA phase (noticeable by high aspect ratios of this LDH phase), whereas the hydrophobic aq. PUR dispersion intercalated into an ionic exchanged LDH-lecithine phase from LDH-NO_3 as original phase, noticable by low aspect ratios.

However, it is remarkable, that the mixture of LDH-ABSA in the commercial aq. polyester dispersion has an upper mixing limit. At about 10 wt.-%, the composite forms an insoluble liquid-crystal like phase and separate from the solvent mixture.
In this work, the organization of colloids is separated in two border cases. The first case is an intact LDH structure, with no considerable change of the inner structure after processing with polymer colloids. These structures are described in the previous section (IV-3, page 94ff) and are shown in **Figure 113**, left. The present chapter is describing the case for intercalating colloids, thereby altering the inner and outer structure notably (Figure 113, right).

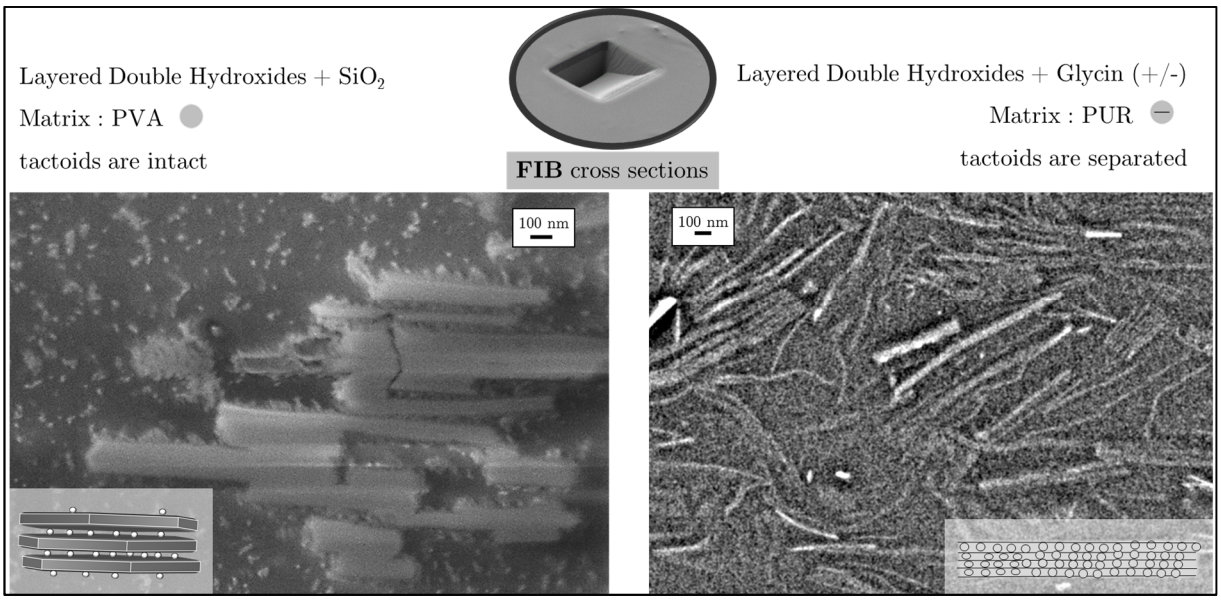


Figure 113: Different kind of stacked assemblies at similar magnifications

The organization of intercalated or exfoliated states of composite materials with layered materials is described much more often than the organization of non-intercalated intact tactoids.

4.2.1 PUR / Kaolinite Composites

The intercalation of DMSO, methanol and the used ammonium salts CTAB, $BuNH_3Cl$ and TPAB into the interlamellar void of kaolinite was monitored by XRD measurements and is shown above in a previous section (III-2.3, page 48). The subsequent mixing of the modified kaolinite colloids intercalated with CTAB & TPAB with an aq. PUR matrix did not lead to intercalation nor full exfoliation. However, an indication was found in a FIB cross-section, where a part of the CTAB-intercalated kaolinite was partially intercalated by the PUR colloids (**Figure 114**). The separation of the sheets could originate from impurities of other layered silicates with higher swelling affinity. The assumed reason for the just partially intercalation was the big amount of water introduced by mixing the colloids with the aq. PUR dispersion (approx. 30 wt.-% NVC). Even when distinct amounts of water are promotive for the DMSO intercalation, bigger amounts of water transform kaolinite into the pristine form (with respect to the d-spacing).[174] The experiment was repeated in a non-aqueous solution of the same PUR formulation in 2-butanone. Surprisingly, in none of these samples an intercalation nor exfoliation could be found in FIB cross-sections.
In the end it can be said, that the intercalation of ions or polymer colloids into kaolinite colloids needs advanced techniques.

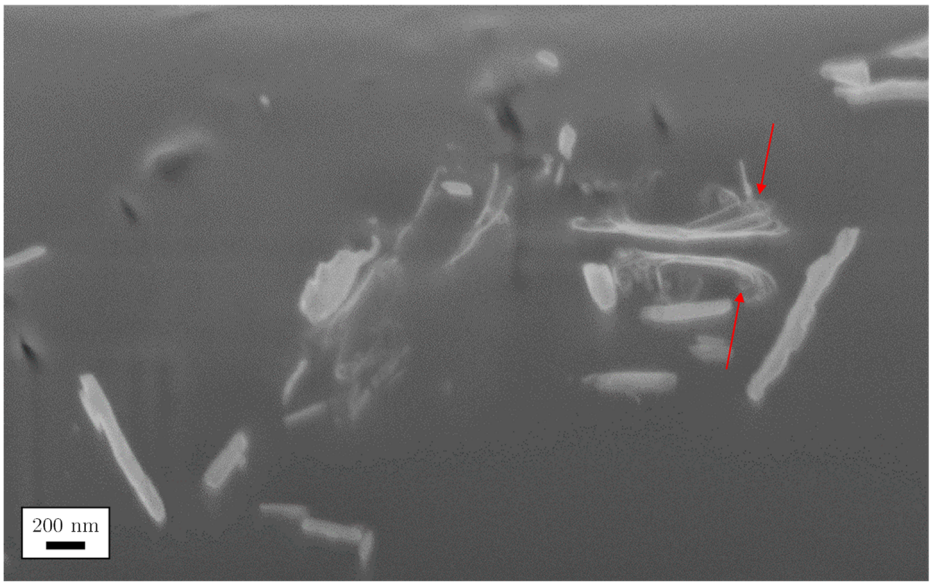


Figure 114: FIB-cross section of CTAB-kaolinite in a PUR matrix

4.2.2 Polymer / LDH Composites - Pretests

In preliminary experiments, the exfoliation behavior of modified LDH phases with non-ionic surfactants in non-ionic polymer matrices (PVA & HMMM) was examined. The obtained FIB cross-sections of these composite films show that no LDH delamination occur for these composites (not shown here).[175]

It was tried to separate the LDH sheets by mixing the LDH colloids with commercial surfactants, namely Pluronic P-123, Tergitol NP-9, Polysorbat 60 and Tween 20. These modified $Zn_2Al(OH)_6[NO_3]$ colloids were mixed with the two non-ionic polymers PVA and HMMM with a 10 wt.-% proportion of LDH in the resulting dry film. The intention behind this work was to weaken H-bonds between the sheets by adsorption and/or intercalation of macromolecules with polar groups. Again, in all FIB cross-sections made on these systems, no intercalation, delamination or exfoliation was observed. This has lead to the assumption, that the charge-driven intercalation mechanism is strongly predominant.

The ionic exchange reactions of Layered Double Hydroxides in water at different pH values lead to a reduction of the primary particle size of the LDH colloids by dissolution (see section III-1.1.8, page 37). Therefore, the ionic strength is kept at a low level (measured as electrical conductivity of the washing water) and the pH was not adjusted. The anionic exchanged phases were tried to be mixed with synthesized anionic PS dispersion (90 nm) with the addition of butoxyethanol as a co-solvent. In this case, the LDH colloids remain in the aggregated state within the composites. Moreover, a phase separation between the PS matrix and floating LDH colloids at the solid/air interface of the coating occurred. The compatibility in terms of polarity of the polymer and LDH phases is therefore also an important parameter if one wants to design composite materials. For example, lecithine is a suitable hydrophobic zwitterion, whereas ABSA is a suitable hydrophilic zwitterion (cf. Figure 112). Zwitterions are assumed to play a key role in delaminating LDH. The delamination of LDH phases do not necessary need zwitterions, because the mechanical force applied on the LDH phases also can lead to a delamination (e.g. melt-intercalation[176]). Within the pretests, the composite dispersions were mostly prepared by magnetic stirring for 5 or more days, so that the mixing state is comparable for all dispersions.

The mixing of LDH-phases with aq. anionic PUR dispersions of different monomodal but polydisperse size distributions (neutralization of carboxyl-groups: 120 %) lead to all of the three main morphologies reported in literature: aggregated, intercalated and exfoliated (**Figure 115**). These different states can also occur in a mixed state, where just the edges are intercalated ("partially intercalated"). This effect was postulated before on α-ZrP colloids based on XRD measurements with different ratios of α-ZrP and intercalating ions in epoxy-based nanocomposites.[177] The partially intercalated structures are desirable in combination with the plate/sphere-stacked structures from an earlier Section (0, page 94f) in order to obtain a well-organized coating material. The control over this phenomenon with the used LDH phases was tried but not accessible in a reproducible manner, because of the emergence of intertwined house of cards structures instead of high aspect ratio LDH-BSA.

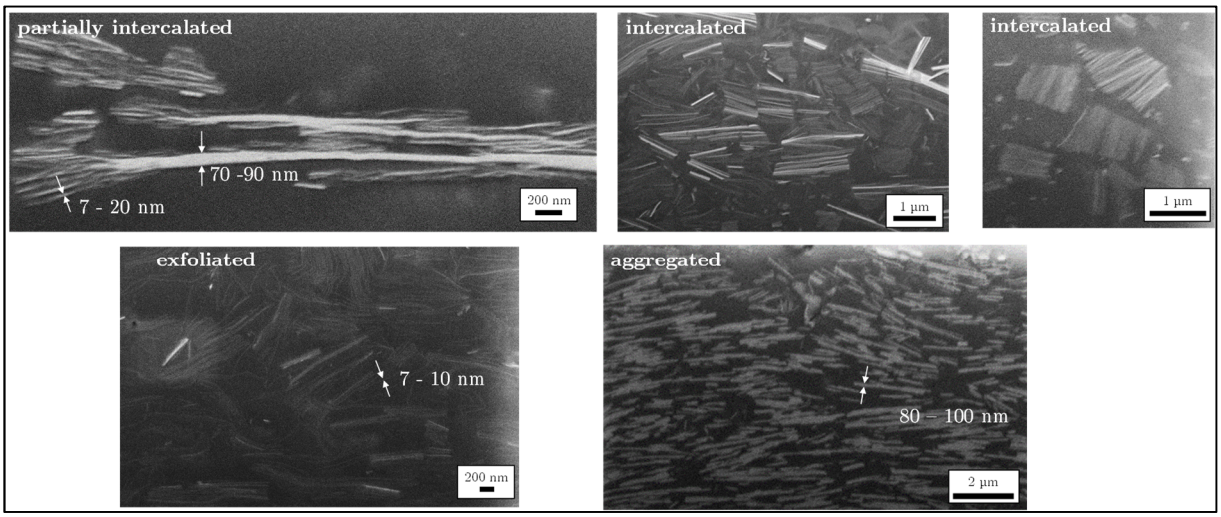


Figure 115: Intercalation and Exfoliation of Layered Double Hydroxides
partially intercalated: 5 µm glycine in aq. polyurethane matrix (diameter 45 nm)
intercalated: biphase exfoliation of LDH-ABSA in commercial polyester dispersion (60 nm) and LDH-Lec in commercial polyurethane dispersion (40 nm). Both dispersions contain additional solvent
exfoliated: LDH-NO3, treated with glycine in a polyurethane dispersion (20 nm) with added butoxyethanol
aggregated: LDH-BSA 1 µm with a polyurethane dispersion, no solvent added (90 nm)

It was found for the magnetical stirring experiments, that besides the intercalation of zwitterions, the chosen primary colloid size of the penetrating PUR colloids plays a role in order to intercalate (or exfoliate) the LDH colloids. It was found, that PUR colloids below approx. 75 nm (d_h, DLS) are able to penetrate some interlamellar voids, whereas bigger PUR colloids are excluded, whereas the compatibility was preserved and no phase separation took place. It is remarkable, that the penetrating PUR colloids have similar thicknesses to the intact lamellar LDH tactoid colloids (approx. 80-100 nm). The aggregated structure in the figure above may imply that parallel oriented stacked LDH platelets are formed.
The XRD analysis of LDH described above (section III-1.2.4, page 42) show no change in basal spacing for glycine, taurine and betaine as intercalants. Moreover, the lateral size of the LDH colloids decrease after ionic exchange with zwitterions, so that the conclusion is, that the zwitterions are not intercalated after the exchange experiment, but promote the dissolution at the edges.

4.2.3 PUR / LDH Composites – Field Study

From the colloidal assembly mechanism and the basic principles of the model system PS/K from the first section of this chapter, another model composite system, namely PUR/LDH, was investigated. For PUR/LDH, the electrostatic interactions @ in water are reversed: the lamellar LDH have a positive charge and the PUR coils have a negative charge, leading to electrostatic attachment PUR @ LDH. The PUR colloids are not visible nor distinguishable in the SEM after drying at r.t. as it is the case for comparable volume ratios of PS/K dispersions above T_g of PS (cf. Appendix, page 223). In both cases, the polymers spread on the platelets surface above Tg to nanometer thin films in the range of the applied Au/Pd sputter coating. Such polymer-coated platelets are known in the literature.[178]
The PUR/LDH composites can be easily processed to form self-standing, transparent, free-films by crosslinking with a melamine resin (HMMM). For example, freeze-dried PS samples emerge into a fluffy powder, whereas the freeze-dried PUR samples emerge into a sticky, viscous liquid - a typical precursor for coating materials. Moreover, LDH colloids can be intercalated by the PUR colloids, whereas kaolinite has no exchangeable ions, therefore is not intercalated by PUR colloids in almost all tests conducted.
During the above described pretests on processing PUR/LDH composites, it already became evident prior any measurement that superior thixotropy was found in composites with PUR colloids ranging around 80 nm in size (DLS, d_N). The platelet height of the LDH colloids in the resulting composites were in the same range (cf. Figure 112), so that the capillary interaction PUR π LDH seem to be the origin of the thixotropic behaviour. The pretests on PUR/LDH composites were all homogenized by magnetical stirring for 5 days. The sample within this series which appear most thixotropic was a $PUR_{90}LDH_{800}$ composite (without added co-solvent, nor HMMM), resulting in nematic ordered samples with a LDH platelet thickness of 80 to 100 nm without any visible intercalation (cf. Figure 112). This finding allows for the suspicion, that the capillary assembly PUR π LDH act in a way where the LDH platelets are accommodated like a monolayer of densely packed spheres in a colloidal crystal, therefore resulting in nematic order of LDH colloids, similar to the morphology of PS π K (cf. Figure 57, page 69).
For the field study, the preparation of the composites were done by shaking, high-shear mixing with a rotor-stator mill and a final stirring step. Within this series, PUR_{75}-based composites have the highest tangible thixotropy. From this result, six batches with six different diameters were chosen for a systematic rheological study. The colloids, colours & symbols used in the following part of the work are:

- **PUR_{10}: black,**
- **PUR_{75}: magenta,**
- **PUR_{115}: green,**
- LDH_{400}: small ○,
- LDH_{800}: intermediate, and
- LDH_{3200}: big ⬡.

The indices are representing the rounded diameters of the six samples. A 3x3 matrix with 9 possible composite combinations result and is further extended by 5 LDH concentrations, resulting in 45 samples. The concentrations were chosen in a way, so that the highest achievable LDH concentration in the aqueous PUR/LDH composites is covered as maximum with

equidistant concentration steps, namely 5, 10, 15, 20 and 25 wt.-% LDH in the solid content. Each sample was examined prior cross-linking in the wet state with a Couette-type rheometer by the help of a shear program (sct. 4.2.5). After rheological measurement, crosslinked composite free films were prepared, and further examined with dynamic mechanical analysis (sct. 4.2.6). For some of the 45 samples, FIB cuts and XRD of the films were made (sct. 4.2.4). The achieved results on the 45 PUR/LDH composites are listed in **Table 22**.

Table 22: Summary of the PUR / LDH field study results

composite type			order	film optic	diameter	spacing	aspect ratio		structural viscosity			DMA results	
ω_{LDH}	d_{PUR}	d_{LDH}	S	o	d_{LDH}	h^*_{LDH}	$d_{LDH}\ h_{LDH}^{-1}$		H	τ vs $\dot{\gamma}$	η vs t	G'	G'/G'' max
wt.-%	/nm	/nm	0 - 1	1,2,3	/nm	/nm	/ nm nm^{-1}		/Pas	shape	shape	/MPa	tan δ
5	10	400		2					24	lin	U	232	0.2
10	10	400		2					18	lin	U	180	0.3
15	10	400	0.46	1	287±68	1	23±18	(2-90)	26	lin	U	260	0.6
20	10	400		1					22	lin	U	141	0.2
25	10	400		1					52	lin	W	11	1.4
5	10	800		2					41	lin	U	341	0.2
10	10	800		2					31	lin	U	99	0.4
15	10	800	0.30	1	287±144	21±8	16±9	(3-34)	39	lin	U	150	0.2
20	10	800		1					51	lin	W		0.4
25	10	800		1					210	thix	W	381	0.2
5	10	1600		2					34	lin	U	209	0.2
10	10	1600		2					17	lin	U	189	0.3
15	10	1600	0.29	1	694±345	1	11±5	(5-21)	27	lin	U	445	0.2
20	10	1600		1					52	lin	U	272	0.3
25	10	1600		1					17	lin	U	385	0.3
5	75	400		2					1672	visc	U	291	1.5
10	75	400		2					19967	visc	U	155	0.1
15	**75**	**400**	**0.79**	**1**	**336±197**	**21±5**	**20±16**	**(5-60)**	**24749**	**thix**	**η**	**125**	**1.5**
20	75	400		1					11574	thix	η	57	1.0
25	75	400		1					4083	thix	mix	137	0.4
5	75	800		2			~		1466	visc	U	143	1.2
10	75	800		2					8658	thix	mix	207	0.1
15	75	800	0.52	1	692±356	1	30±14	(12-57)	16179	thix	mix	152	0.3
20	75	800		1					9107	thix	mix	148	0.3
25	75	800		1					11089	thix	η	89	1.2
5	75	1600		2					2787	visc	U	205	0.2
10	75	1600		1					3001	visc	U	220	0.3
15	75	1600	0.30	1	648±334	1	13±9	(5-39)	337	visc	U	367	0.4
20	75	1600		1					355	visc	U	247	0.2
25	75	1600		2					422	visc	U	184	0.4
5	115	400		1					1169	visc	U	204	0.8
10	115	400		3					3150	visc	U	216	0.8
15	115	400	0.42	3	259±169	54±23	21±19	(4-63)	5780	visc	U	68	0.3
20	115	400		3					5732	thix	U	83	1.4
25	115	400		3					2663	thix	U	103	0.7
5	115	800		1					2190	visc	U	204	0.4
10	115	800		3	~				3094	visc	U	129	0.2
15	115	800	0.40	3	242±141	27±13	20±13	(5-61)	2004	thix	U	88	0.8
20	115	800		3					1327	thix	U	133	0.2
25	115	800		3					129	dila	W	154	0.8
5	115	1600		3					1626	visc	U	224	0.2
10	115	1600		3					1285	visc	U	206	0.3
15	115	1600	0.28	3	607±290	1	12±8	(3-34)	2415	visc	U	56	0.5
20	115	1600		3					628	visc	U	140	0.5
25	115	1600		3					409	visc	U	134	0.2

From Table 22 it is evident, that the sample $PUR_{75}LDH_{400}$ with 15 wt.-% LDH has i) the highest value for for structural viscosity H (cf. Figure 134), ii) the highest order parameter S (cf. Figure 117) and iii) the highest dissipation factor tan δ under oscillatory tensile stress of the free films (cf. Figure **136**).

For the preparation of the films, butoxyethanol (co-solvent) and HMMM (crosslinker) were added to the PUR/LDH composites, so that the former charged DMAE and glycine molecules, butoxyethanol and OH groups from the LDH and PUR colloids react with the HMMM resin. Hexamethoxymethylmelamine (HMMM) was added as a reliable crosslinker molecule with a total mass content of 40 wt.-% in the resulting film. However, since HMMM molecules are very

small compared to the colloids, the HMMM monomers can be interpreted as 0D mass points with respect to the PUR and LDH colloids with diameters of approx. 1 nm, leading to enhanced close-packing. If butoxyethanol is added to the bare PUR dispersions, the appearance turn from milky to transparent and phase separation is observed to happen more likely when these dispersions were mixed with LDH. This effect is attributed to enhanced close-packing by solvation of hydrophobic PUR segments. Besides the intriguing similarity to the capillary interaction of PS π K_{edge} and PUR π LDH_{edge}, both related to the platelet height h_K and h_{LDH}, the experimental design for the electrostatic interaction PUR @ LDH have some intrinsic differences to the PS @ K system. As a major difference, the weight ratios of polymer to clay are reversed, with the PUR part having the lion share.

Also, the LDH colloids are synthetic and the products can easily contain Na+, NO_3^-, $C_6H_5SO_2^-$, Zn^{2+}, Al^{3+} ions and zwitterionic glycine NH_3^+-CH_2-COO^-. However, the conductivity of the last washing water (after 14 centrifugation steps) from LDH slurries prior composite preparation is low with about 60 µS/cm, so that low ion contamination by LDH in the composites can be assumed. The glycine molecules in the LDH samples are believed to enhance intercalation of PUR, as known for other zwitterions in LDHs like amino-BSA.[179] For composites with and without the use of glycine, seemingly different morphologies in FIB/SEM were obtained (cf. Appendix, page 224).

In the PUR dispersions, the ion concentration is made up by the protonated amine concentration alone ($DMAE^+$, 2 to 3 mM). For full deprotonated (PUR^0)-COO^-, the amount of sulfinic acid molecules BSA to be exchanged from (LDH^+)-BSA^- result in following ranges of COO:BSA ratios among the PUR/LDH composite samples: 4.8 to 0.7 for PUR_{10}-composites; 2.3 to 0.3 for PUR_{75}-composites and 1.9 to 0.3 for PUR_{115}-composites. Formally, based on the present charges, these molar ratios demonstrate that full intercalation of PUR colloids into the LDH tactoids is at least possible by the charge as the only driving force. One have to note, that intercalation is more likely found at low DMAE concentrations and high LDH concentrations, inducing osmotic swelling and columnar morphology (cf. **Figure 127**). The restrictive ratio related to the charges in the PUR/LDH composite formulations is the DMAE:COOH molar ratio of the bare PUR dispersions, which was chosen to be 1.2 throughout all PUR batches, in order to derive size-tailoring. Side experiments on a PUR_{15}-equivalent, based on DMAE:COOH = 1.2, the ratios 0.6, 0.8, 0.9 and 1.0 were prepared and mixed with LDH colloids. For the ratios 0.6 and 0.8, a spontaneous phase separation takes place when the PUR dispersions were mixed with LDH colloids: a transparent aqueous phase and a clod containing the colloids form (cf. FIB/SEM image of clod in the Appendix, page 222). For molar ratios of 0.9 and 1.0, no phase separation took place and composites were compatible, whereas the size distributions of the respective diluted PUR dispersions from dynamic light scattering measurements were not unimodal, as desired for the size-tailoring approach for self-organization.

4.2.4 PUR / LDH Composites - Order and Disorder

The colloidal networks of PUR/LDH composites become visible in cross-sections of cross-linked films, shown in **Figure 116** and Figure 123 for the outstanding sample, in Figure 120, Figure **121**, Figure 122, Figure 124, Figure 125, Figure 126 and Figure 127 for some more samples.

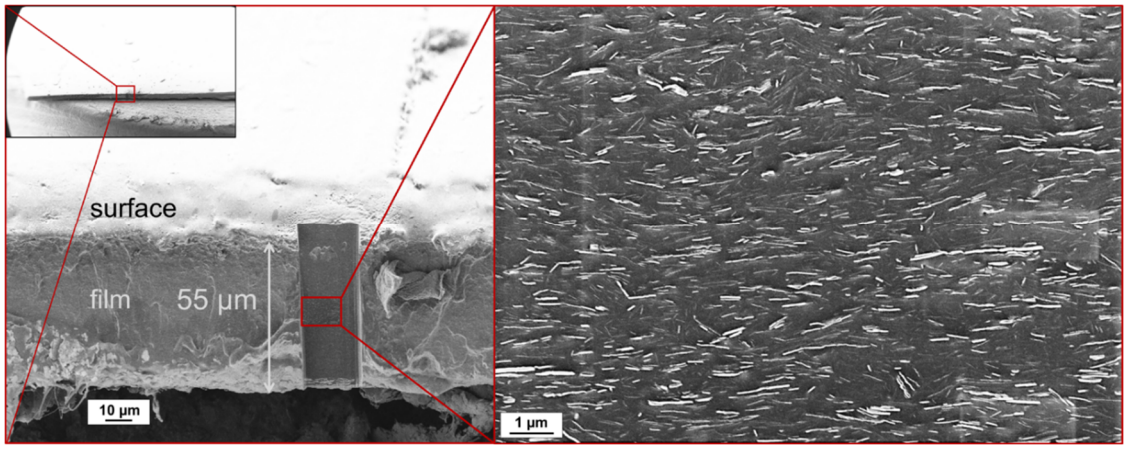


Figure 116: Cross-Section of exemplary PUR/LDH composite film

Some chosen composite films were glued on a sample holder and the films were cut by focussed ion beam technique (FIB) and viewed via SEM. The shown sample has nematic ordered LDH colloids and is the $PUR_{75}LDH_{400}$ with a 15 wt.-% LDH concentration based on the dry film.

From the FIB/SEM images of the composites one can determine LDH diameters d_{LDH}, layer heights h_{LDH}, aspect ratios d_{LDH}/h_{LDH}, layer spacings by intercalation of PUR h^*_{LDH} and the local directors $\vec{n}$ to obtain the order parameter S. The data extracted from the FIB/SEM images (**Figure 117**) is listed among other data in Table 22 and the respective size distributions data is shown in **Figure 118**.

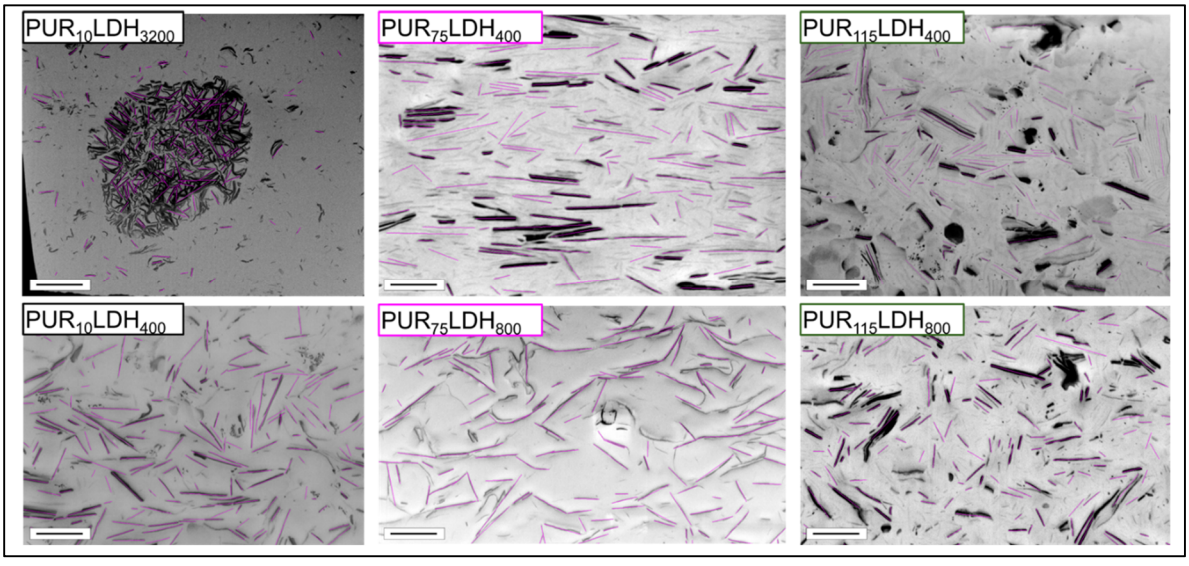


Figure 117: Cross-Sections of six samples with 4.5 vol.-% LDH in composite films

The scale bars measure 500 nm. The pink lines (N=175 per sample) depict the manual measurement of the diameter and the angle θ between individual platelets and the local director in the composite films parallel to surface. To determine the order parameter S, the known equation was used: $S = < \frac{3}{2} cos^2(\theta) - 1 >$. The LDH interlayer spacings and aspect ratios are determined also by manual measurement of the same data and subsequent calculation of an average value (both N=25). The depicted images underwent image processing via ImageJ software. The colours were inverted and a FFT Bandpass filter was applied.

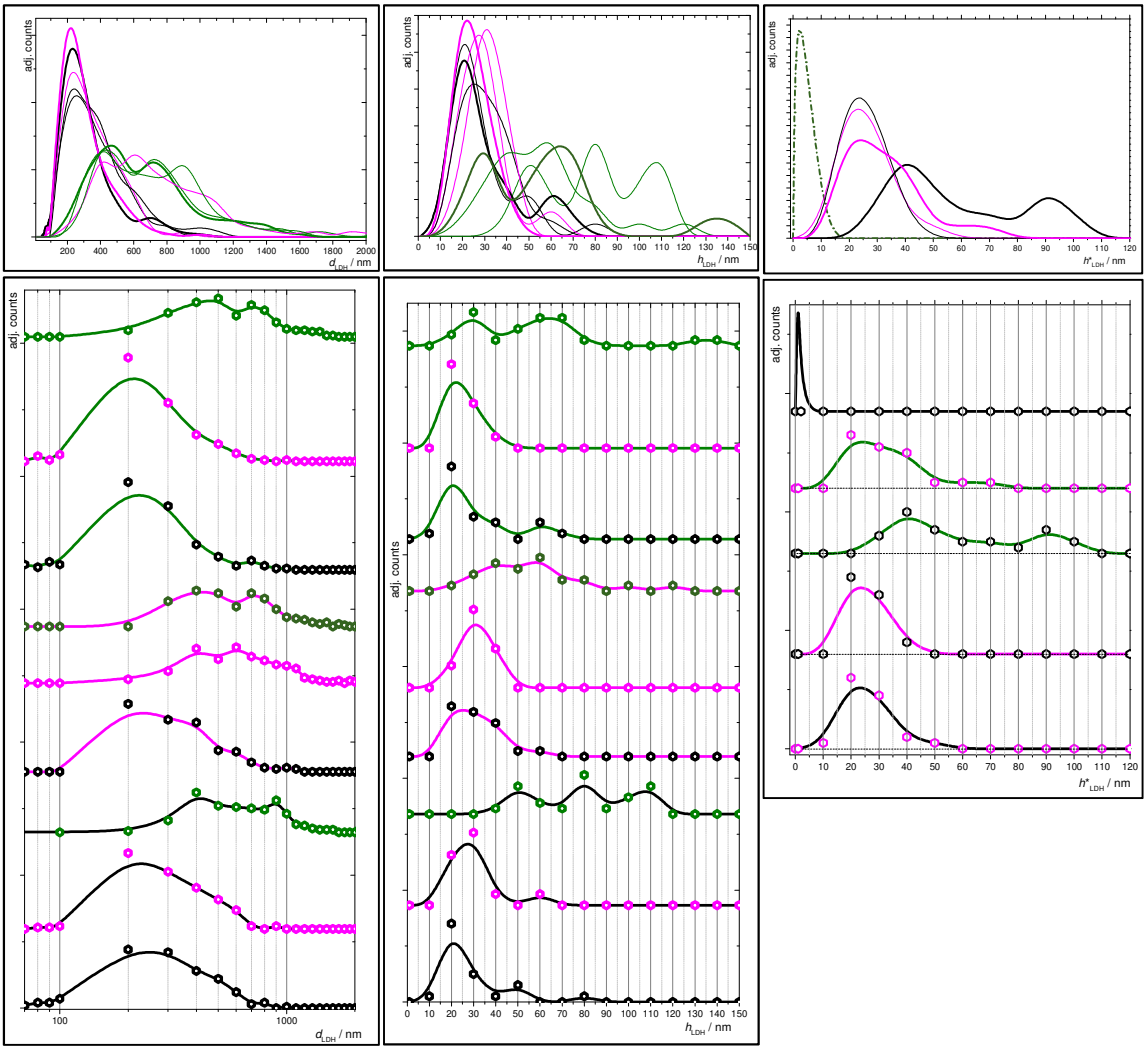


Figure 118: Size Distributions from FIB/SEM images of diameters d_{LDH}, thicknesses h_{LDH} and interlamellar distances h^*_{LDH} with N=175, 25 and 25, respectively. The *top* diagrams show B-splined size distributions in a single diagram with black LDH_{400}, magenta LDH_{800} and green LDH_{3200} lines, with thicknesses indicating the PUR series from thin to thick (small to big). The bottom diagrams show B-splined size distributions with coloured lines, attributed to the PUR series and coloured symbols attributed to the LDH series.

It is clear, that the known interphase morphologies -aggregated, intercalated and exfoliated- are present in either pure, or more likely in a mixed state. In samples with exfoliated LDH (cf. 15 wt.-% $PUR_{75}LDH_{800}$, **Figure 124**), there was no detectable spacing between LDH tactoids h^*_{LDH} whereas the platelet height h_{LDH} was lowered, therefore resulting in higher estimated aspect ratios. For intercalated samples, the interlamellar penetration of PUR into the primary structure of the LDH is evident by the separation of the layers by h^*_{LDH} (cf. 25 wt.-% $PUR_{75}LDH_{800}$, **Figure 127**). Also clear is that the aforementioned magnetic stirred $PUR_{90}LDH_{800}$ composite from pretests is aggregated (cf. Figure 115). Moreover, the comparably low Zn-Al ratio of LDH_{3200} (cf. EDX data, Table 2, page 41) reveal the highest surface charge among the LDH samples, further supported by the FIB/SEM findings, since no intercalation of PUR colloids into the galleries of intertwined LDH_{3200} was found, therefore also categorized as aggregated. As anticipated, the XRD measurements of the crosslinked films result in the highest intensity found for the nematic ordered sample, whereas samples with almost double the concentration of LDH have lower intensities (cf. **Figure 119**)

It is evident, that in some cases the diameter of the LDH colloids seem to decrease after composite formation. This can be explained by LDH dissolution during glycine treatment or poor mixing of the LDH slurries prior mixing the PUR/LDH composites.
As pointed out at the beginning of this section, the LDH structures can be divided into primary, secondary, tertiary and quaternary structures, 1°, 2°, 3°, 4°, respectively. In this context, the 1° LDH structure is only stable and unaffected for aggregated LDH in the composites (cf. Figure **114**). Exfoliation of LDH lead to a decrease of present 1° LDH structures and an increase of the aspect ratio, whereas intercalated LDH have at least locally changed 1° LDH structures. The 2° LDH structure corresponds loosely to the sheet symmetry of the LDH crystals, which is unchanged under intercalation, exfoliation and aggregation. Still, it can be said that just intercalated LDH colloids do change the 1° and 2° structure, resulting for example in an expanded columnar 3° colloidal structure as the colloidal shape (cf. **Figure 127**), resulting from the colloidal assembly 4°.
The colloidal assembly, namely the 4° LDH network structure in the PUR/LDH composites, is based on the interaction of the 3° colloidal structures, best represented by the order parameter S of the platelets in the PUR/LDH colloid network after curing. For example, the cross-sections of LDH_{3200}-containing films support that the 3° intertwined LDH structures remain intact, are seemingly not dispersable into single platelets and have resulting order parameters of S=0.3, which is the minimal value estimated here, whereas the maximum estimated value of S=0.8 shows nematic ordered colloidal LDH networks (cf. FIB/SEM images and respective XRD intensities in **Figure 119**). The range of order parameter S values are also typical for nematic polymer liquid crystals. The 4° LDH structure is best described with the dynamic self-assembly of LDH networks emerging from an ensemble of local interactions of the 3° structures, which depend on the respective volume concentrations and also on the relative diameters of the involved colloids. The spherical appearing LDH_{3200} colloids can be interpreted as tertiary structures 3° based on the interaction of secondary structures 2°, if one accepts that the staples of LDH crystals are the secondary structure 2° (unit cell) based on the composition and interaction of the primary structure 1°, similar to the denotation for the structural hierarchy of biopolymers.
The examinations in the upcoming subsection are based on the impacts of the shearing time t and the shear rate $\dot{\gamma}$ on the 4° colloidal assembly of the composite materials. This was done in the wet state by rheological measurement and in the dry state by dynamic mechanical analysis.

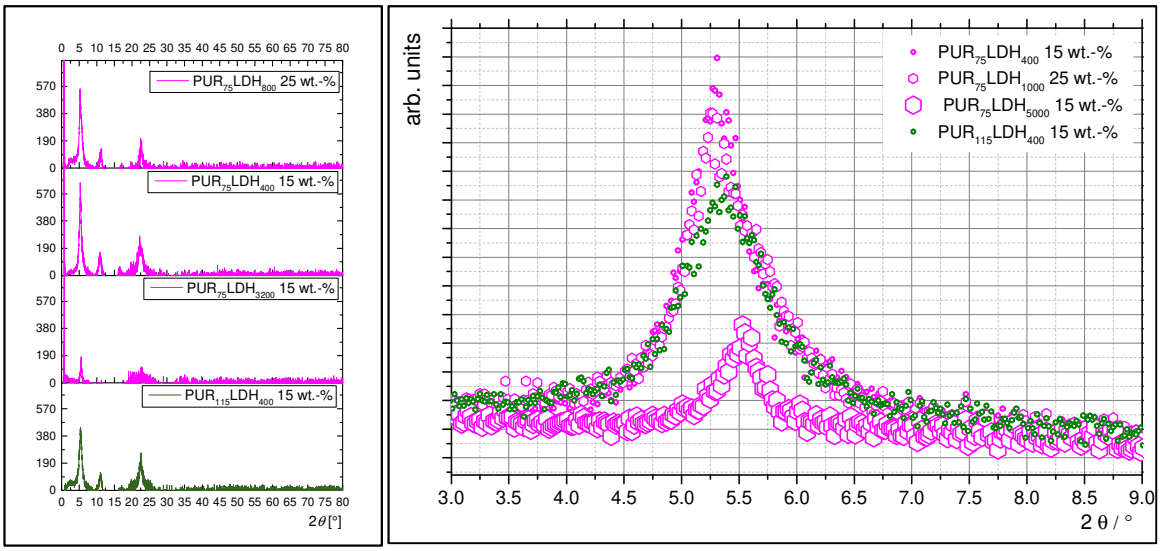


Figure 119: XRD patterns of 4 composite films

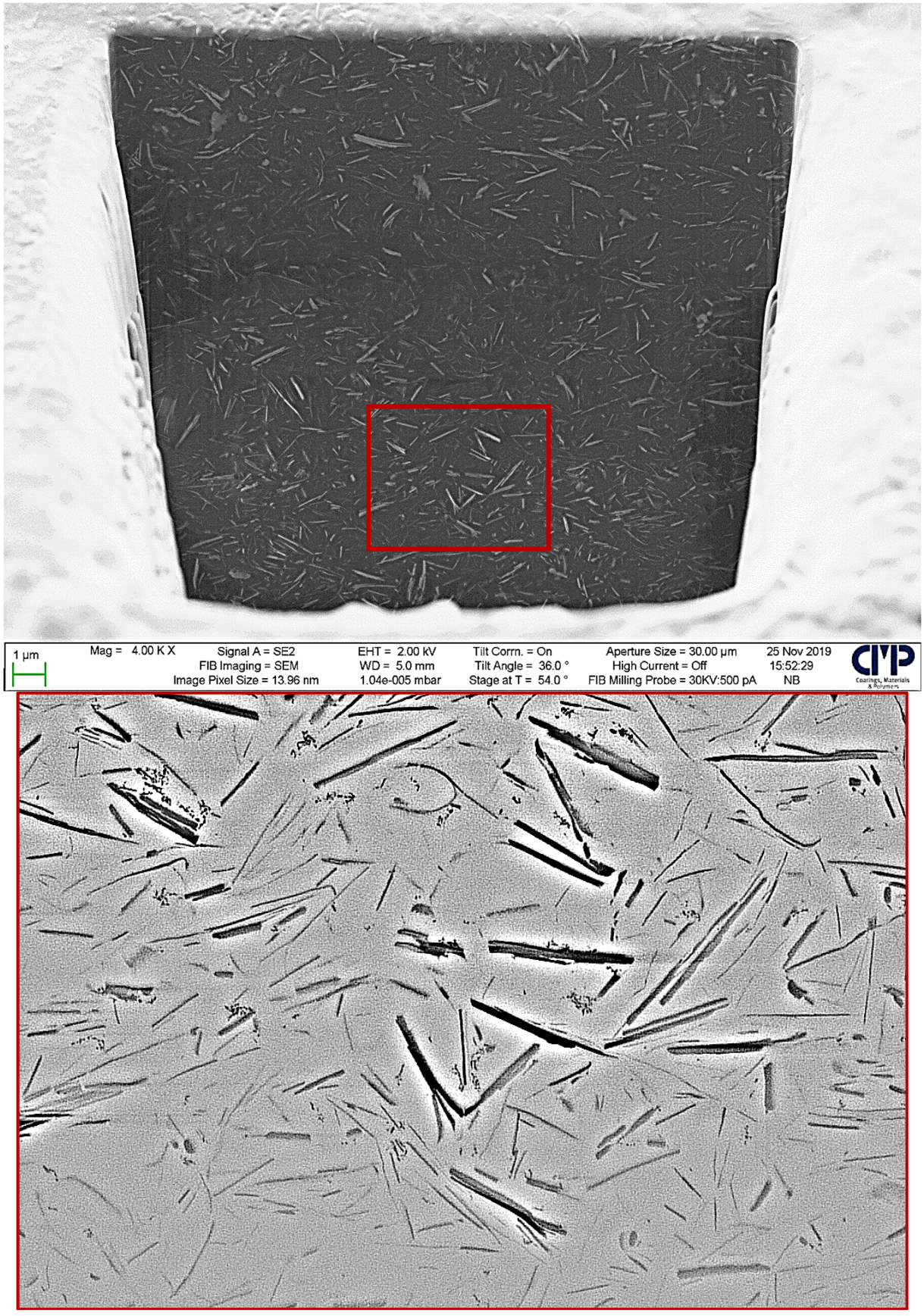


Figure 120: FIB/SEM images of the sample $PUR_{10}LDH_{400}$ with ω_{LDH}=15 wt.-%. The top image shows a deep FIB cut into the film material. The b*ottom* picture underwent enhanced contrast and sharpness by inverting black/white and perfroming a FFT (FastFourierTransform) bandpass filter, performed with ImageJ. This image underwent measurement (cf. maintext).

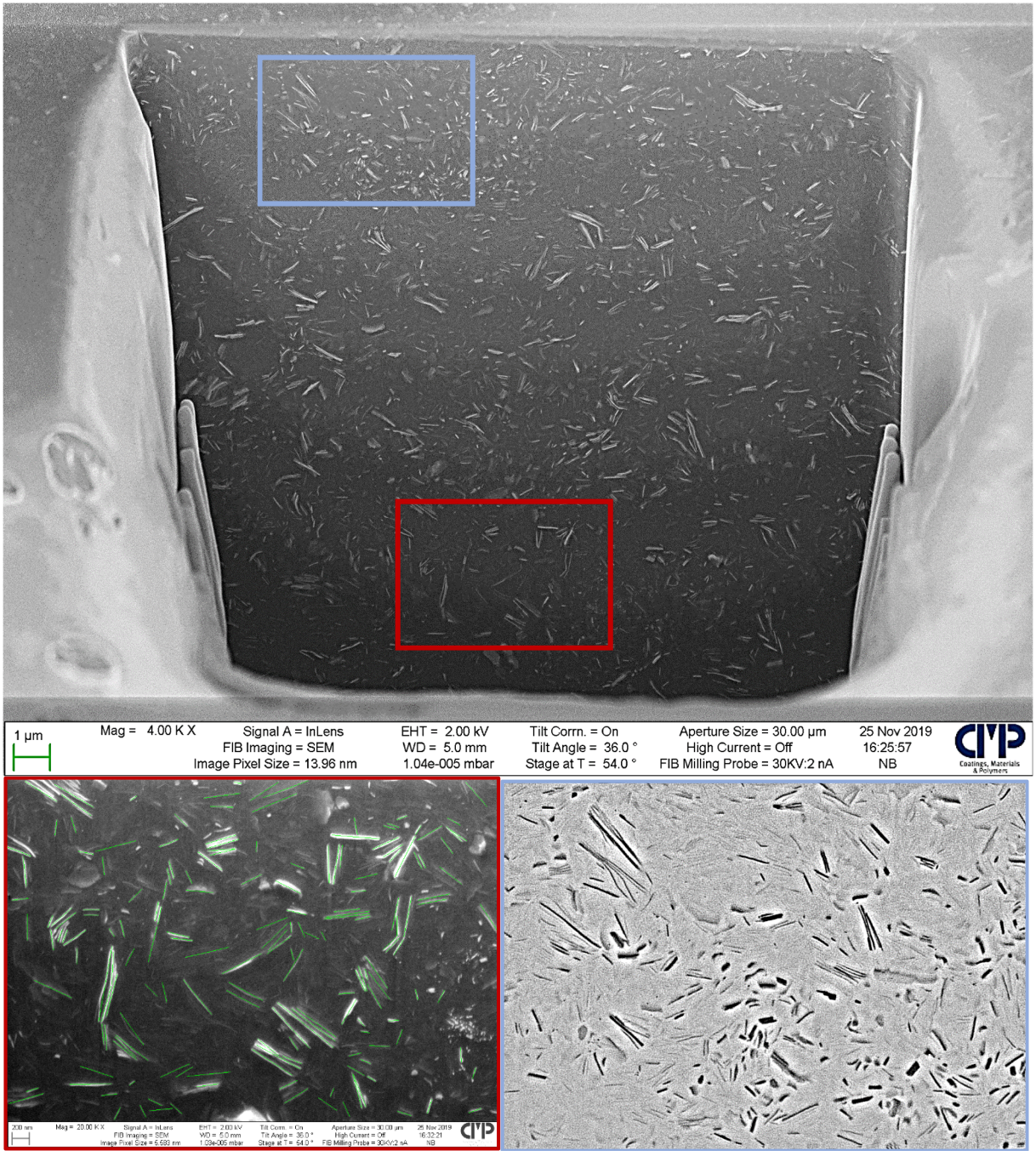


Figure 121: FIB/SEM images of the sample $PUR_{10}LDH_{800}$ with ω_{LDH}=15 wt.-%. The *top* image shows a deep FIB cut into the film material. The *blue-framed* figure underwent image processing with ImageJ. The *red-framed* image underwent measurement.

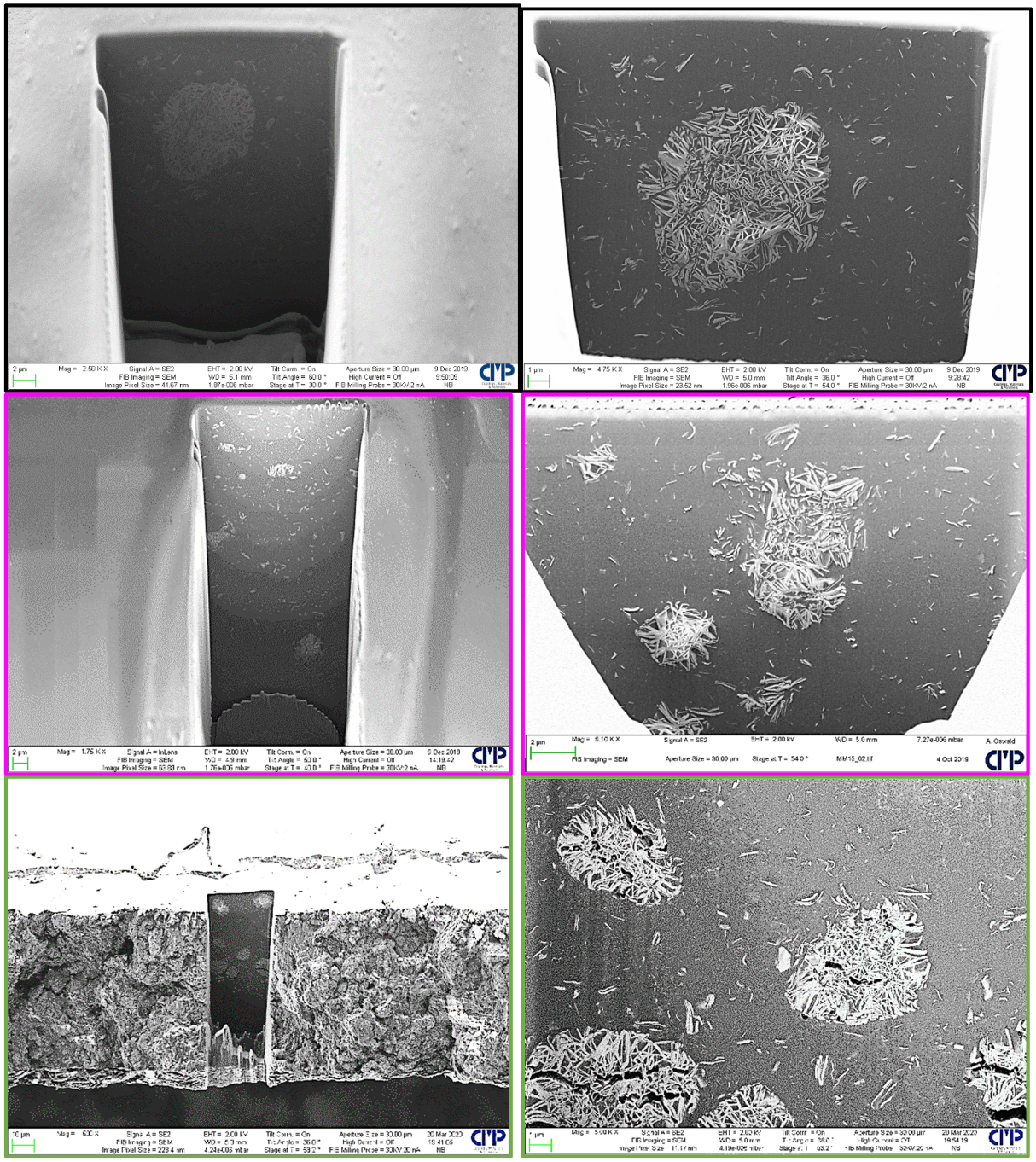
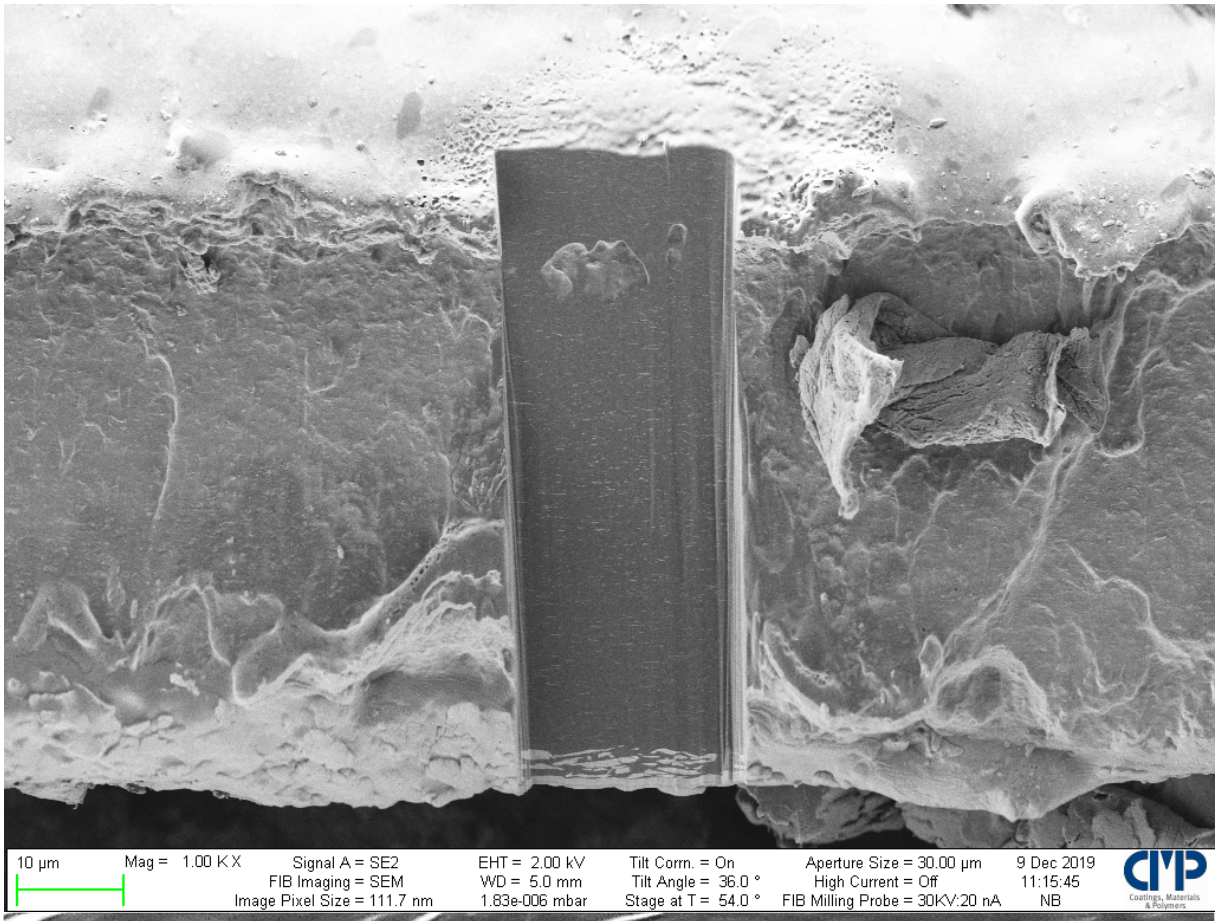
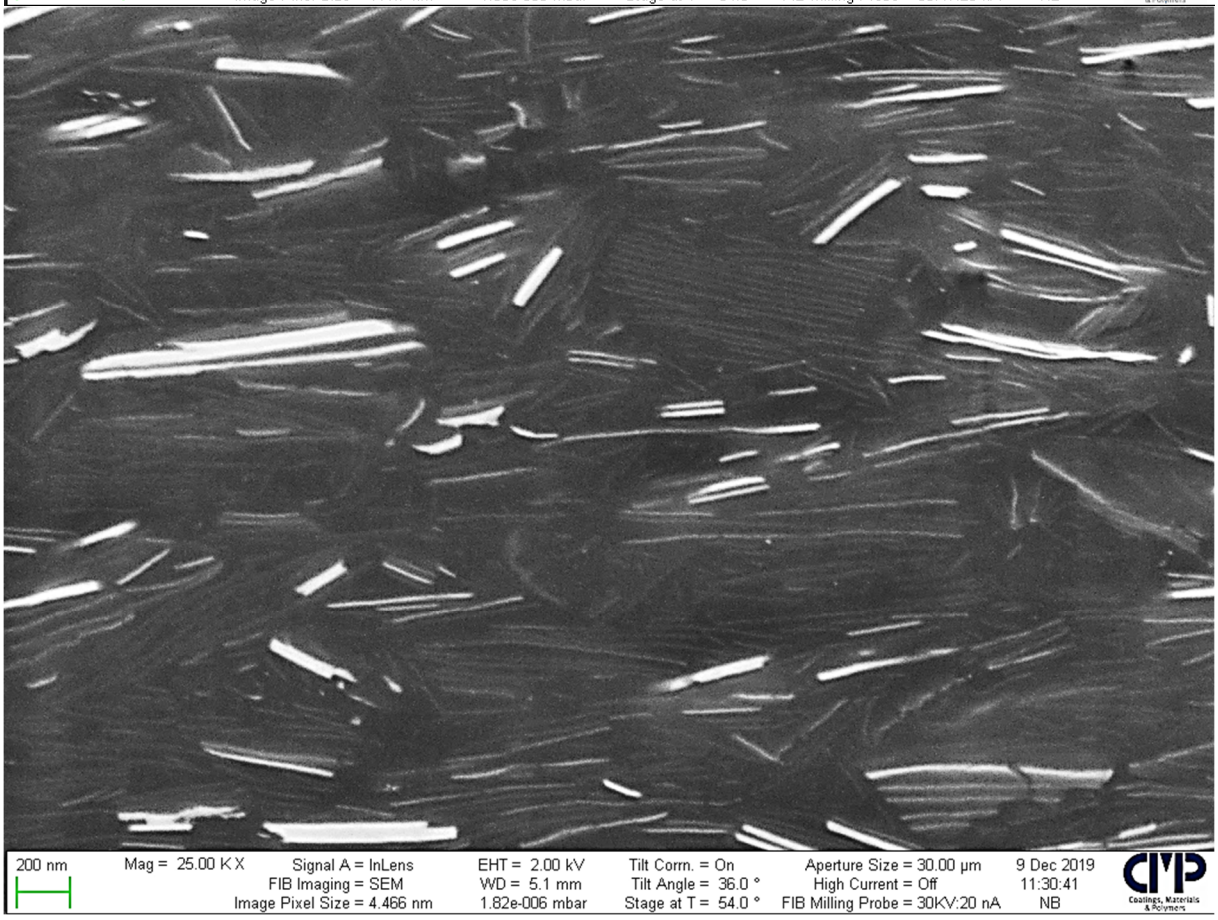


Figure 122: FIB/SEM images of the composite samples comprising LDH_{3200} namely $PUR_{10}LDH_{3200}$, $PUR_{75}LDH_{3200}$ and $PUR_{115}LDH_{3200}$ with ω_{LDH}=15, 15 and 25 wt.-%, respectively, from top to bottom, PUR type is indicated by the frame-colour.


10 µm
Mag = 1.00 K X
Signal A = SE2
FIB Imaging = SEM
Image Pixel Size = 111.7 nm
EHT = 2.00 kV
WD = 5.0 mm
1.83e-006 mbar
Tilt Corrn. = On
Tilt Angle = 36.0 °
Stage at T = 54.0 °
Aperture Size = 30.00 µm
High Current = Off
FIB Milling Probe = 30KV:20 nA
9 Dec 2019
11:15:45
NB


200 nm
Mag = 25.00 K X
Signal A = InLens
FIB Imaging = SEM
Image Pixel Size = 4.466 nm
EHT = 2.00 kV
WD = 5.1 mm
1.82e-006 mbar
Tilt Corrn. = On
Tilt Angle = 36.0 °
Stage at T = 54.0 °
Aperture Size = 30.00 µm
High Current = Off
FIB Milling Probe = 30KV:20 nA
9 Dec 2019
11:30:41
NB

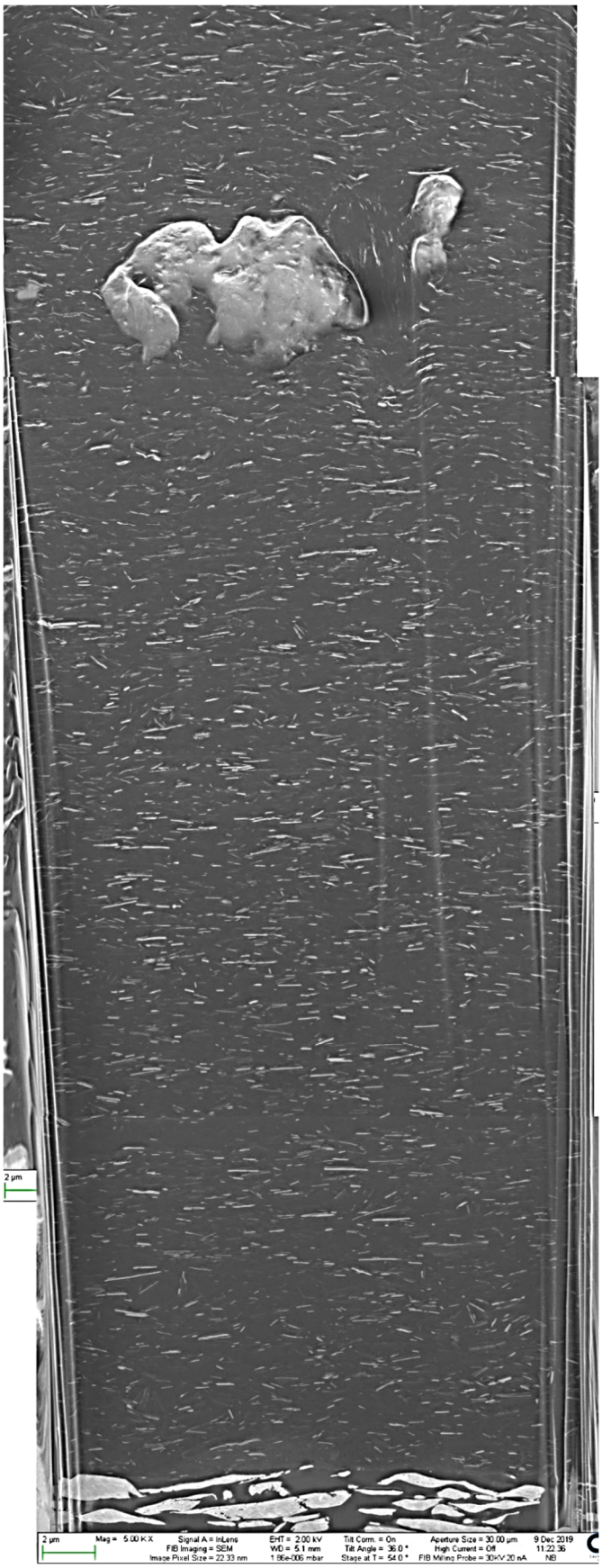


Figure 123: FIB/SEM images of the sample $PUR_{75}LDH_{400}$ with ω_{LDH}=15 wt.-%. Low-magnification, high magnification and merged (from top to bottom) At the top of the sample, an artifact was found (impurity which acts as nucleation point). The LDH colloids are densely packed around and do not have nematic order, exclusively in this region of the sample.

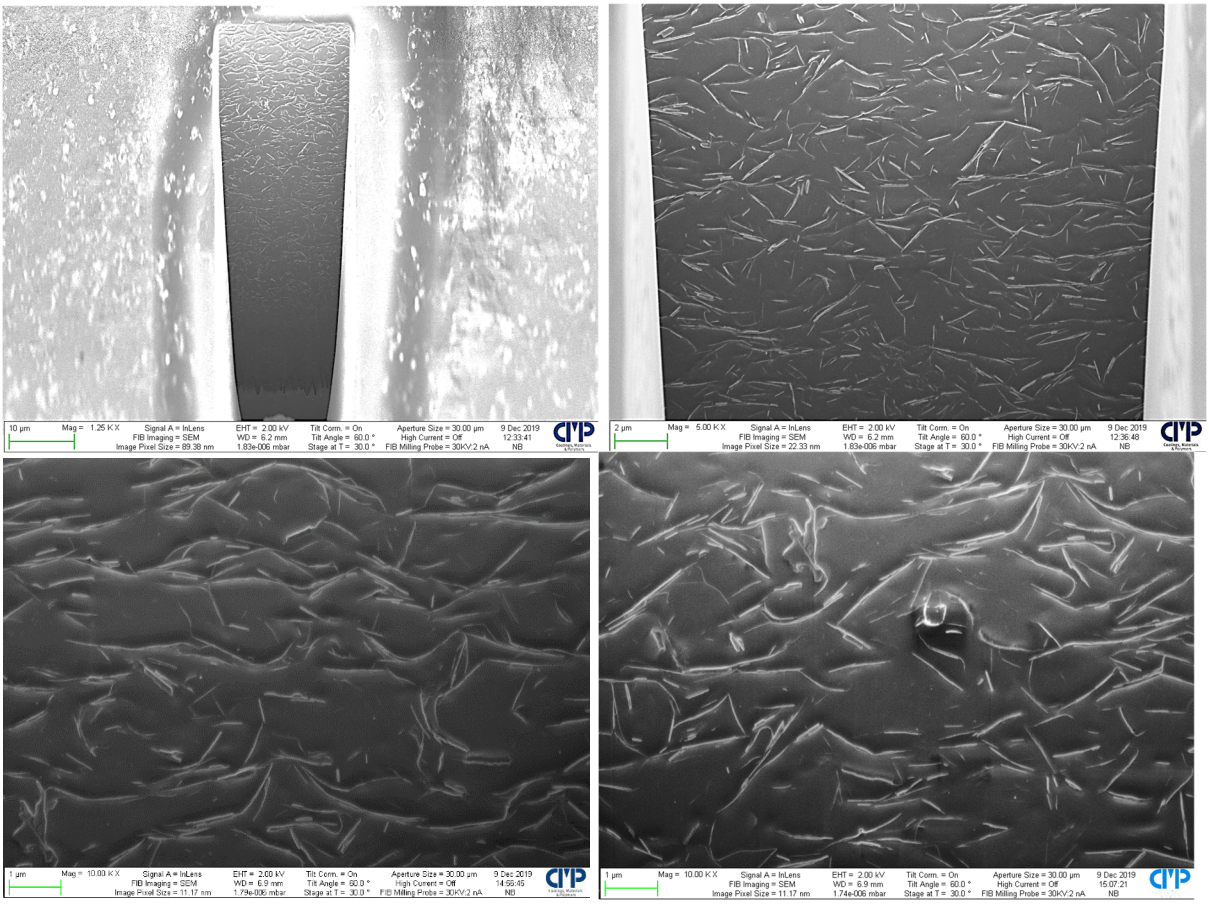


Figure 124: FIB/SEM images of the sample $PUR_{75}LDH_{800}$ with ω_{LDH}=15 wt.-%. The *top* images show lower magnifications of a FIB cut into the film material. The *bottom images* are at the same magnfication at different regions of the film.

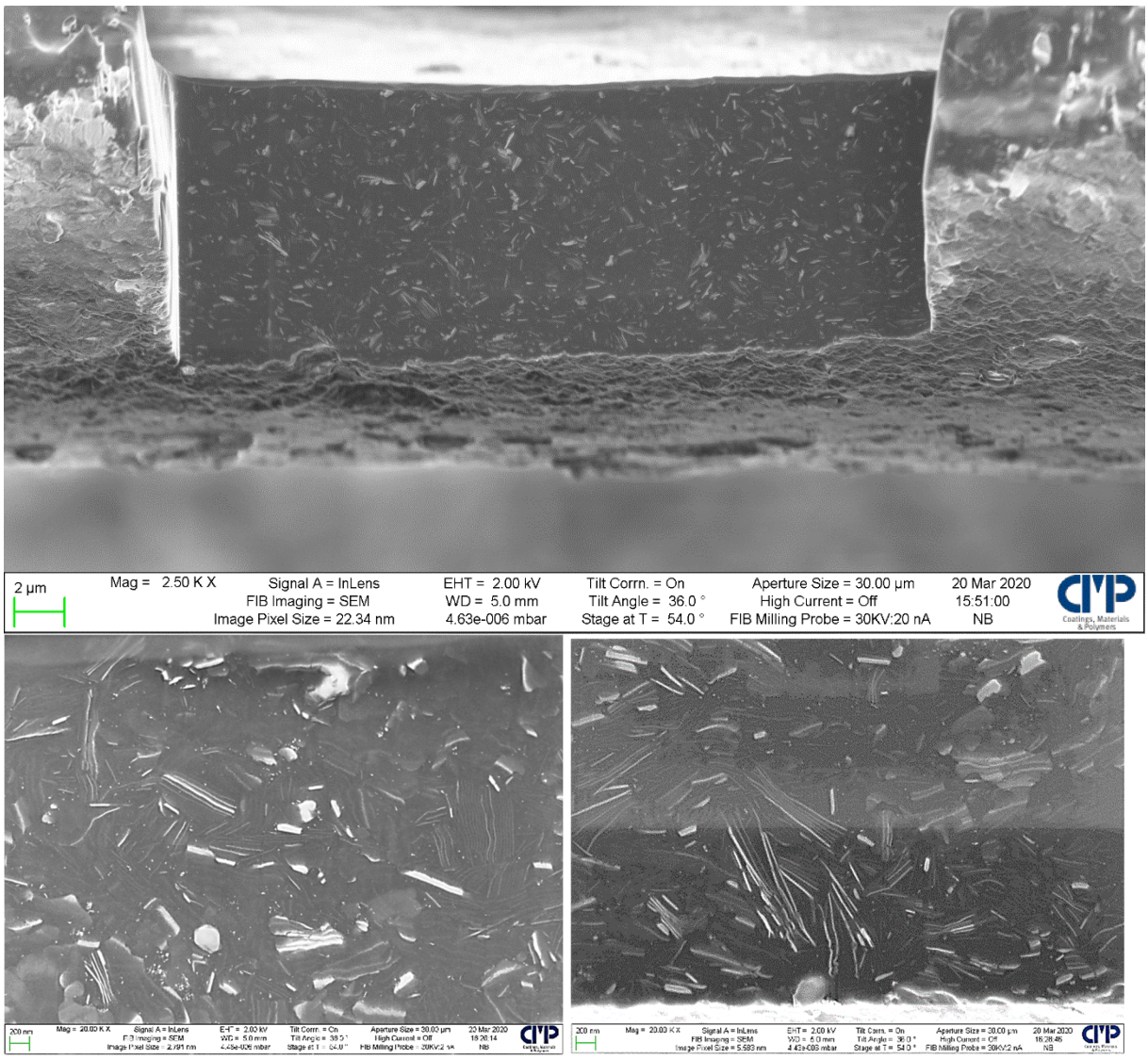


Figure 125: FIB/SEM images of the sample $PUR_{115}LDH_{400}$ with ω_{LDH}=15 wt.-%. The top image has low magnification of a FIB cut into the film material. The bottom images have the same magnfication at different regions of the film.

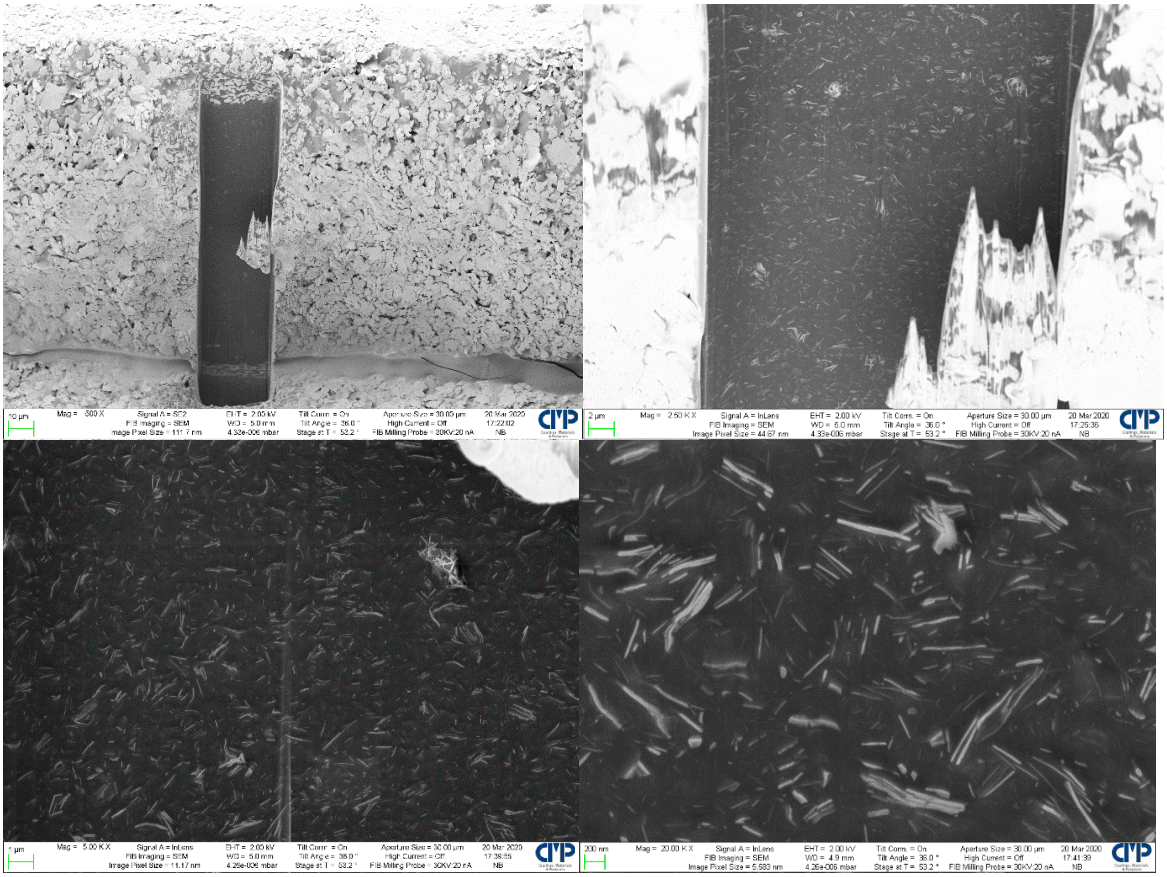


Figure 126: FIB/SEM images of the sample $PUR_{115}LDH_{800}$ with ω_{LDH}=15 wt.-% and increasing magnification.

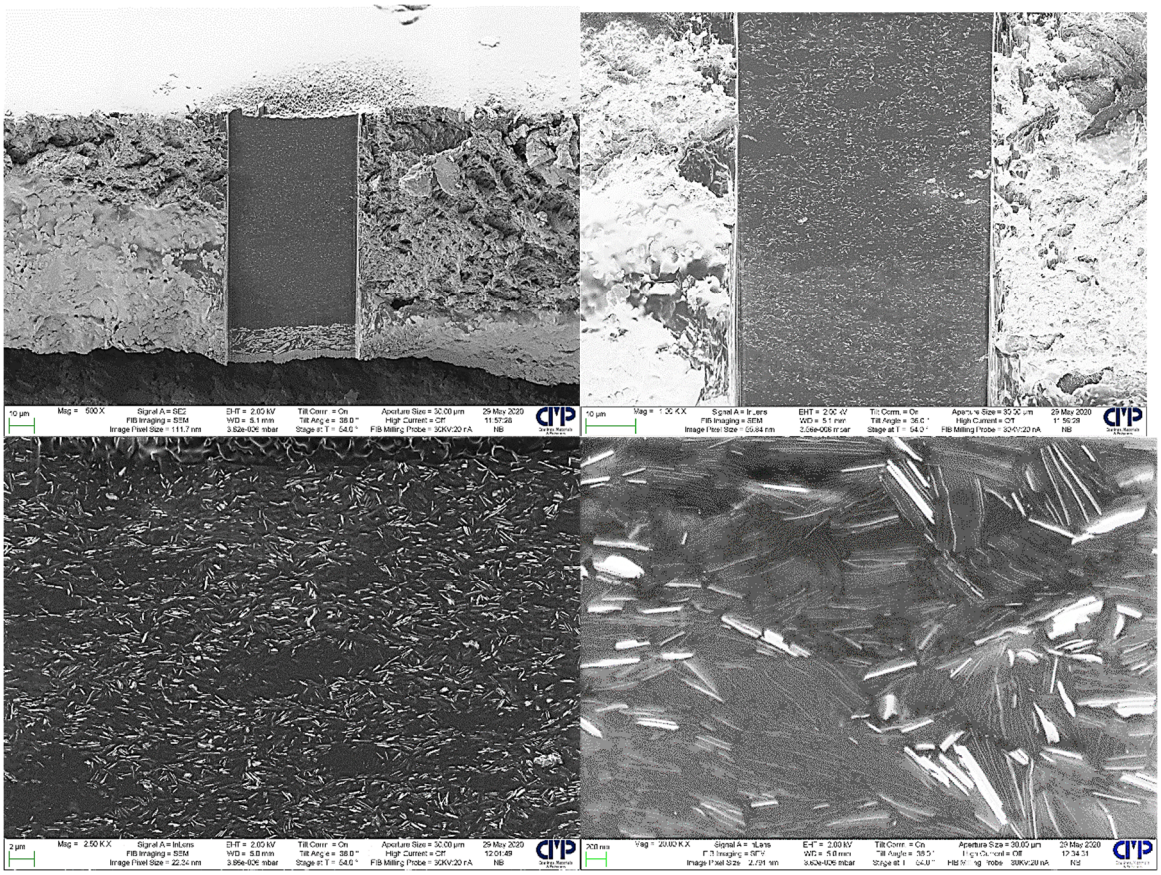


Figure 127: FIB/SEM images of the sample $PUR_{75}LDH_{800}$ with ω_{LDH}=25 wt.-% and increasing magnification

4.2.5 PUR / LDH Composites - Structural Viscosity

The time-dependent rheological measurements are shown in **Figure 128**. The shear program (input: $\dot{\gamma}$ vs t), the resulting shear stress (output: τ vs t) and viscosity (output: η vs t) for the last two up and down ramps is shown, indicated by the red frames. The last ramp underwent analysis (**Figure 129**) and the other ramps provide a constant shear history across the samples. The shear program $\dot{\gamma}$ vs t was developed to give reproducible results for the last approx. 17 minutes of the shearing time t. Within a distinct timeframe Δt, aging is hardly detected. A consecutive measurement after a reasonable timeframe $N\Delta t$ between the measurements, e.g. 24 h of resting, give reproducible results after applying another shear program, whereas for longer becoming timegaps between the measurements, considerably altered results are obtained (cf. Appendix, page 225ff).

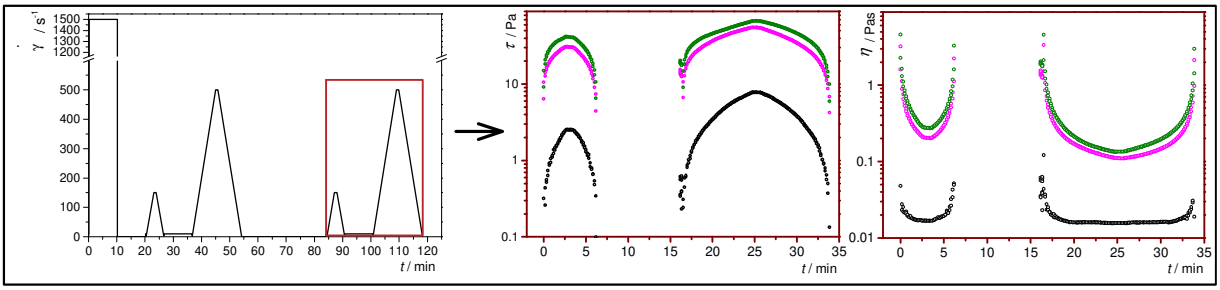


Figure 128: Shear program and output data

The left-hand diagram shows the shear program γ vs t with the shape of a series of hat functions. Every sample was pre-sheared with 1500 s^{-1}, followed by three up and down ramps (150, 500, 150 s^{-1}) to create the same shear history and finished by a last up and down ramp (500 s^{-1}), which give the structural viscosity H from the hysteresis loop area. The middle red box shows the resulting data for the shear stress τ vs time t. The right red box shows the resulting data for the apparent viscosity η vs time t. The shown triplet is from the samples $PUR_{10}PUR_{75}PUR_{115}/LDH_{400}$ with 5 wt.-% LDH in the non-volatile part of the composite dispersion.

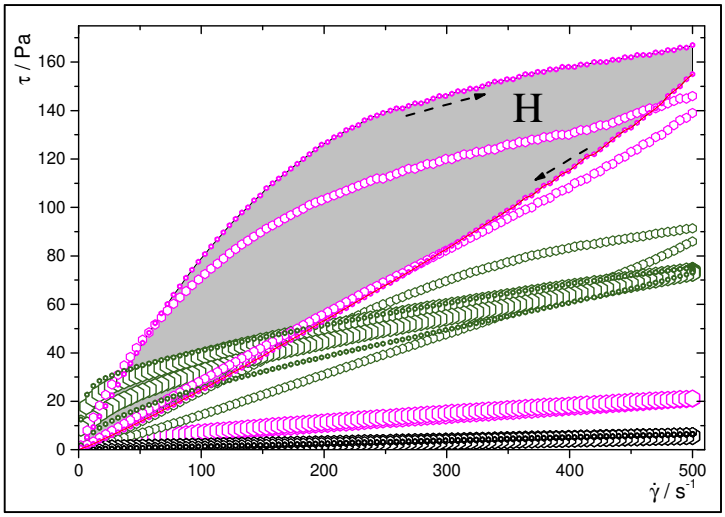


Figure 129: Flow curves of all 15 wt.-% PUR/LDH composites.

The attributions to the symbols are listed in the maintext. The measured shear stress τ versus the applied shear rate $\dot{\gamma}$ are plotted and the structural viscosity H was calculated for all 45 samples by point-to-point integration of the measured hysteresis loops with Origin Software.

In **Figure 129**, a family of flow curves of the last up and down ramp is shown, with different shapes and areas of hysteresis loops, from which the structural viscosity H is calculated. The determined structural viscosities H are spanned over 10^3 Pas^{-1}. In **Figure 130**, the structural viscosity H of all 45 LDH/PUR composite samples including 3 more estimations for the neat PUR dispersions (0% LDH) and the aged samples are shown.

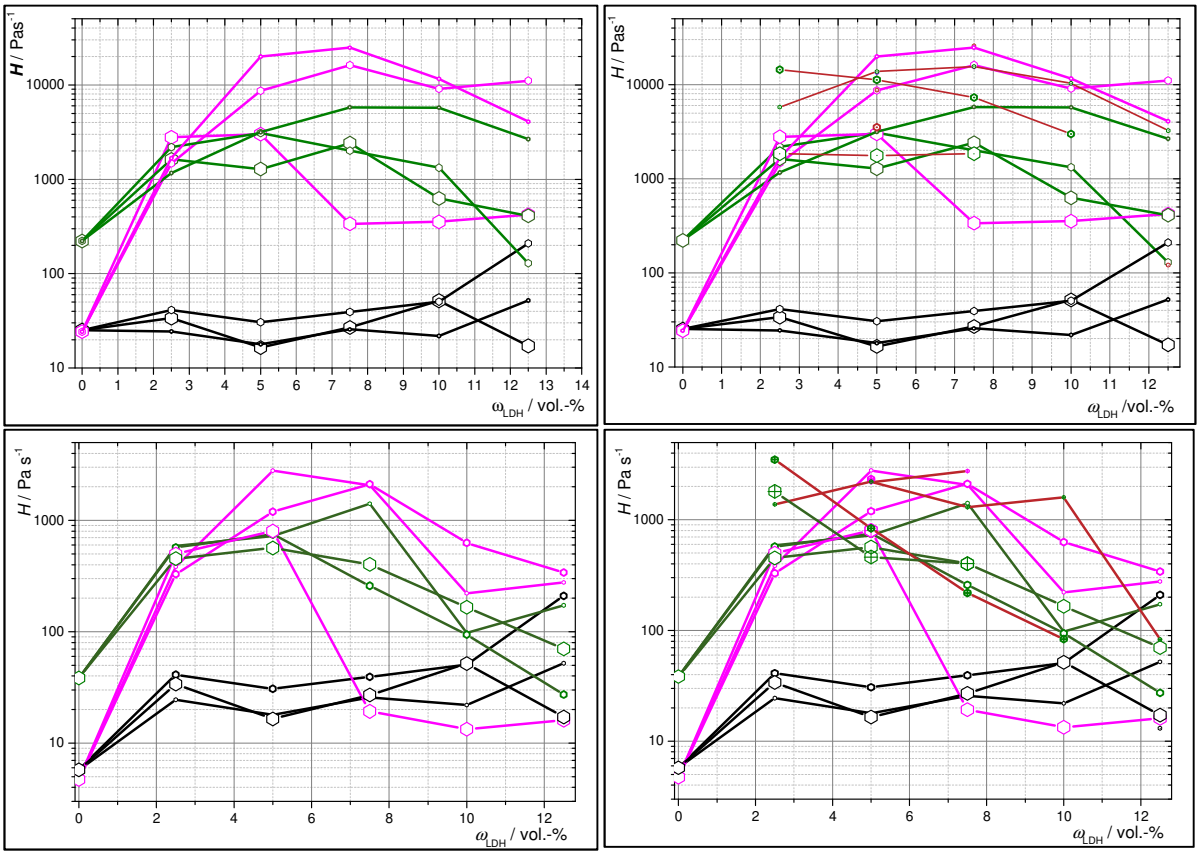


Figure 130: Structural viscosities H vs LDH volume concentration
top: 500 s^{-1} ramps, bottom 150 s^{-1} ramps with and without aging (left vs right)

The apparent viscosity H of the neat PUR dispersions rises with the apparent hydrodynamic size and concentration of PUR, so the applied shear stress τ, the resulting hysteresis area and therefore structural viscosity H. It is evident, that PUR_{10} has the highest ion concentration (DMAE+), the lowest colloid concentration and also the weakest resulting PUR/LDH colloid networks, which is in good agreement on several findings on the NaCl addition to either kaolinite and bentonite dispersions[180] or Mg_2Al-LDH dispersions[181]. For PUR_{75}-dispersions, the structural viscosity H is comparable with PUR_{10}, whereas PUR_{115} show outstanding H among the bare PUR dispersions. Intriguingly, none of the PUR_{10}-based composites reach the structural viscosity H of the bare PUR_{115}-dispersion. As for the composites, the PUR_{115}-based composites have a typical viscoelastic behaviour, whereas almost all PUR_{10}-based composites behave more like a Newtonian liquid with no considerable hysteresis area (cf. Figure 129). For example, by mixing the composites $PUR_{10}LDH_{400}$ ($H = 0.02$ $kPas^{-1}$) and $PUR_{75}LDH_{400}$ ($H = 25.9$ $kPas^{-1}$) with ω_{LDH}=15 wt.-%, in a 50/50 (wt/wt) ratio, a structural viscosity of $H = 0.02$ $kPas^{-1}$ is the result. Another approach was to prepare the composite $PUR_{10}LDH_{400}$, which was then centrifuged and refilled with PUR_{75} dispersion, resulting in a structural viscosity $H = 3.7$ $kPas^{-1}$. Both of these results show, that the charge-carrying units dictate whether a network is stable or not. For the PUR_{10}-based composites it is concluded that the higher ion concentration (DMAE+) lead to the Newtonian behaviour. Based on the maximum structural viscosity H_{max}

among the samples LDH_{400}, LDH_{800} and LDH_{3200} a relation for H_{max} of 8.2 : 5.4 : 1 results, all composites containing PUR_{75}. From a geometric consideration, the ratio of the edge surface per volume is $A_{edge}/V = 2r^{-1}$ for ideal LDH cylinders. The theoretical A_{edge}/V ratios with d_{LDH} = 400, 800 and 3300 nm cylinders is 8.2 : 4.1 : 1, whereas a diameter ratio of d_{LDH}=400, 800, 4300 results into a 10.8 : 5.4 : 1 ratio (cf. Figure 122, diameters between 3200 and 6200 nm are present). Note that the assumed LDH_{3200} diameters are based on the intertwined 3° LDH structures, where the 2° LDH structures therein have diameters in the range of 700 nm (cf. **Table 22**). From this rather simple geometrical model it can be said, that the geometric shape of the LDH platelets can help to approximate the relative strengths of the colloidal networks depending on the aspect ratio, already reported in the literature for clay/polymer nanocomposites by tensile tests of films.[4]

Under high shear stress τ, the LDH platelets $\parallel$ are forced to align to the velocity field $v_{|}$ parallel to the shear surface $v_{|\parallel}$, whereas before measurement, the platelets are organized non-parallel towards the resting shear surface $v_{|\sharp}$. The LDH colloids may surpass a potential barrier during shearing (cf. η vs t curve of 15 wt.-%, $PUR_{75}LDH_{400}$ in Figure 133), whereafter a steady-state of parallel aligned LDH at the shear surface $|\parallel$ is reached. From the geometry of a Couette-type rheometer it is expected that nematic ordering perpendicular to the shear surface $|=$ has the highest potential barrier and is expected to produce the highest values of hysteresis areas, because the director $\vec{n}$ of the platelets have to rotate by the maximum possible angle of 90° in order to get to the parallel alignment $|\parallel$. The highest relaxation time t_r for nematic ordered samples is assumed, since the equilibrium nematic state $|=$ then also has the maximum possible angle to recover its state after resting.

The size of the network entities d_N play a crucial role considering the colloid network dynamics. For the PUR_{75}-based composites for example, it can be assumed, that the charges of the LDH edges are quickly shielded and protected from further heterocoagulation of the type PUR @ LDH_{edge} and LDH_{face} @ LDH_{edge}. One can assume that the colloids have different effective degrees of freedom in the network dependent on the geometrical shape of the network entities, the interaction between the network entities (@, π, μ) and the extent of percolation of the network, determined by the PUR/LDH mass ratios and the overall shear history including the mixing process. The reproducible results of H within a reasonable timeframe Δt on single samples lead to the assumption that the colloidal networks have an equilibrium network shape and geometry, so that the extent of the build-up and the breakdown of the networks reflect the structural viscosity H of a purely dissipative material[182,183,184] .

Further analysis of the rheological data was made by estimating the flow behavior index n for the up- and downramp, based on the Ostwald-de-Waele power-law (cf. **Table 23**). Not surprising, all samples show significant shear-thinning in the upcurve with $n < 1$ and $R^2 > 0.95$. Some of the higher filled samples show dilatant indices with $n > 1$ in the downcurve.

On the next pages, different plots of the rheological data is shown. In **Figure 131**, the η vs t curve for the bare PUR dispersions is shown. In **Figure 132** the η vs t curves, in **Figure 133** the τ vs t curves, in **Figure 134** the τ vs $\dot{\gamma}$ curves and in **Figure 135** the are η vs $\dot{\gamma}$ are shown.

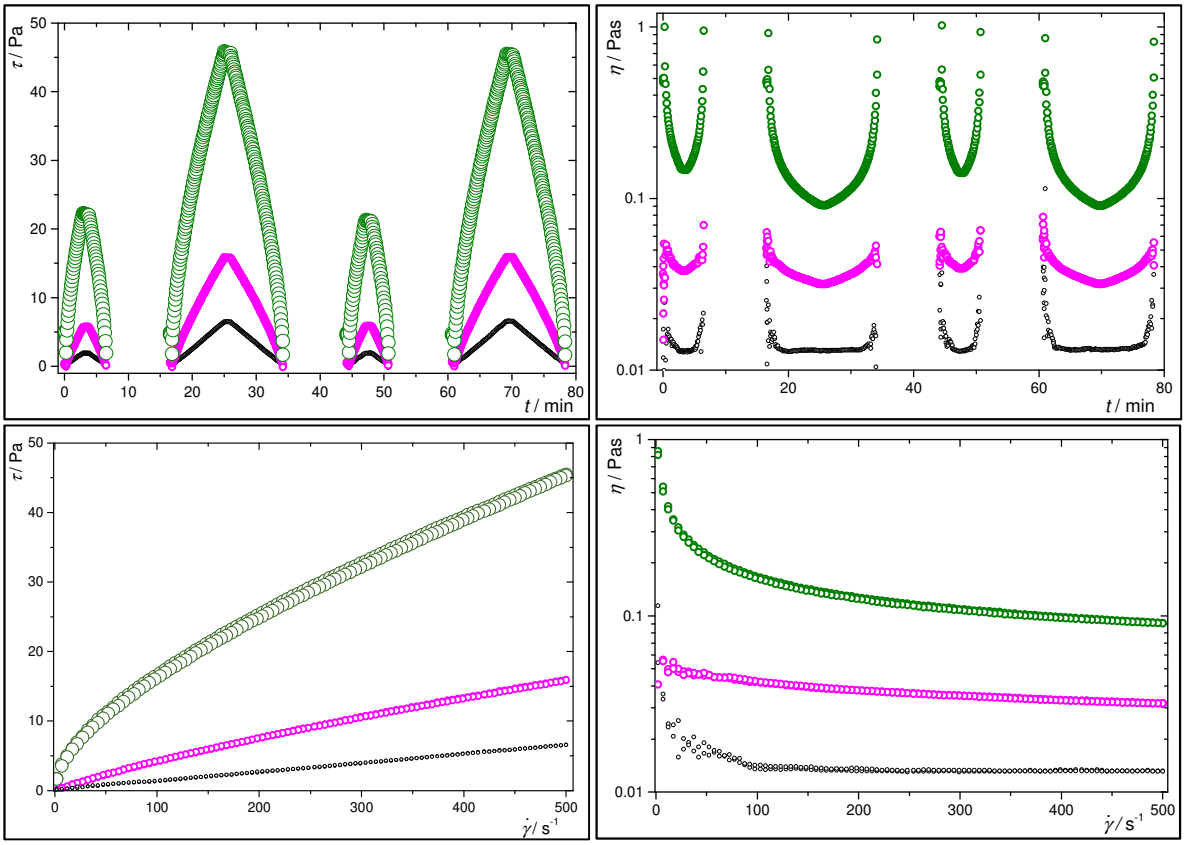


Figure 131: Rheological data of the bare PUR dispersions

PUR$_{10}$, **PUR$_{75}$**, **PUR$_{115}$**: same color attribution as maintext.

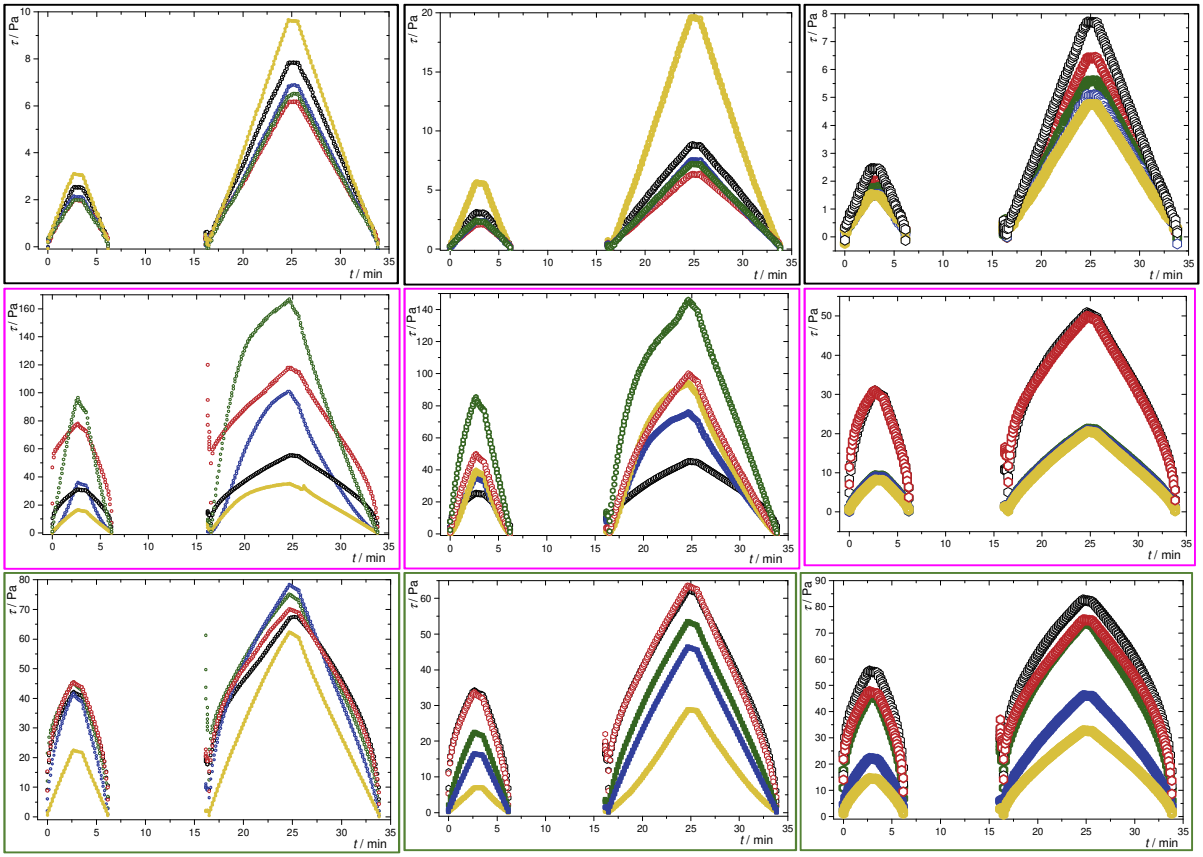


Figure 132: All 45 τ vs t plots of the last two ramps.

Colors indicate the LDH concentration: **black 5%**, **red 10%**, **green 15%**, **blue 20%**, **yellow 25%**.

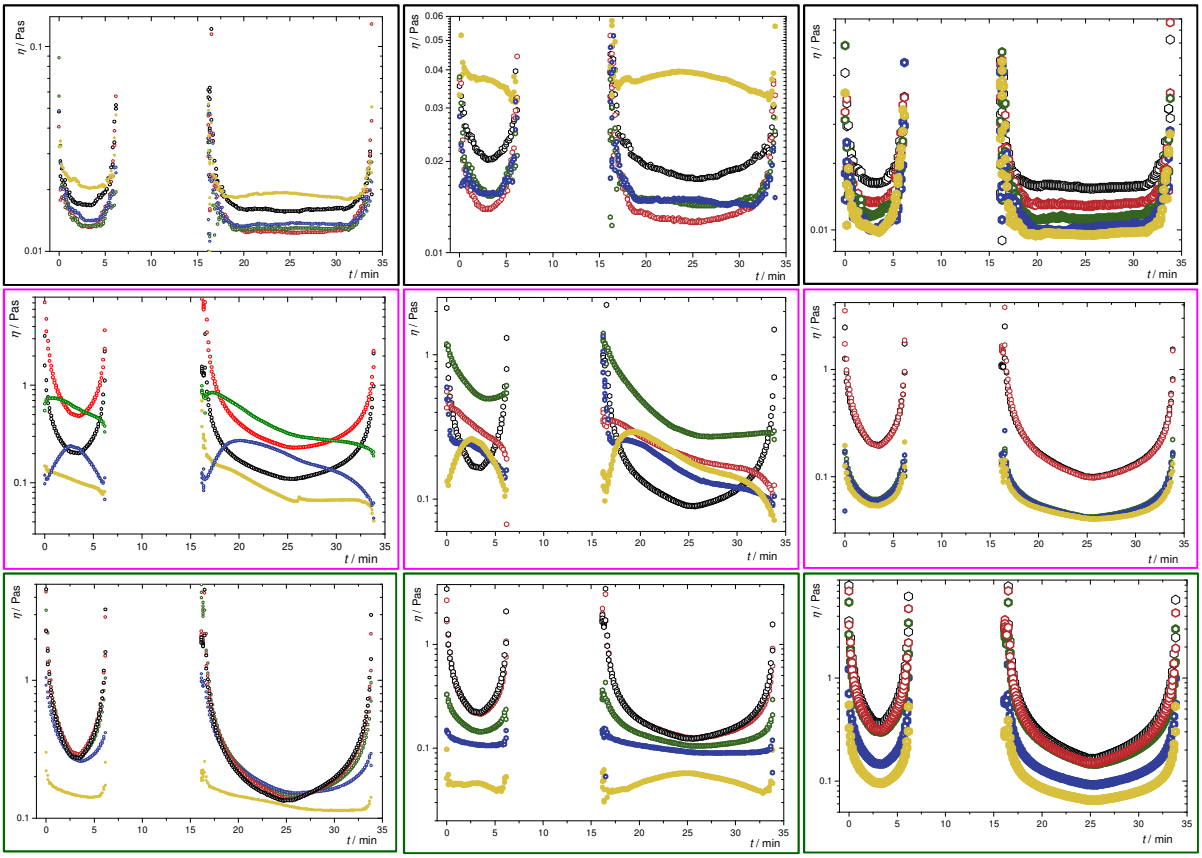


Figure 133: All 45 η vs t plots

Colors indicate the LDH concentration: **black 5%**, **red 10%**, **green 15%**, **blue 20%**, **yellow 25%**.

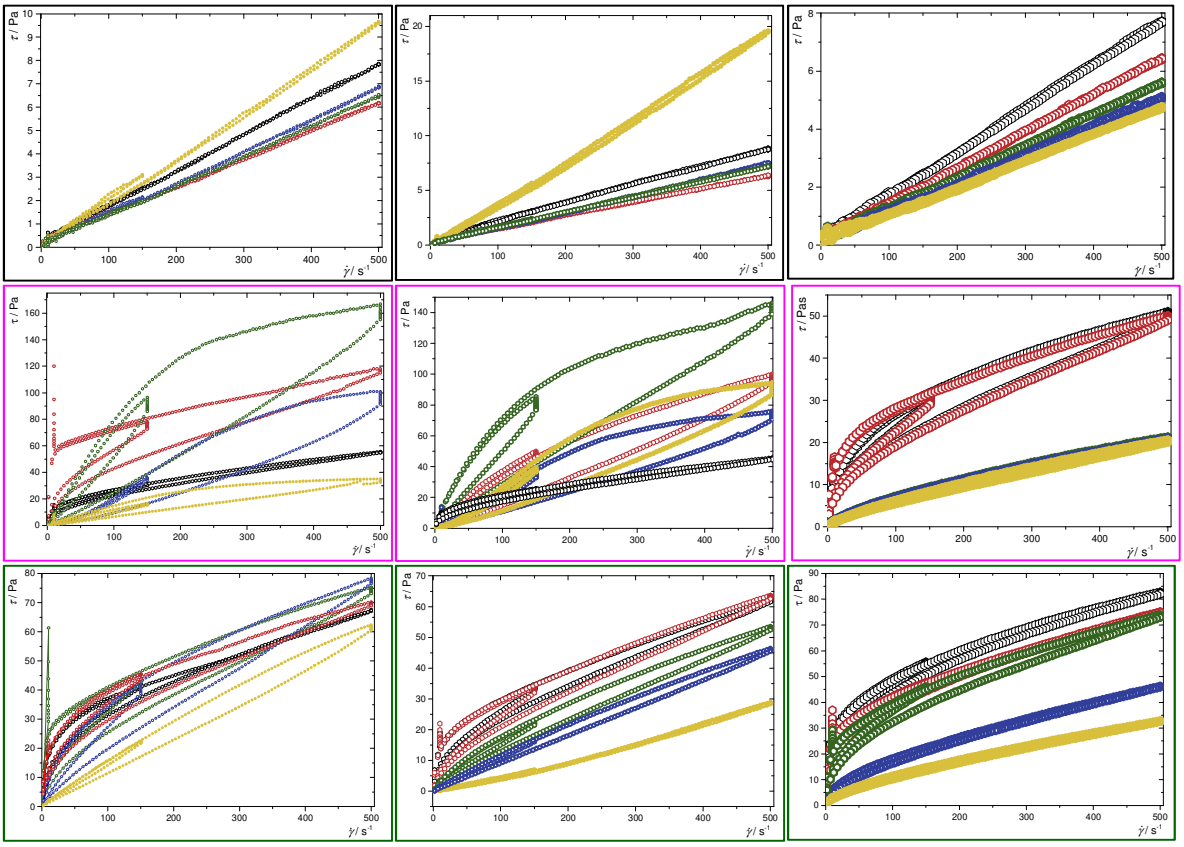


Figure 134: All 45 τ vs $\dot{\gamma}$ plots

Colors indicate the LDH concentration: **black 5%**, **red 10%**, **green 15%**, **blue 20%**, **yellow 25%**.

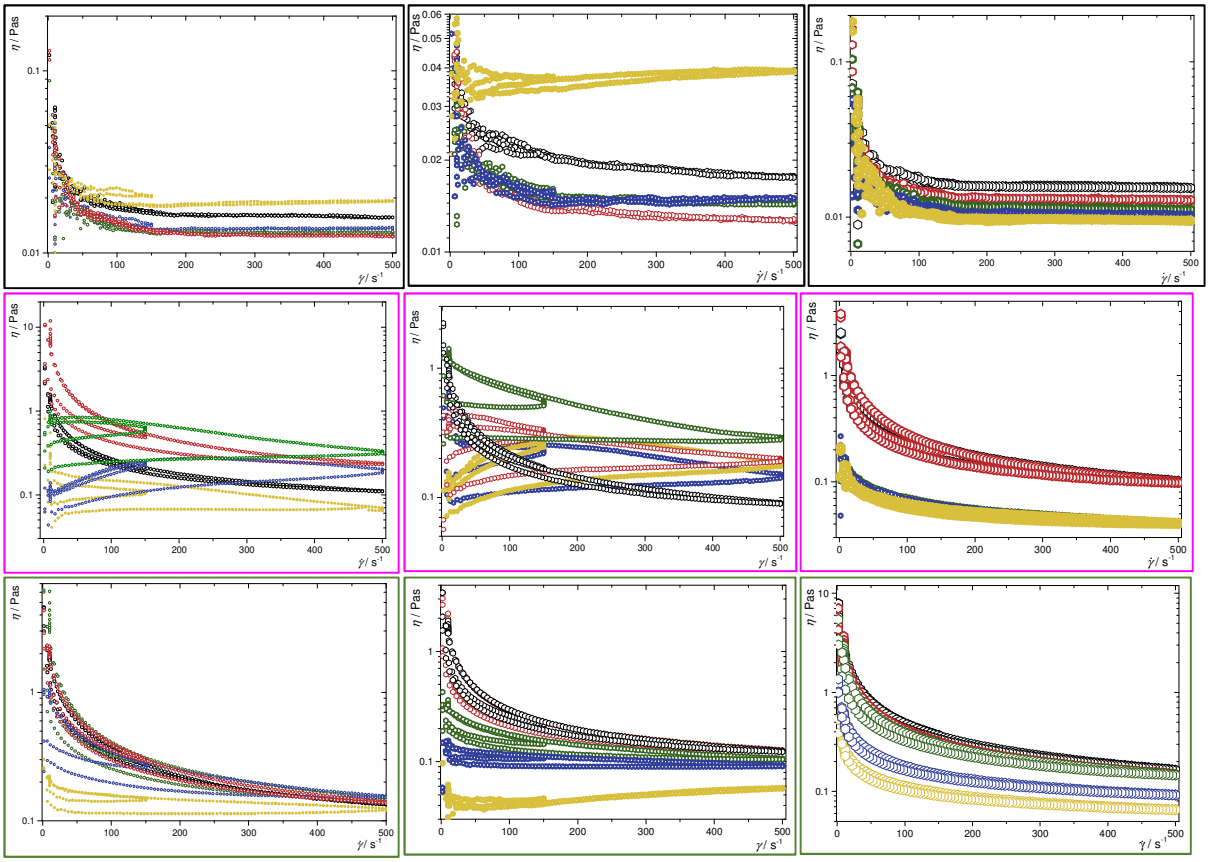


Figure 135: η vs $\dot{\gamma}$ plots

Colors indicate the LDH concentration: **black 5%, red 10%, green 15%, blue 20%, yellow 25%.**

Table 23: Flow index n from Ostwald-de-Waele fits based on logarithmized data from Figure 135

ω_{LDH}	PUR	LDH	n_{up}	R^2	n_{down}	R^2	ω_{LDH}	PUR	LDH	n_{up}	R^2	n_{down}	R^2	ω_{LDH}	PUR	LDH	n_{up}	R^2	n_{down}	R^2
5	10	400	0.9	0.860	0.9	0.600	5	75	400	0.4	1.000	0.5	0.990	5	115	400	0.4	1.000	0.6	0.990
10	10	400	0.8	0.980	0.8	0.900	10	75	400	0.3	1.000	0.6	0.990	10	115	400	0.4	1.000	0.5	1.000
15	10	400	0.7	0.980	0.8	0.970	15	75	400	0.3	1.000	1.1	0.950	15	115	400	0.7	0.970	1.2	0.970
20	10	400	0.8	0.950	0.8	0.840	20	75	400	0.5	0.980	1.4	0.980	20	115	400	0.5	1.000	0.8	0.970
25	10	400	0.8	0.900	0.8	0.890	25	75	400	0.4	0.980	1	0.900	25	115	400	0.9	0.980	0.9	0.960
5	10	800	0.9	0.980	0.9	0.970	5	75	800	0.4	1.000	0.5	0.990	5	115	800	0.4	1.000	0.8	0.990
10	10	800	0.7	0.950	0.8	0.950	10	75	800	0.3	1.000	1.3	0.950	10	115	800	0.8	0.970	1.1	0.980
15	10	800	0.8	0.900	0.8	0.880	15	75	800	0.4	0.990	1	0.980	15	115	800	0.7	0.990	0.8	0.980
20	10	800	0.8	0.970	0.8	0.950	20	75	800	0.6	0.950	1.1	0.990	20	115	800	0.9	0.970	1	0.950
25	10	800	1.1	0.970	1.1	0.990	25	75	800	0.4	0.990	1.2	0.990	25	115	800	1.3	1.000	1.2	1.000
5	10	3200	0.9	0.960	0.8	0.960	5	75	3200	0.4	1.000	0.5	1.000	5	115	3200	0.3	1.000	0.4	1.000
10	10	3200	0.8	0.970	0.9	0.920	10	75	3200	0.3	1.000	0.5	0.990	10	115	3200	0.3	1.000	0.4	1.000
15	10	3200	0.7	0.980	0.8	0.760	15	75	3200	0.7	0.990	0.7	1.000	15	115	3200	0.4	1.000	0.5	1.000
20	10	3200	0.7	0.980	0.8	0.840	20	75	3200	0.7	1.000	0.7	0.990	20	115	3200	0.5	1.000	0.6	0.990
25	10	3200	0.8	0.970	0.9	0.900	25	75	3200	0.7	1.000	0.7	0.980	25	115	3200	0.6	1.000	0.7	0.990

4.2.6 PUR / LDH Composites - Dissipative Properties

The irreversible breakdown of the cross-linked PUR/LDH films was performed by dynamic mechanical analysis with a displacement in the order of the average film thicknesses, cf. **Figure 136** and **Table 22**. The storage modulus G' of cross-linked PUR films (without LDH) is comparable to the outstanding sample with nematic ordered LDH. This can be explained with comparable packing densities of the samples, with respect to the relative scales of the network entities. The dissipation factor tan δ is 2 to 6 times higher for the nematic ordered sample and the highest among all samples, explained by the dissipative breakdown of ordered LDH colloids in the films. The dissipation factor tan δ correlates well with the structural viscosities H, explainable by the purely dissipative, (en)tangled colloidal networks. The bare crosslinked PUR films have similar storage moduli G', with slight difference and same tendencies within the series PUR_{75}>PUR_{115}>PUR_{10}, more pronounced for tan δ. Two samples with 4.7 vol.-% LDH_{3200} have the highest measured storage moduli G' among all samples, confirming the influence of the aspect ratio. [4,82] There are another two samples with G' > 300 MPa, both from $PUR_{10}LDH_{800}$ composites with 1.5 and 8.5 vol.-% LDH in the films (cf. SI). In sum, the DMA results fit the expectation, that a) higher platelet aspect ratios lead to higher storage moduli G',8,11 b) for PUR, higher A/V ratios, hence smaller colloid sizes (cf. Figure 1) lead to higher densities of crosslinks per volume V and therefore higher storage moduli G', and c) for cylindrical shaped LDH, a higher amount of interfaces, hence $A_{edge}/V = 2\ r^{-1}$ ratios lead to more dissipative networks with decreasing LDH diameters.

It is believed that the crack propagation during breakdown has a zipper-like mechanism, known from earlier studies on polyamide-imide/montmorillonite nanocomposites.[2,18]

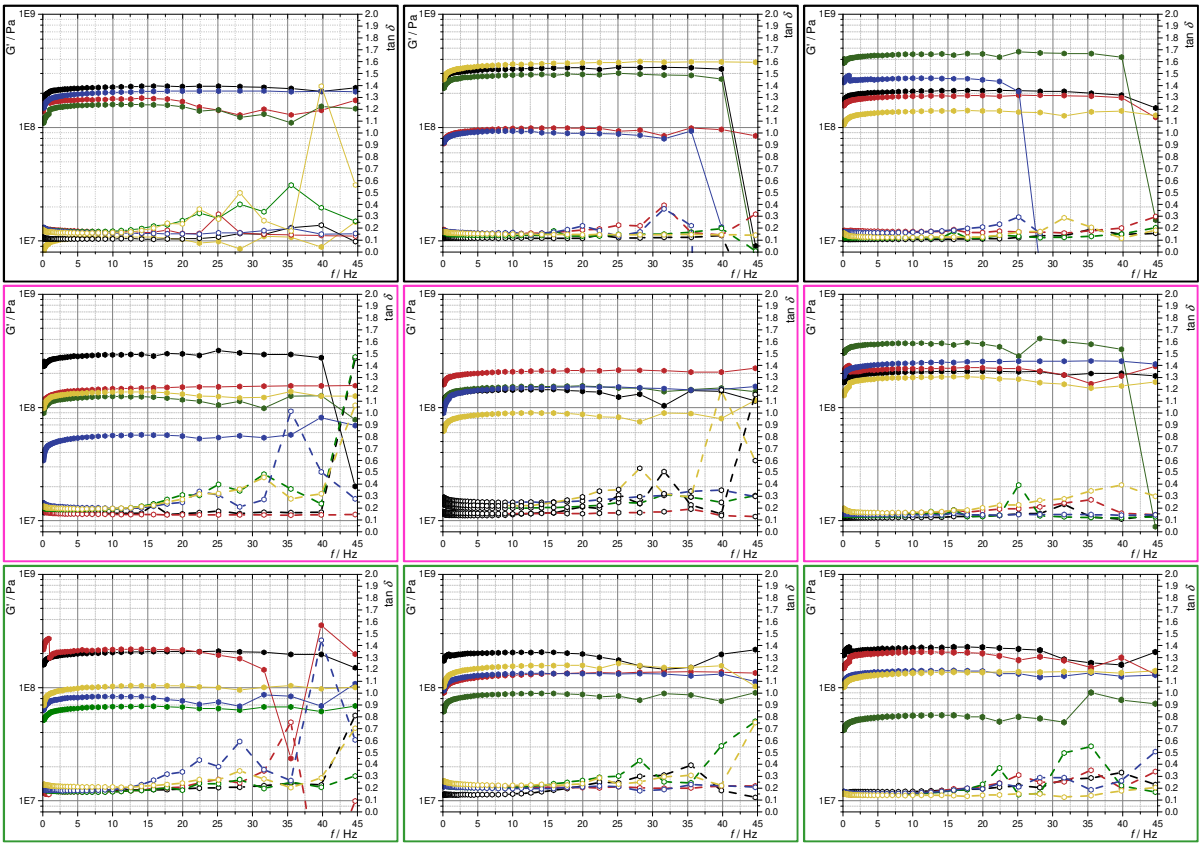


Figure 136: DMA measurement of all PUR/LDH composites

The solid hexagons with solid lines are attributed to the storage modulus G' and the open hexagons with dashed lines are attributed to the dissipation factor tan δ. The frame colour represent the PUR type and the colors indicate the LDH concentrations: **black 5%, red 10%, green 15%, blue 20%, yellow 25%.**

4.2.7 PUR / LDH Composites - Scaling Law Analysis

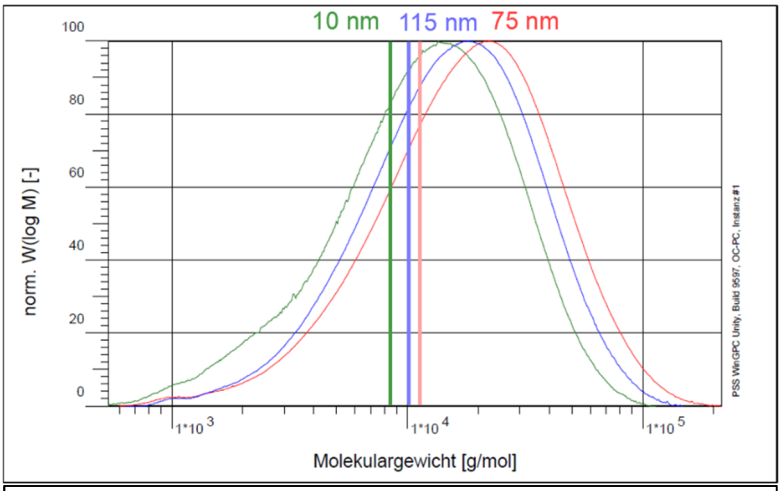
The data of the measured apparent viscosities η (cf. Figure 132) and molar masses M_n of the PUR polymers (cf. table in **Figure 137**) allows to examine numbers based on a model by P.G. de Gennes, which itself describes the movement of entangled polymer chains in a tube-based model,[21] with the resulting scaling law

$$t_r \sim \eta_0 \sim M^{3.0} \tag{17}$$

It is known that experiments give out irrational numbers as exponents, such as

$$\eta_0 \sim M^{3.4} \tag{18}$$

whereas no sufficient physical meaning can be attributed accurately to the numbers. The tube-based model describes entangled 0D units N of a polymer P_N with the molar mass M_N.



	Knauer RI (THF)	Knauer RI (THF)	Knauer RI (THF)	
Mn :	7.3941e3	1.1383e4	1.0299e4	g/mol
Mw :	1.5972e4	2.4600e4	2.0482e4	g/mol
Mz :	2.6631e4	4.2359e4	3.3865e4	g/mol
Mv :	1.4699e4	2.2583e4	1.8924e4	g/mol
D :	2.1601e0	2.1612e0	1.9887e0	
[n]:	1.1553e1	1.5772e1	1.3875e1	ml/g
Vp :	1.7917e1	1.7209e1	1.7515e1	ml
Mp :	1.3561e4	2.2506e4	1.8074e4	g/mol
FI :	1.567e-2	4.068e-2	2.835e-2	ml*V
< 536	0.00	0.00	0.00	
w% :	100.00	100.00	100.00	
> 215852	0.00	0.00	0.00	

Figure 137: GPC data of the chosen PUR colloids.
The number average M_n is highlighted in the upper figure

In the model, the 0D units form a projected 2D plane by defect-driven diffusion through a confined 1D tube during the relaxation time t_r and result in the exponent D = 3.0, all based on the principle of ergodicity. The model and its implications are known to be useful for understanding polymer melts or interdiffusing polymers at melting interfaces. Exponent values of $M^{3.6}$ were estimated by Antonietti et al. for monodisperse and crosslinked organic polymer spheres,[185] already indicating some other mode than the proposed "reptation" in tubes.
The 45 PUR/LDH model composites expose exponents such as

$$\eta_0 \sim M^{11.0} \tag{19}$$

The η vs t data sets of the PUR/LDH composites with the same type and concentration of LDH, e.g. 5 wt.-% LDH_{400}, were fitted with conserved quantities, meaning the respective molar mass M_n of the corresponding PUR type at equal shear rate $\dot{\gamma}$ and time t in each dataset. The underlying equation for the fits is the scaling law

$$\eta = K \cdot M^D \tag{20}$$

The constant K is then represented by

$$K = \frac{A}{V} \cdot \frac{1}{t} \cdot \frac{1}{\bar{m}^{D-1}} \cdot \frac{1}{N_A^D} \tag{21}$$

with A/V as the specific interface of a unit action, t as the elapsed time of a unit action, and $\bar{m}^{D-1}$ as a mass representation with a fractal D as exponent and N_A, the Avogadro constant. The data was calculated by linear regression of the $\log_{10}\eta$ and $\log_{10}M_n$ values. The result of the D values from the slopes of the respective $\log_{10}\eta$ and $\log_{10}M_n$ fits were plotted in a D vs t plot, shown in **Figure 138**.

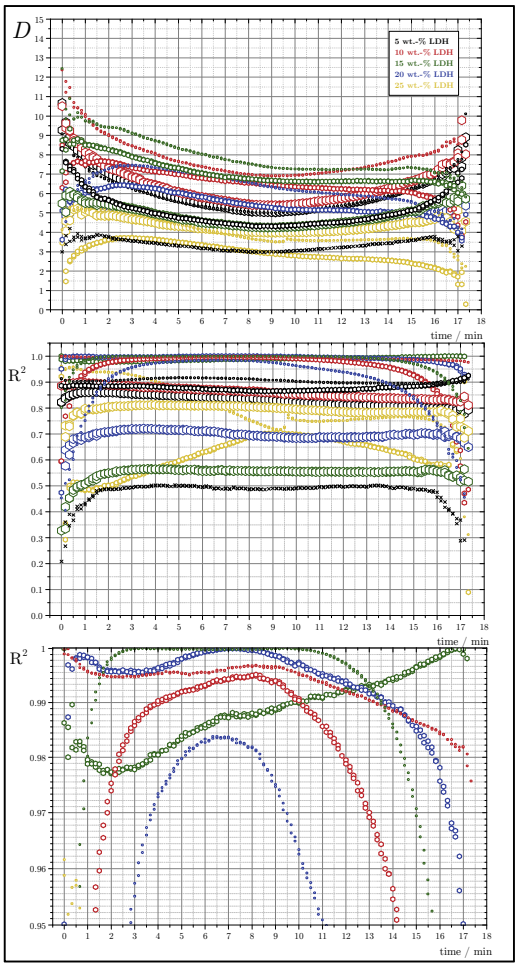


Figure 138: D vs t plots.

The LDH type is attributed by small, medium and big symbols. The LDH weight concentrations ω_{LDH} are attributed to the color: **black 5%, red 10%, green 15%, blue 20%, yellow 25%**. The cross symbols are attributed to the bare PUR dispersions.

For the three bare polyurethane samples, values of D = 3.0 to 4.0 were obtained across the D vs t plot (black crosses). The minimum value D=2.98 was estimated for high shear rates with an intriguing small value for the resulting maximum coefficients of determination R^2_{max}=0.50. The insignificant result for D_{PUR} can be explained by insufficient crowding in

comparison to the other colloid networks, having high significance with a maximum estimated R^2=0.999999995 in this study. The lowest significance among the composite samples was estimated for the LDH_{3200} series, where some rotational actions are known to be inactive by the intertwined structure of the LDH colloids. This is supported by the fact that also low LDH concentrations (black symbols) and high LDH concentrations (yellow symbols) have lowered significance. As for the high concentrations, one can assume inactive rotation by aggregation as the reason for the lowered significance. In sum, the LDH_{400}-based composites at low and high concentrations have more significant values because of its more crowded colloid network structure. One can say from here, that the explanation of the R^2 values fits well the known physical characteristics of the colloid networks. The so-called Mark-Houwink exponent from the GPC measurement is found to be $D = 0.68$ (with R^2=0.96) from fitting the intrinsic viscosity $[\eta]_{PUR}$ of freeze-dried PUR in THF against the thereby obtained molar masses M_n. The resulting fractal number is attributed to flexible polymers and intriguingly resembles the fractal geometry of a Cantor set with Hausdorff- Dimension: $\log_3(2)$ which in turn resembles tortous path trajectories along GPC columns.

The corresponding fits of the shear stress data τ vs t give practically the same values for D, but significant different values and also other physical units for K_τ . This result can be attributed to the kybernetic measurement apparatus, which performs feed-back-loops in order to perform the shear rate program, based on the assumption of a continous sample. The fits of the aforementioned aged PUR/LDH samples were also done with resulting values up to $D = 12.7$. Another approach for the evaluation of the data was to choose single values across η vs t, where the highest and lowest viscosities of the data set were used for fitting the data once per data set. The highest resulting values were found to be $D = 10.6$ and R^2=0.99989.

In the following, the attribution of the D values are represented by natural numbers and degrees of freedom, illustrated in **Figure 139**.

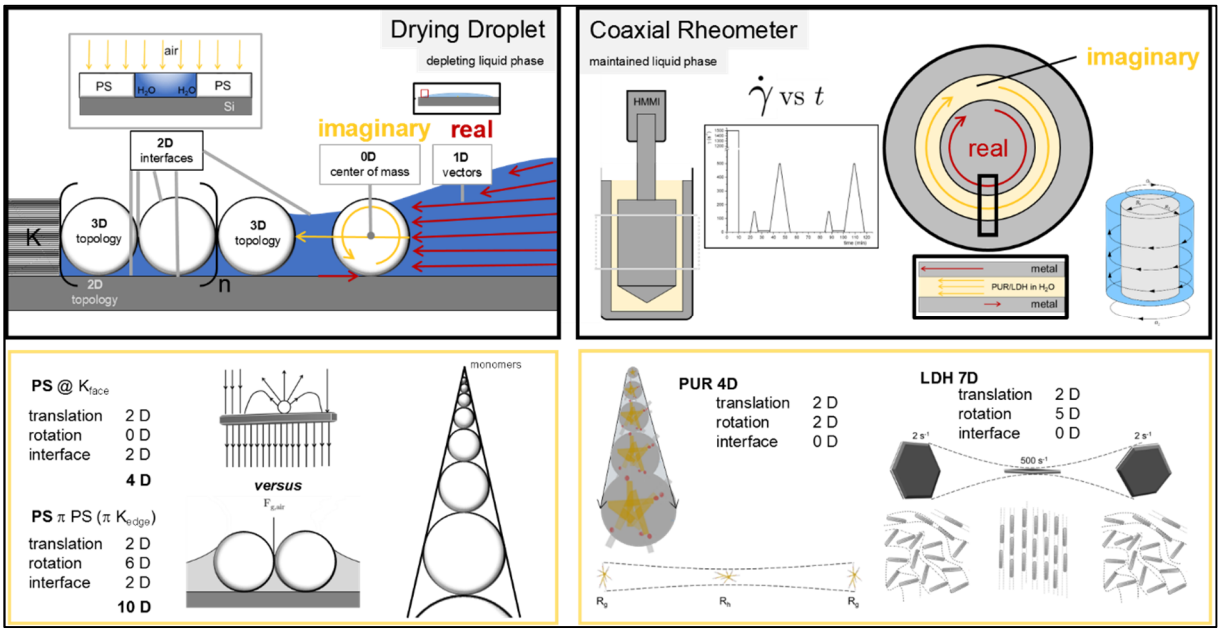


Figure 139: Comparison of drying droplet and rheometer experiments

Attributing for LDH and PUR each 3D for translation (Euclidean: x; y; z), each 6D for rotation (Quaternions, Euclidean rotation axes: x; y; z; -x; -y; -z) and each 2D for the interface (excluded volume, no ghost colloids), one finds 22D. Obviously, the effective 2D interface for composites is still 2D, from where one already can eliminate 2D, coming down to 20D. For the polyurethane

colloids, the rotation between the gyration radius R_g and the hydrodynamic radius R_h are assumed to be the effective two rotation modes, from where 4D were eliminated for invariant PUR rotations, coming down to 16D. For LDH, the invariance of the backward 'frisbee' rotation (rotation axis orthogonal to platelet) in the velocity field is also assumed to be invariant, ending up at 15D in the resting-state without any velocity field. One can assume, that in the moment of measurement, the 2D shear interface is the dominant interface and in the induced Couette-type flow-field, one can assume that 1D of translation for each colloid is at least restricted. From this basic thoughts, one can explain the measurement of 11D at a 4D interface. If one consider the human observer as 11D and the composite as observable on the other side of the measurement, one would end up in 26D during measurement, indicating that this experiment could be a candidate for proving the number of dimensions in the prominent string theories, which itself claim to be a candidate for a "Theory of Everything". An arrangement of the real and imaginary parts that are introduced in Figure 139 are explained by the framework of conservative and dissipative parts, known from dissipative systems, shown in **Table 24**.

Table 24: Hierarchical levels

conservative part (real)	**dissipative part (imaginary)**
human	rheometer
human	computer
human	PUR/LDH in H_2O
computer	rheometer
rheometer	PUR/LDH in H_2O
PUR/LDH	(as medium) H_2O
PUR	LDH
Earth	human
Earth	Si-wafer
Earth	PS/K in H_2O
human	PS/K in H_2O
Si-wafer	PS/K in H_2O
H_2O (as depletant)	PS/K
PS/K	(as medium) H_2O
K	PS

A deeper analysis in terms of the fundamental meaning of the results was beyond the scope of the present work and may be published separately.

5 Nacre-mimetics from protein/salt composites

This section will show some qualitative data and tries to give an explanation based on inductive-reasoning of coincidental findings within a bachelor thesis from Krüger (2015).[186] The initially examined model system was LDH/casein/chymosin with the goal to obtain a "brick-and-cheese" morphology, depicted in **Figure 140**. The simplified colloidal structure of casein micelles consists of a hydrophobic core with charged hydrophilic arms. The rather naive intention behind the model system was to find a suitable polymer that initiate a parallel alignment of LDH platelets, since it was known from nacre, that hydrophilic and hydrophobic parts of the proteins drive the $CaCO_3$-based platelet organization. From a technical polymer scientist's view, the casein/chymosin system opens up the possibility to control over the polymer composition, meaing that a copolymer (κ-casein before cleavage reaction) versus polymer blend (CMP and para-κ-casein after cleavage reaction).

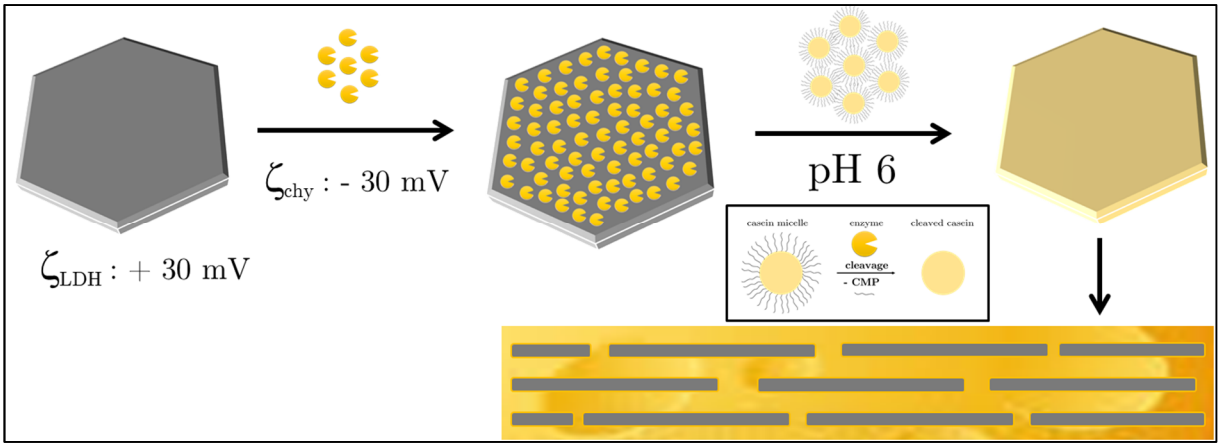


Figure 140: Anticipated coating and organization of LDH colloids with casein

As it is obvious and known in literature, biopolymers, especially proteins consist of hydrophobic and hydrophilic monomers in a manifold of possible combinations with respect to compositions *within* a polymer and also compositions *of* polymers. More fuzzy and hardly tangible is the highly established amino acid sequence which give proteins, especially enzymes its multifunctional properties, emerged from trial-and-error (hyper-)cycles (cf.-II-4, page 26f).

The micelle size distribution of casein is polydisperse and dependent on many parameters, especially solvent type, pH, temperature and ionic strength. In the experiments, the solvent is water, pH is 6, the temperature is 40 °C and the ionic strength was tried to keep at a low level, as in all other organization related experiments in this work. However, the ionic strength in some conducted side-experiments was high enough to give layered and parallel oriented crystal structures consisting of a KCl/protein composites, identified by EDX. In experiments without the presence of LDH colloids, an even more pronounced layered crystal growth occurred. After longer becoming reaction times, 500 nm thick, weakly oriented platelet crystals were observed. Moreover, parallel oriented potassium benzenesulfonate crystals from **K**OH and dissolved LDH-**BSA** were found. The iridescent appearance, SEM images, spatially-resolved elemental analysis (SEM/EDX), MALDI-ToF-MS and also AFM results from the literature indicate similarities to natural nacre growth stages already found by diverse scientists in multidisciplinary fields.

The growth of nacre is a biophysical chemistry topic and reviews exist on the complex interplay of structure, properties and growth.[187] The emphases can be on a lot of interesting topics related to materials science, such as the mechanical properties of the dry *versus* the hydrated state of nacre,[188] the role of the soft part on the mechanical strength,[189] simulation of the

mechanical properties with wavy *versus* flat platelets via finite-element method FEM[80], seasonal and feeding effects on the growth and also evolutionary constraints on the growth[190]. It is also reported, that the chemical structure of some nacre-building proteins have similar structural features to mammalian milk proteins and whey acidic proteins.[191] Such evolutionary relations are also known for silica structure-forming proteins from sponges, Silicatein α[192], that are related to the human cathepsin L and also at other positions resembles other proteases such as trypsin and chymotrypsin.[193,194] From here, one could argue that SiO_2- and $CaCO_3$-containing shells are build by digestive enzymes, based on resource efficiency. This is one of the central evidences why the knowledge on cheese-making may help to successfully mimic nacre or even overcome the properties of nacre and use it for (coating) materials.
A recent publication found an amorphous gradient surface layer between crystalline aragonite $CaCO_3$ und chitin layers, made of amorphous $CaCO_3$ (ACC), whereas no organic part was detected in the 3-5 nm ACC coating.[195] However, the most-cited paper by a group of long-established researchers on the topic of mollusk-shell formation summarized the well-known and recent findings (on ACC) by stating the following (cf. **Figure 141**)[196]:

“

1. The silk phase is a gel that pre-fills the space to be mineralized.
2. The chitin is the ordered structural phase that ultimately dictates the orientation of the mature crystals.
3. The matrix components are spatially differentiated.
4. The first-formed mineral is transient colloidal amorphous calcium carbonate (ACC).
5. Nucleation occurs on the matrix, and the crystal grows at the expense of the ACC phase.
6. During this growth phase some of the acidic proteins are occluded into the crystal.

“

Further, they state a four-stage shell formation mechanism:

“

I) Assembly of the matrix.
II) The first-formed mineral phase
III) Nucleation of individual aragonite tablets.
IV) Growth of the tablets to form the mature tissue

“

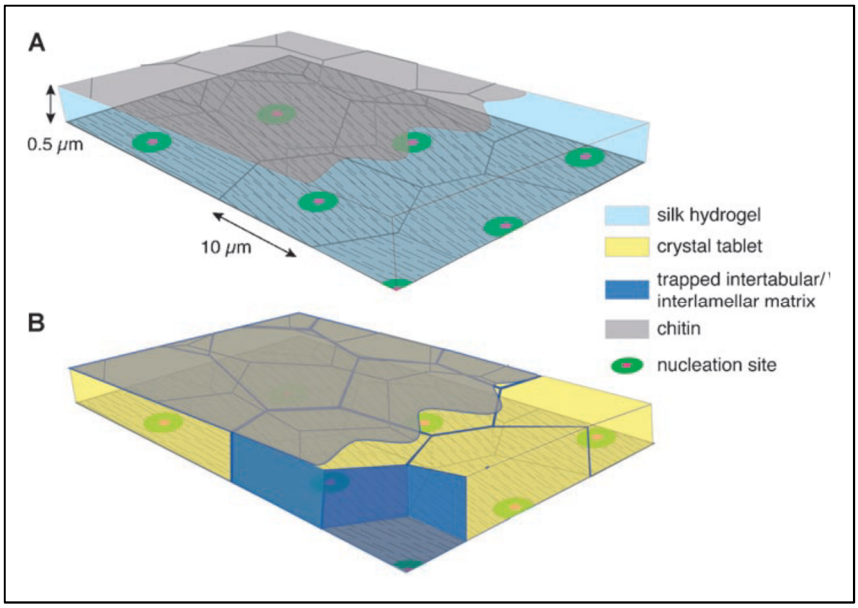


Figure 141: Rrecently postulated mollusk shell formation mechanism

5.1 Experimental Details

Table 25: Materials for Biomineralization experiments

Name	Size/Purity	Supplier/Synthesis
Casein, dephosphorylated		Sigma Aldrich
Calf Rennet Powder (Chymosin)		RENCO
Rennet Powder from Mucor miehei Type II		Sigma Aldrich
KOH, HCl, NaCl		

Dynamic Light Scattering (DLS)
Malvern Zetasizer Nano ZS
Zeta Potential Measurement
Malvern Zetasizer Nano ZS
Scanning Electron Microscopy (SEM)
Zeiss NEON 40
Elementary Analysis
EDX, Zeiss NEON 40
Centrifuge
Hettich Micro 20
BECKMAN COULTER Avanti® J-E with a JA-10 Rotor, equipped with molds for smaller centrifuge bottles
Ultrasonic
BANDELIN "SONOCOOL 255"
pH Electrode
METTLER TOLEDO SevenMulti pH-Meter

5.1.1 Preparation of Casein Dispersion

2 g casein and 200 g water were mixed in a beaker and heated to 50 °C. During the dispersion process, 15 portions of 5 M HCl with a total volume of 350 µL are added (Cl: 1.13 mM, 62 mg, 1.75 mmol) with an Eppendorf pipette to obtain a homogenous dispersion overnight. Subsequently, 20 g of the stable, supernatant dispersion is transferred by decanting into a small glass and small portions of 5 M KOH were added to give a dispersion with pH 6 (45 µL total; K: 8.62mM, 9 mg, 0.23 mmol). The dispersion was stirred overnight at r.t. and the resulting NVC of the dispersion was measured to be approx. 0.27 wt.-% (130 °C, 30 min). The electrical conductivity is below 1 mS/cm.

5.1.2 Preparation of Enzyme Dispersions

The protein content of commercial Calf Rennet Powder from RENCO (New Zealand) contains 92-96 % chymosin, whereas the other part accounts to other enzymes present in the fourth stomach of young milk fed calves (primarily pepsin). The ingredients of the powder according to the safety data sheet refer to NaCl ($< 98\%$), gelatine ($< 2\%$ gelatine, bovine) and the rennet enzymes chymosin ($< 1\%$) and pepsin ($< 1\%$).
The rennet powder from Sigma-Aldrich (Rennet from Mucor miehei Type II) contains maltodextrine and sodium chloride. The protein content of the powder is listed as > 4 % after Lowry in the specification sheet.

Commercial Enzyme

6 g of commercial rennet powder (RENCO) was dissolved in 72 mL pure water. The solution was centrifuged three times 5000 x g for 2 h at 25 °C in the same volume with Amicon® Ultra-15 Centrifugal Filter Devices with a cutoff of 3,000 g/mol. The resulting solid is placed in a round-bottom flask, freeze-dried and stored at 8 °C before use. After the centrifugal filtration, the enzyme content was increased up to 67 wt.-%.[197]

Rennet from Mucor miehei Type II

The rennet powder from Mucor mihei was used as received and stored at -6 °C. The needed amount is dissolved in a small amount of pure water (e.g. 2 g) prior addition.

5.1.3 Biomineralization Experiments

Within the biomineralization experiments, the composition of the dispersions is dependent on the amount of HCl and KOH added to adjust the pH. The proteins used here are in general casein and the enzyme chymosin. The weight percentage of the enzymes in the upcoming subsections is based on the protein powder content of the mixtures.

MALDI sample preparation with 20 wt.-% enzyme content

The pH 6 casein dispersion (75 g, 0.27 wt.-%, 203 mg casein) was heated to 40 °C under magnetic stirring in a beaker covered with a watch glass. 76 mg of chymosin (**RENCO**) were added at $t = 0$ min. After 1 minute of stirring, the first 2 mL of the dispersion is removed. Every 30 minutes, a 2 mL sample was removed, and 1 g of 5 M KOH was added to terminate the cleavage reaction. The samples are centrifuged (30 min, 13.000 rpm) and a droplet of the supernatant is placed on a Si-wafer.

For MALDI measurements, 2,5-Dihydroxybenzoic acid solution (10 mg/mL) is prepared in a 70/30 H_2O/CH_3CN mixture and phosphoric acid was added (1 wt.-%). The DHB solution is added to obtain a mass ratio of 10:1 (DHB : protein). One droplet of the sample solution is placed on the MALDI target prior measurement.

MALDI-type preparation with 30 wt.-% enzyme content

The pH 6 casein dispersion (62 g, 0.27 wt.-%, 167 mg casein) is heated to 40 °C under magnetic stirring. 70 mg enzyme powder (from **Mucor Miehei**) is dissolved in 3.3 g water and added to the mixture at $t = 0$ min. After 1 minute of stirring, the first 2 mL of the dispersion is removed. Every 30 minutes, a 2 mL sample was removed, and 1 g of 5 M KOH was added to terminate the cleavage reaction. The samples are centrifuged (30 min, 13.000 rpm) and a droplet of the supernatant is placed on a Si-wafer.

MALDI-type preparation with $<$ 1 wt.-% enzyme content

The pH 6 casein dispersion (20 g, 0.27 wt.-%, 54 mg casein) is mixed with NaCl solution, so that an electrical conductivity of 3.7 mS/cm is present (approx. 46 mM). Alternatively, the electrical conductivity of the dispersion is adjusted to 30 mS/cm. In both cases, 12 mg of chymosin (**Mucor Miehei**) was added. After 1 minute of stirring, the first 2 mL of the dispersion is removed. Every 30 minutes, 2 mL sample volume was removed, and 1 g of 5 M KOH was added to terminate the cleavage reaction. The samples are centrifuged (30 min, 13.000 rpm) and a droplet of the supernatant is placed on a Si-wafer.

5.1.4 Compositions of biomineralization experiments

In **Table 26**, calculations of the compositions of the biomineralization experiments are listed and the highlighted numbers are attributed to the headings of the previous subsections so that the overall compositions can be put into context with the results.
For the calculation of the enzyme contents it was assumed that the powder from the Mucor Miehei product has 4 wt.-% enzyme content, and the RENCO product has 67 wt.-% enzyme content after concentration by centrifugal filtration described above. The salt contents of the enzyme powders were simplified to be KCl/NaCl. Moreover, for the first experiments based on the B.Sc. thesis of S. Krüger (2015)* and the therein used RENCO product it is not fully clear, how much KOH and HCl solution was used in order to obtain pH 6. However, the experiment was done twice with more acid/base consumption (1^{st*}) and less acid/base consumption (2^{nd*}), both giving similar nacreous structures.

Table 26: Overview of biomineralization experiments

			enzyme in protein	enzyme in solids	protein in solids	KCl/NaCl in solids	KOH in solids	nacreous
#	enzyme type	pH	**wt.-%**	wt.-%	wt.-%	wt.-%	wt.-%	yes/no
***0**	RENCO	6	**20.1%**	3.12%	15.5%	7.3%	77.2%	yes
*0	RENCO	6	**20.1%**	3.12%	15.5%	7.3%	77.2%	yes
0	Mucor	6	**29.5%**	0.68%	2.3%	19.2%	78.5%	yes
0	Mucor	6	**0.9%**	0.02%	2.0%	5.1%	92.9%	no
0	Mucor	6	**0.9%**	0.02%	1.8%	10.8%	87.4%	no

5.2 Results & Discussion

It turned out after the first experiments that the approach for the organization of LDH-BSA platy colloids by the protein system chymosin/casein lead to structures where the LDH colloids rather act as a spectator or to put it different as a source of enzymes, apparent in Figure 144, shown below. Parallel-aligned, mineral crystals made of KCl or K-BSA and protein (cf. EDX results in Appendix, page 230) were found after drying aqueous dispersions on a silicon wafer, which served as an indication that the enzymes enhance the build-up of layered crystal structures similar to nacre during drying - without the necessity of present LDH colloids.
A scheme of the conducted experiments *with* the use of LDH are shown in **Figure 142**. The enzyme chymosin was electrostatically deposited on the surface of the LDH colloids and a subsequent ultrafiltration step was intended in order to remove excess chymosin. Thereafter, the Chy @ LDH_{face} assemblies were mixed with casein and the dispersions were dried on a silicon wafer. Also, the dispersions were centrifuged in order to remove the excessive species, from were core-shell colloids from casein and LDH were obtained. Also, the enzyme chymosin was immobilized by a covalent bond to the LDH surface by the help of an epoxy silane, not shown in the scheme.

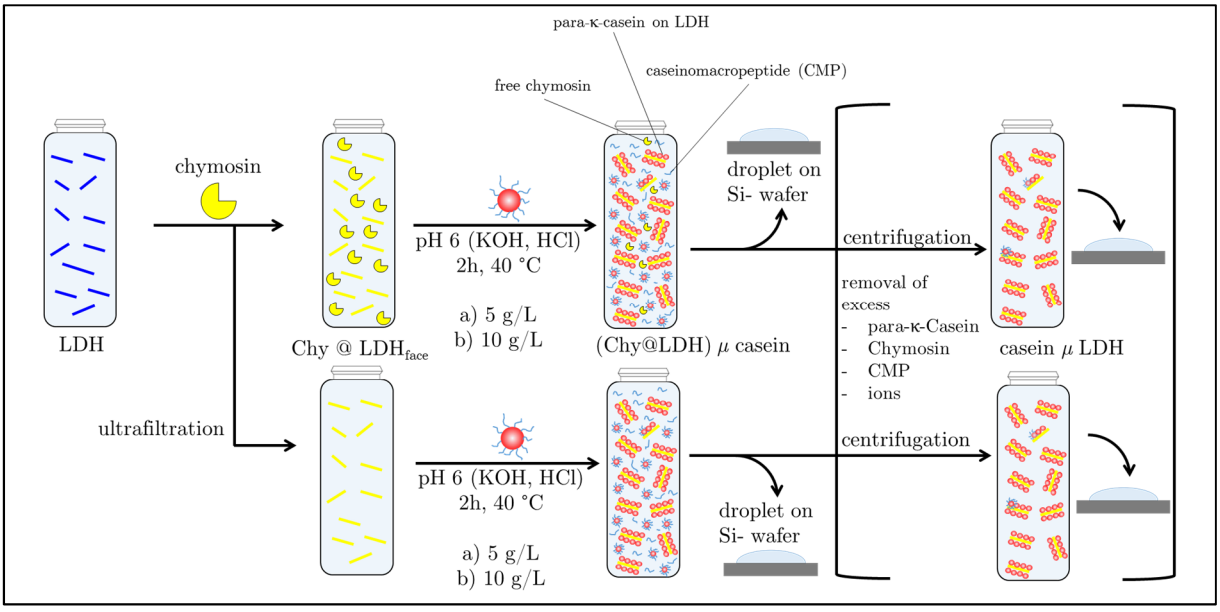


Figure 142: Scheme of examinations on the system Chy/LDH/Cas

The first step was to accomplish the electrostatic deposition of chymosin on the surface of the LDH colloids Chy @ LDH_{face}. Therefore, an isoelectric titration was conducted by measuring the ζ-potential *versus* the mass contents of LDH and chymosin, shown in **Figure 143**, *top*. Surprisingly, after the ultrafiltration of the Chy @ LDH assemblies with a 0.2 µm membrane, agglomerates of chymosin form contiguous to the LDH after drying, whereas without the ultrafiltration step, such chymosin agglomerates were not observed after drying **Figure 143**, *bottom*. Moreover, the chymosin and the Au/Pd nanoparticles from the sputter coating prior SEM imaging are similar in diameter so that it is hard to distinguish between deposited chymosin and Au/Pd nanoparticles. However, based on the ζ-potential measurements it is assumed that thin films of chymosin form on the LDH surface, moreover the intercalation of chymosin can not be excluded.

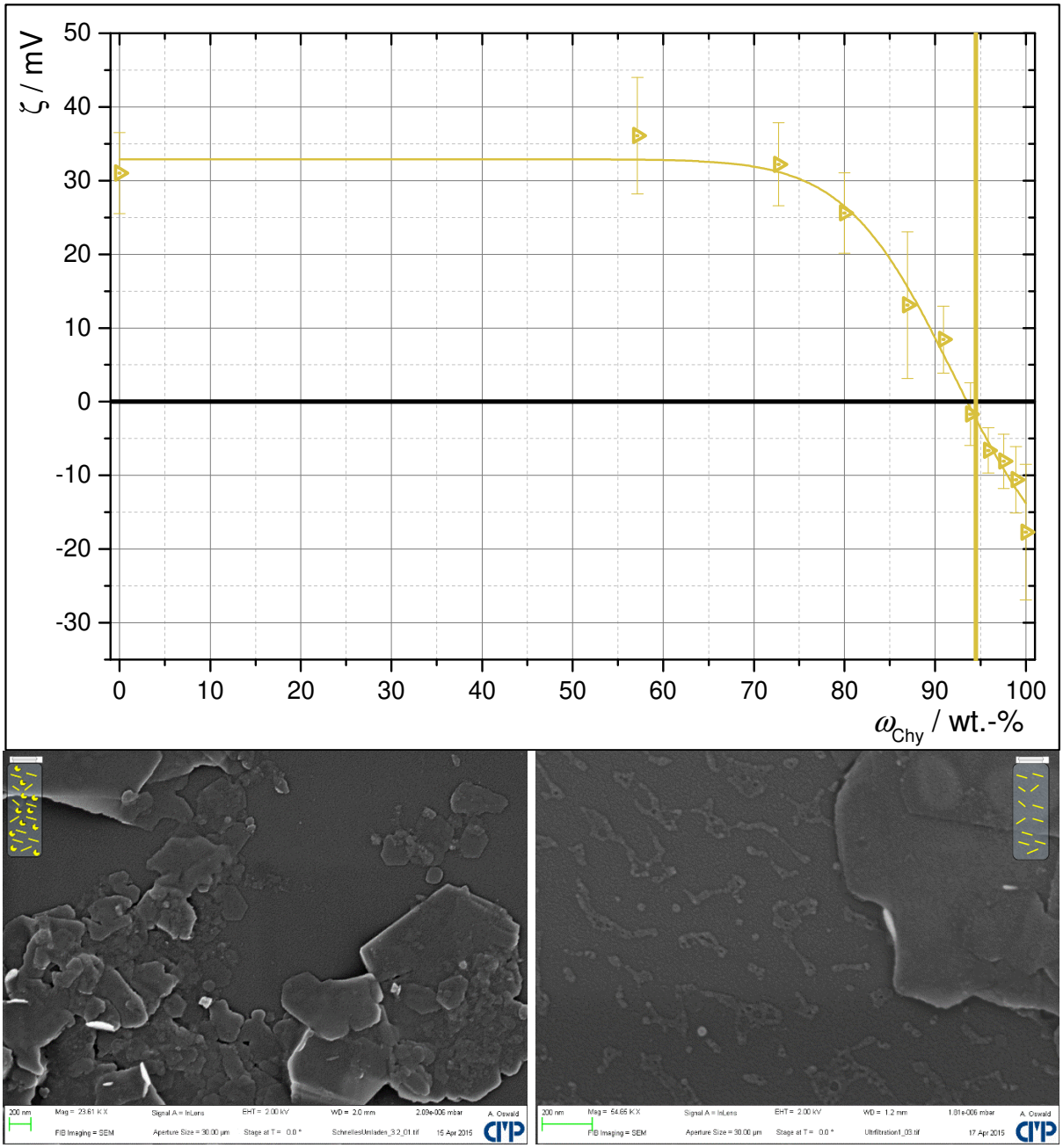


Figure 143: Isolectric titration and SEM morphologies of Chy@LDH$_{face}$ assemblies
For the isolectric titration, the chymosin concentration ω_{Chy} was 0.01 wt.-% and the LDH-NO_3 concentration was ω_{LDH} 0.001 wt.-% in water. The chymosin was added dropwise under stirring and underwent ζ-potential measurement. The line is attributed to a logistic fit which converged with R^2=0.987 and reduced χ^2 = 0.157. The straight yellow line is attributed to the used composition (not shown in experimental part)

After the cleavage reaction between chymosin and casein, the mixtures were dried on silicon wafers without any further treatment (Chy@LDH) μ casein, shown in **Figure 144** and also the mixtures that were dried on silicon wafers after the removal of excessive species Chy μ casein, shown in **Figure 145**. Without the removal step of the excessive species, pronounced dendritic crystal structures form, whereas the LDH colloids are crowded in a clod. From the SEM images it seems, that traces of trajectories of the enzymes are visible. It is assumed, that the latest mobile colloids during drying are the enzymes, since they have the smallest diameter and therefore underwent capillary assembly π in the final seconds or minutes of drying.

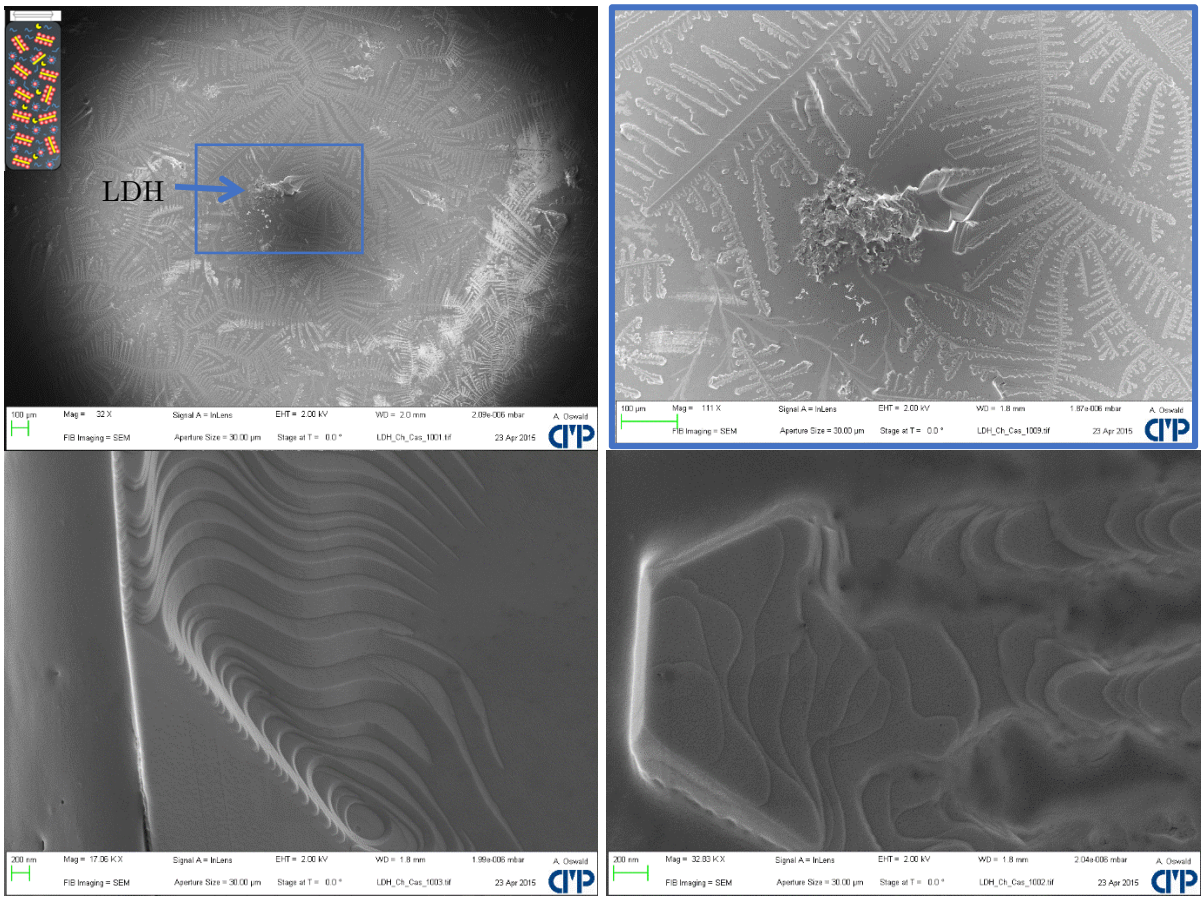


Figure 144: SEM morphology from the (Chy@LDH) μ casein system

The core-shell colloids made of (cleaved) casein colloids on LDH_{face} (casein μ LDH, **Figure 145**) are from minor interest in this chapter, since no parallel alignment was found, which was found to be true also for composite films of LDH with calcium enriched and cleaved casein (not shown herein).

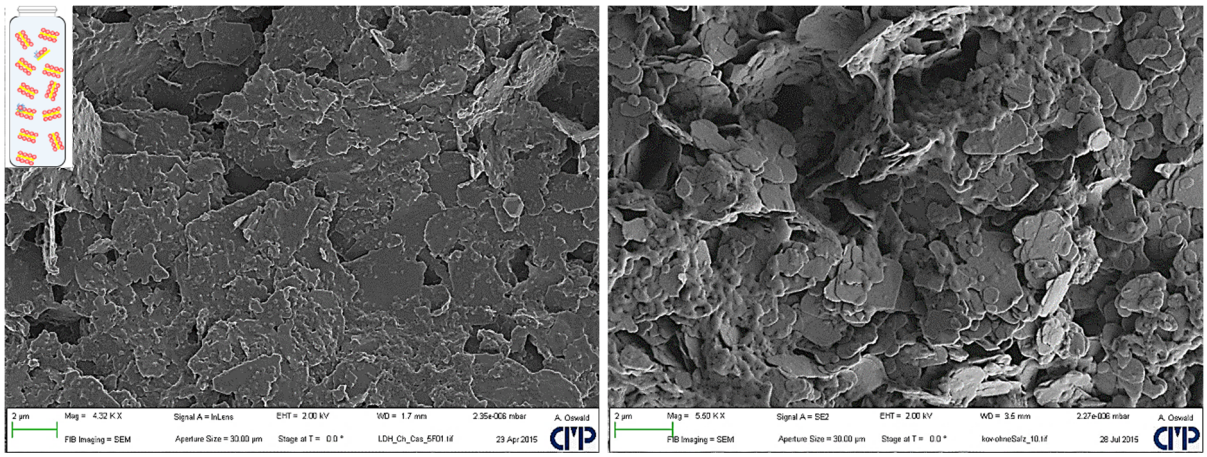


Figure 145: SEM images of casein μ LDH colloids

The *left image* shows the core-shell particles from (Chy @ LDH) μ casein, based on electrostatic assembly @ of chymosin on LDH, whereas the *right image* shows the core-shell particles from (Chy ***μ*** LDH) μ casein, based on immobilized and therefore covalently bonded chymosin by the help of epoxy-functional silane GLYMOS as a linker (Chy μ GLYMOS μ LDH).

As a reference, a mixture of chymosin and KCl was examined, shown in **Figure 146**. In the top row images, single small crystallites are shown, in the middle and bottom row images the edge of a big crystallite at different magnifications is shown. The KCl/chymosin composite crystals have a significantly different morphology compared to samples of further reference samples made of pure KCl (cubic crystallites), pure chymosin (thin coalescent films) and pure KOH (irregular crystal structures), not shown here. In the bottom images, some worm- and circle-shaped crystallites at the edges of layered terraces are shown. The layered terraces are believed to form by the movement of chymosin via capillary forces during late drying stages, described in the theoretical and central part of this work as the mechanism of the buildup of colloidal crystals. Again, when the water level during drying reaches the height of the colloids, the colloids start a collective movement.

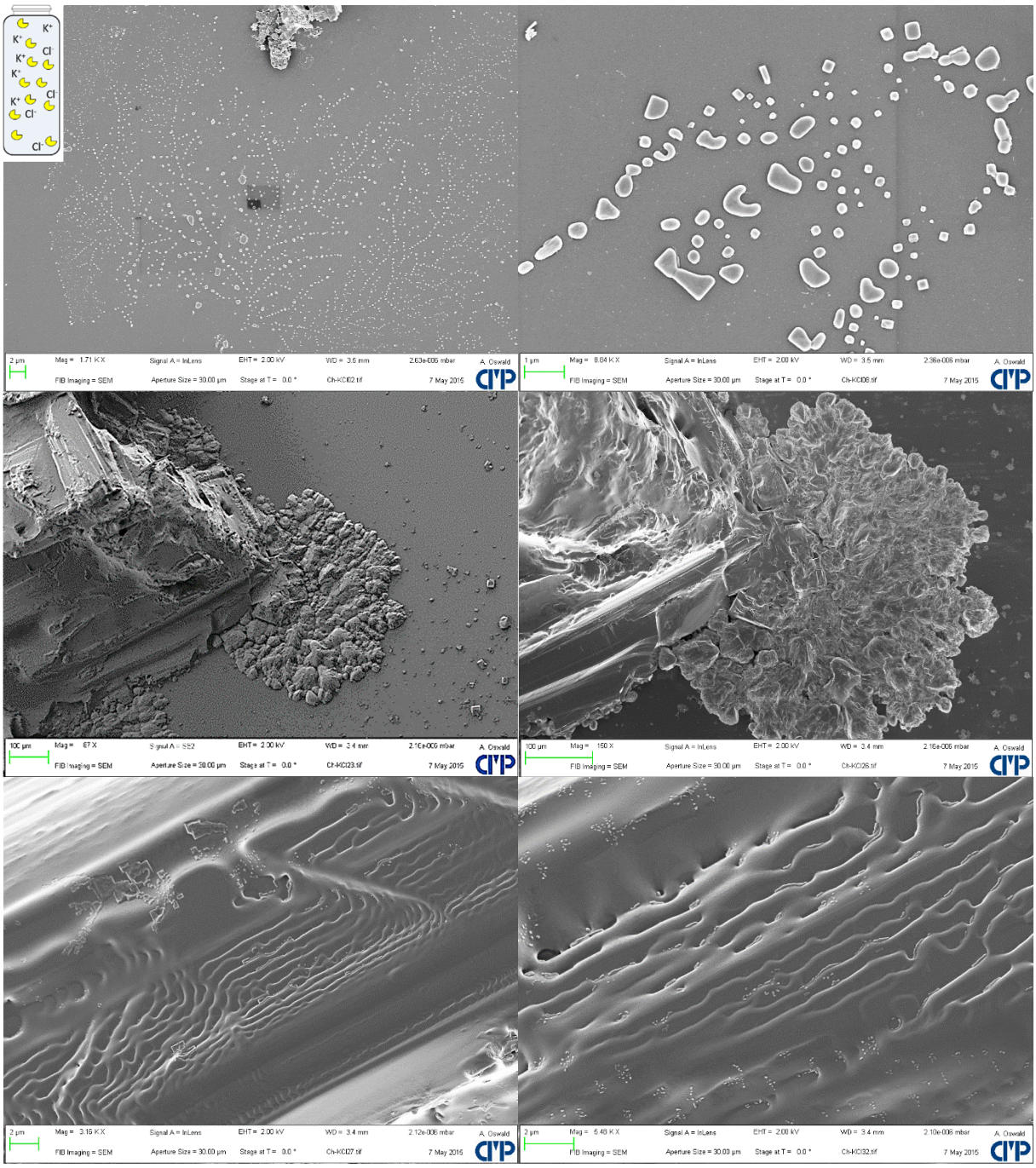


Figure 146: SEM images of the reference sample: KCl & chymosin

The assemblies emerging from non-filtrated samples based on covalent bonding of chymosin (Chy μ GLYMOS μ LDH μ casein) appear to have a remarkable organization into parallel-aligned layered crystals based on sodium benzenesulfonate (KBSA), shown in **Figure 147**. The benzenesulfonate anions BSA^- have its origin from LDH-BSA. The shown structures do not contain zinc Zn nor aluminum Al, measured via EDX spectroscopy (cf. Appendix, page 231). The EDX analysis also shows, that regions of KCl and KBSA are spatially separated.

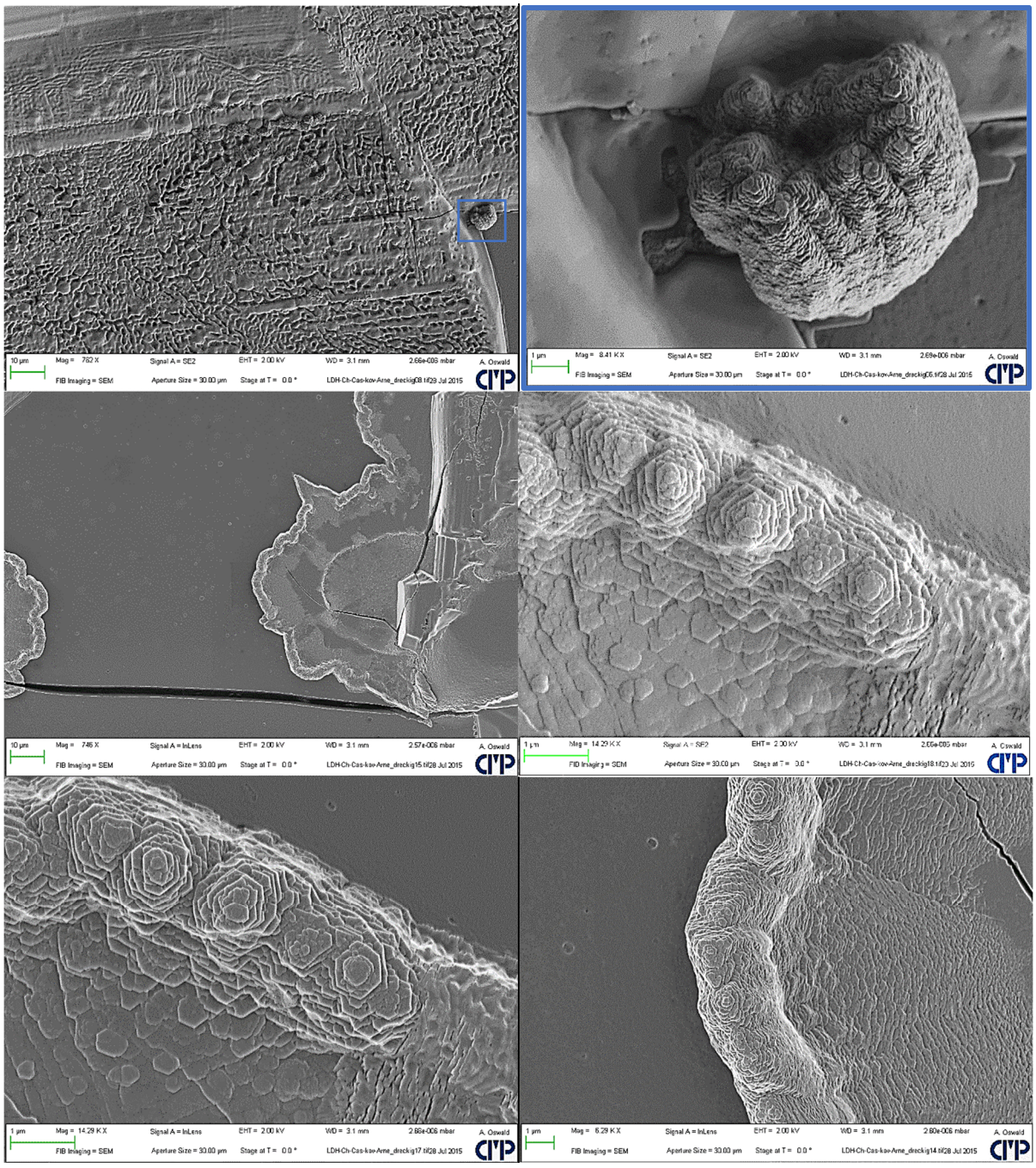


Figure 147: SEM images of composite crystals based on KBSA crystals

In the upcoming subsection, the time-dependent cleavage reaction and the resulting composite crystals *without* the use of LDH colloids are presented and discussed.

5.2.1 Experiments in the absence of LDH colloids

In the first experiments without the use of LDH, a dispersion of casein (pH 6), the enzyme chymosin (from bovine calf or Mucor miehei) and a considerable amount of other dissolved solids resulting in ≈ 85-98 wt.-% of the NVC is dried in a matrix on a MALDI[†††] target, in order to examine the casein cleavage kinetics by detecting fractures of caseinomacropeptide (CMP) molecules by "Time-of-Flight Mass Spectrometry" (ToF-MS). The samples had iridescent appearance. For the examination of the cleavage reaction, pH 6 was chosen in order to compare the structures with the LDH-based experiments. The LDH colloids dissolute strongly at the optimal enzyme activity at pH 3 - shown in **Figure 148** - so that pH 6 was chosen in order to limit the LDH dissolution which already takes place below pH 8.5 and above pH 10 – which is the range of minimal chymosin activity and ζ-potential.

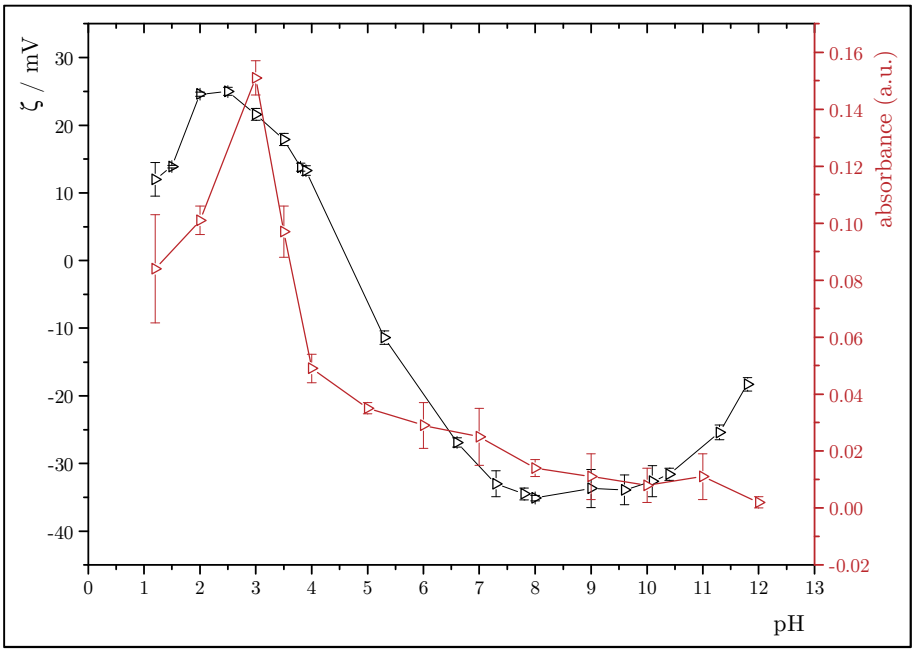


Figure 148: pH-dependent chymosin activity and ζ-potential
The data was taken from the PhD thesis of A. Rüdiger.[197] The activity of chymosin was measured via the Azo-casein method based on UV-spectroscopy and a temperature of 40 °C (red) and the ζ-potential of chymosin was measured at room temperature (black).

The ideal cleavage reaction of casein by the reaction with chymosin is shown in **Figure 149**. The amino acid sequences of the involved proteins are shown in the theoretical part (Figure **29**, page 30).

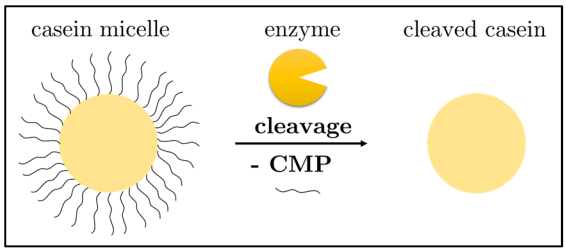


Figure 149: Ideal cleavage reaction of casein micelles

[†††] Matrix-Assisted Laser Desorption/Ionization

It is widely-known that the caseinomacropeptide CMP is part of the κ-casein molecule and after cleavage, the hydrophilic caseinomacropeptide CMP and the hydrophobic para-κ-casein remain. The MALDI-ToF-MS spectra show two major amino acid sequences of caseinomacropeptide CMP present in all mass spectra with an m/z of 885.4329 and 1156.5819 (HH+: 1157.5898):

77-83 (LPYPYYA, H+	885.4258 g/mol,	deviation: 0.08 %
134-143 (NQDKTEIPTI, HH+	1157.5908 g/mol	deviation: 0.01 %
135-144 (QDKTEIPTIN, HH+	1157.5908 g/mol	deviation: 0.01 %

The two signals starting at position 134 or 135 have identical chemical compositions. The whole CMP chain (6.8 kDa) was not detected within all MALDI measurements. The reason might be that the chymosin further cleave the CMP chains or the fact that the used commercial enzyme from calfs is mixed with other enzyme species, so that low molecular weight species are found. Other reasons could be the MALDI process or the choice of the matrix for the measurement.

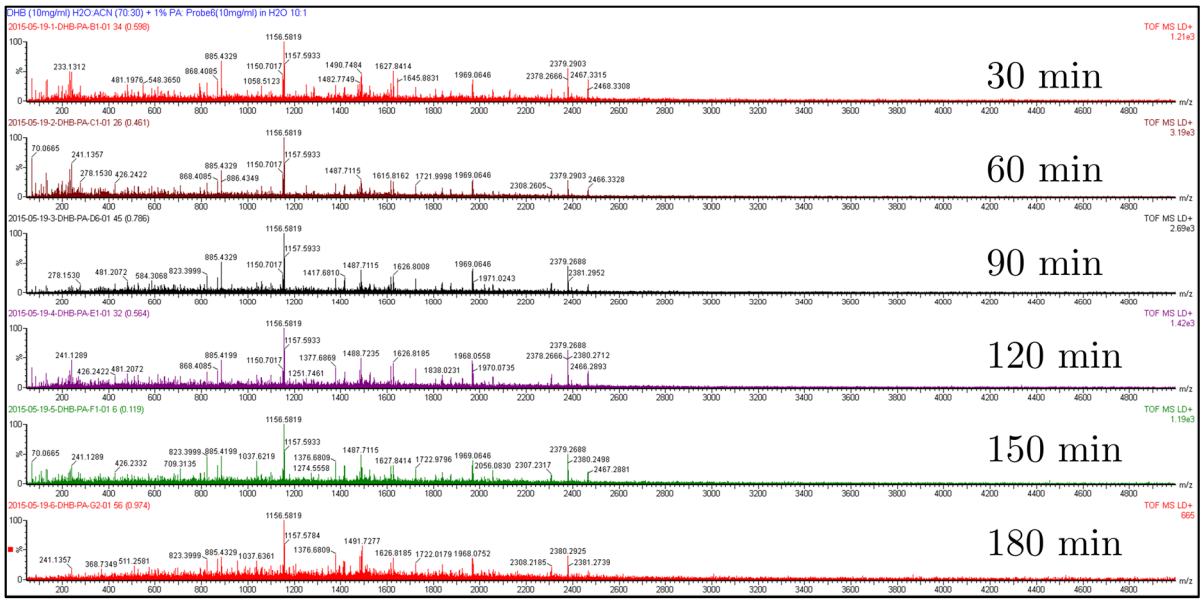


Figure 150: Time-dependent MALDI-ToF-MS results

In the top left, the used matrix is shown. The abbreviations are DHB: 2,5-Dihydroxybenzoic acid; ACN: acetonitrile; PA: phosphoric acid: Probe#: casein/chymosin and H2O: water. The duration of the laser pulse is shown in brackets, e.g. in the spectrum after 30 minutes $t = 0.598$ s, the amount of ions of the most intense signal is shown in the top right, e.g. in the spectrum after 30 minutes $1.21{\cdot}10^3$. The denotation 10:1 is the weight ratio of matrix to sample.

The quantification of MALDI-MS-ToF results to identify the presence of accessible CMP chains in the composite crystals was conducted by taking the highest intensities of the most ominant signal (1156 m/z). It is questionable to what extent the intensity of the mass spectrum signal is usable for quantitative interpretation.

Nevertheless, the emerging thicknesses of cleaved casein films (meas. AFM) by Enzyme-Mediated-Autodeposition (EMA) on glass *versus* time based on A. Rüdigers work[198] are compared with the intensity of the CMP signals of the MALDI mass spectra *versus* time and also the obtained thicknesses of composite crystal platelets *versus* time, all summarized in **Figure 151**.

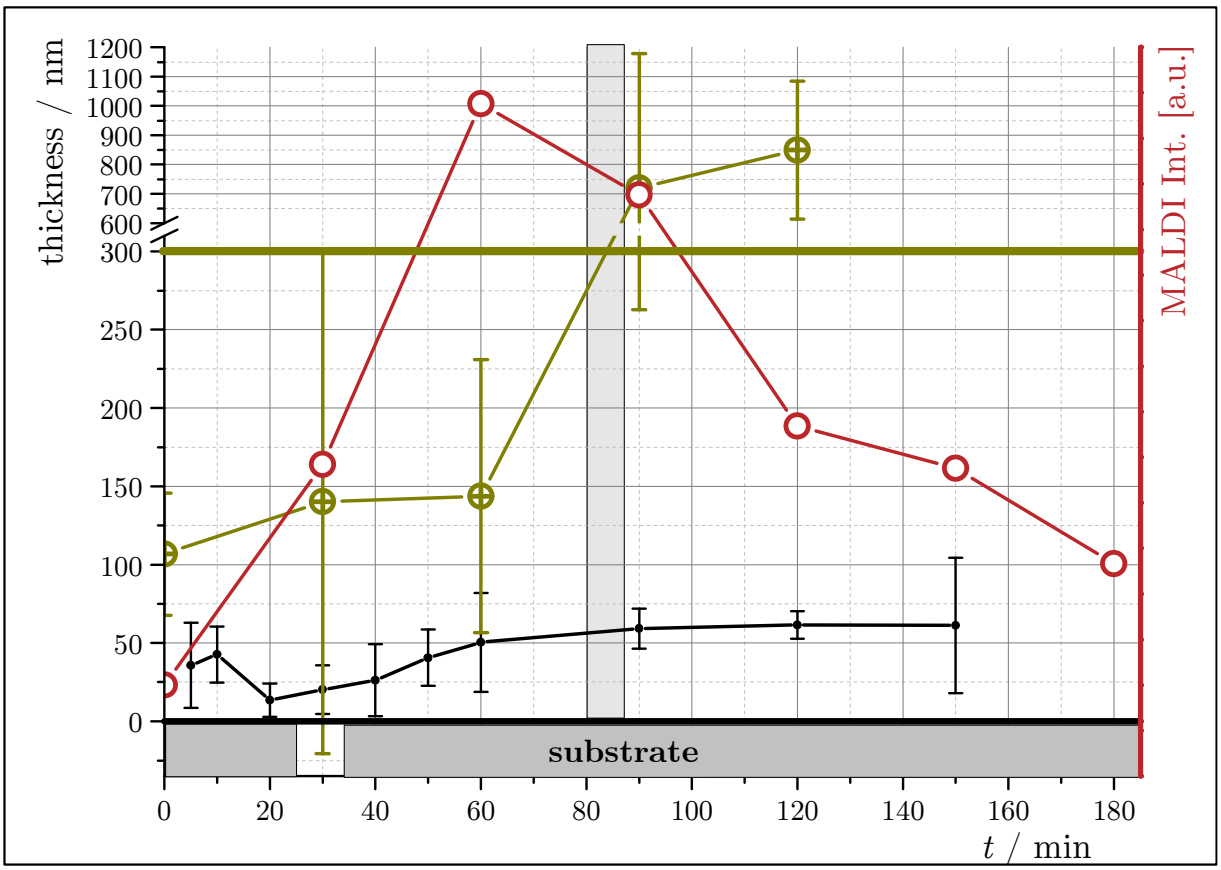


Figure 151: Summary of AFM, MALDI and SEM results

The substrate is drawn into the diagram for better visualization for the black data points. The red data points display the apparent CMP concentration based on the detected maximum intensities from MALDI-ToF-MS data. The black data points display the thicknesses of cleaved casein films by AFM measurements from A. Rüdiger. The dark-yellow data points display the thickness of KCl/protein composite mineral tablets, the dark-yellow line indicates the thickness of a mineral tablet of natural nacre with about 300 nm.

The corresponding SEM images of the underlying morphologies is shown in red-framed **Figure 152** for the MALDI-analogue samples (without the MALDI matrix materials) at low magnifications with enzymes from calfs. The composite crystals show iridescent colors after drying (shown later in Figure 165). The thickness data of the dark-yellow data points are shown in the also dark-yellow-framed **Figure 153**, based on experiments with chymosin produced by a fungus species. For both enzyme products used herein, platelet-like morphologies were found whereas the morphologies seem to be more defined for the enzyme made by fungus. The AFM-based data for the time-dependent casein film thicknesses on glass after enzymatic autodeposition correlate well with the findings from MALDI for the CMP signal intensity in KCl/casein/chymosin$_{calf}$ composites and also for the platelet thicknesses of the KCl/casein/chymosin$_{fungus}$ composites. Two reference samples have morphologies which do not resemble nacre at all after 24 h cleavage time (Appendix, page 232) and also for small enzyme concentrations (<1 wt.-%, Appendix, page 233).

In all three datasets one can see that after 60 minutes of cleavage time the amount of hydrophilic CMP chains reaches a maximum (MALDI) or resemble the behaviour of a saturation curve (emerging thicknesses from AFM & SEM), well known for enzyme kinetics. The colloidal structures resemble the morphology of nacre, albeit with partly distorted platelets but with platelet thicknesses typical for nacre.

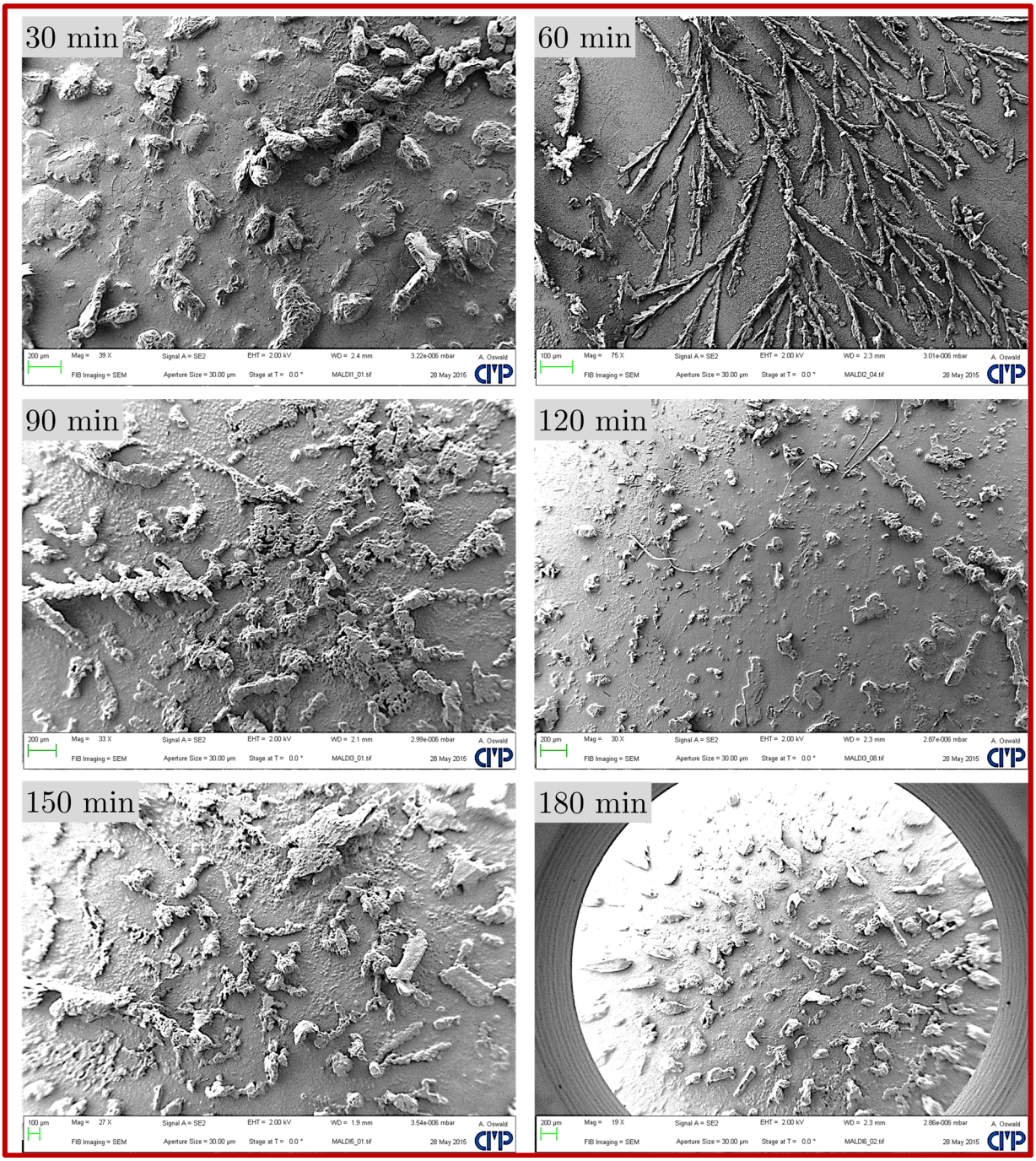


Figure 152: SEM images of KCl/protein composites without MALDI matrix

The macroscopic morphologies can surely not be compared with a continuous coating material in the classical sense. It is evident, that after 60 minutes the most pronounced dendritic structures and also the highest concentration of the acidic caseinomacropeptide CMP were found.

The microscopic morphologies clearly show increasing platelet thicknesses for decreased CMP concentration from the detected MALDI-ToF intensities. The decreased MALDI-ToF intensities can be explained with less accessible CMP fragments, because they are built into the composite crystal.

In the next subsection, the structural features and a proposal for the formation mechanism is described.

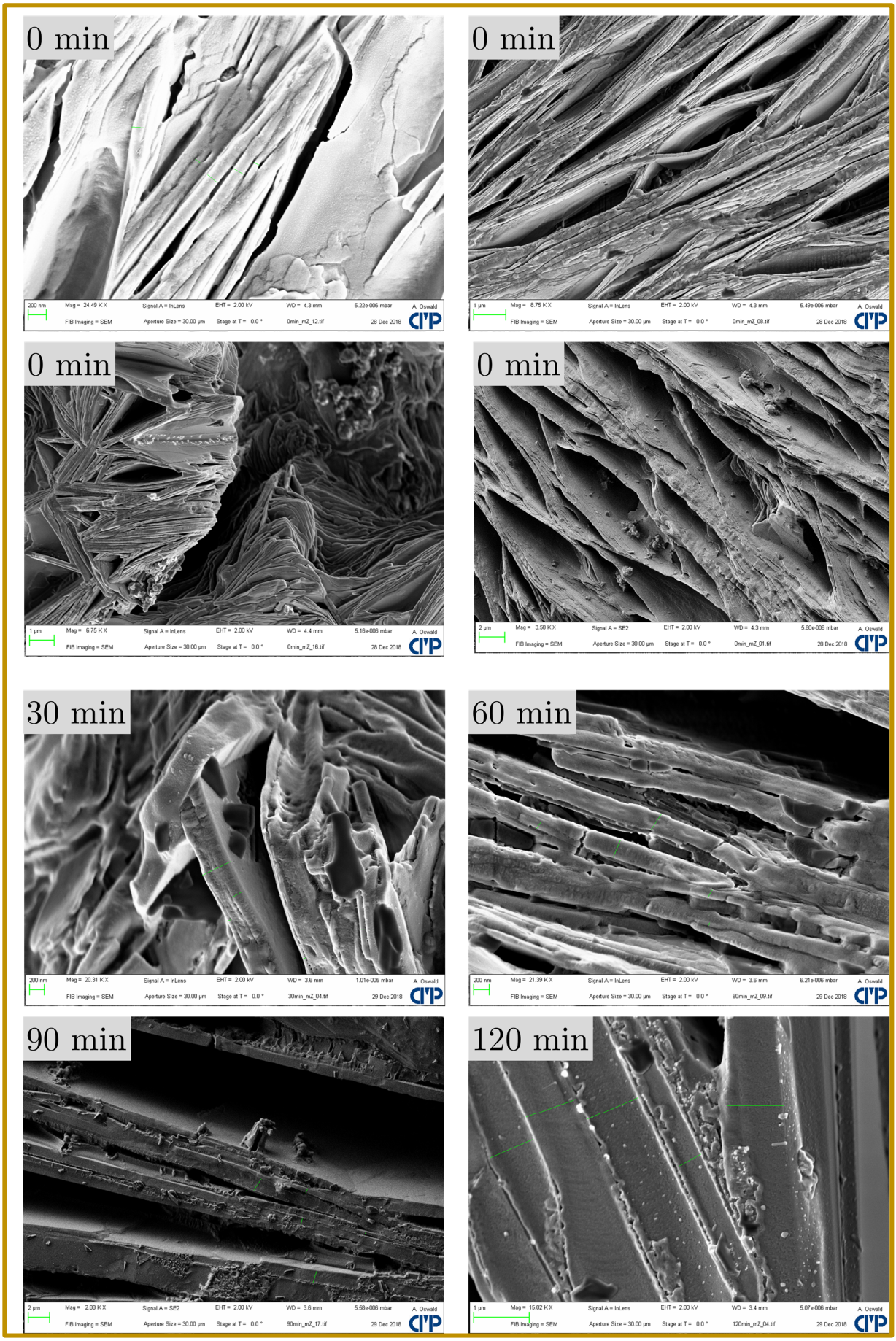


Figure 153: SEM images of salt/protein composites with chymosin from Mucor Miehei
The green lines display the thickness measurements of Figure 151.

5.2.2 Structural Features of Nacre and Formation Mechanism

There is a vast amount and variety of literature about natural nacre of different organisms in the field of biology, moreover, in the field of materials science about approaches to mimic nacre with other materials, such as polymer/layered silicate nanocomposites and also about cheese-making by different food engineering approaches. This subsection will comprehend the data of literature references with different emphases into a mutual framework on the topic of producing artifical nacre. The obtained structures have astonishing similarities to naturally occuring structures, shown in **Figure 154** for the border cases of terraced and towered nacre and also the hierarchical levels in **Figure 155**.

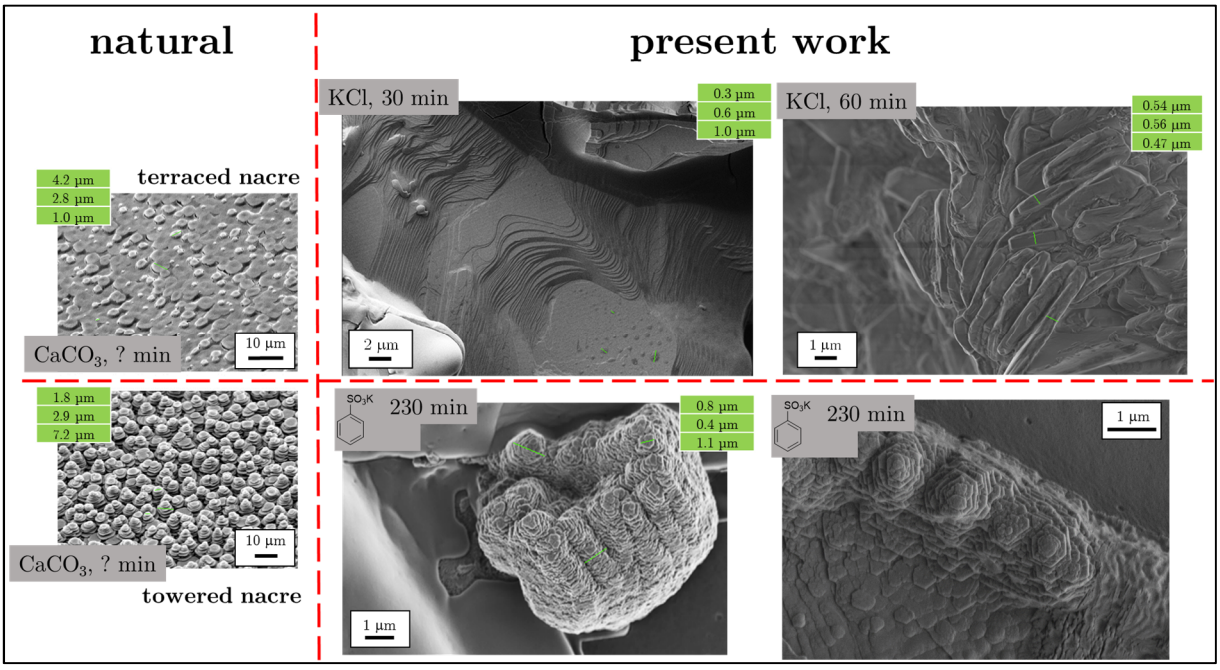


Figure 154: Terraced nacre vs towered nacre
The green lines in the images represent the data with green backgrounds. The left hand images were taken from the literature[199]

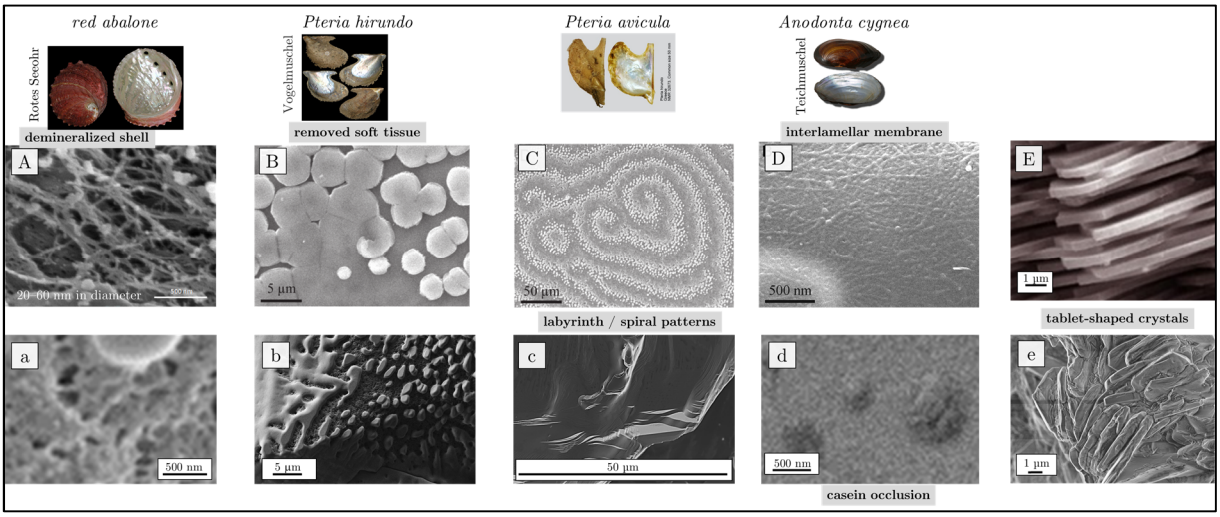


Figure 155: Structures of natural *versus* mimicked nacre on different hierarchical levels
The top row is from natural nacre. Image **A** is from Lopez et al.[200], **B, C** and **D** are from Cartwright et al.[97] and **E** is some typical image of nacre tablets. The bottom row **a-e** are all from the experiments conducted herein. More detailed images are shown in upcoming figures.

As a preliminary point, the already introduced mechanism from the literature[196] would change to the following if one accepts KCl/casein/chymosin as a proper model system for the growth of nacre:

“

1. **The cleaved silk phase** *is a* **hydrogel** *that pre-fills the space to be mineralized.*
2. *The chitin is the ordered structural phase that ultimately dictates the orientation of the mature crystals.*
3. *The matrix components are spatially differentiated.*
4. *The first-formed mineral is transient colloidal amorphous calcium carbonate (ACC).*
5. *Nucleation occurs on the matrix, and the crystal grows at the expense of the ACC phase.*
6. *During this growth phase some of* (**un)cleaved silk protein colloids** *are occluded into the crystal* **and undergo further cleavage.**

“

Moreover, the control over the growth by cyclic patterns as an excitable medium[97] herein are not parallel-aligned but emerge into different directions and have other sizes compared to nacre, merely because the underlying non-equilibrium system is a drying droplet and the growth is not controlled by an organism (**C** vs **c** in Figure **155**; image **c** is shown in more detail below, cf. Figure 162). Organisms producing nacre have chambers with fluids containing the silk and chitin. The growth happens more or less fenced from the surroundings.[200] More details on the topic of cycles and replicative building units is provided in the theoretical part (page 26f).

The cleavage time of the enzyme after which the samples are dried on a silicon wafer lead to tablet-shaped crystals with increasing thicknesses (cf. **Figure 156**) and after a longer period of time (e.g. 24 h), the nacreous structures were not found anymore.

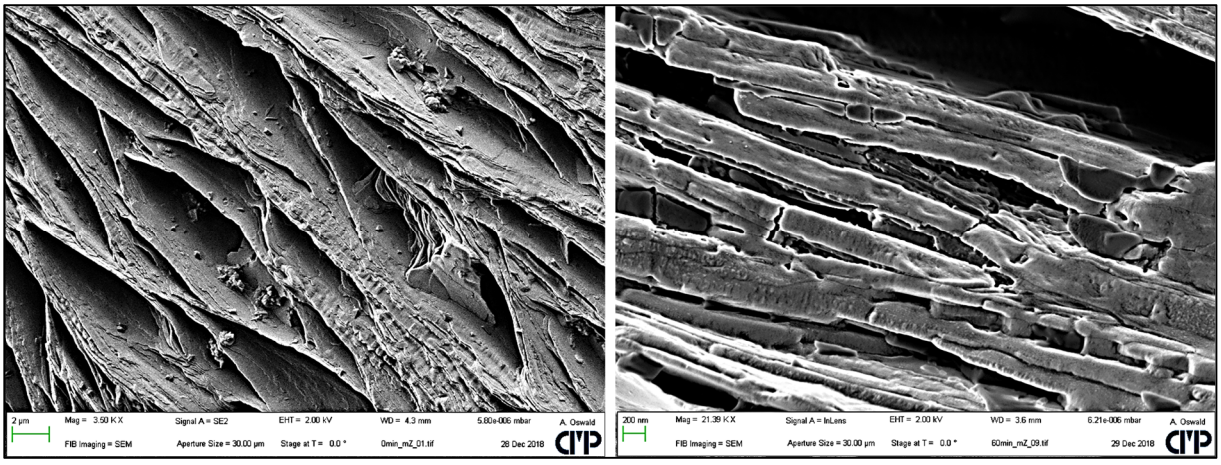


Figure 156: Time-dependent tablet-thicknesses: 0 *versus* 60 minutes cleavage time

Again, the formed structures were examined in dependence of the time the proteins undergo cleavage-reactions. Every 30 minutes of the enzymatic cleavage reaction, a small sample is taken and KOH was added, the sample was centrifuged to remove highly cleaved residues (primarily hydrophobic casein micelles) and a droplet of the supernatant was applied and dried at r.t. on a silicon wafer.

During drying, the coagulation and crystallization of all ingredients (cf. **Table 27**) at different local interfaces, local concentrations, length & time scales leaving structures of different growth states on one single sample at different locations. Strong capillary forces are known for inducing collective movement of colloids during drying, as pointed out in the thesis. The colloids undergo an assembly process leading to closely packed colloidal crystals. The capillary forces have the highest impact on the colloids, when the water level is close to the colloid diameter. In the following, the ingredients, its characteristics and impacts are discussed in more detail.

The structure of caseinomacropeptide (CMP) is from central interest. In many publications, the mimicking of nacre is examined with acid-rich synthetic polymers like linear polyacrylic acid and its carboxyl functions[201], because the literature about nacre identifies the carboxylic acid groups as central functional parts of the organic matter in nacre.

Table 27: Solubilities/dispersibilities of reagents

		solubility/dispersibility at 20 °C / g L^{-1}	diameter / nm
potassium chloride	KCl	347	< 1 nm
casein	Cas	30-50 [197]	50
caseinomacropeptide	CMP	10 [202]	12
para-κ-casein	*p*-κ-Cas	≈ 0	polydisperse Cas: nm to µm
chymosin	Chy	unknown (high)	6 nm

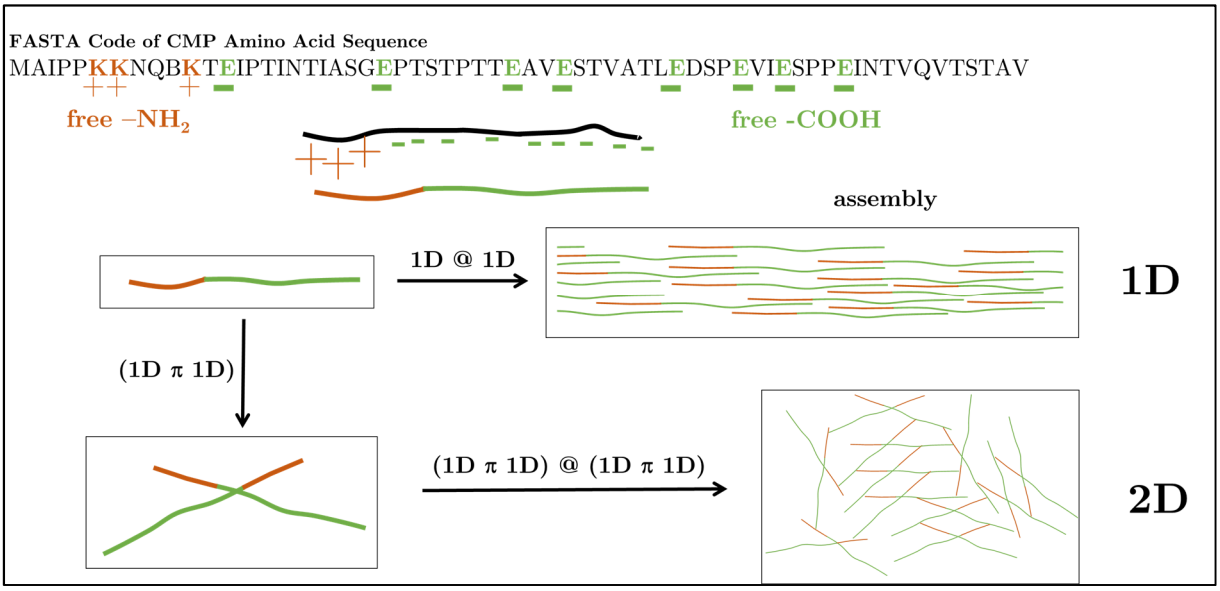


Figure 157: Schematic representation of the postulated border cases of CMP gelation
The occurrence of dimeric (and no monomeric) forms is based on Farías et al. findings [202]

The caseinomacropeptide has hydrophobic parts (e.g. isoleucine, I), free amino-groups (from lysine, K) and free carboxyl groups (from glutamic acid, E), which have an impact on the gelation behaviour of CMP. In **Figure 157**, the amino acid sequence of CMP and the postulated border cases of the CMP gelation are presented. The association of hydrophobic parts by capillary assembly π and hydrophilic parts by electrostatic assembly @ form a 3D hydrogel network made of CMP chains. The gel formation of CMP is suggested to proceed fast, due to comparably high mobility of CMP compared to casein. The matrix of natural occuring nacre (*Pinctada maxima*) was decalcified in a publication, wherein one main glycoprotein with an apparent molecular weight of 20 kDa was discovered.[203] The caseinomacropeptide (CMP) is also a glycoprotein and has a theoretical molecular weight of 6.86 kDa, whereas the uncleaved precursor κ-casein has a theoretical molecular weight of 21.27 kDa, both without attached carbohydrate groups (no glycosylation).
The detection of CMP can be done in different ways. For example, the detection via SEC (Size Exclusion Chromatography) at different pH after filtration lead to different signals.[204] In the study, no observed signal for < 13 kDa was detected. Signals at 20.3 kDa (pH 3.5) and

17.5 kDa (pH 7) were detected. Electrophoresis measurement with SDS-PAGE (Sodium DodecylSulphate - PolyAcrylamide Gel Electrophoresis) analysis revealed that CMP appears in tetrameric (35 kDa) and dimeric fractions appeared as 18-kDa protein bands.[205] The dimeric form (at pH 3) is resistant to separation to CMP monomers by SDS-PAGE. It seems that the CMP monomers are tightly associated to dimers and monomers hardly exist, maybe exist not at all. At pH 6.6, only the tetrameric form is present. ANS-binding (1-Anilino-8-Naphthalene-Sulfonate) experiments revealed, that the tetrameric form of CMP is more hydrophobic than the other associates. The study further suggests, that the high apparent molecular weight is attributed to hydrophobic peptide sequences and/or high hydrodynamic diameters, instead of the initial assumption, that the glycosylation of the CMP chains gain the weight.[205] However, within the CMP hydrogel, uncleaved casein micelles are considered to be trapped by association. The protein-matrix assisted crystal growth is assumed to start with the buildup of loose gels of CMP after its cleavage from κ-casein which is one of the four proteins in casein. The local critical conditions are correlated to the bulk solubility of the components. The ions around the CMP interface begin to form nucleation centers at local critical conditions.

Potassium chloride KCl has the highest solubility of the ingredients in water, whereas the solubility of KOH is approx. 3-fold. With respect to the present experiments it can be assumed that within the hydrogel, nucleation centers of KCl crystals are formed more easily than in the bulk region of a drying water droplet. Moreover it is known, that KOH builds irregular crystals.[206] Due to the addition of KOH, the colour of the dispersion change from white to transparent, because the CMP chains are deprotonated, and K^+ ions may remain near the CMP chains. The CMP gelation during drying may lead to local nucleation at locally high concentrations of KCl during the evaporation (cf. Hofmeister series and the topic extraction of proteins. The major drawback of the "salting out" method for protein extraction is the residual salt in the products[207]). In late stages of the water evaporation, the water film level at the surface and at all involved interfaces becomes lower, so that the capillary assembly can act on the colloids, whereas the smallest present colloid, again, is chymosin.

The agglomeration of chymosin should therefore take place in the very end and could lead to enhanced mobility and therefore activity. In foregoing studies within our working group, the highest enzyme activity is at the same pH, where the electrophoretic mobility is highest[197] (cf. Figure 148). The corresponding pH of these studies is 3 and are measured in the bulk phase, whereas within the present consideration the capillary assembly induce the high mobility and may also enhance the activity, so that cleavage rates in the very end of the drying process increases strongly. It is moreover known that chymosin Chy can also cleave α_{S1}-casein[208] or α_{S2}-casein[209] and β-casein[210]. Moreover, the used commercial enzyme from calfs also contains pepsin, which is also known for cleavage of β-casein, for example.[211,212]

From the collected findings, the mechanism of the growth of KCl/protein composites from drying droplets are illustrated in **Figure 158** and formulated as follows:

I. protein-matrix assisted crystal growth by CMP gels providing cavities for the crystallization of KCl, leading to a CMP/KCl composite
II. occlusion of cleaved, partially cleaved and uncleaved casein micelles into cavities of the CMP/KCl matrix by the aid of the enzyme chymosin (and other enzymes), moving with comparably high velocity during the drying process and thereby enhancing the occlusion, maybe with CMP as a lubricant.

The occurrence of *ion channels* during the nacre growth[200] could actually be also *enzyme channels*, wherein mainly the capillary assembly π, but also the electrostatic assembly @ and the chemical assembly μ lead to concerted actions of enzymes (or

enzyme mixtures) within the mineral/protein composite during growth. Moreover, in case of bovine casein, the κ-casein is glycosylated,[213] meaning there are carbohydrates covalently bonded to the proteins which may further act somehow on the mineralization process (such as chitin in the case of molluscs[214]). Therefore, the often-mentioned "acidic glycoprotein" in the context of nacre growth may moderate the formation of chitin-containing rods.[97,215] Herein, in case of calf-based chymosin, the rods seem to form lamellae, shown in **Figure 159**, whereas such structures were not observed if chymosin from Mucor Miehei was used.

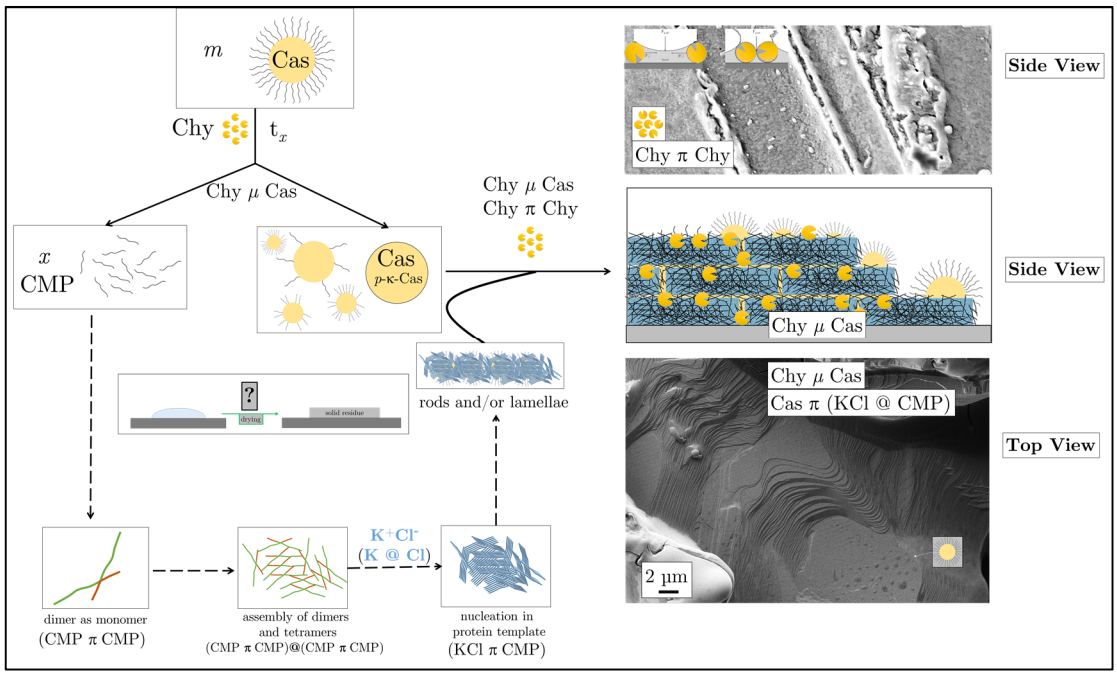


Figure 158: Postulated mechanism of nacreous growth
μ-2D...3D < π {3D @ [(μ-1D π μ-1D) @ (μ-1D π μ-1D)]} > **π 2D$_{inf}$**

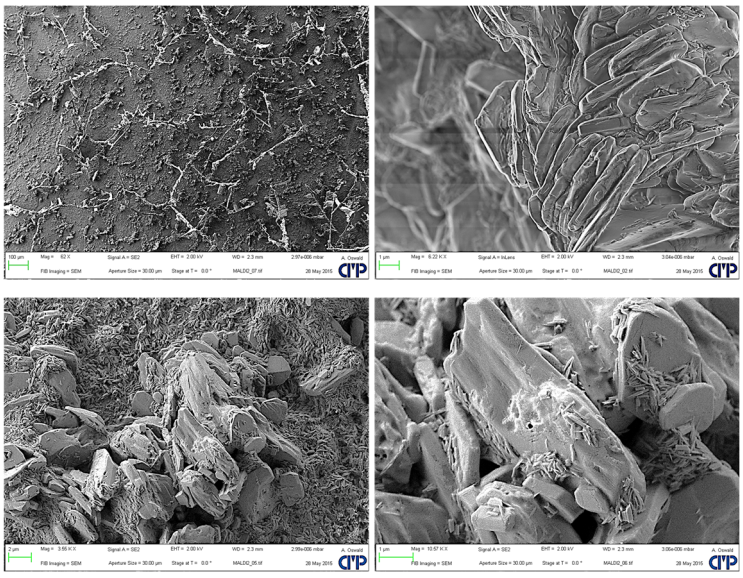


Figure 159: SEM images showing *Platelets from Rods*

The reported "long thin needle crystallites" in nacre, consisting of β-chitin which have diameters of 20-30 nm and hundreds of nanometers in length[97] resemble the here shown rods, having diameters of 50 to 150 nm and 500 nm length. Certainly, the polysaccharides bonded to bovine casein are not made from chitin. Also, bovine caseins are usually phosphorylated, whereas herein, dephosphorylated casein was used so that no definite statement on the role of the

glycosylation can be made, except that glycoproteins, such as κ-casein in bovine milk, are widely known to have a variety of functions in organisms.

On the following pages, some more of the structural features of nacre in the present model systems are shown. The occurrence of asperities and mineral bridges are well-known structural features of nacre and for the present system these features are shown in **Figure 160** and were already visible in Figure 153. The mechanism behind the formation of these asperities and mineral bridges might arise from the occlusion of protein into the mineral/protein composite, shown in **Figure 162**. A summary of findings by Cho et al.[216] on the occlusion mechanism of synthetic copolymer micelles into $CaCO_3$ crystals via in-situ AFM (among other techniques) is shown in **Figure 161**, whereas corresponding SEM images of not occluded proteins within this work is shown in **Figure 163**.

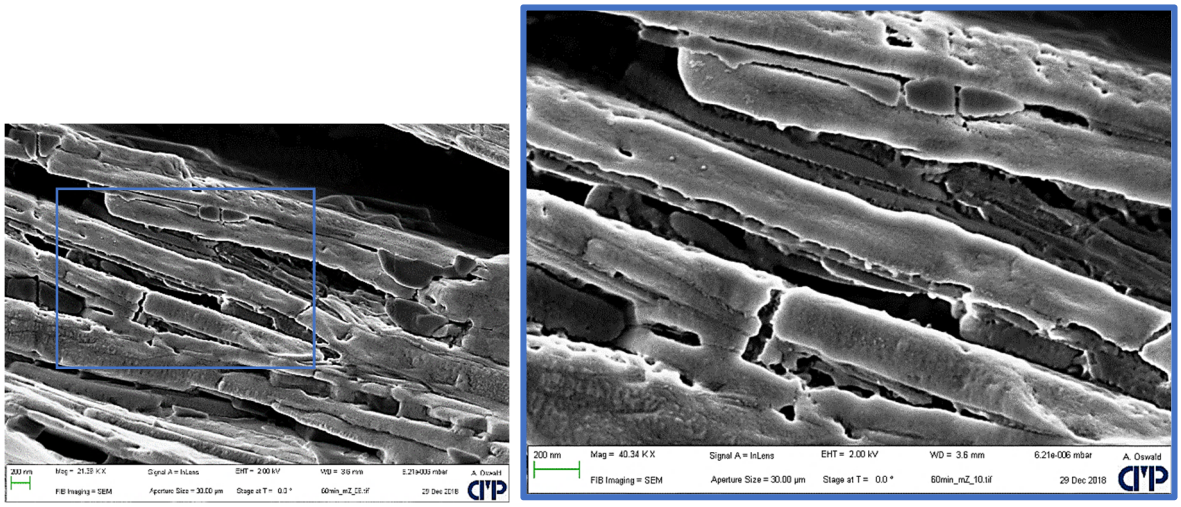


Figure 160: SEM images showing the structural feature *asperities & Mineral Bridges*

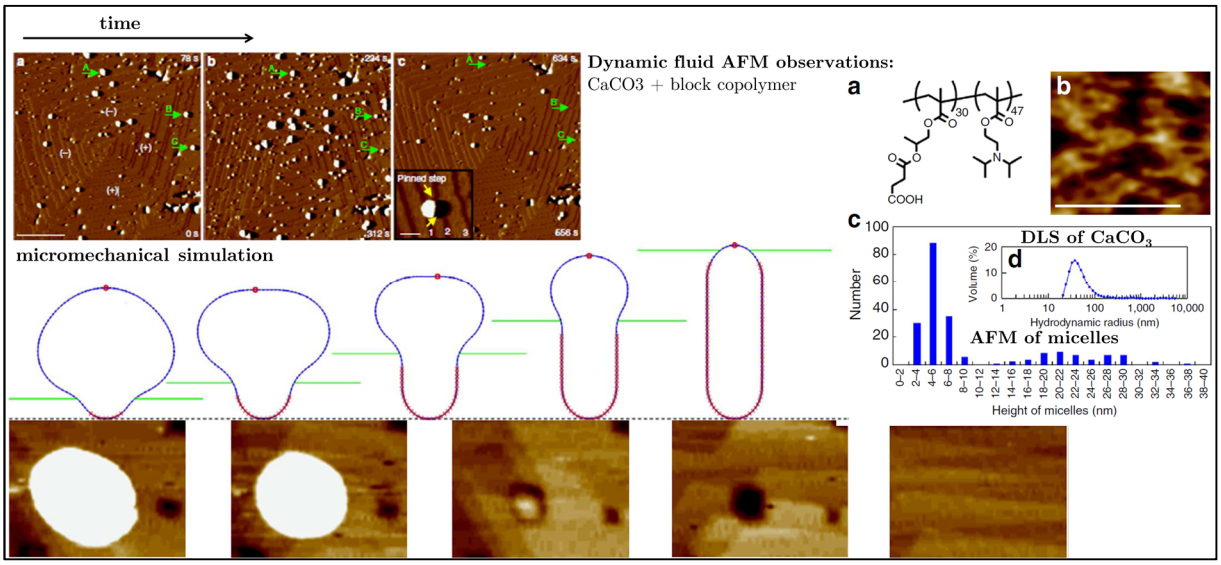


Figure 161: Simulation, AFM and DLS data on the *occlusion mechanism* with synthetic copolymer and $CaCO_3$ *"Both the micelle diameter and height decreased with the passage of each step as the micelles were gradually entrapped"*[216]

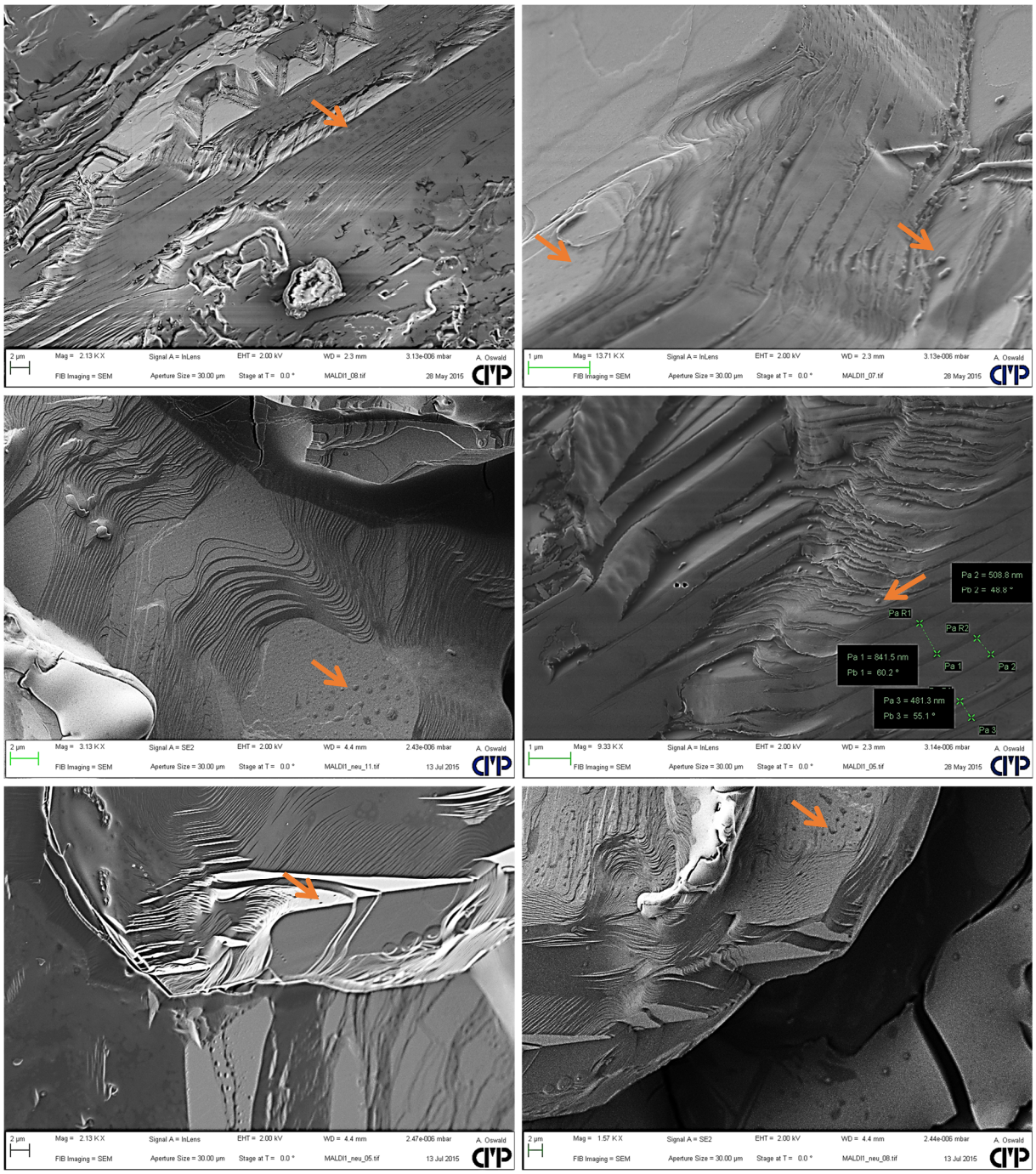


Figure 162: SEM images after 30 minutes cleavage time with bovine calf rennet

In all images, micelles of casein are visible on the surface of the KCl/polymer composite crystals in the *not* occluded, *partly* occluded or *occluded* state, cf. Figure 161.

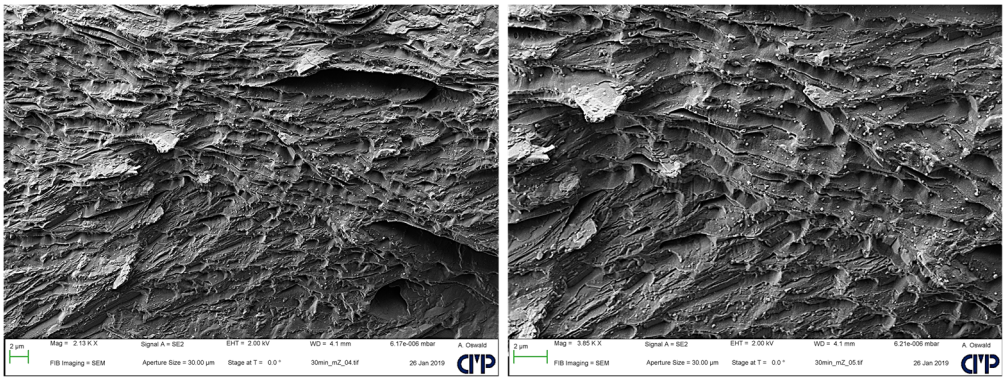


Figure 163: SEM images showing the structural feature of *not occluded protein micelles*

5.2.3 Thoughts on applications of synthetic nacre

The most promising feature speaking for the large-scale production of artificial nacre is the chemical formula of the main component $CaCO_3$, based partially on CO_2 absorbed by the thereby acidified oceans. It is thinkable that 3D printed negative forms of a desired structural component could be immersed into the oceans, making a carbon capture farm. The state-of-the-art already allows for such a technique in lab-scale for rectangular specimens by the use of chitin powder as a precursor (cf. **Figure 164**).
The material could be used for traditional uses such as a **filler for paints** after milling of the formed pieces, so that the actual quality of the artificial nacre in terms of mechanical characteristics is not that important. However, the aspiration for high-quality nacre in terms of mechanical performance could be reached by the use of the present model system based on cheese-making enzymes or similar proteins at ambient temperatures instead of the use of polyacrylic acid and silk fibroin infiltration at 80 °C. Then, the so-formed artificial nacre can be used as a **construction material**.

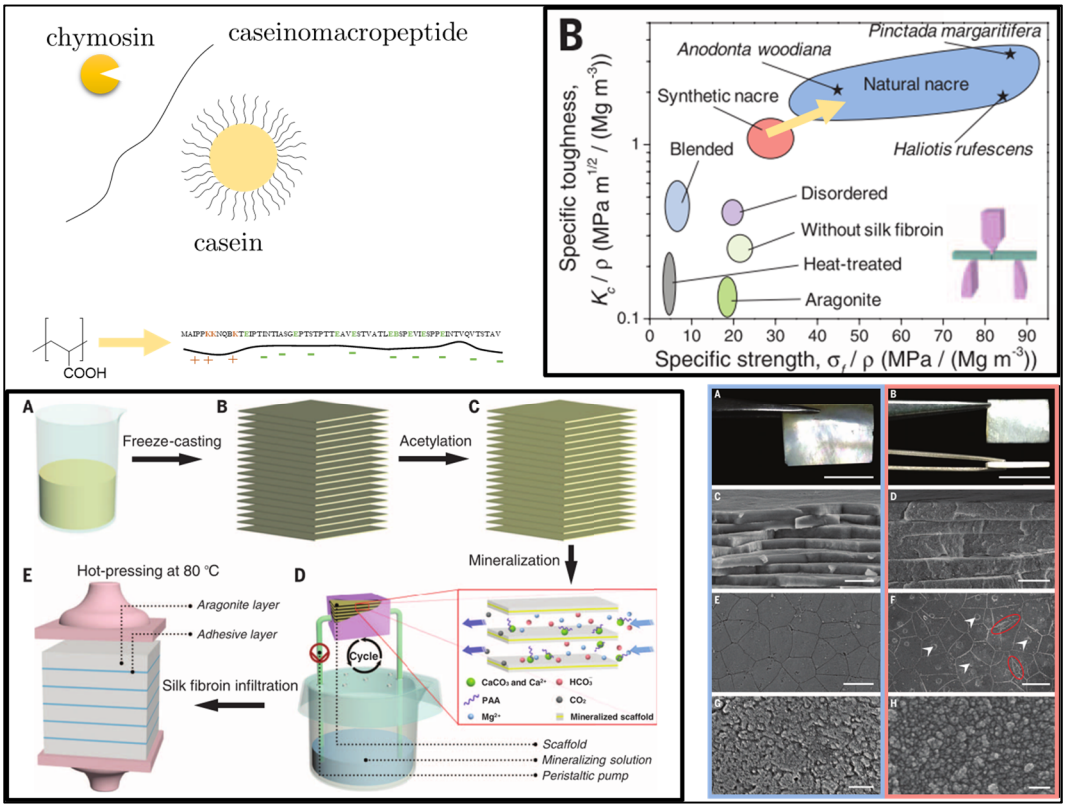


Figure 164: Synthetic nacre by biomineralization in a negative form
The figures and illustrations were taken from the literature (Mao et al.)[217] and are edited by the cheesemaking proteins in yellow.

Utilizing the so-formed carbonate in the oceans in large amounts and form artificial nacre would allow vast amounts of **CO_2-uptake** to take place and may also help to de-acidify the oceans in the long-term. The economic, environmental and ecological impacts in sum then decide over the extent of the implementation of this "CO_2-uptake by artificial nacre" technology, maybe ending up in the rather undesired storage of massive blocks of unused material, if the mechanical characteristics are insufficient.
Another way to use nacre as a high-tech material could be the **medical use**. Nacre appears to be a convenient material for treating bone deficiencies. *In vitro* experiments indicate the

compatibility of bone and nacre by Lopez et al (1992)[218]. Consequently, *in vivo* studies of nacre implants in human bone for 6 months show a perfectly tolerated composition (Lopez et al (1997)[219]). The interfacial anchoring between bone and nacre in a sheep after 10 months was also demonstrated by Lopez et al (1999)[220]. One could therefore use the artificial nacre for the tailored construction of screws, rods, plates or any other structure instead of titanium or other materials, coming with drawbacks such as intolerance and high cost.
One of the most obvious applications is **jewelry**, because of the charming appearance of nacre, which was also found for the present model system, shown in **Figure 165**. Therefore, the artificial nacre approach may also allow for the construction of sculptures or other kinds of **art objects**. Moreover, by changing the $CaCO_3$ matrix and use other components, even higher strengths or modified optical effects are achievable.

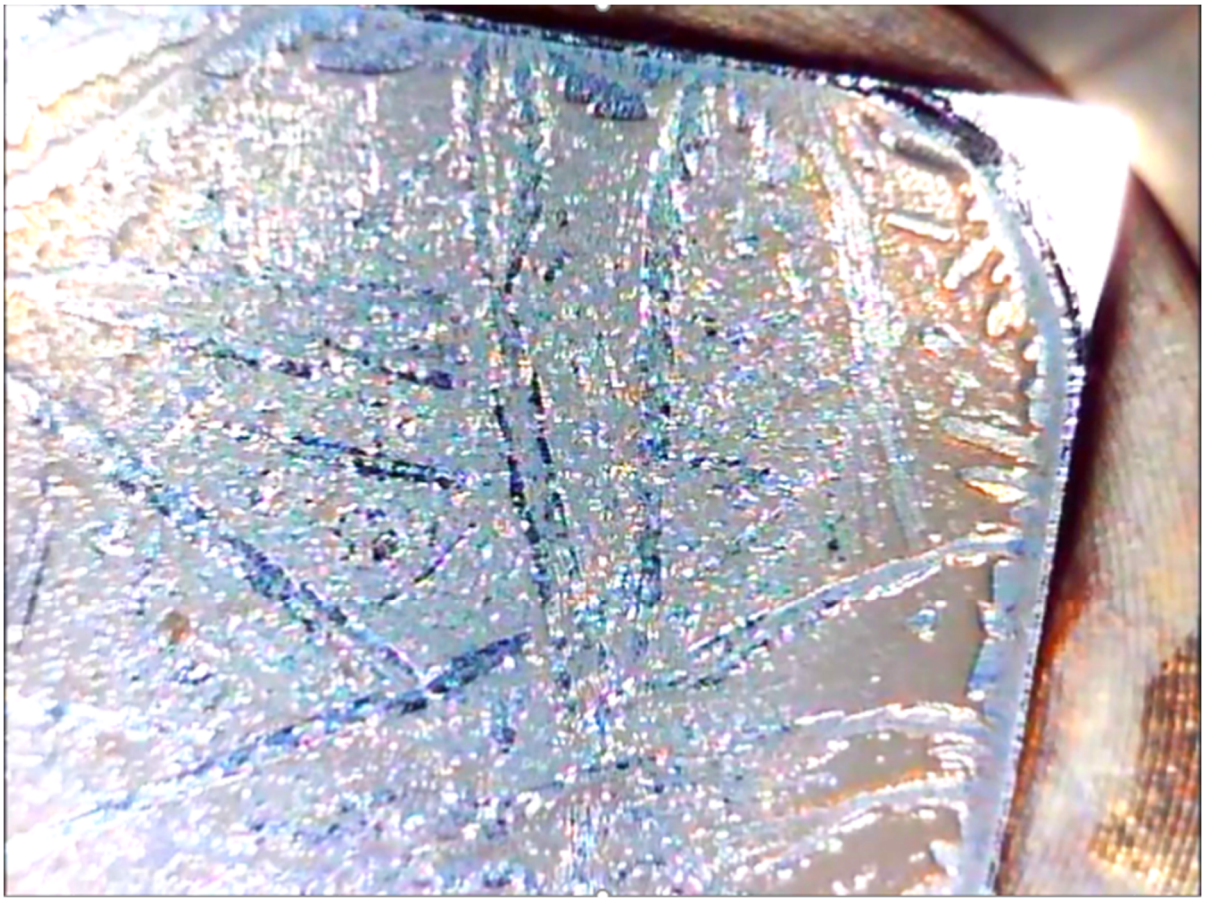


Figure 165: Digital microscope image of dried salt/protein composite on a silicon wafer

As a proposal for the application of artificial nacre is the use as a **symbiotic ship coating**, illustrated in **Figure 166.** It may seem pretentious or pathetic to use the term "symbiotic" in this context, so that in the following some thoughts based on this idea are summarized by stretching the definition of a living system. The defensive symbiosis[221] of such a ship coating in this context imply a host, a symbiont and a common enemy. The host would be the ship, the symbiont would be the living coating and the common enemy would be any fouling organism. It is thinkable that bacteria or fungi can be used in order to form the necessary proteins for the self-repair of the coating. Therefore, the microorganisms can be located at the dock or in a laboratory on board of the ship with tubings supplying the needed proteins for the self-repair or even a multilayer coating, so that an engineered biofilm directly beneath the coating supplies proteins. The last option would need systems like a cooperative community of bacteria[222] and a control over the forming of a biofilm[223], both being recent research topics.

For the most simple approach of a rather dead ship coating, the thickness of the coating could be controlled by a foil, which restricts the growth and removed after completion of growth. It was found that the structure of nacre can act as a thermometer of the oceans temperature[224], therefore leading to the more general conclusion that the formation of nacre can also be controlled by temperature, thus time and quality of the coating can be controlled. However, to make this vision true, more research on this topic has to be made.

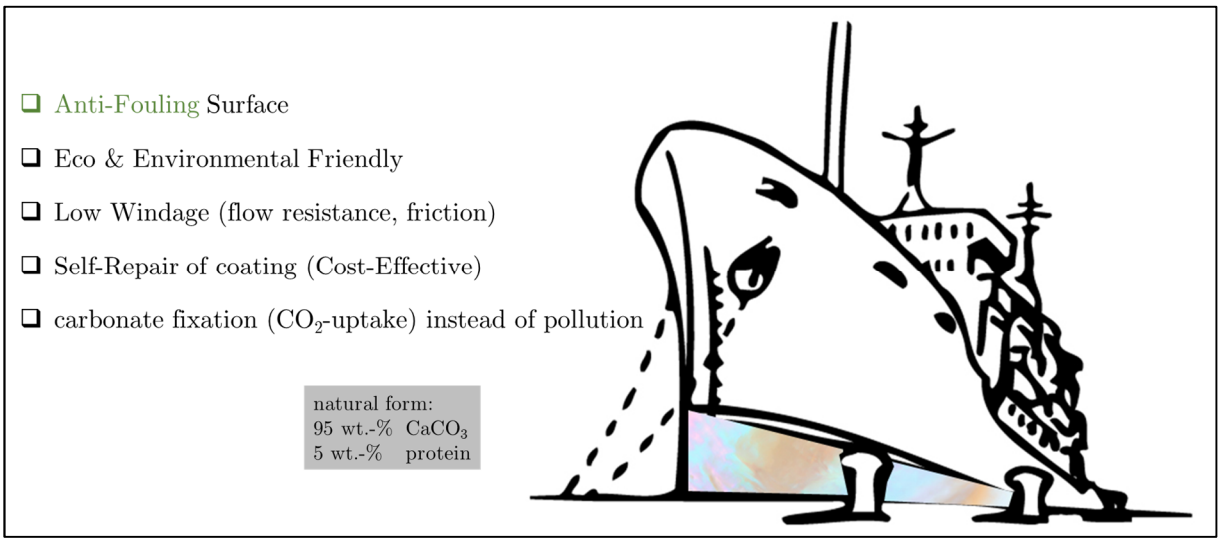


Figure 166: Symbiotic Ship Coating

Among other organisms such as barnacles, mussels are renowned organisms that grow on ship hulls and are called "biofouling" organisms. These organisms, and the mussels themselves also have a defense strategy against such fouling[225] and nacre is known to have a heterogeneous surface where fouling does not succeed easily and the nacreous surface is easy-to-clean. The biofouling on ships leads to increased fuel consumption, poor maneuverability and the blind passengers can also act as parasites in alien waters. Merchant ships usually have to be repainted in dry dock every 5 years[226] as a consequence of biofouling and attrition. In order to prevent fouling on ship hulls, a variety of strategies were applied in the past. For example, toxic tributyltin and other substances were banned from use. State-of-the-art solutions are based on the use of PDMS-based coatings, the cleaning by remotely operated vehicles or cleaning divers. The abrasion of the coatings due to the cleaning operation but also due to high velocities known from nuclear ships lead to massive contamination of the oceans with micro- and/or nanoplastic which undergo bioaccumulation.
From an evolutionary standpoint mussels are one of the first organisms which build an inorganic coating as a protection against the environment, proving that the technology behind this coating can be seen as one of the oldest technologies of organisms which exist on earth. If we as humans could use this "old technology", one could speak of the first step towards symbiosis and reconciliation with mother nature by the help of the prominent mother of pearl.

V Epilog

1 Summary

In the introduction of the thesis, the chemical transformation, physical interaction and the mathematical scaling of colloidal basic building units for designing materials were introduced and illustrated. The parameters from central interest were the electric charge (+/–, measured as ζ-potential) and size of spherical and lamellar colloids (measured by SEM and DLS). The synthesized colloids and the pathways to organized colloids can be understood as model systems and are summarized in **Figure 167**.

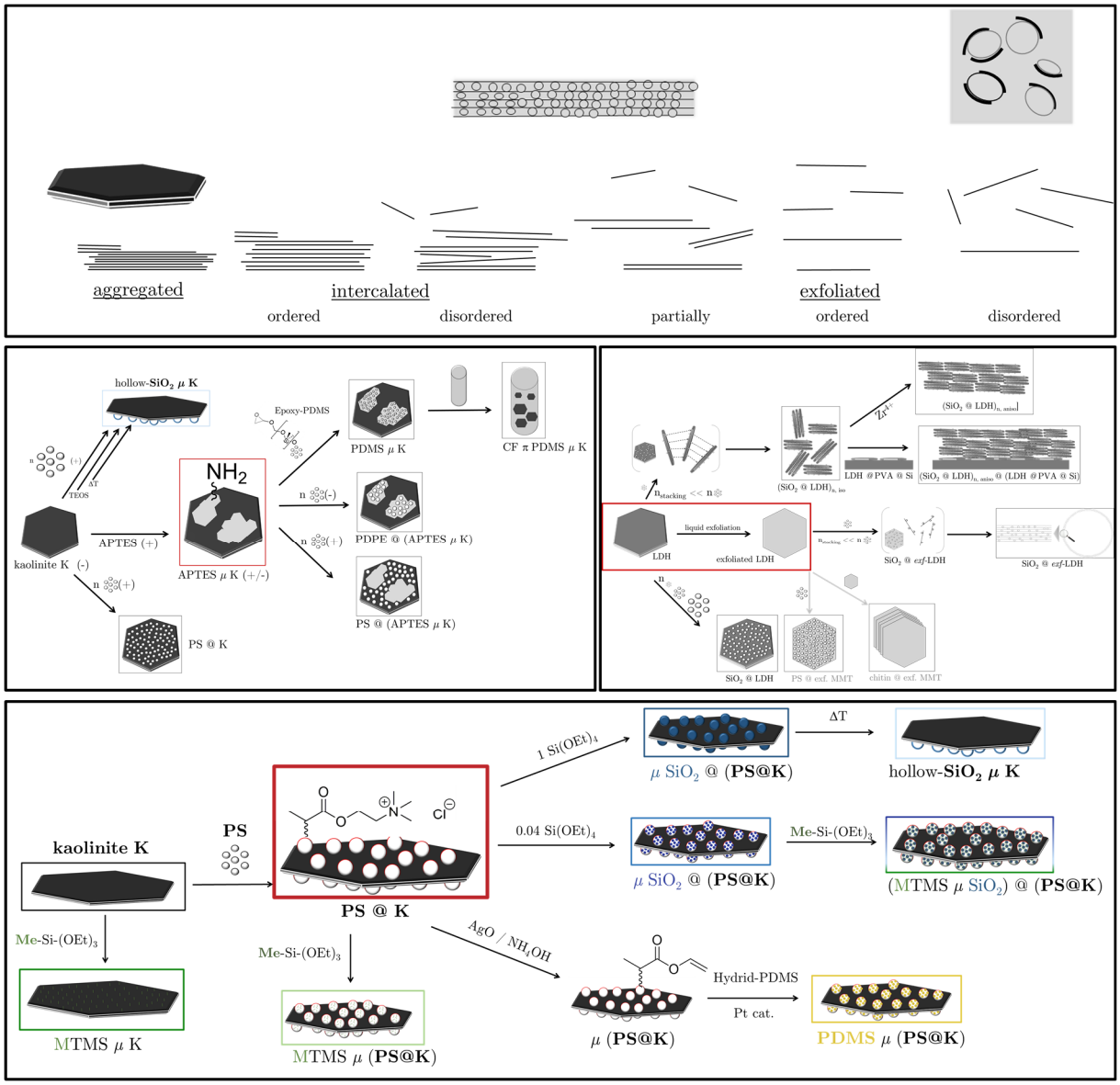


Figure 167: Comprehensive overview of conducted transformations to organized colloids

The **synthesis of the colloids** are summarized in the following. Polyaddition reactions of defined diol mixtures and an isocyanate lead to a prepolymer, which was dispersed in water by addition of amine/water mixtures. The so-obtained PUR colloids (–) in water have different sizes and size distributions, are polydisperse (meas. DLS) and have a coil-like geometry (meas. SLS) and a glass transition temperature T_g of -40°C (measured by DSC). A radical

copolymerization of styrene and an acrylic comonomer lead to monodisperse, spherical PS colloids (+) in water with a T_g of 106 °C.
Lamellar LDH colloids (+) were synthesized from zinc and aluminum monomers to different sizes and keeping the same monomer composition. The composition and the processing of the LDH colloids was varied by the use of a buffer, keeping pH constant at different values using a pH-stat, liquid exfoliation and ionic exchange reactions. Two differently processed lamellar kaolinite colloids (-) were size-separated by sedimentation and centrifugation procedures. Moreover, commercial colloids with different sizes and shapes were examined in side-experiments.
In the first section about **organized colloids**, the electrostatic attraction of spherical colloids on the surface of lamellar colloids PS @ K_{face} was examined. It was found via SEM that the PS colloids are able to occupy the surface with a constant deposition density Λ by electrostatic shielding, even after drying. The electrostatic shielding works up to a critical size where capillary forces overcome the electrostatic forces and lead to a deposition of the PS colloids towards the edges PS π K_{edge}. However, the PS @ K_{face} assemblies as basic building blocks underwent some exemplary modifications (**Figure 167**, *bottom*) in order to modify the resulting surface energy of the organized colloids and allow for the tailoring of its interfaces. Therefore, in the subsequent section, the kaolinite colloids underwent a silylation before the electrostatic deposition of PS colloids in order to make use of the Janus character of kaolinite and for the technical use in Carbon Fiber Reinforced Plastics with PDMS μ kaolinite as carrier particles, [157] promoting dissipative breakdown (**Figure 167**, *middle left*).
The subsequent section deals with the initial emphasis of the thesis, namely the alternating stacking of colloidal spheres and lamellae parallel to a flat substrate as a coating material. Stacked $(SiO_2$ @ $LDH_{face})_n$ assemblies (**Figure 167**, *middle right*) reveal the ability of zirconium-ions to align the stacked assemblies parallel towards a flat substrate by preventing the electrostatic $(LDH_{face}$ @ $LDH_{edge})_n$ assembly which lead to disordered assemblies in the stacked and also in the unstacked state.
The intercalation and exfoliation of lamellae in PUR/LDH composites (**Figure 167**, *top*) was from central interest in the thesis for an application as coating material. A systematic field study was conducted on size-tailored PUR and LDH colloids, leading to at least one sample with superior nematic order by self-organization. The rheological (wet state) and mechanical (solid state) characteristics show a correlation and energy-dissipative effects in the organized coating material, as initially anticipated. Also, a comparably low clay loading in such composites for a parallel orientation was achieved, in contrast to the mentioned literature at the beginning of the thesis, dealing with high clay loadings in the composites. However, the also mentioned and anticipated optical effects were absent and the implementation of hollow spheres in PUR/LDH composites is one of many gaps to be filled in the future.
In fact, optical effects were found for protein/salt composites and additionally a mechanism for the growth of nacre was postulated on the basis of the herein described framework on organized colloids, meaning electrostatic assembly @, capillary assembly π and chemical interaction μ. The used proteins, especially the enzyme chymosin is able to perform all of the three assembly types, whereas in all other experiments of the thesis, the effects were examined in a rather isolated manner.

2 Conclusion

The observed effect for the PS π K_{edge} capillary assemblies after drying from the first section about organized colloids correlate well with the emergence of PUR π LDH_{edge} in the last section about organized colloids, illustrated in **Figure 168** (obtained structure).

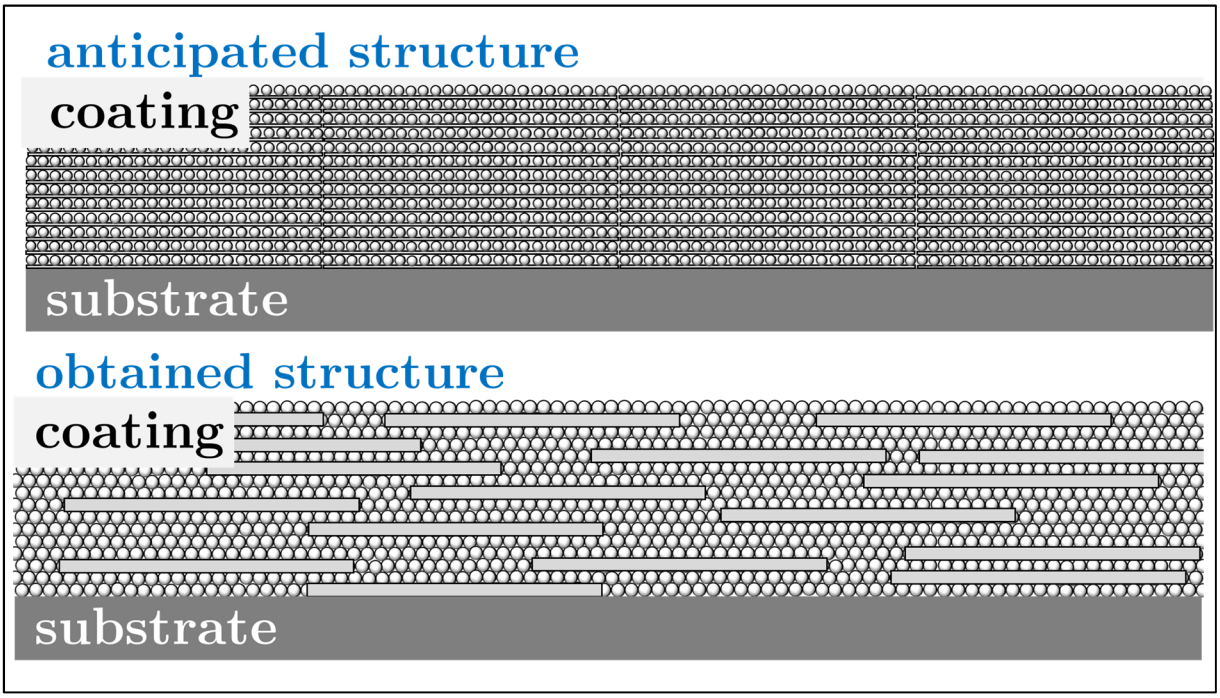


Figure 168: Illustration of anticipated vs obtained cross-sectional coating morphology

The initially anticipated structure was also realized with the already mentioned stacked $(SiO_2$ @ $LDH_{face})_n$ electrostatic assemblies in a PVA matrix by the charge compensation of the edges by the use of zirconium ions.

3 Outlook

The model systems examined herein provide a framework for the further research and development of organized colloids in composites. It has to be noted, that the assembly mechanisms are all made in water as a polar protic solvent. Further examinations on other colloid systems and structures would allow for further confirmation of the proposed assembly mechanisms for the self-organization to (nematic) ordered composites. The implementation of hollow spheres within nematic ordered composites remains a challenge and may further enhance the mechanical performance or provide multifunctional properties with respect to an application as a coating material, such as corrosion inhibition and/or self-repair.

The scaling law analysis of the forelast subsection on PUR/LDH composites provide suspicious numbers that appear in the modern string theories which deserves extra attention so that the experiments can be reproduced by many scientists all over the world, who are in possession of a coaxial rheometer which will then be used in this context as a "colloid collider" or more simply spoken, a "colloider". This may in turn lead to **number-structure-relationships** and the ability to predict ordered states before performing any experiment.

VI References

1. Fan, W., Yan, B., Wang, Z. & Wu, L.
Three-dimensional all-dielectric metamaterial solid immersion lens for subwavelength imaging at visible frequencies. *Sciene Adv.* **2**, 1–8 (2016).
2. Briesenick, D. & Bremser, W.
Synthesis of polyamide-imide-montmorillonite-nanocomposites via new approach of in situ polymerization and solvent casting. *Prog. Org. Coatings* **82**, 26–32 (2015).
3. Sinha Ray, S. & Okamoto, M.
Polymer/layered silicate nanocomposites: a review from preparation to processing. *Prog. Polym. Sci.* **28**, 1539–1641 (2003).
4. Das, P. *et al.*
Nacre-mimetics with synthetic nanoclays up to ultrahigh aspect ratios. *Nat. Commun.* **6**, 5967 (2015).
5. Wang, C., Le, H. & Huang, Y.
Rapid Assembly Processes of Ordered Inorganic / organic Nanocomposites. in *Biomimetics, Learning from nature* (ed. Mukherjee, A.) 217–240 (2010).
6. Bonderer, L. J., Studart, A. R. & Gauckler, L. J.
Bioinspired Design and Assembly of Platelet Reinforced Polymer Films. *Science (80-.).* **319**, 1069–1073 (2008).
7. Shu, Y., Yin, P., Liang, B., Wang, H. & Guo, L.
Bioinspired design and assembly of layered double hydroxide/poly(vinyl alcohol) film with high mechanical performance. *ACS Appl. Mater. Interfaces* **6**, 15154–15161 (2014).
8. Grossman, M. *et al.*
Mineral Nano-Interconnectivity Stiffens and Toughens Nacre-like Composite Materials. *Adv. Mater.* **29**, 1605039 (2017).
9. Graham, T.
Liquid Diffusion Applied to Analysis. *Philos. Trans. R. Soc. London* **151**, 183–224 (1861).
10. Landau, L. & Derjaguin, B. V.
Theory of the stability of strongly charged lyophobic sols and of the adhesion of strongly charged particles in solution of electrolytes. *Acta Physicochim USSR* **14**, 633–662 (1941).
11. Verwey, J. & Overbeek, G. T.
Theory of the stability of lyophobic colloids. *Advances in Colloid Interface Science* **17**, (Elsevier: Amsterdam, 1948).
12. Helmholtz, H. von.
Ueber einige Gesetze der Vertheilung elektrischer Ströme in körperlichen Leitern, mit Anwendung. *Ann. der Phys. und Chemie* **Band LXXXI**, (1853).
13. Gouy, L. G.
Sur la constitution de la charge électrique à la surface d'un électrolyte. *J. Phys. Théorique Appliquée* **9**, 457–468 (1910).
14. Chapman, D. L.
A contribution to the Theory of Electrocapillarity. *Philos. Mag. J. Sci.* **25**, 475–481 (1913).

15. Stern, O.
Zur Theorie der elektrolytische Doppelschicht.
Zeitschrift für Elektrochemie und Angew. Phys. Chemie **30**, 508–516 (1924).
16. Smoluchowski, M. von.
Contribution to the theory of electro-osmosis and related phenomena.
Bull. Int. l'Academie des Sci. Cracovie **3**, 184–199 (1903).
17. Butt, H.-J., Graf, K. & Kappl, M.
Physics and Chemistry of Interfaces.
Wiley-VCH GmbH & Co. KGaA (2003).
18. Briesenick, D.
Reinforced Interphases in PAI-MMT-nanocomposites. (Paderborn University, 2016).
19. Takala, M.
Electrical Insulation Materials towards Nanodielectrics.
(Tampere University of Technology, 2010).
20. Tanaka, T.
Interpretation of Several Key Phenomena Peculiar to Nano Dielectrics in terms of a Multi-Core Model.
Annual Report-Conference on Electrical Insulation and Dielectric Phenomena (2006).
21. de Gennes, P. G.
Reptation of a Polymer Chain in the Presence of Fixed Obstacles.
J. Chem. Phys. **55**, 572–579 (1971).
22. Weiss, A.
Replication and Evolution in Inorganic Systems.
Angew. Chemie Int. Ed. English **20**, 850–860 (1981).
23. Ferris, J. P.
Montmorillonite catalysis of 30-50 mer oligonucleotides: Laboratory demonstration of potential steps in the origin of the RNA world.
Orig. Life Evol. Biosph. **32**, 311–332 (2002).
24. Hill, A. R., Böhler, C. & Orgel, L. E.
Polymerization on the rocks: negatively-charged α-amino acids.
Orig. Life Evol. Biosph. **28**, 235–243 (1998).
25. Cairns-Smith, A. G.
Genetic takeover: and the mineral origins of life. (1982).
26. Goldschmidt, V. M.
Die Gesetze der Krystallochemie. *Naturwissenschaften* **14**, 477–485 (1926).
27. Hintze-Bruening, H. & Leroux, F.
Nanocomposite Based Multifunctional Coatings.
in *New Advances in Vehicular Technology and Automotive Engineering* 61 ff. (2012).
28. Hintze-Bruening, H., Troutier-Thuilliez, A.-L. & Leroux, F.
Layered particle-based polymer composites for coatings: Part II—Stone chip resistant automotive coatings. *Prog. Org. Coatings* **64**, 193–204 (2009).
29. Hintze-Bruening, H., Troutier, A. L. & Leroux, F.
Layered particle based polymer composites for coatings: Part III - Textured coatings obtained via lyotropic liquid crystals. *Prog. Org. Coatings* **70**, 240–244 (2011).
30. Liu, Y., Liang, F., Wang, Q., Qu, X. & Yang, Z.
Flexible responsive Janus nanosheets. *RSC Chem. Commun.* **51**, 3562 (2015).

31. Eklund, P., Beckers, M., Jansson, U., Högberg, H. & Hultman, L.
The MAX phases: Materials science and thin-film processing.
Thin Solid Films **518**, 1851–1878 (2010).
32. Breu, J., Seidl, W., Stoll, A. J., Lange, K. G. & Probst, T. U.
Charge homogeneity in synthetic fluorohectorite. *Chem. Mater.* **13**, 4213–4220 (2001).
33. Weiss, A., Fahn, R. & Hofmann, U.
Nachweis der Gerüststruktur in thixotropen Gelen.
Naturwissenschaften **39**, 351–352 (1952).
34. Lagaly, G. & Dékány, I.
Colloid Clay Science.
in *Handbook of Clay Science* (eds. Bergaya, F. & Lagaly, G.) 286–289 (Elsevier, 2013).
35. Szántó, F. & Gilde, M.
Rheological properties and thixotropic behaviour of kaolinite suspensions.
Acta Univ Szeged. Acta Phys. Chim. XIX 291–297 (1973).
36. Abend, S., Bonnke, N., Gutschner, U. & Lagaly, G.
Stabilization of emulsions by heterocoagulation of clay minerals and layered double hydroxides. *Colloid Polym. Sci.* **276**, 730–737 (1998).
37. BYK Additives & Instruments. *Laponite : Performance Additives.* (2014).
38. Ji, X., Zhang, W., Shan, L., Tian, Y. & Liu, J.
Self-assembly preparation of SiO_2@Ni-Al layered double hydroxide composites and their enhanced electrorheological characteristics. *Sci. Rep.* **5**, 1–10 (2015).
39. Miyata, S. & Okada, A.
Synthesis of Hydrotalcite-like compounds and their physicochemical properties - The Systems Mg^{2+} - Al^{3+} - $SO4^{2-}$ and Mg^{2+} - Al^{3+} - CrO_4^{2-}.
Clays Clay Miner. **25**, 14–18 (1977).
40. Williams, G. & McMurray, H. N.
Inhibition of filiform corrosion on organic-coated AA2024-T3 by smart-release cation and anion-exchange pigments. *Electrochim. Acta* **69**, 287–294 (2012).
41. Michailidou, E., McMurray, H. N. & Williams, G.
Inhibition of Filiform Corrosion on Organic-Coated Magnesium-Containing Galvanized Steel by Smart-Release Ion Exchange Pigments. *ECS Trans.* **80**, 585–591 (2017).
42. Visser, P., Lutz, A., Mol, J. M. C. & Terryn, H.
Study of the formation of a protective layer in a defect from lithium-leaching organic coatings. *Prog. Org. Coatings* **99**, 80–90 (2016).
43. Walther, A., Matussek, K. & Müller, A. H. E.
Engineering nanostructured polymer blends with controlled nanoparticle location using Janus particles. *ACS Nano* **2**, 1167–1178 (2008).
44. Hu, S. H. & Gao, X.
Nanocomposites with spatially separated functionalities for combined imaging and magnetolytic therapy. *J. Am. Chem. Soc.* **132**, 7234–7237 (2010).
45. Baraban, L., Harazim, S. M., Sanchez, S. & Schmidt, O. G.
Chemotactic behavior of catalytic motors in microfluidic channels.
Angew. Chemie - Int. Ed. **125**, 5662–5666 (2013).
46. Rozynek, Z., Zacher, T., Janek, M., Čaplovičová, M. & Fossum, J. O.
Electric-field-induced structuring and rheological properties of kaolinite and halloysite.
Appl. Clay Sci. **77–78**, 1–9 (2013).

47. Dougherty, L. F., Johnsen, S., Caldwell, R. L. & Marshall, N. J.
A dynamic broadband reflector built from microscopic silica spheres in the 'disco' clam Ctenoides ales. *J. R. Soc. Interface* **11**, 1–6 (2014).
48. Schmitz, G. P. & Heaney, M. B.
Bisymmetrical Electric paper and a system therefor. (2006).
49. Yuet, K. P., Hwang, D. K., Haghgooie, R. & Doyle, P. S.
Multifunctional superparamagnetic janus particles. *Langmuir* **26**, 4281–4287 (2010).
50. George, M. C. & Braun, P. V.
Multicompartmental materials by electrohydrodynamic cojetting.
Angew. Chemie - Int. Ed. **48**, 2–6 (2009).
51. Sheridon, N. K.
Method for the fabrication of multicolored balls for a twisting ball display. (1994).
52. Gröschel, A. H. *et al.*
Precise hierarchical self-assembly of multicompartment micelles.
Nat. Commun. **3**, 1–10 (2012).
53. Anderson, K. D. *et al.*
Robust plasma polymerized-Titania/Silica Janus microparticles.
Chem. Mater. **22**, 3259–3264 (2010).
54. Jiang, S. & Granick, S.
A simple method to produce trivalent colloidal particles.
Langmuir **25**, 8915–8918 (2009).
55. Liu, Y., Wang, Q., Qu, X., Liang, F. & Yang, Z.
Amine/acid composite Janus nanosheets. *Sci. China Mater.* **58**, 126–131 (2015).
56. Kogure, T., Elzea-Kogel, J., Johnston, C. T. & Bish, D. L.
Stacking disorder in a sedimentary kaolinite. *Clays Clay Miner.* **58**, 62–71 (2010).
57. Solc, R., Gerzabek, M. H., Lischka, H. & Tunega, D.
Wettability of kaolinite (001) surfaces - Molecular dynamic study.
Geoderma **169**, 47–54 (2011).
58. Shang, J., Flury, M., Harsh, J. B. & Zollars, R. L.
Contact angles of aluminosilicate clays as affected by relative humidity and exchangeable cations. *Colloids Surfaces A Physicochem. Eng. Asp.* **353**, 1–9 (2010).
59. Hirsemann, D. I.
Entwicklung von Janus-Partikeln auf Basis des Schichtsilicats Kaolinit.
(Universität Bayreuth, 2011).
60. Synytska, A. *et al.*
Platelet Janus Particles with Hairy Polymer Shells for Multifunctional Materials.
ACS Appl. Mater. Interfaces **6**, 13106–13144 (2014).
61. Sanders, R. L., Washton, N. M. & Mueller, K. T.
Measurement of the reactive surface area of clay minerals using solid-state NMR studies of a Probe Molecule. *J. Phys. Chem. C* **114**, 5491–5498 (2010).
62. Zhang, S. *et al.*
Intercalation of γ-aminopropyl triethoxysilane (APTES) into kaolinite interlayer with methanol-grafted kaolinite as intermediate. *Appl. Clay Sci.* **114**, 484–490 (2015).
63. Tibbits, S.
The emergence of '4D printing'. (TED - Technology, Entertainment, Design, 2013).
64. Leunissen, M. E. *et al.*
Ionic colloidal crystals of oppositely charged particles. *Nature* **437**, 235–240 (2005).

65. Decher, G. & Jong-Dal Hong.
Buildup of ultrathin multilayer films by a self-assembly process, 1 consecutive adsorption of anionic and cationic bipolar amphiphiles on charged surfaces. *Macromol. Symp.* **46**, 321–327 (1991).
66. Frey, E. & Lagaly, G.
Selective coagulation in mixed colloidal suspensions. *J. Colloid Interface Sci.* **70**, 46–55 (1979).
67. Cong, Y., Chen, K., Zhou, S. & Wu, L.
Synthesis of pH and UV dual-responsive microcapsules with high loading capacity and their application in self-healing hydrophobic coatings. *J. Mater. Chem. A* **3**, 19093–19099 (2015).
68. Briesenick, K.
Selbstorganisierte Kompositpartikel: Untersuchungen zur Herstellung neuartiger Partikelmorphologien. (Universität Paderborn, 2017).
69. Kepler, J.
Ioannis Kepleri … Strena, sei de nove sexangula. (Apud Godefridum Tampach, 1611).
70. Hales, T. C.
A proof of the Kepler conjecture. *Ann. Math.* **162**, 1065–1185 (2005).
71. Kralchevsky, P. A. & Denkov, N. D.
Capillary forces and structuring in layers of colloid particles. *Curr. Opin. Colloid Interface Sci.* **6**, 383–401 (2001).
72. Kralchevsky, P. A., Paunov, V. N., Denkov, N. D., Ivanov, I. B. & Nagayama, K.
Energetical and force approaches to the capillary interactions between particles attached to a liquid-fluid interface. *J. Colloid Interface Sci.* **155**, 420–437 (1993).
73. Kralchevsky, P. A., Paunov, V. N., Ivanov, I. B. & Nagayama, K.
Capillary meniscus interaction between colloidal particles attached to a liquid-fluid interface. *J. Colloid Interface Sci.* **151**, 79–94 (1992).
74. Denkov, D. *et al.*
Mechanism of Formation of Two-Dimensional Crystals from Latex Particles on Substrates. *Langmuir* **8**, 3183–3190 (1992).
75. Routh, A. F. & Russel, W. B.
A Process Model for Latex Film Formation: Limiting Regimes for Individual Driving Forces. *Langmuir* **15**, 7762–7773 (1999).
76. Routh, A. F. & Russel, W. B.
Deformation Mechanisms during Latex Film Formation: Experimental Evidence. *Ind. Eng. Chem. Res.* **40**, 4302–4308 (2001).
77. Routh, A. F.
Drying of thin colloidal films. *Reports Prog. Phys.* **76**, 046603 (2013).
78. Carter, F. T., Kowalczyk, R. M., Millichamp, I., Chainey, M. & Keddie, J. L.
Correlating Particle Deformation with Water Concentration Profiles during Latex Film Formation: Reasons That Softer Latex Films Take Longer to Dry. *Langmuir* **30**, 9672–9681 (2014).
79. van der Kooij, H. M., van de Kerkhof, G. T. & Sprakel, J.
A mechanistic view of drying suspension droplets. *Soft Matter* **12**, 2858–2867 (2016).
80. Espinosa, H. D., Rim, J. E., Barthelat, F. & Buehler, M. J.
Merger of structure and material in nacre and bone - Perspectives on de novo biomimetic materials. *Prog. Mater. Sci.* **54**, 1059–1100 (2009).

81. Finnemore, A. *et al.*
Biomimetic layer-by-layer assembly of artificial nacre. *Nat. Commun.* **3**, 966 (2012).
82. Bonderer, L. J., Studart, A. R. & Gauckler, L. J.
Bioinspired design and assembly of platelet reinforced polymer films.
Science **319**, 1069–1073 (2008).
83. Sun, J. & Bhushan, B.
Hierarchical structure and mechanical properties of nacre: a review.
RSC Adv. **2**, 7617 (2012).
84. Vaia, R. A.
Structural characterization of Polymer-Layered Silicate Nanocomposites.
in *Polymer-Clay Nanocomposites* 244 (2000).
85. Poincaré, H.
Sur les courbes définies par une équation différentielle. *J. Mathématiques* (1882).
86. Hilbert, D.
Mathematische Probleme. in *International Congress of Mathematicians* (1900).
87. Eigen, M. & Schuster, P.
The Hypercycle - A Principle of Natural Self-Organization.
Naturwissenschaften **65**, 7–41 (1978).
88. Eigen, M.
Molecular self-organization and the early stages of evolution.
Quaterly Rev. Biophys. **4**, **2** & **3**, 149–212 (1971).
89. Schmidt, J.
Spiral Galaxy M100. *NASA, ESA* (2018). Available at:
http://hubblesite.org/image/4272/news
90. Sun Release X3.1-class Solar Flare on Oct. 24, 2014. *NASA, SDO* Available at:
https://www.nasa.gov/content/goddard/sun-release-x3.1-class-solar-flare-on-oct-24-2014
91. NASA/JPL. Earth - Pacific Ocean. (1996). Available at:
https://www.jpl.nasa.gov/spaceimages/details.php?id=PIA00123
92. Williams, D. & Fiedlander, J. Earth's Moon - Apollo 16. *NASA* (1972). Available at:
https://nssdc.gsfc.nasa.gov/imgcat/html/object_page/a16_m_3021.html
93. Shirah, G., Mitchell, H., Zhang, H. & Menemenlis, D. Gulf Stream Sea Surface Currents and Temperatures. *Scientific Visulization Studio* (2012). Available at:
http://svs.gsfc.nasa.gov/3913
94. Gallant, J. Largest Braincoral. *Diving Almanac* (2017). Available at:
http://divingalmanac.com/largest-brain-coral/
95. Belousov-Zhabotinsky Reaction. Available at:
http://hopf.chem.brandeis.edu/subpages/main.html
96. Anguelov, R. & Stoltz, S. M.
Stationary and oscillatory patterns in a coupled Brusselator model.
Math. Comput. Simul. **133**, 39–46 (2017).
97. Cartwright, J. H. E., Checa, A. G., Escribano, B. & Sainz-Díaz, C. I.
Spiral and target patterns in bivalve nacre manifest a natural excitable medium from layer growth of a biological liquid crystal.
Proc. Natl. Acad. Sci. **106**, 10499–10504 (2009).

98. Cabrillo, C. *et al.*
A novel real space scattering theory: Efficient characterization of colloidal crystals.
J. Phys. Conf. Ser. **247**, (2010).
99. Belousov, B. P.
A periodic reaction and its mechanism. *Oscil. Travel. Waves Chem. Syst.* (1951).
100. Zhabotinsky, A. M.
Periodic liquid phase reactions. *Proc. Acad. Sci. USSR* **157**, 392–395 (1964).
101. Prigogine, I.
Time, Structure, and Fluctuations. *Science (80-.).* **201**, 777–785 (1978).
102. Turing, A. M.
The chemical basis of morphogenesis.
Philos. Trans. R. Soc. Lond. B. Biol. Sci. **237**, 37–72 (1952).
103. Tan, T. H. *et al.*
Topological turbulence in the membrane of a living cell.
Nat. Phys. Lett. **16**, 657–662 (2020).
104. Gilpin, W., Prakash, V. N. & Prakash, M.
Vortex arrays and ciliary tangles underlie the feeding–swimming trade-off in starfish larvae. *Nat. Phys.* **13**, 380–386 (2017).
105. Bleibel, J., Dietrich, S., Domínguez, A. & Oettel, M.
Shock Waves in Capillary Collapse of Colloids : A Model System for Two-Dimensional Screened Newtonian Gravity. *Phys. Rev. Lett.* **107**, 128302 (2011).
106. Acharya, P. & Rao, N. M.
Stability Studies on a Lipase from Bacillus subtilis in Guanidinium Chloride.
J. Protein Chem. **22**, 51–60 (2002).
107. Bénard, H.
Les tourbillons cellulaires dans une nappe liquide.
Rev. Gen. Sci. Pures Appl. **11**, 1261-1271. (1900).
108. Lord Rayleigh, O. M. F. R. S. LIX .
On convection currents in a horizontal layer of fluid , when the higher temperature is on the under side. *Philos. Mag. Ser. 6* **32**, 529–546 (1916).
109. Urban, P., Hanzelka, P., Musilova, V., Srnka, A. & Skrbek, L.
DESIGN AND TESTS OF THE CRYOSTAT WITH AN EXPERIMENTAL CELL FOR TURBULENT THERMAL CONVECTION.
Colloq. FLUID Dyn. 1–8 (2007).
110. Bae, J. *et al.*
Programmable and reversible assembly of soft capillary multipoles.
Mater. Horizons **4**, 228–235 (2017).
111. Deacon, T. & Koutroufinis, S.
Complexity and dynamical depth.
Information **5**, 404–423 (2014).
112. Shannon, C. E.
A Mathematical Theory of Communication. *Bell Syst. Tech. J.* **27**, 379–423 (1948).
113. Bengoechea, C., Arrachid, A., Guerrero, A., Hill, S. E. & Mitchell, J. R.
Relationship between the glass transition temperature and the melt flow behavior for gluten, casein and soya. *J. Cereal Sci.* **45**, 275–284 (2007).

114. Zhou, W., Apkarian, R. P., Wang, Z. L. & Joy, D.
Fundamentals of Scanning Electron Microscopy.
in *Scanning microscopy for nanotechnology* 1–40 (Springer, 2006).
115. Carl Zeiss AG. Available at: www.zeiss.com.
116. *Introduction to Focused Ion Beams: instrumentation, theory, techniques and practice*.
(Springer Science & Business Media, 2004).
117. Lorber, B., Fischer, F., Bailly, M., Roy, H. & Kern, D.
Protein Analysis by Dynamic Light Scattering: Methods and Techniques for Students.
Biochem. Mol. Biol. Educ. **40**, 372–382 (2012).
118. Bhattacharjee, S.
DLS and zeta potential – What they are and what they are not?
J. Control. Release **235**, 337–351 (2016).
119. Chruszcz, M., Borek, D., Domagalski, M., Otwinowski, Z. & Minor, W.
X-ray diffraction experiment - the last experiment in the structure elucidation process.
Adv Protein Chem Struct Biol. **77**, 23–40 (2009).
120. Chu, B.
Laser Light Scattering: Basic Principles and Practice. (Elsevier Science, 2012).
121. Burchard, W.
Static and Dynamic Light Scattering from Branched Polymers and Biopolymers.
Adv. Polym. Sci. **48**, 1–124 (1983).
122. Sanders, J. K. M. & Hunter, B. K.
Modern NMR Spectroscopy: A Guide for Chemists. (Oxford University Press, 1993).
123. Levitt, M. H.
Spin Dynamics: Basics of Nuclear Magnetic Resonance. (Wiley, 2008).
124. Berger, S. & Braun, S.
200 and more NMR experiments. (Wiley-VCH, 2004).
125. Jacobsen, N. E.
NMR data interpretation explained: understanding 1D and 2D NMR spectra of organic compounds and natural products. (John Wiley & Sons, 2016).
126. Scimeca, M., Bischetti, S., Lamsira, H. K., Bonfiglio, R. & Bonanno, E.
Energy Dispersive X-ray (EDX) microanalysis : A powerful tool in biomedical research and diagnosis. *Eur. J. Histochem. 2018* **62**, 2841 (2018).
127. Hesse, M., Meier, H. & Zeeh, B.
Spektroskopische Methoden in der organischen Chemie. (Thieme, 2005).
128. Socrates, G.
Infrared and Raman characteristic group frequencies. Infrared and Raman characteristic group frequencies (2004).
129. Owens, D. K. & Wendt, R. C.
Estimation of the Surface Free Energy Of Polymers.
J. Appl. Polym. Sci. **13**, 1741–1747 (1969).
130. Rabel, W.
Einige Aspekte der Benetzungstheorie und ihre Anwendung auf die Untersuchung und Veränderung der Oberflächeneigenschaften von Polymeren.
Farbe und Lack **77**, 997–1005 (1971).
131. Kaelble, D. H.
Dispersion-Polar Surface Tension Properties of Organic Solids.
J. Adhes. **2**, 66–81 (1970).

132. Keattch, C. J. *et al.*
Fundamentals and Quantitative Applications of DTA and DSC.
Anal. Proc. **17**, 469–508 (1980).
133. Ruzin, S. E.
Plant Microtechnique and Microscopy. (1999).
134. Rives, V.
Layered Double Hydroxides - Present and Future.
(Nova Science Publishers, Inc., 2001).
135. Haynes, W. M.
Electrical Conductivity of Aqueous Solutions. in *CRC Handbook of Chemistry and Physics, 91th Edition* 5–71 (2010).
136. Vialat, P.
Composition, structure et comportement électrochimique d'Hydroxydes Doubles Lamellaires au cobalt : vers des applications en tant que matériaux d'électrodes.
(Institut de Chimie de Clermont-Ferrand, 2015).
137. Max, J.-J., Trudel, M. & Chapados, C.
Infrared Titration of Aqueous Glycine. *Appl. Spectrosc.* **52**, 226–233 (1998).
138. Guthrie, J. P.
Hydrolysis of esters of oxy acids: pKa values for strong acids; Brflnsted relationship for attack of water at methyl; free energies of hydrolysis of esters of oxy acids; and a linear relationship between free energy of hydrolysis and pKa holding over a ra.
Can. J. Chem. **56**, 1978 (1978).
139. Fatehah, M. O., Aziz, H. A. & Stoll, S.
Stability of ZnO Nanoparticles in Solution. Influence of pH, Dissolution, Aggregation and Disaggregation Effects. *J. Colloid Sci. Biotechnol.* **3**, 75–84 (2014).
140. Hibino, T. & Kobayashi, M.
Delamination of layered double hydroxides in water. *J. Mater. Chem.* **15**, 653 (2005).
141. Ma, R., Liu, Z., Li, L., Iyi, N. & Sasaki, T.
Exfoliating layered double hydroxides in formamide: a method to obtain positively charged nanosheets. *J. Mater. Chem.* **16**, 3809 (2006).
142. Hibino, T. & Jones, W.
New approach to the delamination of layered double hydroxides.
J. Mater. Chem. **11**, 1321–1323 (2001).
143. Gordijo, C. R., Leopoldo Constantino, V. R. & De Oliveira Silva, D.
Evidences for decarbonation and exfoliation of layered double hydroxide in N,N-dimethylformamide–ethanol solvent mixture.
J. Solid State Chem. **180**, 1967–1976 (2007).
144. Adachi-Pagano, M., Forano, C. & Besse, J.-P.
Delamination of layered double hydroxides by use of surfactants.
Chem. Commun. 91–92 (2000).
145. Huertas, F. J., Huertas, F. & Linares, J.
Hydrothermal synthesis of kaolinite: method and characterization of synthetic materials. *Appl. Clay Sci.* **7**, 345–356 (1993).
146. Lamb, H.
Hydrodynamics. (Cambridge University Press, 1975).
147. White, W. A. & Pichler, E.
Water-Sorption Characteristics of Clay Minerals. *Illinois State Geol. Surv.* (1959).

148. Matusik, J. & Kłapyta, Z.
Characterization of kaolinite intercalation compounds with benzylalkylammonium chlorides using XRD, TGA/DTA and CHNS elemental analysis.
Appl. Clay Sci. **83–84**, 433–440 (2013).
149. Antonietti, M., Lohmann, S. & Bremser, W.
Polymerization in microemulsion-size and surface control of ultrafine latex particles.
Prog. Colloid Polym. Sci. **65**, 62–65 (1992).
150. Henning, W., Meckel, W. & Fuhrmann, P.
Process for the continuous production of aqueous polyurethane dispersions and their use as a coating composition or as an adhesive. (1989).
151. Neuhaus, S.
Selbstorganisation von lamellaren und sphärischen Partikeln.
(Paderborn University, 2015).
152. Deng, Z., Chen, M., Zhou, S., You, B. & Wu, L.
A novel method for the fabrication of monodisperse hollow silica spheres.
Langmuir **22**, 6403–6407 (2006).
153. Gu, S., Kondo, T. & Konno, M.
Preparation of silica-polystyrene core-shell particles up to micron sizes.
J. Colloid Interface Sci. **272**, 314–320 (2004).
154. Dong, L., Chu, Y., Zhuo, Y. & Zhang, W.
Two-minute synthesis of PbS nanocubes with high yield and good dispersibility at room temperature. *Nanotechnology* **20**, 125301 (2009).
155. Brochier Salon, M. C., Bayle, P. A., Abdelmouleh, M., Boufi, S. & Belgacem, M. N.
Kinetics of hydrolysis and self condensation reactions of silanes by NMR spectroscopy.
Colloids Surfaces A Physicochem. Eng. Asp. **312**, 83–91 (2008).
156. Bogush, G. H., Tracy, M. A. & Zukoski, C. F.
Preparation of Monodisperse Silica Particles: Control of Size and Mass Fraction.
J. Non. Cryst. Solids **104**, 95-106 (1988).
157. Becker-Staines, A.
Surface modification of carbon fibers. (Paderborn University, 2020).
158. Vaculíková, L., Plevová, E., Vallová, S. & Koutník, I.
Characterization and differentiation of kaolinites from selected Czech deposits using infrared spectroscopy and differential thermal analysis.
Acta Geodyn. Geomater. **8**, 59–67 (2011).
159. Saikia, B. J. & Parthasarathy, G.
Fourier Transform Infrared Spectroscopic Characterization of Kaolinite from Assam and Meghalaya, Northeatern India. *J.Mod.Phys.* **1**, 206–210 (2010).
160. Djomgoue, P. & Njopwouo, D.
FT-IR Spectroscopy Applied for Surface Clays.
J. Surf. Eng. Mater. Adv. Technol. **3**, 275–282 (2013).
161. Rocha, J. & Klinowski, J.
^{29}Si and ^{27}Al Magic-angle-spinning NMR Studies of the Thermal Transformation of Kaolinite. *Phys. Chem. Miner.* **17**, 179–186 (1990).
162. Ishida, H.
A Review Of Recent Progress In The Studies of Molecular and Microstructure of coupling Agents and Their Functions in Composites, Coatings and Adhesive Joints.
Polym. Compos. **5**, 101–123 (1984).

163. Herrera, N. N., Letoffe, J.-M., Reymond, J.-P. & Bourgeat-Lami, E.
Silylation of laponite clay particles with monofunctional and trifunctional vinyl alkoxysilanes. *J. Mater. Chem.* **15**, 863–871 (2005).
164. Becker-Staines, A., Bremser, W. & Tröster, T.
Poly(dimethylsiloxane) as Interphase in Carbon Fiber-Reinforced Epoxy Resin: Topographical Analysis and Single-Fiber Pull-Out Tests.
Ind. Eng. Chem. Res. **58**, 23143–23153 (2019).
165. Tang, M. Functionalization of Carbon Fibers through Polyurethane Coatings with controllable Ductility-and Stiffness-Module. (Paderborn University, 202x).
166. Lagaly, G. & Ziesmer, S.
Colloid chemistry of clay minerals : the coagulation of montmorillonite dispersions.
Adv. Colloid Interface Sci. **100–102**, 105–128 (2003).
167. Tombácz, E. & Szekeres, M.
Surface charge heterogeneity of kaolinite in aqueous suspension in comparison with montmorillonite. *Appl. Clay Sci.* **34**, 105–124 (2006).
168. Guo, X., Zhang, F., Evans, D. G. & Duan, X.
Layered double hydroxide films: synthesis, properties and applications.
Chem. Commun. **46**, 5197–5210 (2010).
169. Guo, X., Zhang, F., Xu, S., Evans, D. G. & Duan, X.
Preparation of layered double hydroxide films with different orientations on the opposite sides of a glass substrate by in situ hydrothermal crystallization.
Chem. Commun. **0**, 6836–6838 (2009).
170. Oswald, A.
Durchschlagsfestigkeiten von Polyamidimid-Kompositen mit lamellaren und sphärischen Nanopartikeln. (Paderborn University, 2014).
171. Mongondry, P., Nicolai, T. & Tassin, J. F.
Influence of pyrophosphate or polyethylene oxide on the aggregation and gelation of aqueous laponite dispersions. *J. Colloid Interface Sci.* **275**, 191–196 (2004).
172. Xu, H. & Van Deventer, J. S. J.
The geopolymerisation of alumino-silicate minerals.
Int. J. Miner. Process. **59**, 247–266 (2000).
173. Troutier-Thuilliez *et al.*
Exfoliation and liquid crystal phase formation of layered double hydroxide into waterborne polyurethane coatings. *Soft Matter* **7**, 4242 (2011).
174. Olejnik, S., Aylmore, L. A. G., Posner, A. M. & Quirk, J. P.
Infrared spectra of kaolin mineral-dimethyl sulfoxide complexes.
J. Phys. Chem. **72**, 241–249 (1968).
175. Malsam, J.
Untersuchung der Interkalations- und Exfolierungseigenschaften von LDH-NO_3-Partikeln. (Paderborn University 2018).
176. Lee, W. D., Im, S. S., Lim, H.-M. & Kim, K.-J.
Preparation and properties of layered double hydroxide/poly (ethylene terephthalate) nanocomposites by direct melt compounding. *Polymer (Guildf).* **47**, 1364–1371 (2006).
177. Sun, L., Boo, W. J., Sun, D., Clearfield, A. & Sue, H. J.
Preparation of Exfoliated Epoxy/α-Zirconium Phosphate Nanocomposites Containing High Aspect Ratio Nanoplatelets. *Chem. Mater.* **19**, 1749–1754 (2007).

178. Voorn, D. J. *et al.*
Controlled heterocoagulation of platelets and spheres. *Langmuir* **21**, 6950–6956 (2005).
179. Troutier-Thuilliez *et al.*
Exfoliation and liquid crystal phase formation of layered double hydroxide into waterborne polyurethane coatings. *Soft Matter* **7**, 4242–4251 (2011).
180. Lagaly, G.
Principles of flow of kaolin and bentonite dispersions.
Appl. Clay Sci. **4**, 105–123 (1989).
181. Zhang, J., Luan, L., Zhu, W., Liu, S. & Sun, D.
Phase Behavior of Aqueous Suspensions of Mg_2Al Layered Double Hydroxide : The Competition among Nematic Ordering, Sedimentation, and Gelation.
Langmuir **23**, 5331–5337 (2007).
182. Goddard, J. D. & Angeles, L.
Dissipative materials as constitutive models for granular media.
Acta Mechanica **63**, 3-13 (1986).
183. Goddard, J. D.
A dissipative anisotropic fluid model for non-colloidal particle dispersions.
J. Fluid Mech. **568**, 1–17 (2006).
184. Cheng, D. C.-H. & Evans, F.
Phenomenological Characterization of the Rheological Behaviour of Inelastic Reversible Thixotropic and Antithixotropic Fluids.
Brit. J. Appl. Phys. **16**, 1599–1617 (1965).
185. Antonietti, M. & Bremser, W.
Rheology of Small Spherical Polystyrene Microgels : A Direct Proof for a New Transport Mechanism in Bulk Polymers besides Reptation.
Macromolecules **28**, 4227–4233 (1995).
186. Krüger, S.
Darstellung eines Lamellarpartikel-Protein-Hybridmaterials durch oberflächennahe, enzymatische Caseinspaltung. (Paderborn University, 2016).
187. Heinemann, F., Launspach, M., Gries, K. & Fritz, M.
Gastropod nacre: Structure, properties and growth - Biological, chemical and physical basics. *Biophys. Chem.* **153**, 126–153 (2011).
188. Barthelat, F., Tang, H., Zavattieri, P. D., Li, C.-M. & Espinosa, H. D.
On the mechanics of mother-of-pearl: A key feature in the material hierarchical structure. *J. Mech. Phys. Solids* **55**, 306–337 (2007).
189. Meyers, M. A., Lin, A. Y.-M., Chen, P.-Y. & Muyco, J.
Mechanical strength of abalone nacre: Role of the soft organic layer.
J. Mech. Behav. Biomed. Mater. I **1**, 76–85 (2008).
190. Schoeppler, V. *et al.*
Crystal growth kinetics as an architectural constraint on the evolution of molluscan shells. *Proc. Natl. Acad. Sci.* **116**, 20388–20397 (2019).
191. Treccani, L., Mann, K., Heinemann, F. & Fritz, M.
Perlwapin, an Abalone Nacre Protein with Three Four-Disulfide Core (Whey Acidic Protein) Domains, Inhibits the Growth of Calcium Carbonate Crystals.
Biophys. J. **91**, 2601–2608 (2006).
192. Shimizu, K., Cha, J., Tucky, G. D. & Morse, D. E.
Silicatein α: Cathepsin L-like protein in sponge biosilica.

Proc. Natl. Acad. Sci. **95**, 6234–6238 (1998).
193. Cha, J. N. *et al.*
Silicatein filaments and subunits from a marine sponge direct the polymerization of silica and silicones in vitro. *Proc. Natl. Acad. Sci.* **96**, 361–365 (1999).
194. Tabatabaei, S. Y. *et al.*
Recombinant silicateins as model biocatalysts in organosiloxane chemistry. *Proc. Natl. Acad. Sci.* **114**, E5285–E5291 (2017).
195. Nassif, N. *et al.*
Amorphous layer around aragonite platelets in nacre. *Proc. Natl. Acad. Sci.* **102**, 12653–12655 (2005).
196. Addadi, L., Joester, D., Nudelman, F. & Weiner, S.
Mollusk shell formation: A source of new concepts for understanding biomineralization processes. *Chem. - A Eur. J.* **12**, 980–987 (2006).
197. Rüdiger, A. A.
The Enzyme Mediated Autodeposition of Casein : From Deposition of Defined Films to Nanostructuring with Single Particles. (Paderborn University, 2017).
198. Ruediger, A. A., Terborg, E., Bremser, W. & Strube, O. I.
Influences on the film thickness in the enzymatic autodeposition process of casein. *Prog. Org. Coatings* **94**, 56–61 (2016).
199. Checa, A. G., Cartwright, J. H. E. & Willinger, M.-G.
The key role of the surface membrane in why gastropod nacre grows in towers. *Proc. Natl. Acad. Sci.* **106**, 38–43 (2009).
200. Lopez, M. I., Chen, P. Y., McKittrick, J. & Meyers, M. A.
Growth of nacre in abalone: Seasonal and feeding effects. *Mater. Sci. Eng. C* **31**, 238–245 (2011).
201. Mao, L.-B. *et al.*
Synthetic nacre by predesigned matrix-directed mineralization. *Science* **354**, 107–110 (2016).
202. Farías, M. E., Martinez, M. J. & Pilosof, A. M. R.
Casein glycomacropeptide pH-dependent self-assembly and cold gelation. *Int. Dairy J.* **20**, 79–88 (2010).
203. Bédouet, L. *et al.*
Soluble proteins of the nacre of the giant oyster Pinctada maxima and of the abalone Haliotis tuberculata:
Comp. Biochem. Physiol. Part B Biochem. Mol. Biol. **128**, 389–400 (2001).
204. Lieske, B., Konrad, G. & Kleinschmidt, T.
Isolation of caseinomacropeptide from rennet whey by a multi-stage ultrafiltration process I . Studies in the apparent molecular weight of caseinomacropeptide as a function of pH. *Milchwissenschaft* **59**, 172–175 (2004).
205. Mikkelsen, T. L. *et al.*
Caseinomacropeptide Self-Association is Dependent on Whether the Peptide is Free or Restricted in κ-Casein. *J. Dairy Sci.* **88**, 4228–4238 (2005).
206. Wells, A. F.
Structural Inorganic Chemistry. (Oxford University Press, 1975).
207. Hyde, A. M. *et al.*
General Principles and Strategies for Salting-Out Informed by the Hofmeister Series. *Org. Process Res. Dev.* **21**, 1355–1370 (2017).

208. McScweeney, P. L. H., Olson, N. F., Fox, P. F., Healy, A. & Hojrup, P.
Proteolytic specificity of chymosin on bovine αS1-casein.
J. Dairy Res. **60**, 401–412 (1993).
209. McSweeney, P. L. H., Olson, N. F., Fox, P. F. & Healy, Á.
Proteolysis of bovine αS2-casein by chymosin.
Z. Lebensm. Unters. Forsch. **199**, 429–432 (1994).
210. Carles, C. & Ribadeau-Dumas, B.
Kinetics of action of Chymosin (Rennin) on some peptide bonds of bovine β-casein.
Biochemistry **23**, 6839–6843 (1984).
211. Monogioudi, E. *et al.*
Effect of enzymatic cross-linking of β-casein on proteolysis by pepsin.
Food Hydrocoll. **25**, 71–81 (2011).
212. Thévenot, J., Cauty, C., Legland, D., Dupont, D. & Floury, J.
Pepsin diffusion in dairy gels depends on casein concentration and microstructure.
Food Chem. **223**, 54–61 (2017).
213. Holt, C.
Structure and stability of bovine casein micelles.
Adv. Protein Chem. **43**, 63–151 (1992).
214. Arroyo-Loranca, R. G. *et al.*
Ps19, a novel chitin binding protein from Pteria sterna capable to mineralize aragonite plates in vitro. *PLoS One* **15**, 1–15 (2020).
215. Cartwright, J. H. E. & Checa, A. G.
The dynamics of nacre self-assembly. *J. R. Soc. Interface* **4**, 491–504 (2007).
216. Rae Cho, K. *et al.*
Direct observation of mineral-organic composite formation reveals occlusion mechanism. *Nat Commun* **7**, 10187 (2016).
217. Mao, L.-B. *et al.*
Synthetic nacre by predesigned matrix-directed mineralization.
Science **354**, 107–110 (2016).
218. Lopez, E. *et al.*
Demonstration of the capacity of nacre to induce bone formation by human osteoblasts maintained in vitro. *Tissue Cell* **24**, 667–679 (1992).
219. Atlan, G., Balmain, N., Berland, S., Vldal, B. & Lopez, E.
Reconstruction of human maxillary defects with nacre powder: Histological evidence for bone regeneration.
Comptes Rendus l'Academie des Sci. - Ser. III **320**, 253–258 (1997).
220. Atlan, G. *et al.*
Interface between bone and nacre implants in sheep.
Biomaterials **20**, 1017–1022 (1999).
221. Clay, K.
Defensive symbiosis : a microbial perspective. *Funct. Ecol.* **28**, 293–298 (2014).
222. Cavaliere, M., Feng, S., Soyer, O. S. & Jiménez, J. I.
Cooperation in microbial communities and their biotechnological applications.
Environ. Microbiol. **19**, 2949–2963 (2017).
223. Epstein, A. K., Hochbaum, A. I., Kim, P. & Aizenberg, J.
Control of bacterial biofilm growth on surfaces by nanostructural mechanics and

geometry. *Nanotechnology* **22**, 494007 (2011).
224. Cartwright, J. H. E., Checa, A. G. & Sainz-Díaz, C. I.
Nacre Is a Liquid-Crystal Thermometer of the Oceans.
ACS Nano **14**, 9277–9281 (2020).
225. Bixler, G. D. & Bhushan, B.
Biofouling : lessons from nature.
Philos. Trans. R. Soc. A Math. Phys. Eng. Sci. **370**, 2381–2417 (2012).
226. Pagoropoulos, A., Laumann Kjaer, L., Dong, Y., Birkved, M. & McAloone, T. C.
Economic and Environmental Impact Trade-Offs Related to In-Water Hull Cleanings of Merchant Vessels. *J. Ind. Ecol.* **22**, 916–929 (2017).
227. Drits, V. A. & Bookin, A. S.
Crystal Structure and X-Ray Identification of Layered Double Hydroxides.
in *Layered Double Hydroxides: Present and Future* 41–100 (2006).

VII Appendix

1 All Methods

Dynamic Light Scattering (DLS)
Malvern Zetasizer Nano ZS: disposable PS cuvettes.
Malvern Mastersizer 2000: MS-1 sample unit and a 300RF lens, which allows detection of colloid sizes from 0.05 to 900 µm or MS-7 Magnetically Stirred Cell (beam length 10 mm, 300F lens)
Zeta Potential Measurement
Malvern "Zetasizer Nano ZS" with Autotitration Unit "MPT-2" + Vacuum Degasser.
measurements were performed in disposable folded capillary cells (U-shaped)
Scanning Electron Microscopy (SEM)
Zeiss NEON 40
Focussed Ion Beam (FIB)
Zeiss NEON 40
Elementary Analysis
elementar vario MicroCube, EDX
X-Ray Diffraction (XRD)
Bruker D5005 (Cu-Kα = 0.154 nm).
Thermogravimetric Analysis (TGA)
Mettler-Toledo TGA/SDTA 851e, optionally Pfeiffer Vacuum OmniStar, mostly 5 °C/min
Dynamic mechanical analysis (DMA)
Triton Technology (TT) DMA
Rheology measurements
Anton Paar Couette Rheometer "Rheolab QC"
Infrared Spectroscopy (ATR-FTIR)
Bruker Alpha-P (λ = 633 nm)
Bruker Attenuated Total Reflection Fourier-Transformed
IRRAS Bruker VERTEX 70
Film thickness
Mahr MarCator 10/5 R
Parallel Reactor System
Hitec Zang LabKit #2026
Centrifuge
Volumes 20 mL to 500 mL: BECKMAN COULTER Avanti® J-E with a JA-10 Rotor
Volumes up to 20 mL : Hettich Micro 20
ULTRA-TURRAX®
small formulations: IKA® T10 basic
big formulations: IKA® T 45
Ultrasonic
BANDELIN "SONOCOOL 255"
pH Electrode
METTLER TOLEDO SevenMulti pH-Meter
Peristaltic Pump
Heidolph PD5201 (constant flow); Heidolph Hei-FLOW Precision 01 (regulated flow)
Rotary Evaporator

Heidolph Laborota 4000 efficient

Syringe Driver

B. Braun PERFUSOR IV

Dissolver

VMA Getzmann DISPERMAT® TU

small formulations: Ø = 20 mm dissolver disk

big formulations: Ø = 40 mm dissolver disk

Contact Angle Measurement

KRÜSS Drop Shape Analyzer 25E

Scanning Electron Microscopy (SEM)

Zeiss NEON 40

Focussed Ion Beam (FIB)

Zeiss NEON 40

X-Ray Diffraction (XRD)

Bruker D5005 (Cu-Kα = 0.154 nm).

Dynamic mechanical analysis (DMA)

Triton Technology (TT) DMA

Rheometer

Anton Paar Couette Rheometer "Rheolab QC"

Film thickness

Mahr MarCator 10/5 R

Centrifuge

BECKMAN COULTER Avanti® J-E with a JA-10 Rotor

ULTRA-TURRAX®

IKA® T10 basic

BANDELIN "SONOCOOL 255"

Sputter Coater

BAL-TEC SCD 500 with BAL-TEC QSG 100 Quartz film thickness monitor

Au/Pd target

Freeze Drying Machine

Zirbus Technology Sublimator VaCo 5

2 Colloids

2.1 LDH synthesis

1st Approach: The manual regulation of the pH during the very slow addition of the metal salts by a syringe driver (0.5 mL/min) requires unachievable skills and did not result in neither wished nor reproducible product, and was therefore quickly discarded.

2nd Approach: The use of a parallel reactor system (HiTec Zang) lead to a non-stoichiometric addition of NaOH (**Figure A-169**). The stoichiometric amount of NaOH (130 mL, 4M) was consumed after approx. 70% of the theoretical metal salt addition time (180 min). The particle size was smaller than 300 nm in lateral size (DLS + SEM).

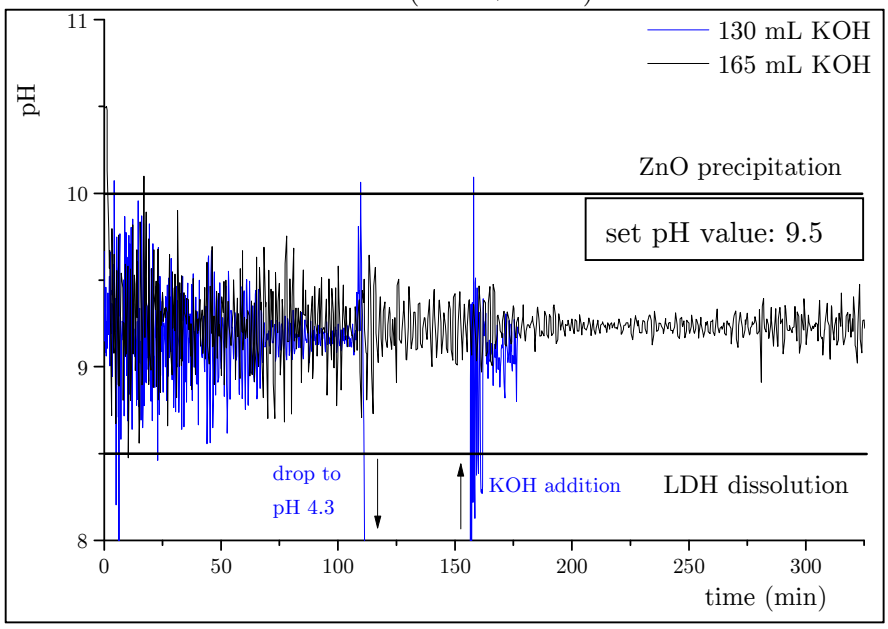


Figure A-169: pH vs time curve of LDH synthesis in parallel reactor (2nd)

Therefore, a second synthesis was conducted with an excess reservoir of 4 M NaOH and a smaller addition rate of the metal salt solution. In the end of the synthesis, 165 mL (approx. 120% excess) were consumed, which lead to small colloids ranging from 200-300 nm.

There are several possible reasons why the synthesis did not lead to a stoichiometric addition. In the beginning of the synthesis, the ionic strength and the buffering capability is very low. Consequently, the regulation of the pH at 9.5 is more challenging in the beginning of the synthesis, what can lead to non-stoichiometric addition in the overall synthesis. The shown curve does not show a surpassing of the upper and lower boundary (pH 8,5-10,0). The pH values can only be measured in 10 second steps. That means, that in the meantime of the synthesis the pH was not reliably recorded. Moreover, the parallel reactor works with the GraviDos® technology, which is based on a traditional dropping funnel with a magnetic valve in between and a weighing instrument.[‡‡‡] This could be the reason why the deviation from the actual set pH value (9.5) could not be held appropriately. The actual pH average in these syntheses is about 9.25. It is assumed, that some of the OH^- ions act as intercalating ion.

3rd Approach: The combination of a constant flow maintained by a syringe driver and a peristaltic pump with a pH-regulating flow lead to distinctly bigger LDH particle sizes. The size of the colloids reaches the same size like in the upcoming 4th Approach. The pH electrode used in this synthesis is able to send signals every three seconds and the overall synthesis is

[‡‡‡] http://www.hitec-zang.de/en/laboratory-devices/gravimetric-dosing.html

shortened towards the 2nd Approach by approx. 100 minutes. The big drawback of this method is the required change of the syringes every 50 mL of added solution. For future experiments on LDH colloids, this method cannot be taken into consideration, because of reproducibility issues for further using.

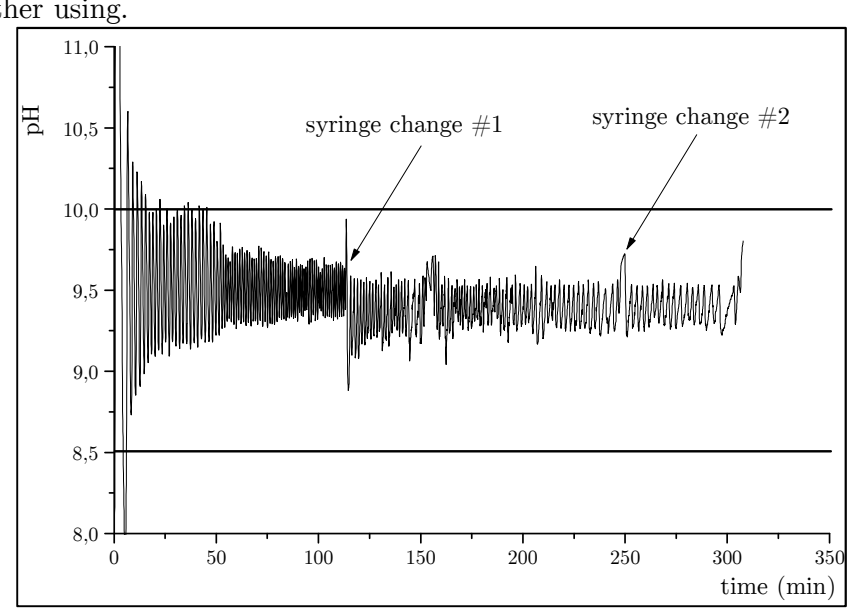


Figure A-170: pH vs time data of LDH synthesis of 3rd approach
Arrows indicate syringe changes.

4th Approach: The combination of two peristaltic pumps leads to the best and reproducible results. The synthesis conditions lead to colloids ten times bigger than in the parallel reactor and took place stoichiometrically. The synthesis time was also 1 hour faster. The comparison of the different approaches can be shown best with the XRD and SEM technique (**Figure A-171**).

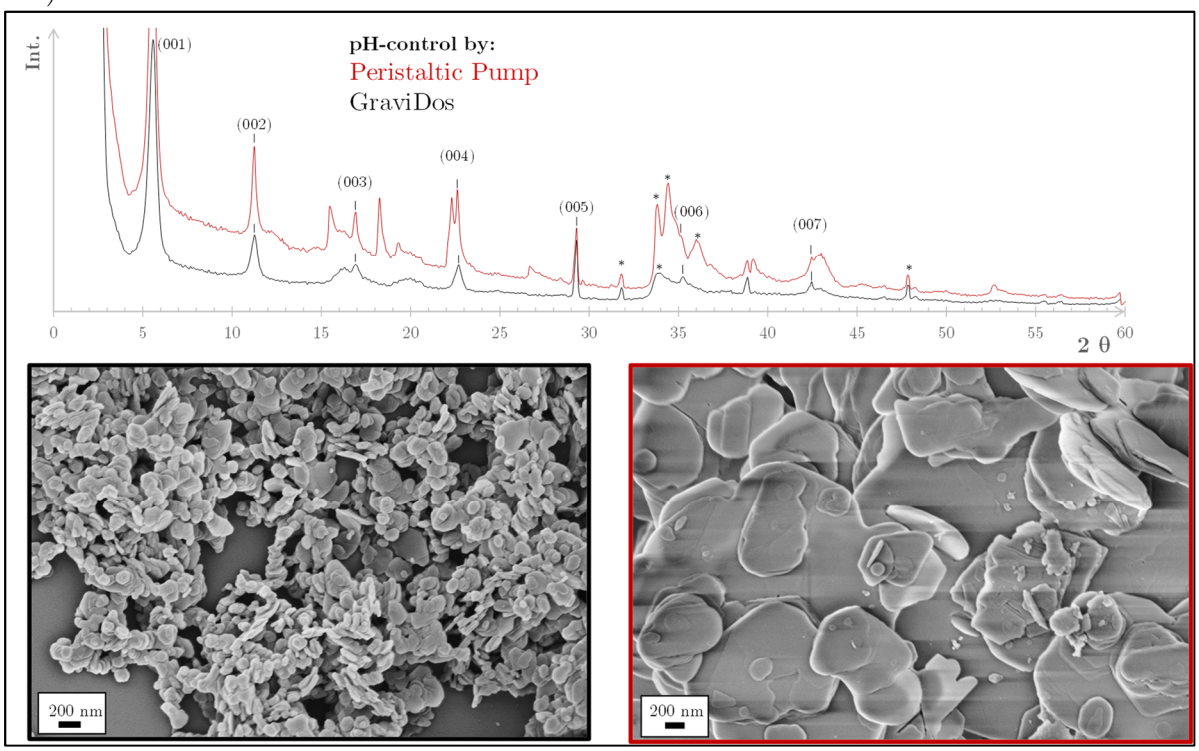


Figure A-171: Evaluation of the synthesized LDH colloids.
Top: XRD diffraction pattern of LDH samples from the 2nd and 4th approach. *Bottom left:* SEM image of small colloids synthesized in parallel reactor; bottom *right*: SEM image of big colloids synthesized with peristaltic pumps

The small LDH colloids made with the GraviDos® technique show broader X-Ray diffraction signals less signals in comparison. There are a lot of reasons why it is very complex to analyze signals from LDH phases by XRD. The high LDH polytype diversity or Zn/Al superstructures lead to additional signals, the broad signals indicate stacking faults and the impurities also show signals (ZnO marked with * in **Figure A-171**).[227] However, the complete and accurate analysis of the XRD spectra was not from further interest within this work.
The SEM images show, that the colloids are a power of magnitude bigger. Dynamic Light Scattering is a fast and reliable method to measure the actual primary particle size. However, in unknown cases the imaging by SEM and the X-Ray diffraction pattern is indispensable.
To sum up, the more precisely the pH is controlled, the bigger the colloids can grow. The condensation of hexa-aqua complex octahedrons is preferred between pH 8.5 and pH 10.

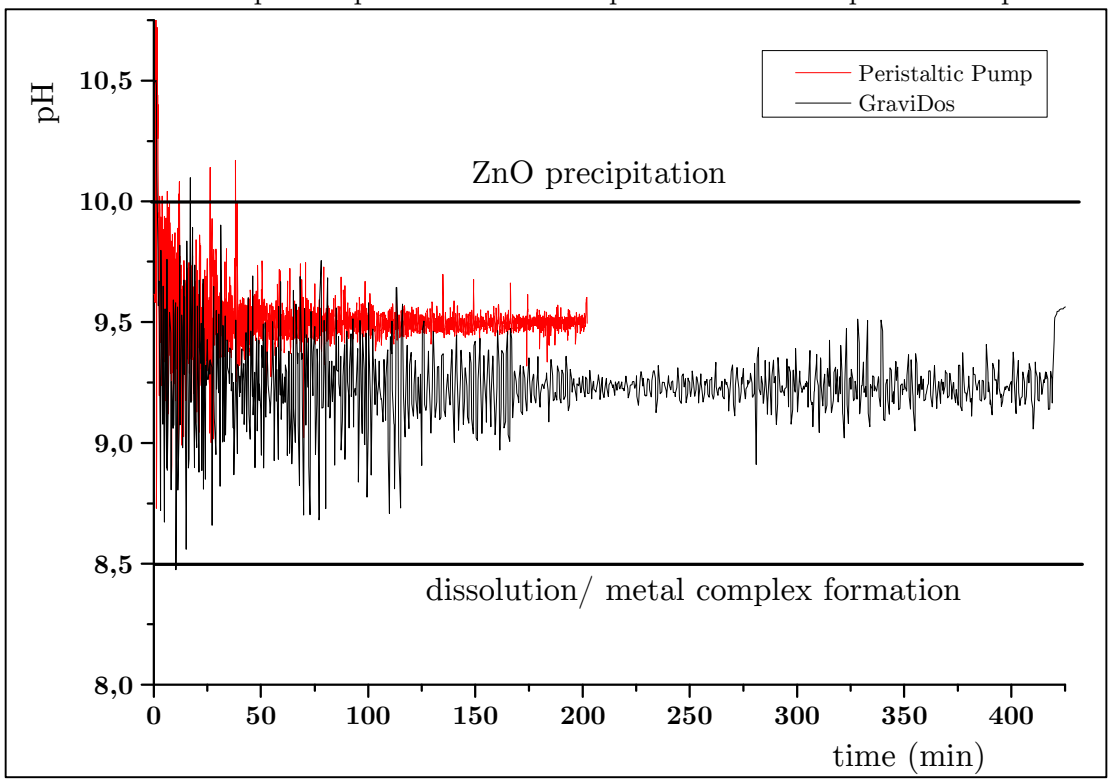


Figure A-172: pH-time data of the 2nd and 4th approach in comparison

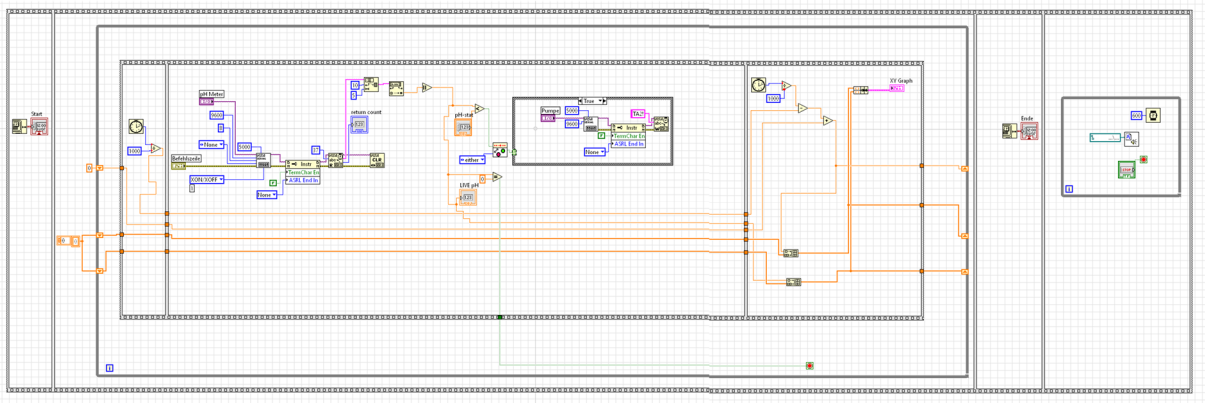


Figure A-173: LabView Block Diagram of pH-stat regulation

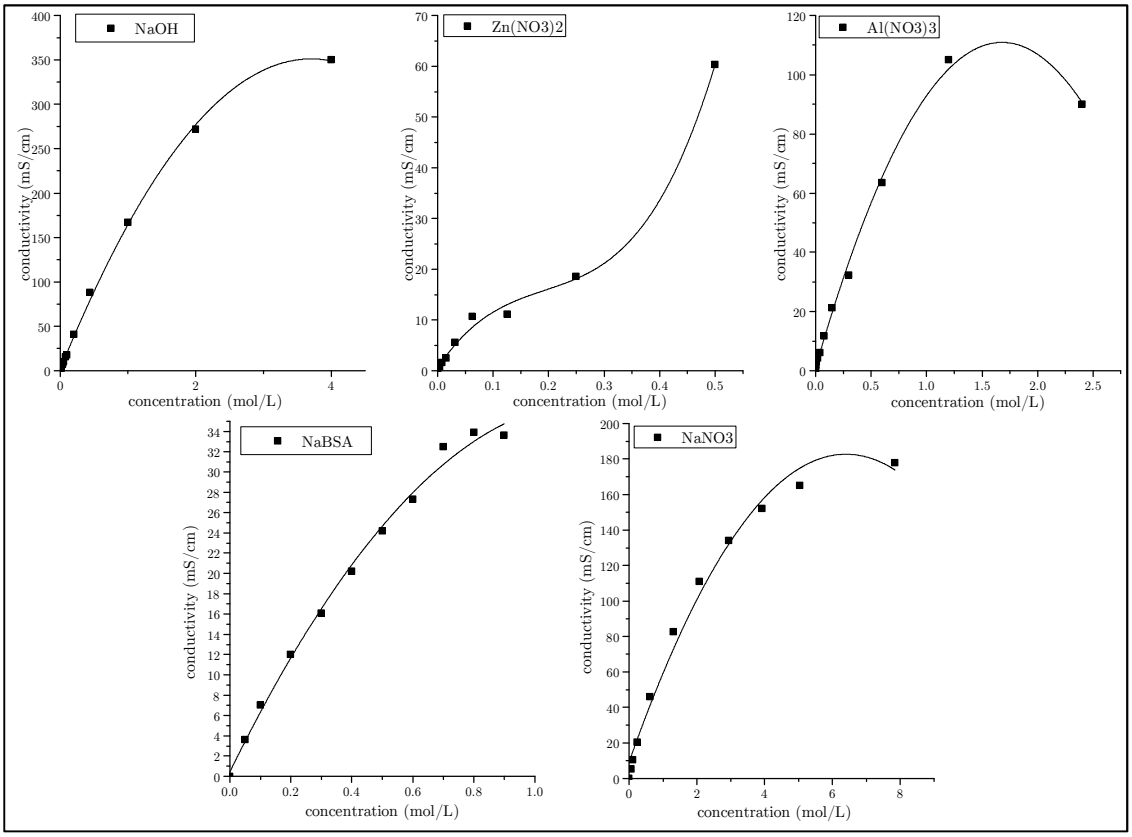


Figure A-174: Net conductivities of LDH synthesis involved solutions

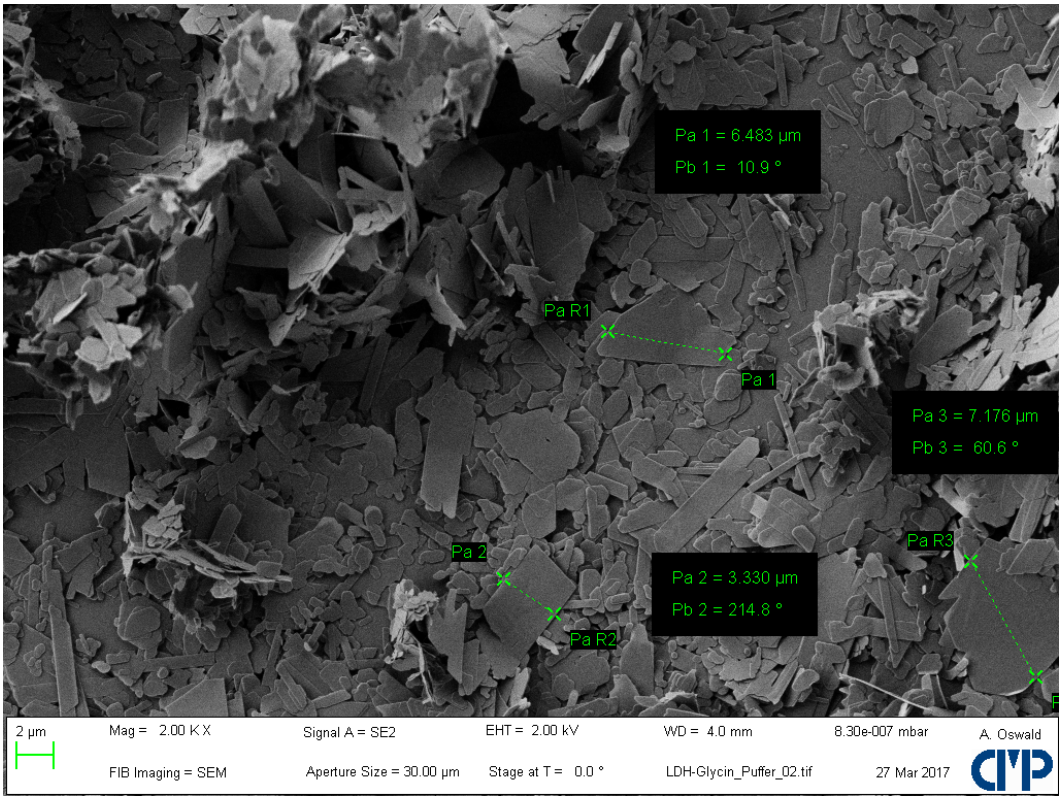


Figure A-175: Morphology of 5 µm LDH phase

2.2 Kaolinite

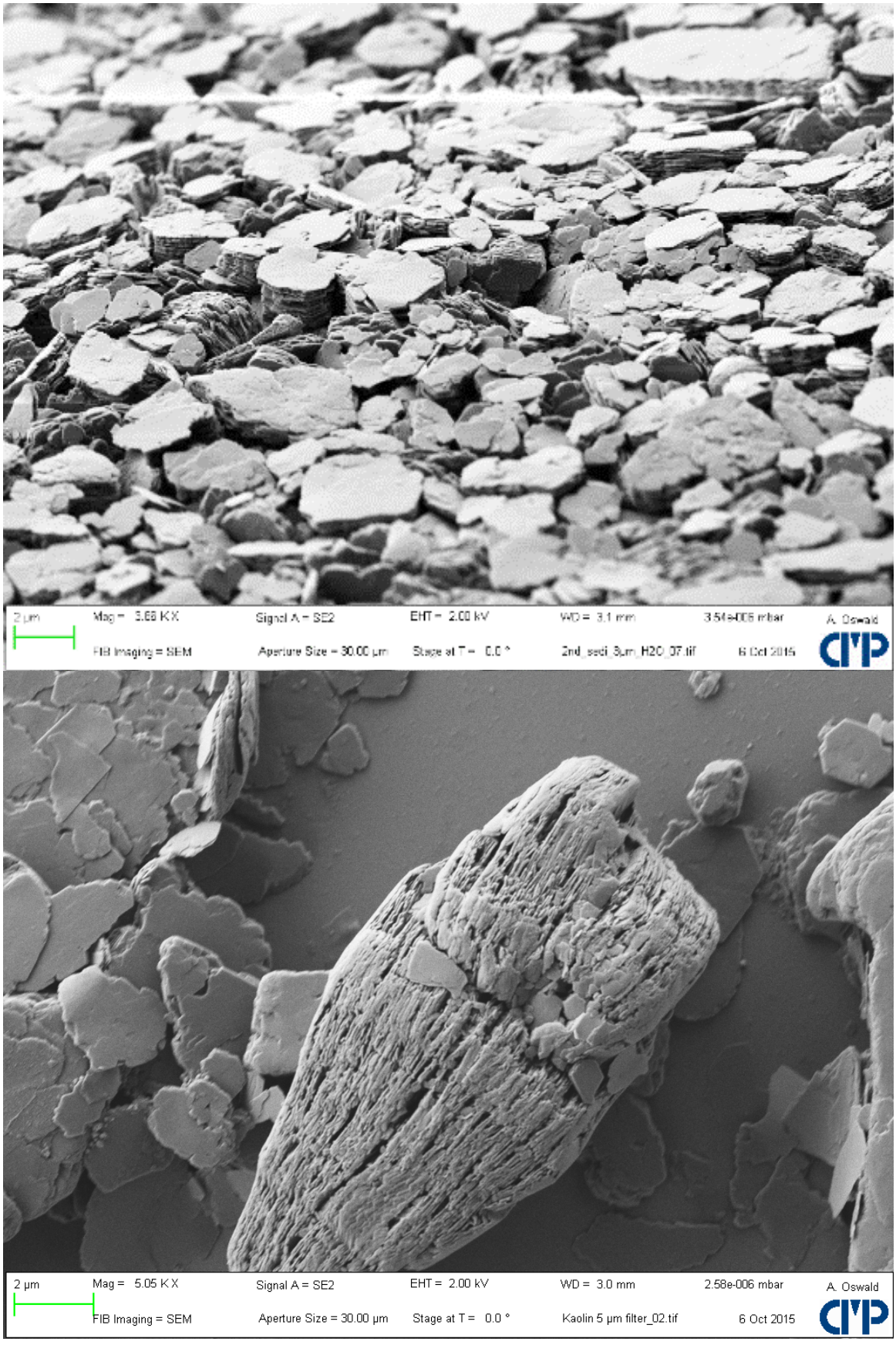


Figure A-176: Book-Like Colloid of Kaolinite

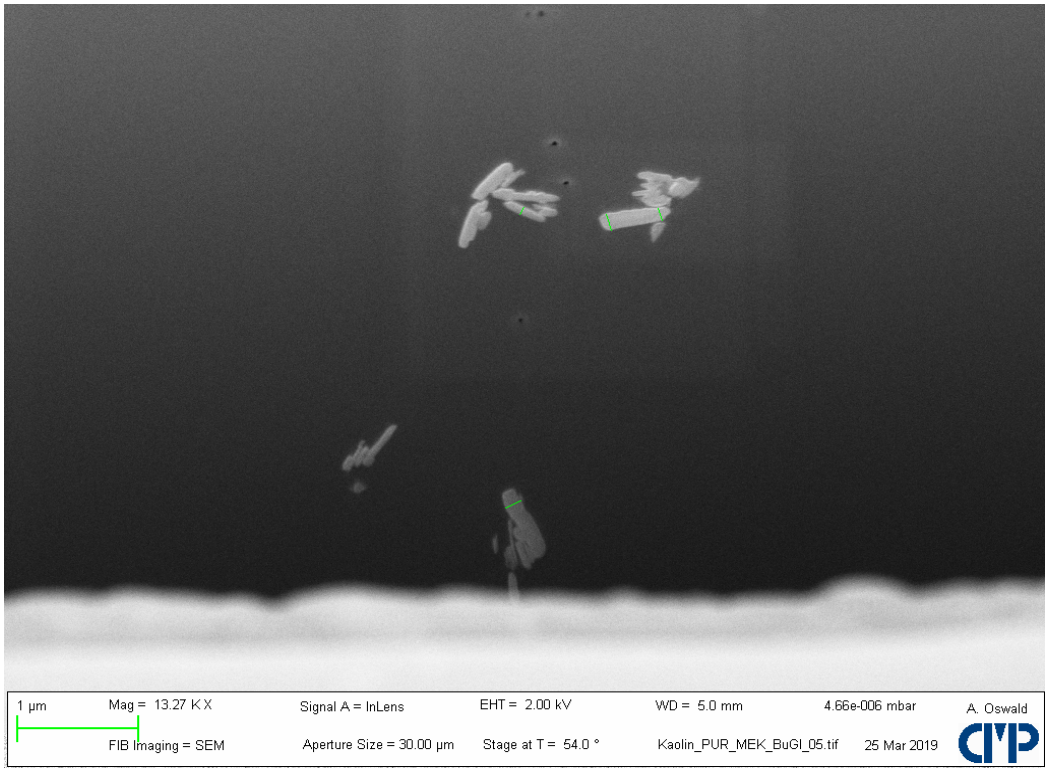


Figure A-177: SEM image of a FIB-cut through a PUR/kaolinite composite.
The four green lines measure kaolinite platelet thicknesses of 70, 108, 138 and 142 nm

2.3 Polystyrene Colloids

Table A-28: Weighed portions of PS colloids

#	PVP [g]	AIBA [g]	St [g]	METAC [g]	water [g]	METAC/St [g/g]	Size (DLS) [nm]	PdI (DLS)	Size (SEM)* [nm]
1	0.6	0.4	7.9	1.1600	103	0.118	65	0.063	61
2	0.6	0.4	7.7	0.8100	102	0.084	58	0.040	66
3	0.6	0.4	7.7	0.6167	103	0.064	75	0.006	80
4	0.6	0.4	7.7	0.4826	103	0.050	86	0.008	93
5	0.6	0.4	7.7	0.3837	103	0.040	97	0.048	110
6	0.6	0.4	7.7	0.3144	103	0.033	106	0.002	105
7	0.6	0.4	7.7	0.2655	103	0.028	145	0.020	139
8	0.6	0.4	7.7	0.2330	103	0.024	172	0.019	140
9	0.6	0.4	7.7	0.4400	103	0.046	88	0.007	85
10	0.6	0.4	7.7	0.3400	103	0.035	107	0.010	111
11	0.6	0.4	7.7	0.3157	103	0.033	123	0.013	123
12	0.6	0.4	7.7	0.4084	102	0.042	95	0.011	95
13	0.6	0.4	7.7	3.3100	103	0.343	95	0.018	-
14	0.6	0.4	7.7	1.7600	104	0.183	90	0.025	-
15	0.6	0.4	7.7	1.5300	103	0.159	84	0.034	-
16	0	0.4	7.7	0.1000	103	0.010	136	0.021	127
17	0	0.4	7.7	0.1240	103	0.013	107	0.020	110
18	0	0.4	7.7	0.1650	103	0.017	103	0.038	99
19	0	0.4	7.7	0.2640	103	0.027	106	0.014	94
20	0	0.4	7.7	0.0400	103	0.004	230	0.027	210

*arithmetic mean, measured by Image J, N=30

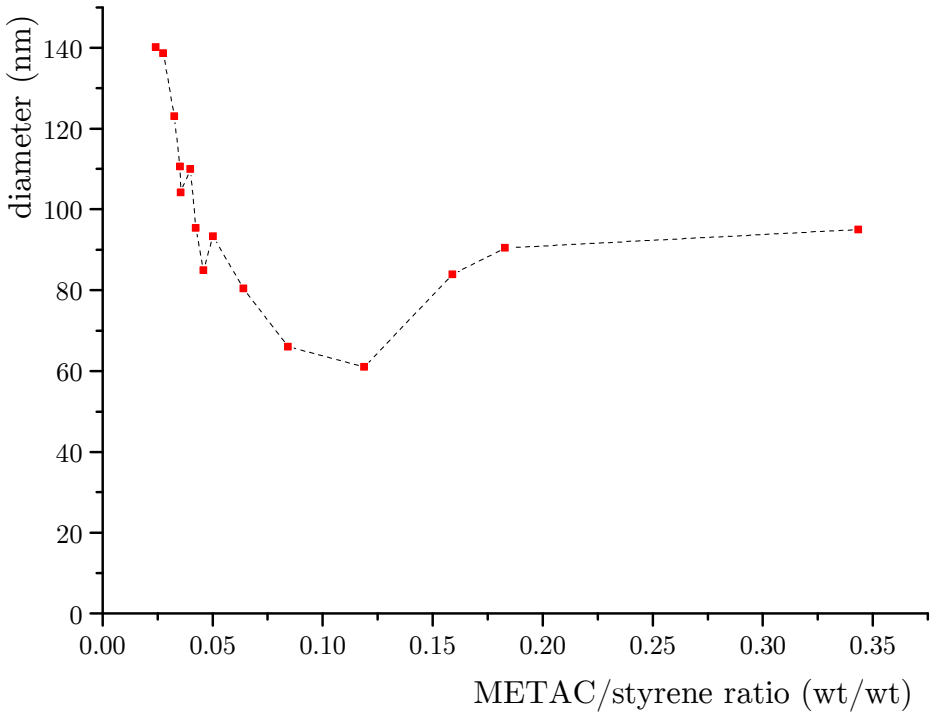


Figure A-178: All PVP containing PS-dispersions (#13-15 added)

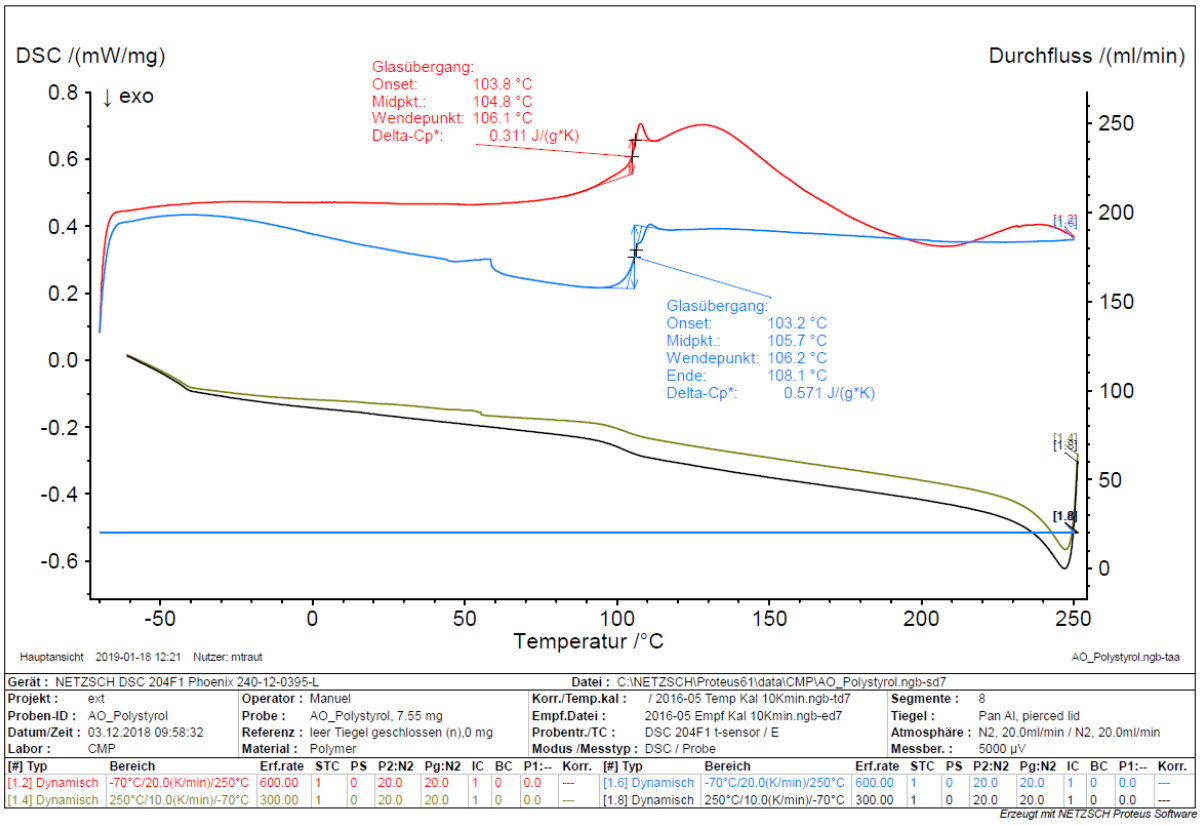


Figure A-179: Glass transition temperature determination of PS via Proteus Software

2.4 Polyurethane Colloids

Table A-29: Weighed portions for PUR synthesis with polyester diol Priplast 1900

#	polyester diol P1900 [g]	DMPA [g]	TMXDI [g]	TMP [g]	DMAE [g]	2-butanone [g]	butanol [g]	water [g]	PdI	N-Avg d.nm
1	114.15	6.06	27.99	2.66	4.88	45	4.63	277	0.24	45
2	128.22	5.17	27.97	2.66	4.16	46	4.64	277	0.15	114*
3	120.24	5.68	28.02	2.66	4.58	45	4.66	277	0.21	97
4	104.83	6.68	28.01	2.66	5.38	45	4.66	277	0.28	13
5	116.69	5.90	27.97	2.66	4.75	45	4.66	277	0.16	75*
6	69.49	8.91	28.04	2.66	7.18	45	4.66	277	0.21	10*
7	109.97	6.33	28.01	2.66	5.10	46	4.66	277	0.18	47

Table A-30: Weighed portions for PUR synthesis with polyester diol P-2010

#	polyester diol P-2010 [g]	DMPA [g]	TMXDI [g]	TMP [g]	DMAE [g]	2-butanone [g]	butanol [g]	water [g]	N-Avg d.nm	PdI
1	19.31	1.3682	5.63	0.5346	0.88	9.1	0.9	56.1	96	0.18
2	9.58	2.0178	5.62	0.538	1.61	9.1	0.9	55.6	11	0.23
3	6.49	2.2273	5.61	0.5387	1.79	9.1	1.0	55.3	17	0.30
4	25.95	0.8962	5.62	0.5343	0.72	9.1	0.9	55.6	190	0.21
5	13	1.7879	5.62	0.5337	1.44	9.1	0.9	55.4	9	0.29
6	31.12	0.5356	5.59	0.5366	0.43	9.1	0.9	56.0	8700	1.00
7	3.53	2.4338	5.62	0.5317	1.96	9.1	0.9	55.5	22	0.37
8	64.62	8.9	28.01	2.6663	7.18	141.7	4.6	276.6	3	0.47
9	17.36	1.4863	5.62	0.537	1.20	9.1	0.9	55.4	9	0.22
10	22.29	1.1367	5.62	0.5336	0.92	9.1	1.0	73.8	80	0.15
11	21.58	1.1902	5.63	0.5528	0.96	9.4	0.9	55.4	76	0.19
12	109.64	5.8148	28.07	2.6637	4.68	45.2	4.6	276.8	92	0.19

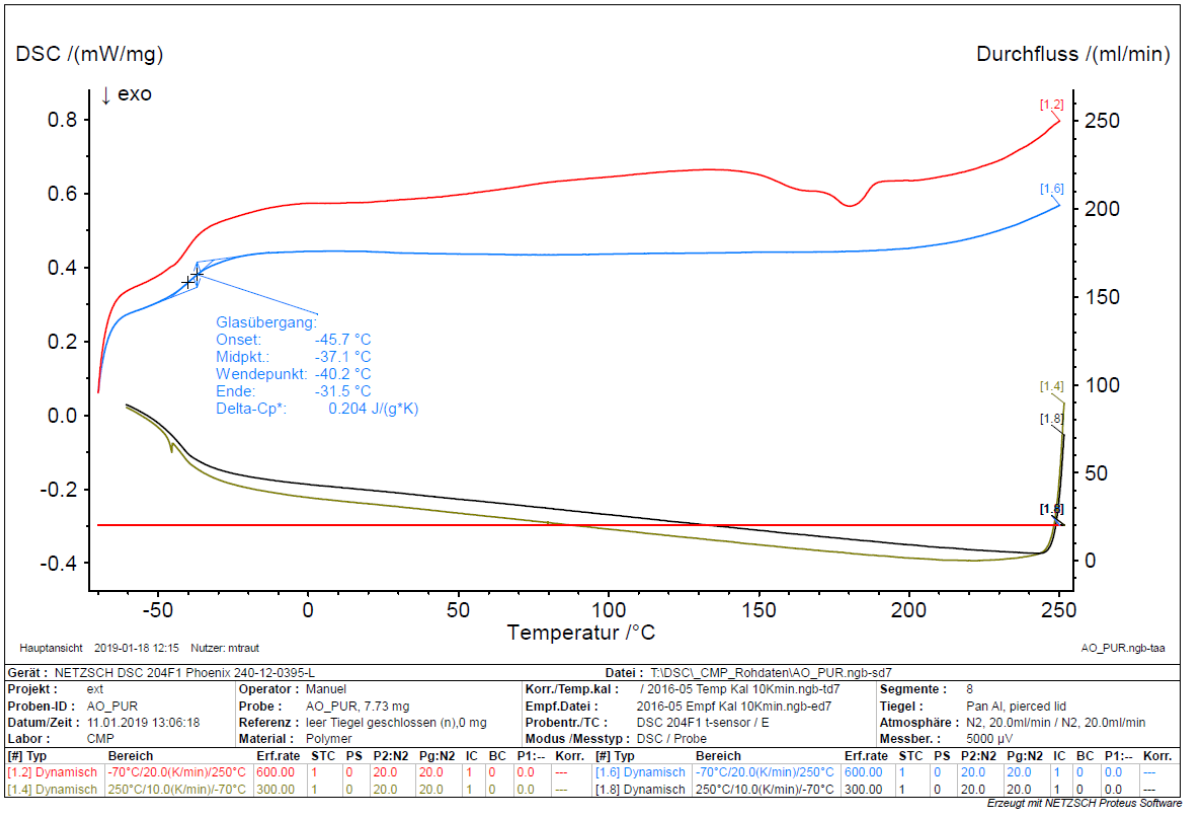
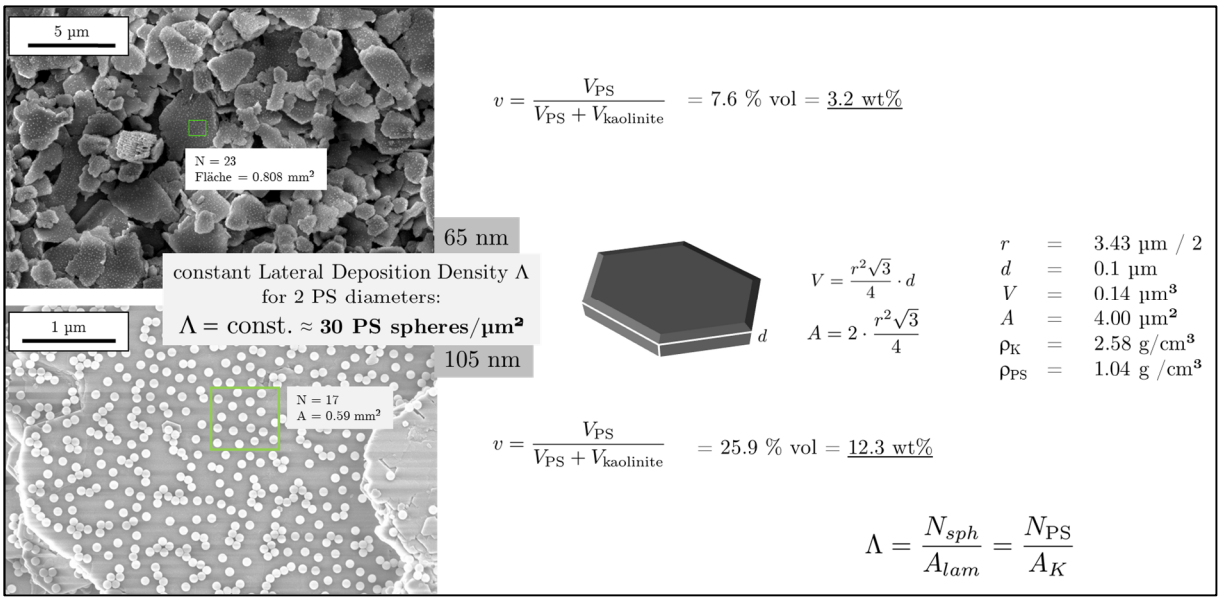


Figure A-180: Glass transition temperature determination of PUR via Proteus Software

3 PS @ kaolinite assemblies

3.1 Lateral Deposition Density Λ and Surface Affinity



$$v = \frac{V_{\mathrm{PS}}}{V_{\mathrm{PS}} + V_{\mathrm{kaolinite}}} = 7.6\ \%\ \mathrm{vol} = \underline{3.2\ \mathrm{wt}\%}$$

$$V = \frac{r^2\sqrt{3}}{4} \cdot d \qquad A = 2 \cdot \frac{r^2\sqrt{3}}{4}$$

$$v = \frac{V_{\mathrm{PS}}}{V_{\mathrm{PS}} + V_{\mathrm{kaolinite}}} = 25.9\ \%\ \mathrm{vol} = \underline{12.3\ \mathrm{wt}\%}$$

$$\Lambda = \frac{N_{sph}}{A_{lam}} = \frac{N_{\mathrm{PS}}}{A_K}$$

Figure A-181: Lateral Deposition Density

The cylindrical model of the 2D colloid give almost the same result.

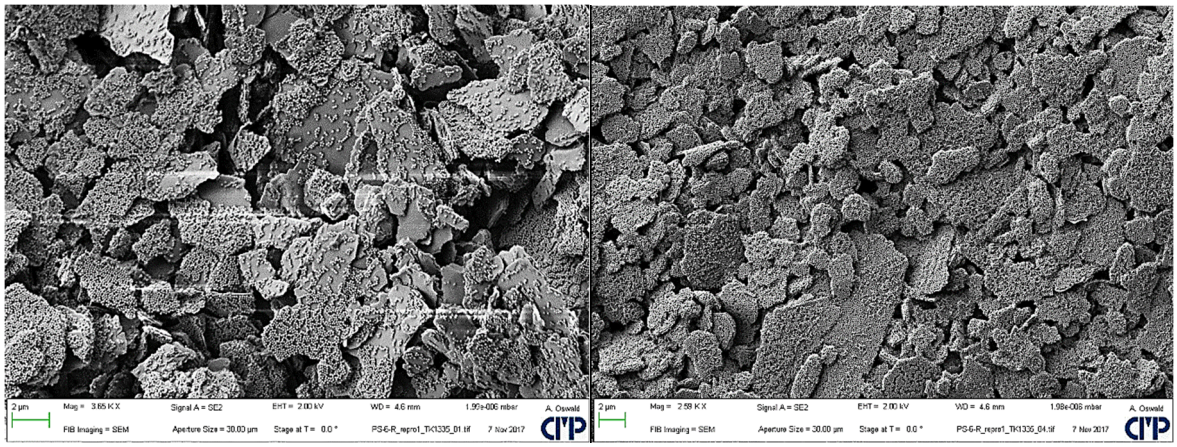


Figure A-182: Full deposition of PS spheres @ kaolinite

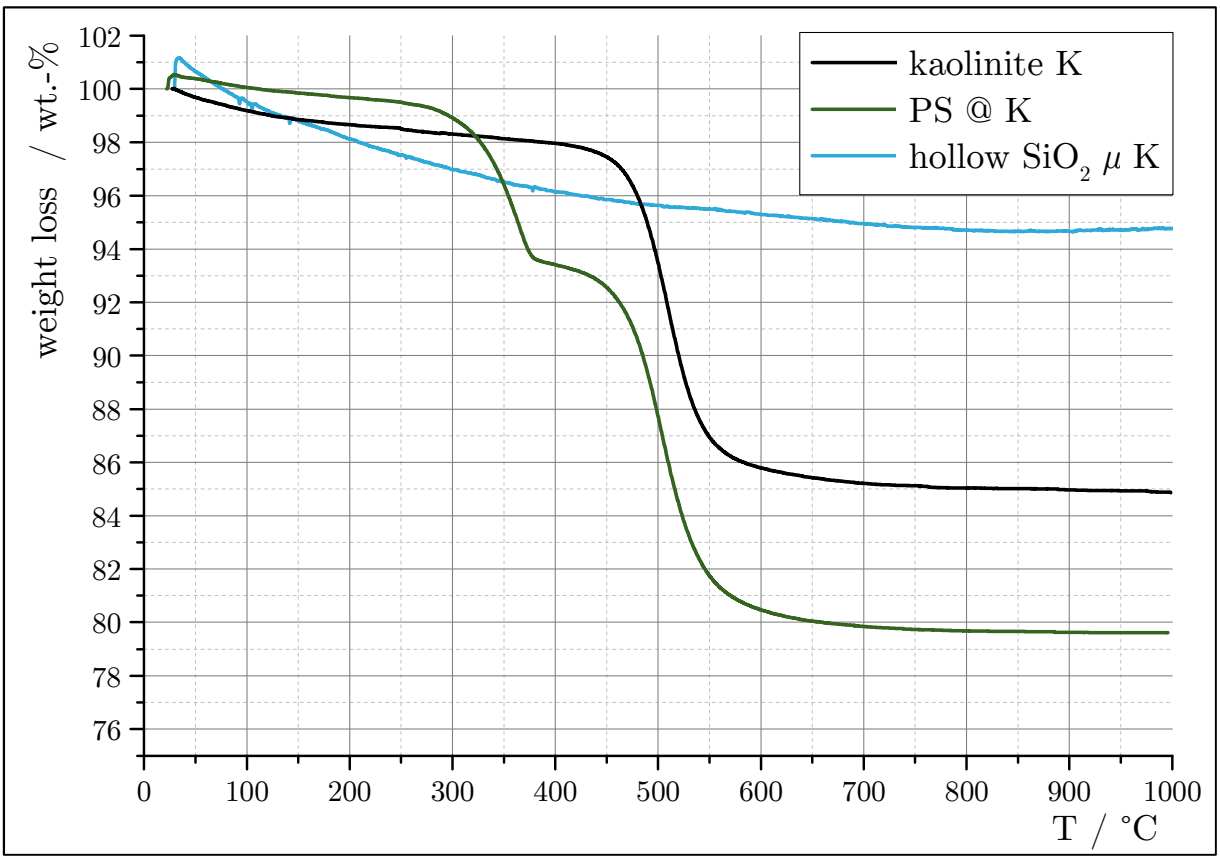


Figure A-183: TGA traces of kaolinite, PS @ kaolinite and hollow SiO_2 μ K

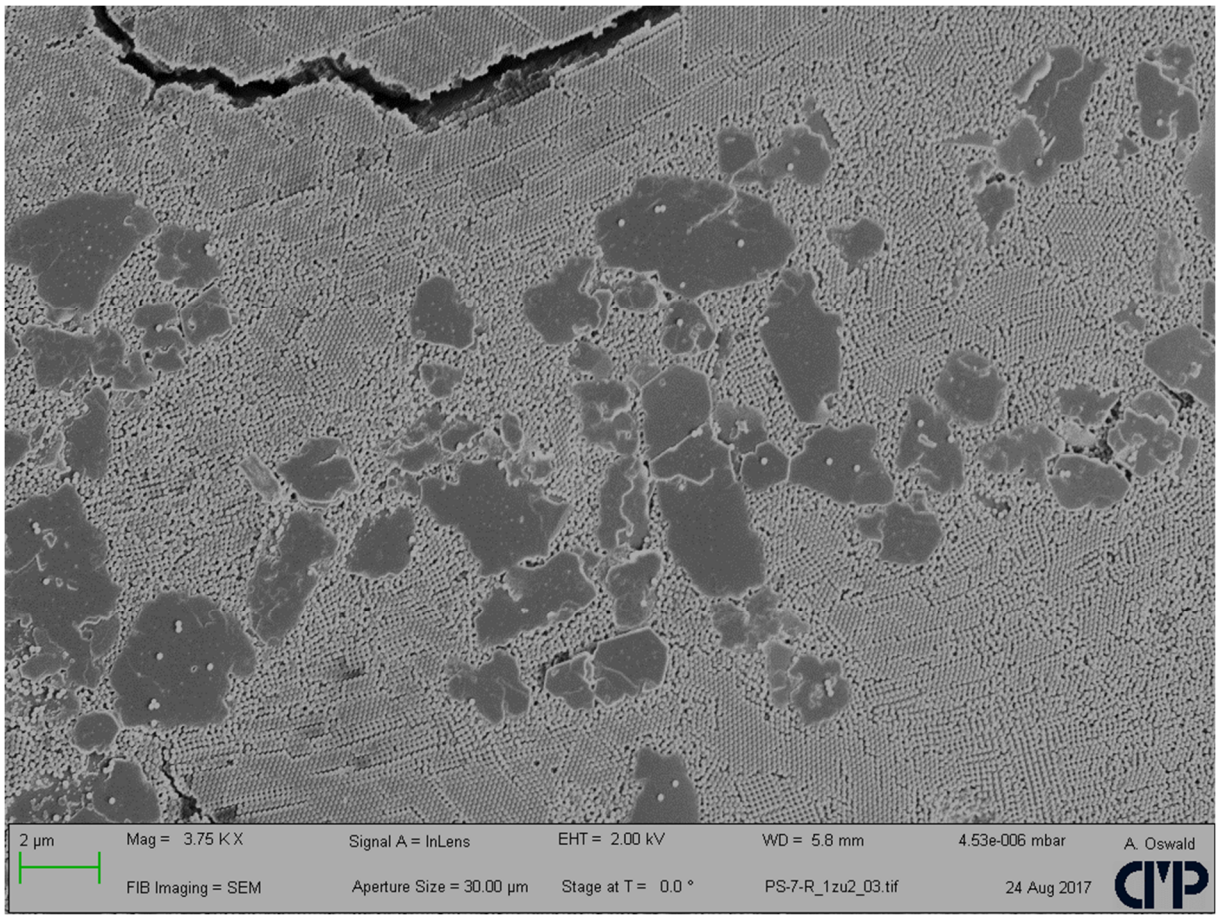


Figure A-184: PS (+) Colloidal Crystals at kaolinite crystal edges (+)
The PS colloids show no surface affinity. The capillary forces between the highly ordered colloids dominate over the electrostatic forces after evaporation of water.

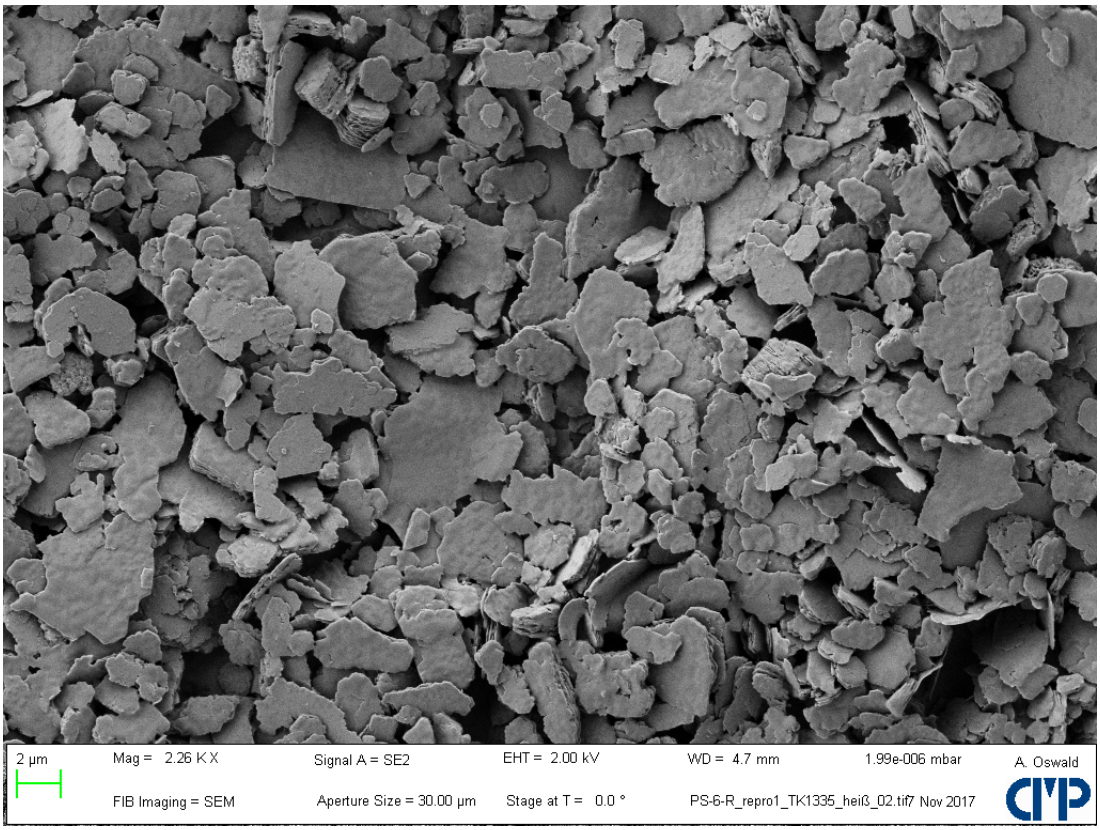


Figure A-185: 105 nm PS spheres on kaolinite after temperature treatment at 120 °C

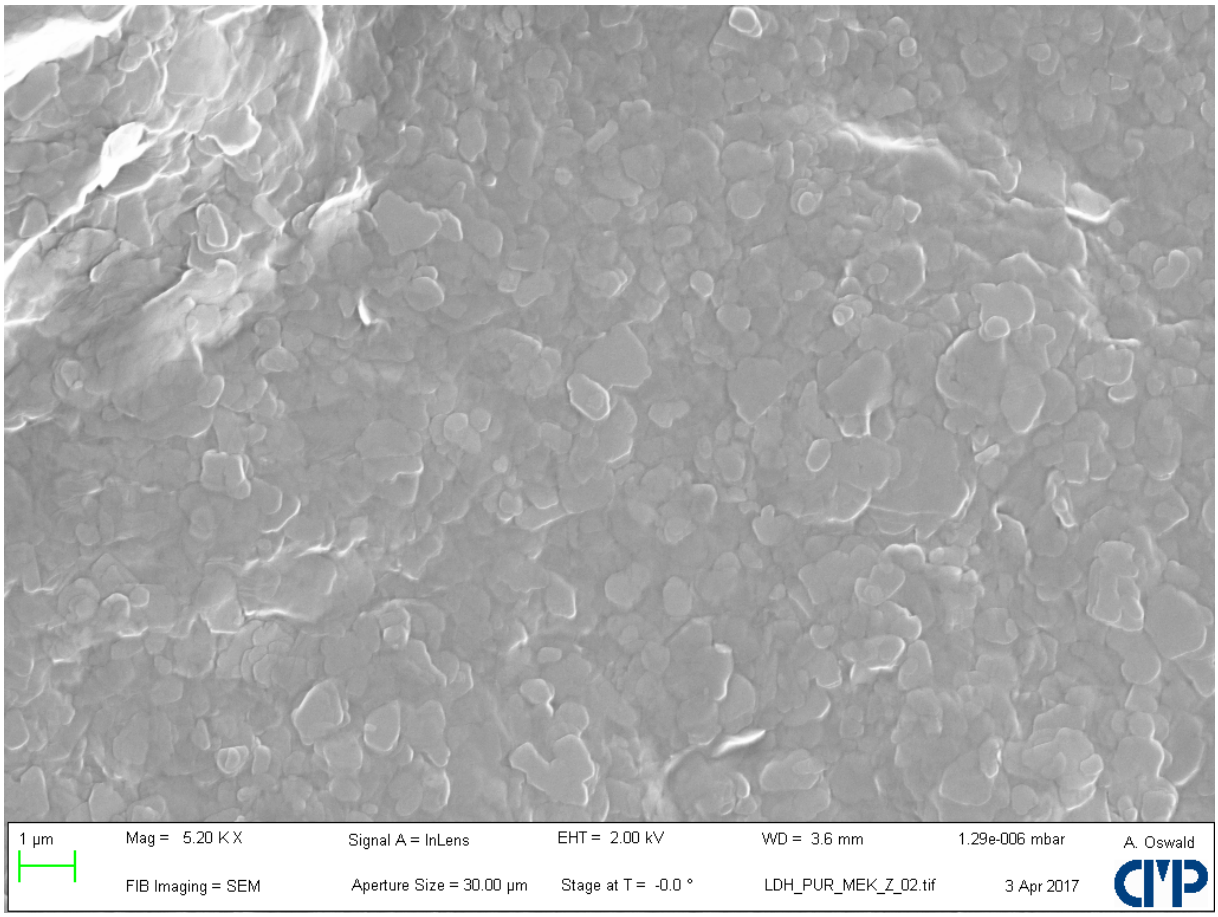


Figure A-186: LDH/PUR composite dispersion after centrifugation

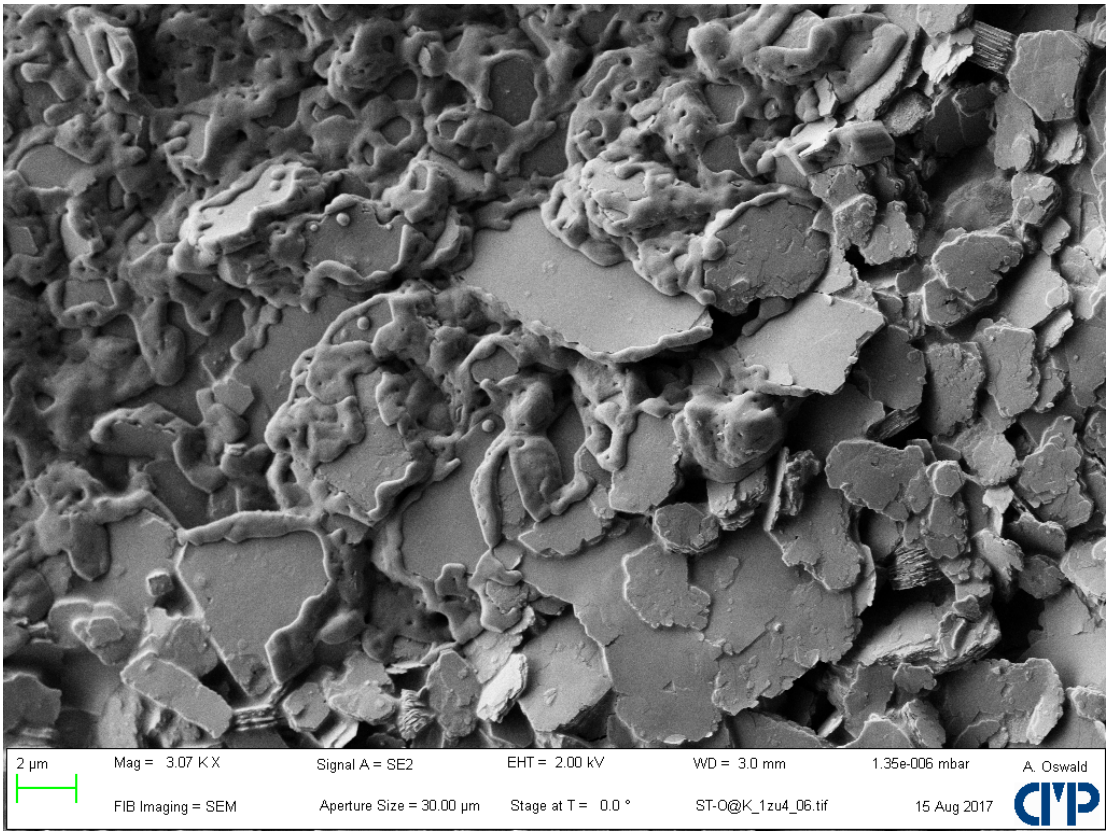


Figure A-187: Electrostatic Deposition of SiO_2 spheres (-) at kaolinite edges (+)

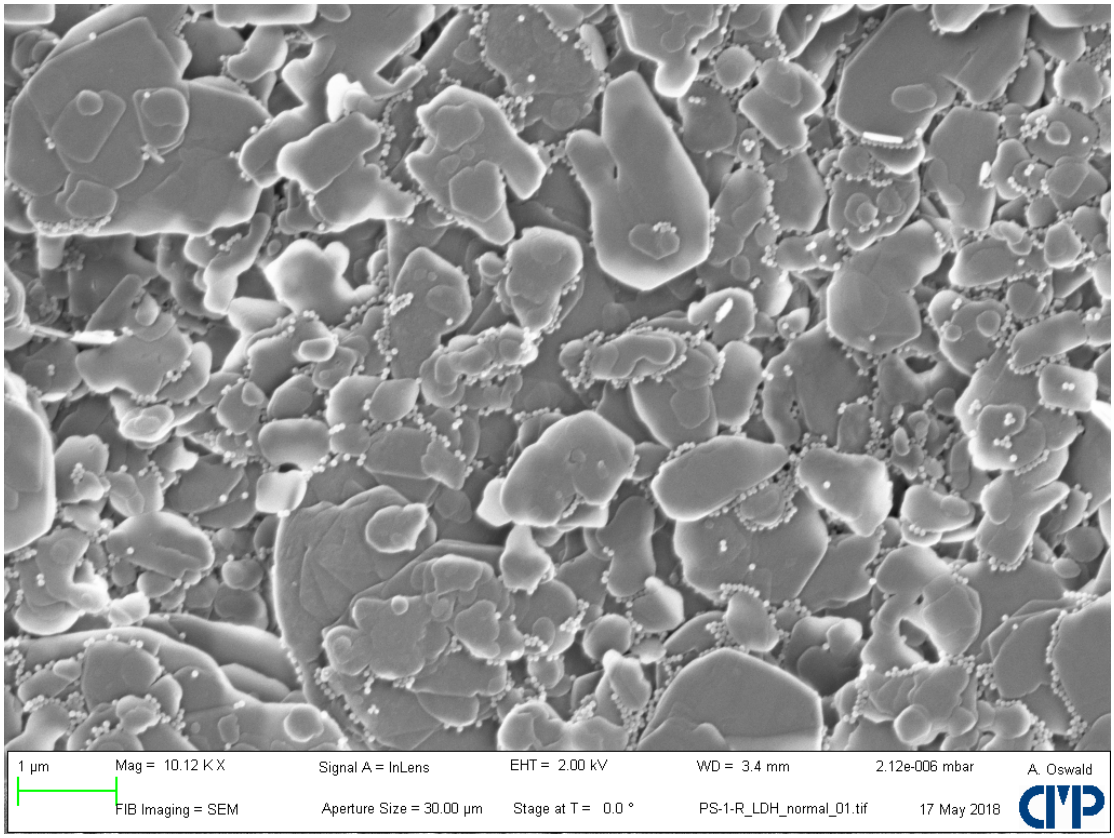


Figure A-188: PS65 @ LDH_{s00}

3.3 Janus deposition pattern of organized kaolinite

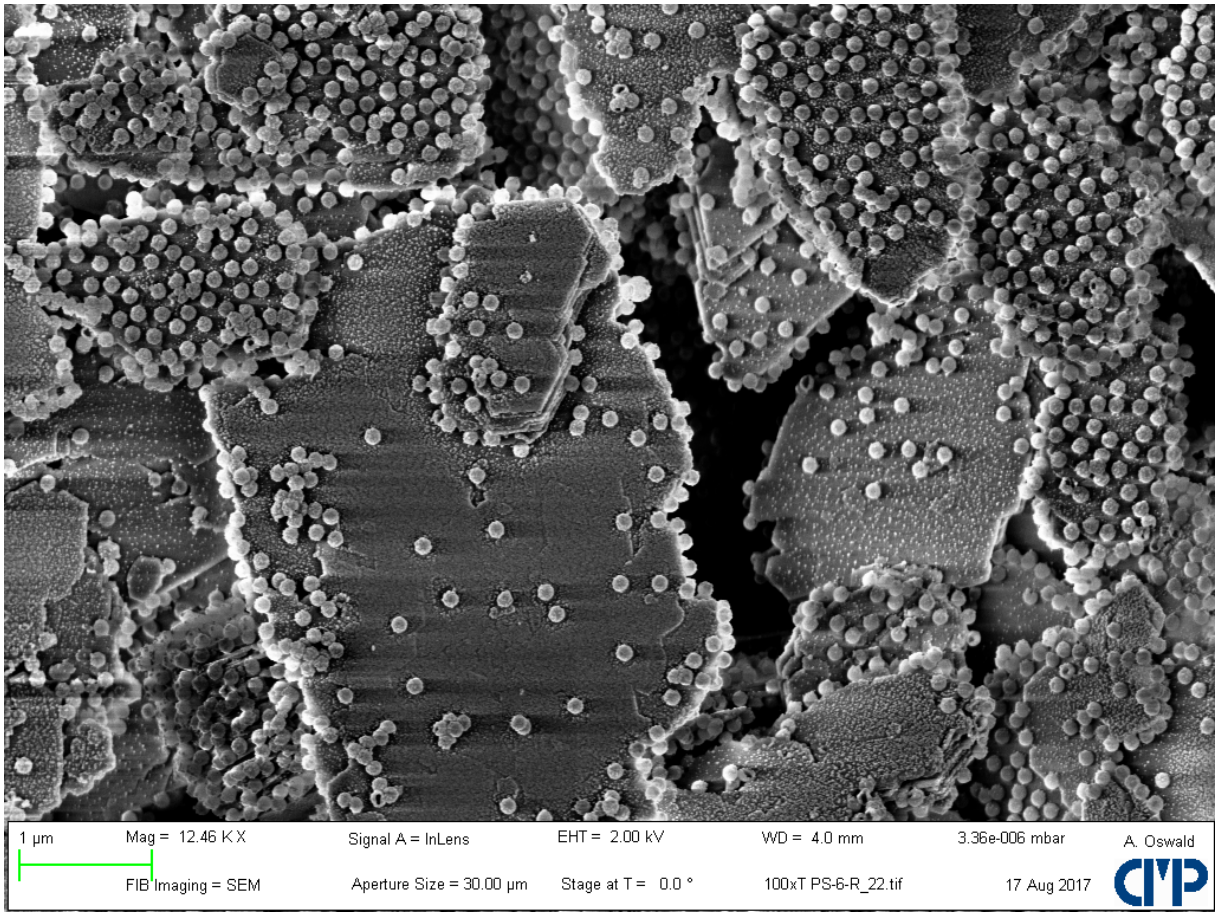


Figure A-189: 1000-fold TEOS before calcination

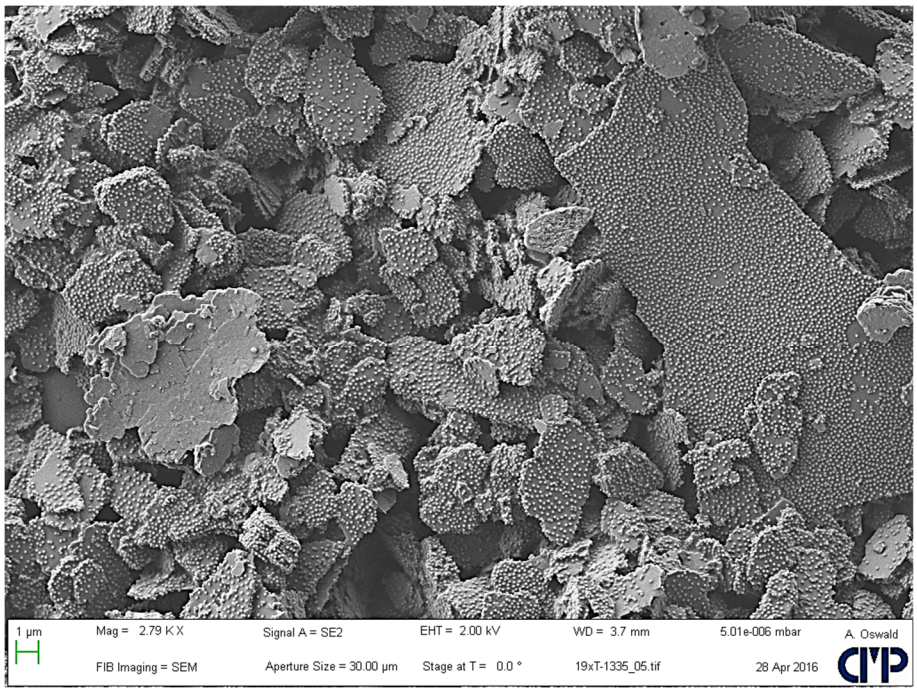


Figure A-190: 19-fold TEOS before calcination

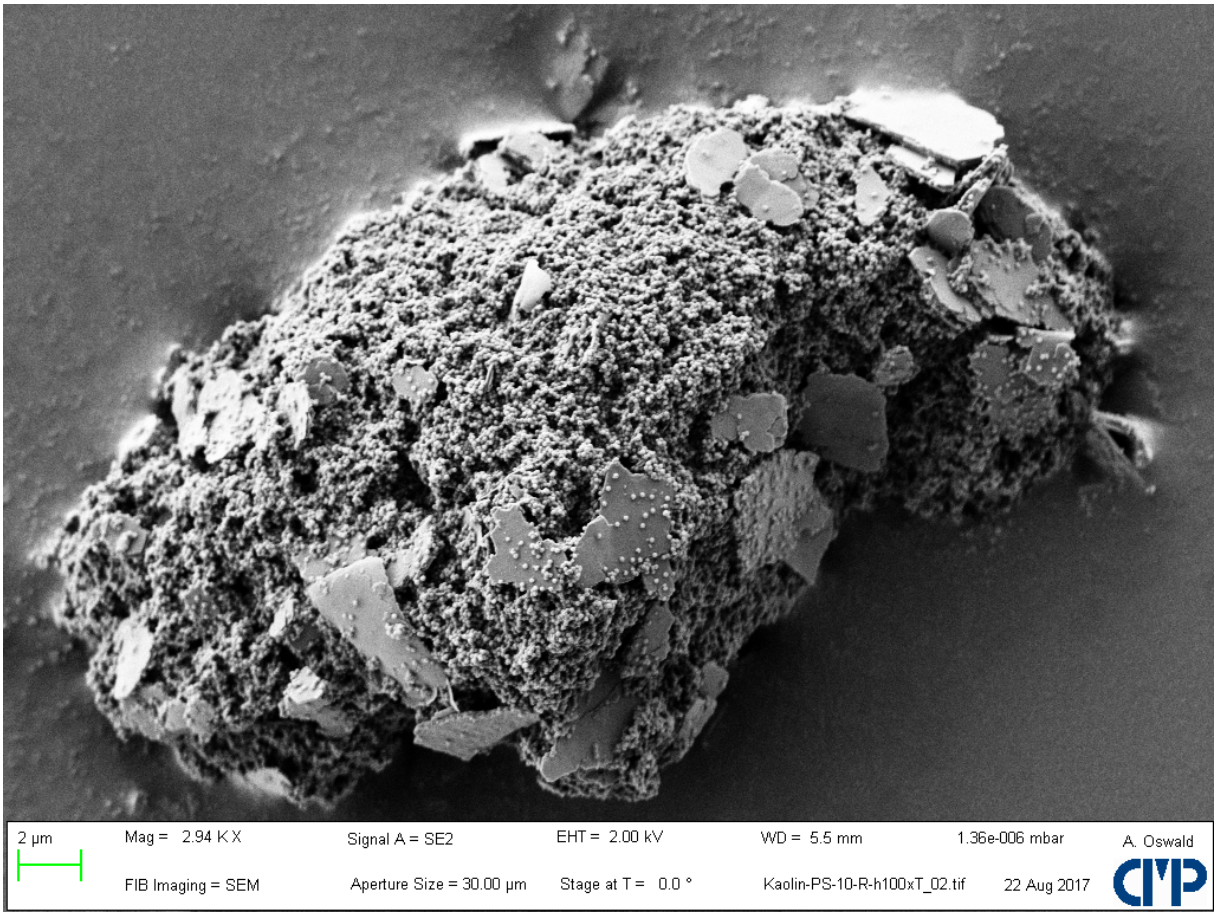


Figure A-191: 1000-fold excess on PS without PVP on kaolinite

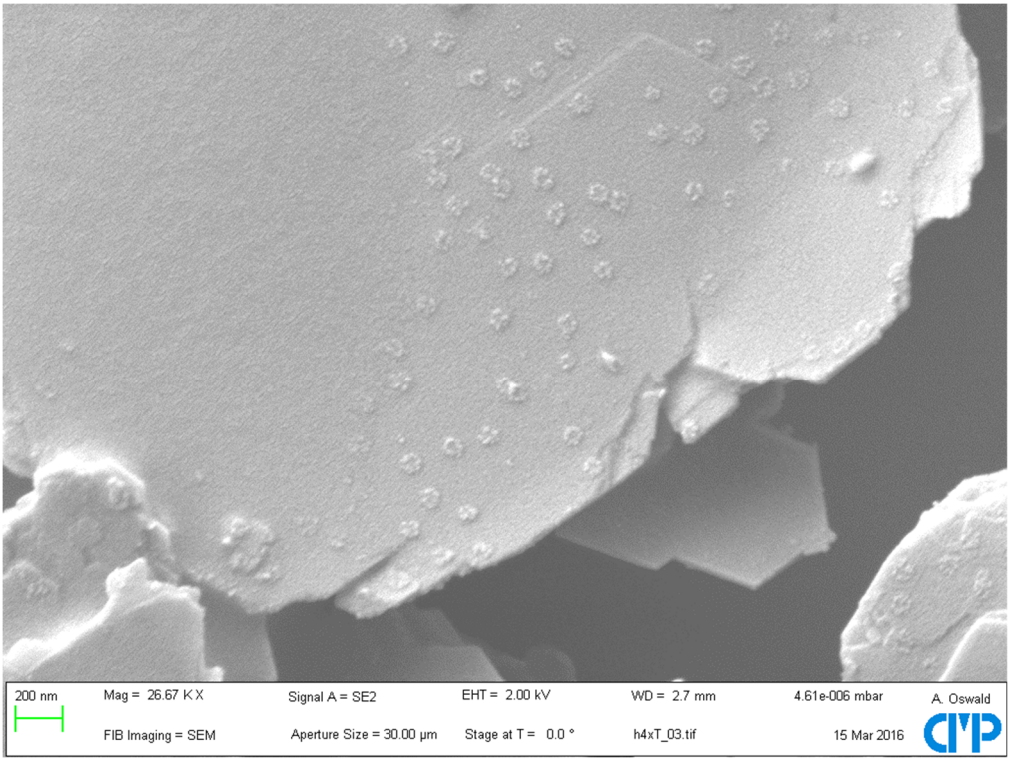


Figure A-192: 4-fold TEOS after calcination

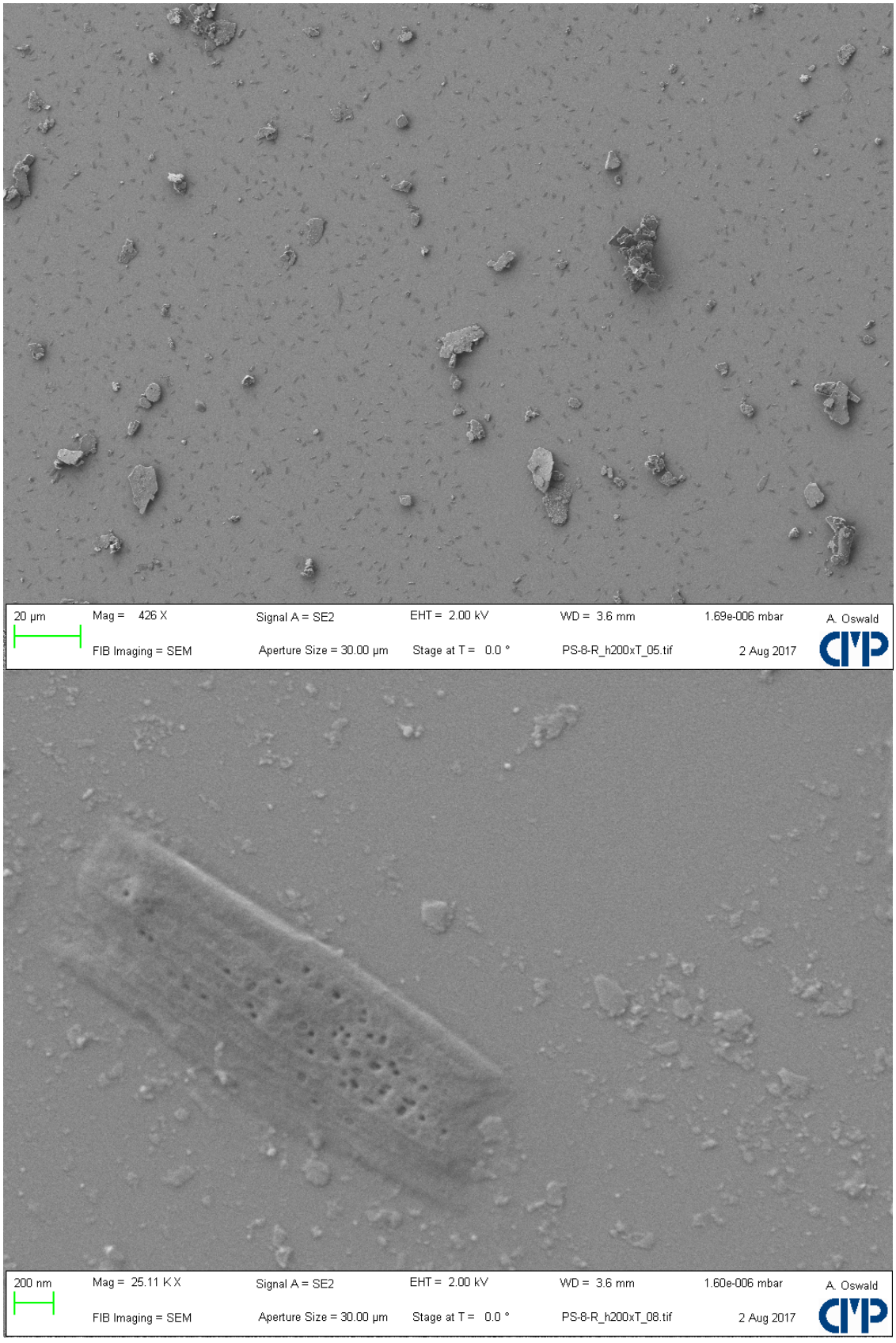


Figure A-193: Lamellar Particles SiO_2 from kaolinite edges

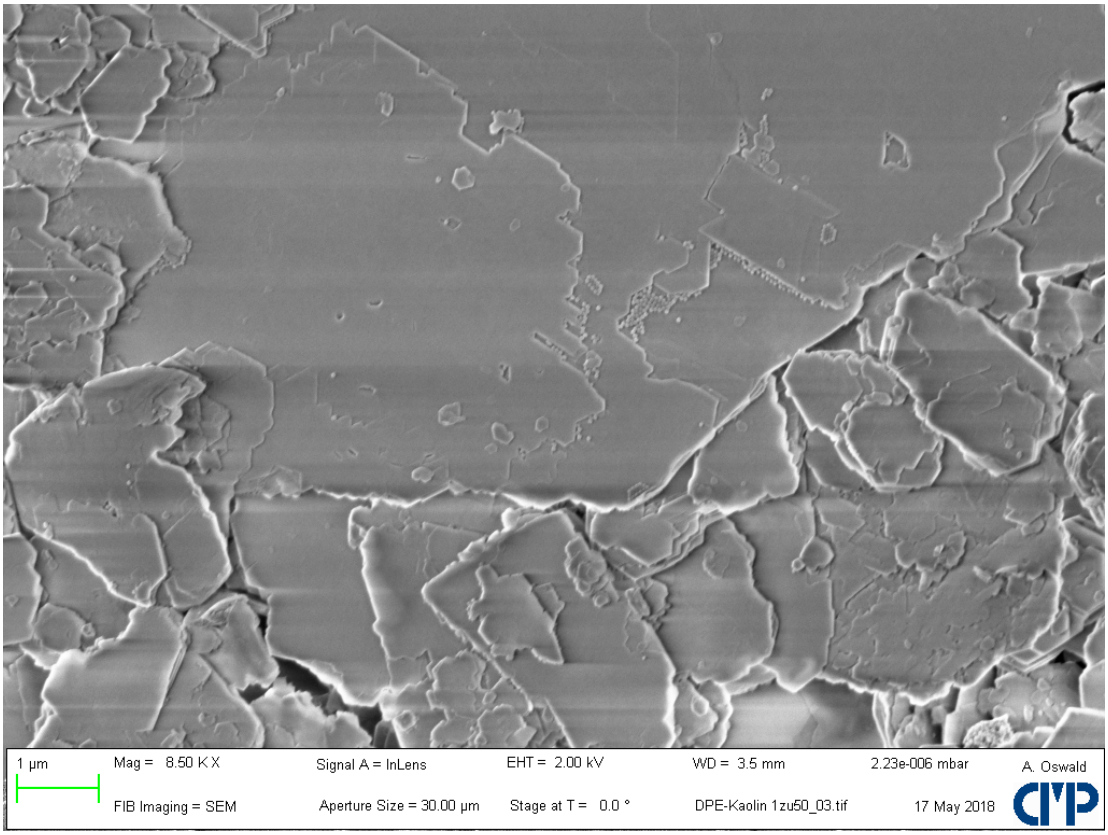


Figure A-194: PDPE @ kaolinite (reference)

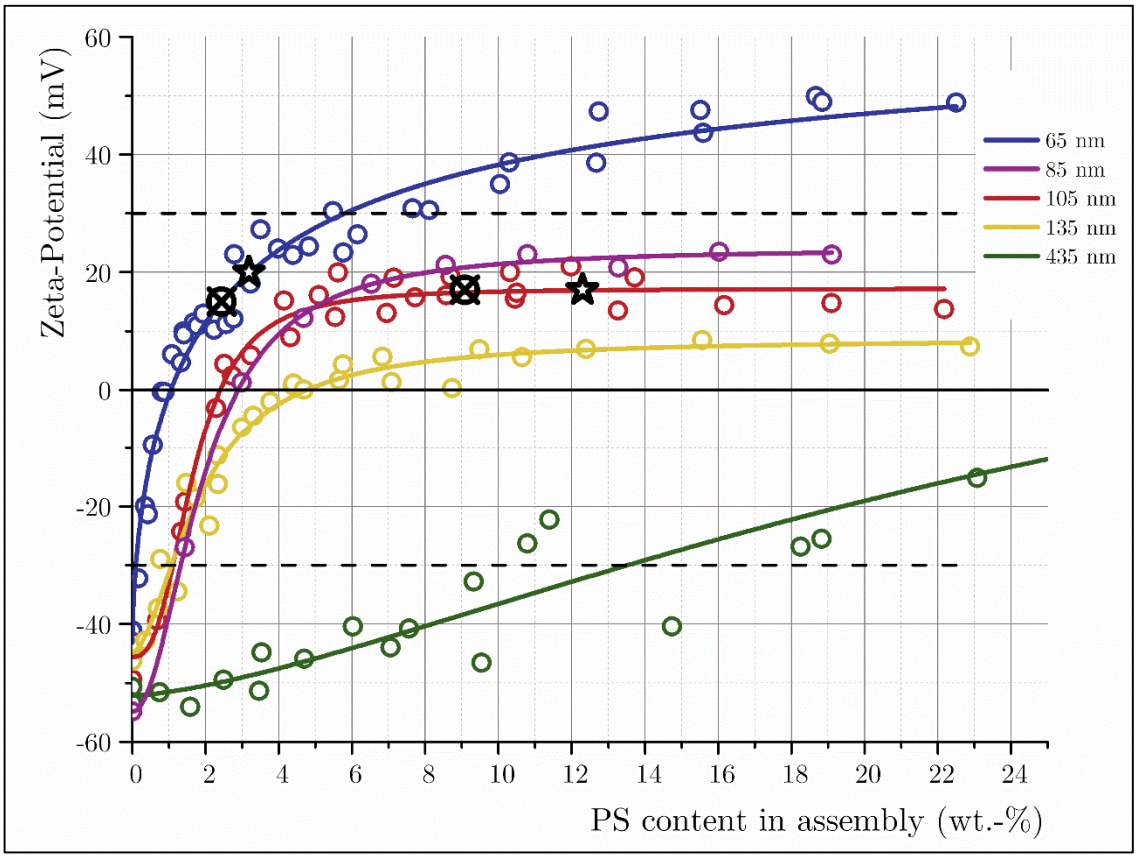


Figure A-195: Zeta-Potential vs. PS content in 3D @ 2D assembly

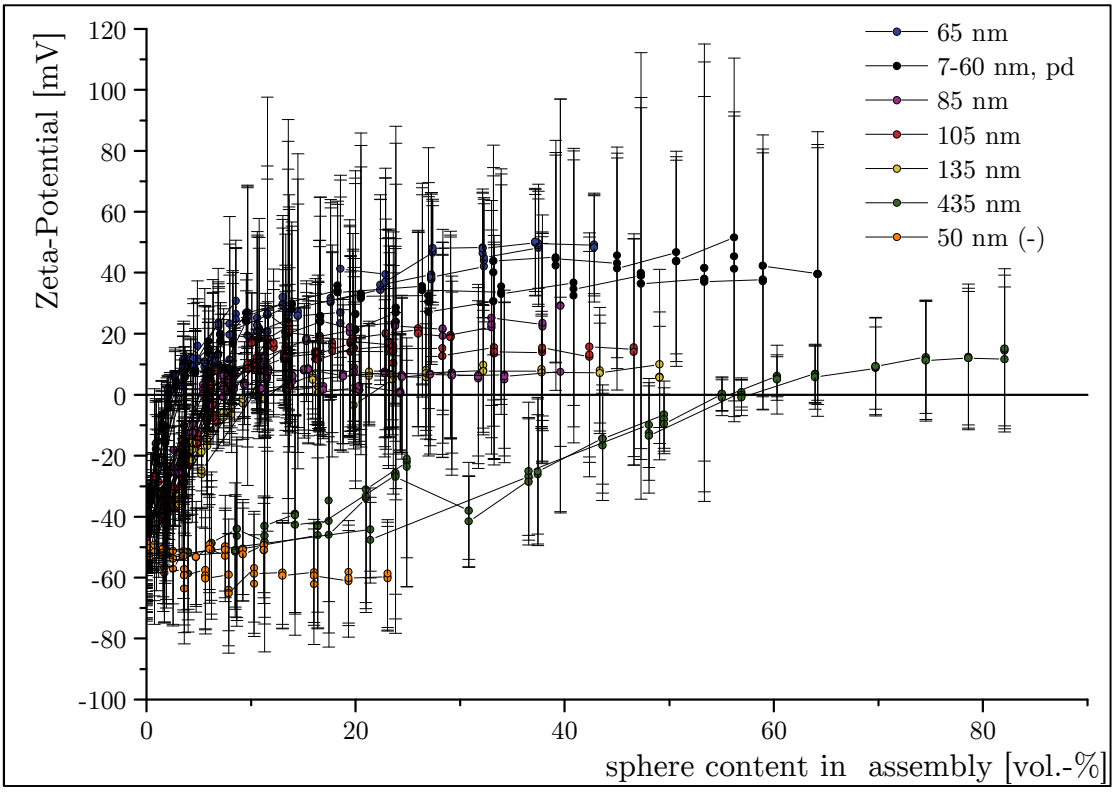


Figure A-196: Isoelectric Titration of Sphere (+) @ kaolinite (-) deposition

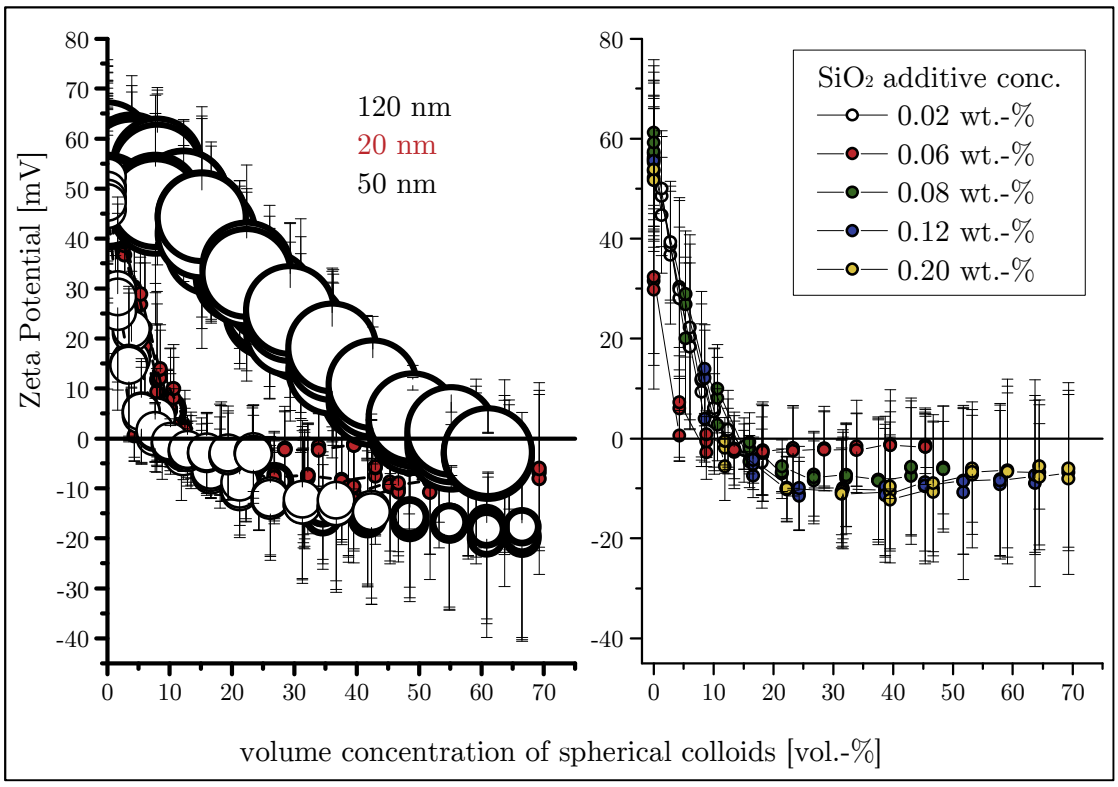


Figure A-197: Isoelectric Titration of SiO_2 (-) @ LDH (+) deposition

3.5 Dissipative CFRP

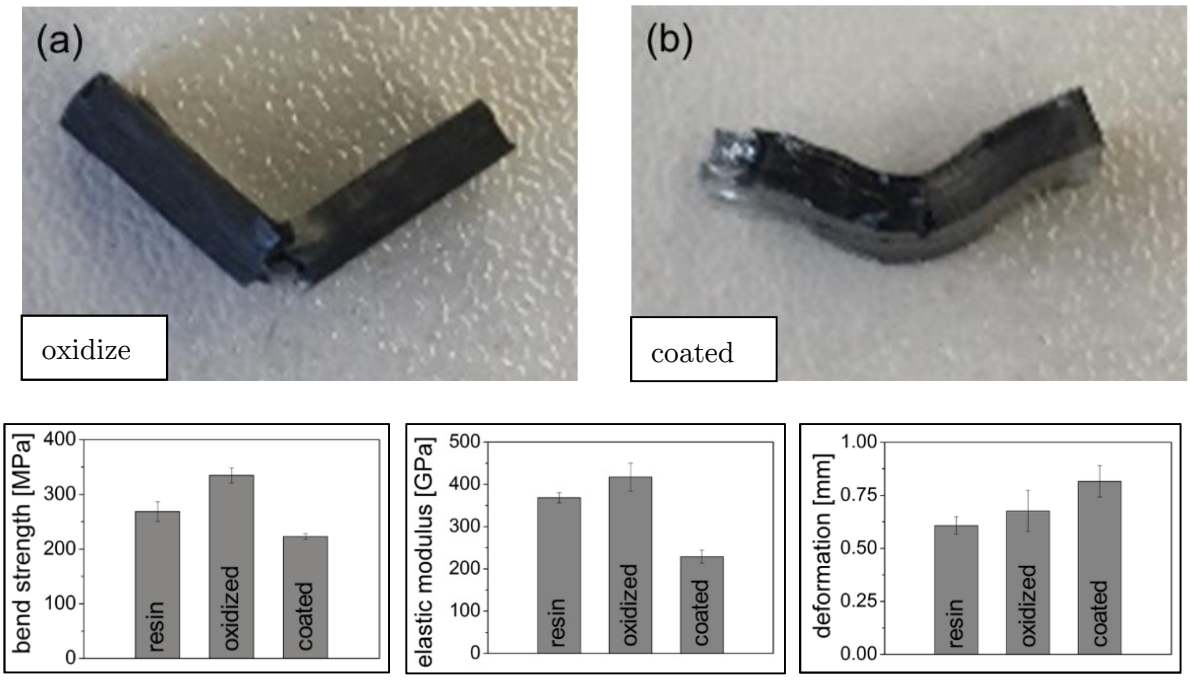


Figure A-198: Results of three-point flexural test on PDMS-coated CF in CFRPs

4 SiO_2 @ LDH assemblies

4.1 Ultrafiltration of lamellar colloids

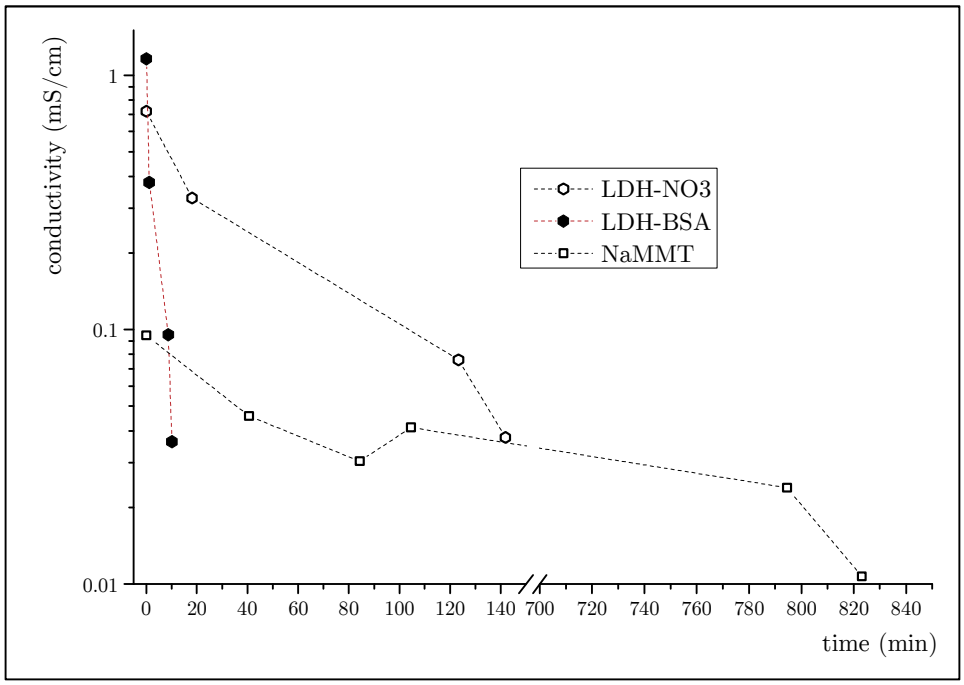


Figure A-199: Conductivity vs. time during ultrafiltration

The ultrafiltration of LDH-BSA particles has the highest decrease in conductivity vs. time. The stiffness of these phases do not block the 50 pore diameter membrane. The LDH-NO_3-phase has a slightly softer character and have comparable decreasing rates. The pressure was not recorded for these conductivity measurements.

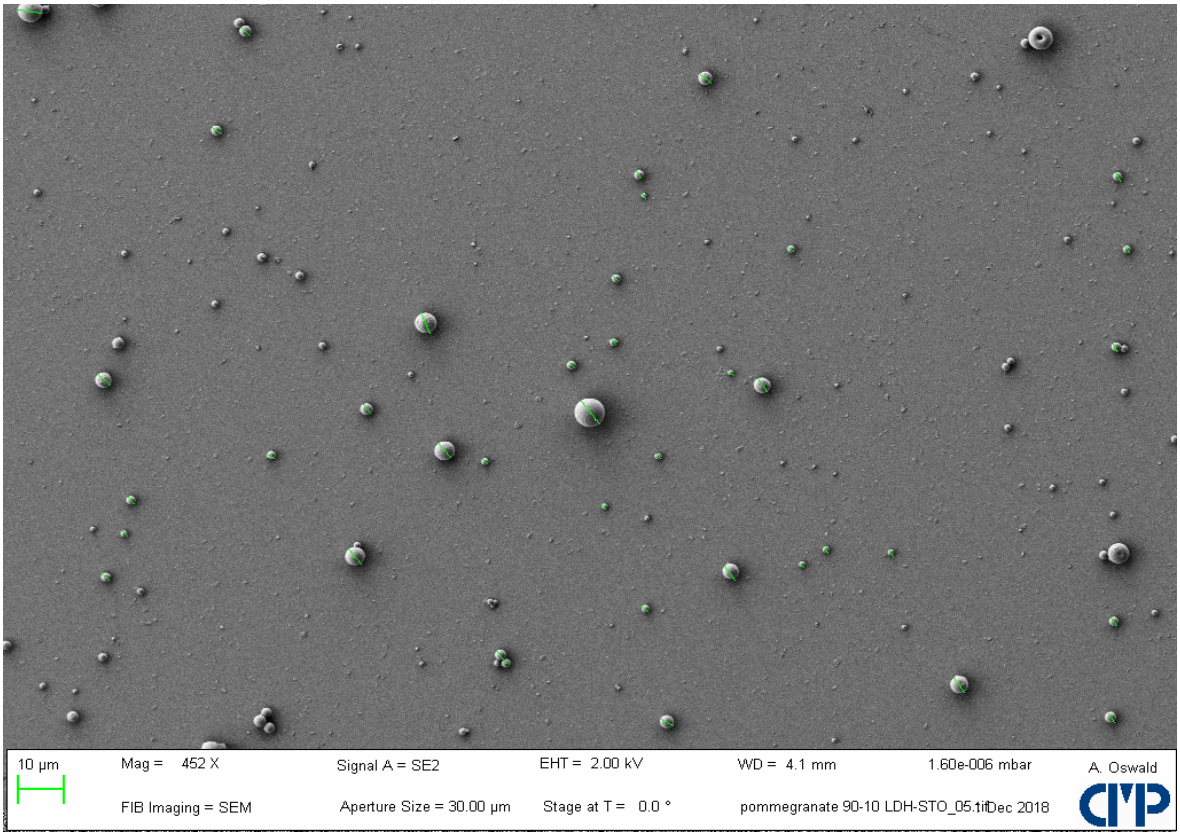


Figure A-200: Size determination of pomegranate structures of LDH-DS from LDH-NO_3

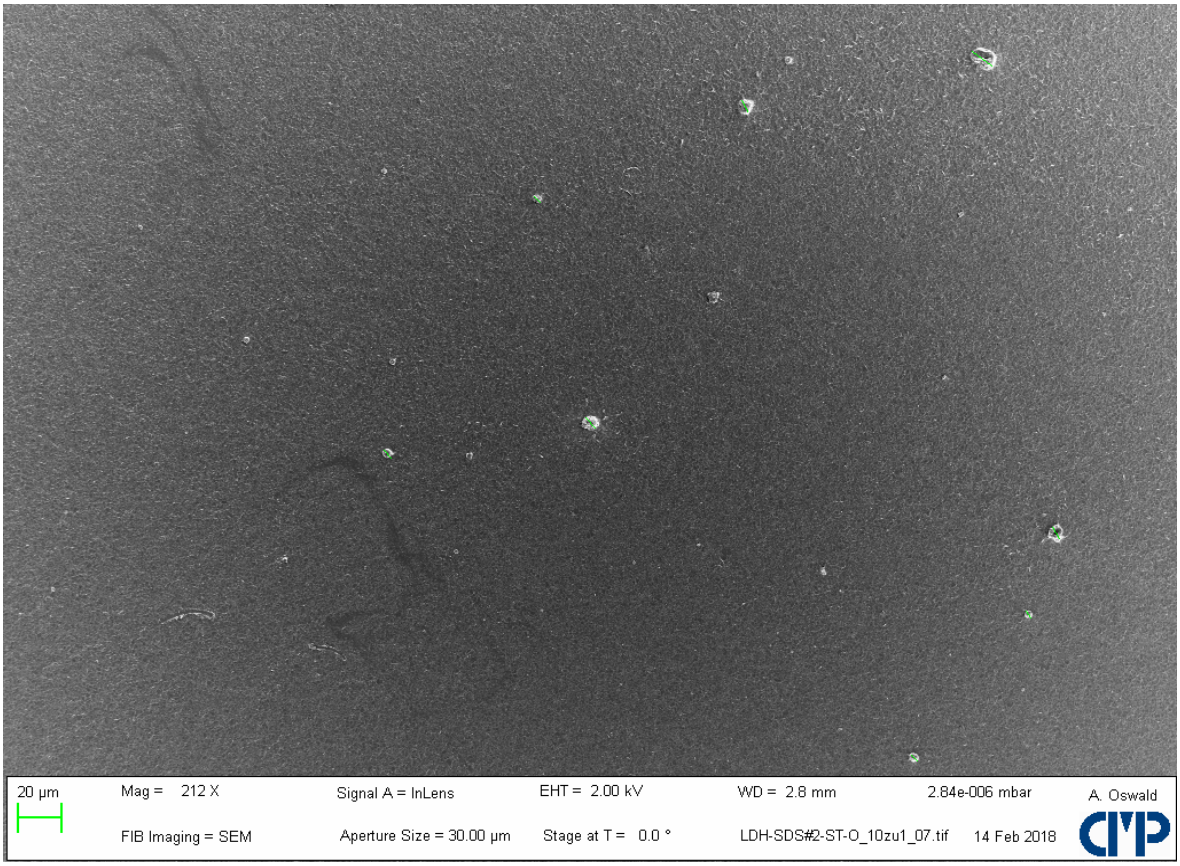


Figure A-201: Pomegranate structures with LDH-DS from LDH-BSA

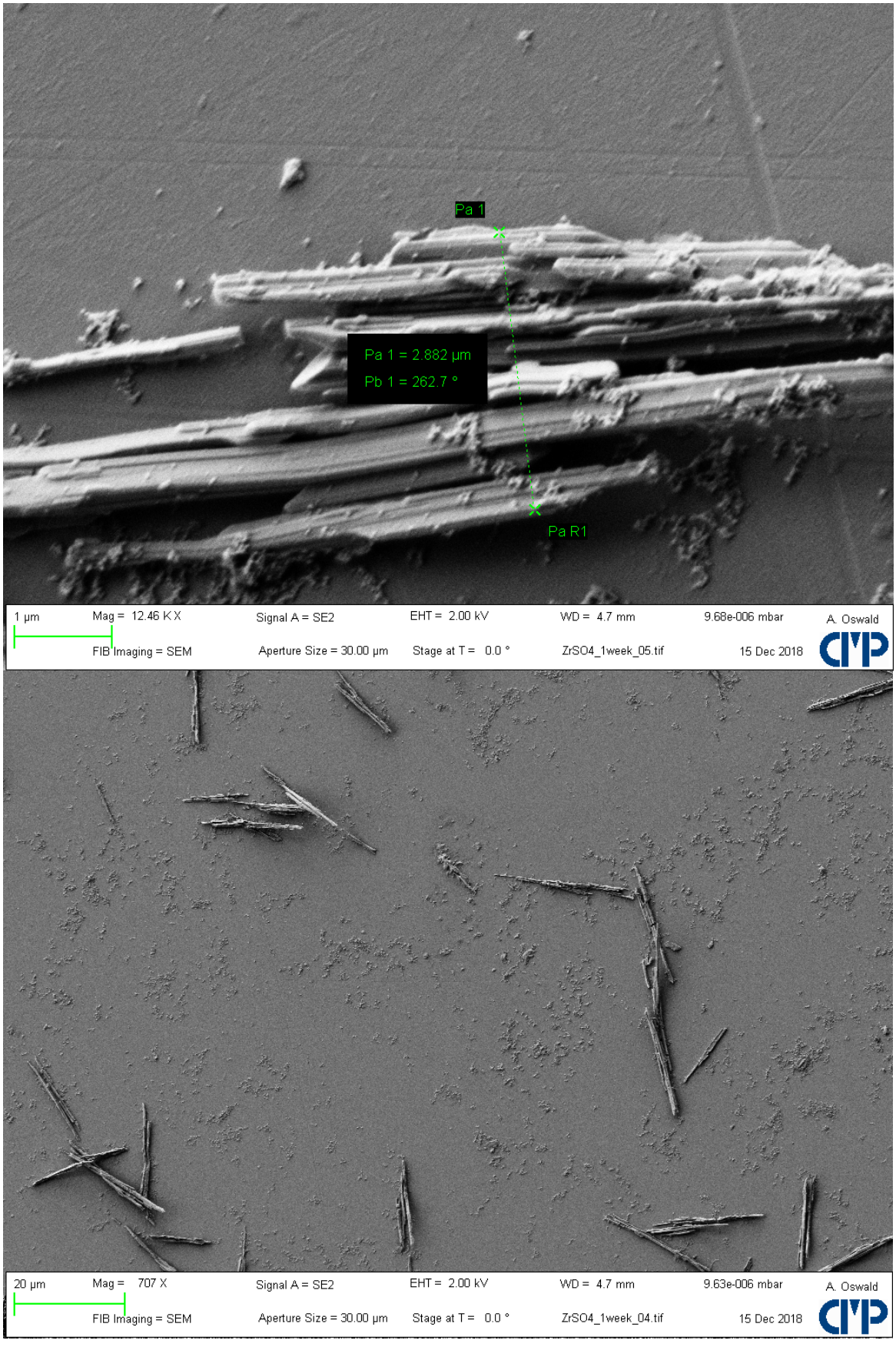


Figure A-202: Morphology of colloids after stirring a $Zr(SO_4)_2$ solution for 1 week.

4.4 Aged morphologies of SiO_2@LDH assemblies

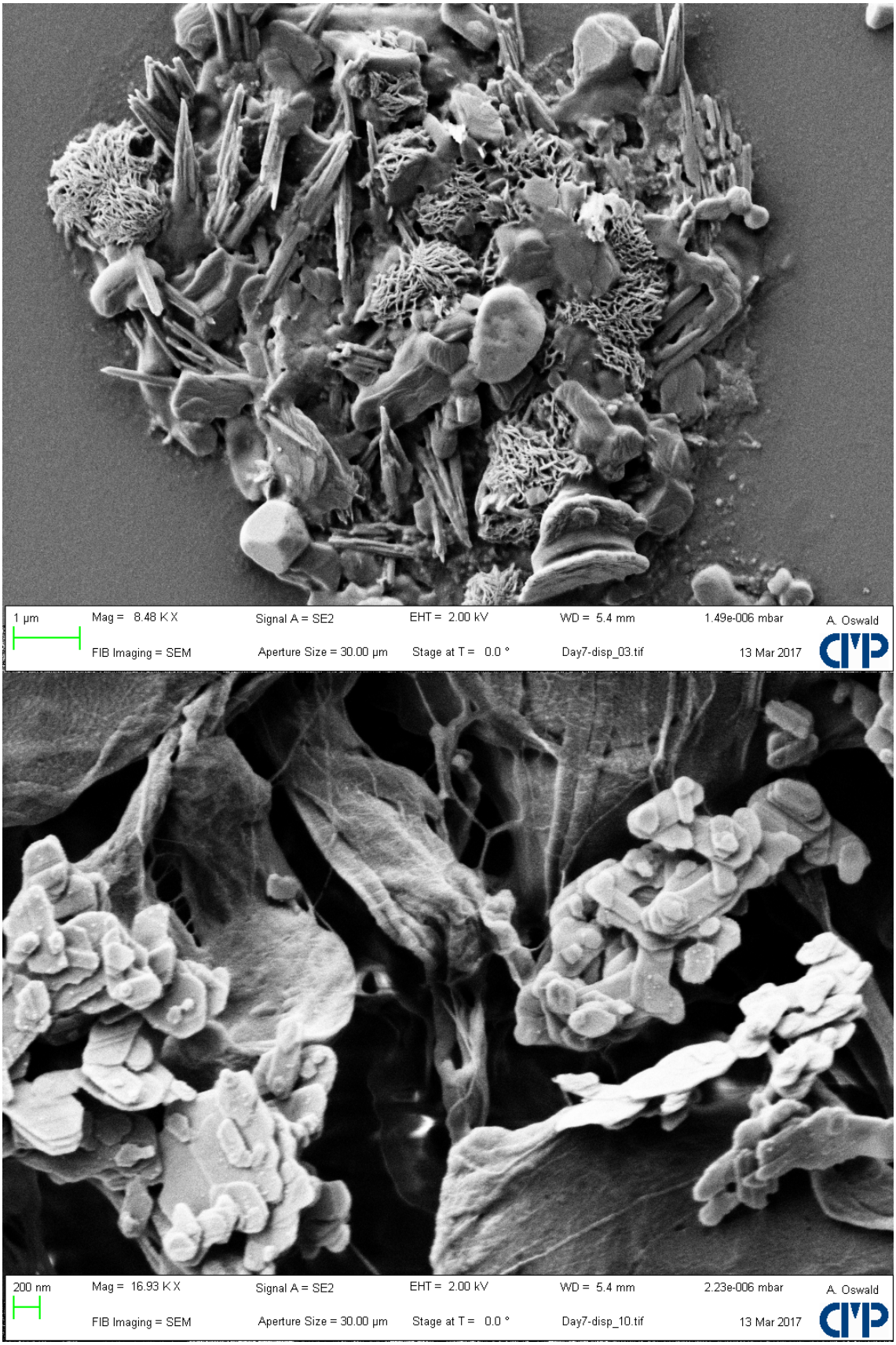
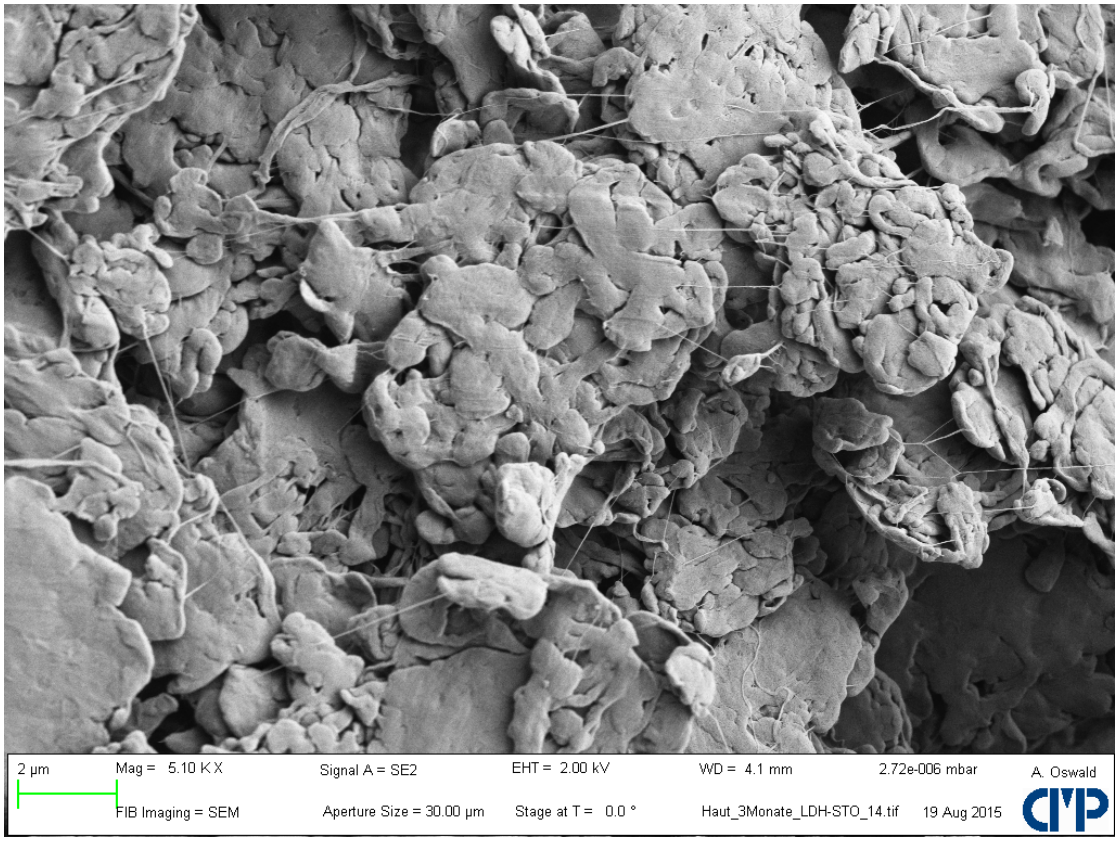


Figure A-203: Morphologies after 7 days of stirring



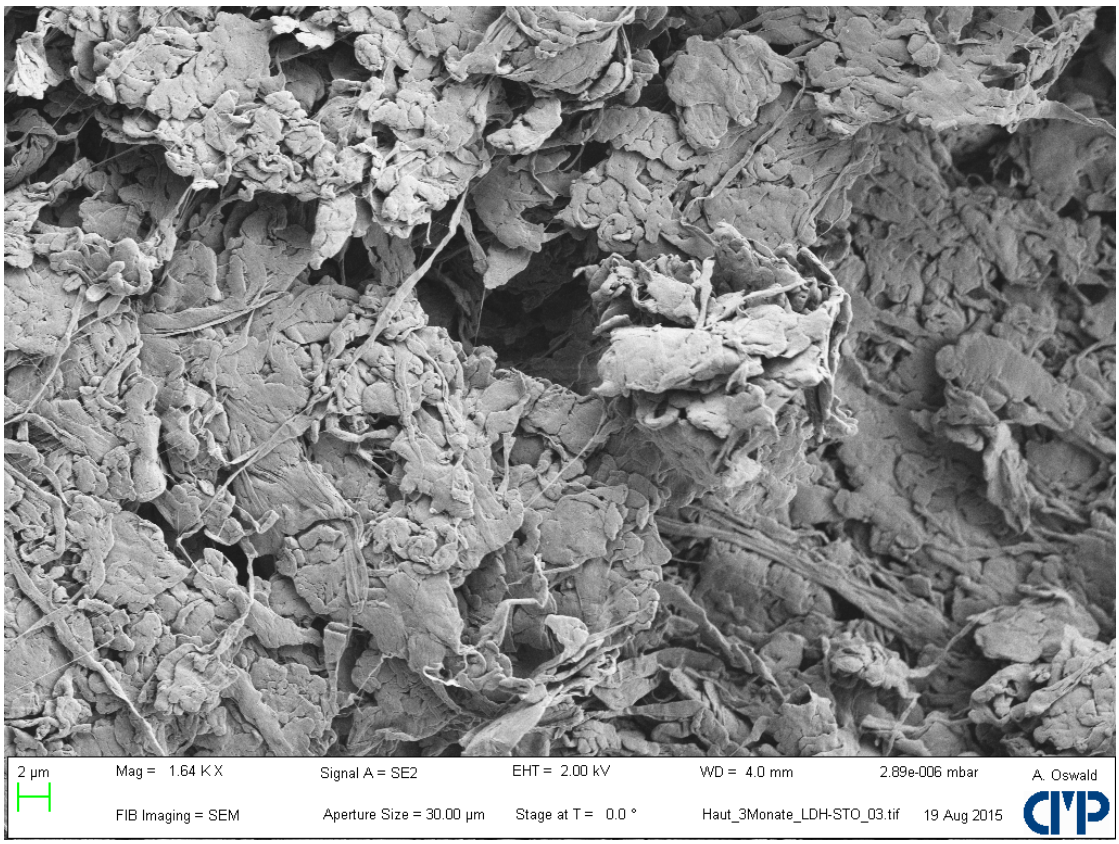


Figure A-204: Morphologies of the flotating fractions after 3 months of stirring

5 PUR/LDH composites

5.1 FIB cross-section of PUR/LDH clod

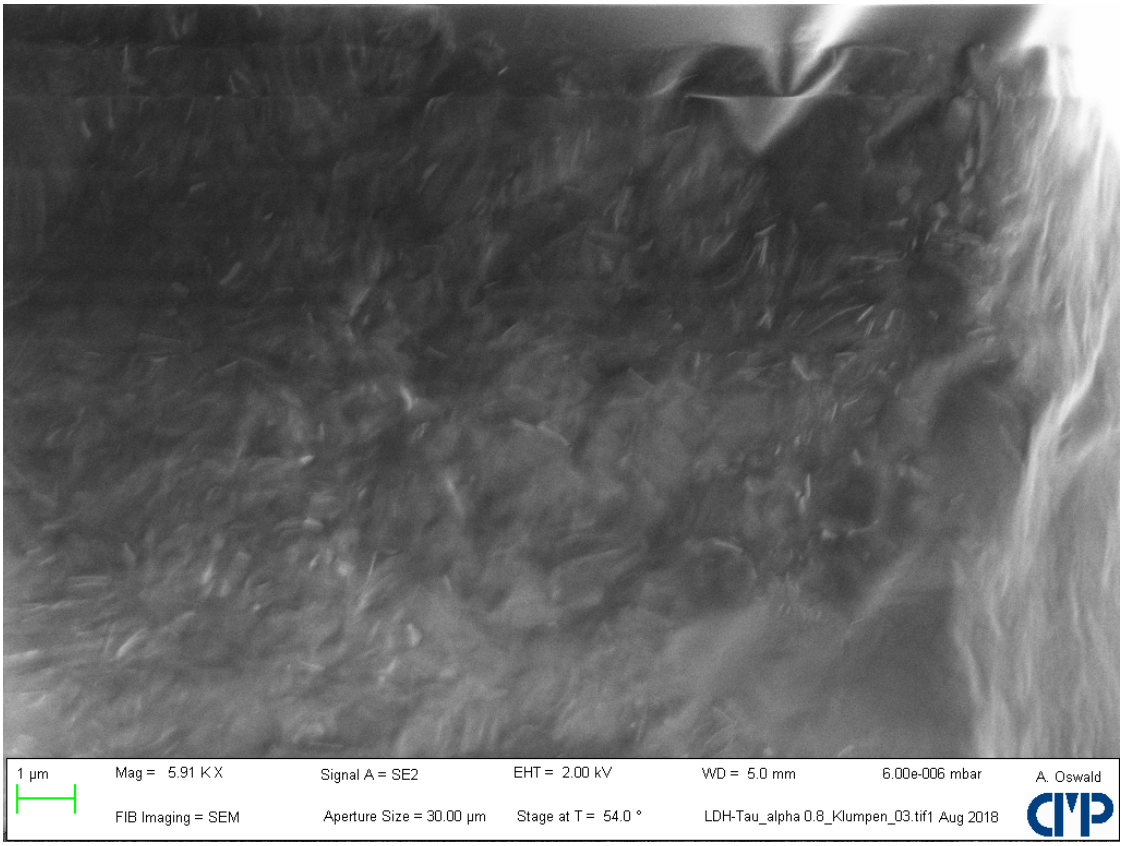


Figure A-205: FIB cut through a clod from pretests.
The LDH was a LDH-NO3, exchanged with taurine. The PUR was a PUR_{15} equivalent, in this case treated with a DMAE:COOH ratio of 0.8.



Figure A-206: LDH-ABSA in a commercial polyester resin containing co-solvent

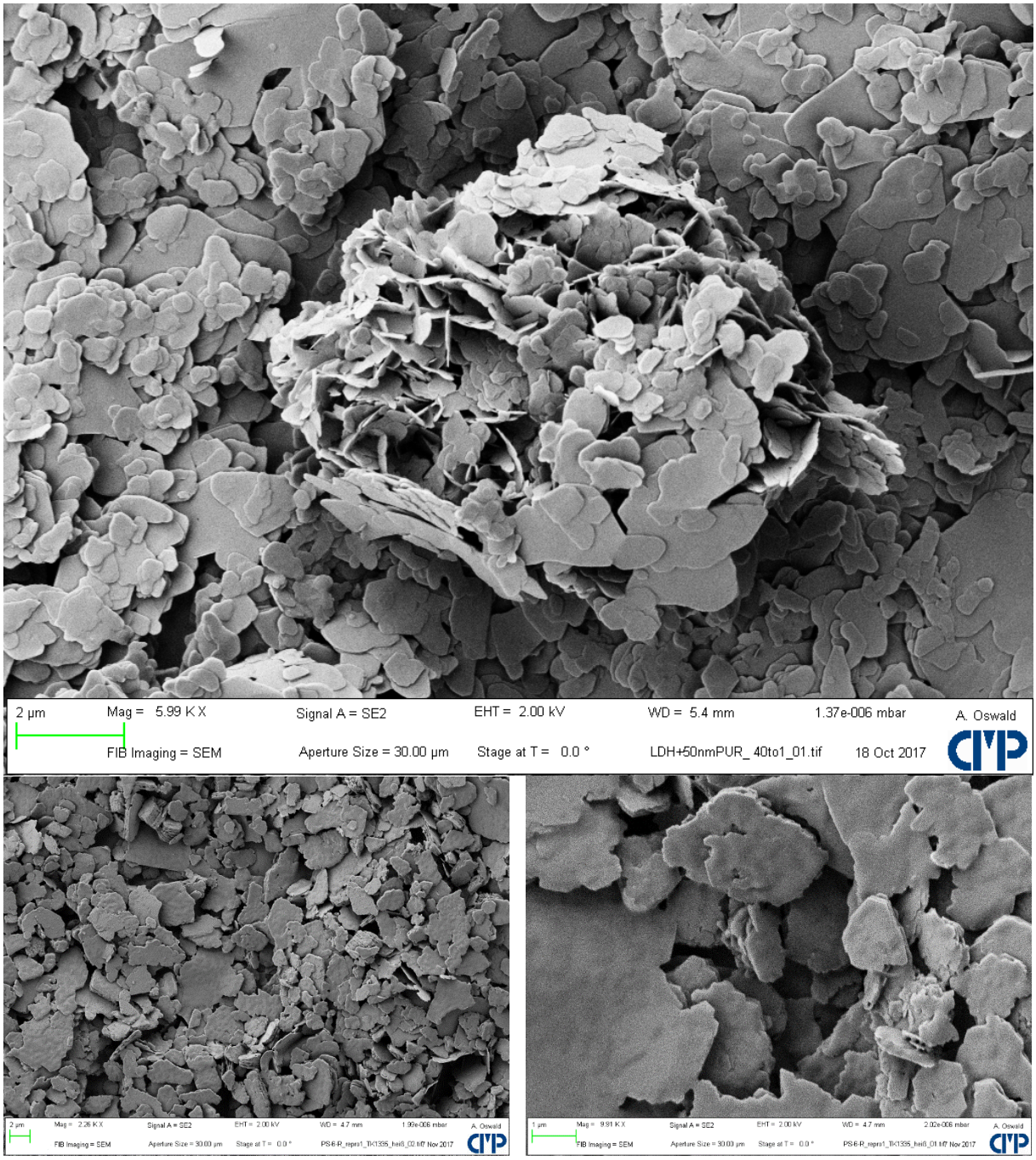


Figure A-207: Comparison between PUR and PS above T_g

PUR_{50} @ LDH_{800} with a 1 to 40 ratio (*top*, wt/wt), dried at room temperature and PS_{95}/K_{face} assemblies, dried at 120 °C.

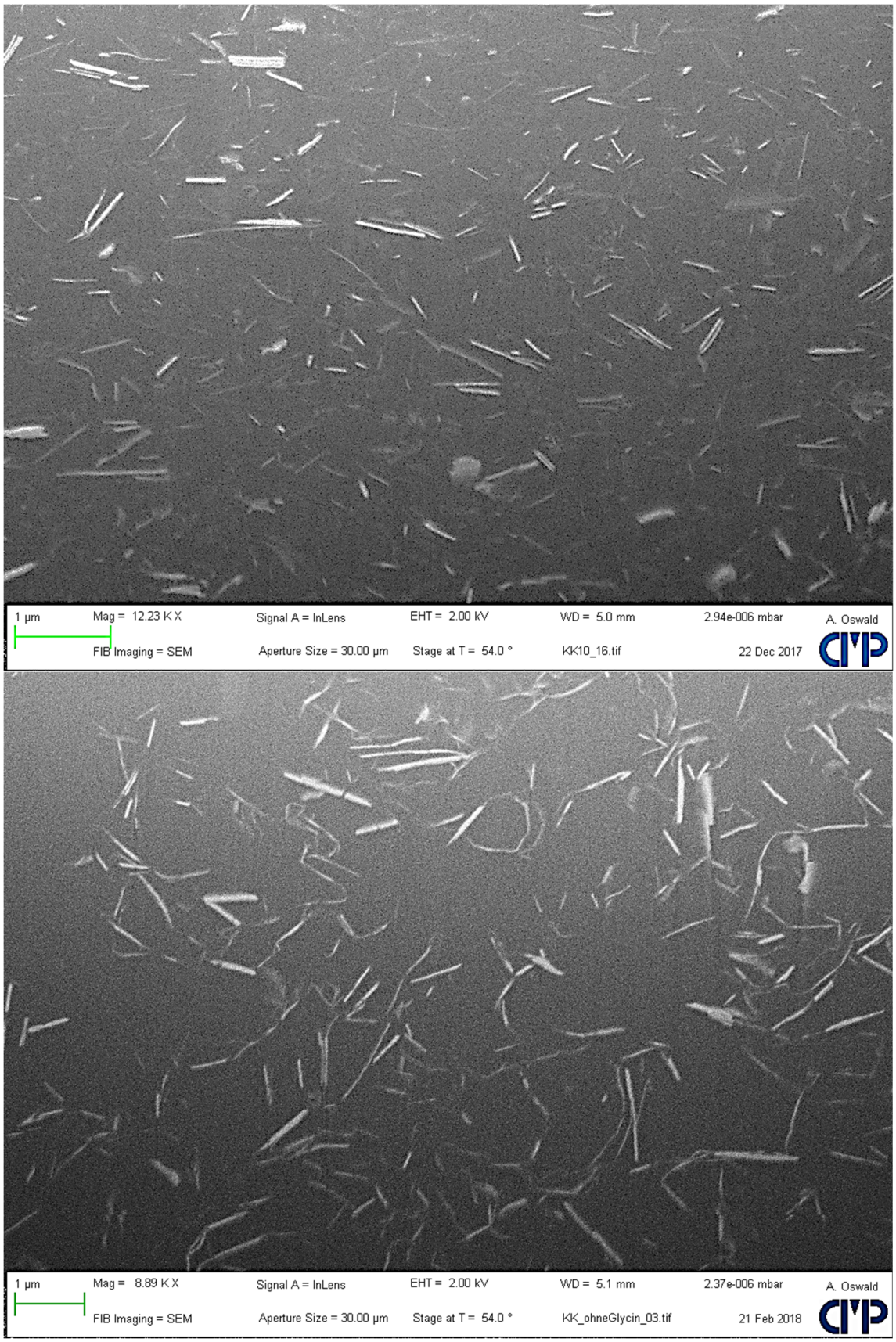


Figure A-208: FIB/SEM images of $PUR_{10}LDH_{S00}$ composites with a 10 wt.-% LDH concentration. The *top* figure shows the morphology with glycine-treated LDH, the *bottom* figure shows the morphology with pristine LDH-BSA.

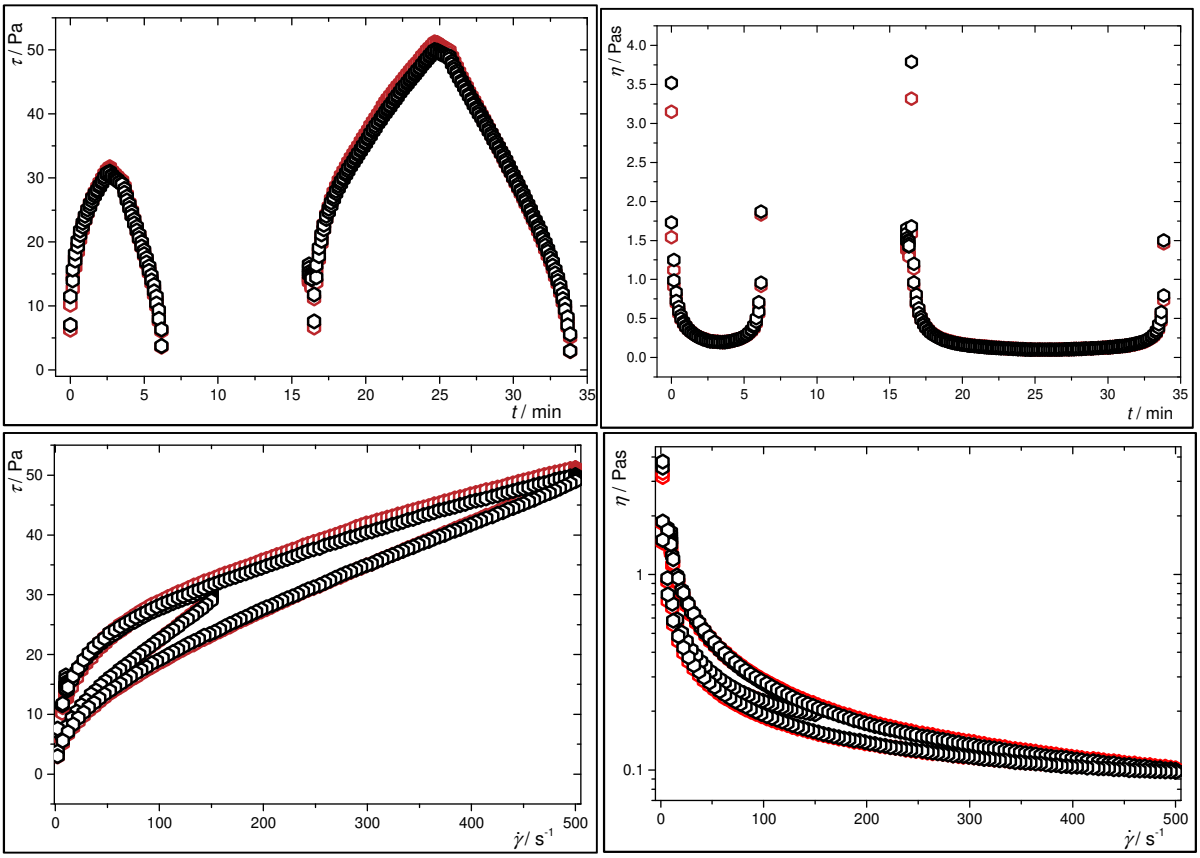


Figure A-209: 1 day aging 10 wt.-\% LDH in $PUR_{75}LDH_{1600}$

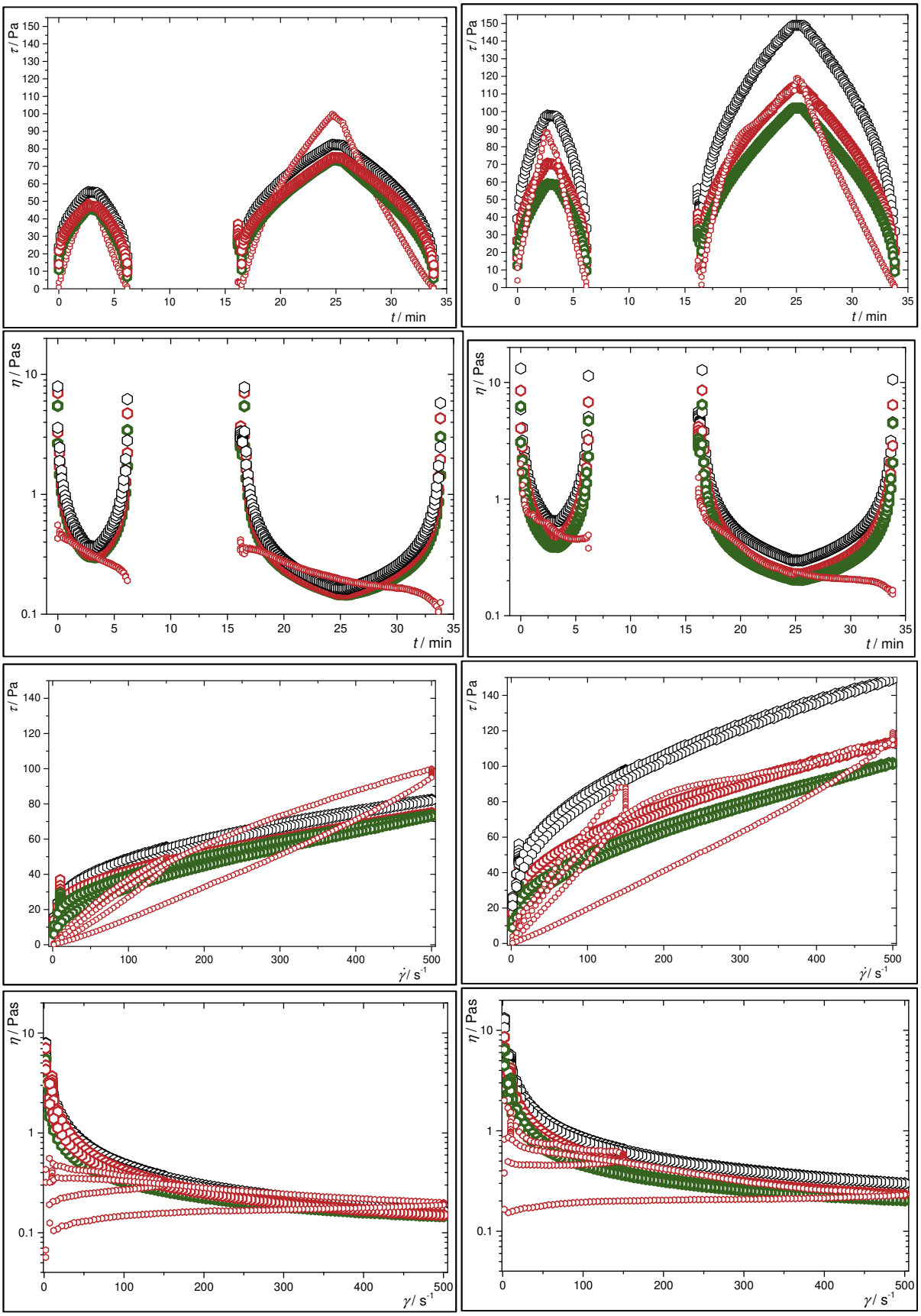


Figure A-210: 9 days aging of 10 wt.-% $PUR_{75}LDH_{800}$ and 5,10,15 wt.-% $PUR_{115}LDH_{3200}$

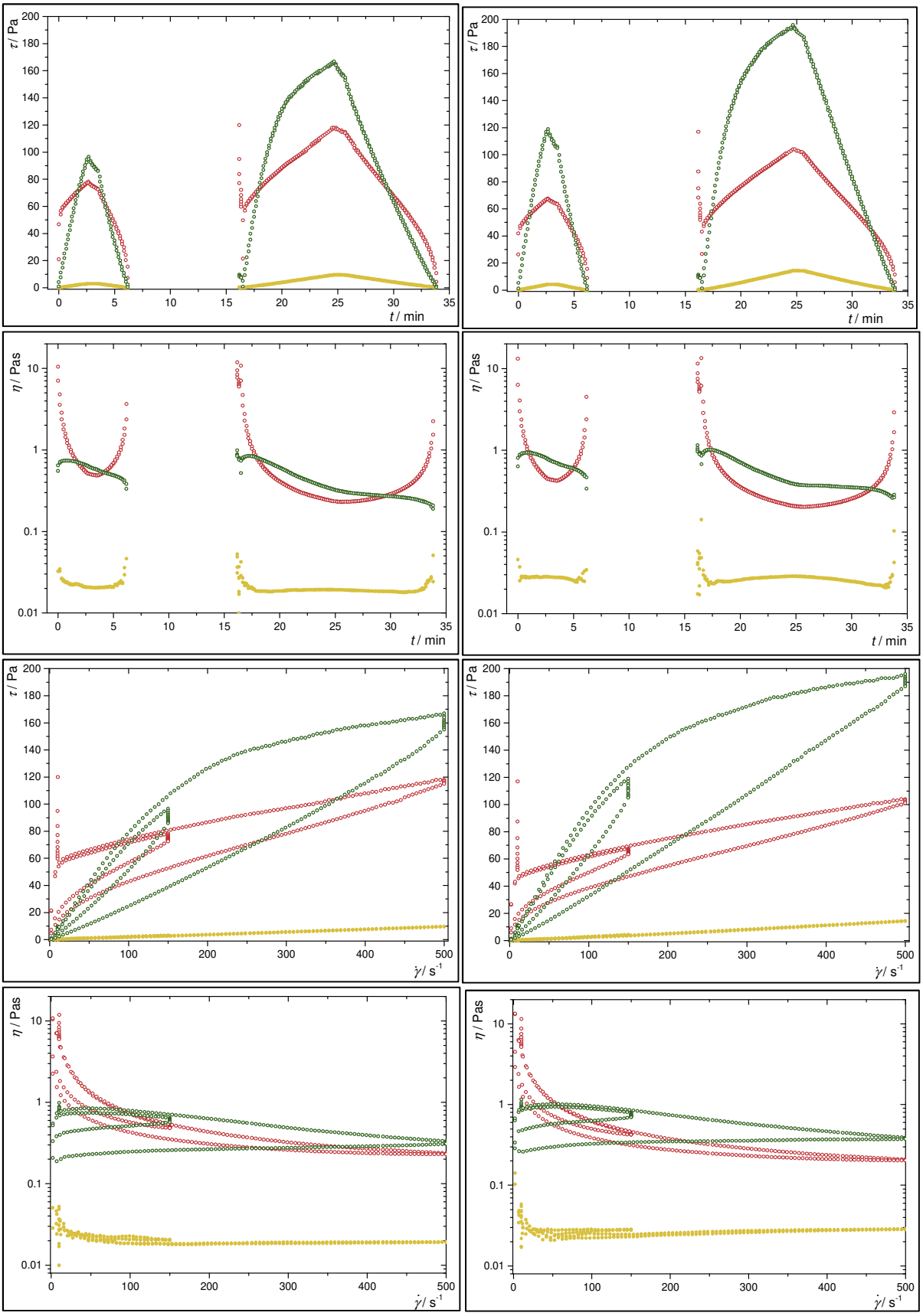


Figure A-211: 18 days aging of 25 wt.-% $PUR_{10}LDH_{400}$ and 10, 15 % $PUR_{75}LDH_{400}$

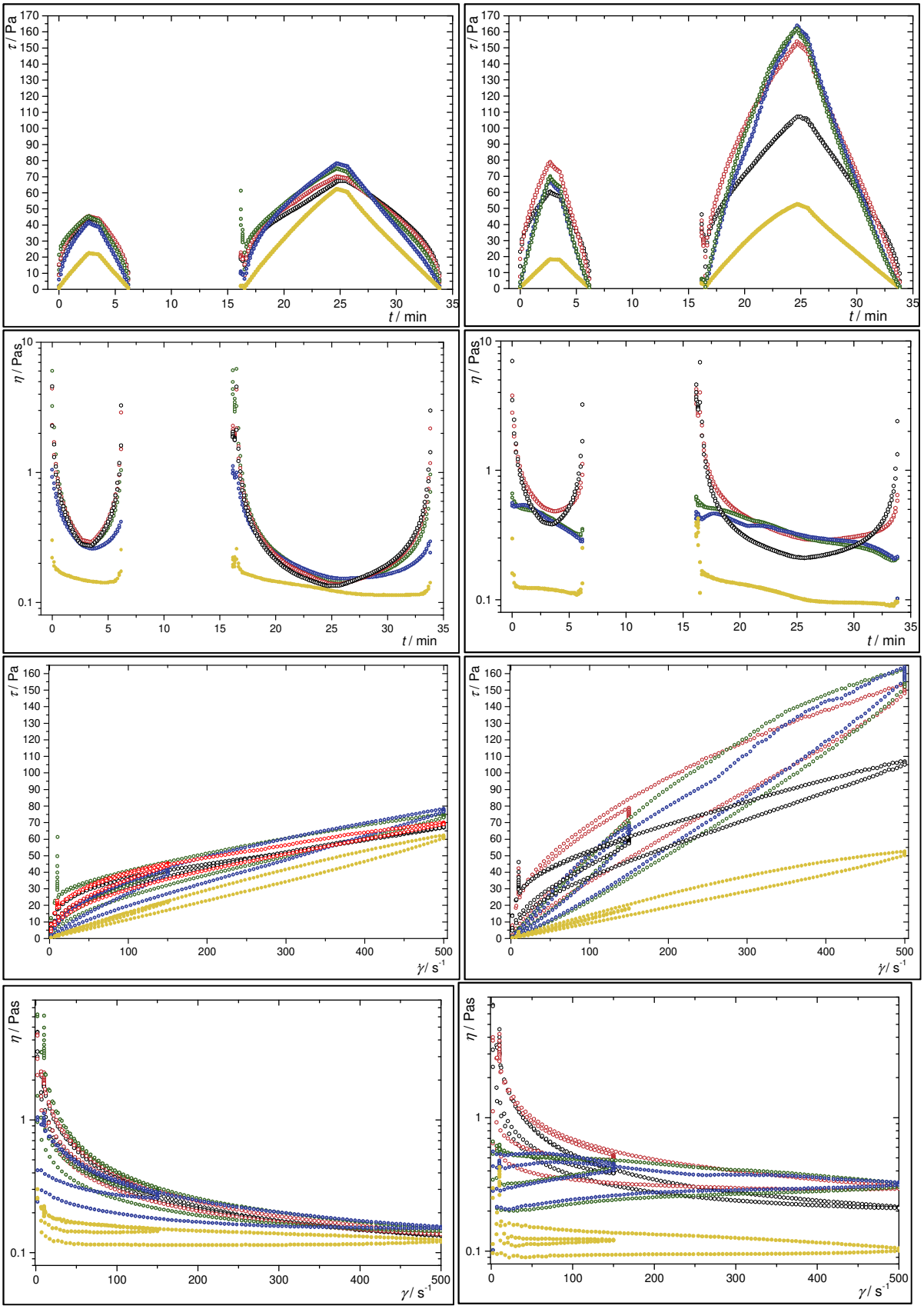


Figure A-212: 36 days aging of all $PUR_{115}LDH_{400}$

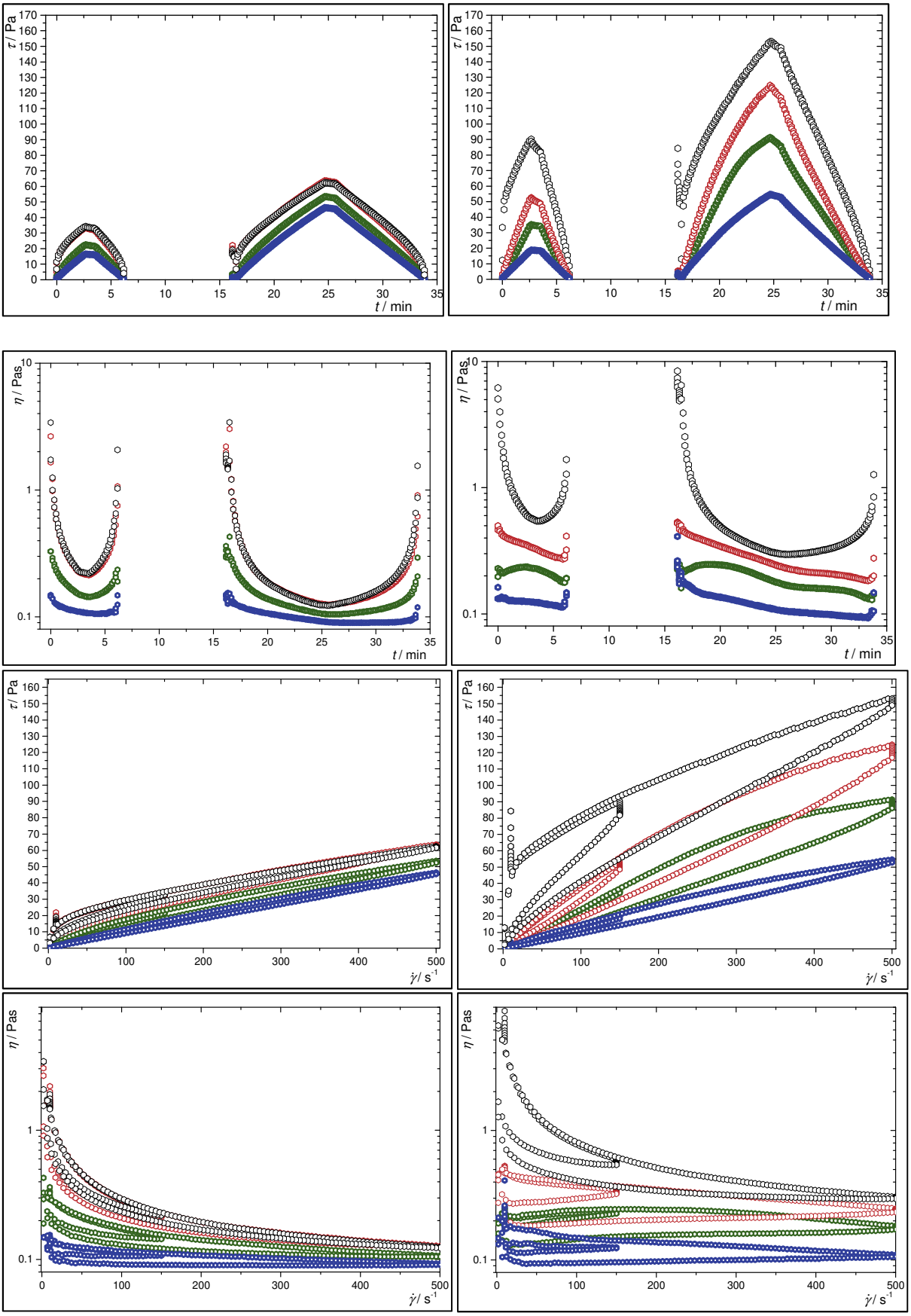


Figure A-213: 36 days aging of 5, 10, 15, 20 wt.-% $PUR_{115}LDH_{800}$

6 Casein / Chymosin / KCl composites

6.1 EDX results

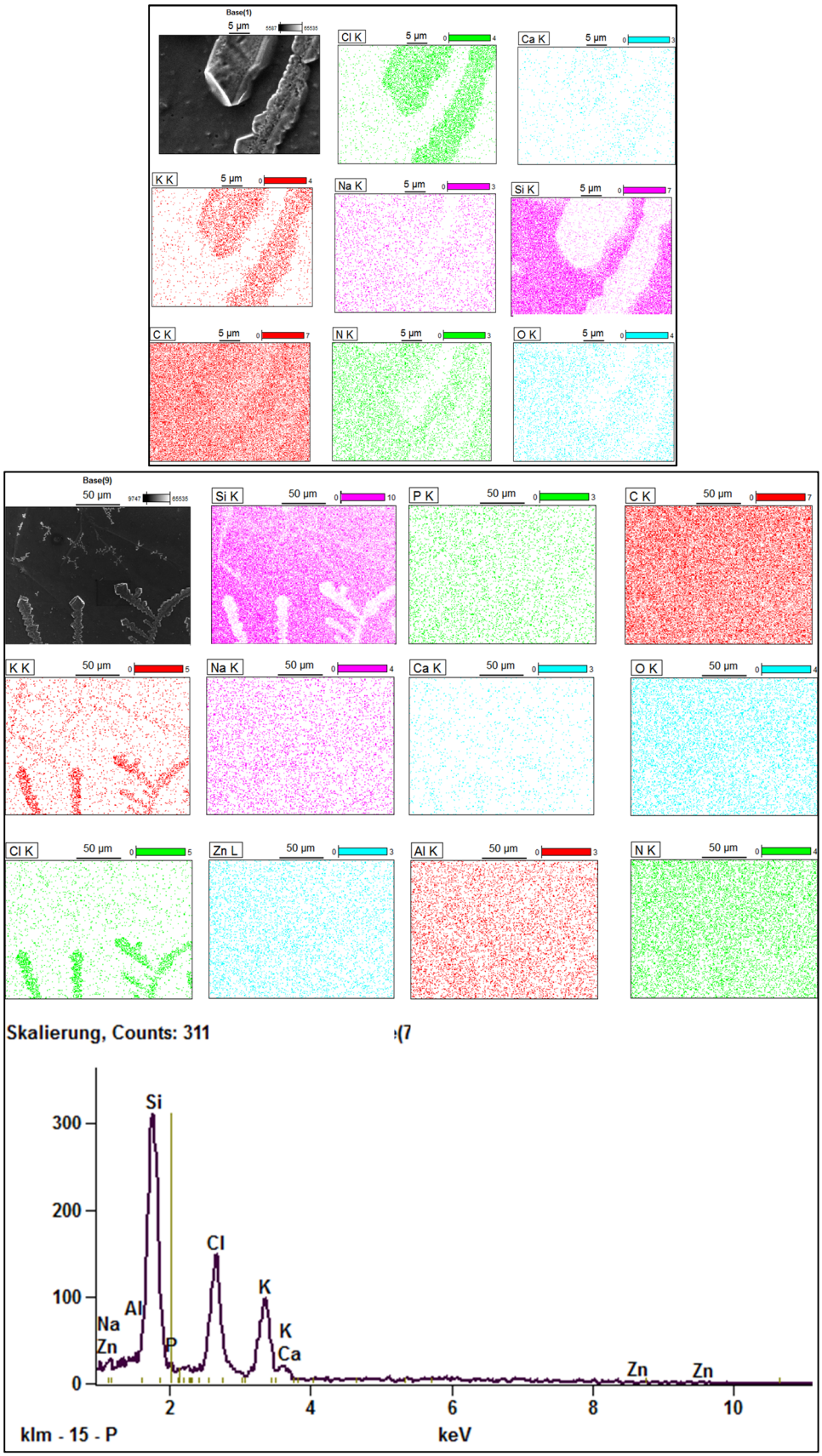


Figure A-214: EDX results on Casein / Chymosin / LDH / KCl composites

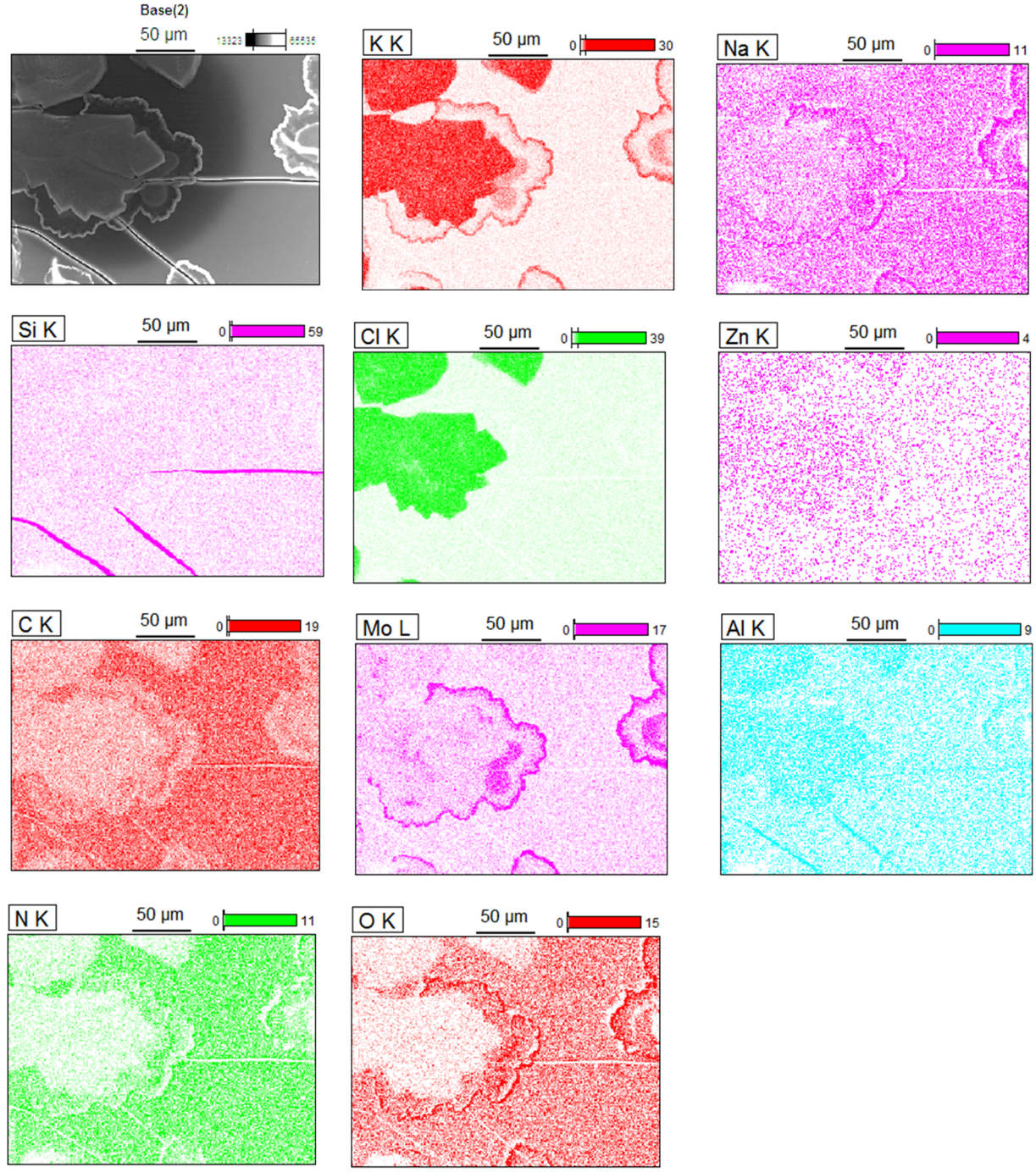


Figure A-215: EDX results on Casein / Chymosin / LDH / KBSA composites

Note: There is sulfur S and no molybdene Mo in the sample: Mo L_α (2.29 keV) *vs* S K_α = (2.307 keV). The EDX software mistakenly treated the signal as molybdene. The sulfur is from the benzenesulfonate molecules from LDH-BSA

6.2 Reference sample after 24 hours cleavage time

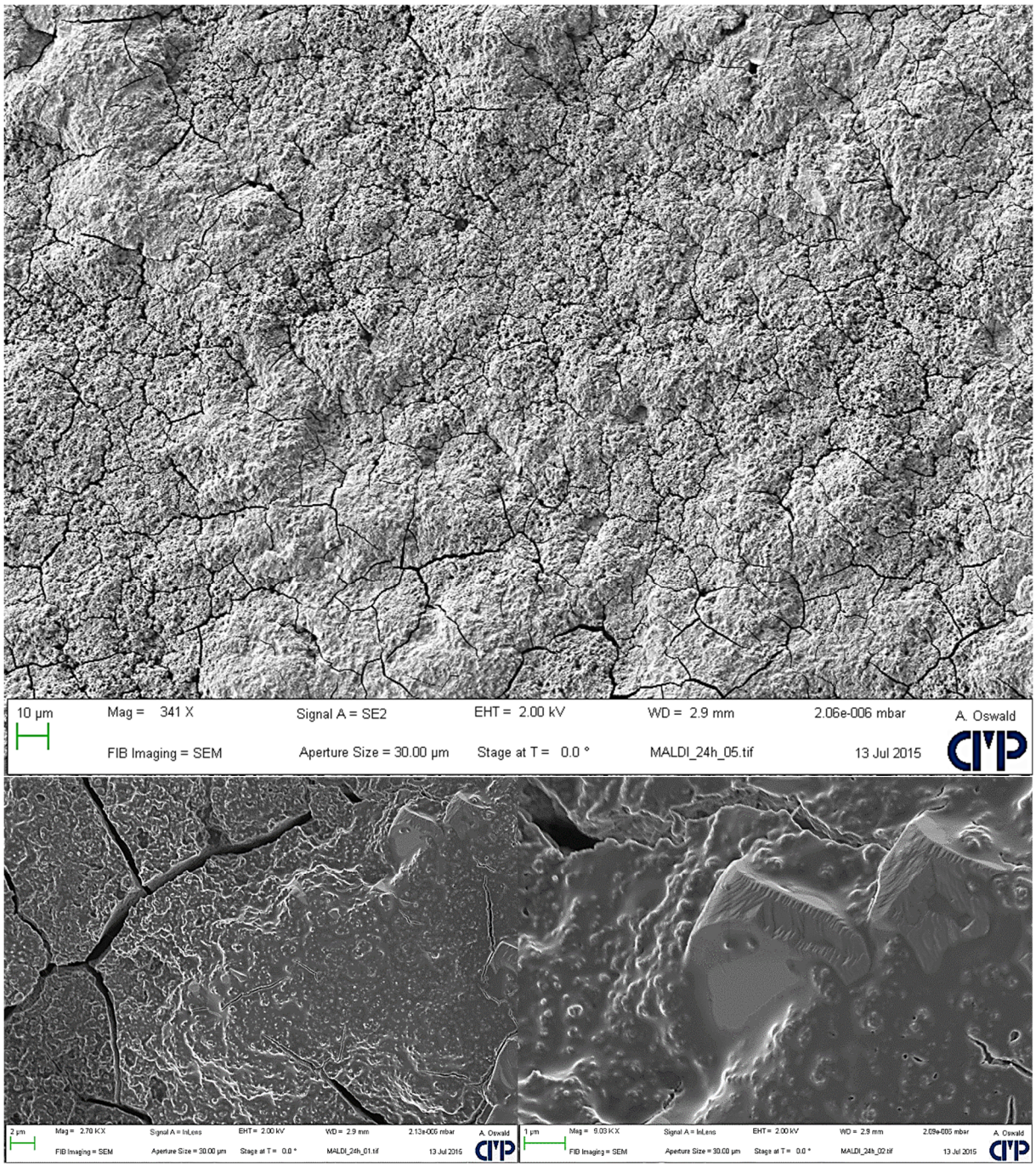


Figure A-216: Morphology of KCl/protein composites after cleavage time of 24 hours

6.3 Reference sample with half the enzyme concentration

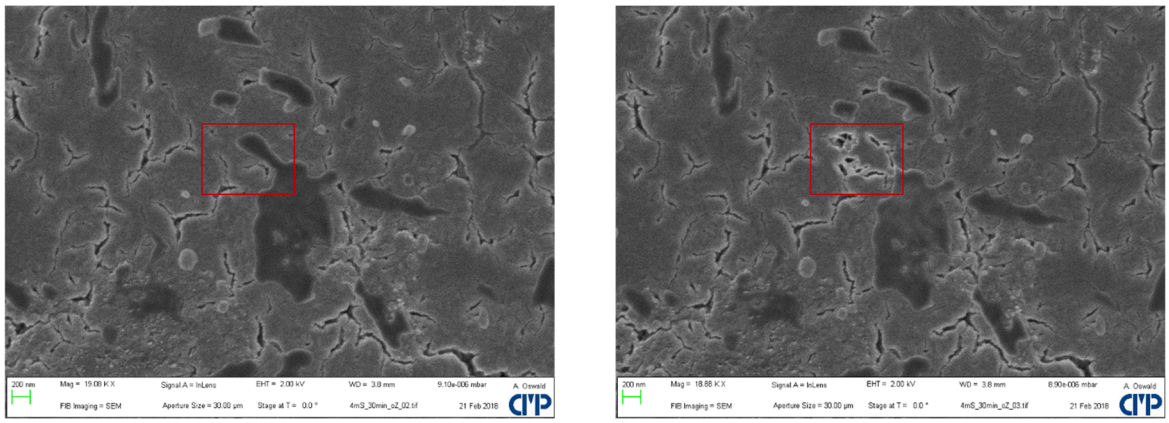


Figure A-217: Identifying soft matter by electron beam

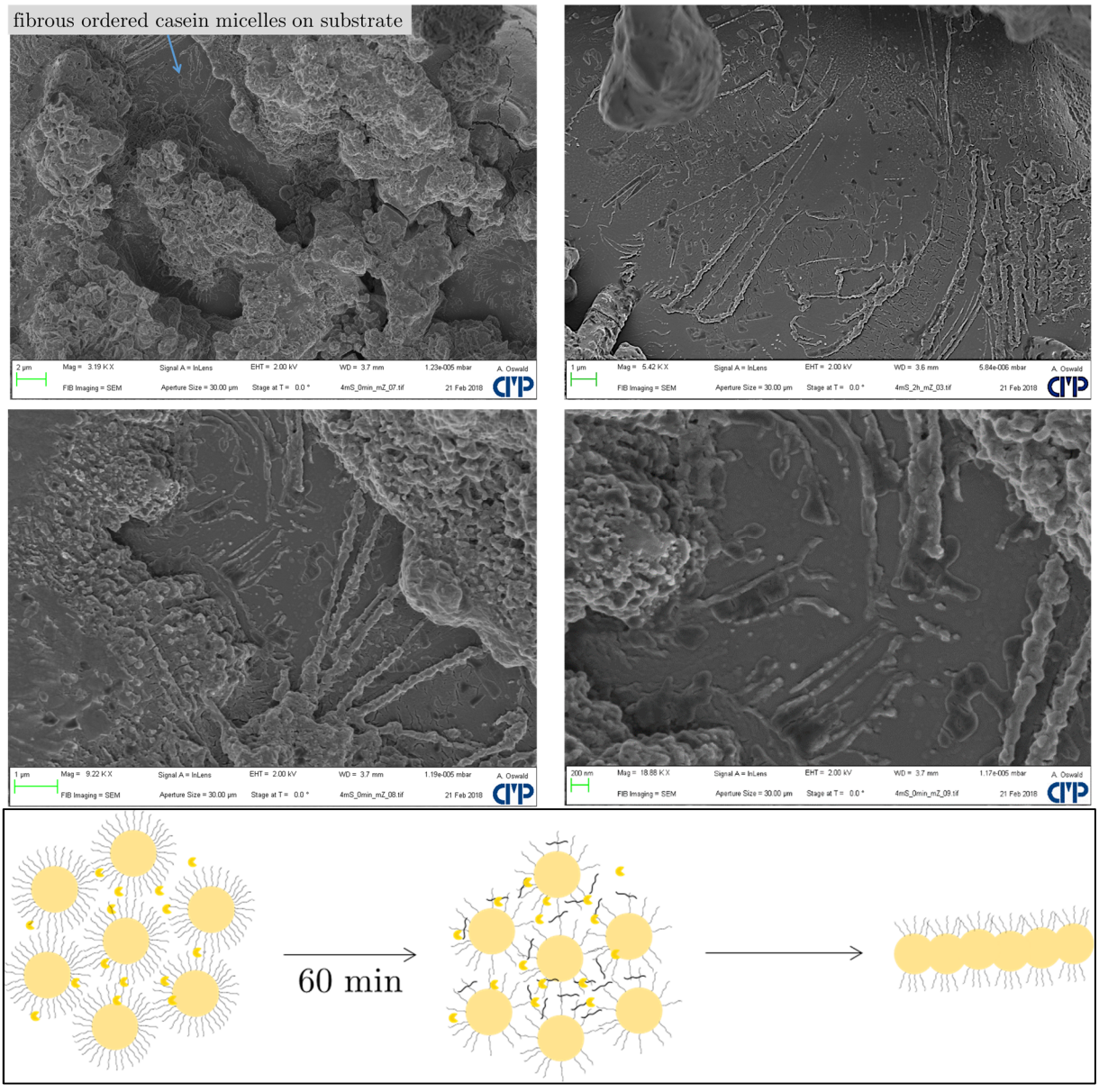


Figure A-218: Images and sketch of fibrous-ordered casein micelles